Volume 12 ● No 1 ● 2024 ● p-ISSN: 2410-9355 ● e-ISSN: 2307-549X

ARO

The Scientific Journal of Koya University

WoS IMPACT FACTOR

2024

www.koyauniversity.org

ARO-The Scientific Journal of Koya University

ARO, meaning "Today" in Hewramí Kurdish, is an esteemed international scientific journal proudly published by Koya University with the following identifiers: p-ISSN: 2410-9355, e-ISSN: 2307-549X, and DOI: 10.14500/2307-549X. As a reputable open-access peer-reviewed journal, ARO is dedicated to publishing original scientific research, global news, and insightful commentary. Recognized for its impact in the academic community, ARO Journal has been awarded an Impact Factor by WoS-ESCI and covers diverse areas of Multidisciplinary Sciences, welcoming both original research articles and review articles. Notably, ARO Journal is committed to providing free access to its content and proudly boasts the absence of both APC (Article Processing Charges) and ASC (Article Submission Charges) fees.

ARO the Scientific Journal Office

Koya University, University Park
Danielle Mitterrand Boulevard, Koya KOY45
Kurdistan Region - F.R. Iraq

E-mail: aro.journal@koyauniversity.org
url: aro.koyauniversity.org

June 2024

ARO

The Scientific Journal of Koya University

Vol XII, No 1(2024)

Contents

Aro Editorial Words iii

Bashdar I. Meena, Hawbash H. Karim, kurdistan F. Aziz, Faten A. Chaqmaqchee, Dashne M. Kokhasmail , Khabat N. Hussein 1
Structural Characterization of Salts Using X-ray Fluorescence Technique: Experiments on Samples Collected from Kurdistan Region of Iraq

Hikmat M. Masyab, Qutaiba S. Al-Nema, Mozahim K. Al-Mallah 8
Glucuronidase Gene: A Strong Evidence of a Novel Interaction of Glucuronidase-labeled Gluconacetobacter diazotrophicus with Spinach, Spinacia oleracea L. Seedlings

Jihad H. Mohammed, Akram N. M. Qaddo, Nabaz A. Muhammad Salih, Faeza B. Omar 13
Synthesis of Some novel Azomethine Oxide Derived from Aromatic Oximes and their Anti-microbial Studies

Aven R. Hamza, Mohammed A. Hussein 19
An Innovative Embedded Processor-Based Signal Phase Shifter Algorithm

Esraa Q. Naamha, Matheel E. Abdulmunim 29
Web Page Ranking Based on Text Content and Link Information Using Data Mining Techniques

Ahmed A. Nafea, Mustafa S. Ibrahim, Abdulrahman A. Mukhlif, Mohammed M. AL-Ani , Nazlia Omar 41
An Ensemble Model for Detection of Adverse Drug Reactions

Kosrat N. Kaka, Rebaz A. Omer, Dyari M. Mamand, Aryan F. Qader 48
Bromination of Chalcone: A Study on Synthesis, Characterization, and Optoelectronic Properties

Ahmed J. Mahmood, Mohammed A. Jubair 54
Permeability Prediction for Carbonate Rocks using a Modified Flow Zone Indicator Method

Zrar Kh. Abdul, Abdulbasit K. Al-Talabani, Chnoor M. Rahman, Safar M. Asaad 61
Electrocardiogram Heartbeat Classification using Convolutional Neural Network-k Nearest Neighbor

Vyan A. Qadir, Kamaran K. Abdoulrahman 68
Analyzing Colorectal Cancer at the Molecular Level through Next-generation Sequencing in Erbil City

DOI: 10.14500/2307-549X ARO p-ISSN: 2410-9355, e-ISSN: 2307-549X

Rana L. Abdulazeez, Fattah Alizadeh ..…….……..……..…..…..…….…….. 79
Deep Learning-Based Optical Music Recognition for Semantic Representation of Non-overlap and Overlap Music Notes

Mohammed Al-Mukhtar, Ameer H. Morad, Hussein L. Hussein, Mina H. Al-hashimi ……..…… 88
Brain Tumor Segmentation Using Enhancement Convolved and Deconvolved CNN Model

Soran S. Badawi ……..…….. 100
Bridging the Gap: Enhancing Kurdish News Classification with RFA-CNN Hybrid Model

Nabaz A. Muhammad Salih ……..…..……..……..……..…… 108
Synthesis, Characterization, and Bioactivity Studies of the Schiff Base Ligand and its Zinc(II) Complex

Vyan A. Qadir, Kamaran K. Abdoulrahman ……..…… 115
Oxidative Stress Assessment in Colorectal Cancer Patients: Erbil Population Study

Anwer H. Dawood, Dana K. Mawlood …..…… 124
Analysis and Design of a Box Culvert Using Bentley Culvert Master Software: Qoshtapa Culvert as a Case Study

Hayder M. Issa, Rezan H. Hama Salih …….. 135
Efficient and Simplified Modeling for Kerosene Processing Quality Detection Using Partial Least Squares-Discriminant Analysis Regression

Ahmed A. Nafea, Manar AL-Mahdawi, Mohammed M. AL-Ani, Nazlia Omar …… 143
A Review on Adverse Drug Reaction Detection Techniques

Hemin F. Ibrahim, Chu K. Loo, Shreeyash Y. Geda, Abdulbasit K. Al-Talabani …..……..…… 154
Optimizing Emotional Insight through Unimodal and Multimodal Long Short-term Memory Models

Leila Nouri, Salah I. Yahya, Abbas Rezaei, Sohrab Majidifar …… 161
Microstrip Passive Components for Energy Harvesting and 5G Applications: A Comprehensive Review

Mardan A. Pirdawood, Shadman R. Kareem, Omar Al-Rassam ……..…….. 170
Encryption of Color Images with a New Framework: Implementation Using the Elzaki Transformation

Bahra Dh. Ghafour, Mohammed J. Hamawandy, Varoujan K. Sissakian ……..…… 181
Geotechnical Assessment of the Slopes of Hamamok Dam, NE of Koya, Kurdistan Region of Iraq

Ahmed K. Ali ……..……..……..……..……..……..……..……..……... 191
A Comprehensive Framework for Integrating Robotics and Digital Twins in Façade Perforation

Halo D. Omar ……..……..……..……..……..……..……..……..……... 203
Upright Pyramid Surface Textures for Light Trapping and MoOx Layer in Ultrathin Crystalline Silicon Solar Cells

Imad M. Ghafor, Asaad I. Mustafa, Ibrahim M. Mohialdeen, Howri Mansurbeg ……..……..… 207
High-resolution biostratigraphic zonation across the Cretaceous/Paleogene (K/Pg) boundary from the Sulaymaniyah area, Kurdistan Region, Northeastern Iraq

ARO Editorial Words

A New Era of Excellence: ARO Achieves 1.2 Impact Factor

Dear Esteemed Readers,

We are very pleased to be launching the 22nd edition of ARO-The Scientific Journal of Koya University, as we celebrate a monumental achievement: ARO has secured a 1.2 Impact Factor from Clarivate Analytics. This remarkable milestone is a testament to the unwavering dedication and collaborative efforts of our authors, reviewers, editorial board, and the entire Koya University community.

ARO's journey to this prestigious recognition has been marked by consistent growth and a steadfast commitment to publishing high-quality research that drives positive change. We are immensely proud to be a leading platform for groundbreaking research in the Kurdistan Region of Iraq and beyond.

This exceptional achievement is a catalyst for further excellence. We are committed to building upon this success by expanding our scope, enhancing our review process, and fostering a vibrant academic community around Aro. We invite researchers from diverse fields to contribute their innovative work to our journal.

We extend our heartfelt gratitude to our authors for sharing their valuable research, and to our reviewers for their meticulous evaluation. Your contributions are instrumental in maintaining ARO's position as a trusted source of knowledge and innovation.

As we continue on this new chapter, we reaffirm our dedication to open access, ensuring that research is freely available to scholars and the public alike. ARO will continue to provide a platform for researchers to share their findings and contribute to the advancement of knowledge.

We look forward to another year of growth and achievement, and we invite you to join us in shaping the future of ARO.

With warm regards,

Dilan M. Rostam
Editor-in-Chief

Mohammed H. S. Zangana
Executive Publisher

Dilan M. Rostam, Salah I. Yahya, Fahmi F. Muhammad, Wali M. Hamad, Jorge Correia, Fouad Mohammed, Jacek Binda, Nadhir Al-Ansari, Howri Mansurbeg, Tara F. Tahir, Yazen A. Khaleel, Mohammad Gh. Faraj and Sahar B. Mahmood.
Executive Editorial Board Members

DOI: 10.14500/2307-549X ARO p-ISSN: 2410-9355, e-ISSN: 2307-549X

Structural Characterization of Salts Using X-ray Fluorescence Technique: Experiments on Samples Collected from Kurdistan Region of Iraq

Bashdar I. Meena[1]*, Hawbash H. Karim[2], Kurdistan F. Aziz[1], Faten A. Chaqmaqchee[2], Dashne M. Kokhasmail[1] and Khabat N. Hussein[3]

[1]Department of Chemistry, Faculty of Science and Health, Koya University, Koya KOY45, Kurdistan Region - F.R. Iraq

[2]Department of Physics, Faculty of Science and Health, Koya University, Koya KOY45, Kurdistan Region - F.R. Iraq

[3]Department of Food Science and Technology, College of Agricultural Engineering Sciences, University of Duhok, Kurdistan Region - F.R. Iraq

***Abstract*—This study investigates the structure of 21 table salts that were collected from different local markets in the Kurdistan region of Iraq. The major trace elements and iodine concentrations in table salt are analyzed through the X-ray fluorescence (XRF) technique and the titration method, respectively. The study shows that using XRF spectral analysis, the collected table salt samples are rich in chlorine, sodium, and contain a lower percentage of bromine, strontium, tin, tellurium, and iodine. Moreover, these samples have a high percentage of sulfur and sirconium, where the molybdenum is >0.2%. Other elements such as zinc and copper are essential and found in low concentrations <0.0086% and 0.001%. Iodine is a trace element that is necessary nutrients for human life, and it is naturally present in some foods. Iodine deficiency is brought on by a lack of iodine consumption. Iodized salt is highly recommended as a source of iodine to prevent iodine deficiency disease. Iodine is added to table salt in two different ways, either through iodate or through iodine. The results show that only 25% of the salt samples have an adequate level of iodine, while the other samples have low or no iodine content. According to the World Health Organization, quality of salt depends on iodine concentration and other trace elements, which are necessary for human health.**

***Index Terms*—Salts, X-ray fluorescence technique, Iodine concentration, Chemical composition.**

I. Introduction

Natural additives such as table salt are vital for human survival. Table salt consists of 97.4% sodium chloride and a small amount of iodine, which is crucial for metabolic activities and the thyroid gland. To meet the daily iodine requirement, potassium iodate is typically added to table salt. Iodine deficiency diseases (IDDs) are known to exist in a number of nations worldwide, particularly in poor nations. The risk of IDD development affects about 38% of the global population (Wulandari and Rosyida, 2017). The thyroid gland stores of the iodine for a person in good health have 70–80%, or around 15–0 mg (Prodhan, et al., 2014). Thyroid-stimulating hormone (TSH) regulates the production of the thyroid hormones T3 (triidothyronine) and T4 (tetraiodothyronine or thyroxine), which are involved in all essential bodily processes. Iodine is a substrate required for this process (De Nayer, 2001, Kitwa, et al., 2012, Diosady, et al., 1997).

As the human body cannot generate iodine, it is important to consume iodine-rich foods frequently. In general, the salt is added into foods during processing, which is typically the main iodine supplier for people. Seafood, meat, milk, eggs, cereals, fruits, and vegetables are some dietary items that contain iodine (Mohammadi, Azizi and Hedayati, 2018). Table salt must contain within 30–80 ppm of iodine in agreement with standard national iodine (SNI) No. 3556:2010. The iodization technique is used to fortify table salt with either potassium iodide or potassium iodate (Wulandari and Rosyida, 2017). Every stage of a person's life is impacted by iodine deficiency, which can cause a number of serious illnesses (Verma and Raghuvanshi, 2001). In addition, depending on the source and technique of salt production, naturally secondary products are often composed of calcium, potassium, magnesium, sodium sulfates, carbonates, bromides, calcium, potassium, and magnesium chlorides, which may be found in edible salt in varying amounts (Alimentarius, 2001). Salts production with impurities causes absorb moisture and break, making it complicated to use, they must all be minimized throughout

ARO-The Scientific Journal of Koya University
Vol. XII, No. 1 (2024), Article ID: ARO.11418. 7 pages
Doi: 10.14500/aro.11418
Received: 23 September 2023; Accepted: 14 December 2023
Regular research paper: Published: 06 January 2024
Corresponding author's e-mail: bashdar.ismael@koyauniversity.org

the purification process to an acceptable standard level (Kumar, et al., 2001, Nerín, Aznar and Carrizo, 2016).

In the US, salt was first infused with iodine in 1924 (Markel, 1987). Universal salt iodization (USI) was suggested as the primary source for reducing IDD by the World Health Organization and UNICEF in 1994. Almost 20% about the iodine within salt is removed during manufacture for home use, and an additional 20% is lost during cooking. Through packaging, storage, and heating, an additional 50% might be lost (Organization, 2007). About 120 nations across the world started salt iodization projects in 2006. In some nations, it has successfully eradicated iodine deficient illnesses by iodizing all salt (USI) (UNICEF, et al., 2008). Around 123 nations approved the iodization of salt between 1942 and 2020 and 124 nations required salt iodization laws in place by 2021(Meena, et al., 2018, Zimmermann and Andersson, 2021). Based on data gathered between 2013 and 2018, UNICEF estimates that 88% of the world's population consumed iodized salt in 2018. East Asia, South Asia, and the pacific had the highest home iodized salt coverage rates, at 89% and 92% respectively, as shown in Fig. 1. Although the coverage of iodized salt in central and western Africa was the lowest, more than three out of every four families had access to it in the area (Andersson, et al., 2007).

II. Methodology

Twenty-one table salts purchased from local stores of Kurdistan Region-Iraq were analyzed using X-ray fluorescence (XRF). The XRF method allowed for the analysis of the chemical composition or elements present in twenty-one samples in <3 h. The X-ray measuring time was only 200 s for the Al target and 100 s for other including RX9, Cu, and Mo secondary targets at room temperature at around 27°C. A detailed description of the XRF technique can be found elsewhere (Chaqmaqchee, Baker and Salih, 2017). Twenty-one salt samples have been collected from different locations in Kurdistan Regions-Iraq. All measurements of salts were carried out under vacuum, using a Rigaku Next-generation Energy dispersive Cartesian Geometry (NEX CG) with four targets. Chemical elements of Na, Cl, I, and other trace elements were calculated with almost the same salt concentration. The Kα-lines intensities were measured for most salt sample, in which the applied voltage increased in general with the required lines energies. In addition, titration method is one of the common methods used globally to estimation iodine in iodized salt. This is due to easy method and low cost. Titration is a process in which unknown solution's concentration can be determined using a solution with known concentration. Iodometric titration technique was used to determine the iodine content in 21 different samples of iodized salt. An unknown solution's concentration is determined by adding a known volume of the titrant (the known solution) to a known volume of the analyte (the unknown solution) until the reaction is completed. Indicator is used as a signaling to end of the reaction. The endpoint can be detected by observing color change from light brown to colorless as shown in Fig. 1. The endpoint of a titration is the point at which titrant addition should be prevented. The unknown concentration can be determined by knowing the amount of titrant added. A standard solution of 0.005 N sodium thiosulfate as a titrant in addition to its two drops of indicator (1% starch), which changed the solution's color from yellow to light brown then the color of the solution tuned to colorless after the reaction occurs completely.

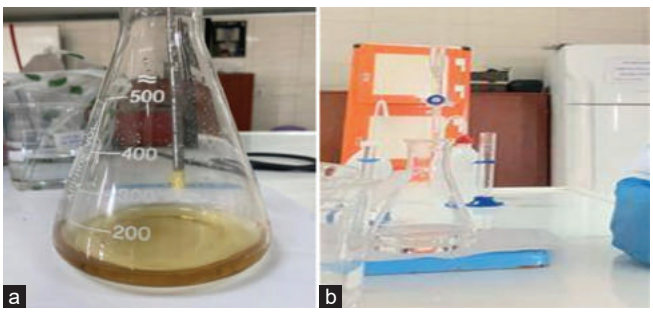

Fig. 1. (a) Before starting titration and (b) after ending titration.

A. Preparation of Standard Solution in Titration Method

Preparation of 0.005 M sodium thiosulfate ($Na_2S_2O_3$)

Dissolve 1.24 g of sodium thiosulfate in 1 litter hot distilled water.

Preparation of 2N sulfuric acid (H_2SO_4)

Add 5.56 ml concentrated sulfuric acid drop-wise into a 90 ml of chilled distilled water and make the final volume up to 100 ml (Sepahvand, et al., 2018).

Preparation of potassium iodide (KI)

Dissolve 10 g of potassium iodide in 100 ml of distilled water.

Preparation of saturated salt solution

Take 100 ml of distilled water in a conical flask and add sodium chloride until the salt is insoluble. Heat the solution till the sodium chloride crystals are formed on the sides of the vessel. After cooling down the saturated salt solution at room temperature, transfer the supernatant to a clean bottle (Sepahvand, et al., 2018).

Preparation of 1% Starch solution

Take 1 g of starch and prepare slurry in 50 ml of water. Add the slurry slowly to 50 ml of boiling water (Sepahvand, et al., 2018).

B. Procedure and Working Step

Dissolve 10 g of salt in 50 ml of distilled water, then added 1–2 ml of (2N) sulphuric acid and 5 ml of 10% KI to the solution with constant shaking the solution, it turns to a yellow color. The flask is closed with stopper and keeps it in the dark for about 10 min. Then, the sample is taken out of the dark place and titrated against a sodium thiosulfate solution until it turns a pale yellowish color. Subsequently, add a few drops of 1% starch solution. The solution will turn a deep purple color. Thiosulfate drops are added drop by drop from the burette until the solution becomes colorless, and note the final reading targets.

III. Results and Discussion

The salts were subjected to XRF to analyze the chemical composition or elements present in the sample as summarized in Tables IA and B, for which the salt samples were measured in advanced research laboratory of physics at Koya University of Kurdistan Region-Iraq. Some major and trace elements were identified in 21 salt samples coded between H1 and H21.

The results from the analysis of XRF were based on characteristic Kα lines from the XRF spectral analysis of the salts, the salts contained less percentage of bromine, strontium, tin, tellurium, and Iodine and high percentage of zirconium and molybdenum. Other elements as zinc and copper are essential element and found in low concentrations <0.0086% and 0.001%. However, it can be potential hazard when presented in an over concentration, which can affect both animal's life and human health (Papagiannis, et al., 2004).

When the samples are irradiated with X-rays, the intensity as a function of energy can be calculated over the energy range 1-20 keV at the same computing conditions. Fig. 2 shows two essential peaks in the ranges of ~1.85 and 7.12 keV corresponding to Na- kα and Cl- kα lines for all 21 salt elements. Note that the peak intensity of Cl-k_α has a higher intensity than Na-kα intensity due to the salts being comparatively rich in Cl and Na contents that can be interpreted as good sources of Cl and Na as shown in Fig. 2a. In addition, the peak intensities of 11.91, 14.17, 15.76, 17.69, 25.25, 27.41, and 28.57 keV that corresponding to Br-k_α, Sr-k_α, Zr-k_α Mo-k_α, Sn-k_α, Te-k_α, and I-k_β lines are indicated in Fig. 2b. It was noticed that Zr element has high intensity than the rest elements.

Fig. 3 shows that the peak intensity of element Cl is higher than that of elements of Na and I. The mass concentrations of salt samples are increasing from around 45–69 mg/cm^2. Where the elements coded between H1 and H21 are indicated in the chart in Fig. 4.

As shown in Table II, the samples labeled from H1 to H21, measuring iodine concentration for all samples, during the titration observed that big different in iodine content in 21 samples. Titrant ($Na_2S_2O_3$) volume increases indicate a higher concentration of iodine present in the solution or in the nature of the salt.

TABLE IA
Chemical Compositions for Salt Samples Coded H1 to H10 Under the Same Measuring Conditions

No.	Elements	Mass concentration % (mg/cm^2)									
		H1	H2	H3	H4	H5	H6	H7	H8	H9	H10
1	Cl	65.9	51.4	68.9	45.6	64.8	67.3	67.5	67.3	67.1	68.0
2	Na	31.7	40.5	29.6	42.0	31.7	30.6	30.2	31.5	30.4	30.6
3	Si	0.766	0.561	0.498	0.484	1.01	0.623	0.551	0.501	0.587	0.542
4	S	0.722	0.769	0.432	1.89	1.00	0.582	0.688	0.232	1.18	0.321
5	Ca	0.578	4.37	0.251	8.28	0.395	0.471	0.595	0.0483	0.154	0.164
6	Zr	0.241	1.22	0.265	1.24	0.301	0.270	0.340	0.299	0.218	0.315
7	K	0.0321	0.656	0.0206	0.270	0.519	0.0332	0.0523	0.0359	0.241	0.0250
8	Fe	0.0167	0.241	0.0063	0.0301	0.0378	0.0074	0.0069	0.0032	0.0038	0.0034
9	Sn	0.0061	0.0312	0.0064	0.0370	0.0081	0.0065	0.0091	0.0078	0.0058	0.0086
10	W	0.0031	--	0.0013	--	0.0028	0.0024	0.0036	0.0039	0.0019	0.0014
11	Ti	0.0030	--	--	--	0.0118	--	--	--	--	--
12	Sr	0.0025	0.0582	0.0027	0.0394	0.0039	0.0026	0.0033	0.0007	0.0018	0.0016
13	Co	0.0019	0.0163	0.0026	--	0.0013	0.0009	0.0021	--	--	--
14	Re	0.0011	0.0040	0.0011	0.0032	0.0016	--	--	--	--	--
15	Au	0.0010	0.0048	0.0009	--	0.0010	0.0007	0.0010	0.0009	0.0006	0.0007
16	Cu	0.0005	0.0057	0.0011	0.0017	0.0007	0.0009	0.0011	0.0010	0.0005	0.0009
17	Br	0.0004	0.0534	0.0050	0.0556	0.0049	0.0024	0.0031	0.0075	0.0038	0.0033
18	SC	--	0.0879	--	--	--	--	--	--	--	--
19	Cr	--	0.0154	--	--	0.0021	--	--	--	--	--
20	Zn	--	0.0086	--	0.0014	--	--	--	--	--	--
21	Ta	--	0.0060	--	0.0046	0.0013	--	--	--	--	0.0011
22	Ni	--	0.0034	--	--	--	--	--	--	--	--
23	Rb	--	0.0033	0.0005	0.0054	0.0009	0.0004	0.0004	0.0010	0.0007	0.0008
24	Fr	--	--	--	0.0451	0.0032	0.0012	0.0019	0.0076	0.0042	0.0044
25	Mn	--	--	--	0.0138	--	--	--	--	--	--
26	V	--	--	--	--	0.0011	--	--	--	--	--
27	Ag	--	--	--	--	0.0006	--	--	--	--	--
28	I	--	--	--	--	0.0090	--	0.0033	0.0029	0.0060	
29	P	--	--	--	--	--	--	0.0960	--	--	--
30	Os	--	--	--	--	--	--	0.0010	--	--	--
31	Hg	--	--	--	--	--	--	0.0009	--	--	--
32	Po	--	--	--	--	--	--	0.0005	--	--	--
33	Te	--	--	--	--	--	--	--	0.0011	0.0011	--
34	Ge	--	--	--	--	--	--	--	--	--	0.0004

 http://dx.doi.org/10.14500/aro.11418

TABLE IB
CHEMICAL COMPOSITIONS FOR SALT SAMPLES CODED H11 TO H21 UNDER THE SAME MEASURING CONDITIONS

No.	Elements	Mass concentration % (mg/cm^2)										
		H11	H12	H13	H14	H15	H16	H17	H18	H19	H20	H21
1	Cl	68.8	65.9	58.3	67.6	66.2	66.5	63.2	66.2	65.1	64.5	65.4
2	Na	29.6	30.3	37.9	31.5	33.0	31.8	34.7	31.2	34.3	32.0	32.5
3	Si	0.569	0.456	0.618	--	0.504	0.491	0.549	0.476	0.481	0.886	0.529
4	S	0.346	1.60	1.50	0.452	--	0.866	0.680	1.19	--	1.55	0.689
5	Ca	0.188	1.11	0.280	--	--	--	0.507	0.219	0.0123	0.295	0.476
6	Zr	0.340	0.305	0.241	0.322	0.247	0.272	0.287	0.327	0.101	0.174	0.264
7	K	--	0.0432	0.278	--	--	--	0.0416	0.249	0.0105	0.325	0.0726
8	Fe	0.0047	0.0031	0.0046	0.0046	0.0017	0.0024	0.0097	0.0044	--	0.0187	0.0085
9	Sn	0.0093	0.0069	0.0068	0.0087	0.0064	0.0068	0.0073	0.0086	0.0024	0.0043	0.0062
10	W	0.0031	0.0026	--	0.0030	--	0.0022	--	0.0096	0.0027	0.0064	--
11	Ti	--	--	--	--	--	--	0.0033	--	--	0.0043	--
12	Sr	0.0030	0.0097	0.0052	0.0037	0.0009	0.0030	0.0029	0.0045	0.0003	0.0024	0.0024
13	Co	--	0.0009	--	--	--	0.0009	--	0.0011	--	--	--
14	Re	0.0019	--	--	--	--	--	--		--	--	--
15	Au	0.0012	0.0010		0.0009	0.0008	0.0006	--	0.0006	--	--	--
16	Cu	0.0007	0.0006	0.0006	0.0006	0.0010	--	--	0.0007	--	0.0004	0.0005
17	Br	0.0047	0.0214	0.0153	0.0048	0.0026	0.0144	0.0006	0.0070	0.0022	0.0026	0.0034
18	SC	--	0.0095	--	--	--	--	--	--	--	--	--
19	Cr	--	--	0.0017	--	--	--	--	--	--	--	--
20	Zn	--	--	--	--	--	--	--	--	--	--	--
21	Ta	0.0013	0.0017	0.0009	0.0012	--	--	--	0.0015	--	--	--
22	Ni	0.0009	--	--	--	--	--	--	--	--	--	--
23	Rb	0.0005	0.0017	0.0015	0.0008	0.0006	0.0014	--	0.0011	0.0004	0.0005	0.0006
24	Fr	--	0.0138	0.0115	0.0052	0.0034	0.0105	--	0.0054	0.0023	0.0016	0.0031
25	Mn	--	--	--	--	--	--	--	--	--	--	--
26	V	--	--	--	--	--	--	--	--	--	0.0011	0.0009
27	Ag	--	--	--	--	--	--	--	--	--	--	--
28	I	0.0062				0.0038		0.0062	0.0032	--	--	--
29	P	0.0940	0.113	--	--	--	--	--		--	--	--
30	Os	--	--	--	--	--	--	--	0.0008	--	--	--
31	Hg	--	--	--	--	0.0007			0.0011	--	--	--
32	Po	--	--	--	--	--	--	--	--	--	--	--
33	Te	0.0012		0.0008	0.0009	--	--	--	--	--	--	--
34	Ge	--	--	--	--	--	--	--	--	--	--	--
35	Mg	--	0.539	--	--	--	--	--	--	--	--	--
36	Al	--	--	0.228		--	--	--	--	--	--	--
38	At	--	--	--	--	--	--	0.0004	0.0005	0.0003	--	--

Titration method is used for determining the trace element such as iodine with a highly accuracy and precise as indicated in Table II. Result show that from 21 samples of iodized salt only seven sample of salts were present iodine and the rest of it not present iodine in salt sample, as well as three samples from these seven samples are not contain the recommended amount of iodine which means the concentration of iodine is less than that recommended to be. However, sample six (H6) showed the highest concentration of iodine, due to reactivity of iodine the rate of iodine decrease with the increasing temperature; moreover, iodine loss from iodine-containing materials is probably influenced by exposure to air and light not only that also inadequate storage might result in loss iodine and humidity affect the iodine, recommendation iodine intake based on the literature is (30–80) ppm, six samples are exiting iodine in the recommendation range, exclusively for the reason of diminish iodine level in salts and foods by increasing heat exposure during cooking 30% of the 20 different household salt are recommended to take advantage. Figs. 5 and 6 show household salt which is iodine is specified with X-ray fluorescence method, which realizes the same result for the titration method.

Most salt samples contain lower amount of iodine compared to standard salt sample, in one of the salt's label indicates that it contains 50–80 mg/kg of potassium iodide.

However, the sample of number six (H6) which is named (Al-Nema salt) contains the highest quantity of iodine (74.02 ppm). The lowest iodine content was 2.11 ppm with in H12 and H13 (Taban table salt and Henan salt), respectively, contain the least quantity of iodine. Iodine content was below 15 ppm in 70% of samples, additionally 30% was significantly contained iodine higher than 15 ppm. The sample number six with the highest concentration of iodine is similar with the result by the XRF analyzed. The main sources of iodized salt imported into the Kurdistan from Iran and Turkey. The salt may refer to coarse rock salt and H1, which is the concentration of iodine, equal to (8.46 ppm). To reduce the range of error, we repeated the titration 2 times.

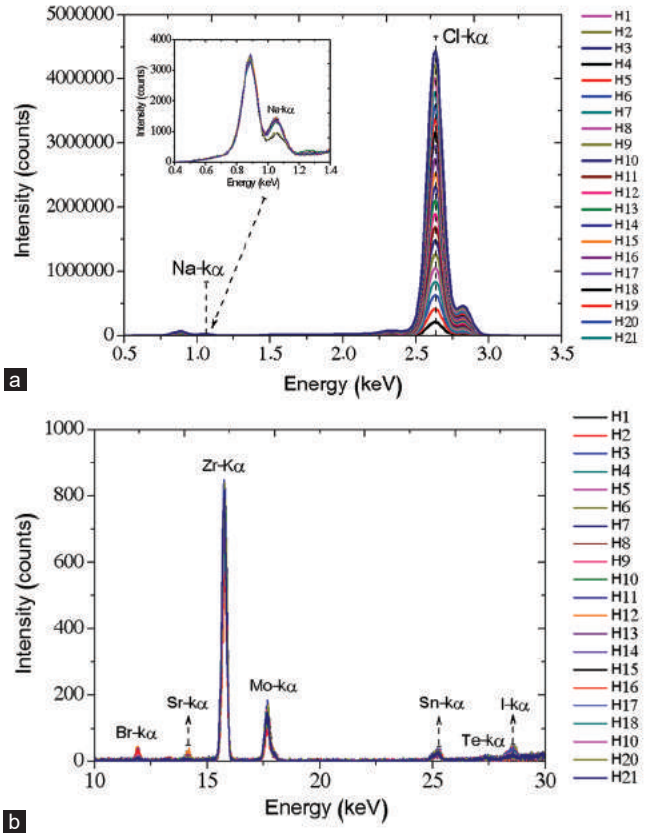

Fig. 2: Energies of X-ray spectra for various salts samples coded from H1 to H12 at (a) high intensity with zoomed Na-kα peak and (b) low intensity using X-ray fluorescence technique.

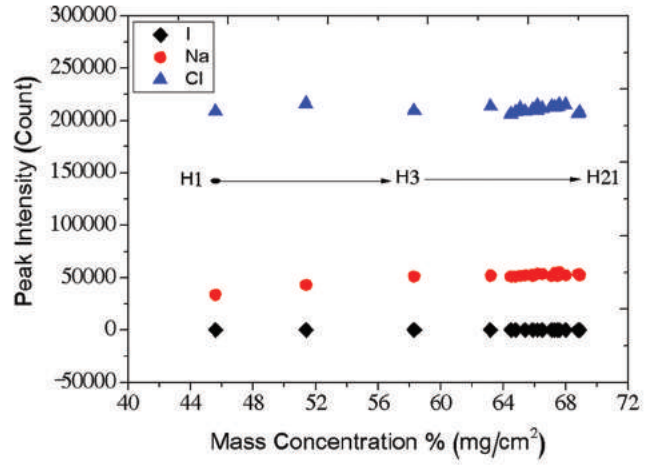

Fig. 3: Dependence of the X-ray fluorescence intensity on the salts concentration coded from H1 to H21.

The result in ppm value of iodine content is displayed in the Fig. 7. However, titration method used commonly but result compared to analytical technique such as XRF not high precise result, may due to technique error and personal error during titration and end point detection.

To investigate the structure of salt and iodine concentration, we used two different methods, such as the titration method and the XRF technique. The main goal of this study is to compare the concentration of iodine in 21 different brands of

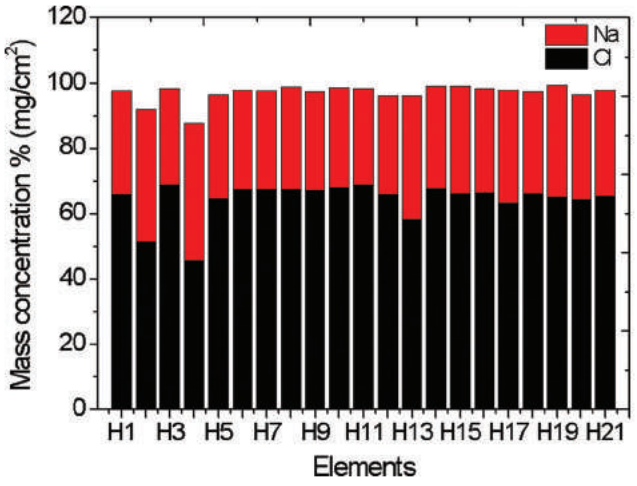

Fig. 4: Mass concentration of Cl and Na elements in the salt samples coded between H1 and H21.

TABLE II
CALCULATION OF IODINE CONCENTRATION IN PPM

Samples number	Volume of 1st titration in ml	Volume of 2nd titration in ml	Average in ml	Iodine conc. in ppm
H1	1	0.6	0.8	8.46
H2	1	1.2	1.1	11.63
H3	0.6	0.5	0.55	5.81
H4	0.5	0.5	0.5	5.2
H5	0.7	0.8	0.75	7.9
H6	7	7	7	74.02
H7	1.5	1.3	1.4	14.8
H8	3	2.8	2.9	30.66
H9	5	4	5.5	58.1
H10	0.2	0.3	0.25	2.64
H11	1.4	1	1.2	12.69
H12	0.3	0.1	0.2	2.11
H13	0.2	0.2	0.2	2.11
H14	1	0.6	0.8	8.4
H15	4	3.8	3.9	41.22
H16	0.5	0.3	0.4	4.22
H17	1.8	1.2	1.5	15.85
H18	2.7	2.5	2.6	27.48
H19	1.5	1.3	1.4	14.8
H20	0.7	0.7	0.7	7.40
H21	0.4	0.5	0.3	4.12

table salt or iodized salt. The sample salt has been iodized, which mean that iodine was added to salt sample. Iodine cannot be produced by human body, despite the fact that it is necessary for a functioning thyroid and other bodily processes. Iodine is used by the thyroid gland to produce thyroid hormones that promote a healthy metabolism, manage growth, and repair damaged cells. There is various sources of iodine but the most common one is iodized salt which is used daily and cheap.

Adequate amount of iodine content in iodized salt should concentration of iodine between (30 and 80) ppm. Unfortunately, the iodized salt available on the local market does not contain adequate iodine, there are many factors that have negative impact on iodine concentration such as, light when sunlight strikes the iodized salt loses between 47.8%

http://dx.doi.org/10.14500/aro.11418

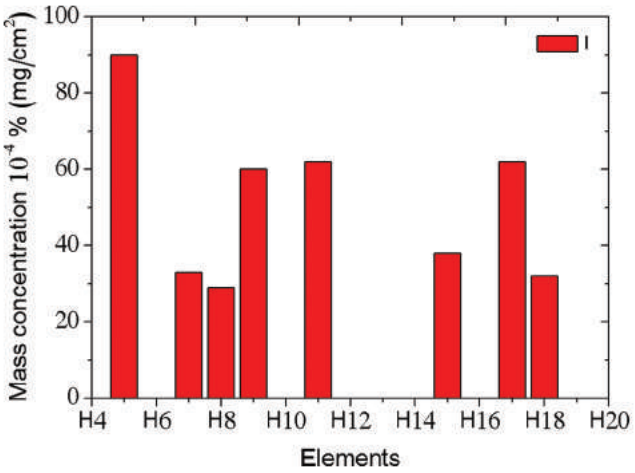

Fig. 5: Mass concentration of I element in the samples coded between H1 and H21.

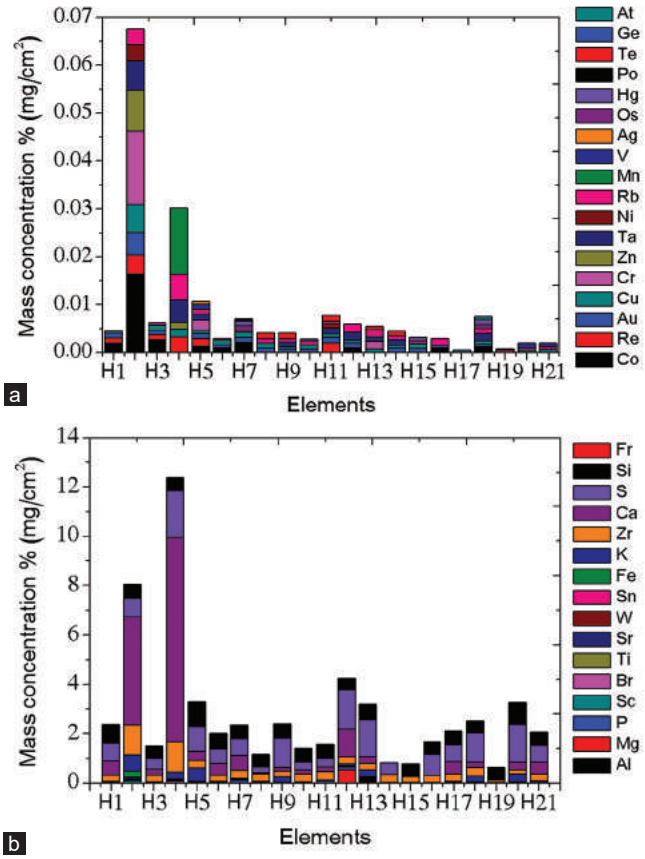

Fig. 6: Mass concentration of trace elements in the samples coded between H1 and H21 from elements between (a) Co and At, and (b) Al and Fr.

and 49.1% of its iodine content, also another factor that might affect iodine content and decrease its concentration in iodized salt is heating and packing. Compared to XRF result, the titration approach is less accurate may due to error at endpoint detection, leading to significant errors in titration process.

XRF result is showed that 70% of samples does not contain enough concentration of iodine, where both techniques proved

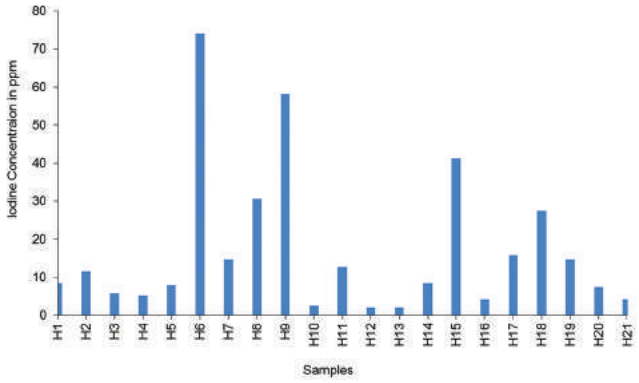

Fig. 7: The concentration of iodine in salts based on the titration method.

that the S.6 (Al-Nema salt) contains the highest concentration of iodine that is equal to 74.02 ppm by titration and 90 ppm by XRF. In addition, the titration method revealed the lowest iodine concentration in H11 and H12.

Based on the literature, the lack of iodine content in iodized salt may be due to various factors, such as the nature of the salt and exposure to direct sunlight. The amount of iodine concentration in iodized salt might also be affected by how it is packaged and stored. Sometimes, iodine is lost from salt samples during cooking. However, each different salt brand had various results. The result from the XRF method detects iodine only in 30% of samples; more than half the samples do not contain iodine.

IV. Conclusion

The purpose of this study is to estimate the major and trace elements in 21 different brands of table salt or iodized salt. To valuate iodine concentration, we used two different methods (the titration method and the XRF technique). The study showed that the table salts using XRF spectral analysis were rich in chlorine and sodium and contained a lower percentage of bromine, strontium, tin, tellurium, iodine and a high percentage of sulfur, sirconium, and molybdenum <0.2%. Other elements such as zinc and copper are essential and found in low concentrations, >0.0086% and 0.001%, respectively. An adequate amount of iodine content in iodized salt should have a concentration of iodine between (30 and 80) ppm. Unfortunately, the iodized salt available on the local market does not contain adequate iodine. Many factors hurt iodine concentration, such as light when sunlight strikes the iodized salt, which loses between 47.8% and 49.1% of its iodine content. Furthermore, another factor that might affect iodine content and decrease its concentration in iodized salt is heating and packing. Compared to the XRF result, the titration approach is inaccurate may be due to error at end-point detection, leading to significant errors in the titration process. The result of the XRF showed that 70% of samples did not contain enough concentrations of iodine, and both techniques proved that sample H6 (Al-Nema salt) contains the highest concentration of iodine which is equal to 74.02 ppm by titration and 90 ppm by XRF. In addition, H11 and H12 showed the lowest concentrations of iodine with the titration method.

Acknowledgement

The authors are grateful to the department of chemistry and the department of physics at Koya University for their support and cooperation.

Declaration

We declare that this study is not to defame any product or harm the reputation of the product.

References

Andersson, M., De Benoist, B., Darnton-Hill, I., and Delange, F. 2007. Iodine deficiency in Europe: A continuing public health problem. World Health Organization, Geneva.

Chaqmaqchee, F.A.I., Baker, A.G., and Salih, N.F. 2017. Comparison of various plastics wastes using X-ray fluorescence. *American Journal of Materials Synthesis and Processing*, 5, pp.24-27.

Codex Alimentarius Commission, 2021. *Codex Standard for Food Grade Salt. CX STAN 150-1985*, Rev. 1-1997 Amend. 1-1999, Amend. 2-2001. Codex Alimentarius Commission, Rome, pp.1-9.

De Nayer, P. 2001. Actions multiples des hormones thyroïdiennes. La thyroïde. Des concepts à la pratique clinique. Elsevier, Amsterdam, pp.129-136.

Diosady, L.L., Alberti, J.O., Mannar, M.G., and Stone, TG. 1997. Stability of iodine in iodized salt used for correction of iodine-deficiency disorders. *Food and Nutrition Bulletin*, 18, pp.388-396.

Kitwa, K.E., Habimana, L., Lumbu, S.J., Donnen, P., Twite, K.E., Mpoyo, K.E., De Nayer, P., Kalenga, M.K., and Robert, A. 2012. Evaluation of iodine content in table salt consumed in democratic republic of Congo. *Food and Nutrition Bulletin*, 33, pp.217-223.

Kumar, S., Maiti, B., and Mathur, P. 2001. Determination of iodate and sulphate in iodized common salt by ion chromatography with conductivity detection. *Talanta*, 53, pp.701-705.

Markel, H. 1987. When it rains it pours: Endemic goiter, iodized salt, and David Murray Cowie, MD. *American Journal of Public Health*, 77, pp.219-229.

Meena, B.I., Omar, K.A., Khan, A., Chaqmaqchee, F.A.I., and Alsalihi, E. 2018. Characterization and comparison of clay from Iraq and Iran for bricks production. *Clay Research*, 37, pp.8-13.

Mohammadi, M., Azizi, F., and Hedayati, M. 2018. Iodine deficiency status in the WHO Eastern Mediterranean region: A systematic review. *Environmental Geochemistry and Health*, 40, pp.87-97.

Nerín, C., Aznar, M., and Carrizo, D. 2016. Food contamination during food process. *Trends in food Science and Technology*, 48, pp.63-68.

Organization, W.H. 2007. Assessment of Iodine Deficiency Disorders and Monitoring their Elimination: A Guide for Programme Managers. Switzerland: World Health Organization.

Papagiannis, I., Kagalou, I., Leonardos, J., Petridis, D., and Kalfakakou, V. 2004. Copper and zinc in four freshwater fish species from Lake Pamvotis (Greece). Environment International, 30, pp.357-362.

Prodhan, U., Alim, M.A., Kabir, M.H., and Pulak, M.R. 2014. Measurement of iodine availability and stability of some iodized salts in Bangladesh. *International Journal of Engineering Research and Technology*, 3, pp.470-474.

Sepahvand, R., Hatamikia, M., Hassanzadazar, H., Moridi, S., Bahari, K., Sepahvand, H., Fatehi, R., Bagheri, A., Belghadr, I., and Javadi, K. 2018. Iodine concentration in iodized salts marketed in Lorestan Province, West of Iran. Journal of Chemical Health Risks, 6, p.99-103.

UNICEF, Section, U.N, Division, U.P., and Communication, U.D.O. 2008. Sustainable Elimination of Iodine Deficiency: Progress since the 1990 World Summit for Children. United States: UNICEF.

Verma, M., and Raghuvanshi, R.S. 2001. Dietary iodine intake and prevalence of iodine deficiency disorders in adults. *Journal of Nutritional Environmental Medicine*, 11, pp.175-180.

Wulandari, E.R., and Rosyida, N. 2017. Analysis of iodine content in table salt. *Jurnal Vokasi Indonesia*, 5, p.5.

Zimmermann, M.B., and Andersson, M. 2021. Global Endocrinology: Global perspectives in endocrinology: Coverage of iodized salt programs and iodine status in 2020. *European Journal of Endocrinology*, 185, pp.R13-R21.

http://dx.doi.org/10.14500/aro.11239

Glucuronidase Gene: A Strong Evidence of a Novel Interaction of Glucuronidase-labeled Gluconacetobacter diazotrophicus with Spinach, *Spinacia oleracea* L. Seedlings

Hikmat M. Masyeb[1], Qutaiba S. Al-Nema[2] and Mozahim K. Al-Mallah[3,*]

[1]Department of Biology, Faculty of Science and Health, Koya University, Koya KOY45, Kurdistan Region - F.R. Iraq

[2]Department of Biology, College Education for Pure Sciences, University of Mosul, Mosul, F.R. Iraq

[3]Department of MLT, Al-Hadbaa University College, Mosul, F.R. Iraq

***Abstract*—*Gluconacetobacter diazotrophicus* lives inside plant tissue cells in the form of colonies and excretes about half of the fixed nitrogen, which offers potential power that improves plant growth. The aim of this study is to find the interaction of glucuronidase (*GUS*)-labeled *G. diazotrophicus* with spinach seedlings and the detection of *GUS* genes using X-gluc dye (5-bromo-4-chloro-3-indolyl-β-D-glucuronic acid). The GUS protocol is used to detect GUS-labeled *G. diazotrophicus* in spinach seedling tissues by chemical detection using X-gluc dye. The results show that the spinach seedlings are successfully infected with GUS-labeled *G. diazotrophicus*, with the survival of the seedlings throughout their growth period and an improvement in the growth of pollinated seedlings. The outcomes of the microscopic inspection of the root slices reveal the presence of bacterial cells at the root tips and their concentration in the area of the cell walls of the peripheral cells. Furthermore, the findings of microscopic examinations of longitudinal sections for cotyledons show the presence of a number of bacteria within epidermal cell walls. This indicates that the determinants of the interaction between these bacteria and spinach seedlings are suitable for the expression of the gene responsible for the formation of the nitrogenase enzyme.**

***Index Terms* — Glucuronidase protocol, *Gluconacetobacter diazotrophicus*, Interaction, Nitrogen fixation, Spinach.**

I. Introduction

Spinach (*Spinacia oleracea* L.) is one of the leafy green vegetables rich in nutrients; it stores great quantities of carotenoids, Vitamin C, folate, Vitamin K, calcium, and iron (Furness, et al., 2013). *Gluconacetobacter diazotrophicus* bacteria were isolated for the first time from the roots and stems of sugarcane plants, *Saccharum officinarum* L., and it was previously called *Acetobacter diazotrophicus*. The endophytic, non-rhizobial bacterium has been similarly separated from other monocot plants (Eskin, Vessey, and Tian, 2014). The 15N2 tests demonstrated the ability of this bacteria to fix atmospheric nitrogen in sugarcane plants (Boddey, et al., 2003), thus acting as a biostimulant (Grillo-Puertas, et al., 2018). The use of reporter genes has become widespread nowadays with plant or animal tissues and with microorganisms as a quick and direct way to observe the expected results, and the most important genes are *GUS* (an enzyme from the bacterium *Escherichia coli* is a competing reporter gene that uses a histochemical technique to analyze promoter activity of an induced gene)*, NPT II, GFP, CAT,* and *LUC* (Miki, 2008). One of the studies followed the *GUS* gene in genetically transformed hairy root cultures emerging from tomato and potato plants using the X-gluc dye and stained it with a blue color. This is evidence of the transmission of this gene with the genes of the *Agrobacterium rhizogenes* bacterial vector to the genome of plants inoculated with these bacteria. Then, the hairy roots emerge from them (Al-Mallah and Masyeb, 2014). This investigation aimed to find the interaction of *GUS*-labeled *G. diazotrophicus* with spinach seedlings and the detection of *GUS* genes using X-gluc dye.

II. Materials and Methods

A. Seeds Growth and Plant Cultivation

Seeds of *S. oleracea* were exterior uncontaminated by soaking in 70% ethanol solution for 2 min and properly diluting “Domestos” bleach with 5% of sodium hypochlorite (Lever Fabergé; Kingston upon Thames, UK) 2:4, v: v for

ARO-The Scientific Journal of Koya University
Vol. XII, No. 1 (2024), Article ID: ARO.11239. 5 pages
DOI: 10.14500/aro.11239
Received: 07 July 2023; Accepted: 20 December 2023
Regular review paper: Published: 08 January 2024
Corresponding author’s e-mail: hikmat.mustafa@koyauniversity.org

30 min. Later, it was rinsed in sterile distal water (Shojaei, et al., 2010). Overlay disinfected seeds were grown in autoclaved vermiculite and antiseptic water for up to 5 days/28°C, 16 h photoperiod. After 5 days, seedlings (root approximately 1.0 cm in length) were transferred to sterile MSO (Murashige and Skoog, 1962), 3% sucrose, and 0.8% agar in small jars (one seedling per jar). They were kept in a growth room at 25°C with light for 4 days.

B. Preparation of G. diazotrophicus inoculum

Nine dilutions of *GUS*-labeled *G. diazotrophicus* were provided by Azotic Technologies, Ltd., Nottingham, United Kingdom; suspensions were prepared; and the optical density (O.D 600) was fixed at 1.2. *G. diazotrophicus* bacterium type 5541, UAP5541/pRGS561 expressing the *GUS* was cultured on AT-*GUS* medium (Sebring, et al., 2022).

C. Inoculation Procedures

The last dilution (10^9) was used to inoculate 25 seedlings whose root system was in MSO medium by adding 1.0 ml of suspension to it. Twenty-five other seedlings were vaccinated by adding 1.0 ml of sterile distilled water only (comparison). Inoculated samples were kept in the development room under the same previous conditions (Rasheed, 2014; Ruhullah, et al., 2017).

D. Histochemical Staining using X-GLUC

Three of the bacteria-inoculated seedlings and three of the control seedlings, after 4 days of inoculation, were removed from the medium and their root aggregates were carefully removed from the suspended agar. Whole inoculated seedlings were placed in sterile 10 ml vials, including 5.0 ml fresh X-gluc dye mixture (Kong, et al., 2023). Similarly, the comparison seedlings were transferred to another tube containing the same volume of the same dye solution as well. The bottles were placed inside a desiccator container with the lids left open and connected to a vacuum pump for 30 min. Formerly, the sections were taken and saved in the darkness at 37°C for 24 h (Rasheed, 2014; Mohammed and Masyab, 2020).

E. Direct Microscopic Observation

The steps for preparing all histological sections of inoculated plant samples were carried out according to Cocking, Stone and Davey (2006). At each sampling time, roots and cotyledon leaves were excised, and histochemical staining was done through X-gluc and seen by light field microscopy. To observe, slices of roots and cotyledon leaves, samples displaying blue color, were restored in glutaraldehyde (2%) with dissolved sodium phosphate (0.1 M) buffer reaching 24 h in the refrigerator, dried by ethanol, and set in white medium-grade acrylic resin (Agar Aids, UK). Later, sections with 1.4 µm thickness stained with safranin (0.01%), and observed under 10X and 100X objective lenses. Experiments were repeated (histochemical staining and observation) after 12 days of inoculation (Ruhullah, et al., 2017).

III. Results

The results recognized that intracellular occupation for the tips of the root appears after injection of spinach plants through *G. diazotrophicus*. It was also found for all samples examined that the most extensive intracellular colonization was in shoots and roots cultivated in a semisolid MS medium. Yet young seedlings grown on MS agar medium with 109 CFU were inoculated, the quantity typically runs down for inoculations of plants by *G. diazotrophicus* strain UAP5541.

Data showed that the color of the X-gluc dye solution after 24 h was changed from colorless to blue for inoculated seedlings and remained colorless for un-inoculated seedlings. Furthermore, the leaves of inoculated seedlings were dyed blue compared with the un-inoculated seedling leaves.

Microscopic assessments for root tips verified the existence of bacterial cells within the cell walls of these roots 4 days after inoculation through *GUSA–G. diazotrophicus* (Fig. 1a), whereas the absence of bacteria was observed in the root tips of control samples (Fig. 1b). Pieces of roots that are embedded in resin 12 days after inoculation

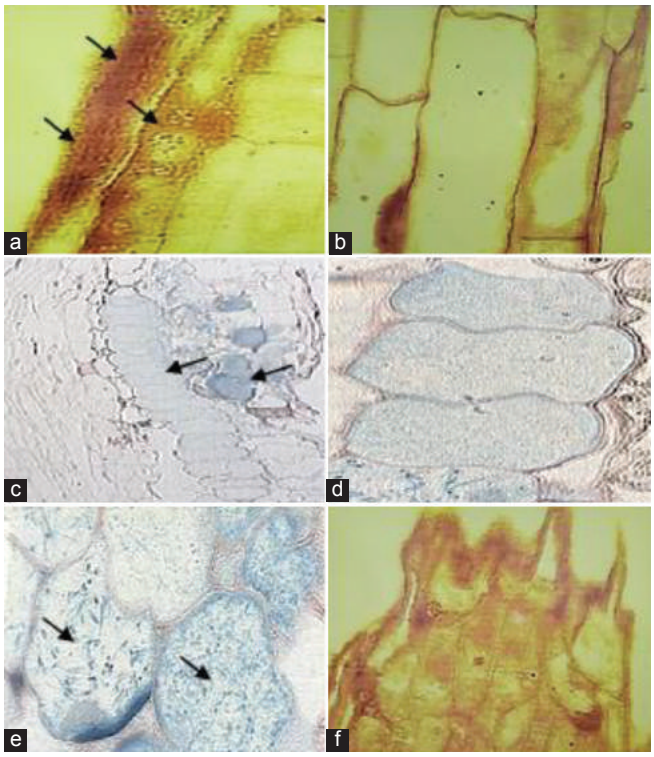

Fig. 1. Illumination micrographs of roots of *Spinacia oleracea* L. inoculated with *Gluconacetobacter diazotrophicus* 4 days and 12 days after inoculation and un-inoculated control. (a) Root section inoculated through *GUS*A–*G. diazotrophicus* viewing bacteria inside the cells and within the walls (arrows) 4 days after inoculation. (b) Longitudinal section of the stained un-inoculated root tip (control). (c) Root section inoculated through *GUS*A–*G. diazotrophicus* screening bacteria inside the cells (arrows) 12 days after inoculation. (d and e) Section of root inoculated through *GUS*A–*G. diazotrophicus*, displaying widespread intracellular occupation and the existence of micro-colonies (arrows). (f) Root apex peripheral cells stained section of un-inoculated (control). Scale bars ¼ 10 mm (a-f).

http://dx.doi.org/10.14500/aro.11239

through *GUSA–G. diazotrophicus* presented dim blue-dyed *G. diazotrophicus* inside the cells and similarly in the cell walls (Fig. 1c). Bacterial invasion of the elongation zone and their spread were heavy (Fig. 1d and e). The absence of dim blue-dyed *G. diazotrophicus* was noted within stained slices of un-inoculated root tips (control) (Fig. 1f).

Moreover, the results demonstrated the presence of bacterial cells within cellular walls for cotyledon leaf epidermal cells (Fig. 2a); in some sections, bacterial cells were closely associated with vesicles (Fig. 2b). Data from microscopic observations detected leaf cells' intracellular occupation with blue-dyed *G. diazotrophicus* clearly (Fig. 2c) and also viewed numerous bacterial cells within the guard cells (Fig. 2d). Again, the absence of dim blue dyed *G. diazotrophicus* in divisions of un-inoculated dyed leaves (control) (Fig. 2e and f).

IV. Discussion

The success of the interaction of spinach seedlings with *GUS*-labeled *G. diazotrophicus* bacteria and the improvement in its growth reflects the access of this bacterium to the cell walls of the roots and its concentration among these cells. Their concentration between these cells was known for its effective role in resisting the diffusion of oxygen to enable it to fix nitrogen in conditions of high concentrations of oxygen, thus preserving the effectiveness of the *nitrogenase* enzyme from the flow of oxygen (Dong, et al., 2002). The mutual signals in the response between the plant and then the *G. diazotrophicus* bacteria, which enabled bacteria to penetrate the plant cell walls and then settle inside cells, may be attributed to the fact that the inoculation and growth conditions in the MS medium containing sucrose were suitable for both bacteria and plants (Rodriguez, et al., 2019). It is likely that the contributing reason for this point is that *G. diazotrophicus* creates great quantities of indole acetic acid, and plant development is usually inhibited through extreme intensities of auxin hormone (Rocafull, et al., 2016). However, small quantities of IAA are known to function such as a common signifying iota in plant and bacteria relations, with microbial-liberated IAA stimulating a reaction differing from useful to harmful in plant cells. This is determined by the endogenous level of IAA in the root cells (Duca, et al., 2014). Subsequent cell wall access through *G. diazotrophicus*, intracellular bacteria occupation in vesicles might produce as sucrose caused the endocytosis (Rodriguez, et al., 2019). Exopolysaccharides manufactured through *G. diazotrophicus* are in charge of mucoid bacteria development (Lambrecht, et al., 2000). *G. diazotrophicus* culture is able to utilize a mucoid medium as an operative challenge to the diffusion of oxygen, allowing bacteria cells to do nitrogen fixation in a great range of oxygen levels, thus keeping nitrogenase action from extreme oxygen change (Dong, et al., 2002). In general, this is due to *GUS* gene expression carried in *G. diazotrophicus* which is loaded with *nifH* promoter and *GUS*A promoter, which is in charge of changing the color of the X-gluc dye from colorless to blue when incubating the inoculated spinach seedling (Masyab, 2018). Herein, dye explains the color change to the formation of dichloro-dibromoindigo (ClBr-indigo) compound as a result of the oxidation of X-gluc dye by *β-glucuronidase* (*GUS*) enzyme (Xiong, et al., 2011). This proves that the interaction determinants between these bacteria and spinach seedlings were suitable for the expression of the gene responsible for forming *nitrogenase* enzyme (Varghese, et al., 2019). Whereas, the similar *G. diazotrophicus nifH–GUSA* form existed within dead wood vessels of sugarcane-negative *GUS* expression was identified (Eskin, Vessey and Tian, 2014). Prospect acts through mutants influenced exopolysaccharide production (Sevilla and Kennedy, 2000). This might aid to verify if exopolysaccharides are in charge of the development of *G. diazotrophicus;* moreover, *nifH* gene expression is associated with exopolysaccharide production (Dietz, 2022). The lengthy pleomorphic cells of intracellular *G. diazotrophicus* are a feature of *G. diazotrophicus* development at great concentrations of nitrogen (NH_4NO_3, NH_4Cl, KNO_3, and Urea) representing in MS media as a source for plant development (Muthukumarasamy, Revathi and Loganathan, 2002). The *G. diazotrophicus* has extreme tolerance to acid, growth, and nitrogen fixation much at the pH (3.0) and less than that (Grillo-Puertas, et al., 2018).

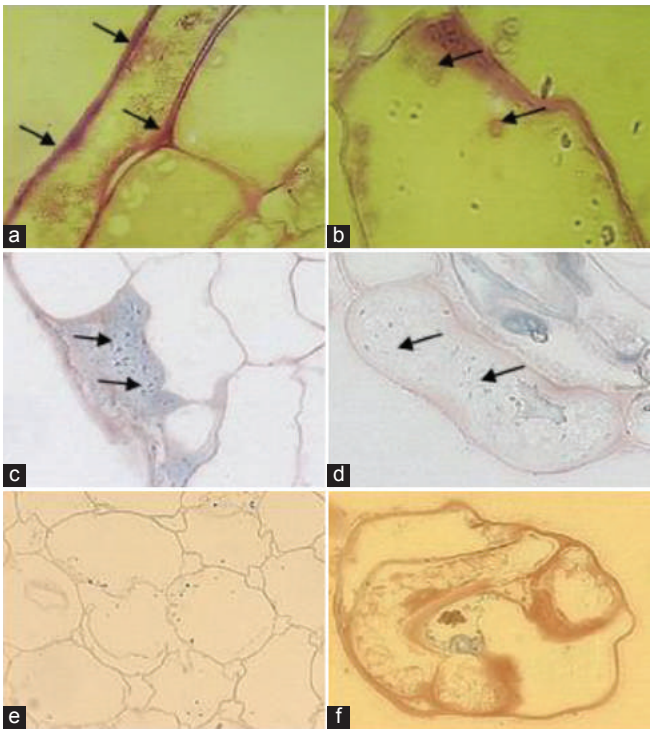

Fig. 2. Illumination micrographs of cotyledon leaves for *Spinacia oleracea* L. inoculated with *Gluconacetobacter diazotrophicus* 4 days and 12 days after inoculation and un-inoculated control. (a) Inoculated leaf section through *GUS*A–*G. diazotrophicus* viewing bacteria inside the cells beside the cell walls (arrows). (b) Leaf section at 4 days after inoculation through *GUS*A–*G. diazotrophicus*, displaying stretched pleomorphic bacterial cells in addition to massive intracellular occupation for leaves cells through bacteria strictly coupled with vesicles (arrows). **(c)** Intracellular colonization in leaf displaying blue-stained *G. diazotrophicus* within cells (arrows). (d) Bacterial cells were invading guard cells (arrows). (e and f) Cotyledon un-inoculated section stained (control). Scale bars ¼ 10 mm (a-f).

Furthermore, ammonia (NH_4) affects incomplete inhibition for *nitrogenase* lone (Medeiros, Polidoro, and Reis, 2006). The collaboration between non-rhizobial *G. diazotrophicus* bacteria together with the apex of a plant root has seen firm resemblances to that taking place among angiosperm genera and nitrogen-fixing cyanobacteria such as Nostoc sp. (Chiu, et al., 2005). These cyanobacteria enter the meristematic cells through their thin walls at the stem by liquefying the wall of cells and then are immersed in vesicles within the host cell by endocytosis. In general, they become intracellular and surrounded by a layer primarily in a band together with the host plasma membrane. The conclusion is that this is analog to symbiosome membrane enclosing bacteroids in the nodule of rhizobium legume interaction (Parniske, 2000); however, nodules are not formed.

V. Conclusion

The research indicates that the determinants of the interaction between the *G. diazotrophicus* bacteria and spinach seedlings were suitable for the expression of the gene responsible for the formation of the *nitrogenase* enzyme. *G. diazotrophicus* lives inside plant tissue cells in the form of colonies and excretes about half of the fixed nitrogen, which offers potential power that improves plant growth.

Acknowledgment

The authors would like to thank Professor E. C. Cocking, School of Biology, and Nottingham University, UK, for supplying *G. diazotrophicus* bacteria. Once again, the authors are very grateful to the Department of Biology, Faculty of Science and Health, Koya University and University of Mosul/College of Education for Pure Sciences, and Al-Hadba University Colleges for their facilities that sustained this investigation.

References

AL-Mallah, M.K., and Masyab, H.M., 2014. Expression of GUS and GFP reporter genes in transgenic hairy roots of tomato and potato plants via *Agrobacterium rhizogenes* mediated transformation. *Australian Journal of Basic and Applied Sciences*, 8(2), pp.234-239.

Boddey, R.M., Urquiaga, S., Alves, B.J.R., and Reis, V., 2003. Endophytic nitrogen fixation in sugarcane: Present knowledge and future applications. *Plant and Soil*, 252, pp.139-149.

Chiu, W., Peters, G.A., Levieille, G., Still, P.C., Cousins, S., Osborne, B., and Elhai J., 2005. Nitrogen deprivation stimulates symbiotic gland development in *Gunnera manicata*. *Plant Physiology*, 139, pp.224-230.

Cocking, E.C., Stone, P.J., and Davey, M.R., 2006. Intracellular colonization of roots of *Arabidopsis* and crop plants by *Gluconacetobacter diazotrophicus*. *In Vitro Cellular and Developmental Biology-Plant*, 42, pp.74-82.

Dietz, B.R., 2022. *Genetic Manipulations in Known Endophytes Furthering the Application as a Biofertilizer. M. Sc. Thesis*. University of Minnesota, Minnesota, U.S.A.

Dong, Z., Zelmer, C.D., Canny, M.J., McCully, M.E., Luit, B., Pan, B., Faustino, R.S., Pierce, G.N., and Vessey, J.K., 2002. Evidence for protection of nitrogenase from O_2 by colony structure in the aerobic diazotroph *Gluconacetobacter diazotrophicus*. *Microbiology* (*Reading*), 148, pp.2293-2298.

Duca, D., Lorv, J., Patten, C.L., Rose, D., and Glick, B.R., 2014. Indole-3-acetic acid in plant-microbe interactions. *Antonie van Leeuwenhoek*, 106, pp.85-125.

Eskin, N., Vessey, K., and Tian, L., 2014. Research progress and perspectives of nitrogen fixing bacterium, *Gluconacetobacter diazotrophicus*, in monocot plants. *International Journal of Agronomy*, 2014, p.208383

Furness, D., Fenech, M., Dekker, G., Khong, T.Y., Roberts, C., and Hague, W., 2013. Folate, Vitamin B12, Vitamin B6 and homocysteine: Impact on pregnancy outcome. *Maternal and Child Nutrition*, 9(2), pp.155-166.

Grillo-Puertas, M., Delaporte-Quintana, P., Pedraza, R.O., and Rapisarda, V.A., 2018. Intracellular polyphosphate levels in *Gluconacetobacter diazotrophicus* affect tolerance to abiotic stressors and biofilm formation. *Microbes and Environment*, 33(4), pp.440-445.

Kong, Q., Li, J., Wang, S., Feng, X., and Shou, H., 2023. Combination of hairy root and whole-plant transformation protocols to achieve efficient CRISPR/Cas9 genome editing in soybean. *Plants* (*Basel*), 12, p.1017.

Lambrecht, M., Okon, Y., Vande Broek, A., and Vanderleyden, J., 2000. Indole-3-acetic acid: A reciprocal signalling molecule in bacteria-plant interactions. *Trends Microbiology*, 8, pp.298-300.

Masyab, H.M., 2018. Expression patterns of *GUS* gene in five different strains of *Arabidopsis thaliana* plants. In: *International Conference on Pure and Applied Sciences (ICPAS 2018)*, pp.59-63.

Medeiros, A.F.A., Polidoro, J.C., and Reis, V.M., 2006. Nitrogen source effect on *Gluconacetobacter diazotrophicus* colonization of sugarcane (*Saccharum* spp.). *Plant and Soil*, 279(1-2), pp.141-152.

Miki, B., 2008. Marker genes and promoters. In: Stewart, C.N., editor. *Plant Biotechnology and Genetics: Principles, Techniques, and Applications*. John Wiley and Sons, Ltd., New Jersey, U.S.A.

Mohammed, A.A.H., and Masyab, H.M., 2020. Genetic transformation of *Nigella sativa* L. Plants with *Agrobacterium rhizogenes* 35S GUS R1000 and estimation of thymoquinone level in transformed hairy roots cultures. *Plant Archives*, 20(Suppl 1), pp.3649-3652.

Murashige, T., and Skoog, F., 1962. A revised medium for rapid growth and bio assays with tobacco tissue culture. *Physiologia Plantarum*, 15, pp.473-497.

Muthukumarasamy, R., Revathi, G., and Loganathan, P., 2002. Effect of inorganic N on the population, *in vitro* colonization and morphology of *Acetobacter diazotrophicus* (syn. *Gluconacetobacter diazotrophicus*). *Plant and Soil*, 243, pp.91-102.

Parniske, M., 2000. Intracellular accommodation of microbes by plants: A common developmental program for symbiosis and disease. *Current Opinion in Plant Biology*, 3, pp.320-328.

Rasheed, J.H., 2014. *GUS*-gene as a visual marker for *Gluconacetobacter diazotrophicus* co-cultivated with carrot plantlets. *International Journal of Science and Technology*, 3, pp.776-779.

Rocafull, Y.R., Badia, M.J., Garciea, M.O., Álvarez, B.D., and Sánchez, J.R., 2016. Isolation and characterization of *Gluconacetobacter diazotrophicus* strains. *Cultivos Tropicales*, 37(1), pp.34-39.

Rodriguez, M.V., Tano, J., Ansaldi, N., Carrau, A., Srebot, M.S., Ferreira, V., Martínez, M.L., Cortadi, A.A., Siri, M.I., and Orellano, E.G., 2019. Anatomical and biochemical changes induced by *Gluconacetobacter diazotrophicus* stand up for *Arabidopsis thaliana* seedlings from *Ralstonia solanacearum* infection. *Frontiers in Plant Science*, 10, p.1618.

Ruhullah, M., Rahman, M.S., Sarafat, A.M.D., Mohsin G.M., and Khalekuzzaman, M., 2017. Establishment of agrobacterium mediated genetic transformation in popular rice cultivar BRRI dhan-29 through reporter GUS gene expression system in Bangladesh. *FPI*, 1(2), pp.67-75.

Sebring, R.L., Duiker, S.W., Berghage, R.D., Regan, J.M., Lambert, J.D., and

Bryant, R.B., 2022. *Gluconacetobacter diazotrophicus* inoculation of two lettuce cultivars affects leaf and root growth under hydroponic conditions. *Applied Sciences*, 12, p.1585.

Sevilla, M., and Kennedy, C., 2000. Genetic analysis of nitrogen fixation and plant growth stimulating properties of *Acetobacter diazotrophicus*, an endophyte of sugarcane. In: Triplett, E.W., editor. *Prokaryotic Nitrogen Fixation: A Model System for Analysis of a Biological Process*. Scientific Press, Wymondham, UK, Horizon, pp.737-760.

Shojaei, T.R., Salari, V., Ramazan, D., Ehyaei, M., Gharechahi, J., and Chaleshtori, R.M., 2010. The effect of plant growth regulators, explants and cultivars on spinach (*Spinacia oleracea* L.) Tissue culture. *African Journal of Biotechnology*, 9(27), pp.4179-4185.

Varghese, F., Kabasakal, B.V., Cotton, C.A.R., Schumacher, J., Rutherford, A.W., Fantuzzi, A., and Murray, J.W., 2019. A low-potential terminal *oxidase* associated with the iron-only *Nitrogenase* from the nitrogen-fixing bacterium *Azotobacter vinelandii*. *Journal of Biological Chemistry*, 294(24), pp.9367-9376.

Xiong, A.S., Peng, R.H., Zhuang, J., Chen, J.M., Zhang, B., Zhang, J., and Yao, Q.H., 2011. A thermostable β-glucuronidase obtained by directed evolution as a reporter gene in transgenic plants. *PLoS One*, 6(11), e26773.

Synthesis of Some novel Azomethine Oxide Derived from Aromatic Oximes and their Anti-microbial Studies

Jihad H. Mohammed[1], Akram N. M. Qaddo[2], Nabaz A. Muhammad Salih[1,*] and Faeza B. Omar[3]

[1]Department of Chemistry, Faculty of Science, Soran University,
Kurdistan Region – F.R. Iraq

[2]Department of Chemistry, Education College for Girls,
University of Mosul – F.R. Iraq

[3]Department of Biology, Faculty of Science, Soran University,
Kurdistan Region – F.R. Iraq

***Abstract*—The organic compound category known as azomethine oxides has garnered significant attention due to its potential for bioactive and pharmacological effects, as well as its role in organic syntheses. Existing literature offers various methods for producing derivatives of these compounds. This study, in particular, concentrates on the creation of several aromatic oximes through the reduction of corresponding aldehydes. Furthermore, these oximes are employed in the generation of new azomethine oxides through a condensation reaction with selected aldehydes. The molecular structure of the synthesized azomethine oxides is determined using techniques such as Fourier-transform infrared spectroscopy, ^{1}H-NMR, and ^{13}C-NMR. Finally, the antimicrobial effectiveness of these compounds was assessed against *Escherichia coli* (gram-negative bacteria), *Staphylococcus aureus* (gram-positive bacteria), and *Candida albicans* (fungus). The synthesized compounds were obtained with high purity and yielded excellent results. Furthermore, the data demonstrates that these azomethine oxides exhibit significant antimicrobial activity when compared to standard drugs.**

***Index Terms*—Aromatic oximes, Azomethine-*N*-oxide, Biological activity, Condensation reaction.**

I. Introduction

Nitrone, specifically the azomethine-*N*-oxide, is represented by the chemical structure R'-CH=N(O)-R" in its simplest form. It is a class of organic compounds that contain a nitrogen-oxygen double bond (El Bouakher, Martel, and Comesse, 2019). Nitrones are versatile compounds with diverse applications in organic synthesis and medicinal chemistry (Murahashi and Imada, 2019; Hiraoka, et al., 2019). Nitrones are typically synthesized by the condensation reaction between a carbonyl compound (such as an aldehyde or a ketone) and hydroxylamine, followed by oxidation. This reaction forms the N-O double bond and creates a stable nitronate intermediate, which can be isolated or used directly in subsequent reactions (Murahashi and Imada, 2019). One of the most notable characteristics of nitrones is their ability to undergo 1,3-dipolar cycloaddition reactions with alkenes or alkynes, known as the "nitrone-alkene/alkyne" cycloaddition (Yang, et al., 2017; Alshreimi, et al., 2020). This reaction forms isoxazolidine or isoxazole derivatives, depending on the specific conditions used (Qaddo and Abed, 2022; Li, et al., 2021). The resulting products can have interesting biological activities and can serve as building blocks for the synthesis of more complex molecules (Anderson, et al., 2016). Nitrones are widely used in the synthesis of natural products, pharmaceuticals, and other biologically active compounds (Mohammed and Salih, 2022). They have been employed in the development of drugs for various therapeutic areas, including neurodegenerative diseases, cancer, antimicrobial, antitumor, anti-inflammatory properties, and infectious diseases (Yang, et al., 2017; McKay, et al., 2011; Sandmeier and Carreira, 2021). In addition to their synthetic applications, nitrones also exhibit antioxidant properties, which make them useful in the fields of free radical biology and medicine (Floyd, et al., 2002; Floyd, et al., 2008).

Considering all the aforementioned information, we hereby present the synthesis of several new azomethine-*N*-oxide derivatives and an assessment of their biological properties.

II. Experimental

A. Materials and Instrumentation

The study utilized commercially obtained materials and instrumentation. These included sodium sulfate anhydrous,

ARO-The Scientific Journal of Koya University
Vol. XII, No. 1 (2024), Article ID: ARO.11471. 6 pages
DOI: 10.14500/aro.11471
Received: 12 November 2023; Accepted: 01 February 2024
Regular research paper: Published: 15 February 2024
Corresponding author's e-mail: nabaz.mohammad@soran.edu.iq

diethyl ether, petroleum ether (Scharlau), NaOH, KOH (SDFCL), HNO_3, methanol (Romil), and methyl orange (BDH). Hydroxylamine hydrochloride and aldehydes were also acquired from a commercial laboratory. The materials and solvents were used directly from their containers without any further purification steps. The uncorrected melting points of the nitrones were determined using a Stuart Scientific melting point apparatus (SMP3). Fourier-transform infrared spectroscopy (FT-IR) spectra were recorded at Salahaddin University-Erbil using a Shimadzu 8300 instrument with KBr disks. ^{1}H-NMR and ^{13}C-NMR spectra were obtained at the Kurdistan Central Research Center in Iran using a 500 MHz and 125 MHz spectrometer, respectively. Tetramethylsilane was used as an internal reference, and deuterated chloroform $CDCl_3$ was used as the solvent. The chemical shifts were measured in units of parts per million (ppm), with the residual solvent as the reference. Coupling constants (J) were reported in Hertz. The ChemDraw software was utilized for the nomenclature of the compounds.

B. Synthesis of Phenylhydroxylamine Derivatives (Kliegel, Metge, and Rettig, 1997)

General Procedure A: 34 mmol, 1.36 g of NaOH was dissolved in 25 mL of H_2O and then 15 mmol of one of the substituted benzaldehydes. The solution was supplemented with 18 mmol, 1.25 g of hydroxylamine hydrochloride, and the resulting mixture was stirred at ambient temperature for duration of 45 min. Subsequently, the solution was acidified by adding 10% aqueous HCl. The resulting mixture was extracted with 3*15 mL of methylene chloride. The organic layer was then dried using anhydrous sodium sulfate (Na_2SO_4) and concentrated by a rotary evaporator.

In the next step, 10 mmol of the obtained material was dissolved in 20 mL of MeOH, and then, 6.7 mmol, 0.42 g of $NaBH_3CN$ was added to it. A very small amount of methyl orange was added to the solution as an indicator. The solution was acidified by adding 4N HCl/MeOH until a pink solution was observed. The mixture was stirred for 1.5 h, which MeOH was removed using a rotary evaporator. To the resulting aqueous solution, 20 mL of H_2O and 4M KOH were added to adjust the pH to 9. The mixture was extracted with 3*15 mL of CH_2Cl_2. The CH_2Cl_2 layer was dried with Na_2SO_4 and removed *via* rotary evaporation.

C. Synthesis of Azomethine Oxides

General Procedure B: In a solution containing *N*-phenylhydroxylamine derivative (10 mmol, 1.0 eq.) in dichloromethane (10 ml), an equivalent amount of aldehyde (10 mmol, 1.0 eq.) was added while stirring. The mixture was then heated to 60°C and stirred until the starting material was fully consumed, as monitored by TLC. The solvent was evaporated under reduced pressure to obtain the crude product, which subsequently precipitated. The resulting precipitate was purified by recrystallization with hot ethanol to obtain pure azomethine oxide. The purified compound was stored in a cool and dark place (Qaddo and Abed, 2022).

(E)-N-benzyl-1-(p-tolyl)methanimine oxide (5)

Following the general procedure B, white crystal (1.8 g, 80%), m.p.= 109–111°C; R_f = 0.51 (10:90 methanol/dichloromethane); ^{1}H-NMR (500 MHz, $CDCl_3$) δ ppm: δ 8.13 (d, 2H, N=C*H* + 1H, aromatic proton), 7.65–7.13 (m, 8H, aromatic protons), 5.05 (s, 2H, Ph-CH_2), (s, 3H, CH_3). ^{13}C-NMR (126 MHz, $CDCl_3$) δ 140.97, 134.43, 133.37, 129.22, 129.21, 129.17, 129.16, 128.95, 128.91, 128.70, 128.69, 128.66, 127.77, 71.01, 21.68.

(E)-N-benzyl-1-(3,4-dimethoxyphenyl)methanimine oxide (6)

Following the general procedure B, light yellow solid (2.4 g, 89%), m.p.= 103–105°C; R_f = 0.36 (10:90 methanol/dichloromethane); ^{1}H-NMR (500 MHz, $CDCl_3$) δ ppm: δ 8.35 (s, 1H, N=C*H*), 7.51–7.29 (m, 8H, aromatic protons), 4.99 (s, 2H, Ph-CH_2), 3.88 (s, 3H, OCH_3), 3.87 (s, 3H, OCH_3). ^{13}C-NMR (126 MHz, $CDCl_3$) δ 150.72, 148.42, 134.32, 133.35, 129.21, 129.20, 128.92, 128.91, 128.89, 123.73, 123.17, 110.93, 110.55, 70.78, 70.77, 55.87.

(E)-N-(4-methylbenzyl)-1-phenylmethanimine oxide (7)

Following the general procedure B, white crystal (2.0 g, 88%), m.p.= 116–118°C; R_f = 0.56 (10:90 methanol/dichloromethane); ^{1}H-NMR (500 MHz, $CDCl_3$) δ ppm: δ 8.30–8.20 (m, 1H, aromatic proton), 8.15 (s, 1H, N=C*H*), 7.51–7.17 (m, 8H, aromatic protons), 5.10 (s, 1H, Ph-CH*H*), 2.37 (s, 4H, Ph-C*H*H + CH_3). ^{13}C-NMR (126 MHz, $CDCl_3$) δ 149.95, 149.94, 140.03, 140.00, 135.29, 130.78, 129.74, 129.55, 129.47, 129.13, 128.48, 126.96, 70.74, 21.47, 21.46.

(E)-N-(4-methylbenzyl)-1-(p-tolyl)methanimine oxide (8)

Following the general procedure B, white crystal (2.2 g, 92%), m.p. = 89–91°C; R_f = 0.52 (10:90 methanol/dichloromethane); ^{1}H NMR (500 MHz, $CDCl_3$) δ ppm: 8.12 (d, J = 7.9 Hz, 2H, aromatic protons + N=C*H*), 7.38–7.12 (m, 7H, aromatic protons), 4.94 (s, 2H, Ph-CH_2), 2.33 (s, 6H, 2*CH_3). ^{13}C-NMR (126 MHz, $CDCl_3$) δ 140.76, 138.71, 134.15, 130.49, 129.57, 129.25, 129.12, 128.69, 127.94, 70.65, 21.67, 21.25.

(E)-1-(3,4-dimethoxyphenyl)-N-(4-methylbenzyl) methanimine oxide (9)

Following the general procedure B, yellow crystal (2.6 g, 91%), m.p.= 66–68°C; R_f = 0.76 (10:90 methanol/dichloromethane); ^{1}H-NMR (500 MHz, $CDCl_3$) δ ppm: δ 8.37 (s, 1H, N=C*H*), 7.45–6.81 (m, 7H, aromatic protons), 4.98 (s, 2H, Ph-CH_2), 3.90 (s, 6H, 2*OCH_3), 2.36 (s, 3H, CH_3). ^{13}C-NMR (126 MHz, $CDCl_3$) δ 148.43, 148.40, 138.93, 138.91, 130.21, 129.67, 129.66, 129.36, 129.31, 123.71, 123.29, 111.06, 110.49, 70.51, 56.05, 55.89, 21.20.

(E)-N-(3,4-dimethoxybenzyl)-1-(p-tolyl)methanimine oxide (10)

Following the general procedure B, white crystal (2.6 g, 91%), m.p.= 100–101°C; R_f = 0.55 (10:90 methanol/dichloromethane); ^{1}H-NMR (500 MHz, $CDCl_3$) δ ppm: 8.05 (d, J = 8.0 Hz, 2H, aromatic protons), 7.30 (s, 1H, N=C*H*), 7.15–6.75 (m, 5H, aromatic protons), 4.88 (s, 2H, Ph-CH_2), 3.79 (s, 6H, 2*OCH_3), 2.27 (s, 3H, Ph-CH_3). ^{13}C-NMR (126 MHz, $CDCl_3$) δ 149.49, 149.09, 140.79, 134.02, 133.96, 129.12, 129.05, 128.63, 128.59, 127.79, 125.76, 122.15, 122.10, 112.40, 112.32, 111.14, 21.62.

(E)-N-(3,4-dimethoxybenzyl)-1-(3,4-dimethoxyphenyl) methanimine oxide (11)

In accordance with the general procedure B, light yellow solid (3.0 g, 91%), m.p.= 127–129°C; R_f = 0.64 (10:90 methanol/dichloromethane); ^{1}H-NMR (500 MHz, $CDCl_3$) δ ppm: δ 8.32 (s, 1H, N=C*H*), 7.46–6.73 (m, 6H, aromatic protons), 4.91 (s, 2H, Ph-CH_2), 3.88–3.81 (m, 12H, 4*OCH_3). ^{13}C-NMR (126 MHz, $CDCl_3$) δ 150.71, 149.65, 149.24, 148.41, 134.01, 133.90, 125.64, 123.73, 123.14, 122.25, 112.49, 111.30, 110.95, 110.52, 55.96, 55.93, 55.86, 55.80.

(E)-N-(3,4-dimethoxybenzyl)-1-(2-nitrophenyl) methanimine oxide (12)

Using the general procedure B, light yellow solid (2.8 g, 89%), m.p.= 161–163°C; R_f = 0.67 (10:90 methanol/dichloromethane); ^{1}H-NMR (500 MHz, $CDCl_3$) δ ppm: δ 9.07 (s, 1H, N=C*H*), 8.06–6.83 (m, 7H, aromatic protons), 5.02 (s, 2H, Ph-CH_2), 3.90 (s, 3H, OCH_3), 3.88 (s, 3H, OCH_3). ^{13}C-NMR (126 MHz, $CDCl_3$) δ 149.90, 149.33, 149.32, 133.40, 130.08, 129.46, 128.09, 124.95, 124.81, 124.44, 122.39, 112.39, 111.26, 72.20, 55.99, 55.94.

(E)-1-(3,4-dimethoxyphenyl)-N-(2-nitrobenzyl) methanimine oxide (13)

According to the general procedure B, light yellow solid (2.5 g, 79%), m.p.= 161–163°C; R_f = 0.5 (10:90 methanol/dichloromethane); ^{1}H-NMR (500 MHz, $CDCl_3$) δ ppm: 8.33 (s, 1H, N=C*H*), 8.18–6.85 (m, 7H, aromatic protons), 5.44 (s, 2H, Ph-CH_2), 3.91 (s, 6H, 2*OCH_3). ^{13}C-NMR (126 MHz, $CDCl_3$) δ 151.14, 148.50, 148.12, 134.04, 132.38, 129.74, 129.72, 128.84, 125.22, 123.67, 123.34, 111.06, 110.63, 66.99, 55.93, 55.89.

D. The Antibacterial and Antifungal Activity of the Synthesized Nitrones

The antibacterial and antifungal effects of the synthesized azomethine oxides (5-13) were evaluated by dissolving them in two different concentrations, 500 μg and 1000 μg, in 1 mL of dimethyl sulfoxide (DMSO). These concentrations were tested against Gram-positive *Staphylococcus aureus* bacteria and Gram-negative *Escherichia coli* bacteria, as well as their antifungal activity against *Candida albicans*. The agar-well diffusion method was employed to assess the antibacterial activity. Initially, Muller–Hinton agar was sterilized using an autoclave, then cooled to 50–55°C, and poured into petri dishes to form a uniform layer. Sterilized swabs were used to streak *S. aureus* and *E. coli* bacteria onto the agar surface, allowing them to solidify for 30 min. Subsequently, four wells with an 8 mm diameter were created in the agar layer, and 100 μL of each concentration of the prepared azomethine oxides, as well as dimethyl sulfoxide, levofloxacin, and clotrimazole (used as a standard drug for comparison), were added to the respective wells. The petri dishes were incubated at 37°C for 48 h, following which the diameter of the inhibitory zone was measured in millimeters.

III. Results and Discussion

The objective of this study is to produce new azomethine oxides through the transformation of specific substituted benzaldehydes into their corresponding hydroxylamines, as shown in Scheme 1 and Table I. Scheme 2 provides a general mechanism of the process for synthesizing phenylhydroxylamine derivatives (Mohammed, et al., 2023).

For the synthesis of azomethine oxides (5-13), a condensation strategy between *N*-phenylhydroxylamines and various substituted benzaldehydes was employed. This process is exemplified in Scheme 3 and summarized in Table II. Furthermore, Scheme 4 outlines the general mechanism involved in the synthesis of the desired compounds (Mohammed, et al., 2023)

The FT-IR spectra of the synthesized azomethine oxides clearly demonstrated that the carbonyl stretching band of the aldehyde disappeared, located between 1740 and –1720 cm^{-1}. Instead, new bands corresponding to (C=N), (C-N), and (N-O) vibrations appeared in the spectra within the following ranges: (1597–1583) cm^{-1}, (1346–1317) cm^{-1}, and (1112–1020) cm^{-1}, respectively.

A. Determining the Configuration of Compound 11

Inouye's research findings indicate that the configuration of nitrones is influenced by the solvent used. Surprisingly, it has been observed that in non-polar solvents, *E*-configuration is the major product, whereas in polar solvents, *Z*-configuration is the major product (Inouye, 1980). Furthermore, the steric effect experienced by the *E*-isomer of azomethine oxide is lower compared to the *Z*-isomer, resulting in greater stability for the *E*-isomer (Figure 1). These results have been further supported by the findings of Qaddo and Abed, which align closely with Inouye's conclusions (Qaddo and Abed, 2022).

B. Determining the Configuration of 11 by ^{1}H-NMR

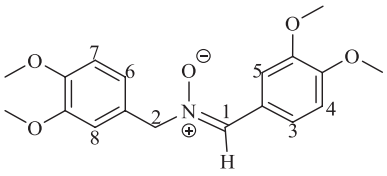

Compound 11's structure has been established using ^{1}H-NMR spectroscopy. It was emerged that the H at C-1 exhibited a singlet peak at 8.32 ppm, two protons at C-2

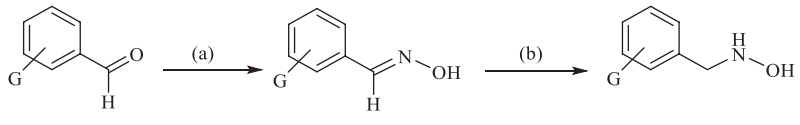

(1-4)

(a)= NaOH, H_2O, $NH_2OH.HCl$, HCl and CH_2Cl_2.
(b)= $NaBH_3CN$, MeOH, HCl-MeOH, KOH, H_2O and CH_2Cl_2

Scheme 1. General scheme of phenylhydroxylamine derivatives syntheses (**1-4**).

http://dx.doi.org/10.14500/aro.11471

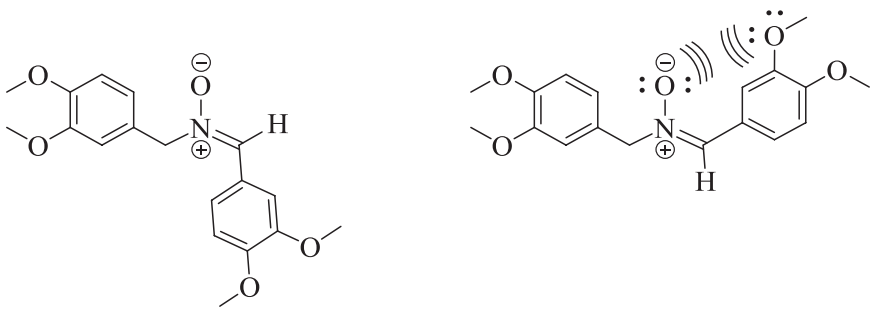

Fig. 1. *Z*-isomer and E-isomer azomethine oxide (Compound 11).

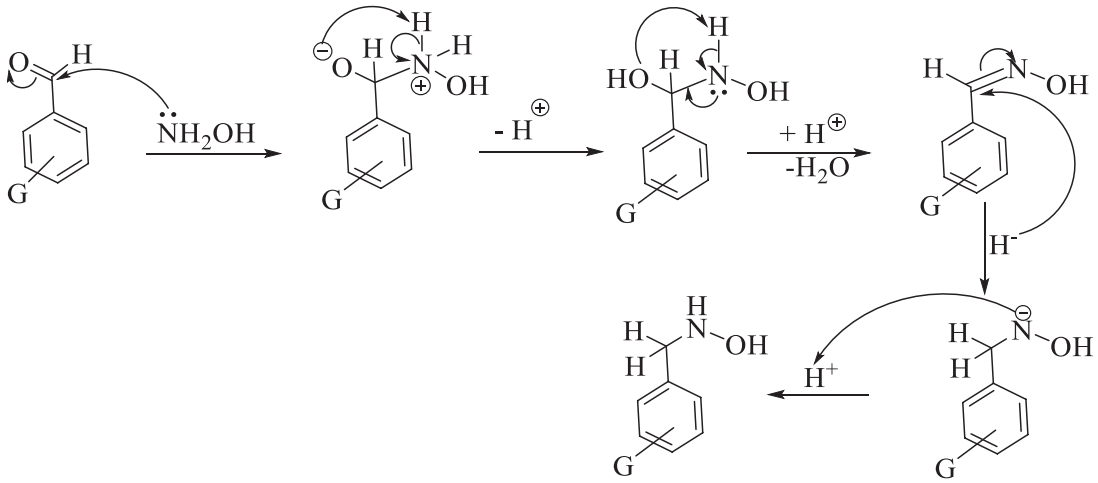

Scheme 2. General mechanism for the synthesis of phenylhydroxylamine derivatives (**1-4**).

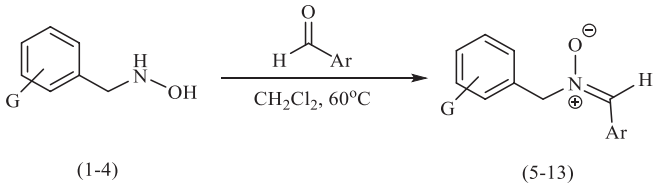

Scheme 3. General scheme of azomethine oxide synthesis (**5-13**).

TABLE I
PHENYLHYDROXYLAMINE DERIVATIVES SYNTHESIS (1-4)

Entry	Product No.	Product Name	Yield %
Benzaldehyde	1	*N*-benzylhydroxylamine	94
3-methylbenzaldehyde	2	*N*-(3-methylbenzyl) hydroxylamine	96
3,4-dimethoxybenzaldehyde	3	*N*-(3,4-dimethoxybenzyl) hydroxylamine	96
2-nitrobenzaldehyde	4	*N*-(2-nitrobenzyl) hydroxylamine	93

TABLE II
SYNTHESIS OF AZOMETHINE OXIDES (5-13)

N-phenylhydroxylamine derivative	Aldehyde	Azomethine oxide	Yield %
N-benzylhydroxylamine	3-methylbenzaldehyde	5	80
N-benzylhydroxylamine	3,4-dimethoxybenzaldehyde	6	89
N-(3-methylbenzyl) hydroxylamine	Benzaldehyde	7	88
N-(3-methylbenzyl) hydroxylamine	3-methylbenzaldehyde	8	92
N-(3-methylbenzyl) hydroxylamine	3,4-dimethoxybenzaldehyde	9	91
N-(3,4-dimethoxybenzyl) hydroxylamine	3-methylbenzaldehyde	10	91
N-(3,4-dimethoxybenzyl) hydroxylamine	3,4-dimethoxybenzaldehyde	11	91
N-(3,4-dimethoxybenzyl) hydroxylamine	2-nitrobenzaldehyde	12	89
N-(2-nitrobenzyl) hydroxylamine	3,4-dimethoxybenzaldehyde	13	79

appeared as a singlet at 4.91 ppm, and the aromatic protons of the phenyl group showed a multiplet from 7.46–6.73 ppm. Additionally, the protons of the methoxy groups appeared as a multiplet from 3.88–3.81 ppm. Furthermore, the ^{13}C-NMR analysis of this compound yielded the following results in ppm: 150.71, 149.65, 149.24, 148.41, 134.01, 133.90, 125.64, 123.73, 123.14, 122.25, 112.49, 111.30, 110.95, 110.52, 55.96, 55.93, 55.86, 55.80. The combined analysis of the ^{1}H-NMR and ^{13}C-NMR spectra provided strong confirmation of the correct structure of compound 11.

The confirmation of the configuration of compound 11 is crucial, as it serves as a vital reference point for determining the configuration of the remaining azomethine oxide compounds using only ^{1}H-NMR spectroscopy.

Table III presents the results of the study on the antibacterial and antifungal properties of synthetic

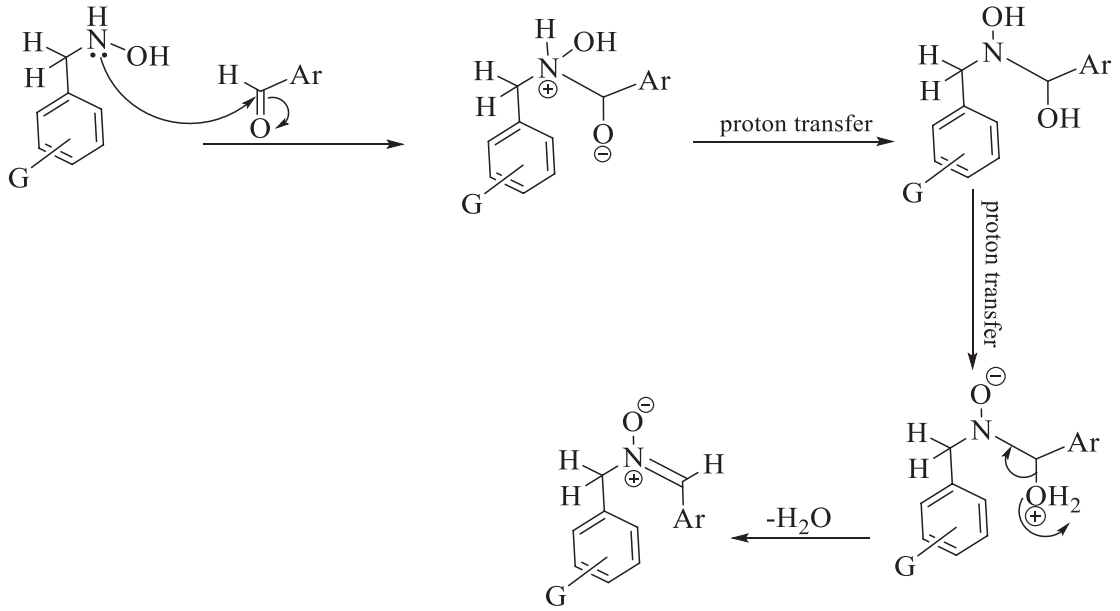

Scheme 4. General mechanism for the synthesis of azomethine oxides (**5-13**).

TABLE III
ANTIMICROBIAL ACTIVITY OF AZOMETHINE OXIDES (5-13)

Compound	Microorganism	500 µg/mL in 1 mL DMSO in mm	1000 µg/mL in 1 mL DMSO in mm
5.	*Escherichia coli*	NI	11
	Staphylococcus aureus	12	13
	Candida (Fungi)	13	15
6.	*Escherichia coli*	8	25
	Staphylococcus aureus	12	22
	Candida albicans	6	19
7.	*Escherichia coli*	7	15
	Staphylococcus aureus	11	15
	Candida albicans	NI	9
8.	*Escherichia coli*	NI	13
	Staphylococcus aureus	7	14
	Candida albicans	8	17
9.	*Escherichia coli*	7	15
	Staphylococcus aureus	10	15
	Candida albicans	8	11
10.	*Escherichia coli*	6	15
	Staphylococcus aureus	8	14
	Candida albicans	9	19
11.	*Escherichia coli*	NI	NI
	Staphylococcus aureus	NI	NI
	Candida (Fungi)	13	14
12.	*Escherichia coli*	11	12
	Staphylococcus aureus	NI	17
	Candida albicans	9	15
13.	*Escherichia coli*	9	17
	Staphylococcus aureus	11	20
	Candida albicans	13	25

Levofloxacin was effective against *E. coli* and *S. aureus*, with inhibition zones of 24 mm and 26 mm, respectively.
Clotrimazole was also effective against *C. albicans*, with an inhibition zone of 23 mm.
NI: No inhibition was observed

azomethine oxides against *C. albicans* fungus, *E. coli,* and *S. aureus* bacteria.

IV. Conclusion

To summarize, the structure of a synthetic azomethine oxide compound was confirmed through analysis of FT-IR, ^{1}H-NMR, and ^{13}C-NMR spectra. The experimental data validated the structure of this compound. In terms of biological activities, the synthesized azomethine oxides displayed remarkable antifungal properties against the *C. albicans* fungus, surpassing their antibacterial effects against *E. coli* and *S. aureus* bacteria.

References

Alshreimi, A.S., Zhang, G., Reidl, T.W., Peña, R.L., Koto, N.G., Islam, S.M., Wink, D.J., and Anderson, L.L., 2020. Synthesis of spirocyclic 1-pyrrolines from nitrones and arynes through a dearomative [3,3′]-sigmatropic rearrangement. *Angewandte Chemie - International Edition*, 59(35), pp.15244-15248.

Anderson, L.L., Kroc, M.A., Reidl, T.W., and Son, J., 2016. Cascade reactions of nitrones and allenes for the synthesis of indole derivatives. *Journal of Organic Chemistry*, 81(20), pp.9521-9529.

El Bouakher, A., Martel, A., and Comesse, S., 2019. α-halogenoacetamides: Versatile and efficient tools for the synthesis of complex aza-heterocycles. *Organic and Biomolecular Chemistry*, 17(37), pp.8467-8485.

Floyd, R.A., Hensley, K., Forster, M.J., Kelleher-Anderson, J.A., and Wood, P.L., 2002. Nitrones as neuroprotectants and antiaging drugs. *Annals of the New York Academy of Sciences*, 959, pp.321-329.

Floyd, R.A., Kopke, R.D., Choi, C.H., Foster, S.B., Doblas, S., and Towner, R.A., 2008. Nitrones as therapeutics. *Free Radical Biology and Medicine*, 45(10), pp.1361-1374.

Hiraoka, S., Matsumoto, T., Matsuzaka, K., Sato, T., and Chida, N., 2019. Approach to fully substituted cyclic nitrones from N-hydroxylactam derivatives: Development and application to the total synthesis of cylindricine C. *Angewandte Chemie - International Edition*, 58(13), pp.4381-4385.

Inouye, Y., Hara, J., and Kakisawa, H., 1980. Novel E-Z equilibrium of N-alkyl-alpha-alkoxycarbonylnitrone in solution. *Chemistry Letters*, 9, pp.1407-1410.

Kliegel, W., Metge, J., and Rettig, S.J., 1997. Synthesis of C-aryl-N-(2-hydroxyphenylmethyl)-nitrones and their reaction with diphenylborinic or carboxylic acid derivatives. Crystal and molecular structures of a free nitrone ligand and its diphenyl-boron chelate. *Canadian Journal of Chemistry*, 75, pp.1830-1843.

Li, T.Z., Liu, S.J., Sun, Y.W., Deng, S., Tan, W., Jiao, Y., Zhang, Y.C., and Shi, F., 2021. Regio- and enantioselective (3+3) cycloaddition of nitrones with 2-indolylmethanols enabled by cooperative organocatalysis. *Angewandte Chemie - International Edition*, 60(5), pp.2355-2363.

McKay, C.S., Blake, J.A., Cheng, J., Danielson, D.C., and Pezacki, J.P., 2011. Strain-promoted cycloadditions of cyclic nitrones with cyclooctynes for labeling human cancer cells. *Chemical Communications*, 47(36), pp.10040-10042.

Mohammed, J.H., and Salih, N.A.M., 2022. Synthesis and characterization of some new nitrones derivatives and screening their biological activities. *Science Journal of University of Zakho*, 10(4), pp.268-273.

Mohammed, J.H., Qaddo, A.N.M., Salih, N.A.M., and Omar, F.B., 2023. The synthesis of some imine derivatives via condensation reactions between some aromatic phenylhydroxylamine derivatives with glyoxylic acid and the study of their biological activity. *Tikrit Journal of Pure Science*, 28(6), pp.34-41.

Murahashi, S.I., and Imada, Y., 2019. Synthesis and transformations of nitrones for organic synthesis. *Chemical Reviews*, 119(7), 4684-4716.

Qaddo, A.N.M., and Abed, A.A., 2022. Heterocyclic synthesis of some new isoxazolidine derivatives via 1,3-dipolar cycloaddition of nitrones to styrene. *Iraqi Journal of Science*, 63(10), pp.4175-4184.

Sandmeier, T., and Carreira, E.M., 2021. Enantioselective synthesis of cyclic nitrones by chemoselective intramolecular allylic alkylation of oximes. *Angewandte Chemie - International Edition*, 60(18), pp.9913-9918.

Yang, X., Cheng, F., Kou, Y.D., Pang, S., Shen, Y.C., Huang, Y.Y., and Shibata, N., 2017. Catalytic asymmetric 1,3-dipolar cycloaddition of β-fluoroalkylated α,β-unsaturated 2-pyridylsulfones with nitrones for chiral fluoroalkylated isoxazolidines and γ-amino alcohols. *Angewandte Chemie*, 129(6), pp.1532-1536.

An Innovative Embedded Processor-Based Signal Phase Shifter Algorithm

Aven R. Hamza[1] and Mohammed A. Hussein[2]

[1]Department of Communication Engineering, Sulaimani Polytechnic University, Sulaimani, Kurdistan region – F.R. Iraq

[2]Department of Electrical Engineering, University of Sulaimani, Sulaimani, Kurdistan region – F.R. Iraq

***Abstract*—Digital filtration is widely used today in many application fields, and with the increased use of low-cost embedded processors, it can be applied to vast areas. A drawback of digital filtration algorithms is the introduction of phase angle shifts in the filtered signals, thereby creating undesirable characteristics in many application fields. In this work, low-pass filters of finite impulse response and infinite impulse response types are designed with an innovative buffering scheme to delay a digitally low-passed signal by an angle ranging from 0° to 180° for real-time signals. The application of the filtration and buffering scheme on a cost-effective embedded processor with limited signal processing capabilities opens the horizons for its applicability in many signal processing fields. In assessing its practicality, the generated filtered output signal is correlated with the original signal (a low-passed version), revealing correlation values reaching 0.99 in certain instances. The novelty of the proposed approach enables its application to a broad-spectrum area of digital signal filtration.**

***Index Terms*—Finite impulse response digital filter, Infinite impulse response Digital filter, Phase angle shifting algorithms, Signal correlation, Signals buffering.**

I. Introduction

Nowadays, most signal processing electronic systems depend on digital signal processing (DSP) systems as they are more effective in handling complex signal manipulation operations compared to analog techniques (Pandey and Pratibha, 2022). Digital filters offer advantages of easy design modifications using software as they do not rely on the environmental parameters such as temperature change and magnetic declination in addition to its cost-effectiveness and capabilities of storing digital data (Ozkan and Saday, 2018). Digital filters play a crucial role in various signal processing implementations, including spectrum analysis, digital image manipulation, audio and video processing, sonar and radar systems, as well as pattern recognition (Wang, 2022; Dallalbashi, 2020). They are operated on discrete-time signals and are classified as linear time-invariant (LTI) systems. Digital filters also have several significant properties, such as causality, stability, and feedback (recursivity), in addition to definability by unit impulse responses in the time domain. The unit impulse response sequence can have a finite or infinite duration, a classification that comprises finite impulse response (FIR) and infinite impulse response (IIR) (Dallalbashi, 2020).

Based on the mentioned properties of LTI systems, FIR filter is a non-recursive filter with a linear phase response, meaning it introduces a constant phase shift for all frequencies without distorting their relative timing. It is always stable due to its FIR (Kockanat and Karaboga, 2015; Hannah and Agordzo, 2020). In contrary, IIR filter is a recursive filter that combines both input and output samples for calculating the output signal a characteristic that can lead to instability. One significant distinction of IIR filter is its non-linear phase response, causing distinct frequency components of the input signal to undergo varying amounts of phase shift, leading to phase distortions between the output and input signals (potentially affecting the timing relationships of different frequencies). As a result, the non-linear phase response of the IIR filter may have implications in applications that depend on accurate timing relationships (Kockanat and Karaboga, 2015; Pal, 2017).

Enhancing digital filtration characteristics is under the scope of many research works. Some samples are surveyed here, and the start is with Lai and Lin (2016), who used two iterative reweighted minimax phase-error algorithms to develop linear phase IIR filters. These algorithms involve two steps in each iteration that results in phase-error function exhibiting equi-ripple characteristics over most of the passband, except for small areas near the passband edges. Furthermore, the filter's group delay response achieves nearly equi-ripple characteristics across the entire passband. In Lai (2009), one- and two-dimensional non-linear phase FIR filters with prescribed phase-error are designed. They focused on constrained least-squares and constrained chebyshev designs. This approach resulted in a minimax filter with

ARO-The Scientific Journal of Koya University
Vol. XII, No. 1 (2024), Article ID: ARO.11358. 10 pages
Doi: 10.14500/aro.11358
Received: 20 August 2023; Accepted: 27 January 2024
Regular research paper: Published: 15 February 2024
Corresponding author's email: aven.rawf@spu.edu.iq

 http://dx.doi.org/10.14500/aro.11358

the lowest energy of complex errors among the various nonunique minimax solutions, providing an effective solution for achieving desired filter performance.

In Xiao, Olivier and Agathoklis (2001), the authors introduced a new approach to implement linear phase IIR filter. The method is based on the frequency weighted least-square error optimization and integrates the Broyden-Flether-Goldfarb-Shanno (BFGS) method. The method minimizes the weighted least square cost function using the BFGS method and the results demonstrate the effectiveness of this approach in achieving excellent filter design outcomes. The work by Vijay, et al. (2022) proposes an IIR filter model referred to as parallel pipeline, which is built upon a FIR filter including the two-level pipeline-based IIR filter and a look-ahead-based models, both of which have been reported to yield substantial enhancements in filter efficiency.

In Agrawal, Kumar, and Bajaj (2020), an innovative technique is presented to design IIR filters with an almost linear phase response that uses fractional derivative constraints (FDCs). The proposed technique improves the passband response and provides a better transition width; however, there is a slight reduction in stopband attenuation in comparison to non-fractional design methods. The designed filter ensures immunity to word length issues and can be extended to accommodate larger numbers of FDCs. Moreover, the method is applicable for designing multiplier less IIR filters. In Tan and Burrus (2019) employed the Gauss-Newton method to create a linear phase IIR filter. Comparisons with an FIR filter revealed that the designed IIR filter achieves lower magnitude error, a smaller order, and reduced group delay. It maintains a consistent phase response with a linearity of $R^2 \geq 0.99$, making it particularly well-suited for applications demanding an approximately linear phase response.

In this research, a circular buffering technique is employed, exhibiting its applicability in various fields highlighted below:

1. Employing it to introduce phase correction between the original and filtered signals to single-tone signals. Besides, the circular buffering algorithm can be helpful in digitally manipulating the phase angle between transmitted and received signals within the range of 0–180°. This digital phase angle adjustment is particularly valuable in specific applications where precise control over phase relationships is crucial such as noise cancellation, audio processing in music production, communication system, medical imaging, radar, and sonar.
2. In real-time processing, acoustic delays introduce latency. The application of a circular buffering algorithm effectively mitigates this issue by compensating for the acoustic delay and it provides the capability of precisely adjusting the phase angles according to specific application's requirements.

II. Digital Filters

Digital filters that can be categorized as FIR or IIR filters hold a crucial part in the area of DSP, as they are used to attenuate unwanted signals and extract desired signals. One of the most prevalent approaches in designing digital filters is to first design an analog filter and then converts it into a corresponding digital filter. A digital filter is defined by its transfer function or difference equation, which mathematically describes its response to various input signals. The implementation usually involves basic arithmetic operations such as addition, multiplication, and division (Kuo and Lee, 2001).

A. Non-Recursive Filter (FIR Filter)

The essential component within a DSP system is the FIR filter. The unit impulse response is finite (h(n)=0 for $n < 0$ and $n \geq M$) and therefore, the unit sample response is present in the range from 0 to M-1. The transfer function of FIR filter H(z) is determined by Zhao (2022):

$$H(z) = \sum_{n=0}^{N-1} h_n z^{-n} \quad h_0 \quad h_1 z^{-1} \quad h_2 z^{-2} \qquad h_{N-1} z^{-(N-1)} \quad (1)$$

The coefficient h_n, referred to as zeros is used to design different types of filters where the end of the summation term N-1 is the filter's order. FIRs filters have the advantages of stability and linear phase response, and are non-recursive filters widely used in signal processing. In addition, they employ Fast Fourier Transform (FFT) to optimize their implementation, enabling efficient convolution computation. However, meeting design specifications often necessitates a higher number of coefficients (Nor, et al., n.d.).

B. Recursive Filter (IIR Filter)

IIR filter is a zero-pole filter, and it has an IIR (i.e., h(n)=0 for $n < 0$), hence, the unit sample response persists indefinitely from 0 to ∞. This type of filter is generally realized using feedback structure, so it is called a recursive filter. The transfer function of IIR filter is expressed as follows (Kuo and Lee, 2001)**:**

$$H(z) = \frac{\sum_{l=0}^{L-1} b_l z^{-l}}{1 + \sum_{m=1}^{M} a_m z^{-m}} \quad (2)$$

In this equation, b_1 and a_m are filter's weight coefficients. Various types of filters, including Butterworth, Chebyshev (Type I and II), and Elliptic filters, are available in which MATLAB software offers functions tailored for each specific filter type (Li, 2022). One notable advantage of IIR filters is their ability to fulfill design specifications using a reduced number of filter coefficients compared to FIR filters. Nevertheless, IIR filters can exhibit instability, potentially leading to unpredictable outputs due to their feedback-based nature. It also introduces non-linear phase shifts, causing different frequency components to experience varying delays that affect the sequential relationships within the signal (Nor, et al., n.d.).

III. Correlation Analysis

Correlation analyses play a key role in various applications, particularly in DSP. It is widely used to assess the similarity

between two signals, making it invaluable for tasks such as detecting signals corrupted by noise, measuring time delays between signals, and defining the impulse response of a system. Correlation functions are extensively employed in the analysis of random processes, where the statistical attributes of a stochastic signal such as mean, variance, and correlation functions, commonly vary over time. For a random variable signal x(n), the mean can be formulated by Kuo and Lee (2001):

$$m_x = E\left[x(n)\right] = \frac{1}{N}\sum_{n=0}^{N-1} x(n) \tag{3}$$

Where m_x is the sample mean of x(n), E [] is the expectation operator, and N is the number of samples in the short-time analysis interval. The variance of random signal x(n) can be determined by Kuo and Lee (2001):

$$\sigma_x^{\,2} = E\left[x(n)\right] = \frac{1}{N}\sum_{n=0}^{N-1}[x(n) - m_x]^2 \tag{4}$$

Correlation can be characterized into two main types: autocorrelation and cross-correlation. Auto-correlation is employed to measure the correspondence between different segments of the same signal, such as x(n). Autocorrelation can be calculated for the time instances n and k by Kuo and Lee (2001):

$$r_{xx}(n,k) = E\left[x(n)x(k)\right]$$
$$= E\left[x(n)\right]E(x(k)] = \begin{cases} 0, & n \neq k \\ \sigma_x^{\,2}, & n = k \end{cases} \tag{5}$$

Cross-correlation is utilized to measure the similarity between two different signals, such as x(n) and y(n) that can be calculated by Kuo and Lee (2001):

$$r_{xy}(n,k) = E\left[x(n)y(k)\right] = E\left[x(n)\right]E(y(k)] \tag{6}$$

The correlation coefficient, often referred to as an index of correlation, allows analyzing the connection between two signals, and it ranges from −1 to +1, providing a measure on the strength and direction of the correlation between the signals. The two random variables have a strong positive linear correlation if the correlation coefficient approaches +1 and they have a strong negative linear correlation if the correlation coefficients are nearly −1. In addition, a correlation coefficient of zero indicates that the two signals are not linearly correlated (Kohn, 2006). The calculation of cross-correlation coefficients (ρ_{xy}) between the input signal x(n) and the filtered signal y(n) is accomplished through the following equation (Kohn, 2006):

$$\rho_{xy} = \frac{\frac{1}{N}\sum_{n=0}^{N-1}\left[x(n) - m_x\right].[y(n) - m_y]}{\sqrt{\frac{1}{N}\sum_{n=0}^{N-1} x(n) - m_x^{\,2} \;\; y(n) - m_y^{\,2}}} \tag{7}$$

IV. Proposed Circular Buffer Algorithm

A circular buffer, often referred to as a ring buffer, is a simple buffer data structure that follows the First-In-First-Out ordering principle. In a circular buffer, the element that is initially added to the buffer is the first one to be subsequently out from it. Fig. 1 shows the basic mechanism used for buffering P data elements. In general, it uses two pointers: one for writing the sample in the buffer, and the other for reading it. The process begins with the initialization of the buffer, typically represented as an array of fixed-size with cyclic behavior. Initially, all buffer locations are empty and as new data arrives, it is placed at the beginning of the buffer (buf [0]), overwriting the previous data sample stored there. New data are stored in the next buffer location (buf [1]), overwriting what is available there and effectively moving clockwise. This process of replacing the oldest data with the newest data is key to the functioning of circular buffers. By continuously updating the buffer in this manner, only one location in the buffer needs to be modified for each new data sample (Smith, 2013; Tan and Jiang, 2018).

Real-time signal processing, commonly observed in the field of digital signal processors, involves the simultaneous production of the output signal while acquiring the input signal. In this field, real-time applications efficiently utilize algorithms to process groups of input samples, generating corresponding groups of output signals. To implement a real-time FIR or IIR digital filter, as depicted in Fig. 2a and b, it is necessary to have access to a specific number of the most recent samples from both the input and output. For instance, in considering the second-order IIR filter, the values of the coefficients b_0, b_1, b_2, a_0, a_1, a_2 from the input signals x(n), x(n-1), and x(n-2), in addition to the output signals y(n), y(n-1), and y(n-2), need to be known. To achieve this, these coefficients must be stored in memory and continuously updated as new samples are acquired. Circular buffering is typically employed to facilitate this process.

The proposed algorithm for aligning the phase shift of FIR and IIR digital filters involves applying circular buffering to both filters, with a chosen buffering size of 1024 for this research. When implementing circular buffering, it is essential to consider several parameters for effective processing, including:

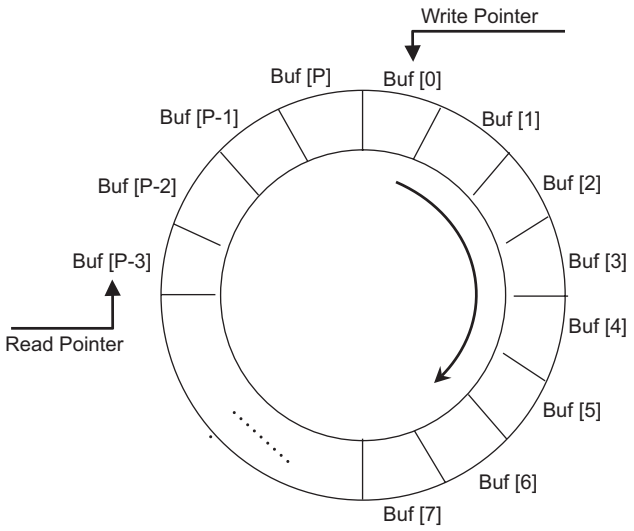

Fig. 1. Circular buffering.

http://dx.doi.org/10.14500/aro.11358

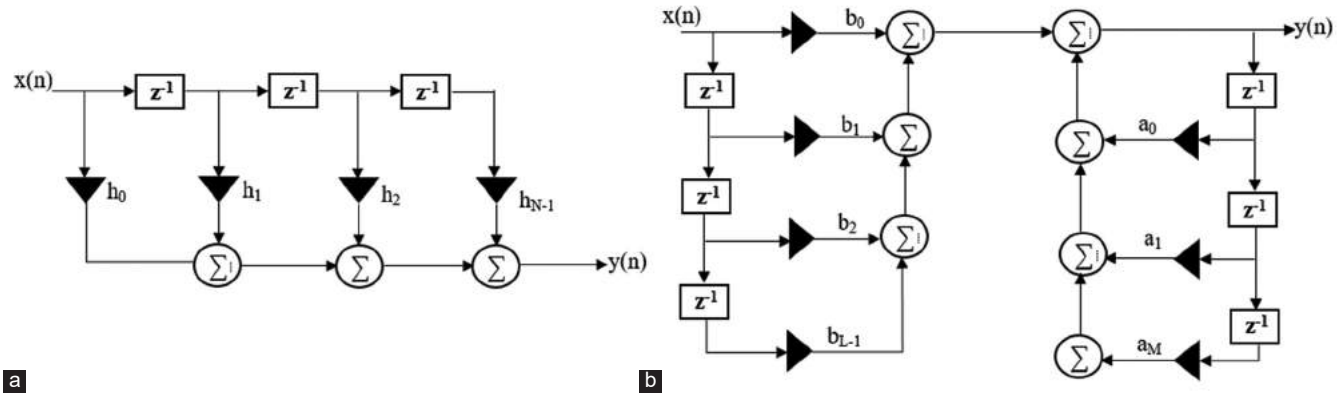

Fig. 2. Digital filter structures for (a) finite impulse response filter and (b) infinite impulse response filter.

1. Buffer Length: The circular buffer holds a total number of samples.
2. Read Pointer: This index indicates the current read position within the circular buffer x(n).
3. Write Pointer: The index is for the current write position within the circular buffer.
4. Step Size: The step size of memory in the algorithm is set to one, indicating that each sample is sequentially stored in memory.
5. Update Frequency: It is the rate at which the circular buffer is updated with new samples.

By carefully managing these parameters, the circular buffering technique enables effective phase correction of signals filtered digitally, allowing accurate signal processing and alignment.

The algorithm used for circular buffering is shown in Fig. 3. The start is with initializing the buffer and inputting signals after it gets conditioned for proper processing, from scaling to DC-offsetting till it reaches the phase of applying the filtration algorithm. The resulting filtered signal is stored in the buffer at the current index. Subsequently, the program proceeds to determine the required phase shift by analyzing signal B and assigning the calculated value to the variable J. To ensure the correctness of the required phase shift, the code checks whether J falls within the desired range. If it does not meet the criteria, corrective actions are taken to make them valid and to obtain a correct shift value. Once the condition is satisfied, signal B advances to proper buffer output position through B(J). The program continuously repeats this process until it reaches the end of the buffer and start again entering new inputs to the buffer at the start location. The filtration algorithm continues till the user ends it.

Fig. 4 shows the graphical abstract that briefly describes the proposed algorithm's methodology in addressing phase delay issues in digital filters. It provides a visual overview of the used approach and allows quick understanding of the algorithm's significance in DSP.

V. Results and Discussion

A digital FIR and IIR low pass were designed using MATLAB and Table I shows the filters parameters.

TABLE I
Digital Filters Parameters

Parameters	FIR low-pass filter	IIR low-pass filter	FIR low-pass filter	IIR low-pass filter
Sampling frequency (Hz)	44100	44100	44100	44100
Cut-off frequency (Hz)	500	500	500	500
Filter order	2	2	4	4
Frequency of the input signal	200	200	200	200

FIR: Finite impulse response, IIR: Infinite impulse response

Different filter orders were used to show performances variations effect in phase correction. The MATLAB function fir1(n,2πfc, ftype) is used to design the FIR low-pass filter. Here 'n' is the filter order, 'fc' is the normalized cut-off frequency, and 'ftype' is the type of the filter (low-pass, high-pass, band-pass, and band-stop filters). Furthermore, for designing IIR low-pass filter, the MATLAB function butter (n, 2πfc, 'low') is used. In this function, 'butter' referred to Butterworth IIR filter type, 'n' represents the order of the digital filter, 'fc' denotes the normalized cut-off frequency, and 'low' signifies that it is a low-pass filter (The MathWorks, Inc., 2023). The obtained results are presented in the next two subsections in which the first is on ones obtained from the MATLAB program, and the next is on outcomes obtained from the embedded processor.

A. MATLAB

Fig. 5a and b shows the comparison between the original signal and the filtered signal using 2nd and 4th orders FIR low-pass filters using MATLAB. The original signal is depicted by the blue line, while the filtered signal is represented by the red line. The input signal has a frequency of 200 Hz, and the filter is designed to have a cut-off frequency of 500 Hz. It is significant to mention that FIR filters have linear phase characteristics, meaning that all frequency components of the input signal experience a consistent time delay. This property ensures that the relative timing relationships within the signal are preserved without introducing significant phase distortions. The small group delay exhibited by the FIR filters contributes to the minimal phase shift between the original and filtered signals.

Fig. 6a and b depict the original and filtered signals for both a 2nd and 4th orders IIR low-pass filter using MATLAB.

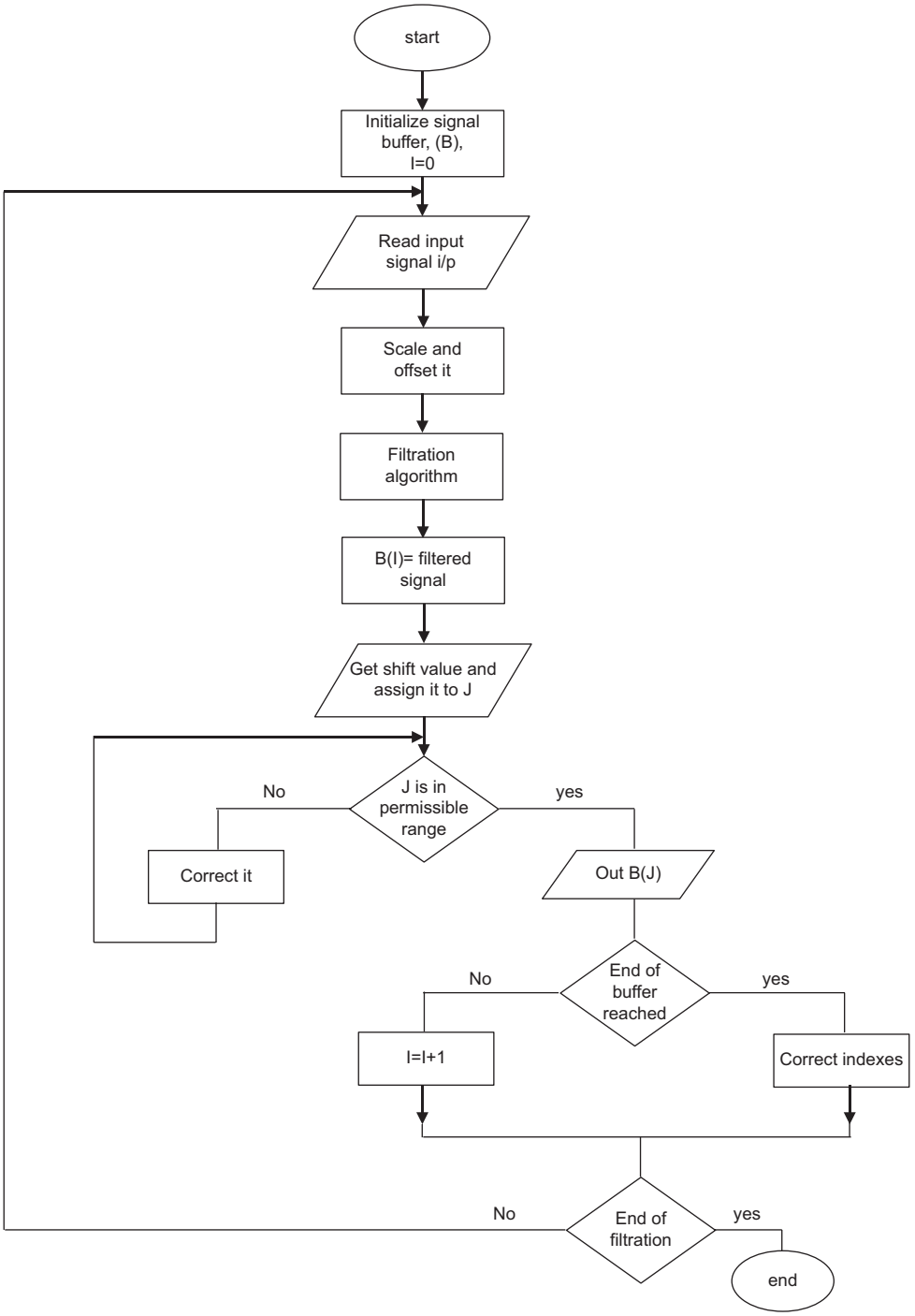

Fig. 3. Flowchart of circular buffering algorithm.

The aim of this analysis is to explore the consequences of employing an IIR low-pass filter on an input signal with a frequency of 200 Hz. Using a sampling frequency of 44100 Hz (to ensure an accurate representation of the signal's characteristics) a Butterworth filter was designed with a cut-off frequency of 200 Hz. From the figure, it is observed that the original signal and the filtered signal exhibited noticeable differences due to the non-linear phase and large group delay properties of the IIR filter. A property causing phase shift between the original and filtered signals and by increasing the filter order the phase shift increases in value.

B. Digital Processor

The connection setup for phase correction of digital filters using an embedded processor is illustrated in Fig. 7. The process can be subdivided into four distinct phases. During the initial phase, the input signals are generated according to the specifications provided in Table II (refer to section 5 results and discussion). In the second stage, a microphone is used to capture the signal. Before passing the signal to the Arduino, it is biased (dc-offset correction) to 1.4 V, as the Arduino is unable to read negative voltage values. Subsequently, in the third stage, the filter coefficients

http://dx.doi.org/10.14500/aro.11358

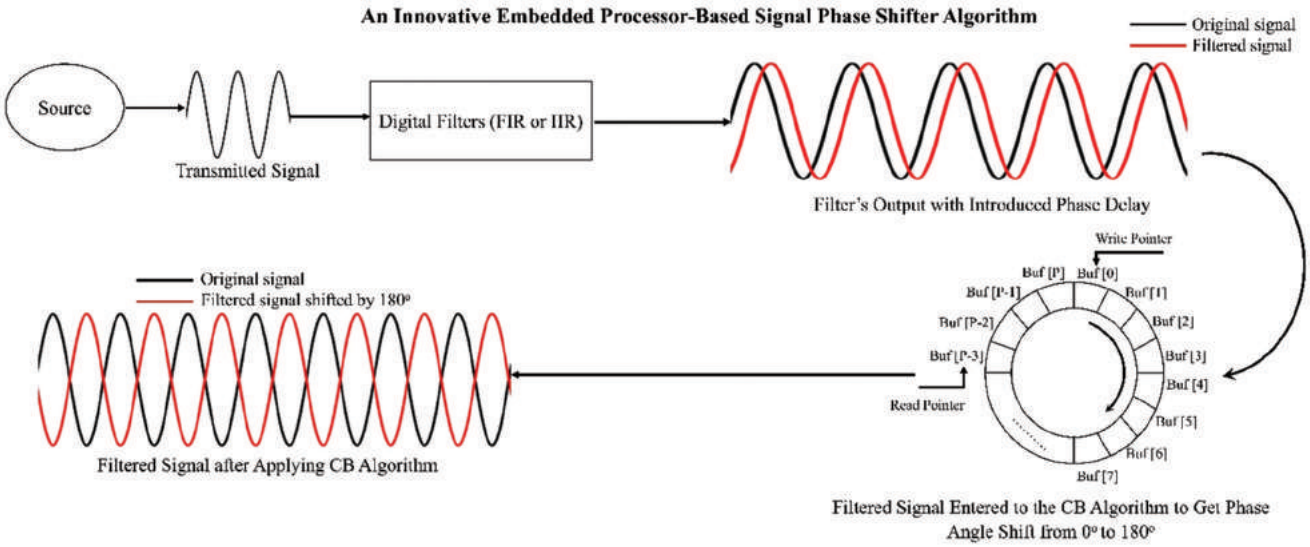

Fig. 4. Graphical abstract showing the algorithm's success in addressing phase delays in digital filters.

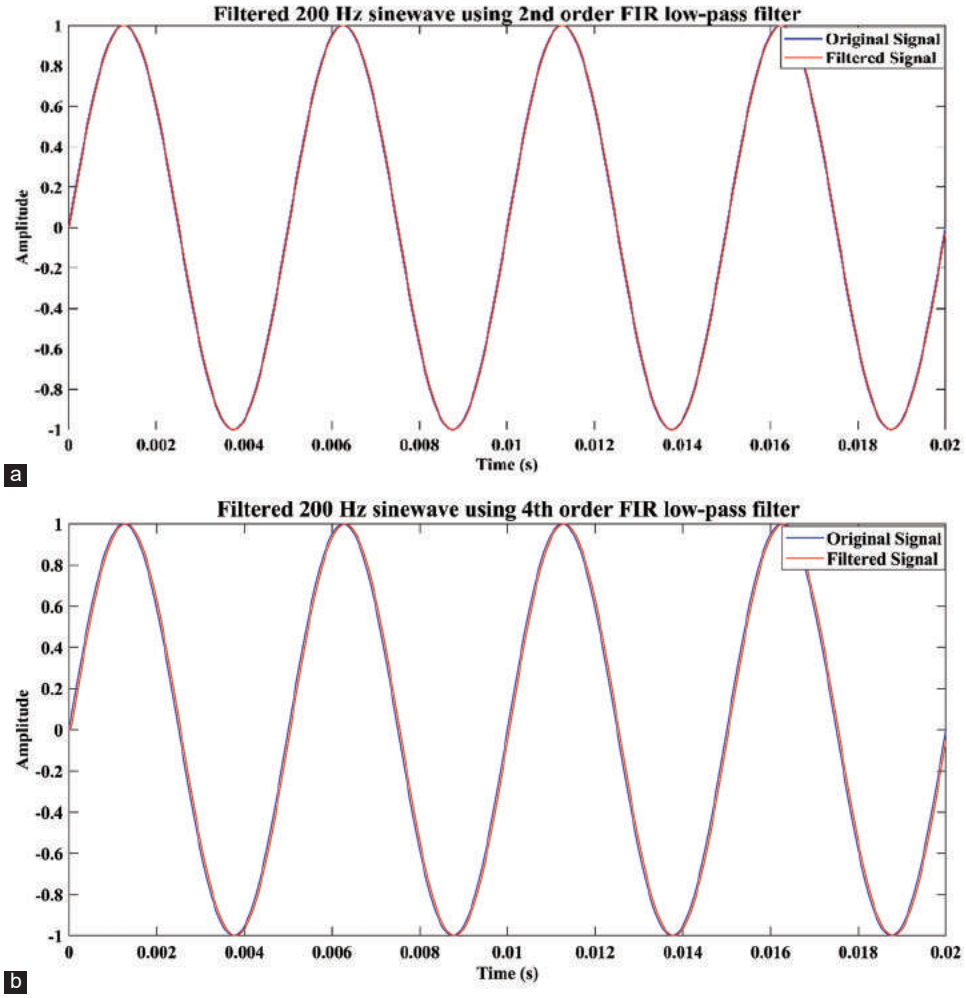

Fig. 5. Original and filtered signals for (a) 2nd order finite impulse response (FIR) low-pass filter and (b) 4th order FIR low-pass filter.

from MATLAB software are transferred to the Arduino IDE and the signals are filtered using both FIR and IIR filters implemented with the proposed algorithm. The algorithm ensures the availability of the necessary number of the

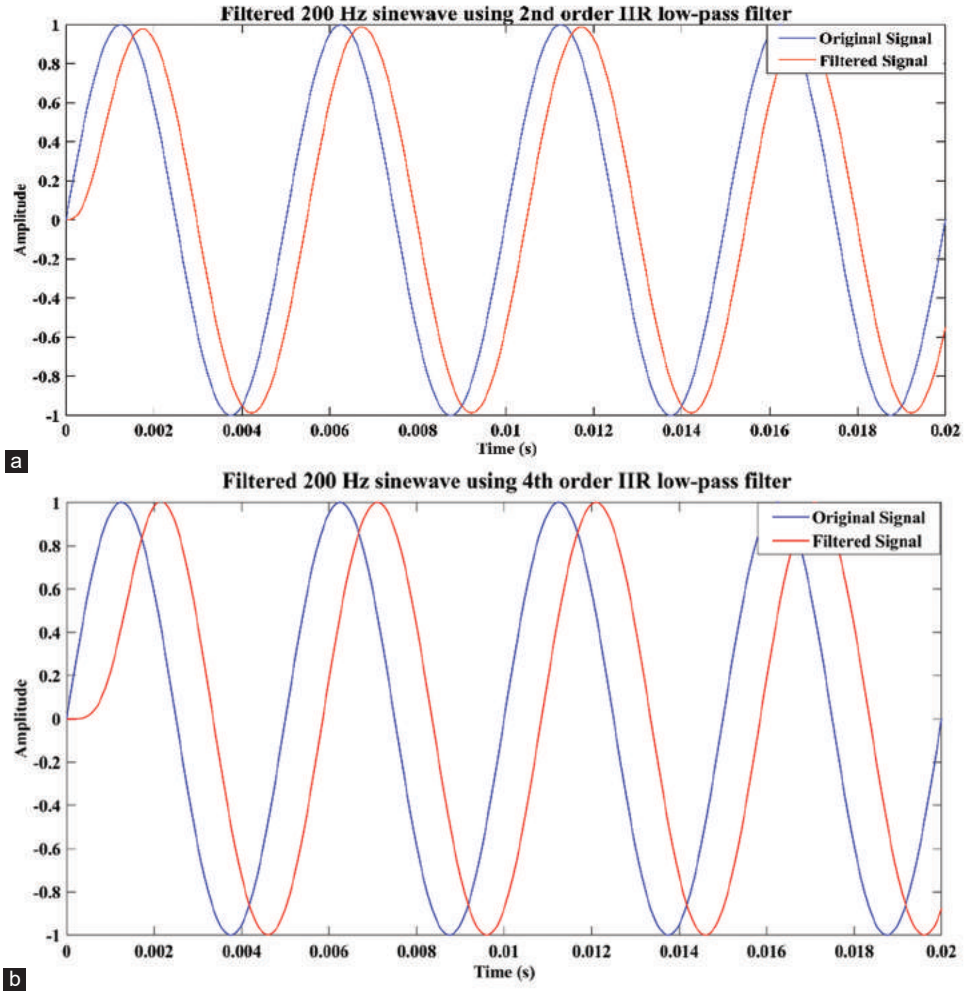

Fig. 6. Original and filtered signals for (a) 2nd order infinite impulse response (IIR) low-pass filter and (b) 4th order IIR low-pass filter.

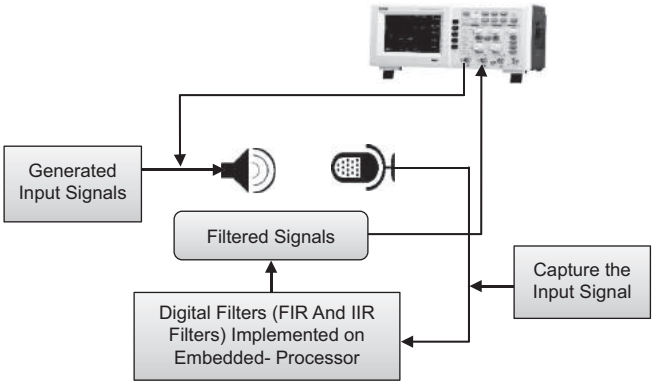

Fig. 7. Connection setup for filtration of various signals.

most recent samples for computation and by adjusting a potentiometer, the phase shift between the two signals is controlled and the refinements could be seen on channels A and B of the oscilloscope. The correlation coefficients are then obtained and monitored through the Arduino serial monitor.

Fig. 8 shows the output of the second order FIR low-pass filter. The original signal is presented by the blue color and the filtered signal is represented by the yellow color. The second-order FIR filters exhibit minimal group delay, typically just one sample, resulting in negligible impact on the filter's output. While the difference between the original and filtered signals may not be readily apparent Fig. 8a, the introduction of a circular buffer allows for the adjustment of the phase shift between the input signal and the filtered signal, ranging from 0° to 180°, as illustrated in Fig. 8b and c.

Fig. 9 illustrates the results obtained from applying a fourth order FIR low-pass filter. The filter's output is minimally affected, since FIR filter has linear phase response as shown in Fig. 9a, where the difference between the original and filtered signals is not visibly distinct. However, by implementing a circular buffer, it is possible to adjust the phase shift between the input signal and the filtered signal. In Fig. 9b and c, the circular buffer is utilized to achieve phase shifts from 0° to 180°.

Fig. 10 shows the second order IIR low-pass filter for various phase angles. Due to non-linearities of IIR filters, there is a phase shift between the original and the filtered signals of approximately 40.3°, as shown in Fig. 10a. To counteract by employing the proposed algorithm, the phase shift can be corrected, including higher ranges from 0° to

180°. Fig. 10b and c reveal the filtered signal after applying the proposed algorithm and adjusting the phase shift from 0° to 180°, as required.

Fig. 11 displays the fourth order IIR low-pass filter at different phase angles. Due to inherited non-linearity of IIR filters, a phase shift is introduced between the original and filtered signals. In this case, the phase shift is approximately 103.7°, as shown in Fig. 11a. To tackle this issue, the proposed algorithm is employed, providing the capability to dynamically adjust the phase shift within a range of 0–180°. In Fig. 11b and c, the filtered signals are presented after applying the proposed algorithm with phase shifts adjustment from 0° to 180°, as required. These figures demonstrate the effectiveness of the algorithm in manipulating the phase shift, resulting in altered phase relationships between the original and filtered signals.

A tabular approach is employed to compare the cross-correlation coefficients between FIR and IIR low-pass filters with various filtering orders and circular buffering algorithms. The cross-correlation coefficients are calculated in MATLAB and by the embedded processor. The results were nearly the same for all filter orders except the 4th order IIR low-pass filter. The proposed algorithm yields approximately a 0.99 correlation coefficient for both digital filters with different filter's orders using a 200 Hz sine wave as an input frequency, as shown in Table II.

Fig. 12 shows that the proposed algorithm results in achieving good performances values. Its versatility lies in the

TABLE II
COMPARISON OF CROSS-CORRELATION COEFFICIENTS

Filter order	Correlation coefficients from MATLAB	Correlation coefficients from Arduino	Correlation coefficients using proposed algorithm to align input and output signals	Correlation coefficients using proposed algorithm to make 180° phase shift between input and output signals
FIR 2nd order	0.99959	1	1	−0.99
FIR 4th order	0.99838	0.99	0.99	−0.98
IIR 2nd order	0.82969	0.74	0.99	−0.98
IIR 4th order	0.47993	−0.37	0.99	−0.99

FIR: Finite impulse response, IIR: Infinite impulse response

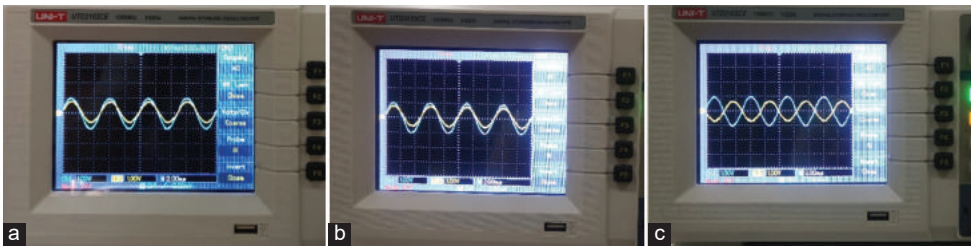

Fig. 8. Second order finite impulse response low-pass filter (a) output of the filter, (b) phase angle between the input and output of the filter is 0°, and (c) phase angle between the input and output of the filter is 180°.

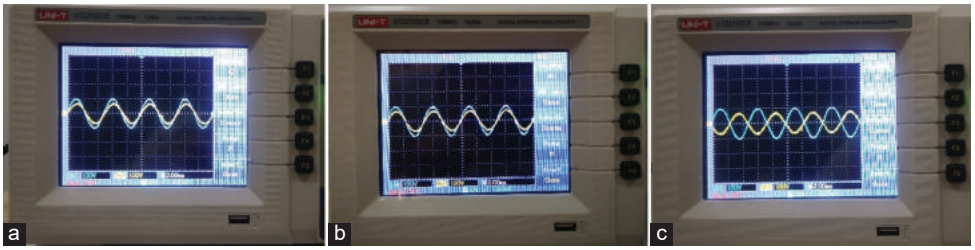

Fig. 9. Fourth order finite impulse response low-pass filter (a) output of the filter, (b) phase angle between the input and output of the filter is 0°, and (c) phase angle between the input and output of the filter is 180°.

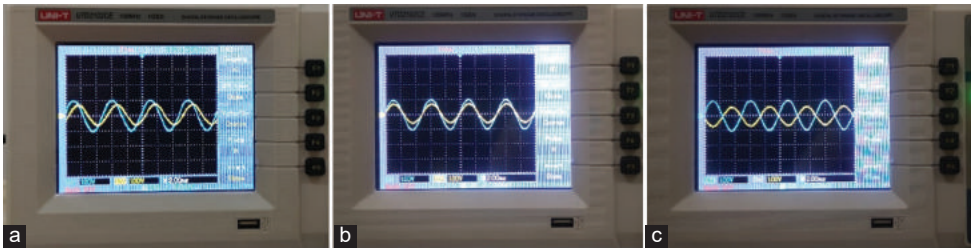

Fig. 10. Second order infinite impulse response low-pass filter (a) output of the filter, (b) phase angle between the input and output of the filter is 0°, and (c) phase angle between the input and output of the filter is 180°.

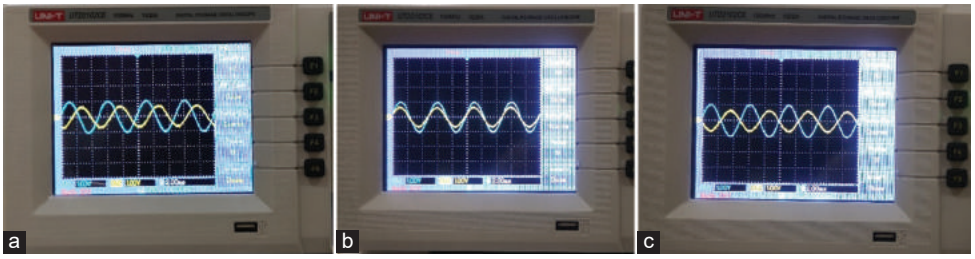

Fig. 11. Fourth order infinite impulse response low-pass filter (a) output of the filter, (b) phase angle between the input and output of the filter is 0°, and (c) phase angle between the input and output of the filter is 180°.

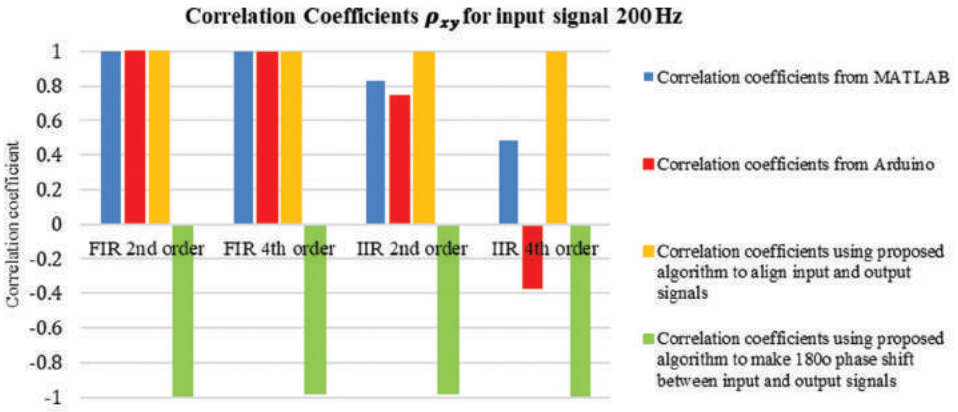

Fig. 12. Cross-correlation coefficients for finite impulse response low-pass, infinite impulse response low-pass filters with and without using circular buffering algorithm.

TABLE III
Comparison between Proposed Algorithm and Previous Works

References	Name of the Algorithm	Achievements
Lai and Lin, 2016	Two iterative reweighted minimax phase-error algorithms were used to develop linear phase IIR filters.	Filter's group delay response achieves nearly equi-ripple characteristics across the entire passband.
Tan and Burrus, 2019	Gauss-Newton method was employed to create a linear phase IIR filter.	Comparisons with an FIR filter revealed that the designed IIR filter achieves lower magnitude error, a smaller order, and reduced group delay. It maintains a consistent phase response with a linearity of $R^2 \geq 0.99$
Agrawal, Kumar, and Bajaj, 2020	An innovative technique is presented to design IIR filters with an almost linear phase response that uses fractional derivative constraints.	The proposed technique improves the passband response and provides a better transition width, however, there is a slight reduction in stopband attenuation in comparison to non-fractional design methods
Current work	New algorithm named circular buffering algorithm was used to digitally change the phase angle of both FIR and IIR digital filters.	The results show that by applying this novel buffering method, both the phase shift and the correlation between the original and filtered signals are effectively corrected. Furthermore, the proposed technique allows users to adjust values of phase shifts and obtained correlations in a flexible manner, ranging from 0° to 180° and−1 to+1, respectively.

FIR: Finite impulse response, IIR: Infinite impulse response

ability to adjust correlation coefficients according to specific application's requirement, making it highly adaptable. Consequently, the algorithm enables the alignment of a signal with another desired signal or creates any required phase shift between them. These customizable adjustments offer enhanced flexibility and optimize the algorithm's performance for various practical scenarios.

The primary objective of the current work is to enhance the efficiency of delayed signals processing in various applications. Table III presents a comparative analysis between the algorithm proposed in this work and prior research ones by precisely examining and contrasting it against them.

VI. Conclusion

This paper introduces an innovative circular buffering technique applicable to both FIR and IIR filters. In digital filters, the non-linear phase response and the large group delay create a phase shift between the input and output signals, affecting the correlation between them. To address this issue, the proposed approach involves designing digital filters using MATLAB and implementing them on an embedded processor to be applicable for real-worlds applications. To assess the effectiveness of the proposed algorithm, correlation coefficients are computed through simulations and practical implementation. The outcomes

show that by applying this novel buffering method, both the phase shift and the correlation between the original and filtered signals are effectively corrected. Furthermore, the proposed technique allows users to adjust values of phase shifts and obtained correlations in a flexible manner, ranging from 0° to 180° and -1 to +1, respectively.

In conclusion, this innovative buffering technique offers a promising solution to reduce phase shifts and enhance correlations in the DSP. It also opens possibilities for improved signal manipulation and analysis in a variety of real-world applications.

VII. Limitation and Future Work

Arduino based digital filtration and circular buffering is used as a platform in this work. It is important to acknowledge the limitation inherited by this choice, as the filter order and circular buffer length increases, the computational complexity will be a restricting factor. To address this limitation and potentially enhance the computational efficiency, future implementation of this research could explore the utilization of Field-Programmable Gate Array devices. Their parallel processing capabilities may offer a more scalable and efficient solution to handle the increased complexity associated with higher filter's orders and longer circular buffers. Thus, ensuring that the circular buffering algorithm will be capable of addressing phase delays across wide ranges of frequencies and make it frequency-independent, to effectively correct delays in complex signals with various frequency components.

References

Agrawal, N., Kumar, A., and Bajaj, V., 2020. A new design approach for nearly linear phase stable IIR filter using fractional derivative. *IEEE/CAA Journal of Automatica Sinica*, 7(2), pp.527-538.

Dallalbashi, Z.E., 2020. MatLab based design and implemetation of digita filter. *IJCSNS International Journal of Computer Science and Network Security*, 20(1), p.95.

Hannah, A.A.S., and Agordzo, G.K., 2020. A design of a low-pass FIR filter using hamming window functions in Matlab. *Computer Engineering and Intelligent Systems*, 11(2), pp.24-30.

Kockanat, S., and Karaboga, N., 2015. The design approaches of two-dimensional digital filters based on metaheuristic optimization algorithms: A review of the literature. *Artificial Intelligence Review*, 44, pp.265-287.

Kohn, A.F., 2006. Autocorrelation and Cross-Correlation Methods. In: *Wiley Encyclopedia of Biomedical Engineering*. Wiley, United States.

Kuo, S.M., and Lee, B.H., 2001. *Real-Time Digital Signal Processing: Implementaions, Applications and Experiements with the TMS320C55X*. Wiley, Hoboken, NJ, USA.

Lai, X., 2009. Optimal design of nonlinear-phase FIR filters with prescribed phase error. *IEEE Transactions on Signal Processing*, 57(9), pp.3399-3410.

Lai, X., and Lin, Z., 2016. Iterative reweighted minimax phase error designs of IIR digital filters with nearly linear phases. *IEEE Transactions on Signal Processing*, 64(9), pp.2416-2428.

Li, J., 2022. A Comparative Study of Different Filters for Speech Signals. In: *International Conference on Intelligent Systems, Communications, and Computer Networks, China*, pp.394-403.

Nor, N.M., Hashim, N.M.Z., Rosli, S.N., and Aziz, K.A.A., n.d. A *Study on Application Digital Filtering for Audio Signal Processing in Digital Signal Processing*. IEEE, United States.

Ozkan, I.A., and Saday, A., 2018. *Design and Implementation of FIR Filter based on FPGA*. Marketlinks Logo, Bulgaria.

Pal, R., 2017. *Comparison of the Design of FIR and IIR Filters for a Given Specification and Removal of Phase Distortion from IIR Filters*. IEEE, United States, pp.1-3.

Pandey, A., and Pratibha, E., 2022. A review of techniques for optimization and implementation of digital filters on FPGA. *International Journal for Research in Applied Science and Engineering Technology* (*IJRASET*), 10(6), pp.133-139.

Smith, S.K., 2013. *Digital Signal Processing: A Practical Guide for Engineers and Scientists*. Elsevier, Netherlands.

Tan, J., and Burrus, C.S., 2019. *Near-Linear-Phase IIR Filters Using Gauss-Newton Optimization*. IEEE, United States, pp.876-879.

Tan, L., and Jiang, J., 2018. *Digital Signal Processing: Fundamentals and Applications*. Academic Press, United States.

The MathWorks, Inc., 2023. *MathWorks*. Available from: https://www.mathworks.com/help/signal/ref/fir1.html [Last access on 2023 Aug 15].

Vijay, V., Rao, V., Chaitanya, K.R., Venkateshwarlu, S.C., Pittala, S., and Vallabhuni, R.R., 2022. *High-Performance IIR Filter Implementation Using FPGA*. IEEE, United States, pp.354-358.

Wang, Z., 2022. Different methods of linear phase IIR filer realization. *Highlights in Science, Engineering and Technology*, 27, pp.167-171.

Xiao, C., Olivier, J.C., and Agathoklis, P., 2001. *Design of linear phase IIR filters via Weighted Least-Squares Approximation. Proceedings* (*Cat. No. 01CH37221*). IEEE, United States, pp.3817-3820.

Zhao, H., 2022. Analysis of FIR Filter and IIR Filter for Human Speech Signal different Effects. In: *Society of Photo-Optical Instrumentation Engineers (SPIE) Conference Series, China*, pp.272-280.

Web Page Ranking Based on Text Content and Link Information Using Data Mining Techniques

Esraa Q. Naamha and Matheel E. Abdulmunim

Department of Computer Science, University of Technology-Iraq,
Baghdad, Iraq

***Abstract*–Thanks to the rapid expansion of the Internet, anyone can now access a vast array of information online. However, as the volume of web content continues to grow exponentially, search engines face challenges in delivering relevant results. Early search engines primarily relied on the words or phrases found within web pages to index and rank them. While this approach had its merits, it often resulted in irrelevant or inaccurate results. To address this issue, more advanced search engines began incorporating the hyperlink structures of web pages to help determine their relevance. While this method improved retrieval accuracy to some extent, it still had limitations, as it did not consider the actual content of web pages. The objective of the work is to enhance Web Information Retrieval methods by leveraging three key components: text content analysis, link analysis, and log file analysis. By integrating insights from these multiple data sources, the goal is to achieve a more accurate and effective ranking of relevant web pages in the retrieved document set, ultimately enhancing the user experience and delivering more precise search results the proposed system was tested with both multi-word and single-word queries, and the results were evaluated using metrics such as relative recall, precision, and F-measure. When compared to Google's PageRank algorithm, the proposed system demonstrated superior performance, achieving an 81% mean average precision, 56% average relative recall, and a 66% F-measure.**

***Index Terms*—Information retrieval, JSON API, Programmable (CSE), Search engine, World Wide Web, Web page ranking.**

I. Introduction

The World Wide Web (WWW) is evolving rapidly as a dynamic, explosive, diverse, vast, and unstructured data repository. It currently serves as an extensive knowledge reference, but it poses several challenges. Web pages are semi-structured, the web is vast, and the meaning of web information varies, affecting the quality of extracted knowledge. A comprehensive understanding and analysis of the web's data structure are essential for efficient IR. Web mining methods, including IR, Natural Language Processing (NLP), Machine Learning (ML), and Database (DB) techniques, address these challenges. To access information on the WWW, individuals utilize search engines such as Bing, Web Crawler, Iwon, Yahoo, Google, and similar platforms. These search engines consist of three main components: a crawler (spider or robot) that navigates the web and captures pages, an indexing module that parses downloaded pages, constructs an index using keywords, and stores Uniform Resource Locators (URLs) of relevant pages. When users enter keywords into a search engine's interface, the query processor compares these keywords to the index and provides users with a list of relevant pages. However, before displaying the results, search engines employ a ranking mechanism to prioritize the most relevant pages at the top and the least relevant ones at the bottom (Sharma, Yadav and Garg, 2020; Alhaidari, Alwarthan and Alamoudi, 2020). The use of web search engines has become immensely popular for efficiently finding valuable information (Sharma, et al., 2019; Guwta, 2021). These engines can be divided into two generations based on their indexing techniques (Ali and Khusro, 2021). In the early days of the web, first-generation search engines relied solely on index terms extracted from web page content. Consequently, web page searches followed a conventional document retrieval approach. However, the unique characteristics of web pages, such as their hyperlink structures and vast quantity, posed challenges for efficient searching. Consequently, users often found the retrieval accuracy and usability of these search engines unsatisfactory (Mustafa, et al., 2022; Afolabi, Makinde and Oladipupo, 2019; Phyu and Thu, 2021). First-generation search engines did not fully leverage the unique features of web pages. Second-generation search engines addressed these issues by considering the hyperlink structures associated with web pages. For instance, techniques such as Hypertext-Induced Topic Search (HITS) and Page Rank (PR) utilize web pages' hyperlink structures. Compared to first-generation search engines, algorithms like these achieve higher retrieval accuracy by assigning weights to web pages based on their hyperlink structures. However, these algorithms have a limitation in that they primarily assess the importance of web pages without taking into account the relative significance of the content between hyperlinked pages (Tyagi and Gupta,

ARO-The Scientific Journal of Koya University
Vol. XII, No. 1 (2024), Article ID: ARO.11397. 12 pages
Doi: 10.14500/aro.11397
Received: 11 September 2023; Accepted: 01 February 2024
Regular research paper: Published: 15 February 2024
Corresponding author's e-mail: cs.20.29@grad.uotechnology.edu.iq

2018; S. and A., 2019; Payal, 2020). As a result, the problem of irrelevant web pages ranking highly in response to a user's query persists. Therefore, a technique must be developed to accurately represent web page contents and provide users with relevant results (Sharma, Yadav and Thakur, 2022; Team, et al., 2023).

The aim of this study is to propose a Web IR approach that could incorporate the analysis of the page's text content, link information, and log files to rank relevant Web pages higher in the retrieved document set. By incorporating text content analysis, link analysis, and log file analysis, this approach seeks to leverage multiple component to gain a deeper understanding of Web pages, user behavior, and relevance. Each component provides valuable insights that, when integrated, can enhance the accuracy and effectiveness of Web IR. This enables the algorithm to rank relevant Web pages higher in the retrieved document set, resulting in an improved user experience and more accurate search results.

Robert and Brown (2004) introduced the PR algorithm for ranking web pages. The web consists of a complex structure of interlinked web pages, and PR calculates page rankings based on their link structures. When a page has important incoming links, the PR algorithm also considers the pages it connects to as important. PR spreads ranking influence through backlinks, assigning a high rank to a page if the sum of its backlink ranks is substantial.

Xing and Ghorbani (2004) introduced the Weighted PageRank (WPR) algorithm as an enhanced version of the PR algorithm. This system evaluates a page's popularity, determines its page rank, and takes into account the relevance of both outgoing and incoming links. The number of outgoing and incoming links a page has influences its popularity. Unlike the PR algorithm, the WPR algorithm does not evenly distribute a page's rank among its outgoing links. Instead, it assigns weight values to both inbound and outbound links based on their importance.

Kleinberg (2011) suggested the HITS algorithm, which classifies web pages into two categories known as Hubs and Authorities. Authorities are pages that contain essential content and are linked to by numerous hyperlinks. This algorithm determines a web page's rank by analyzing its content in relation to a given query. Moreover, the HITS algorithm relies on the web's structure after collecting web pages.

This paper provides the following main contributions:

- A Google programmable Customized Search Engine (CSE) is created and implemented to extract links and their associated metadata from web pages in the Google database and save it in JavaScript Object Notation (JSON) format using the Google Application Programming Interface (API), where a web site offers a set of structured Hypertext Transfer Protocol (HTTP) requests that return JSON files.
- An innovative ranking method has been proposed to re-rank links retrieved by Google using semantic metadata analysis. This method takes into account several factors, such as the number of links visited across different time periods, regions, and related topics and queries. By incorporating these elements, a novel ranking algorithm has been developed to deliver more accurate and relevant search results.
- The top link from each semantic metadata criterion serves as the root web page or seed URL for the web crawling algorithm. The goal of this step is to initiate the extraction of hyperlinks or URLs from web pages, saving them in a local database for further analysis and retrieval purposes. By starting the web crawling process with seed URLs derived from the top links of the semantic metadata criteria, the approach focuses the crawling effort on specific web pages that are likely to be more relevant or representative based on these criteria. This allows for a targeted collection of URLs, which can then be used for subsequent retrieval and analysis tasks.
- The Singular Value Decomposition (SVD) algorithm has been improved by selecting the top-k dominant features from the global feature vector and retaining 95% of the energy to determine which top-k features to consider based on the eigenvalues of the words or features. This transformation reduces a larger, high-dimensional, sparse matrix to a smaller, more manageable one.
- A new similarity measure is employed to assess the similarity between documents and a user's query. This measure takes into account multiple aspects, including syntactic, semantic, and sentiment-related similarities. By considering these various dimensions, a more comprehensive understanding of document similarity is achieved. This holistic understanding enables the ranking of documents based on their relevance to the user's query, considering multiple dimensions of similarity.

II. Background

A. Vector Space Model (VSM)

After preprocessing, handling document complexity involves transforming the resulting documents from complete text representations into document vectors that describe their contents. This vector space IR system is known as VCM. One key advantage of this representation is its ability to leverage the algebraic structure of the vector space. VCM facilitates information filtering, IR implementation, indexing, and ranking of information relevance. Using vectors in natural language, documents are represented as vectors of index terms in a multidimensional linear space. VCM possesses several attractive properties, some of which are listed below (Allahyari, et al., 2017; Shahmirzadi, Lugowski and Younge, 2019):

- It can handle heterogeneous document formats.
- It can process various types of multimedia data.
- It can work with documents in multiple languages.
- The IR process can be fully automated.
- Computational work can be performed entirely during the preprocessing stage, enabling real-time query processing.

B. Term Weighting Schemes

Clarifying term weighting involves balancing inclusiveness and accuracy in the search process, where inclusiveness relates to recall and accuracy relates to specificity. Term weighting schemes impact the performance of VSMs, which

are the functions that determine the component vectors (Jain, Vishwakarma and Jain, 2023). The performance of the VSM can be significantly enhanced through appropriate term weighting. Initially, single-term statistics were employed to weight the VSM. Term weighting involves three primary factors, with local weights assigned based on the number of term appearances within a document (Jain, Jain and Vishwakarma, 2020; Rathi and Mustafi, 2023).

Because a term that appears ten times in a document may not necessarily be 10 times as relevant as a term that appears only once in the same document, Logarithmic Term Frequency (LTF) is introduced as a local weight to adjust within-document frequency. The following equation can be employed to calculate LTF (Wu and Gu, 2014; Nassar, Kanaan and Awad, 2010):

$$LTF\left(L_{ij}\right) = Log\left(f_{ij} + 1\right) \tag{1}$$

Global weights are determined by assessing the occurrences of each term across the entire collection. Global Frequency Inverse Document Frequency (GFIDF) is often the most effective global weight. In cases where a term is present in every document or occurs only once in a single document, its weight is set to one, the minimum weight possible. Terms that occur frequently are assigned a significant weight, which is proportional to the number of documents they appear in. The GFIDF equation can be calculated as follows (Wu and Gu, 2014; Nassar, Kanaan and Awad, 2010):

$$GFIDF\left(G_i\right) = \frac{\sum_{j=1}^{n} f_{ij}}{\sum_{j=1}^{n} x\left(f_{ij}\right)} \tag{2}$$

The normalization factor takes into account differences in document lengths. Among the commonly used normalization methods in the VSM, Cosine Normalization (CN) is prominent. CN divides by the weighted document vector to ensure that the magnitude of these vectors becomes one. This method allows us to examine the angle separating the weighted vectors. Longer documents receive reduced individual term weights, which favors retrieval for shorter documents over longer ones. The CN equation can be calculated as follows (Wu and Gu, 2014; Nassar, Kanaan and Awad, 2010):

$$CN(N_j) = \left[\sum_{i=1}^{m}\left(g_i * t_{ij}\right)^2\right]^{-\frac{1}{2}} \tag{3}$$

C. Latent Semantic Indexing (LSI)

When implemented, this technique compresses document vectors into a lower-dimensional space characterized by dimensions obtained from co-occurrence patterns. LSI determines the structure of relationships between words and documents by analyzing word co-occurrence patterns. This process organizes data into a semantic arrangement that maximizes the advantages of implicit higher-level associations between text objects and words. Furthermore, it addresses challenges arising from polysemy (words with diverse meanings) and synonymy (multiple words representing the same concept) within efficient IR (Al-Anzi and Abuzeina, 2020). The SVD approach retains the most relevant distance information by reducing the dimensionality of document vectors. This reduction results in some information loss and the overlapping of content words. However, this information loss can have a positive aspect. According to P. P., (2020), loss represents noise in the initial term-document matrix, revealing latent similarities in the document collection. SVD, an orthogonal decomposition, is employed to compute the rank-t approximation where (t<*min* (*m*,*n*)) in a m × n matrix A once it has been properly constructed and weighted. As stated by Qi, Hessen and van der Heijden (2023), the original matrix A is decomposed into three new matrices—S, U, and V using the SVD method.

$$A = USV^T \tag{4}$$

The diagonal elements of S, which monotonically decrease in value and are known as the singular values of matrix A, are represented by the left and right singular vectors in the columns of U and V, respectively.

D. Similarity Measure

The measurement of similarity between a query and a document in a document collection is a crucial component of the IR system. This similarity is mathematically quantified, with the higher values indicating greater likeness. Typically, non-negative values within the range of [0,1] are used to represent similarity measures. A value of 1 indicates complete similarity, while a value of 0 indicates no similarity (Reddy, et al., 2018; Ghani and Hussain, 2021; Wang and Dong, 2020). There are many similarity measures, including cosine similarity, Jensen Shannon Divergence (JSD) similarity, sentiment similarity, and more.

A widely favored measure in IR models is cosine similarity. In this approach, queries and documents are treated as vectors in term space, allowing for easy computation through vector operations. Cosine similarity is defined as (Thakur, et al., 2019):

$$sim_{cosine} = \frac{\sum_{k=1}^{n} w_{kj}.w_{kq}}{\sqrt{\sum_{k=1}^{n} w_{kj}^{\,2}}\sqrt{\sum_{k=1}^{n} w_{kq}^{\,2}}} \tag{5}$$

JSD is a metric that quantifies the distance between two probability distributions, indicating their degree of dissimilarity or similarity. It is built on the foundation of Kullback-Leibler divergence, which is used to compare two probability distributions. The JSD between two probability distributions, Q and P, is defined as (Lu, Henchion and Namee, 2020):

$$JSD(P\,||Q) = \left(KL(P\,||M) + KL(Q\,||M)\right)/2 \tag{6}$$

Where M is the average distribution, defined as:

$$M = (P+Q)/2 \tag{7}$$

http://dx.doi.org/10.14500/aro.11397

In addition, $KL(P||Q)$ is the Kullback-Leibler divergence between Q and P, specified as:

$$KL(P||Q)=\sum p(i)*log(p(i)/q(i)) \quad (8)$$

The sum is taken over all possible values of i, where $q(i)$ and $p(i)$ represent the probabilities of i in the distributions Q and P, respectively.

According to Zheng and Fang (2010), sentiment similarity in the context of IR quantifies the similarity between queries or documents based on their emotional or sentimental content. A Python library for NLP known as TextBlob actively utilizes the Natural Language Toolkit (NLTK) to accomplish its tasks. NLTK is a library that simplifies user access to various lexical resources and enables tasks such as classification and categorization (Hazarika, Konwar and Bora, 2020).

III. Proposed System

The concept behind the proposed system relies on various measures to enhance result quality, avoiding reliance on a single measure. In this regard, diverse actions are taken for web page ranking, incorporating content, structure, and log data. The proposed system is implemented using the Python 3 language. The proposed system consists of three stages: dataset collection (link's metadata scraping), semantic metadata analysis, and Web IR. The framework of the proposed system is illustrated in Fig. 1. An overview of the proposed system for each level is provided in the following steps:

A. The first stage of the proposed system is dataset collection (link's metadata scraping), in which a Google programmable CSE is created and implemented to extract links and their

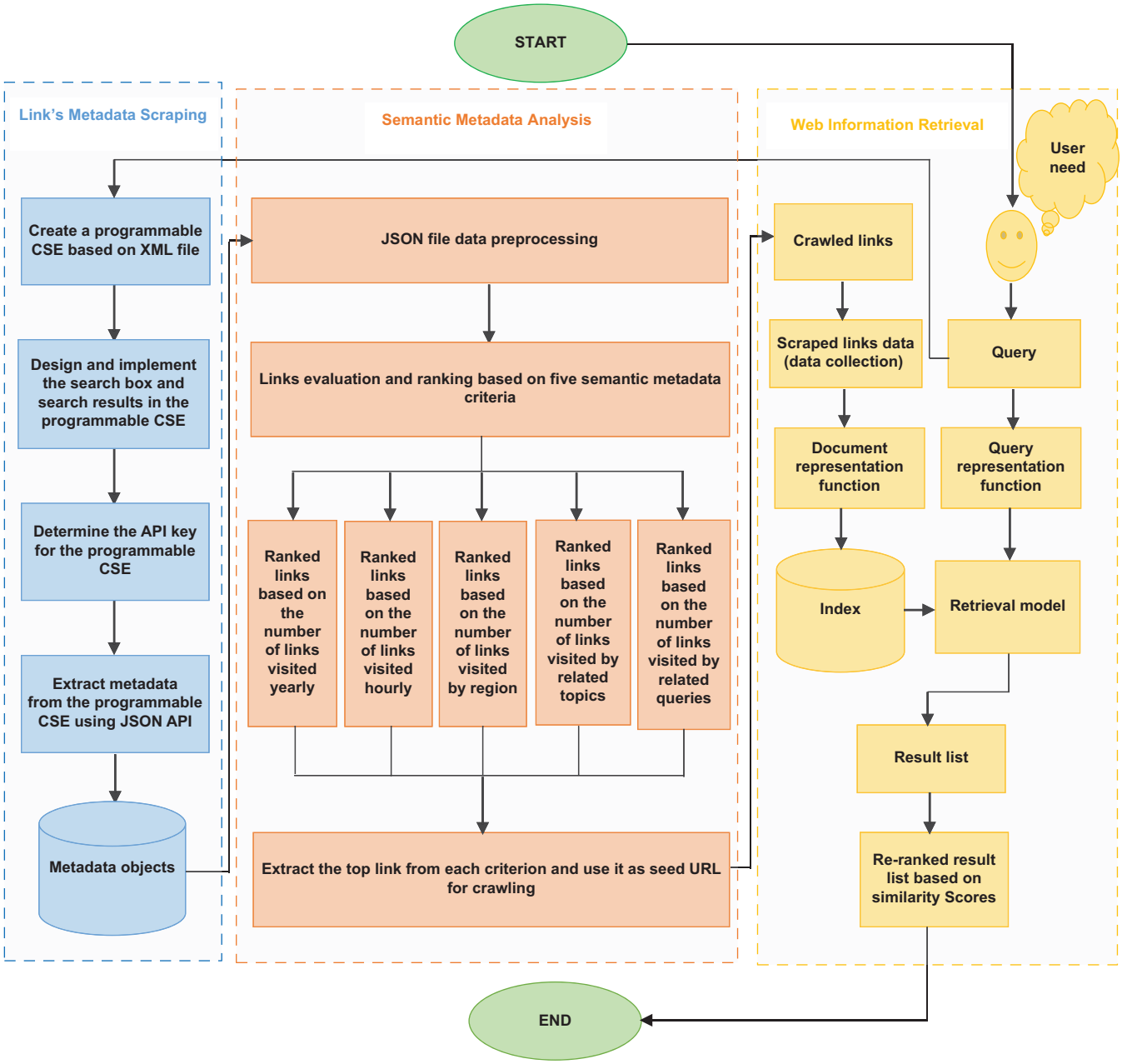

Fig. 1. Framework of the proposed system.

associated metadata from web pages in the Google database and save it in a JSON format using the Google API, where a web site offers a set of structured HTTP requests that return JSON files. The following are the details:

1. The first step involves creating a basic search engine using a programmable search engine control panel. This control panel allows users to configure and customize the search engine to meet their specific requirements. Once the search engine is set up, the control panel's overview page provides access to download annotations and context XML files. These files offer enhanced control, flexibility, and access to advanced features of the programmable search engine."
2. Once the programmable CSE has been created and configured, the next step involves integrating programmable search elements into an HTML file. This includes adding both the search box and search results to the desired location on the web site where the search engine will be embedded.
3. Afterward, the API is utilized, playing a crucial role in enabling communication between the programmable CSE and the service provider, in this case, Google. It serves as the interface through which users can interact with the programmable CSE and retrieve the desired search results and metadata. To use the API for the programmable CSE, both the search engine ID and API key should be identified and obtained initially. These are essential components that provide access to the search engine's functionalities and authenticate API requests.
4. Finally, the Custom Search JSON API is one of the powerful tools that enable developers to programmatically retrieve search results from a programmable CSE and display them on their applications or web sites. This API allows developers to make RESTful requests to obtain search results, both for web and image searches, in JSON format.

B. The second stage of the proposed system, semantic metadata analysis, is a crucial step towards improving the ranking of the links extracted by Google in the first stage. By leveraging semantic metadata criteria, the new ranking approach aims to assess the significance of these links across various dimensions such as time periods, regions, and related queries and topics. The following provides more details:

1. The first step involves pre-processing JSON file data. The JSON file is opened in write mode, and a Python dictionary is serialized as a JSON formatted stream to the opened file using the json.dump() function. This function should be set to ASCII = False if the JSON data contain non-ASCII characters. Subsequently, the json.load() function automatically returns a Python dictionary, making it easier to work with the JSON data.
2. The next step involves re-ranking the links retrieved by Google based on semantic metadata criteria. This process helps prioritize more relevant and significant links for a given query. After the re-ranking is completed, the top 10 links with the highest hits from each criterion's results are extracted and presented to users as the most relevant and significant results for their query.

C. The third stage of the proposed system, Web IR, is a critical step in further refining the ranking of relevant pages from the retrieved document set. In this stage, data mining techniques are employed to analyze both the text content and link information of the web pages to ascertain their relevance and importance. The following provides more details:

1. The first step is web page crawling, which is crucial for gathering the relevant data needed for further processing and analysis. This process involves extracting the top link from each semantic metadata criterion and using them as seed URLs in a web crawling algorithm. The objective is to retrieve all the hyperlinks or URLs present within the content of those web pages.
2. The next step involves collecting text data from each crawled link using BeautifulSoup, a powerful Python library for web scraping and parsing HTML or XML documents. Once the relevant text data are extracted, it will be saved into a local database for further analysis and processing.
3. Subsequently, the necessity for data cleansing becomes evident to generate meaningful results. In essence, meaningful terms must be extracted from the text through a series of pre-processing actions. During the preprocessing stage, tasks such as tokenization, removal of stop words, and stemming are performed.
4. Using a statistically based VCM, a document is theoretically represented as a vector of keywords, with associated weights indicating the significance of keywords within the document and across the entire document collection. Similarly, a query is represented as a list of keywords with corresponding weights, signifying the importance of keywords in the query. A term's weight in a document vector can be calculated by combining weighting algorithms for local, global, and normalization. Once term weights are determined, a document-term matrix is constructed, with content words in columns and documents in rows.
5. However, when dealing with a complex document database, the number of terms involved is often substantial. This increased dimensionality poses the challenge of inefficient calculations. Furthermore, the higher dimensionality leads to exceedingly sparse vectors and complicates the identification and utilization of relationships between terms. To address these issues, the use of LSI comes into play. This technique employs the SVD approach to effectively reduce the dimensions of the document-term matrix, facilitating analysis.
6. The final step in the IR process involves developing a ranking function that measures the similarity between query and document vectors. The proposed new similarity considers semantic, syntactic, and sentiment-related aspects to evaluate the relevance of the documents to the user's query. These similarities are then combined to obtain a final quantitative value, indicating how similar the documents are to the user's query. Based on this value, the documents are ranked accordingly.

IV. Experimental Results

This section provides an overview of the stages involved in implementing the proposed system, which include link's metadata scraping results, semantic metadata analysis results, and Web IR results.

A. First Stage Experimental Results: Link's Metadata Scraping

In this stage, the user interacts with the system by entering a search query, which in this case is "information retrieval." The system takes this query as input and proceeds to fetch relevant search results. It imports a JSON file containing links and their associated metadata, which may include page titles, keywords, descriptions, URLs, and other relevant information about the web pages. The system then creates a list of search results that are most pertinent to the user's query, based on metadata analysis and relevance evaluation. These results may be presented as a list of links, accompanied by additional information such as page titles and descriptions to help the user identify the content of each link, as illustrated in Table I.

B. Second Stage Experimental Results: Semantic Metadata Analysis

In this stage, following the creation and implementation of a programmable CSE to extract links and their associated metadata from web pages and retrieve relevant links ranked using Google's PageRank algorithm, as displayed in Table I, the links are re-ranked based on five semantic metadata criteria. The links are independently evaluated for each of the five criteria, considering their hits or occurrences related to each category. For each criterion, the top 10 links with the highest hits are selected as the most significant and relevant links for that specific criterion. The following presents the results for each of the five semantic metadata criteria:

- Criteria 1: Links are ranked based on the number of links visited yearly, which indicates the popularity and traffic of each link over the course of a year, as shown in Table II.
- Criteria 2: Links are ranked based on the number of links visited hourly, reflecting the current popularity and recent traffic patterns for each link, as shown in Table III.
- Criteria 3: Links are ranked based on the number of links visited by region, assessing the popularity of links in specific geographic locations or their relevance to different audiences in different regions, as shown in Table IV.
- Criteria 4: Links are ranked based on the number of links visited by related keyword topics. This criterion may involve identifying links that are frequently visited in the context of related keyword topics to the user's query, as shown in Table V.
- Criteria 5: Links are ranked based on the number of links visited by related search queries, identifying links that are frequently visited in the context of searches similar to the user's query, as shown in Table VI.

C. Third Stage Experimental Results: Web IR

In this stage, after re-ranking the links using the five semantic metadata criteria, the top-ranked link from each criterion is

TABLE I
The List of Relevance Search Results to the User's Search Query, "Information Retrieval"

Rank	Metadata		
	URL	Title	Description
1	https://en.wikipedia.org/wiki/Information_retrieval	Information retrieval.	Resources from a collection of information system resources which are relevant to a particular information demand.
2	https://www.geeksforgeeks.org/what-is-information-retrieval/	What is information retrieval?	A software program which stores, organizes, retrieves, and evaluates information from document repositories, especially textual information, is known as information retrieval (IR).
3	https://nlp.stanford.edu/IR-book/information-retrieval-book.html	Introduction to information retrieval.	The purpose of the book is to present a contemporary computer science perspective on IR. It depends on a course taught at the University of Stuttgart, Stanford University, and the University of Munich in a variety of formats.
4	https://www.engati.com/glossary/information-retrieval	What are the three classic models in information retrieval systems?	The three types of IR models are the non-classical IR model, the alternative IR model, and the classical IR model.
5	https://www.coveo.com/blog/information-retrieval/	The three parts of any information retrieval system.	IR systems serve as a link between users and data repositories. Querying, indexing, and presentation are, at a high level, the three major components of IR system.
6	https://www.upgrad.com/blog/information-retrieval-system-explained/	Information retrieval system explained: types, comparison and components.	An IR system is a collection of algorithms which makes it easier for documents to be shown that are relevant to searches. Simply put, it works to sort and rank documents according to user queries.
7	https://www.librarianshipstudies.com/2020/02/information-retrieval.html	Information retrieval models.	Searching for, locating, and obtaining recorded data and information from a file or database is referred to as IR.
8	https://www.sciencedirect.com/topics/computer-science/information-retrieval-systems	Information retrieval systems.	A conventional IR system experiment consists of the following elements: a set of documents, an indexing system, a predetermined set of queries, and assessment standards.
9	https://www.ncbi.nlm.nih.gov/pmc/articles/PMC3137130/	An introduction to information retrieval.	The area of computer science known as IR is concerned with processing documents which contain free text so that they may be quickly retrieved depending on keywords entered by a user.
10	https://paperswithcode.com/task/information-retrieval	Information retrieval progress.	Ranking a list of documents or search results in response to a query is the work of IR.

TABLE II
Web Page Ranking Based On Interest Over Time

Rank	URL	Hits
1	https://www.geeksforgeeks.org/what-is-information-retrieval/	100
2	https://en.wikipedia.org/wiki/Information_retrieval	74
3	https://www.upgrad.com/blog/information-retrieval-system-explained/	40
4	https://www.coveo.com/blog/information-retrieval/	26
5	https://www.ncbi.nlm.nih.gov/pmc/articles/PMC3137130/	20
6	https://paperswithcode.com/task/information-retrieval	18
7	https://nlp.stanford.edu/IR-book/information-retrieval-book.html	14
8	https://www.engati.com/glossary/information-retrieval	12
9	https://www.librarianshipstudies.com/2020/02/information-retrieval.html	11
10	https://www.sciencedirect.com/topics/computer-science/information-retrieval-systems	10

TABLE III
Web Page Ranking Based on Hourly Historical Interest

Rank	URL	Hits
1	https://en.wikipedia.org/wiki/Information_retrieval	73
2	https://www.upgrad.com/blog/information-retrieval-system-explained/	70
3	https://www.librarianshipstudies.com/2020/02/information-retrieval.html	69
4	https://paperswithcode.com/task/information-retrieval	68
5	https://www.ncbi.nlm.nih.gov/pmc/articles/PMC3137130/	63
6	https://www.geeksforgeeks.org/what-is-information-retrieval/	52
7	https://www.coveo.com/blog/information-retrieval/	44
8	https://www.engati.com/glossary/information-retrieval	42
9	https://nlp.stanford.edu/IR-book/information-retrieval-book.html	34
10	https://www.sciencedirect.com/topics/computer-science/information-retrieval-systems	28

TABLE IV
Web Page Ranking based on Interest by Region

Rank	URL	Hits
1	https://paperswithcode.com/task/information-retrieval	100
2	https://www.upgrad.com/blog/information-retrieval-system-explained/	79
3	https://www.ncbi.nlm.nih.gov/pmc/articles/PMC3137130/	36
4	https://www.geeksforgeeks.org/what-is-information-retrieval/	31
5	https://www.geeksforgeeks.org/what-is-information-retrieval/	30
6	https://www.coveo.com/blog/information-retrieval/	28
7	https://www.sciencedirect.com/topics/computer-science/information-retrieval-systems	25
8	https://www.librarianshipstudies.com/2020/02/information-retrieval.html	22
9	https://www.upgrad.com/blog/information-retrieval-system-explained/	20
10	https://www.engati.com/glossary/information-retrieval	17

TABLE V
Web Page Ranking Based on Related Topics

Rank	URL	Hits
1	https://www.sciencedirect.com/topics/computer-science/information-retrieval-systems	100
2	https://www.engati.com/glossary/information-retrieval	99
3	https://nlp.stanford.edu/IR-book/information-retrieval-book.html	66
4	https://en.wikipedia.org/wiki/Information_retrieval	30
5	https://www.coveo.com/blog/information-retrieval/	17
6	https://www.upgrad.com/blog/information-retrieval-system-explained/	10
7	https://www.librarianshipstudies.com/2020/02/information-retrieval.html	5
8	https://www.geeksforgeeks.org/what-is-information-retrieval/	4
9	https://paperswithcode.com/task/information-retrieval	3
10	https://www.ncbi.nlm.nih.gov/pmc/articles/PMC3137130/	2

TABLE VI
Web Page Ranking Based On Related Search Queries

Rank	URL	Hits
1	https://nlp.stanford.edu/IR-book/information-retrieval-book.html	100
2	https://www.geeksforgeeks.org/what-is-information-retrieval/	71
3	https://www.sciencedirect.com/topics/computer-science/information-retrieval-systems	70
4	https://www.librarianshipstudies.com/2020/02/information-retrieval.html	69
5	https://www.upgrad.com/blog/information-retrieval-system-explained/	68
6	https://www.coveo.com/blog/information-retrieval/	57
7	https://en.wikipedia.org/wiki/Information_retrieval	48
8	https://paperswithcode.com/task/information-retrieval	44
9	https://www.engati.com/glossary/information-retrieval	37
10	https://www.ncbi.nlm.nih.gov/pmc/articles/PMC3137130/	28

extracted, representing the most significant and relevant link for that criterion. These top-ranked links are then used as seed URLs for crawling. A web crawling algorithm is employed to systematically collect all the links within the content of these web pages. The objective is to explore and discover additional web pages linked from the root web pages, thereby expanding the search space and gathering more information. After extracting each possible link from the top links, the web page text data are collected from each extracted link using the BeautifulSoup scraping tool. Subsequently, the collected text data undergoes preprocessing through several techniques: tokenization, stop word removal, and stemming. At this point, the documents containing only content words are represented as vectors following the VSM of IR. The terms in the query are also represented as a query vector. The content words from the documents are placed in the columns, and the corresponding documents are in the rows of the document-term matrix. The cells in the matrix contain binary values, indicating the presence or absence of terms in the corresponding documents. Terms that occur frequently and those that appear only once are not distinguished by binary weight; instead, term frequency (how often a word or phrase appears in the relevant document) is considered. A term's weight is determined by considering its local, global, and normalization weighting schemes. The resulting document-term matrix is typically high dimensional and sparse due to the large number of terms. To address this, the SVD method, commonly used for LSI, is applied to reduce the dimensionality while retaining dominant and significant features. For example, consider a sample document-term matrix denoted as X in the context of dimensionality reduction using SVD. Table VII shows a document-term matrix with nine documents and ten terms, initially forming the feature set.

Tables VIII-X display the resulting matrix elements obtained through the SVD applied to the document-term matrix X. The SVD factorizes the matrix X into three

 http://dx.doi.org/10.14500/aro.11397

TABLE VII
DOCUMENT-TERM MATRIX

Documents	Terms (Features)									
	T_1	T_2	T_3	T_4	T_5	T_6	T_7	T_8	T_9	T_{10}
D_1	0.0000	0.5695	0.0000	0.0000	0. 4796	0.4055	0.0000	0.0000	0.0000	0.4796
D_2	0.0000	0.0000	0.0000	0.0000	0.0000	0.6931	0.3757	0.3465	0.0000	0.0000
D_3	0.0000	0.0000	0.0000	0.0000	0.0000	0.0000	0.3757	0.0000	0.0000	0.0000
D_4	0.0000	0.0000	0.2310	0.0000	0.6931	0.4435	0.3757	0.5695	0.0000	0.4796
D_5	0.0000	0.0000	0.0000	0.5695	0.0000	0.3465	0.0000	0.0000	0.3857	0.0000
D_6	0.6931	0.4435	0.3857	0.0000	0.0000	0.4055	0.0000	0.0000	0.2310	0.0000
D_7	1.0986	0.6931	0.4055	1.0986	0.0000	0.2310	0.0000	0.3857	0.3465	0.0000
D_8	0.4435	0.0000	0.2310	0.4435	0.0000	0.3465	0.0000	0.0000	0.0000	0.0000
D_9	0.4435	0.5695	0.3857	0.5695	0.0000	0.0000	0.0000	0.0000	0.0000	0.0000

TABLE VIII
MATRIX U (DOCUMENT×DOCUMENT MATRIX)

−0.1349	−0.2729	−0.1618	−0.4403	0.7357	−0.0484	−0.2167	−0.2213	−0.2186
−0.1525	−0.4215	0.6911	−0.0219	−0.1221	−0.3667	0.3545	−0.0364	0.2114
−0.0137	−0.1428	−0.0284	0.1846	−0.2607	−0.236	−0.2333	−0.7336	−0.4778
−0.1920	−0.7976	−0.3913	0.1966	−0.1377	0.1438	−0.1904	0.2228	0.0982
−0.1642	−0.0298	−0.4653	0.1179	0.332	0.4638	−0.5669	−0.2121	0.2238
−0.3748	0.0532	−0.0049	−0.7739	−0.4096	−0.0031	−0.2974	0.0224	0.0319
−0.7796	0.2643	−0.0444	0.3361	0.1631	−0.3178	−0.0662	0.221	−0.1632
−0.2689	−0.0040	0.1456	0.0412	−0.2158	0.6781	0.4732	−0.0094	−0.4176
−0.2720	0.1330	−0.3204	0.0738	−0.076	0.1047	0.3139	−0.5171	0.6462

TABLE IX
EIGEN VALUE MATRIX S

6.3313	0.0000	0.0000	0.0000	0.0000	0.0000	0.0000	0.0000	0.0000	0.0000
0.0000	3.8887	0.0000	0.0000	0.0000	0.0000	0.0000	0.0000	0.0000	0.0000
0.0000	0.0000	2.0543	0.0000	0.0000	0.0000	0.0000	0.0000	0.0000	0.0000
0.0000	0.0000	0.0000	1.735	0.0000	0.0000	0.0000	0.0000	0.0000	0.0000
0.0000	0.0000	0.0000	0.0000	1.5891	0.0000	0.0000	0.0000	0.0000	0.0000
0.0000	0.0000	0.0000	0.0000	0.0000	1.1554	0.0000	0.0000	0.0000	0.0000
0.0000	0.0000	0.0000	0.0000	0.0000	0.0000	1.0549	0.0000	0.0000	0.0000
0.0000	0.0000	0.0000	0.0000	0.0000	0.0000	0.0000	0.665	0.0000	0.0000
0.0000	0.0000	0.0000	0.0000	0.0000	0.0000	0.0000	0.0000	0.3829	0.0000

matrices: a diagonal matrix (Eigenvalue matrix), a left singular matrix (document x document matrix), and a right singular matrix (term x term matrix), as shown in Eq. (4):

$$X = [Document\ Matrix]x$$
$$[Eigenvalue\ Matrix]x\ [Term\ Matrix]^T$$

The diagonal matrix, presented in Table IX, displays a distinct arrangement, with Eigenvalues neatly ordered along the diagonal. These Eigenvalues symbolize the relevance assigned to corresponding terms or features in the initial document-term matrix.

Consider the absolute values in the first column of the term matrix, which, when sorted, represents the terms in order of their relative importance. Term T1 emerges as the most significant, while term T10 is the least significant. By selecting the top-k most significant terms, all inconsequential terms can be removed from the global feature set once the significant terms are identified. The criteria for selecting the top-k terms are to retain 95% of the energy from the Eigen values of the term vectors. The sorted characteristics and their corresponding Eigenvalues are presented in Table XI.

The sum of all Eigenvalues, which equals 18.8566, represents the total energy of the Eigenvalue matrix. The energy for the top-k Eigenvalues, where k can be one of 6, 7, 8, 9, or 10. To retain 95% of the energy, the top 7 terms are considered, leading to a reduction in the dimensions of the initial matrix from 10 terms to 7 terms. After achieving dimension reduction and structuring the information systematically in a semantic format within the document-term matrix, the next step involves introducing a ranking function. This function assesses the similarity between query and document vectors, aiding in document retrieval. In this system, a new similarity measure is proposed, incorporating three different measures: syntactic similarity, semantic similarity, and sentiment similarity, resulting in a more accurate and meaningful document ranking. Syntactic similarity utilizes the cosine similarity measure, which calculates the cosine of the angle between the query and document vectors, as shown in Eq. (9):

$$\text{Syntactic Simalirity}(d,q) = \text{Coscos}(d,q) \quad (9)$$

The JSD similarity metric is employed to assess the semantic similarity between the query and document vectors. To measure the semantic relationship between terms in the query and document, JSD calculates the divergence between their probability distributions, as indicated in Eq. (10):

$$\text{Semantic similarity}(d,q) = \text{JSD}(\theta_d, \theta_q) \quad (10)$$

To analyze sentiment polarity, TextBlob, a Python library for sentiment analysis, is utilized to determine whether the sentiment expressed in the query matches that of the documents, as shown in Eq. (11):

$$\text{Sentiment Simalirity}(d,q) = \text{Polarity}(d) \times \text{Polarity}(q) \quad (11)$$

After calculating the individual similarity values for each aspect, the final similarity score is determined by combining them using the arithmetic mean. The average similarity is calculated by summing up the similarity scores for syntactic similarity, semantic similarity, and sentiment-related similarity, and then dividing the sum by 3, as shown in Eq. (12):

$$\frac{\text{Syntactic Simalirity+Semantic similarity} \\ \text{+Sentiment Simalirity}}{3} \quad (12)$$

TABLE X
MATRIX V (TREM X TERM MATRIX)

0.5732	0.2644	−0.1547	−0.2447	−0.3912	−0.153	−0.0059	0.2726	−0.5145	−0.0462
0.3697	0.1136	−0.2804	−0.2699	0.3627	−0.504	0.0956	−0.4121	0.348	−0.1155
0.2981	−0.0903	−0.2996	−0.0728	−0.4254	0.5242	0.221	−0.0907	0.5108	0.1849
0.4808	0.2294	0.0765	0.7154	0.3332	0.2537	0.0205	−0.1136	−0.0968	−0.0231
0.0819	−0.4804	−0.4597	−0.0272	0.2896	0.207	−0.1555	0.3372	−0.058	−0.5314
0.3505	−0.4191	0.6769	−0.3264	0.1406	0.1585	0.2636	−0.0745	−0.0593	−0.1155
0.0869	−0.5553	−0.0584	0.3203	−0.4143	−0.2726	−0.2461	−0.4879	−0.1829	0.0000
0.1775	−0.2456	0.1243	0.2943	−0.0609	−0.4679	0.0928	0.6126	0.3824	0.2311
0.2083	0.074	0.2025	−0.1844	0.0538	0.1237	−0.8821	0.047	−0.2418	0.1386
0.0516	−0.2753	−0.2692	−0.1405	0.3763	0.0826	0.025	0.0022	−0.3144	0.7625

TABLE XI
SORTED FEATURE CORRESPONDING EIGEN VALUES

Features before sorting		Features after sorting		Eigen values	
T1	0.5732	T1	0.5732	EV1	6.3313
T2	0.3697	T4	0.4808	EV2	3.8887
T3	0.2981	T2	0.3697	EV3	2.0543
T4	0.4808	T6	0.3505	EV4	1.7350
T5	0.0819	T3	0.2981	EV5	1.5891
T6	0.3505	T9	0.2083	EV6	1.1554
T7	0.0869	T8	0.1775	EV7	1.0549
T8	0.1775	T7	0.0869	EV8	0.6650
T9	0.2083	T5	0.0819	EV9	0.3829
T10	0.0516	T10	0.0516	EV10	0.0000

Subsequently, the documents are ranked in descending order of their final similarity scores. Documents with higher similarity scores are given higher priority in search results, as they are considered more relevant to the user's query, as shown in Table XII.

V. EVALUATION AND DISCUSSIONS

The proposed system's performance is assessed using three measures: precision, recall, and the F-measure. Precision gauges the accuracy of the system and is calculated by dividing the number of relevant web pages retrieved by the total number of web pages retrieved. Recall measures the quantity of relevant web pages retrieved and is calculated by dividing the number of relevant web pages retrieved by the total number of relevant web pages retrieved by both the proposed system and Google. Average Precision (AP) or Average Relative Recall (AR) values are calculated as the average of all precision or relative recall values for single-word and multi-word queries, respectively. Mean Average Precision (MAP) or Mean Average Relative Recall (MAR) is determined by computing the mean of the average precision or average relative recall values for single-word and multi-word queries. The F-measure is a composite metric that balances precision and recall, yielding a single score that encapsulates the overall system performance. The evaluation criteria for the proposed system are described below.

$$\text{Precision} = \frac{\text{Total Web pages relevant for each query}}{\text{Total Web pages retrieved for that query}} \quad (13)$$

$$\text{Recall} = \frac{\text{Total Web pages retrieved by proposed system}}{\text{Total Web pages retrieved by the proposed system and Google}} \quad (14)$$

$$\text{F}-\text{measure} = \frac{2 \times \text{MAP} \times \text{MAR}}{\text{MAP} + \text{MAR}} \quad (15)$$

The search results of the proposed system are compared to those of Google. Google's page ranks are checked by either installing the Google toolbar or using one of the page rank checking tools, such as www.prchecker.info. When compared to Google's search results, the proposed system consistently exhibits superior relative recall, precision, and F-measure values. This demonstrates that the proposed system performs better in terms of quantity, accuracy, and overall performance. The proposed system has been tested with single-word and multi-word queries. Figs. 2-7 present the results graphically.

The precision values of the proposed system, compared to Google, for single-word and multi-word queries are displayed in Figs. 2 and 3, respectively. These values assess the accuracy and relevance of the retrieved results, calculated as the precision in relation to the total number of results. In both figures, the Y-axis represents accuracy values, which indicate the ratio of relevant web pages retrieved to the total number of retrieved web pages for each query. The X-axis represents various queries, labeled as Q1 to Q10. Both figures clearly demonstrate that the proposed system outperforms Google in terms of precision for both multi-word and single-word queries. This suggests that the proposed system excels in locating relevant web pages across a wide range of search query types.

Figs. 4 and 5 focus on the relative recall values of the proposed system compared to Google for both multi-word and single-word queries. Recall is a measure of how effectively a system retrieves all relevant results, and relative recall indicates the ratio of relevant results retrieved by a system compared to the total number of relevant results available. In both figures, the X-axis represents different queries, labeled as Q1 to Q10, and the Y-axis represents relative recall values. Both figures clearly demonstrate that the proposed system outperforms Google in terms of relative recall for both multi-word and single-word queries. This suggests that the proposed system is more effective at retrieving a higher proportion of relevant web pages, making it advantageous for users who prioritize comprehensive and relevant search results.

 http://dx.doi.org/10.14500/aro.11397

TABLE XII
RANKED WEB PAGES BASED ON THEIR SIMILARITY TO THE USER'S QUERY USING THE PROPOSED NEW SIMILARITY

No.	URL	Semantic Similarity	Syntactic Similarity	Sentiment Similarity	Average Similarity
1	https://en.wikipedia.org/wiki/Information_retrieval	0.9961	0.9547	0.9871	0.9793
2	https://www.geeksforgeeks.org/issues-in-information-retrieval	0.9944	0.9172	0.9663	0.9593
3	https://nlp.stanford.edu/IR-book/information-retrieval.html	0.9914	0.8687	0.9601	0.9401
4	https://paperswithcode.com/methods/category/information-retrieval-methods	0.9897	0.8475	0.9856	0.9409
5	https://www.sciencedirect.com/topics/computer-science/information-retrieval-systems	0.9860	0.8034	0.9678	0.9191
6	https://www.sciencedirect.com/topics/computer-science/information-retrieval-systems	0.9834	0.7838	0.9854	0.9175
7	https://medium.com/@soumya.vkshukla/information-retrieval-a-brief-overview-173bba8fe0e9	0.9799	0.7605	0.9760	0.9055
8	https://www.linkedin.com/pulse/information-retrieval-basics-sagar-khatavkar	0.9769	0.7280	0.9648	0.8899
9	https://www.kaggle.com/code/vabatista/introduction-to-information-retrieval	0.9740	0.6866	0.9802	0.8803
10	https://en.wikipedia.org/wiki/Compound-term_processing	0.9727	0.6383	0.9695	0.8601

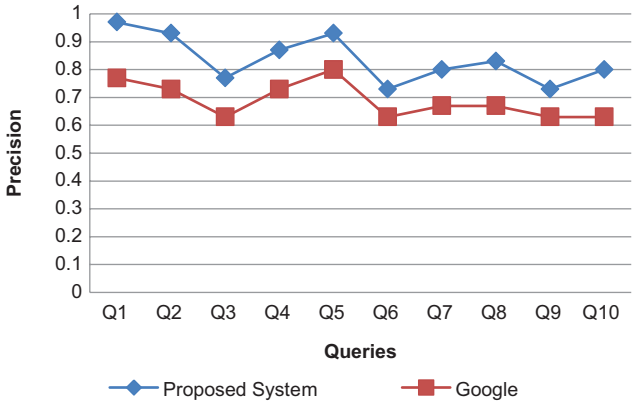

Fig. 2. Precision of single-word queries.

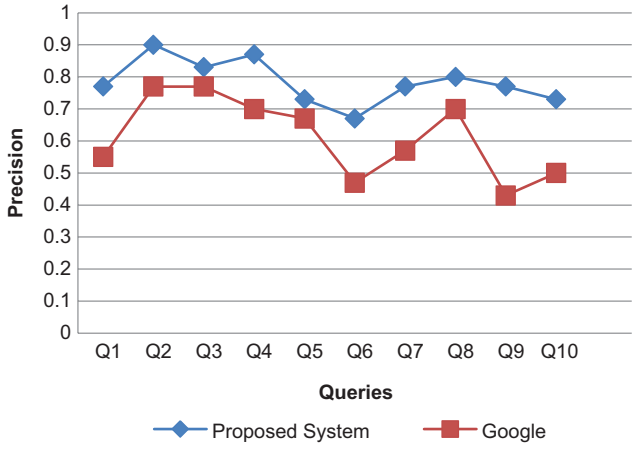

Fig. 3. Precision of multi-word queries.

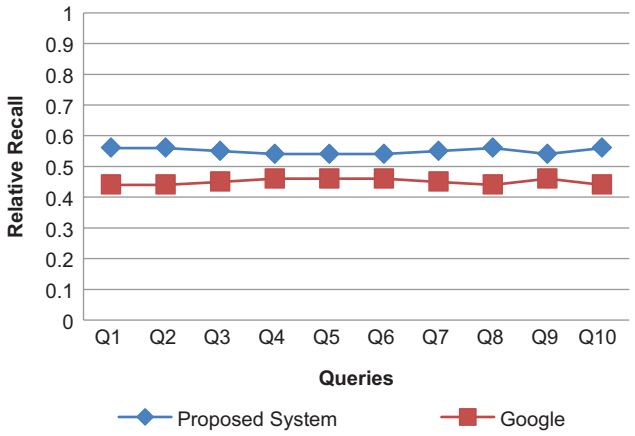

Fig. 4. Relative recall of single-word queries.

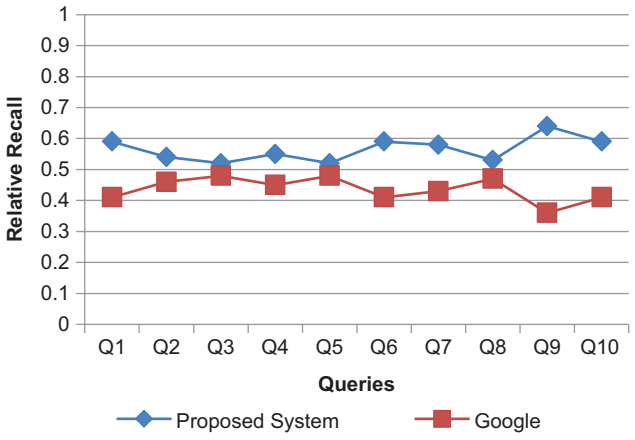

Fig. 5. Relative recall of multi-word queries.

Fig. 6 presents the AR and AP values of the proposed system and Google for both multi-word and single-word queries. The X-axis displays the evaluation measures, including APS (Average Precision of Single-Word Queries), APM (Average Precision of Multi-Word Queries), ARS (Average Relative Recall of Single-Word Queries), and ARM (Average Relative Recall of Multi-Word Queries), while the Y-axis represents the values of AR and AP. The graph clearly illustrates that, for both multi-word and single-word queries, the AR and AP values of the proposed system surpass those of Google. In other words, on average, the proposed system retrieves a higher proportion of relevant web pages compared to Google's search results for both query types. Users who

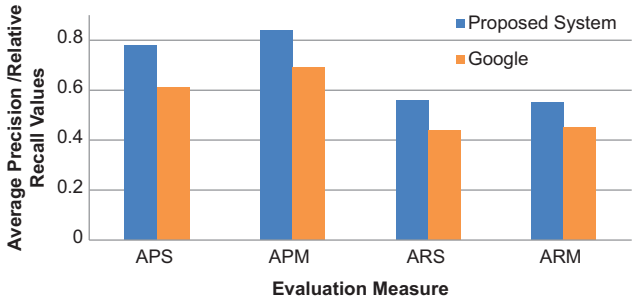

Fig. 6. Average Precision and Average Relative Recall of the proposed system and Google.

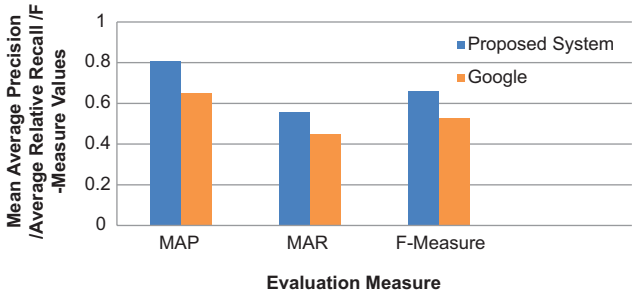

Fig. 7. F-measure of the proposed system and Google.

prioritize accuracy and comprehensiveness in their search results may find the proposed system to be the superior choice due to its consistently higher AP and AR performance compared to Google.

Fig. 7 compares the F-measure values of the proposed system and Google. The X-axis represents the evaluation measures: MAP, MAR, and F-measure. The Y-axis represents the values of these measures in fractions. Fig. 7 clearly demonstrates that the proposed system outperforms Google in terms of relative recall, precision, and F-measure. This indicates that the proposed system excels in retrieving relevant web pages with greater accuracy and comprehensiveness compared to Google's search results.

VI. Conclusions

This paper aims to develop an efficient approach for Web IR to enhance the search process and assist users in finding relevant content based on their queries. The proposed system ranks web pages by considering both the structural links of the pages, the content within them, and log files, resulting in high precision. By adopting this approach, we achieve high-quality results. The proposed method involves data collection from Google using an API, followed by storing this data in a database for further analysis. Utilizing an API for data retrieval offers advantages such as automated data collection, customizable requests, speed, efficiency, security, standardization, scalability, and real-time data updates. These qualities make it a preferred choice for many developers and researchers. Rate limiting is a challenge associated with using API for data collection from Web sites. Rate limiting refers to a restriction on the number of API requests that can be made within a certain time frame. This is done to prevent server overload and maintain Web site performance. Therefore, developers must optimize their code and implement techniques such as throttling to avoid exceeding the rate limit. To address the limitations of traditional ranking methods, such as Google's PageRank algorithm, a web page ranking method based on the number of links visited is proposed. This approach integrates semantic metadata analysis and considers factors such as visitation frequency, regional relevance, and related topics and queries to re-rank the links retrieved from Google. The goal is to provide more relevant, personalized, and context-aware search results. However, there are extra effort on crawlers to fetch the visit counts of Web pages from Web servers. Initiating the web crawling process with seed URLs derived from the top links of each semantic metadata criterion is a strategic approach that allows for targeted and efficient URL collection. Focusing the crawling effort on specific web pages, deemed relevant based on semantic criteria, enhances the quality and relevance of collected data, leading to improved retrieval and analysis tasks. Term-weighting schemes are vital in the VSM for document representation and IR. By judiciously selecting and combining term-weighting schemes, VSM can effectively rank documents, improving the accuracy and relevance of search results. Improved SVD is a powerful technique for dimensionality reduction in text mining and other data analysis tasks. It effectively filters out noise and less significant variations in data, resulting in a cleaner representation and enabling more efficient and effective data analysis with reduced memory and computational requirements. Finally, this paper introduces a new similarity measure for document retrieval, offering a more comprehensive understanding of how documents relate to user queries. This measure enables a more precise ranking of content.

VII. Future Work

Research work illustrated in this paper can be stretched in many directions that will help in enhancing the results thus obtained.

1. Web page data may be collected by using screen scraping, where data are extracted from the source code of a Web site with an HTML parser or regular expression matching.
2. The weight of a term in a document vector may be determined by using information gain.
3. The high dimensionality problem may be addressed by performing the rough set based on feature selection and by designing the rough set based on membership functions.
4. The system may be modified to have the provision of refining the input query by using the relevance feedback technique.
5. Evaluation can be carried out on techniques for documents in various languages, as well as on the study of how language affects the performance of the retrieval process.

References

Afolabi, I.T., Makinde, O.S., and Oladipupo, O.O., 2019. Semantic web mining for content-based online shopping recommender systems. *International Journal of Intelligent Information Technologies*, 15(4), pp.41-56.

Al-Anzi, F., and Abuzeina, D., 2020. Enhanced latent semantic indexing using cosine similarity measures for medical application. *International Arab Journal of Information Technology*, 17(5), pp.742-749.

Alhaidari, F., Alwarthan, S., and Alamoudi, A., 2020. User preference based weighted page ranking algorithm. In: *ICCAIS 2020-3rd International Conference on Computer Applications and Information Security*, pp.1-6.

Ali, F., and Khusro, S., 2021. Content and link-structure perspective of ranking webpages: A review. *Computer Science Review*, 40, p.100397.

Allahyari, M., Pouriyeh, S., Assefi, M., Safaei, S., Trippe, E.D., Gutierrez, J.B., and Kochut, K., 2017. A Brief Survey of Text Mining: Classification, Clustering and Extraction Techniques. *Journal of Intelligent Information Systems,* 2017, 1(1), pp.1-13

Ghani, W.A., and Hussain, A., 2021. Applying similarity measures to improve query expansion. *Iraqi Journal of Science*, 62(6), pp.2053-2063.

Guwta, M., 2021. *Information Retrieval for Silt'e Text Using Latent Semantic Indexing*. M.C. Thesis. Bahir Dar University.

Hazarika, D., Konwar, D., and Bora, D.J., 2020. Sentiment Analysis on Twitter by Using TextBlob for Natural Language Processing. In: *Proceedings of the International Conference on Research in Management and Technovation 2020*. Vol. 24, pp.63-67.

Jain, S., Jain, S.C., and Vishwakarma, S.K., 2020. Analysis of text classification with various term weighting schemes in vector space model. *International Journal of Innovative Technology and Exploring Engineering*, 9(10), pp.390-393.

Jain, S., Vishwakarma, S., and Jain, S.C., 2023. Analysis of term weighting schemes in vector space model for text classification. *Journal of Integrated Science and Technology*, 11(2), p.469.

Joby, P.P., 2020. Expedient information retrieval system for web pages using the natural language modelling. *Journal of Artificial Intelligence and Capsule Network*s, 2(2), pp.100-110.

Kleinberg, J.M., 2011. Authoritative sources in a hyperlinked environment. In: *The Structure and Dynamics of Networks*. Princeton University Press, Princeton, pp.514-542.

Lu, J., Henchion, M., and Namee, B.M., 2020. Diverging Divergences: Examining Variants of Jensen Shannon Divergence for Corpus Comparison Tasks. In: *LREC 2020-12th International Conference on Language Resources and Evaluation, Conference Proceedings*. Vol. 2, pp.6740-6744.

Mustafa, A.B., Ghulam, S.K., Naadiya, M., and Sheeba, M., 2022. Web content mining techniques for structured data: A review. *Sindh Journal of Headways in Software Engineering*, 1(1), pp.1-10.

Nassar, M.O., Kanaan, G., and Awad, H.A.H., 2010. Comparison between Different Global Weighting Schemes. In: *Proceedings of the International MultiConference of Engineers and Computer Scientists 2010, IMECS 2010*. Vol. I, pp.690-692.

Patel, S.H., and Desai, A.A., 2019. Link analysis to discover relevant documents using information retrieval. *International Journal of Computer Application*s, 178(10), pp.23-27.

Payal, L.S., 2020. A study of different web mining types. *Anveshana's International Journal of Research in Engineering and Applied Sciences*, 5(3), pp.30-33.

Phyu, A.P., and Thu, E.E., 2021. Short survey of data mining and web mining using cloud computing. *International Journal of Advanced Networking and Applications*, 12(05), pp.4725-4731.

Qi, Q., Hessen, D.J., and van der Heijden, P.G.M., 2023. Improving Information Retrieval Through Correspondence Analysis Instead of Latent Semantic Analysis. *Journal of Intelligent Information Systems*, 2023, 1(1), pp.1-44.

Rathi, R.N., and Mustafi, A., 2023. The importance of term weighting in semantic understanding of text: A review of techniques. *Multimedia Tools and Applications*, 82(7), pp.9761-9783.

Reddy, K.P., Reddy, T.R., Naidu, G.A., and Vardhan, B.V., 2018. Impact of similarity measures in information retrieval. *International Journal of Computational Engineering Research*, 8(6), pp.54-59.

Robert, B., and Brown, E.B., 2004. *The PageRank Citation Ranking: Bringing Order to the Web*. Vol. 1, University of Pennsylvania, Philadelphia, PA, pp.1-14.

Shahmirzadi, O., Lugowski, A., and Younge, K., 2019. Text Similarity in Vector Space Models: A Comparative Study. In: *Proceeding-18th IEEE International Conference on Machine Learning and Applications, ICMLA 2019*, pp.659-666.

Sharma, D., Shukla, R., Giri, A.K., and Kumar, S., 2019. A Brief Review on Search ENGINE Optimization. In: *Proceedings of the 9th International Conference On Cloud Computing, Data Science and Engineering, Confluence 2019*, pp.687-692.

Sharma, P.S., Yadav, D., and Garg, P., 2020. A systematic review on page ranking algorithms. *International Journal of Information Technology*, 12(2), pp.329-337.

Sharma, P.S., Yadav, D., and Thakur, R.N., 2022. Web page ranking using web mining techniques: A comprehensive survey. *Mobile Information Systems*, 2022, p.7519573.

Ilo, P.I., Nkiko, C., Izuagbe, R., and Furfuri, I.M.M., 2023. *Course Guide Lis 303 Information Retrieval (Cataloguing ii)*. National Open University of Nigeria, Nsukka.

Thakur, N., Mehrotra, D., Bansal A., and Bala M., 2019. Comparative analysis of ranking functions for retrieving information from medical repository. *Malaysian Journal of Computer Science*, 32(1), pp.18-30.

Tyagi, N., and Gupta, S.K., 2018. Web structure mining algorithms: A survey. *Advances in Intelligent Systems and Computing*, 654, pp.305-317.

Wang, J., and Dong, Y., 2020. Measurement of text similarity: A survey. *Information*, 11(9), p.421.

Wu, H., and Gu, X., 2014. Reducing Over-weighting in Supervised Term Weighting for Sentiment Analysis. In: *COLING 2014-25th International Conference on Computational Linguistics, Proceedings of COLING 2014: Technical Papers*, pp.1322-1330.

Xing, W., and Ghorbani, A., 2004. Weighted PageRank Algorithm. In: *Proceedings-Second Annual Conference on Communication Networks and Services Research*, pp.305-314.

Zheng, W., and Fang, H., 2010. *A Retrieval System based on Sentiment Analysis*. HCIR. [Preprint].

An Ensemble Model for Detection of Adverse Drug Reactions

Ahmed A. Nafea[1,*], Mustafa S. Ibrahim[2], Abdulrahman A. Mukhlif[3], Mohammed M. AL-Ani[4] and Nazlia Omar[4]

[1]Department of Artificial Intelligence, College of Computer Science and IT, University of Anbar 31001, Ramadi, Anbar, Iraq

[2]Department of Computer Science, University of Anbar 31001, Ramadi, Anbar, Iraq

[3]Registration and Students Affairs, University Headquarter, University of Anbar 31001, Ramadi, Anbar, Iraq

[4]Center for Artificial Intelligence Technology (CAIT), Faculty of Information Science and Technology, Universiti Kebangsaan Malaysia (UKM), Bangi, Selangor, Malaysia

***Abstract*—The detection of adverse drug reactions (ADRs) plays a necessary role in comprehending the safety and benefit profiles of medicines. Although spontaneous reporting stays the standard approach for ADR documents, it suffers from significant under-reporting rates and limitations in terms of treatment inspection. This study proposes an ensemble model that combines decision trees, support vector machines, random forests, and adaptive boosting (ADA-boost) to improve ADR detection. The experimental evaluation applied the benchmark data set and many preprocessing techniques such as tokenization, stop-word removal, stemming, and utilization of Point-wise Mutual Information. In addition, two-term representations, namely, term frequency-inverse document frequency and term frequency, are utilized. The proposed ensemble model achieves an F-measure of 89% on the dataset. The proposed ensemble model shows its ability in detecting ADR to be a favored option in achieving both accuracy and clarity.**

***Index Terms*—Adverse drug reactions, Classification, Ensemble Model, Machine Learning, Point-wise Mutual Information.**

1. Introduction

Adverse drug reactions (ADRs) are a harmful side effect that happens when patients are taking drugs. These effects can be severe and may arise either from the pharmacological properties of the drug, interactions with other drugs, or existing medical conditions (Edwards and Aronson, 2000; Kiritchenko; Zhu and Mohammad, 2014). ADRs establish a significant public health concern, with approximately 2.2 million serious cases occurring annually in the United States alone. Identifying and monitoring ADRs are vital to ensuring patient safety and appropriate medication usage (Yadesa et al., 2021; Ebrahimi et al., 2016). Early detection of ADRs is necessary in avoiding consequences and improving patient effects. The development of accurate and efficient is importance methods for detecting ADR (Kiritchenko et al., 2018).

Machine learning is an automatic detection of ADR from unstructured clinical text and has been greatly enabled by latest developments in natural language processing (NLP) and ML. This improvement is useful into the large data within health-care systems using these methods focused on data that show significant in ADR detection and elevating patient safety (Sørup et al., 2020). It is a must to implement challenges, like accuracy of ADR detection, to fully understand the advantages presented by these methods.

This study focuses on detecting ADR by the proposed of an ensemble model. This study utilized random forest (RF), support vector machines (SVM), decision trees (DT), and ADA-boost algorithms, with the aims to improve the accuracy and efficiency of ADR detection. This study utilized dataset from a benchmark collection by (Yates and Goharian, 2013), and this study by Yousef et al. (2019) has been extended this dataset by combining supplementary meaningful attributes.

The organization of this study as follows: Firstly, a comprehensive review of previous research on ADR detection using ML is presented. The second section describes the methodology applied in this study which includes the pre-processing, feature engineering, and model training. The results of the study, including performance metrics of the ensemble model utilizing RF, SVM, DT, and ADA-boost algorithms, are then presented and compared to different approaches. Finally, the effects of the findings are discussed and potential ways for future research on ADR detection using deep learning techniques.

ARO-The Scientific Journal of Koya University
Vol. XII, No. 1 (2024), Article ID: ARO.11403. 7 pages
DOI: 10.14500/aro.11403
Received: 14 September 2023; Accepted: 25 January 2024
Regular research paper: Published: 20 February 2024
Corresponding author's e-mail: ahmed.a.n@uoanbar.edu.iq

II. Related Work

Wang et al. (2019) proposed a deep neural network (DNN) to develop model reserved for the automated detection of ADR, utilizing chemical, biological, and biomedical information pertaining to drugs. This model was designed with two primary objectives. The first is the sensitivity of potential ADR related to established drugs. The second one prediction of possible ADRs linked to novel drugs. The model combined word-embedding techniques to efficiently get complex drug relationships present in extensive biomedical literature to account for new drugs, to another place from the dataset, a mapping function was created.

In this study by Zhang et al. (2020), the authors proposed a Gated Iterative Capsule Network (GICN) was established as an modern model for detecting ADR. This model combined character embedding to proficiently operate abbreviations and typographical errors. Given the multi-word nature of ADR, the model utilized CNN to cover comprehensive phrase-related information to extract deep semantic degrees, a case network featuring a gated iteration unit was proposed. This mechanism helped the classified grouping from lower level to higher-level cases while retaining related information. Experimental findings show that the GICN model displayed enhanced performance in ADR prediction from social media text compared to other current approaches. This model's efficacy contributes significantly to the improvement of ADR detection within the realm of text analysis.

This research by Yousef et al. (2020) was focused on the problems around the identification of ADR within the large area of medical information accessible via social networks. The previse studies methods commonly depend on medical dictionaries for ADR extraction often utilized trigger terms or text extension techniques. These techniques have a limitation regarding the treatment of abbreviations and effect on whole text contexts. This study proposed a lexicon alternative approach relate on the replacement of individual terms rather than entire sentences to overcome these limits. There are different previous works; this approach combined a medically pre-trained word embedding model to support in another task. Experimental evaluations including medical review benchmark datasets and three classifiers SVM, LR, and NB showed developments in classification accuracy through the proposed lexicon replacement method. This contribution highlights the advantage of the created approach compared to normal techniques in the field of ADR extraction from social network data.

This research by Li et al. (2020) focused on difficult challenged task of detection ADR. This study proposed models for ADR detection showed limitations including small-scale benchmark measures and the necessary for additional manually explained amounts or co-training with entity-mentioning extraction tasks, which might introduce noise or escalate explanation pains to address these challenges, this researcher focuses on ADR detection as a text classification task and introduced an adversarial transfer learning framework. This approach controlled a source quantity to reinforce performance within limited training cases in smaller target measures. Adversarial learning was deployed to avoid the advance of corpus-specific features into the shared area, ensuring the effective utilization of diverse corpora. The experiential results among three benchmark corpora supported the advantage of the proposed method, particularly in the context of small-scale corpora, outperforming existing state-of-the-art strategies. This study proposed transfer learning and adversarial mechanisms for improving ADR detection.

This paper by Zhang et al. (2021) focuses on the complex task of detecting ADR entities within text, uniquely within the field of social media data. While social media offers real-time and dynamically evolving drug reaction information, the lack of explained social media data has presented a challenge for research in this area. In addition, the informal and informal expressions prevalent in social media posts introduce significant problems for ADR-named entity recognition (NER). To improve these difficulties, the study proposed an adversarial transfer learning architecture for ADR NER. This architecture benefits from on biomedical domain information derived from PubMed to enhance performance within Twitter data. This proposed approach achieved state-of-the-art performance without depending on manually engineered features, yielding a notable F1 score of 68.58% on Twitter ADR data. This research highlights the might of adversarial transfer learning in addressing the challenges unique to ADR identification in the context of social media data.

Chen et al. (2021) proposed focus on challenged of detecting ADR events using social media data, particularly from platforms like Twitter. Conventional post-marketing surveillance systems, trusting on natural reports, are susceptible to underreporting issues, needing alternative data sources. However, research within this domain works with limitations stemming from limited explained datasets, which can delay the efficacy of deep learning models that often trust on large training samples. In response, the study introduced two regularization techniques at the representation level graph embedding-based data augmentation and adversarial training. These techniques aimed to amplify the performance of ADR within the constraints of data lack. The study analyzed and deliberated upon the applicability of these techniques through rigorous experiments. This study proposed an adverse drug event detection framework merging these regularization methods with a convolutional neural network to extract the full advantages. This research significantly contributes to filtering the detection of adverse events in the field of social media data and presents innovative regularization strategies to implement challenges related with limited explained datasets.

In Nafea, Omar and AL-Ani (2021), this study proposed LSA to detecting ADR from social networks, where individuals articulate their perspectives on medications. The previous studies predominantly leaned on trigger terms for ADR detection, this method needed regular updates to hold novel side effects and pertinent medical entities. The feature space built only on trigger terms lacked latent semantic comprehension. To surmount these limitations, the study proposed a semantic approach rooted in LSA to enhance

ADR detection. Experimental studies concerned a benchmark dataset and encompassed preprocessing operations such as stopping word removal, tokenization, and stemming. Three classifiers (SVM, NB, and LR) were trained on the proposed LSA, useful two document representations as TF and TFIDF. The results underscored the superiority of the proposed LSA methodology over the baseline extended trigger term approach, achieving an F-measure of 82% on the dataset. This elevation highlights the effectiveness of LSA in identifying accurate semantic similarities, transcending the utility of predefined trigger term lists. The study explains the relevance of combining semantic insights for ADR detection, thereby contributing to advancements within this domain.

In Nafea, Omar and Al-qfail (2023), this study focuses on the extraction of ADR from user-generated comments and reviews. While previous research mostly focused on machine learning techniques for ADR detection and applied noted medical review data for training classification models, the domain still challenges with relating to detection accuracy. To solve these complexities, this study introduced a composite approach involving LSA and ANN classifiers for the accurate ADR detection. Experimental findings supported the efficacy of merging LSA in tandem with ANN for accurate ADR extraction. This study has the potential to refine ADR detection methodologies and highlights the significance of combining LSA and ANN classifiers to realize accurate ADR extraction.

The key limitation of previous studies depends just on word embeddings that focused on term sequences and required pre-training the model specifically using those embeddings and they used only one model to detect ADR; there is still area for improving the accuracy of ADR detection. This study aims to address these challenges by proposed an ensemble model to enhance ADR detection performance. The proposed ensemble model approach combines multiple individual models as RF, SVM, DT, and ADA-boost to achieve more accurate predictions compared to using a single model. By utilizing and combining different models, the ensemble can capture a wider range of information leading to improved accuracy of ADR detection.

III. Research Methodology

The method of this study contains five stages, as shown in Fig. 1. The first step shows the explanation of drug reviews through the use of a dataset from Yates and Goharian (2013) benchmark datasets. This data set has been enhanced with additional valuable data fields by Yousef, Tiun, and Omar (2019). Following that, several preprocessing tasks include stemming, stop word removal, and tokenization. Then, the terms within the drug reviews are represented in a vector space using term frequency-inverse document frequency (TF-IDF) and TF. After that, PMI is applied. Finally, the classification process uses an ensemble model that combines RF, SVM, DT, and ADA-boost algorithms. The following section shows a more comprehensive and detailed elucidation of the research methodology.

A. Dataset

This study used dataset created by Yates and Goharian (2013), which was enhanced with additional informative data columns from Yousef et al. (2019). The dataset utilized in this research consisted of 2500 reviews, out of which 246 were labeled documents. Every document contained one or more sentences. The texts extracted from Twitter contained a total of 945 sentences. Among all the texts, there were 982 ADR identified. The documents were written in English as shown in Table I; the dataset details in Table II show a sample of dataset. Data from three prominent platforms specializing in drug reviews on social media, namely, askapatient.com,

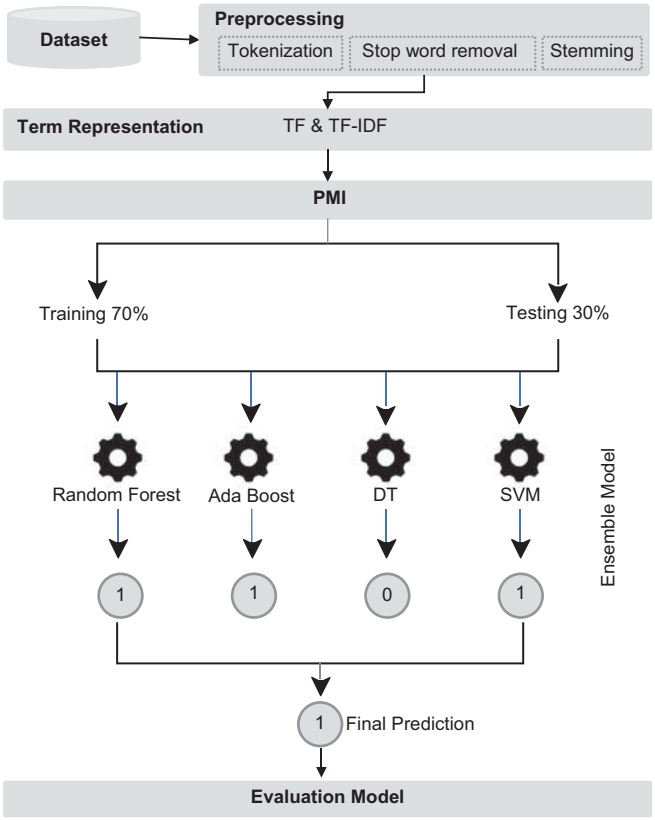

Fig. 1. Research methodology.

TABLE I
Dataset Details

Attribute	Total
Number of ADR	982
Number of Reviews	2500 (labeled 246)
Number of Sentences	944

ADR: Adverse drug reactions

TABLE II
Sample of the Dataset

Doc	Sen	Class	Review	ADR
1	1	0	I had been on Tamoxofin for 5 years.	[]
1	2	1	I still have the neuropathy, but I can deal with that	['neuropathy']
2	1	1	The night sweats were the worst!	['sweats']
3	1	0	I have been taking Femara for 5 months. []	[]
4	1	1	Lower back pain.	['pain']
4	2	0	Vaginal dryness is the other symptom I have.	[]

http://dx.doi.org/10.14500/aro.11403

drugratingz.com, and drugs.com, were gathered for the review analysis. There are two class types the first one ADR is 1 and the second non-ADR is 0.

B. Preprocessing

Pre-processing plays an essential role in NLP, as it shows the cleansing and transformation of unstructured text data into a suitable format for analysis and modeling using machine learning algorithms. This study applies three preprocessing techniques as a stop word removal, stemming, and tokenization.

- Tokenization: It is an initial step in preprocessing, where the text is divided into individual words or tokens (Oyebode and Orji, 2023).
- Stop words: It is commonly used words that have limited meaning. There is an example of these words including "the," "and" "of," and "to." the removal of these words reduces the dimensionality of text data, leading to improved performance of ML models by reducing noise and improving their ability to extract valuable information (McMaster et al., 2023).
- Stemming: It is used to cause the reduction of a word to its fundamental showed by the move of words like "running" to "run." This approach helps the reduction of the number of unique words in the text data, thus enhancing the performance of ML models through a decrease in data sparsity (Brueckle et al., 2023).

C. Term Representation

This study utilized TF and TF-IDF for feature extraction. The TF is utilized for calculates word frequency within a document (Azam and Yao, 2012) while the TF-IDF is used for word frequency between all documents in a corpus and it is utilized in text data analysis for ML approaches like sentiment analysis and text classification (Martin et al., 2022).

D. Pointwise Mutual Information (PMI)

PMI is a metric utilized to measure the connection between two events within a dataset. It is a common technique in the field of NLP (Ahanin and Ismail, 2022).

This work utilized PMI of significant importance in various domains, but not limited to word sense clarification, information retrieval, and text mining. It enables the detection of significant word relations and can be utilized to create semantic models and extract valuable samples from large text datasets.

The PMI equation is as follows:

$$\text{PMI}(x, y) = \frac{\log_2 P(x, y)}{(P(x) * P(y))} \quad (1)$$

In this equation, P(x, y) is the likelihood of the joint occurrence of events x and y, while P(x) and P(y) are the probabilities of events x and y explaining autonomously.

PMI creates a positive value when the cooccurrence of events x and y is higher than expected, indicating a positive association. A value of 0 signifies independence between the events, while negative values indicate a lower -occurrence than expected, implying a negative association.

E. Proposed Ensemble model

In this study, proposed an ensemble model that combines RF, DT, SVM, and AdaBoost for the detection of ADR is a effective technique for increasing accuracy classifier. Fig. 2 shows the proposed ensemble model proposed. The following describes each of the models used:

DT

DT algorithms are flexible methods for constructing tree-like models using various features and their corresponding thresholds by iterative data partitioning. This algorithm provides a simple and understandable framework for capturing complex patterns within the data, incorporating both categorical and numerical attributes. It is sensitive to overfitting, which causes the use of regularization methods such as reducing to improve this potential point (Alheeti et al., 2023; Charbuty and Abdulazeez, 2021).

RF

RF is a prevalent ensemble ML method appropriate for both classification and regression assignments. Operational on the foundation of DT values, it combines many DTs, each honed on a definite subset of training data, to formulate predictions. Its resilience and adaptability, RF bests in helping high-dimensional dataset brimming with numerous features, rendering it especially accurate in comparison with conventional classification methods (Sheykhmousa et al., 2020; Alsumaidaie et al., 2023).

SVM

SVM is a focus primarily on binary classification, but its means extend to multiclass classification. The core objective of SVM is to decide the best decision limits to maximize the difference between different classes. It is a competent program for dealing with linear separated data and can deal with nonlinear separated data using kernel tricks. SVM is highly regarded for its generalization characteristics and shows effectiveness in high-dimensional characteristic spaces. However, when faced with overlapping or indistinct classes, challenges arise, underlining the importance of the selection of careful kernels and hyperparameters (Cervantes et al., 2020; Alsumaidaie et al., 2023; Bassel et al., 2022).

AdaBoost (adaptive boost)

AdaBoost operates as a set technology that iteratively trains a weak classifier sequence (typically decision boards, characterized by a small structure characterized by only one split) on different subgroups of the training dataset. Each of these weak classifications was designed to emphasize cases that had previously been misclassified or showed a higher error rate. During the training process, AdaBoost assigns more weight to these challenging cases, allowing the later weaker classifiers to focus more on them. The final prediction made by the AdaBoost model is a weighted fusion of the predictions generated by individual weak classifications (Pham et al., 2021).

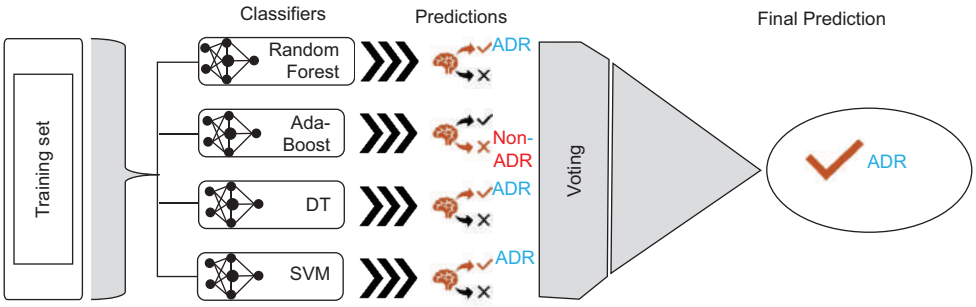

Fig. 2. Proposed ensemble model.

F. Voting

Voting contains each individual classifier in the ensemble making its prediction, and the final prediction is determined by selecting the class that receives the majority of votes. The class with the majority of votes among the individual classifiers is chosen as the final prediction of the ensemble model. The variety of classifiers helps catch different aspects of the data and can lead to more strong predictions.

This proposed utilized combining four algorithms as AdaBoost, SVM, DT, and RF strengths the ensemble model improves classification accuracy of ADR detection and performance, rather than using every algorithm individually. The combined models have improved predictive performance by effectively qualifying bias and errors through combining multiple model outputs. Each ensemble's basic model shows an important role in final prediction and produces more accurate results. Through the combination of RF, SVM, DT, and AdaBoost, the ensemble model develops its unique experiences to focus the several views of ADR detection challenges.

G. Evaluation

There are several performance metrics, such as precision, recall, and F-measure that usually utilized to evaluate the efficiency of ML models.

Precision is used to determine and correctly detect positive cases out of the total predicted positives, showing a low false positive rate (Mukhlif, Al-Khateeb and Mohammed, 2023).

$$\text{Precision} = \frac{\text{True positives (TP)}}{\text{True positives (TP)} + \text{False positives (FP))}} \quad (2)$$

Recall utilized to evaluates the model's capability to detect all positive cases out of the total actual positives, highlighting a low false negative rate (Kareem and Alheeti, 2022).

$$\text{Recall} = \frac{\text{TP}}{\text{TP} + \text{False Negatives(FN)}} \quad (3)$$

F-measure is used for merging precision and recall to show a single metric that balances both measures (Alsumaidaie, et al., 2023).

$$F - \text{measure} = \frac{2 \times (\text{Precision} * \text{Recall})}{\text{Precision} + \text{Recall}} \quad (4)$$

IV. Results and Discussion

This section shows the proposed ensemble models results by combining (RF, SVM, and DT with ADA-boost). The objective of the experimentation was to evaluate the effectiveness of the proposed study with a baseline methodology. The baseline approach applied identical data sourced from a benchmark dataset, precisely the annotated ADR review dataset introduced by (Yates et al., 2013). This dataset had been subsequently enriched by Yousef et al. (2019) through the incorporation of supplementary meaningful attributes.

The first baseline proposed LSA with ML algorithms (Nafea, Omar and AL-Ani, 2021), while the second baseline utilized LSA with ANN (Nafea, Omar and Al-qfail, 2023). Both baselines and current study utilized TF or TF-IDF for feature extraction. The testing and training were conducted with the same distribution as the baseline, with 30% of the data allocated for testing and 70% for training.

The first baseline utilized different ML classifiers such as SVM, NB, and LR, while the second baseline used ANN for classifiers. In this study, proposed ensemble models combining RF, SVM, and DT with ADA-boost were applied.

The outcomes of the proposed ensemble models using RF, SVM, and DT with ADA-boost, along with the baseline results, are presented in Table 1. The classification results based on F-measure are shown in Fig. 3, a comparison between the ADR proposed work using ensemble models and baselines research.

The results show the method established, utilizing RF, SVM, DT, and ADA-boost, showed enhancement in F-measure performance when compared with the baseline research. Specifically, when using TF, the proposed ensemble models achieved an enhanced F-measure result of 89%, surpassing the baseline LR result of 82%, while the second baseline using ANN achieved 85%. Similarly, when using TF-IDF, the proposed ensemble models achieved an enhanced F-measure result of 86%, outstanding the baseline LR result of 80%, while the second baseline using ANN achieved 83%.

These results indicate the promising potential of ensemble models, specifically ensemble models, for extracting ADRs. Table III, a comparison between baseline and proposed results.

In addition to the conventional baseline approach, it is essential to explore state-of-the-art methods that apply machine learning or deep learning methods as shown in

http://dx.doi.org/10.14500/aro.11403

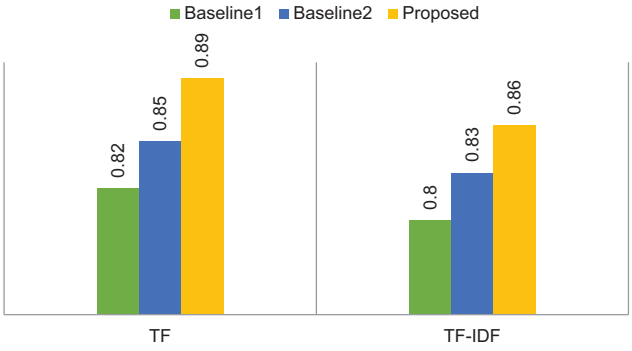

Fig. 3. Comparative of outcomes between the proposed approach and baseline methods.

TABLE III
COMPARATIVE OF OUTCOMES BETWEEN THE PROPOSED APPROACH AND BASELINE METHODS

Comparison	TF			TF-IDF		
	Precision	Recall	F-measure	Precision	Recall	F-measure
Baseline1	0.83	0.82	0.82	0.82	0.81	0.80
Baseline2	0.85	0.85	0.85	0.83	0.83	0.83
Proposed	0.89	0.89	0.89	0.87	0.86	0.86

TABLE IV
A COMPARISON OF RESULTS BETWEEN RELATED WORKS

Author's	Proposed used	F-measure (%)
Yousef et al. (2019)	SVM, NB and LR with trigger terms w	69
Wang et al. (2019)	DNN	84.4
Zhang et al. (2020)	CNN	67
Zhang et al. (2021)	Bi-LSTM	68
Shen et al. (2021)	GAR	74
Nafea, Omar and AL-Ani (2021)	SVM, NB, and LR with LSA	82
Nafea, Omar and Al-qfail (2023)	ANN with LSA	85
Proposed Method	Ensemble Model (RF+SVM+DT+ADA-boost)	89

DNN: Deep neural network, RF: Random forest, SVM: Support vector machines, DT: Decision trees, NLP: Natural language processing

Table IV. Wang et al. (2019) utilized DNN method and achieved an impressive f-measure of 84.4%. Zhang et al. (2020) developed adversarial transfer learning and applied the private CNN method to identify ADRs, achieving an f-measure of 67%. Zhang et al. (2021) utilized adversarial transfer learning to extract ADRs by using Bi-LSTM, resulting in an f-measure of 68%. In this study by Shen et al. (2021) used a graph adversary representation framework (GAR) that included word embedding. Their approach yielded an f-measure of 74% for the extraction of ADRs. It is essential to acknowledge that making direct comparisons using the provided technique may not be practicable owing to disparities in the dataset used. The efficacy of these deep learning approaches is contingent upon a multitude of parameters, with the size of the dataset being a notable determinant of their success. However, the ensemble model that has been suggested continues to be competitive, especially in situations where small-scale data is being used.

V. CONCLUSION

The findings of this research using ensemble models using term frequency (TF) achieved an f-measure of 89%, better than the baseline's f-measures of 82% and 85%. This finding shows that when utilizing ensemble models to improve the detection of ADR. Thus, the results show that proposed ensemble models are efficacious in extracting ADR. It is important to acknowledge that this research has several limitations due to its exclusive focus on real-time evaluations. Nevertheless, these issues may play a role in the discovery of novel medication side effects, particularly those associated with COVID-19. In future work, there is potential value in integrating advanced word embedding methodologies with deep learning frameworks. This approach may have been possible to enhance the efficacy of ADR detection.

VI. APPENDIX

Appendixes, if needed, appear before the acknowledgment.

VII. ACKNOWLEDGMENT

None.

REFERENCES

Ahanin, Z., and Ismail, M.A., 2022. A multi-label emoji classification method using balanced pointwise mutual information-based feature selection. *Computer Speech and Language*, 73, p.101330.

Alheeti, K.M.A., Alzahrani, A., Alamri, M., Kareem, A.K., and Al_Dosary, D., 2023. A comparative study for SDN security based on machine learning. *International Journal of Interactive Mobile Technologies*, 17(11), pp.131-140.

Alsumaidaie, M.S.I., Alheeti, K.M.A., and Al-Aloosy, A.K., 2023. Intelligent Detection System for a Distributed Denial-of-Service (DDoS) Attack Based on Time Series. In: *2023 15th International Conference on Developments in eSystems Engineering (DeSE)*. IEEE, pp.445-450.

Alsumaidaie, M.S.I., Alheeti, K.M.A., and Alaloosy, A.K., 2023. Intelligent detection of distributed denial of service attacks: A supervised machine learning and ensemble approach. *Iraqi Journal for Computer Science and Mathematics*, 4(3), pp.12-24.

Azam, N., and Yao, J., 2012. Comparison of term frequency and document frequency based feature selection metrics in text categorization. *Expert Systems with Applications*, 39(5), pp.4760-4768.

Bassel, A., Abdulkareem, A.B., Alyasseri, Z.A.A., Sani, N.S., and Mohammed, H.J., 2022. Automatic malignant and benign skin cancer classification using a hybrid deep learning approach. *Diagnostics* (*Basel*), 12(10), p.2472.

Brueckle, M.S., Thomas, E.T., Seide, S.E., Pilz, M., Gonzalez-Gonzalez, A.I., Dinh, T.S., Gerlach, F.M., Harder, S., Glasziou, P.P., and Muth, C., 2023. Amitriptyline's anticholinergic adverse drug reactions-a systematic multiple-indication review and meta-analysis. *PLoS One*, 18(4), p.e0284168.

Cervantes, J., Garcia-Lamont, F., Rodríguez-Mazahua, L., and Lopez A., 2020. A comprehensive survey on support vector machine classification: Applications, challenges and trends. *Neurocomputing*, 408, pp.189-215.

Charbuty, B., and Abdulazeez, A., 2021. Classification based on decision tree algorithm for machine learning. *Journal of Applied Science and Technology Trends*, 2(01), pp.20-28.

Ebrahimi, M., Yazdavar, A.H., Salim, N., and Eltyeb, S., 2016. Recognition

of side effects as implicit-opinion words in drug reviews. *Online Information Review*, 40(7), pp.1018-1032.

Edwards, I.R., and Aronson, J.K., 2000. Adverse drug reactions: Definitions, diagnosis, and management. *The Lancet*, 356(9237), pp.1255-1259.

Kareem, A.K., and Alheeti, K.M.A., 2022. Multimodal Approach for Fall Detection based on Support Vector Machine. In: *AIP Conference Proceedings.* AIP Publishing.

Kiritchenko, S., Mohammad, S.M., Morin, J., De Bruijn, B., 2017. NRC-Canada at SMM4H Shared Task: Classifying Tweets Mentioning Adverse Drug Reactions and Medication Intake. In: *CEUR Workshop Proceedings*, p.1-11.

Kiritchenko, S., Zhu, X., and Mohammad, S.M., 2014. Sentiment analysis of short informal texts. *Journal of Artificial Intelligence Research*, 50, pp.723-762.

Li, Z., Yang, Z., Luo, L., Xiang, Y., and Lin, H., 2020. Exploiting adversarial transfer learning for adverse drug reaction detection from texts. *Journal of Biomedical Informatics*, 106, p.103431.

Martin, G.L., Jouganous, J., Savidan, R., Bellec, A., Goehrs, C., Benkebil, M., Miremont, G., Micallef, J., Salvo, F., Pariente, A., and Létinier, L., 2022. Validation of artificial intelligence to support the automatic coding of patient adverse drug reaction reports, using nationwide pharmacovigilance data. *Drug Safety*, 45(5), pp.535-548.

McMaster, C., Chan, J., Liew, D.F.L., Su, E., Frauman, A.G., Chapman, W.W., and Pires, D.E.V., 2023. Developing a deep learning natural language processing algorithm for automated reporting of adverse drug reactions. *Journal of Biomedical Informatics*, 137, p.104265.

Mukhlif, A.A., Al-Khateeb, B., and Mohammed, M., 2023. Classification of breast cancer images using new transfer learning techniques. *Iraqi Journal for Computer Science and Mathematics*, 4(1), pp.167-180.

Nafea, A.A., Omar, N., and AL-Ani, M.M., 2021. Adverse drug reaction detection using latent semantic analysis. *Journal of Computer Science*, 17(10), pp.960-970.

Nafea, A.A., Omar, N. and Al-Qfail, Z.M., 2024. Artificial neural network and latent semantic analysis for adverse drug reaction detection. *Baghdad Science Journal*, 21(1), pp.0226-0233.

Oyebode, O., and Orji, R., 2023. Identifying adverse drug reactions from patient reviews on social media using natural language processing. *Health Informatics Journal,* 29(1).

Pham, B.T., Nguyen, M.D., Nguyen-Thoi, T., Ho, L.S., Koopialipoor, M., Quoc, N.K., Armaghani, D.J., and Van Le H., 2021. A novel approach for classification of soils based on laboratory tests using adaboost, tree and ANN modeling. *Transportation Geotechnics*, 27, p.100508.

Shen, C., Li, Z., Chu, Y., and Zhao Z., 2021. GAR: Graph adversarial representation for adverse drug event detection on Twitter. *Applied Soft Computing*, 106, p.107324.

Sheykhmousa, M., Mahdianpari, M., Mohammadimanesh, F., Ghamisi, P., and Hom, S., 2020. Support vector machine versus random forest for remote sensing image classification: A meta-analysis and systematic review. *IEEE Journal of Selected Topics in Applied Earth Observations and Remote Sensing*, 13, pp.6308-6325.

Sørup, F.K.H., Eriksson, R., Westergaard, D., Hallas, J., Brunak, S., and Ejdrup Andersen, S., 2020. Sex differences in text-mined possible adverse drug events associated with drugs for psychosis. *Journal of Psychopharmacology*, 34(5), pp.532-539.

Wang, C.S., Lin, P.J., Cheng, C.L., Tai, S.H., Kao Yang, Y.H., and Chiang, J.H., 2019. Detecting potential adverse drug reactions using a deep neural network model. *Journal of Medical Internet Research*, 21(2), p.e11016.

Yadesa, T.M., Kitutu, F.E., Deyno, S., Ogwang, P.E., Tamukong, R., and Alele, P.E., 2021. Prevalence, characteristics and predicting risk factors of adverse drug reactions among hospitalized older adults: A systematic review and meta-analysis. *SAGE Open Medicine*, 9.

Yates, A., and Goharian, N., 2013. ADRTrace: Detecting expected and unexpected adverse drug reactions from user reviews on social media sites. In: *European Conference on Information Retrieval*. Springer, Berlin, Heidelberg, pp.816-819.

Yousef, R.N., Tiun, S., and Omar, N., 2019. Extended trigger terms for extracting adverse drug reactions in social media texts. *Journal of Computer Science*, 15(6), pp.873-879.

Yousef, R.N.M., Tiun S., Omar N., and Alshari, E.A., 2020. Lexicon replacement method using word embedding technique for extracting adverse drug reaction. *International Journal of Technology Management and Information System*, 2(1), pp.113-122.

Zhang, T., Lin, H., Ren.,Y., Yang, Z., Wang, J., Duan, X., and Xu, B., 2021. Identifying adverse drug reaction entities from social media with adversarial transfer learning model. *Neurocomputing*, 453, pp.254-262.

Zhang, T., Lin, H., Xu, B., Ren, Y., Yang, Z., Wang, J., and Duan, X., 2020. Gated iterative capsule network for adverse drug reaction detection from social media. In: *2020 IEEE International Conference on Bioinformatics and Biomedicine (BIBM)*. IEEE, pp.387-390.

 http://dx.doi.org/10.14500/aro.11431

Bromination of Chalcone: A Study on Synthesis, Characterization, and Optoelectronic Properties

Kosrat N. Kaka[1], Rebaz A. Omer[1], Dyari M. Mamand[2] and Aryan F. Qader[1]*

[1]Department of Chemistry, Faculty of Science and Health, Koya University, Danielle Mitterrand Boulevard, Koya KOY45, Kurdistan Region – F.R. Iraq

[2]Department of Physics, College of Science, University of Raparin, Sulaymani, Kurdistan Region – F.R. Iraq

***Abstract*–In this research work, a new compound, namely 2,6-dibromo-2,6-bis(bromo(phenyl)methyl)cyclohexanone (1), is synthesized and characterized for possible applications in organic electronic devices. The formation of the compound was confirmed by Fourier-transform infrared spectroscopy, ^{1}H-, and ^{13}C-NMR spectroscopy measurements. Furthermore, the spectroscopic and optoelectronic properties of the chemical compound were theoretically investigated using density-functional theory (DFT). Herein, the B3LYP/cc-pVDZ level was used to discover the compound electrostatic potentials and frontier molecular orbitals. The theoretical investigations predicted by DFT were compared with the experimentally obtained results from the ultraviolet visible spectra of the compound after being dissolved in various solvents. Results showed that the experimental band-gap energy of the compound is 3.17 eV, whereas its theoretical value was calculated to be 3.33 eV. The outcome of the achieved results suggests the viability of 2,6-dibromo-2,6-bis(bromo(phenyl) methyl)cyclohexanone for possible applications in organic electronic devices.**

***Index Terms*—Bromination of Chalcone, Density-functional theory, Optoelectronic, Molecular reactivity, Ultraviolet visible.**

I. Introduction

Chalcones exhibit a wide range of diverse biological activities. These substances can be easily manufactured or found naturally, but there has been no recent review describing the therapeutic (and on occasion, dystherapeutic) activities of this Chalcone (Elias, et al., 1999; Rani, et al., 2019). Chalcone is a naturally occurring substance that exhibits many pharmacological properties, including anticancer activity. One intriguing mechanism is its ability to alter the production of return on sales (ROS). Pyroptosis has long had anti-cancer properties. Adding a unit of a,β-unsaturated ketone to chalcone may be a successful method for creating chemotherapeutic medicines (Zhu, et al., 2018; Tajuddeen, et al., 2018). Using various substituted amines in basic conditions, a variety of *β*-chalcone derivatives was produced through the Claisen-Schmidt condensation procedure. Density-functional theory (DFT) has been optimized for HOMO-LUMO energy calculations using *β*-chalcones. Vertical excitation energies, absorption wavelengths, and oscillator strengths of the *β*-chalcone derivative were determined using an optimal time-dependent DFT analysis (Arif, et al., 2020; Priya, et al., 2019). Another class of Chalcone derivatives CO–CH═CH– is regarded as a desirable species since it has a ketoethylenic component moiety. Chalcones and their derivatives have a wide range of antiproliferative, antifungal, antibacterial, antiviral, antileishmanial, antimalarial pharmacological activities, antitubercular, antioxidant, and anti-inflammatory because they contain a reactive unsaturated carbonyl group (Elkanzi, et al., 2022; Tekale, et al., 2020). The chalcones undergo several reactions since they contain C=C and C=O active sites, for example, dibromo compounds formation by the reactions with bromine (Lévai, 2004; Haji, 2013). An environmentally friendly method for brominating chalcones was developed by combining a number of acetophenone derivatives with aromatic aldehydes. Tetrabutylammonium tribromide helped to simplify this process. The antibacterial activity of each produced chalcone dibromide was tested against Aspergillus flavus, Rhizopus sp., Fusarium solani, and Aspergillus niger, and Asymmetric bromination of chalcone and benzylideneacetone (trans isomer) in a crystalline *β*-cyclodextrin complex was studied (Adokar, 2013; Pitchumani, et al., 1994).

Among the modeling methodologies, the DFT formalism stands out because it allows for the calculation of the physicochemical properties of the investigated molecules at a microscopic level with high precision and low processing cosine (Parlak, et al., 2022). This quantum approach, for example, can determine the molecule's frontier orbitals, nucleophilic and/or electrophilic sites, kinetics, and thermodynamic properties (Koparir, et al., 2022b; Rebaz, et al., 2021). The DFT method can compute the geometric optimization of organic molecules. Infrared (IR) spectra and

ARO-The Scientific Journal of Koya University
Vol. XII, No. 1 (2024), Article ID: ARO.11431. 6 pages
DOI: 10.14500/aro.11431
Received: 07 October 2023; Accepted: 02 January 2024
Regular research paper: Published: 28 February 2024
Corresponding author's email: aryan.qader@koyauniversity.org

frontier molecular orbitals simulated can be generated for electronic characterization and the generation of quantum reactivity descriptors to comprehend the overall reaction of the molecule's behavior as a nucleophile or electrophile (Omer, et al., 2022b; Omer, et al., 2022c).

The principal aim of this investigation is to comprehensively assess the efficacy of the organic compounds under examination, with a particular focus on their optoelectronic characteristics. The research aims to elucidate the interaction mechanisms between these organic compounds and light, a parameter of paramount importance in various applications such as sensors, solar cells, and light-emitting devices. To deepen our comprehension of the structural attributes of these organic compounds, the B3LYP/cc-pVDZ method is employed in this study. The evaluation entails the examination of the ultraviolet (UV) spectrum of the organic compounds in four distinct solvents. Furthermore, the exploration of the energy band of the target molecule in an alternative solvent serves a dual purpose.

II. Experimental

A. Physical Measurements

The ^{1}H-NMR spectrum in DMSO-d6 was recorded with a Bruker F2-processing parameter (SF-300 MHz) spectrometer. The melting point was determined using the BUCHI B-540 apparatus.

B. Synthesis of Title Compound (1)

Preparation of compound (1). Preparation involves mixing 1 mole of 2,6-dibenzylidenecyclohexanone (Chalcone) in 10 ml of chloroform as a solvent with (0.1 ml) of (bromine, 96%) in 10 ml of the same solvent (Chloroform), then stirring for 1 h at room temperature. Finally, the solvent was evaporated using a rotary evaporator, and the precipitate was dried and recrystallized in acetone (if the precipitate became gelatin, use petroleum ether and a refrigerator to cool until 1 day to liquidate the gelatin precipitate) (Fig. 1). The structure of the product compound (1) was identified using Fourier-transform infrared spectroscopy (FT-IR), ^{1}H-NMR, and ^{13}C-NMR instruments. Color is red-yellow; yield is 60%; melting point 105–106°C; FT-IR (KBr, cm^{-1}, υ): 1449 (C⎯⎯⎯C), 1717(υC=O), 625 (υC=Br), 984 (υC-C); ^{1}H-NMR (300 MHz, DMSO-d6, δ, ppm): 2.261 (m, 2H, CH_2-Cyclo-none), 1.816 (m, 2H, CH_2-Cyclo-none), 6.095 (s, 2H, CH-Br), 7.319 (dd, 10H, Ar-H); ^{13}C-NMR (100 MHz, DMSO-d6, δ, ppm): 16.839, 34.59, 55.86, 66.45, 198.17, 136.47.

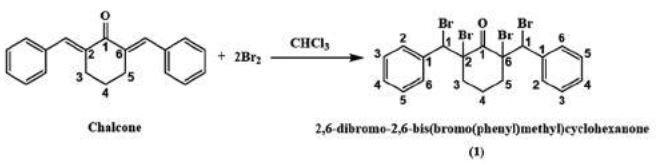

Fig. 1. Reaction pathway for the synthesis of compound (1).

C. Computational Details

Gaussian 09 used a theoretical investigation to calculate quantum computing theory (Medvedev, et al., 2017; Omar, et al., 2023). DFT rounded calculations with the first basis set, cc-pVDZ. Becky's three functional hybrid exchange restrictions (*B3LYP*) are functional (Becke, 1996; Parlak, et al., 2022). After optimizing the structure of compound (1), a quantum computational calculation can get an excitation state. UV-visible (UV-Vis) is more suitable for investigating optoelectronic behaviors that can benefit from maximum UV-Vis absorption. In the high absorption graph region, the highest peak has the most effective, predictable excitation state. It is possible to predict or show an excitable state in the amount of oscillator strength that is related to the highest peak intensity, as shown in some different solvents.

III. Results and Discussion

A. NMR Characterization

Compound (1) was synthesized by the reaction of two moles of bromine with Chalcone in chloroform as a solvent. The formation of the products was confirmed based on their FT-IR, 1H-, and 13C-NMR spectroscopy. The IR spectrum for compound (1) showed a strong band at 1717 cm^{-1}, which corresponded to the C=O stretching vibration, the C⎯⎯⎯C stretching vibration appeared near 1449 cm^{-1}, and the C-Br stretching vibration appeared near 625 cm^{-1}. The ^{1}H-NMR showed multiple signals at δ2.225 ppm for the four protons of the cyclohexanone (H2, H4), whereas (H3) showed the pentest signal because of the two protons at δ1.837 ppm, (H8, H9) showed a singlet signal for the two protons at δ6.240 ppm, and the (Ar-H) showed multiple signals for the five aromatic protons between 7.703 and 7.951 ppm. The ^{13}C-NMR spectrum showed a variable peak, which is attributed to the following carbons: (C3) at δ16.839 ppm, (C2, C4) at δ34.592 ppm, (C8, C9) at δ55.861 ppm, (C1, C5) at δ66.453 ppm, (C6) at δ198.178 ppm, and (Ar-C) at δ136.472 ppm.

B. UV-Vis Spectroscopy Characteristics of Compound (1) Dissolved in Different Solvents

UV-Vis has a wide range of applications today. It is a scientific category that includes arrangements. It entails studying the electromagnetic radiation of materials besides light. The significance of UV-Vis application stems from its ease and usefulness in investigating the optical and structural properties of materials, such as polymers and polymer nanostructures, as well as light-emitting organic materials. The UV spectrum can depict the material sample's basic electronic behavior. The theoretical calculation associated with the DFT approximation corresponds to the absorption spectra and optical density of the compound (1) molecule, dissolved in different solvents. Each theoretical and experimental approach has more similarities that are close to the amount of the result value. As shown in Fig. 2, the experimental result of UV toward the highest peak is 320.93 nm in dimethyl sulfoxide and the second is 319.97 nm

 http://dx.doi.org/10.14500/aro.11431

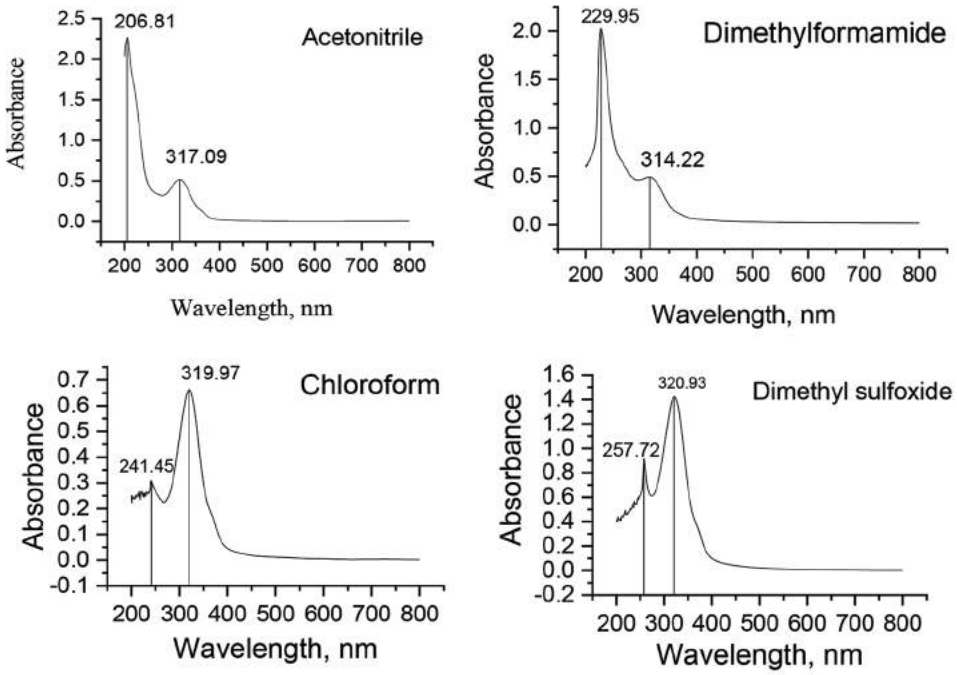

Fig. 2. Experimental ultra-violet visible of compound (1) using different solvent.

in chloroform. However, when compared to the theoretical result, good similarities are shown. The highest peak was observed in chloroform, which is equal to 331.25 nm, and the second highest peak was observed at 330 nm in dimethyl sulfoxide. The experimental ultraviolet result (in DMSO as an example) revealed only two peaks in two different ranges: The first at 320.93 nm and the second peak at 257.72 nm, which are very close to the visible region of light.

As shown in theory (Fig. 3), the first peak in acetonitrile solvent was determined at 329.61 nm with an oscillator strength of 0.0005, whereas the peak in dimethyl formamide was observed at 330.43 nm with an oscillator strength of 0.0005. For both chloroform and dimethyl sulfoxide solvents, the peaks were determined at 331.25 and 330.43 nm with an oscillator strength of 0.0005 and 0.0005, respectively. When the wavelength value approaches 800 nm, the absorbance of compound (1) in the ultraviolet range is experimentally nearly constant. Here, DMSO is a significantly excellent solvent rather than other solvents.

Extremely important for semiconductors is the ability to express the basic property of light absorption of materials in the absorption's expression, where α is absorbance, *Eg* is band gap, and *hv* is photon energy (Kumara, et al., 2013; Salih, et al., 2023). The optical transition of a semiconductor associated with a forbidden bandwidth or optical band gap can be detected and expressed using the equation below.

$$\alpha\ hv = (hv - E_g)^m \quad (1)$$

The direct transition is provided by *m* equal to 1/2, and the prohibited direct transition is provided by *m* 3/2. The value of m was determined by dividing it in half.

$$\alpha\ hv = (hv - E_g)^{\frac{1}{2}} \quad (2)$$

The graph between $(hv)^2$ and photon energy (E) was plotted to determine the allowable band gap value, as shown in Fig. 4. The DMSO solvent was chosen to determine the band gap for both experimental and theoretical data. The experimentally band-gap energy value is equal to 3.166 eV. The results show that the title compound is an excellent semiconductor when dissolved in DMSO. Compared to the theoretical method, the experimental band-gap value for DFT/cc-pVDZ is equal to 3.326, as shown in Fig. 4. The theoretical result is very close to the experimental result, and DFT was an acceptable method for measuring band gap with a cc-pVDZ basis set. The results obtained in our practice suggest that the band-gap energy of the title compound is low, making it a good conductor when using chemically doped with p-type and n-type materials. Another factor that influences the ratio band-gap is the type of solvent used. A material's optical transfer properties can be described as permeable, which is a function of it. It follows Lambert–Beer law because the transmitted radiation density is represented by work, which has an inverse relationship with the original material's penetration depth or length, and permeability is determined by the molecule's geometry.

C. Descriptors of Global Reactivity and Frontier Molecular Orbitals

The theory of frontier molecular orbitals uses fine molecular properties through HOMO-LUMO interactions. In the literature, softness, hardness, and electronegativity are used as global reactivity descriptors (Parlak, et al., 2022; Aktaş, et al., 2022; Koparir, Omar, and Koparir, 2022a; Koparir, et al., 2022c; Rebaz, et al., 2022). Fig. 5 shows that the HOMO electrons are delocalized on the dibromocyclohexane and benzene rings, whereas the LUMO

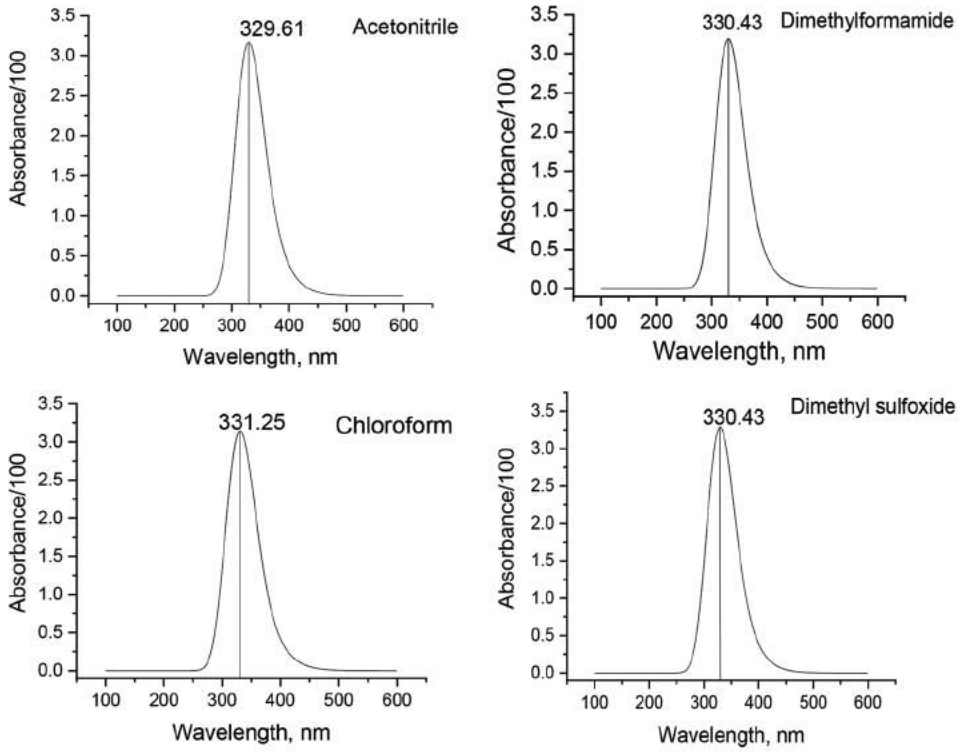

Fig. 3. Theoretical ultraviolet visible of compound (1) using density-functional theory/cc-pVDZ methods.

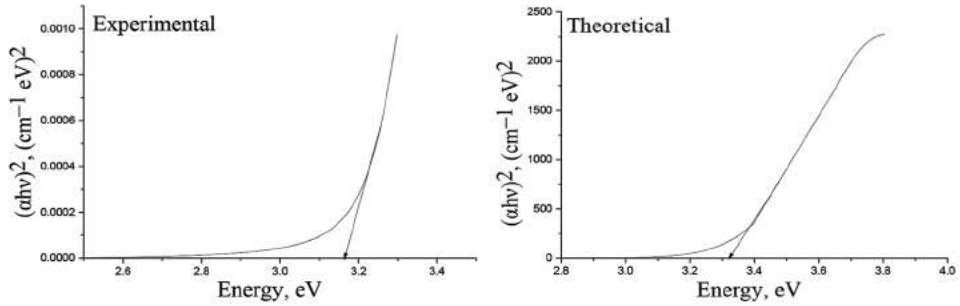

Fig. 4. Band-gap energy $(hv)^2$ plot versus E of compound (1) experimentally and theoretically.

electrons are only delocalized on the cyclobenzene ring. The energy separation between the HOMO and the LUMO is 4.325 eV, which shows that the energy gap reflects the molecule's chemical activity. The following parameters for a molecule can be calculated using HOMO and LUMO energy values:

The ionization potential is the amount of energy required to remove an electron from a gaseous atom or molecule. The amount of energy released when an electron is added to a gaseous molecule is defined as electron affinity. Electronegativity is an atom's proclivity to attract electrons. Chemical hardness is a measure of how well molecules resist weight transfer. The molecules with higher chemical hardness values have little or no weight transfer. Table I displays the electronic structure parameter values calculated by the *B3LYP* method with cc-pVDZ.

Because neighboring orbitals in the boundary region may have quasi-degenerate energy levels, only the HOMO and LUMO may not yield a realistic description of the frontier orbitals. The Gauss Sum 3.0 program does not calculate the density of the mode but displays it from the calculation results of the Gaussian 09 program (Zandiyeh and Ghiasi, 2019). The density of states (DOS) diagram for the title compound is shown in Fig. 6.

TABLE I
Descript ors of Global Reactivity for Compound (1)

Parameters	Results (eV) with *B3LYP*/cc-pVDZ
E_{HOMO}	−6.6861
E_{LUMO}	−2.3611
Eg	−4.325
$I = -E_{HOMO}$ (Plakhutin and Davidson, 2009)	6.6861
$A = -E_{LUMO}$ (Plakhutin and Davidson, 2009)	2.3611
$\chi = (I+A)/2$ (Masoud, et al., 2012)	4.5236
$\eta = (I - A)/2$ (Gökce and Bahceli, 2011)	2.1625
$\sigma = 1/\eta$ (Arivazhagan and Subhasini, 2012)	0.4624
$\Delta E = (E_{LUMO} - E_{HOMO})$ (Jesudason, et al., 2009)	4.325

http://dx.doi.org/10.14500/aro.11431

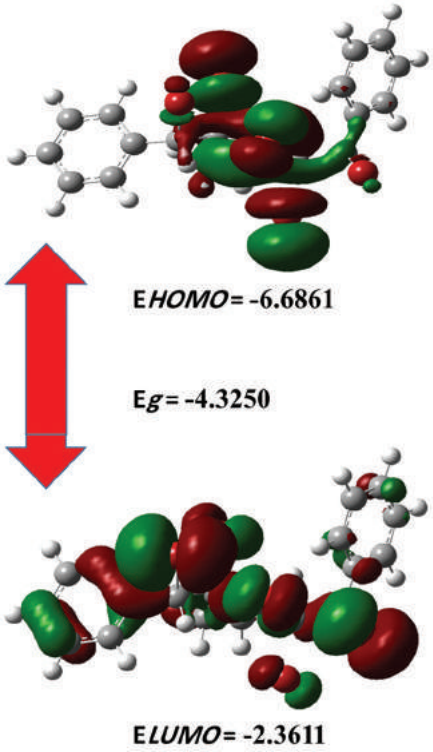

Fig. 5. Energy levels of HOMO and LUMO of the title compound computed at *B3LYP*/cc-pVDZ level in a gas phase.

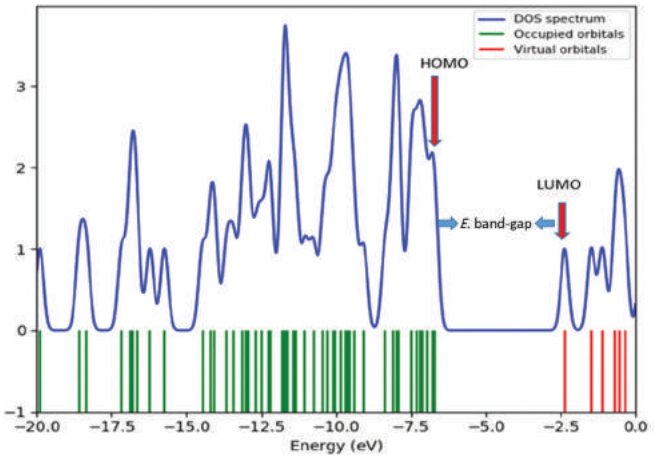

Fig. 6. Density states diagrams for compound (1).

D. Molecular Electrostatic Potential (MEP)

The MEP is linked to the dipole moment, electronegativity, partial charges, and chemical reactivity region of the molecule (Koparir, et al., 2020; Omer, et al., 2022a). It provides a visual method for understanding the molecule's relative polarity. The negative electrostatic potential is the region of the molecule where the electron density is greater than the nucleus (colored in red tones on the ESP surface); the positive electrostatic potential is the region where the electron density is low (the ESP surface is colored in blue tones) (Omer, et al., 2021; Rebaz, et al., 2021; Politzer and Murray, 2002; Rasul, et al., 2023). Fig. 7 shows the MEP map for the title compound. According to the figure, the

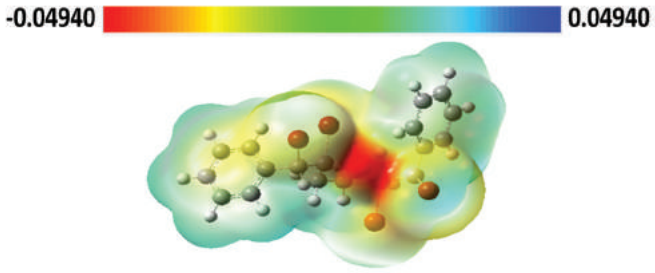

Fig. 7. Molecular electrostatic potential map calculated at *B3LYP*/cc-pVDZ level for compound (1).

negative regions in the molecule are on the two bromine (0.0324 and 0.0247 a.u.), carbon for cyclohexane (0.308, 0.339, 0.006, 0.020, 0.047, and 0.024 a.u.), and oxygen O (0.202 a.u.) atoms. These are the most suitable regions for electrophilic attack. The two benzene rings attached to the cyclohexane ring were the most susceptible to nucleophilic attack in the positive regions.

IV. Conclusion

The compound (1) was synthesized and experimentally reported using FT-IR, ^{1}H-, and ^{13}C-NMR spectroscopic techniques. The optical and electronic properties of the mentioned compound when dissolved in different solvents are investigated for both experimental and theoretical purposes. The experimental correlation was compared to the theoretical result using the Gaussian 09 program. The compound (1) has an energy gap of 3.166 eV experimentally, but the theoretical result is equal to 3.326 eV. DFT showed good agreement with the experiment results. According to graphs and results estimated from the band-gap value, they have significant similarities. The MEP map shows positive potential locations around carbon atoms of cyclohexane and negative potential locations around bromine atoms.

V. Appendix

Appendixes, if needed, appear before the acknowledgment.

VI. Acknowledgment

Koya University Chemistry Department wishes to express its appreciation to the authors who contributed to their work.

References

Adokar, M.R., 2013. Synthesis and green bromination of some chalcones and their antimicrobial screening. *International Research Journal of Pharmacy*, 4, pp.194-196.

Aktaş, A.E., Omer, R.A., Koparir, P., and Koparir, M., 2022. Synthesis, characterization and theoretical anti-corrosion study for substitute thiazole contained cyclobutane ring. *Journal of Physical Chemistry and Functional Materials*, 5, pp.111-120.

Arif, R., Rana, M., Yasmeen, S., Khan, M.S., Abid, M., and Khan, M.S., (2020). Facile synthesis of chalcone derivatives as antibacterial agents: Synthesis, DNA

binding, molecular docking, DFT and antioxidant studies. *Journal of Molecular Structure*, 1208, p.127905.

Arivazhagan, M., and Subhasini, V., 2012. Quantum chemical studies on structure of 2-amino-5-nitropyrimidine. *Spectrochimica Acta Part A: Molecular and Biomolecular Spectroscopy*, 91, pp.402-410.

Becke, A.D., 1996. Density-functional thermochemistry. IV. A new dynamical correlation functional and implications for exact-exchange mixing. *The Journal of Chemical Physics*, 104, pp.1040-1046.

Elias, D.W., Beazely, M.A., and Kandepu, N.M., 1999. Bioactivities of chalcones. *Current Medicinal Chemistry*, 6, p.1125.

Elkanzi, N.A., Hrichi, H., Alolayan, R.A., Derafa, W., Zahou, F.M., and Bakr, R.B., 2022. Synthesis of chalcones derivatives and their biological activities: A review. *ACS Omega*, 7, pp.27769-27786.

Medvedev, M.G., Bushmarinov, I.S., Sun, J., Perdew, J.P., and Lyssenko, K.A., 2017. Density functional theory is straying from the path toward the exact functional. Science, 355, pp.49-52.

Gökce, H., and Bahceli, S., 2011. A study on quantum chemical calculations of 3-, 4-nitrobenzaldehyde oximes. *Spectrochimica Acta Part A: Molecular and Biomolecular Spectroscopy,* 79, pp.1783-1793.

Haji, K., 2013. *Kinetics and Mechanistic on the Formationof Some Alpha, Beta-Unsaturated Ketons in ent Solvents and thier Reaction with Bromine and Hydrazine.* University of Mousel.

Jesudason, E.P., Sridhar, S., Malar, E.P., Shanmugapandiyan, P., Inayathullah, M., Arul, V., Selvaraj, D., and Jayakumar, R., 2009. Synthesis, pharmacological screening, quantum chemical and *in vitro* permeability studies of N-Mannich bases of benzimidazoles through bovine cornea. *European Journal of Medicinal Chemistry*, 44, pp.2307-2312.

Koparir, P., Omar, R., and Koparir, M., 2022a. Synthesis and molecular characterization with DFT: Study of 2-chloro-1-(3-methyl-3-mesityl-cyclobutyl)-ethanone. *Indian Journal of Chemistry*, 61, pp.858-865.

Koparir, P., Omar, R.A., Sarac, K., Ahmed, L.O., Karatepe, A., Taskin-Tok, T., and Safin, D.A., 2022b. Synthesis, characterization and computational analysis of thiophene-2, 5-diylbis ((3-mesityl-3-methylcyclobutyl) methanone). *Polycyclic Aromatic Compounds*, 43, pp.1-19.

Koparir, P., Rebaz, O., Karatepe, M., and Ahmed, L., 2020. Synthesis, characterization, and theoretical inhibitor study for (1E, 1'E)-2, 2'-thiobis (1-(3-mesityl-3-methylcyclobutyl) ethan-1-one) dioxime. *El-Cezeri Journal of Science and Engineering*, 8, pp.1495-1510.

Koparir, P., Sarac, K., and Omar, R.A., 2022c. Synthesis, molecular characterization, biological and computational studies of new molecule contain 1, 2, 4-triazole, and coumarin bearing 6, 8-dimethyl. *Biointerface Research in Applied Chemistry*, 12, pp.809-823.

Kumara, N., Kooh, M.R.R., Lim, A., Petra, M.I., Voo, N.Y., Lim, C.M., and Ekanayake, P., 2013. DFT/TDDFT and experimental studies of natural pigments extracted from black tea waste for DSSC application. *International Journal of Photoenergy*, 2013, p.109843.

Lévai, A., 2004. Synthesis of exocyclic α, β-unsaturated ketones. *ARKIVOC*, 2004, pp.15-33.

Masoud, M.S., Ali, A.E., Shaker, M.A., and Elasala, G.S., 2012. Synthesis, computational, spectroscopic, thermal and antimicrobial activity studies on some metal-urate complexes. *Spectrochimica Acta Part A: Molecular and Biomolecular Spectroscopy*, 90, pp.93-108.

Omar, S.Y., Mamand, D.M., Omer, R.A., Rashid, R.F., and Salih, M.I., 2023. Investigating the role of metoclopramide and hyoscine-N-butyl bromide in colon motility. , 11, pp.109-115.

Omer, R., Koparir, P., Koparir, M., Rashid, R., Ahmed, L., and Hama, J., 2022a. Synthesis, characterization and DFT study of 1-(3-mesityl-3-methylcyclobutyl)-2-((4-phenyl-5-(thiophen-2-yl)-4H-1, 2, 4-triazol-3-yl) thio) ethan-1-one. *Protection of Metals and Physical Chemistry of Surfaces*, 58, pp.1-13.

Omer, R.A., Koparir, P., Ahmed, L., and Koparir, M., 2021. Computational and spectroscopy study of melatonin. *Indian Journal of Chemistry*, 60, pp.732-741.

Omer, R.A., Koparir, P., and Ahmed, L.O., 2022b. Characterization and inhibitor activity of two newly synthesized thiazole. *Journal of Bio-and Tribo-Corrosion*, 8, pp.1-12.

Omer, R.A., Koparir, P., Qader, I.N., and Ahmed, L.O., 2022c. Theoretical determination of corrosion inhibitor activities of naphthalene and tetralin. *Gazi University Journal of Science*, 35, pp.434-444.

Parlak, A.E., Omar, R.A., Koparir, P., and Salih, M.I., 2022. Experimental, DFT and theoretical corrosion study for 4-(((4-ethyl-5-(thiophen-2-yl)-4H-1, 2, 4-triazole-3-yl) thio) methyl)-7, 8-dimethyl-2H-chromen-2-one. *Arabian Journal of Chemistry*, 15, p.104088.

Pitchumani, K., Velusamy, P., Sabithamala, S., and Srinivasan, C., 1994. Modification of chemical reactivity upon cyclodextrin encapsulation: Asymmetric bromination of chalcone and benzylideneacetone. *Tetrahedron*, 50, pp.7903-7912.

Plakhutin, B.N., and Davidson, E.R., 2009. Koopmans' theorem in the restricted open-shell hartree-fock method. 1. A variational approach. *The Journal of Physical Chemistry A*, 113, pp.12386-12395.

Politzer, P., and Murray, J.S., 2002. The fundamental nature and role of the electrostatic potential in atoms and molecules. *Theoretical Chemistry Accounts*, 108, pp.134-142.

Priya, M.K., Revathi, B., Renuka, V., Sathya, S., and Asirvatham, P.S., 2019. Molecular structure, spectroscopic (FT-IR, FT-raman, 13C and 1H NMR) analysis, HOMO-LUMO energies, Mulliken, MEP and thermal properties of new chalcone derivative by DFT calculation. *Materials Today Proceedings*, 8, pp.37-46.

Rani, A., Anand, A., Kumar, K., and Kumar, V., (2019). Recent developments in biological aspects of chalcones: The Odyssey continues. *Expert Opinion on Drug Discovery*, 14, pp.249-288.

Rasul, H.H., Mamad, D.M., Azeez, Y.H., Omer, R.A., and Omer, K.A., 2023. Theoretical investigation on corrosion inhibition efficiency of some amino acid compounds. *Computational and Theoretical Chemistry*, 1225, p.114177.

Rebaz, O., Ahmed, L., Jwameer, H., and Koparir, P., 2021. Structural analysis of epinephrine by combination of density functional theory and hartree-fock methods. *El-Cezeri Journal of Science and Engineering*, 9, pp.760-776.

Rebaz, O., Ahmed, L., Qader, I., and Koparir, P., 2022. Theoretical analysis of the reactivity of carmustine and lomustine drugs. *Journal of Physical Chemistry and Functional Materials*, 5, pp.84-96.

Rebaz, O., Koparir, P., Qader, I.N., and Ahmed, L., 2021. Structure reactivity analysis for phenylalanine and tyrosine. *Cumhuriyet Science Journal*, 42, pp.576-585.

Salih, S.K., Mustafa, R.M., Mamad, D.M., Kaka, K.N., Omer, R.A., and Hamad, W.M., 2023. Synthesis of liquid crystalline benzothiazole based derivatives: Theoretical and experimental study of their optical and electrical properties. *ZANCO Journal of Pure and Applied Sciences*, 35, pp.143-162.

Tajuddeen, N., Isah, M.B., Suleiman, M.A., Van Heerden, F.R., and Ibrahim, M.A., 2018. The chemotherapeutic potential of chalcones against leishmaniases: A review. *International Journal of Antimicrobial Agents*, 51, pp.311-318.

Tekale, S., Mashele, S., Pooe, O., Thore, S., Kendrekar, P., and Pawar, R., 2020. Biological role of chalcones in medicinal chemistry. In: *Vector-Borne Diseases-Recent Developments in Epidemiology and Control.* IntechOpen, London.

Zandiyeh, Z., and Ghiasi, R., 2019. A theoretical approach towards identification of external electric field effect on (η5-C5H5) Me2Ta (η2-C6H4). *Russian Journal of Physical Chemistry A*, 93, pp.482-487.

Zhu, M., Wang, J., Xie, J., Chen, L., Wei, X., Jiang, X., Bao, M., Qiu, Y., Chen, Q., Li, W., Jiang, C., Zhou, X., Jiang, L., Qiu, P., and Wu, J., 2018. Design, synthesis, and evaluation of chalcone analogues incorporate α, β-Unsaturated ketone functionality as anti-lung cancer agents via evoking ROS to induce pyroptosis. *European Journal of Medicinal Chemistry*, 157, pp.1395-1405.

http://dx.doi.org/10.14500/aro.11314

Permeability Prediction for Carbonate Rocks using a Modified Flow Zone Indicator Method

Ahmed J. Mahmood[1*] and Mohammed A. Jubair[2]

[1]Department of Petroleum Engineering, Al-Farabi University College, Baghdad, Iraq

[2]Department of Computer Technical Engineering, College of Information Technology, Imam Ja'afar Al-Sadiq University, Al-Muthanna, 66002, Iraq

***Abstract*–Carbonate reservoir rocks are usually heterogeneous, so it is not an easy task to establish a relation between porosity and permeability in these types of reservoir rocks. First, Kozney and Kozney-carmen formulas were used to establish these relations. Later, the flow zone indicator (FZI) method was introduced, which was widely used to find such a relation since it shows better results than the two former methods. In this work, the classical FZI method and a modified form of the FZI method were utilized to identify the hydraulic flow units and rock quality index to predict permeability. In the modified FZI method, the cementation factor (m) was introduced in calculating the value of FZI. The data collected from core analysis of the cored intervals in the Tanuma and Khasib formations were used as a database for this work. The classical and the modified FZI methods were applied using the database to predict core permeability. The value of the cementation factor was tuned to get a better match between the predicted permeability resulting from applying the modified method and the measured permeability values. Results show that the correlation coefficients resulting from applying the modified FZI method are closer to unity compared with that resulting from the classical FZI method. Cementation factor (m) of m = 3 for Tanuma formation and m = 3 for Khasib formation are the best values used with the modified FZI method. The modified FZI method shows a regression factor of 0.9986 for Tanuma and 0.9942 for Khasib formation.**

***Index Terms* – Cementation factor, FZI, Hydraulic flow unit, Modified FZI, Permeability prediction.**

I. Introduction

The flow capacity and storage of petroleum reservoirs are mainly dependent on two important rock properties. They are permeability and porosity; because of their heterogeneity and inclination to be tight because of depositional and digenetic processes, carbonate reservoirs provide several obstacles when attempting to characterize them (Alobaidi, 2016; Haghighi, Shabaninejad and Afsari, 2011; Riazi, 2018).

In cored intervals, both permeability and porosity could be measured, but in uncored wells, permeability evaluation depends on the porosity evaluated by well logs. Many methods were proposed to calculate permeability, earlier The Kozeny, Kozeny–Carmen (K–C) correlation and their modifications are widely acceptable methodologies in the oil industry (Kozeny, 1927; Carman, 1937; Carman, 1938 and Shun, Yuzuru and Hide, 2018).

Amaefule, et al. (1993) presented a modification for K–C correlation. The reservoir quality index (RQI) and flow zone indicator (FZI) were proposed to improve its ability to represent the various behaviors of reservoir flow based on its respective characteristics. This was done to improve the capability of K–C correlation. However, there are difficulties associated with employing the initial correlation because of the inherent limits and oversimplified assumptions that it contains, both of which hinder correct definitions of the hydraulic flow unit (HFU) (Davies and Vessell, 1996; Barach, et al., 2022).

The concept introduced by Amaefule, et al. (1993), was modified by many researchers to establish a porosity permeability correlation having a correlation coefficient better than that resulting from the Amaefule method. Nooruddin and Hossain (2012) provided a modified K–C correlation by addressing the tortuosity factor in a more powerful manner. The model was validated with the help of core data taken from important carbonate reservoirs in Saudi Arabia. To demonstrate that the suggested model is applicable on a worldwide scale, additional data sets that were gleaned from the existing body of scholarly research on sandstone reservoirs were utilized. The findings indicate that one should anticipate a greater range of permeability values within a single HFU. Their results show that the traditional model greatly underestimates the permeability values found within a given HFU compared to the modified model.

Based on the well-log and core data, Abed (2014) was able to establish the flow zone indicator and then use K-means to divide the reservoir into several different HFUs. The next step is to develop a correlation between the HFUs from the core and the well-log data. This correlation is used

ARO-The Scientific Journal of Koya University
Vol. XII, No. 1 (2024), Article ID: ARO.11314. 7 pages
DOI: 10.14500/aro.11314
Received: 02 August 2023; Accepted: 04 December 2023
Regular research paper: Published: 28 February 2024
Corresponding author's email: dr.ahmed.jabir@alfarabiuc.edu.iq

to estimate permeability in un-cored wells; moreover, these correlations enable reservoir permeability to be estimated at the "flow unit" scale. After obtaining an effective porosity and flow zone indicator, the final step was to determine the permeability in each HFU. The results of permeability prediction based on HFU were studied for several wells, and the measured permeability value of cores was compared with those results. A strong relationship was shown between the expected and measured permeability.

Onuh, David and Onuh (2017) updated the reservoir quality indicator (RQI) approach for HFU characterization using the normalized pore throat concept. A correlation coefficient of 0.78 for the proposed modified RQI demonstrates an improvement over a correlation coefficient of 0.31 for the classical RQI method. This improvement was demonstrated by the result of an analysis that was conducted on various genetic reservoir units.

The first K–C formula was as follows:

$$K = (1/f_g\tau\ S^2)(\varnothing^3/(1-\varnothing)^2) \quad (1)$$

Where: - k is permeability in μm², fg is the shape factor, dimensionless, τ is the tortuosity (dimensionless), S is the surface area per unit bulk volume (*L2*/*L3*), and *Ø*. is the effective porosity (fraction). Mathematical resolutions are applied on Eq. (1) to become as follows:

$$0.0314\sqrt{k/\varnothing} = \left[1/s\sqrt{fg\,\tau}\right]\left[\varnothing/(1-\varnothing)\right] \quad (2)$$

K in millidarcy. Amaefule, et al. (1993) introduced the following definitions.

$$RQI = 0.0314\sqrt{k/\varnothing} \quad (3)$$

$$\varnothing_z = \varnothing/(1-\varnothing) \quad (4)$$

And

$$FZI = 1/s\sqrt{fg\ \tau} \quad (5)$$

Hence.

$$RQI = FZI * \varnothing_z \quad (6)$$

Then RQI versus $\varnothing_z$ can be plotted on (log–log) paper, where similar FZI values of the core sample will appear as a straight line, whereas various FZI values of the core sample shown on other parallel straight lines (Amaefule, et al., 1993; Davies and Vessell, 1996). Based on a modified K–C model Nooruddin and Hossain (2012) incorporated the tortuosity term as:

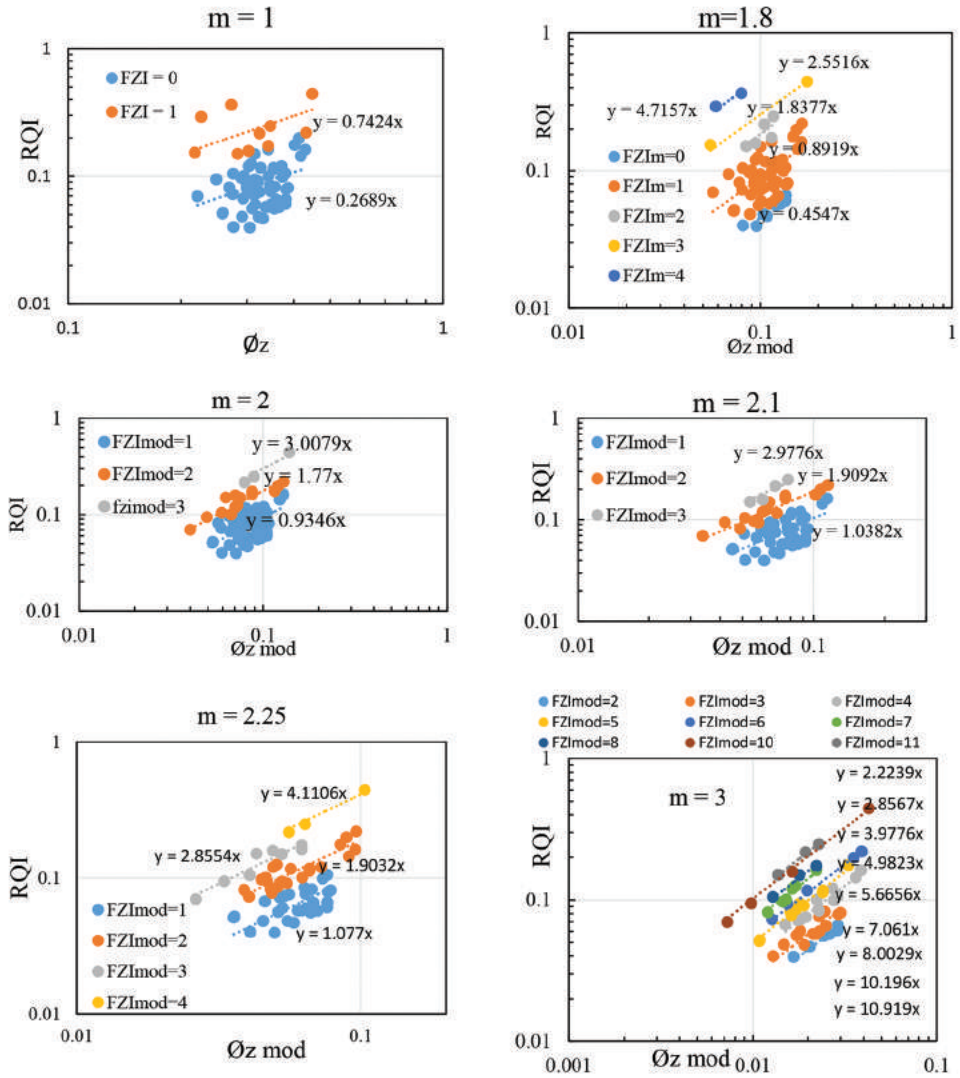

Fig. 1. Reservoir quality index versus Øz for conventional (m = 1) and modified method (m = 1.8, 2, 2.1, 2.25, and 3) for Tanuma formation.

http://dx.doi.org/10.14500/aro.11314

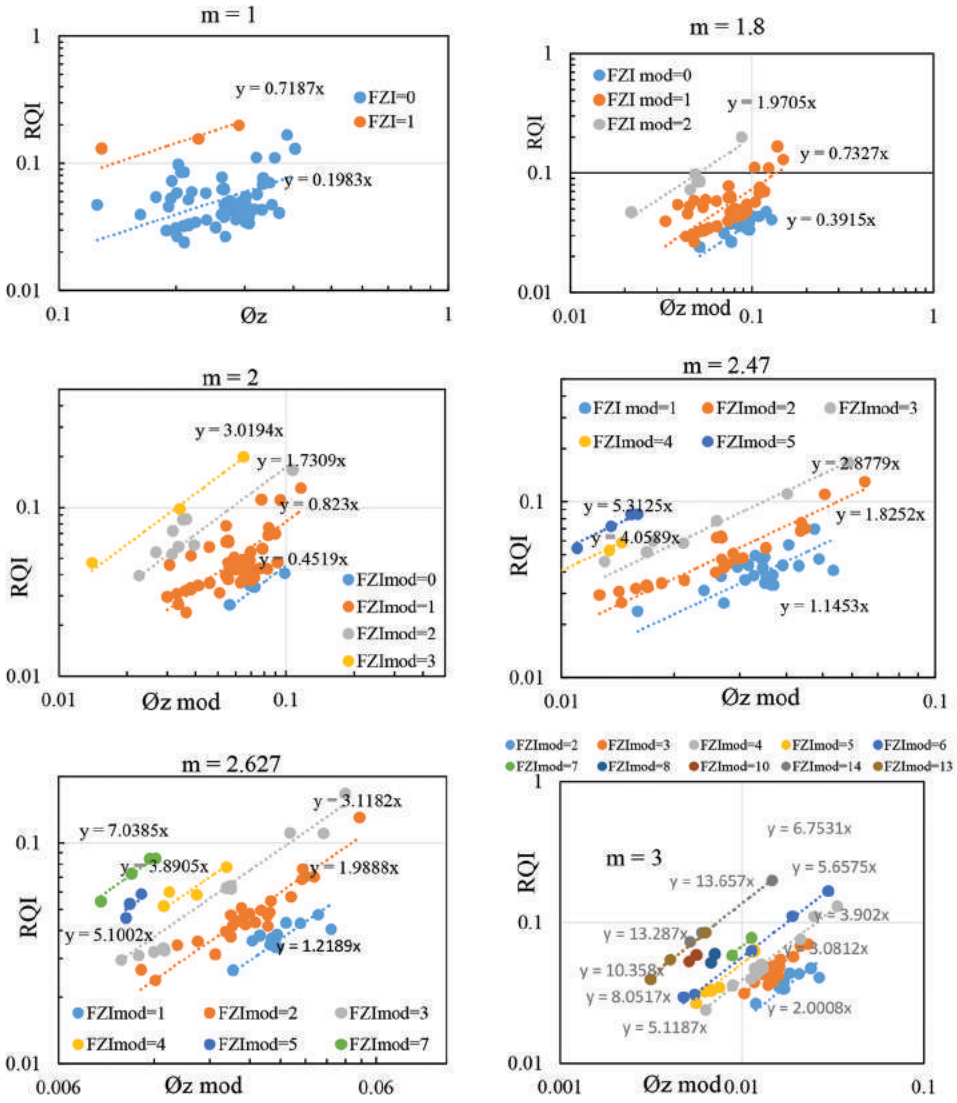

Fig. 2. Reservoir quality index versus Øz for conventional (m = 1) and modified method (m = 1.8, 2, 2.47, 2.627, and 3) for Khasib formation.

$$\tau = \left(a / \varnothing^{m-1}\right)^2 \tag{7}$$

Where a is the lithology factor and m is the cementation factor. Eq. (7) demonstrates the non-linear relationship between tortuosity and porosity and was incorporated into the original K–C model (Eq. 1). The proposed model is:

$$K = (1/f_g a^2 \ \ S^2)(\varnothing^{2m+1}/(1-\varnothing)^2) \tag{8}$$

Rearranging and taking the square root of Eq. (8) resulting in the following form:

$$0.0314\sqrt{k/\varnothing} = \left[1/a\ s\sqrt{fg}\right]\varnothing^m/(1-\varnothing) \tag{9}$$

Using the relations in Eqs. (3) and (4) and considering the first part of RHS (1/a s $\sqrt{fg}$) as the modified flow zone indicator (FZIm) yields:

$$RQI = FZIm^* \varnothing z^* \varnothing^{m-1} = FZIm^* \varnothing_{zmod} \tag{10}$$

Where,

$$\varnothing_{zmod} = \varnothing z^* \varnothing^{m-1} \tag{11}$$

Taking the logarithm of both sides of Eq. (10) results in the following relationship:

$$\log RQI = \log FZIm + \log \varnothing_{zmod} \tag{12}$$

If the cementation exponent, (m), is equal to one, then Eq. (12) is the same as the model that Amaefule, et al. (1993) developed. The slope of the lines in the plot of RQI versus $\varnothing_{zmod}$ on a log–log scale becomes steeper as the value of m grows. Every collection of rocks with a comparable FZI will be considered an HFU (Onuh, David and Onuh, 2017). Mathematically, the cementation factor (m) can vary from 1.0 to infinity. Practically, the cementation factor (m) for carbonate rocks ranges from 1.0 to 3.0 (Kadhim, Samsuri and Kamal, 2013). In this study, the value of m is considered between 1.0 and 3.0.

II. Methodology

The data set used in this work was from a well in the East-Baghdad oil field. The field is an Iraqi oil field. Tanuma and Khasib formations were recognized as reservoir rocks in this field. Tanuma formation is porous limestone having small vugs with evidence of shale in some sections. Khasib

formation is a porous limestone with shelly lime and chalky lime in some sections. The data set are readings of porosity and permeability at different depths resulting from core analysis for the cored intervals in well East-Baghdad – 35 (Ministry of Oil, 1983). The porosity range is (6–29.24) % and the permeability range is (0.1–28.9) md.

When applying the conventional FZI method, the porosity-permeability values for each formation were used to calculate RQI and $Ø_z$ adopting Eqs. (3) and (4). After calculating FZI from Eq. (6), different HFUs could be recognized corresponding to the rounded value of FZI. From the plot of RQI versus $Ø_z$ mathematical relation between porosity and permeability was derived for each rounded FZI value. These mathematical relations are employed to calculate core permeability depending on the measured porosity value. The former steps were followed when the modified FZI method was employed but Eq. (11) was utilized to calculate $Ø_{zmod}$ instead of Eq. (4) and FZIm was calculated through Eq. (10). The magnitude of m was used to calculate $Ø_{zmod}$ was ranging from 1 to 3 and calculation steps were repeated for each m value. Permeability could be predicted depending on the mathematical relations resulting from plots of RQI versus $Ø_{zmod}$ for each m value.

To study the effectuality of the different FZI techniques, plots of the calculated permeability resulting from the different approaches versus the measured permeability were achieved. The correlation coefficients of these plots are considered the base for comparison between the different porosity–permeability relations for formations under study.

III. Results and Discussion

The conventional FZI method (m = 1) and the modified FZI method (m = 1.8, 2, 2.1, 2.25, and 3) were applied using the porosity and permeability data for Tanuma formation. Plots of RQI versus Øz and RQI versus $Ø_{zmod}$ in log–log scale are shown in Fig. 1.

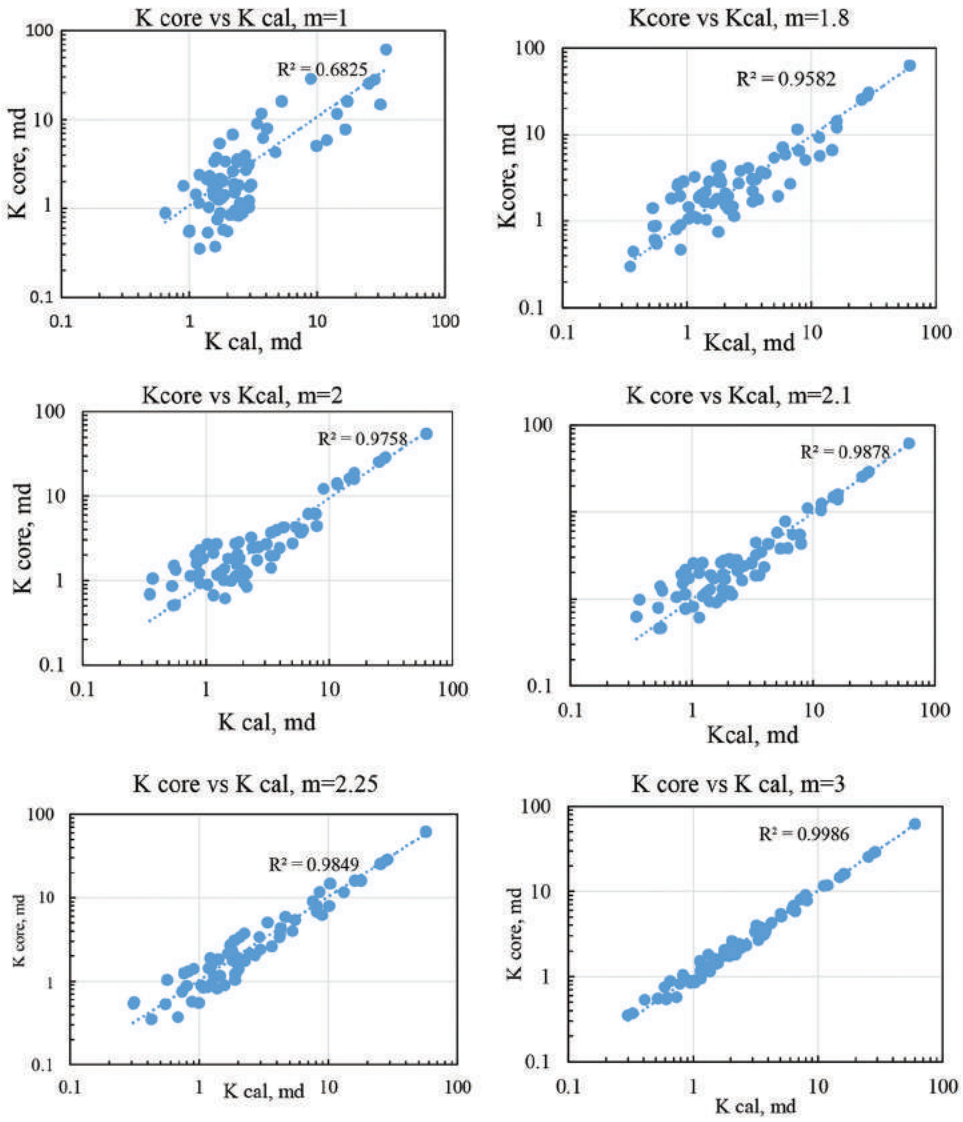

Fig. 3. Core permeability versus calculated permeability applying the conventional (m = 1) and the modified method (m = 1.8, 2, 2.1, 2.25, and 3) Tanuma formation.

http://dx.doi.org/10.14500/aro.11314

The same methods (conventional and modified FZI) were applied using the porosity and permeability data for Khasib formation. Plots of RQI versus Øz and RQI versus $Ø_{zmod}$ in log–log scale are shown in Fig. 2.

The plots in Figs. 1 and 2 clarify that applying the modified method increases the number of HFUs (zones) as the value of m increases, more zones are identified. Mathematical relations between porosity and permeability were derived from x and y equations that appear with each specific FZI value. These derived relations were used to calculate core permeability depending on the measured porosity. To compare the measured core permeability values for each individual formation with the calculated permeability values resulting from applying the mathematical relations. Plots of core permeability versus the calculated permeability resulting from applying the conventional and the modified FZI methods are presented in Fig. 3 for Tanuma formation and Fig. 4 for Khasib formation.

In Figs. 3 and 4, it is clearly seen that the conventional method (m = 1) yields a lower correlation coefficient (R^2 = 0.6825 for Tanuma and R^2 = 0.5971 for Khasib) compared to that resulted from the modified method. The value of the correlation coefficients is closer to unity as m increased in modified method. The best values of R^2 are at m = 3 for both formations (0.9986 for Tanuma and 0.9942 for Khasib). The improvement of the R^2 values as m increases is attributed to the increase of the HFU as m increases, this implies that more porosity – permeability relation will be identified. The different values of m and correlation coefficient are in Table I below.

The values in Table I indicate that generally, values of R^2 when applying the modified method are better (closer to

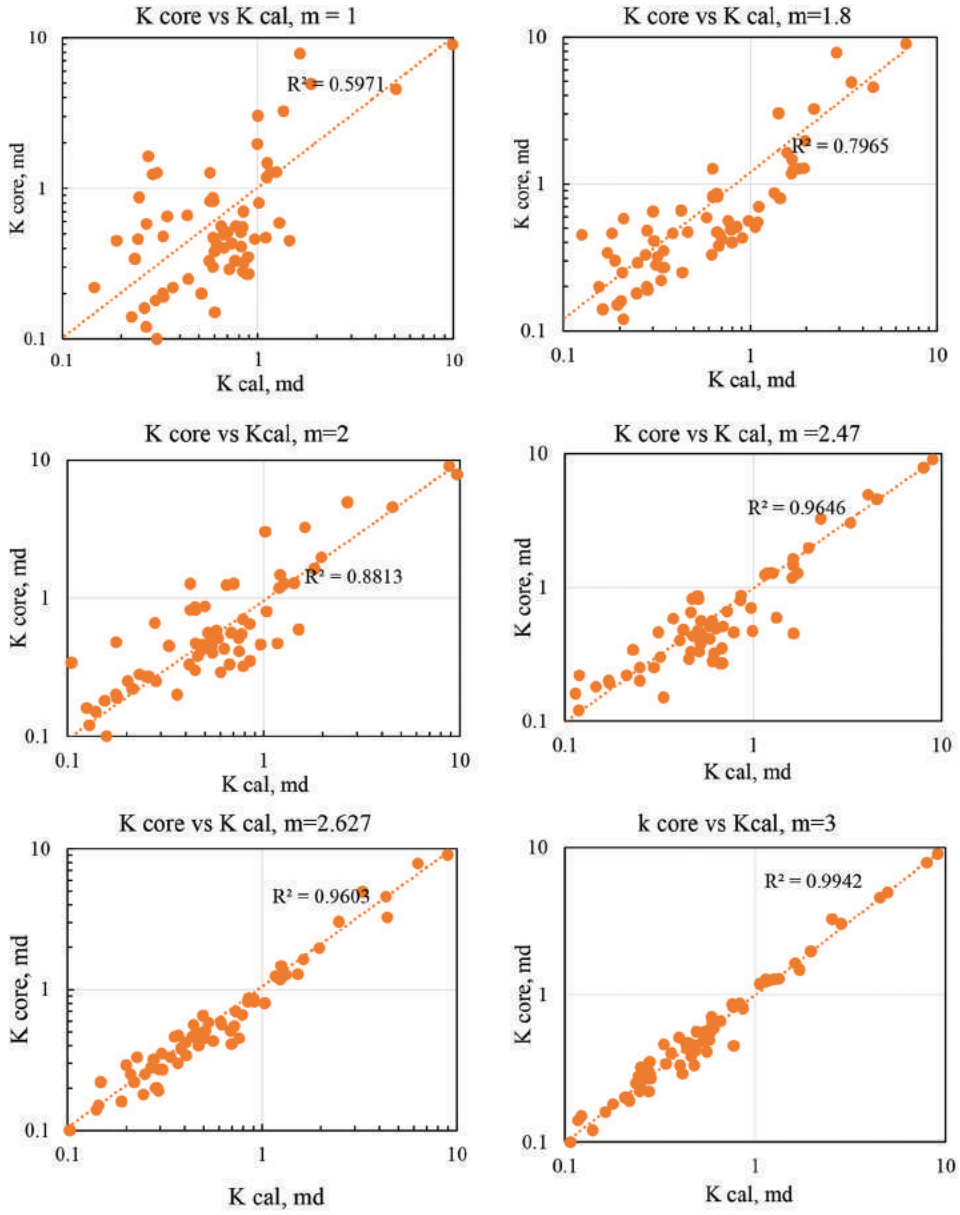

Fig. 4. Core permeability versus calculated permeability applying the conventional (m = 1) and the modified method (m = 1.8, 2, 2.47, 2.647, and 3) Khasib formation.

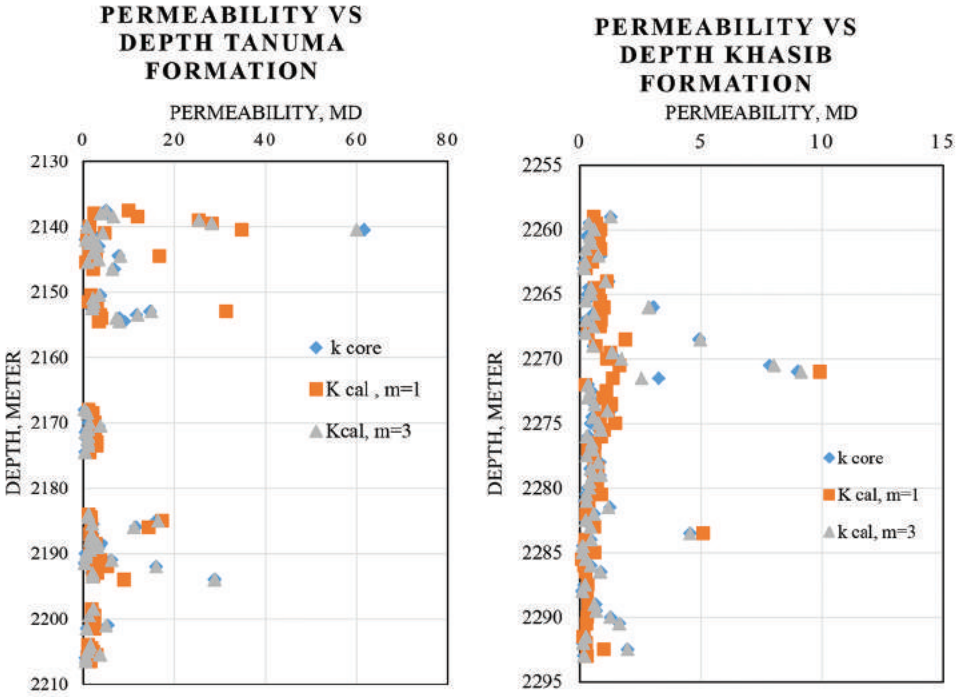

Fig. 5. Calculated permeability and core permeability versus depth for Tanuma and Khasib formations.

TABLE I
VALUES OF CORRELATION COEFFICIENT FOR TANUMA AND KHASIB FORMATIONS

Tanuma Formation		Khasib Formation	
m	R^2	m	R^2
1 (conventional)	0.6825	1 (conventional)	0.5971
1.8	0.9582	1.8	0.7965
2	0.9758	2	0.8813
2.1	0.9878	2.47	0.9646
2.25	0.9849	2.627	0.9603
3	0.9986	3	0.9942

unity) than that resulting from applying the conventional one. In Tanuma formation, R^2 increases from 0.6825 to 0.9582 when m increases from 1 to 1.8, whereas m needs to be 2.47 to reach R^2 value of 0.9646 in Khasib formation.

The plot of measured core permeability, permeability calculated by the conventional method, and permeability calculated by the modified method (m = 3) versus depth for Tanuma and Khasib formations are in Fig. 5.

IV. CONCLUSIONS

The modified FZI method is more accurate in permeability prediction than the conventional method. Better matches between calculated and measured permeability are recognized as the value of the cementation factor (m) increases. The best match between the measured and the predicted permeability is at m = 3 for both formations. It is better than the conventional method, so it is better to use the modified method for predicting permeability in uncored intervals. When applying the modified method to any other formations, different values of cementation factor (m) must be tested to select the one having the best correlation coefficient.

REFERENCES

Abed, A.A., 2014. Hydraulic flow units and permeability prediction in a carbonate reservoir, Southern Iraq from well log data using non-parametric correlation. *International Journal of Enhanced Research in Science Technology and Engineering*, 3(1), pp.480-486.

Alobaidi, D.A., 2016. Permeability prediction in one of Iraqi carbonate reservoir using hydraulic flow units and neural networks. *Iraqi Journal of Chemical and Petroleum Engineering*, 17(1), pp.1-11.

Amaefule, J.O., Altunbay, M., Tiab, D., Kersey, D.G., and Keelan, D.K., 1993. Enhanced Reservoir Description: Using Core and Log Data to Identify Hydraulic (Flow) Units and Predict Permeability in Uncored Intervals/Wells. In*: SPE Annual Technical Conference and Exhibition*, OnePetro.

Barach, B., Jaafar, M., Gaafar, G., Agi, A., Junin, R., Sidek, A., Gbadamosi, A., Yakasai, F., Oseh, J., and Gbonhibor, J., 2022. Development and Identification of Petrophysical Rock Typing for Effective Reservoir Characterization. In: *SPE Nigeria Annual International Conference and Exhibition*, Onepetro.

Carman, P.C., 1937. Fluid flow through granular beds. *Transactions of the Institution of Chemical Engineers*, 15, pp.150-166.

Carman, P.C., 1938. Fundamental principles of industrial filtration. *Transactions of the Institution of Chemical Engineers*, 16, pp.168-188.

Davies, D.K., and Vessell, R.K., 1996. Identification and Distribution of Hydraulic Flow Units in a Heterogeneous Carbonate Reservoir: North Robertson Unit, West Texas. In: *SPE Permian Basin Oil and Gas Recovery Conference, Paper Number SPE-35183*, SPE.

Haghighi, M.B., Shabaninejad, M., and Afsari, K., 2011. A permeability predictive model based on hydraulic flow unit for one of Iranian carbonate tight gas reservoir. In: *SPE Middle East Unconventional Resources Conference and Exhibition, Paper Number SPE-142183*, SPE.

Kadhim, F.S., Samsuri, A., and Kamal, A., 2013. A review in correlations between cementation factor and carbonate rocks properties. *Life Science Journal*, 10(4), pp.2451-2458.

Kozeny, J., 1927. *Über Kapillare Leitung des Wassers im Boden*. Vol. 136. Akademie der Wissenschaften, Sitz der Wien, pp.271-306.

Ministry of Oil, 1985. *Routine Core analysis (RCA) for Wells (EB-35)*. Reservoir Solutions (RES), United States.

Nooruddin, H.A., and Hossain, M.E., 2012. Modified Kozeny-correlation for enhanced hydraulic flow unit characterization. *Journal of Petroleum Science and Engineering*, 80, pp.107-115.

Onuh, H.M., David, O.O., and Onuh, C.Y., 2017. Modified reservoir quality indicator methodology for improved hydraulic flow unit characterization using the normalized pore throat methodology (Niger Delta field as case study). *Journal of Petroleum Exploration and Production Technology*, 7, pp.409-416.

Riazi, Z., 2018. Application of integrated rock typing and flow units identification methods for an Iranian carbonate reservoir. *Journal of Petroleum Science and Engineering*, 160, pp.483-497.

Shun, N., Yuzuru, Y., and Hide, S., 2018. Modified expression of Kozeny-Carman equation based on semilog-sigmoid function. *Soils and Foundations*, 58, pp.1350-1357.

Electrocardiogram Heartbeat Classification using Convolutional Neural Network-k Nearest Neighbor

Zrar Kh. Abdul[1], Abdulbasit K. Al-Talabani[2], Chnoor M. Rahman[1] and Safar M. Asaad[2]*

[1]Department of Computer Science, College of Science, Charmo University
46023, Chamchamal, Sulaimani, Kurdistan Region – F.R. Iraq

[2]Department of Software Engineering, Faculty of Engineering, Koya University
Koya KOY45, Kurdistan Region – F.R. Iraq

***Abstract*–Electrocardiogram (ECG) analysis is widely used by cardiologists and medical practitioners for monitoring cardiac health. A high-performance automatic ECG classification system is challenging because there is difficulty in detecting and categorizing different waveforms in the signal, especially in manual analysis of ECG signals, which means, a better classification system is needed in terms of performance and accuracy. Hence, in this paper, the authors propose an accurate ECG classification and monitoring system called convolutional neural network-k nearest neighbor (CNN-kNN). The proposed method utilizes 1D-CNN and kNN. Unlike the existing techniques, the examined technique does not need training during classifying the ECG signals. The CNN-kNN is evaluated against the PhysioNet's MIT-BIH and PTB diagnostics datasets. The CNN is fed using the ECG beat raw signal directly. In addition, the learned features are extracted from the 1D-CNN model and its dimensions are reduced using two fully connected layers and then fed to the k-NN classifier. The CNN-kNN model achieved average accuracies of 98% and 97.4% on arrhythmia and myocardial infarction classifications, respectively. These results are evidence of the great ability of the proposed model compared to the mentioned models in this article.**

***Index Terms*—Convolutional neural network, Electrocardiogram classification arrhythmia, K-nearest neighbor.**

I. Introduction

An electrical activity generated by the heart is called an electrocardiogram (ECG) signal. The ECG signal conveys information which is reflection the properties of the heart health condition. Therefore, diagnosis of the ECG signal is the main way to know the heart health condition. Consequently, analysis of the ECG signal became interesting to categorize the heart health condition. Due to certain limitations in disease classification based on the ECG including variance ECG morphology, Machine learning techniques have been widely applied to develop automatic heartbeat classification systems (Luz, et al., 2016). Machine learning techniques have been widely applied to develop automatic heartbeat classification systems (Luz, et al., 2016). Three different architectures of machine learning have been used for ECG diagnosis, namely traditional machine learning, deep machine learning, and hybrid machine learning architecture.

Effective feature extraction technique is the key success of traditional machine learning. In Saini, Singh, and Khosla (2013), a model developed based on the k nearest neighbor (kNN) classifier and some features that were adopted by applying a digital band-pass filter. Discrete wavelet transform (DWT) was addressed to an effective feature for the ECG signal and fed to the kNN algorithm (Bouaziz, Boutana and Oulhadj, 2019). The DWT was to train support vector machine (SVM). Venkatesan, et al. (2018) and Smíšek, et al. (2017) reported that a trained SVM through some morphological features could improve the accuracy rate for ECG classification. Mel Frequency Cepstrum Coefficient was used to feed artificial neuron networks for ECG Signals Classification Boussaa, et al. (2016). Due to the ECG signal is non-stationary signal, more complex methods for feature extraction have been conducted. Therefore, determining the best suited features is time-consuming and tedious work (Khatibi and Rabinezhadsadatmahaleh, 2019).

For deep machine learning, mass consideration is about having enough data to train the machine and turn parameters Litjens, et al. (2017), Shima, Nakashima and Yasuda (2018). Convolutional neural network (CNN) has widely been used for variance applications including ECG classification (Labati, et al., 2018), (Zubair, Kim and Yoon, 2016). They all reported that the CNN model is straightforward to apply and can improve the automatic heartbeat classification system. CNN has been used in two forms 1 and 2 directional. For instance, Kiranyaz, Ince, and Gabbouj, 2016a developed an ECG diagnosis system based on 1D-CNN and the ECG signal was fed to the 1D-CNN directly. However, for 2D-CNN, the ECG signal must be transformed into two two-dimensional forms. For instance, in Zhai and Tin (2018), a model based on 2D-CNN was proposed, where the heartbeats were transformed into dual dual-beat coupling matrix and given to the CNN model as 2-D input.

ARO-The Scientific Journal of Koya University
Vol. XII, No. 1 (2024), Article ID: ARO.11444. 7 pages
DOI: 10.14500/aro.11444
Received: 16 October 2023; Accepted: 14 February 2024
Regular research paper: Published: 29 February 2024
Corresponding author's email: safar.maghdid@koyauniversity.org

http://dx.doi.org/10.14500/aro.11444

The hybrid machine learning system is a model that consists of traditional machine learning and deep learning algorithms or a combination of two deep learning algorithms. In Khatibi and Rabinezhadsadatmahaleh (2019), CNN and kNN have participated in extracting the features. The features were later given to the SVM for ECG beat classification and arrhythmia detection. Wang in (Wang, 2020) proposed a model by combining CNN and the modified Elman neural network, and his results show that the model can improve the accuracy of the ECG beat classification system. The CNN and long short-term memory (LSTM) were examined in Oh, et al. (2018). The CNN part was responsible for extracting features and LSTM was responsible for classifying the categories of the ECG beat.

As mentioned, in most of the existing techniques, one more technique was utilized for training the features, which may affect the performance of the model. To date, no techniques exist for utilizing the kNN classifier for classifying the features without requiring to train the features. Moreover, as mentioned by Homaeinezhad, et al. (2012) and Zhang and Zhou (2005), kNN is counted as one of the well-known and fastest machine learning classifiers. Hence, utilizing it in computing any models will affect the model's accuracy and prediction. In this paper, a hybrid machine-learning model is developed for heartbeat classification. The model contains the 1D-CNN to extract the features and the kNN classifier to classify the feature signal. The CNN-kNN model is a featureless model as it does not need to have any Handcrafted features. The novelty and importance of the proposed work are that the kNN does not need further training to classify the ECG. The main contributions of the proposed model are as follows:

- Designing and implementing a high-performance ECG classification system.
- Utilizing the 1D-CNN as feature extractor.
- Using the kNN classifier for the feature classification.
- For classifying the ECG, no further training of the extracted features is required.

The rest of this paper is organized as follows. Section 2 explains the background of the area. Section 3 presents the proposed method. Section 4 presents results and a discussion of the proposed method on different tasks and a comparing it with the works in the literature. Finally, Section 5 concludes the paper.

II. Background

The traditional main steps involved in any classification system are preprocessing, feature extraction, and classifier learning. Automatic heartbeat classification is one of the applications that should follow the same process. In this paper, since the prepared data in Li and Zhou (2016); Acharya, et al., (2017a); Kachuee, Fazeli, and Sarrafzadeh (2018) are utilized, the preprocessing step is not focused on. For the feature extraction step, the 1D-CNN employed to extract the learned features which they fed the kNN classifier. In this section, a brief background about CNN and k-NN is presented.

A. k-Nearest Neighbors Classifier

kNN is one of the well-known classification methods in the world of machine learning, which is a supervised algorithm with a desirable computational speed along with acceptable classification accuracy (Zhang and Zhi-Hua, 2005). The training stage is not required for the kNN classifier but rather it is based on a simple mathematical theory (Jiang, et al., 2007). The kNN classifier imposes the lowest computational rate N compared to the most of the other classification methods, such as SVM and artificial neural networks (ANN) classifiers (Homaeinezhad, et al., 2012). Consequently, kNN is much faster than the SVM and ANN algorithms. To formulate the kNN classification algorithm, assume that the pair (x_i, $f(x_i)$) contains the feature vector x_i and its corresponding label $f(x_i)$ where $f(x_i) \in \{1,2,\ldots, n\}$ and $i = 1,2,\ldots, N$ (n and N is the number of classes and the number of train feature vectors, respectively). The principal idea behind kNN is to measure the distance between feature vectors such that the nearest neighbor for the tested sample makes a decision about the label of the features (Aljojo, 2022). The majority voting strategy among the k-nearest samples is basically adopted in this classifier. The distance for the features can be formulated in (1) Homaeinezhad, et al. (2012).

$$d(i,j) = f\left(x_i, x_j\right) \tag{1}$$

Where, $f(x_i, x_j)$ is a scalar distances function. Three common distance functions have been widely used for determining the distance as given in (2), (3), and (4) Homaeinezhad, et al. (2012).

$$f\left(x_i, x_j\right) = (x_i - x_j)^T \sum \left(x_i - x_j\right) \tag{2}$$

$$f\left(x_i, x_j\right) = \left(\sum_{k=1}^{p} (x_i(k) - x_j(k))\right)^{1/r} \tag{3}$$

$$f\left(x_i, x_j\right) = \frac{1}{p} \sum_{k=1}^{p} abs\left(x_i(k) - x_j(k)\right) \tag{4}$$

Where, Equation (2) is named generalized distance and when the weight matrix $\Sigma = I$, the famous Euclidean norm will be reached. Equation (3) is called Minkowski distance of degree r and when $r = 2$, again the Euclidean distance appears. Furthermore, Equation (4) is known as City Block distance and it is used in many pattern recognition cases (Homaeinezhad, et al., 2012).

B. CNN

CNN is a kind of deep neural network that was originally proposed for 2D input. It is a powerful machine learning tool for learning features from the input raw data. CNN outperforms the traditional machine learning models for image classification (Khan, et al., 2020). One of the modifications of 2D-CNNs is the 1D-CNNs, which has recently been applied in many applications (Ince, et al., 2016; Kiranyaz, Ince, and Gabbouj, 2016b; Acharya, et al., 2017b; Kiranyaz, et al., 2019). These researches have clarified that for certain applications, 1D-CNNs are preferable one-dimensional-based applications due to the low complexity, small number of hidden layers and neurons, and low cost of implementation. Typically, any CNN

models are mainly composed of two parts: Feature extraction and classification. The feature extraction section is responsible for extracting features from the ECG signals automatically, which usually consists of some layers such as convolution and pooling layers, whereas the classification part is in charge of classification decisions. The classification part is identical to a typical Multi-layer Perceptron (MLP) and is often referred to as fully connected layers (Kiranyaz, et al., 2015).

The configuration of any 1D-CNN explores some important processes as shown below:

- Initialize weights and biases
- Feed forward process applies from the input layer to the output layer to find outputs of each neuron at each layer. The process is formulated in (5) (Kiranyaz, et al., 2020; Rautela, et al., 2020).

$$x_k^l = b_k^l + \sum_{i=1}^{Nl-1} \text{conv1D}\left(w_{ik}^{l-1}, s_i^{l-1}\right) \quad (5)$$

Where, x_k^l represents the input of the k^{th} neuron at layer l, b_k^l is a bias of the k^{th} neuron at layer l, s_i^{l-1} and w_{ik}^{l-1} are the output of the i^{th} neuron at layer $l-1$ and the kernel from the i^{th} neuron at layer $l-1$ to the k^{th} neuron at layer l, respectively. Moreover, $conv1D$ is used to perform the convolution process between w_{ik}^{l-1} and s_i^{l-1}.

- Backpropagation process: start from computing delta error at the output layer and back-propagate it to the first hidden layer to compute the delta errors. The Equation (6) is a delta error (Kiranyaz, et al., 2020).

$$\frac{\partial E}{\partial w_{ik}^{l-1}} = \Delta_k^t y_i^{l-1} \text{ and } \frac{\partial E}{\partial b_k^l} = \Delta_k^t \quad (6)$$

Where, E is the mean-squared error (MSE), y_i^{l-1} is intermediate output, and Δ_k^t is defined as a delta error.

- Post-process to compute the weight and bias sensitivities.
- Update the weights and biases.

III. Methodology

A. Datasets

In studies that set out to classify ECG records, authors Martis, et al. (2013a); Li and Zhou (2016); Acharya, et al. (2017b); Kachuee, Fazeli, and Sarrafzadeh (2018) used two different sources of data, namely PTB Diagnostic ECG and PhysioNet MIT-BIH Arrhythmia. Both of the sources are composed of ECG records which were recorded from different subjects; the PTB diagnostics dataset registered from 290 subjects at a sample rate of 1000 Hz (Sadhukhan and Mitra, 2012), whereas the PhysioNet MIT-BIH Arrhythmia dataset are recordings of 47 subjects at a sample rate of 360 Hz (Goldberger, et al., 2000). Table I illustrates a summary of mappings between beat annotations in five categories in accordance with the Association for the Advancement of Medical Instrumentation (AAMI) standard (AAMI and others, 1998). In this paper, the author uses ECG lead II resampled to the frequency sample of 125 Hz for MIT-BIH.

B. Preprocessing

A preprocessing for the ECG signals is performed in this work based on a set of steps as shown below:

1. Picking a 10-s window from a signal of ECG after division of the signal to 10-s windows.
2. The values of the amplitude were normalized to the range of zero and one.
3. Relying on the zero crossing of the first derivative, trace the set of all local maximums.
4. Implementing a threshold of 0.9 on the normalized value of the local maximums to find the set of ECG R peak candidates.
5. The median of the R-R time interval was considered as the nominal heartbeat period of that window (T).
6. Choosing a signal part of 1.2T length for each R-peak.
7. Unify the signal length by applying padding.

It is important to note that in the extracting R-R interval method, no form of filtering was used and to use these extracted beats as an input to the subsequent processing parts, all the beats have equal length.

C. CNN-kNN Proposed Model

The proposed model for heartbeat classification is developed based on an integration between CNN and kNN as shown in Fig. 1. The proposed model is developed based on integrating into two common machine learning algorithms, including the CNN and the kNN. The CNN

TABLE I
Summary of Mappings between Beat Annotations and AAMI EC57

AAMI class	MIT-BIH heartbeat types				
Normal beat (N)	Normal beat (N)	Left bundle branch block beat (L)	Right bundle branch block beat (R)	Atrial escape beat (e)	Nodal (junctional) escape beat (j)
Supraventricular ectopic beat (S)	Atrial premature beat (A)	Aberrated atrial premature beat (a)	Nodal (junctional) premature beat (J)	Supraventricular premature beat (S)	
Ventricular ectopic beat (V)	Premature ventricular contraction (V)	Ventricular escape beat (E)			
Fusion beat (F)	Fusion of ventricular and normal beat (F)				
Unknown beat (Q)	Paced beat (/)	Fusion of paced and normal beat (f)	Unclassified beat (Q)		

AAMI: Association for the Advancement of Medical Instrumentation

http://dx.doi.org/10.14500/aro.11444

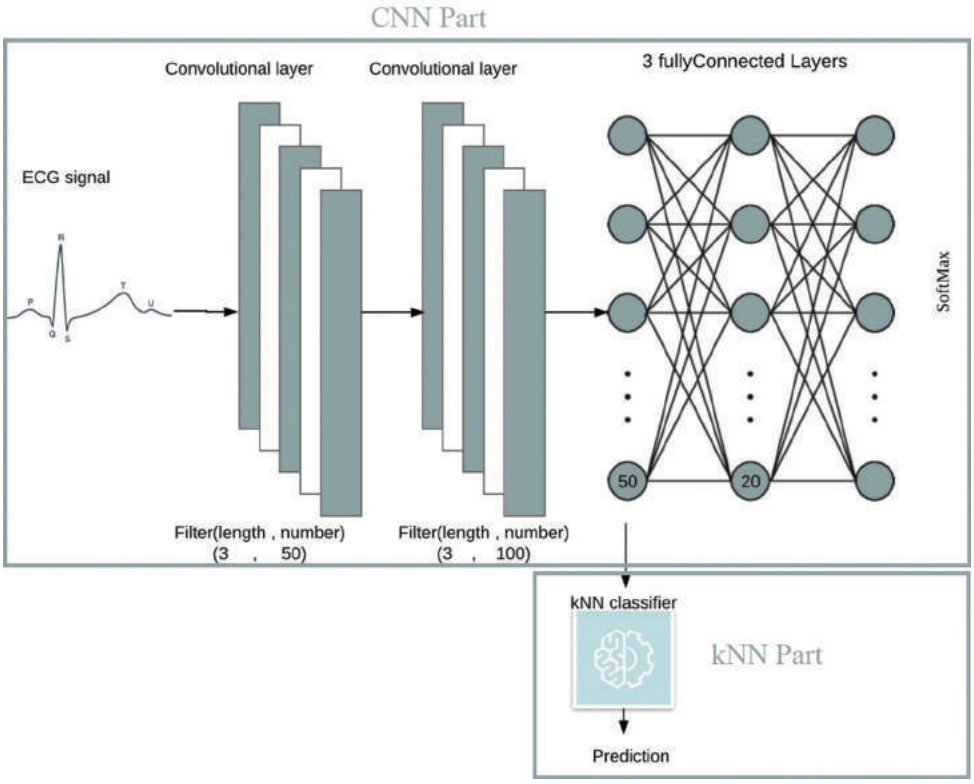

Fig. 1. Architecture of convolutional neural network-k nearest neighbor proposed model.

structure contains 8 layers including two convolutional and three fully connected layers. The number of neurons in the output layer depends on the adopted dataset (for instance, 5 neurons for PhysioNet's MIT-BIH and 2 neurons for PTB Diagnostics datasets). The other details of the CNN model can be found in Table II. In the first stage, the CNN is trained by the ECG datasets, where the hyperparameters of the CNN model were tuned using nine-fold cross-validation to get the least error rate. Then, the features are adopted from all the fully connected layers. The obtained features from each of the layers are fed to the kNN separately and the best optimum features are observed from the first fully connected layer which consists 50 nodes. In the final stage, the obtained features are classified by the kNN, where the number of k was tuned by the same strategy (cross-validation) that was used to tune the hyperparameter of CNN. In general, the CNN part of the proposed model is responsible for executing two vital tasks, which are extracting the effective features from the heartbeat signal and reducing the number of features using the fully connected layers. Moreover, the kNN part is responsible for classifying the learned features.

TABLE II
Detail of the 1D-CNN Model

No. layer	Name	Description
1	Input	187 × 1 × 1 input with 'zero center' normalization
2	Convolution	50 3 × 3 convolutions with stride [1 1] and padding 'same'
3	Convolution	100 3 × 3 convolutions with stride [1 1] and padding 'same'
4	Fully connected	50 fully connected layer
5	Fully connected	20 fully connected layer
6	Fully connected	Either 2 or 5 fully connected layer depending on the dataset
7	Softmax	Activation function for the last Fully Connected layer
8	Classification	Output cross-entropy

TABLE III
NN Parameters

Parameters	Value	Parameters	Value
Optimization method	Adam	Mini batch size	128
Initial learn rate	0.01	Number of iteration	864
Number of epochs	25	Activation function in output layer	Softmax

D. Performance Metrics

Inspired by the previous studies that have proposed models for ECG arrhythmia detection [1], [3], [7], [15], [21], [26] (Luz, et al., 2016; Oh, et al., 2018; Zhai and Tin, 2018; Bouaziz, Boutana and Oulhadj, 2019), the performance metrics that are conducted in this study include accuracy, precision, and recall. The accuracy rate shows the overall ability of the model to classify ECG signals correctly as presented in (7). Recall is the rate of correctly classified beats of one class and the total beats classified as that class. It can be calculated by (8). Precision is the ratio of correctly classified beats of one class among the total beats belonging to that class, which is formulated as (9) (Foody, 2023)

$$\text{Accuracy}=\frac{TP+TN}{TP+TN+FP+FN} \quad (7)$$

Table IV
Accuracy of All Experiments

Dataset/layers	First fully-connected (50 nodes)	Second fully-connected (20 nodes)	Last fully connected 5, 2 nodes for MIB, PTB	Softmax layer
MIB	98	97.93	97.18	96.86
PTB	97.4	96.6	94.23	93.25

$$\text{Recall} = \frac{TP}{TP + FN} \quad (8)$$

$$\text{Precision} = \frac{TP}{TP + FP} \quad (9)$$

Where, TP is true positive, FP is false positive, TN is true negative, and FN is false negative.

E. Experiments' Setup

For any model like CNN and KNN, some parameters should be tuned to obtain the optimum values to improve the performance of the model. Regarding the kNN model, and to tune the parameter k, a 9-fold cross-validation approach is adopted. The k parameter is tuned to 5 and the metric is fixed as Euclidean distance. Following the same 9-fold cross-validation presented above, the number of convolutional layers is tuned to 2 layers, where they include 50 and 100 nodes, respectively, both with ReLu activation function. The number of hidden fully connected layers is set as two with the number of nodes equal to 50 and 20, respectively. The output layer's number of nodes is set according to the number of classes involved in the experiments. The optimization technique adopted in this network is Adam (Table III). The learned features are extracted from different fully connected layers to produce four versions of features. Consequently, four experiments per each dataset are conducted in this work as shown in the next section.

IV. Results and Discussion

To present the usefulness of the proposed model and validate the performance of each of the four versions of the learned features, four experiments per dataset are conducted and their accuracy is presented in Table IV. In both of the datasets, the same pattern of having the highest accuracy using the larger feature number is clearly seen. Learn features transformed into 50 dimensions outperform other versions of extracted features. Another observation is reducing the accuracy when the features are extracted from the softmax layer, i.e., after the softmax function is applied to the values of the features that are mapped to the output layer. This shows the non-usefulness of the softmax transformation for the kNN classifier.

The implementation of the proposed model includes two phases since the CNN-kNN method is an integrated model using CNN for extracting features and kNN as the classifier. In the first phase, an MPL-based 1D-CNN model is evaluated on PhysioNet MIT-BIH Arrhythmia dataset. Inspired by the previous works, which are cited in Table V, the dataset is set as 21892 and 87554 heartbeats for testing and training, respectively. As shown in the table, the accuracy rate of the proposed model is 98%, which is much higher compared to the second highest rate by the 1D-CNN, which is 96.8%. The reasonable accuracy of the CNN-kNN refers to the ability of the kNN classifier to classify the features of ECG. The second phase is about extracting features from the same 1D-CNN model but instead of utilizing the MLP, kNN is adopted as a classifier called CNN-kNN. The result shows that, in terms of accuracy, the ability to identify correct samples, and the quality of prediction, the 1D-CNN model and CNN-kNN model outperformed several state-of-the-art studies. It is noticeable that the proposed CNN-kNN is able to outperform the 1D-CNN as presented in Table V.

TABLE V
Comparison of Heartbeat Classification Results

Work	Approach	Accuracy (%)
Proposed (CNN-kNN)	CNN-kNN	98
CNN	1D-CNN	96.8
Kachuee, Fazeli and Sarrafzadeh (2018)	Deep residual CNN	93.4
Acharya, et al. (2017c)	Augmentation+CNN	93.5
Martis, et al. (2013b)	DWT+SVM	93.8
Li and Zhou (2016)	DWT+Random forest	94.6

CNN-kNN: Convolutional neural network-k nearest neighbor, DWT: Discrete Wavelet Transform, SVM: Support vector machine

TABLE VI
Comparison of MI Classification Results

Work	Accuracy (%)	Precision (%)	Recall (%)
Proposed (CNN-kNN)	96.78	95.9	96.26
1D-CNN	93.64	92.7	92.05
Kachuee Fazeli and Sarrafzadeh, 2018	95.9	95.2	95.1
Acharya, et al. (2017a)	93.5	92.8	93.7
Safdarian Dabanloo and Attarodi (2014)	94.7	-	-

CNN-kNN: Convolutional neural network-k nearest neighbor

MI detection is also treated as a two-class classification problem (infracted and non-infracted classes). The length of PTB diagnostics dataset is 14552 samples including 4046 normal and 10506 abnormal. Based on relevant research in the literature, k fold and hold out (20% testing and 80% training) cross-validation have been used to evaluate the utilized dataset for MI classification. In this paper, a 5-fold cross-validation is adopted. The result in Table VI shows that the performance of 1D-CNN does not surpass all the state of art results. However, the proposed CNN-kNN outperforms the state-of-the-art model performances. As shown in Table VI, the proposed model has a great ability in classifying and predicting the heartbeats compared to the participated algorithms, and the result of the accuracy metric is an evidence for this. In addition to the superior accuracy

of the propose method, the CNN-kNN technique has a great prediction, which outperformed the participated models in the table. The great prediction of the proposed model is supported by the result of the Precision. The result of the Recall metric proves the ability of the model to identify high percentage of samples correctly.

V. Conclusion

This study has proposed a model for ECG heartbeat classification based on CNN-kNN models. The 1D-CNN model is used to extract the features from the ECG signal and then fed to the kNN classifier. According to the results, the proposed method is able to make predictions on both arrhythmia and MI tasks whereas outperforming the accuracies of the state-of-the-art methods in the literature. The CNN-kNN model does not require the handcrafted feature as well as no further training is needed unlike any integrated model, as the kNN classifier has no training stage. However, the proposed model still needed to be validated by various datasets in this field to be more generalized.

References

Acharya, U.R., Fujita, H., Oh, S.L., Hagiwara, Y., Tan, J.H., and Adam, M., 2017a. Application of deep convolutional neural network for automated detection of myocardial infarction using ECG signals. *Information Sciences*, 415-416, pp.190-198.

Acharya, U.R., Oh, S.L., Hagiwara, Y., Tan, J.H., Adam, M., Gertych, A., and Tan, R.S., 2017b. A deep convolutional neural network model to classify heartbeats. *Computers in Biology and Medicine*, 89, pp.389-396.

Acharya, U.R., Oh, S.L., Hagiwara, Y., Tan, J.H., Adam, M., Gertych, A., and Tan, R.S., 2017c. A deep convolutional neural network model to classify heartbeats. *Computers in Biology and Medicine*, 89, pp.389-396.

Aljojo, N., 2022. Network transmission flags data affinity-based classification by K-nearest neighbor. *Aro-The Scientific Journal of Koya University*, 10(1), pp.35-43.

Association for the Advancement of Medical Instrumentation., 1998. *Testing and Reporting Performance Results of Cardiac Rhythm and St Segment Measurement Algorithms*. Association for the Advancement of Medical Instrumentation, Arlington.

Bouaziz, F., Boutana, D., and Oulhadj, H., 2019. Diagnostic of ECG Arrhythmia using Wavelet Analysis and K-Nearest Neighbor Algorithm. In: *Proceedings of the 2018 International Conference on Applied Smart Systems*, *ICASS 2018*, pp.1-6.

Boussaa, M., Atouf, I., Atibi, M., and Bennis, A., 2016. ECG signals classification using MFCC coefficients and ANN classifier. In: *Proceedings of 2016 International Conference on Electrical and Information Technologies, ICEIT 2016*, pp.480-484.

Foody, G.M., 2023. Challenges in the real world use of classification accuracy metrics: From recall and precision to the Matthews correlation coefficient. *PLoS One*, 18(10), p.e0291908.

Goldberger, A.L., Amaral, L.A.N., Glass, L., Hausdorff, J.M., Ivanov, P.C., Mark, R.G., Mietus, J.E., Moody, G.B., Peng, C., and Stanley, H.E., 2000. PhysioBank, PhysioToolkit, and PhysioNet: Components of a new research resource for complex physiologic signals. *Circulation*, 101(23), pp.E215-E220.

Homaeinezhad, M.R., Atyabi, S.A., Tavakkoli, E., Toosi, H.N., Ghaffari, A., and Ebrahimpour, R., 2012. ECG arrhythmia recognition via a neuro-SVM-KNN hybrid classifier with virtual QRS image-based geometrical features. *Expert Systems with Applications*, 39(2), pp.2047-2058.

Ince, T., Kiranyaz, S., Eren, L., Askar, M., and Gabbouj, M., 2016. Real-time motor fault detection by 1-D convolutional neural networks. *IEEE Transactions on Industrial Electronics*, 63(11), pp.7067-7075.

Jiang, L., Cai, Z., Wang, D., and Jiang, S., 2007. Survey of Improving K-Nearest-Neighbor for Classification. In: *Proceedings-Fourth International Conference on Fuzzy Systems and Knowledge Discovery, FSKD 2007*. Vol. 1, pp.679-683.

Kachuee, M., Fazeli, S., and Sarrafzadeh, M., 2018. ECG Heartbeat Classification: A Deep Transferable Representation. In: *Proceedings-2018 IEEE International Conference on Healthcare Informatics, ICHI 2018*, pp.443-444.

Khan, A., Sohail, A., Zahoora, U., and Qureshi, A.S., 2020. A survey of the recent architectures of deep convolutional neural networks. *Artificial Intelligence Review*, 53, pp.5455-5516.

Khatibi, T., and Rabinezhadsadatmahaleh, N., 2019. Proposing feature engineering method based on deep learning and K-NNs for ECG beat classification and arrhythmia detection. *Australasian Physical and Engineering Sciences in Medicine*, 43, pp.49-68.

Kiranyaz, S., Avci, O., Abdeljaber, O., Ince, T., Gabbouj, M., and Inman, D.J., 2021. 1D convolutional neural networks and applications: A survey. *Mechanical Systems and Signal Processing*, 151, p.107398.

Kiranyaz, S., Gastli, A., Ben-Brahim, L., Al-Emadi, N., and Gabbouj, M., 2019. Real-time fault detection and identification for MMC using 1-D convolutional neural networks. *IEEE Transactions on Industrial Electronics*, 66(11), pp.8760-8771.

Kiranyaz, S., Ince, T., and Gabbouj, M., 2016a. Real-time patient-specific ECG classification by 1-D convolutional neural networks. *IEEE Transactions on Biomedical Engineering*, 63(3), pp.664-675.

Kiranyaz, S., Ince, T., and Gabbouj, M., 2016b. Real-time patient-specific ECG classification by 1-D convolutional neural networks. *IEEE Transactions on Biomedical Engineering*, 63(3), pp.664-675.

Kiranyaz, S., Ince, T., Hamila, R., and Gabbouj, M., 2015. Convolutional Neural Networks for Patient-Specific ECG Classification. In: *Proceedings of the Annual International Conference of the IEEE Engineering in Medicine and Biology Society, EMBS*, *2015*, pp.2608-2611.

Labati, R.D., Enrique, M., Piuri, P., Sassi, R., and Scotti, R., 2018. Deep-ECG: Convolutional neural networks for ECG biometric recognition. *Pattern Recognition Letters*, 126, pp.78-85.

Li, T., and Zhou, M., 2016. ECG classification using wavelet packet entropy and random forests. *Entropy*, 18(8), p.285.

Litjens, G., Kooi, T., Bejnordi, B.E., Setio, A.A.A., Ciompi, F., Ghafoorian, M., Van der Laak, J.A.W.M., Van Ginneken, B., and Sánchez, C.I., 2017. A survey on deep learning in medical image analysis. *Medical Image Analysis*, 42, pp.60-88.

Luz, E.J.S., Schwartz, W.R., Cámara-Chávez, G., and Menotti, D., 2016. ECG-based heartbeat classification for arrhythmia detection: A survey. *Computer Methods and Programs in Biomedicine*, 127, pp.144-164.

Martis, R.J., Acharya, U.R., Lim, C.M., Mandana, K.M., Ray, A.K., and Chakraborty, C., 2013a. Application of higher order cumulant features for cardiac health diagnosis using ECG signals. *International Journal of Neural Systems*, 23(4), p.1350014.

Martis, R.J., Acharya, U.R., Lim, C.M., Mandana, K.M., Ray, A.K., and Chakraborty, C., 2013b. Application of higher order cumulant features for cardiac health diagnosis using ECG signals. *International Journal of Neural Systems*, 23(4), p.1350014.

Oh, S.L., Ng, E.Y.K., Tan, R.S., and Acharya, U.R., 2018. Automated diagnosis of arrhythmia using combination of CNN and LSTM techniques with variable length heart beats. *Computers in Biology and Medicine*, 102, pp.278-287.

Rautela, M., Gopalakrishnan, S., Gopalakrishnan, K., and Deng, Y., 2020. Ultrasonic Guided Waves Based Identification of Elastic Properties Using

1D-Convolutional Neural Networks. In: *2020 IEEE International Conference on Prognostics and Health Management (ICPHM)*. IEEE, United States, pp.1-7.

Sadhukhan, D., and Mitra, M., 2012. R-peak detection algorithm for Ecg using double difference and RR interval processing. *Procedia Technology*, 4, pp.873-877.

Safdarian, N., Dabanloo, N.J., and Attarodi, G., 2014. A new pattern recognition method for detection and localization of myocardial infarction using T-wave integral and total integral as extracted features from one cycle of ECG signal. *Journal of Biomedical Science and Engineering*, 7, pp.818-824.

Saini, I., Singh, D., and Khosla, A., 2013. QRS detection using K-Nearest Neighbor algorithm (KNN) and evaluation on standard ECG databases. *Journal of Advanced Research*, 4(4), pp.331-344.

Shima, Y., Nakashima, Y., and Yasuda, M., 2018. Pattern Augmentation for Handwritten Digit Classification Based on Combination of Pre-Trained CNN and SVM. In: *2017 6th International Conference on Informatics, Electronics and Vision and 2017 7th International Symposium in Computational Medical and Health Technology*, *ICIEV-ISCMHT 2017*, pp.1-6.

Smíšek, R., Hejč, J., Ronzhina, M., Němcová, A., Maršánová, L., Chmelík, J., Kolářová, J., Provazník, I., Smital, L., and Vítek, M., 2017. SVM Based ECG classification using rhythm and morphology features, cluster analysis and multilevel noise estimation. *Computing in Cardiology*, 44, pp.1-4.

Venkatesan, C., Karthigaikumar, P., Paul, A., Satheeskumaran, S., and Kumar, R., 2018. ECG signal preprocessing and SVM classifier-based abnormality detection in remote healthcare applications. *IEEE Access*, 6, pp.9767-9773.

Wang, J., 2020. A deep learning approach for atrial fibrillation signals classification based on convolutional and modified Elman neural network. *Future Generation Computer Systems*, 102, pp.670-679.

Zhai, X., and Tin, C., 2018. Automated ECG classification using dual heartbeat coupling based on convolutional neural network. *IEEE Access*, 6, pp.27465-27472.

Zhang, M.Z., and Zhou, Z.H., 2005. *A K-Nearest Neighbor Based Algorithm for Multi-Label Classification*. Vol. 2. IEEE, United States, pp.718-721.

Zubair, M., Kim, J., and Yoon, C., 2016. An Automated ECG Beat Classification System Using Convolutional Neural Networks. In: *2016 6th International Conference on IT Convergence and Security, ICITCS 2016*.

http://dx.doi.org/10.14500/aro.11495

Analyzing Colorectal Cancer at the Molecular Level through Next-generation Sequencing in Erbil City

Vyan A. Qadir[1] and Kamaran K. Abdoulrahman[2]

[1]Department of Chemistry, Faculty of Science and Health, Koya University, Koya KOY45, Kurdistan Region - F.R. Iraq

[2]Department of Chemistry, College of Science, Salahaddin University-Erbil, Erbil, Kurdistan Region - F.R. Iraq

***Abstract*—Colorectal cancer (CRC) ranks as the third leading cause of cancer-related deaths globally. It is characterized as a genomic disorder marked by diverse genomic anomalies, including point mutations, genomic rearrangements, gene fusions, and alterations in chromosomal copy numbers. This research aims to identify previously undisclosed genetic variants associated with an increased risk of CRC by employing next-generation sequencing technology. Genomic DNA was extracted from blood specimens of five CRC patients. The sequencing data of the samples are utilized for variant identification. In addition, the Integrative Genomic Viewer software (IGV) is used to visualize the identified variants. Furthermore, various *in silico* tools, including Mutation Taster and Align GVGD, are used to predict the potential impact of mutations on structural features and protein function. Based on the findings of this research, 12 different genetic variations are detected among individuals with CRC. Inherited variations are located within the following genes: MSH6, MSH2, PTPRJ, PMS2, TP53, BRAF, APC, and PIK3CA.**

***Index Terms*—Colorectal, Cancer, Gene, Molecular level, Mutation.**

I. Introduction

Colorectal cancer (CRC) is a significant worldwide contributor to illness and health-related issues (Arbyn, et al., 2020). Globally, CRC leads to substantial sickness and loss of life. It stands as the prevalent form of internal cancer in both men and women within Western communities. The occurrence of CRC is progressively increasing in Asian countries as well. Among the genetic triggers of CRC, Lynch syndrome (LS), alternatively known as hereditary non-polyposis CRC, holds the highest prevalence, contributing to about 3–4% of all global cases of CRC (Sinicrope, 2018). Certainly, both inherited and acquired genetic alterations, along with external environmental influences, undoubtedly play a role in its development. CRC displays significant diversity in terms of tumor location, genetic variations, and racial distinctions. The interplay of various factors, including environmental elements, dietary choices, and lifestyle, exerts multiple influences on the progression of the disease(Murphy, et al., 2019). Risk factors for CRC encompass a range of factors such as genetic predisposition (like hereditary non-polyposis CRC), susceptibility to polyp development, inflammatory conditions in the large bowel, obesity, consumption of high-fat diets, alcohol consumption, smoking, and psychological stress (Murphy, et al., 2019; Tariq and Ghias, 2016; Barrasa, et al., 2013). For a considerable time, it has been acknowledged that certain families exhibit a dominant inclination toward developing colorectal adenomas and/or cancers. However, the discovery of the specific genes and mutations accountable for this heightened familial susceptibility is a relatively recent development (Peltokallio and Peltokallio, 1966; Lynch and Lynch, 1985). The risk levels elevate significantly when multiple family members are impacted or if an individual within the family is diagnosed at an early age (Fuchs, et al., 1994; Winawer, et al., 2003). The development of CRC results from the progressive buildup of genetic modifications (such as gene mutations and amplification) and epigenetic modifications including abnormal DNA methylation and changes in chromatin structure (Bardhan and Liu, 2013). These alterations collectively convert normal colonic epithelial cells into malignant colon adenocarcinoma cells. The initial stages of tumorigenesis involve the loss of genomic stability, leading to genetic changes. This process is pivotal in acquiring the necessary mutations in tumor suppressor genes and oncogenes, which drive the transformation of cells and facilitate the advancement of tumors (Kontomanolis, et al., 2020). Two primary types of genomic instability, namely, microsatellite instability and chromosome instability, have been recognized as predominant in colon cancer (Rao and Yamada, 2013). The impacts of diverse types of genomic instability on the biological and clinical characteristics of colon tumors were examined (Hause, et al., 2016). Investigating the origins and functions of genomic and epigenomic instability in the development of colon tumors holds the promise of generating improved approaches for preventing and treating CRC

ARO-The Scientific Journal of Koya University
Vol. XII, No. 1 (2024), Article ID: ARO.11495. 11 pages
DOI: 10.14500/aro.11495
Received: 03 December 2023; Accepted: 03 February 2024
Regular research paper: Published: 04 March 2024
Corresponding author's e-mail: vyan.asad@koyauniversity.org

in patients. Next-generation sequencing (NGS) is a gene sequencing technology that offers very high throughput, scalability, and speed, allowing sequencing of whole cancer genomes (whole genome sequencing or WGS) from dozens to hundreds of patients within a few days. Significant variations in the lifetime susceptibility to cancer have been documented among carriers of MMR (mismatch repair) mutations, with the greatest risk associated with mutations found in either MLH1 or MSH2 genes. Cancer occurrences within families possessing a pathogenic alteration in MSH6 are typically detected at a later stage, and the associated cancer risks are relatively diminished, except in the case of endometrial cancer (Berends, et al., 2002; Hendriks, et al., 2004; Baglietto, et al., 2010). Most investigations detailing the molecular makeup of LS families have been carried out in regions encompassing North America, Europe, and Asia (Dominguez-Valentin, et al., 2013). A limited number of studies have outlined the occurrence and specific varieties of MMR (mismatch repair) mutations in Latin America, particularly within the context of Brazil (Cossio, et al., 2010; Da Silva, et al., 2010; Carneiro Da Silva, et al., 2015).

The objective of this research was to assess the effectiveness of next-generation sequencing (NGS) in a standard clinical environment involving patients with CRC. Exome sequencing was employed to reveal previously unidentified variants that predispose individuals to CRC.

II. Materials and Methods

A. Collection of Samples

The present study included five CRC patients recruited from Rezgari Hospital, Erbil/Iraq. A case–control study design was established from (August 01, 2022, to December 01, 2022) to study the effect of some genetic effects in patients with CRC who visited Rezgari Hospital Cancer Department, Erbil/Iraq.

B. Extraction of Genome

Genomic DNA from blood specimens was prepared using a DNA extraction kit (Thermofisher, USA), following the manufacturer's instructions with minor modifications. Qualification and quantification of DNA concentration were performed using NanoDrop (Biometrical). Samples of genomic DNA with (A260–A230)/(A280–A320) ratios of more than 1.7 and outputs more than 30 ng/μl were obtained.

C. Mutation Analysis

Twist Human Core Exome Enzymatic Fragmentation (EF) Multiplex Complete kit was used for library construction, and MGIEasy FS DNA Library Prep Kit was performed for the library to be ready for sequencing on the MGI system. The library was sequenced on the (MGI-DNBSEQ-G400, China) instrument generating 150 bp paired-end read with 100X mean target coverage. Fast QC, and Raw fastq files were quality controlled. The reads were aligned to the reference human genome (hg19) using Burrows-Wheeler Aligner (BWA). Variants were identified with the Genome Analysis Toolkit (GATK). Integrative Genomic Viewer software (IGV) was used for variants visualization Intergen Genetics and Rare Diseases Diagnostic Center, (Ankara, Turkey).

D. In Silico Analysis

Different *in silico* tools were used to predict the effect of mutation on the structural features or protein function. Polymorphism Phenotyping (PolyPhen-2) (Vaser, et al., 2016) and Sorting Intolerant from Tolerant (SIFT) (Schwarz, et al., 2014) were used to assess the functional effects of variants. A mutation Taster was used for the evaluation of the mutation effect on protein function and structure (Tavtigian, et al., 2006). Align GVGD was used to compute a biochemical distance score prepared manuscript methods according to previous international published NGS data. In the thesis, we explained and clarified the method section in detail (Tavtigian, et al., 2006; Mathe, et al., 2006).

III. Results and Discussion

In this study, NGS was employed for the exploration of the genetic mutation landscape within a cohort of five CRC patients residing in Erbil City/Iraq. Previously, immunohistochemical and molecular studies were conducted to target the expression of specific genes (Kamal and Jalal, 2019; Ali Hama, 2019). In addition, other studies attempted to determine mutations in target genes among patients with CRC (Abid, Qadir and Salihi, 2021). To the best of our knowledge, this is the inaugural study conducted in Erbil City/Iraq to evaluate the use of NGS in a typical clinical setting with CRC patients. Exome sequencing was utilized to identify previously unknown genetic variations that may increase an individual's susceptibility to CRC. The 12 variants in CRC patients were identified and the inherited variants were found in MSH6, MSH2, PTPRJ, PMS2, TP53, BRAF, APC, and PIK3CA genes. Table I shows the variants and the results of *in silico* predictions.

For predicting the effects and potential significance of variants, many *in silico* tools have been developed. Polymorphism Phenotyping (PolyPhen), SIFT, and MutationTaster were applied to investigate the functional effects of 12 variants. The PolyPhen gives predictions to find structural features and sequence alignment changes caused by amino acid substitution. PolyPhen predicts the functional significance of an allele substitution. Variants with scores of 0.0 are predicted to be benign, the scores 0.15–0.85 are predicted as possibly damaging, the score more than 0.85 are more confidently considered as damaging. PolyPhen predicted uncertain significance function for a variant of MSH2, TP53, BRAF, and a variant of APC. Furthermore, it predicted probably damaging function for a variant of MHS6 (ENST00000234420.11 c.276A>G).

The functional effect of SIFT on the variants is assessed by evaluating the sequence homology and investigating the conservation degree of amino acid residues among species. SIFT predicts whether an amino acid substitution in a protein will have a phenotypic influence. A score ≤0.05 is predicted

http://dx.doi.org/10.14500/aro.11495

TABLE I
MUTATIONS IDENTIFIED IN COLORECTAL CANCER PATIENTS

Gene	Variant coordinates	Amino acid change	Zygosity	*In silico* parameters*	Type and Classification
MSH6	ENST00000234420.11 c.276A >G	p.P92P	Heterozygote	PolyPhen: - Align-GVGD: N/A SIFT: N/A Mutation Taster: N/A Conservation_nt: N/A Conservation_aa: N/A	Likely pathogenic
MSH2	47403411 C >G	Splicing site	Homozygote	PolyPhen: - Align-GVGD: N/A SIFT: N/A MutationTaster: N/A Conservation_nt: N/A Conservation_aa: N/A	Uncertain significance
PTPRJ	ENST00000418331.7 c.827A >C	p.Q276P	Heterozygote	PolyPhen: - Align-GVGD: N/A SIFT: N/A MutationTaster: N/A Conservation_nt: N/A Conservation_aa: N/A	Pathogenic
PMS2	5982995 C >T	Splicing site	Heterozygote	PolyPhen: - Align-GVGD: N/A SIFT: N/A MutationTaster: N/A Conservation_nt: N/A Conservation_aa: N/A	Likely pathogenic
TP53	ENST00000359597.8 c.215C >G	p.P72R	Homozygote	PolyPhen: - Align-GVGD: N/A SIFT: N/A MutationTaster: N/A Conservation_nt: N/A Conservation_aa: N/A	Uncertain_significance
BRAF	140734797 C>A	Intronic	Homozygote	PolyPhen: - Align-GVGD: N/A SIFT: N/A MutationTaster: N/A Conservation_nt: N/A Conservation_aa: N/A	Uncertain_significance
APC	ENST00000257430.9 c.5880G >A	p.P1960P	Heterozygote	PolyPhen: - Align-GVGD: N/A SIFT: N/A MutationTaster: N/A Conservation_nt: N/A Conservation_aa: N/A	Likely_pathogenic
APC	ENST00000257430.9 c.5034G >A	p.G1678G	Heterozygote	PolyPhen: - Align-GVGD: N/A SIFT: N/A MutationTaster: N/A Conservation_nt: N/A Conservation_aa: N/A	Uncertain_significance
APC	ENST00000257430.9 c.4479G >A	p.T1493T	Heterozygote	PolyPhen: - Align-GVGD: N/A SIFT: N/A MutationTaster: N/A Conservation_nt: N/A Conservation_aa: N/A	Uncertain_significance
APC	ENST00000504915.2 c.147T >C	p.Y49Y	Heterozygote	PolyPhen: - Align-GVGD: N/A SIFT: N/A MutationTaster: N/A Conservation_nt: N/A Conservation_aa: N/A	Uncertain_significance
APC	112707585 C >G	Intronic	Heterozygote	PolyPhen: - Align-GVGD: N/A SIFT: N/A MutationTaster: N/A Conservation_nt: N/A Conservation_aa: N/A	Uncertain_significance
PIK3CA	179199217 A >G	Intronic	Homozygote	PolyPhen: - Align-GVGD: N/A SIFT: N/A MutationTaster: N/A Conservation_nt: N/A Conservation_aa: N/A	Likely pathogenic

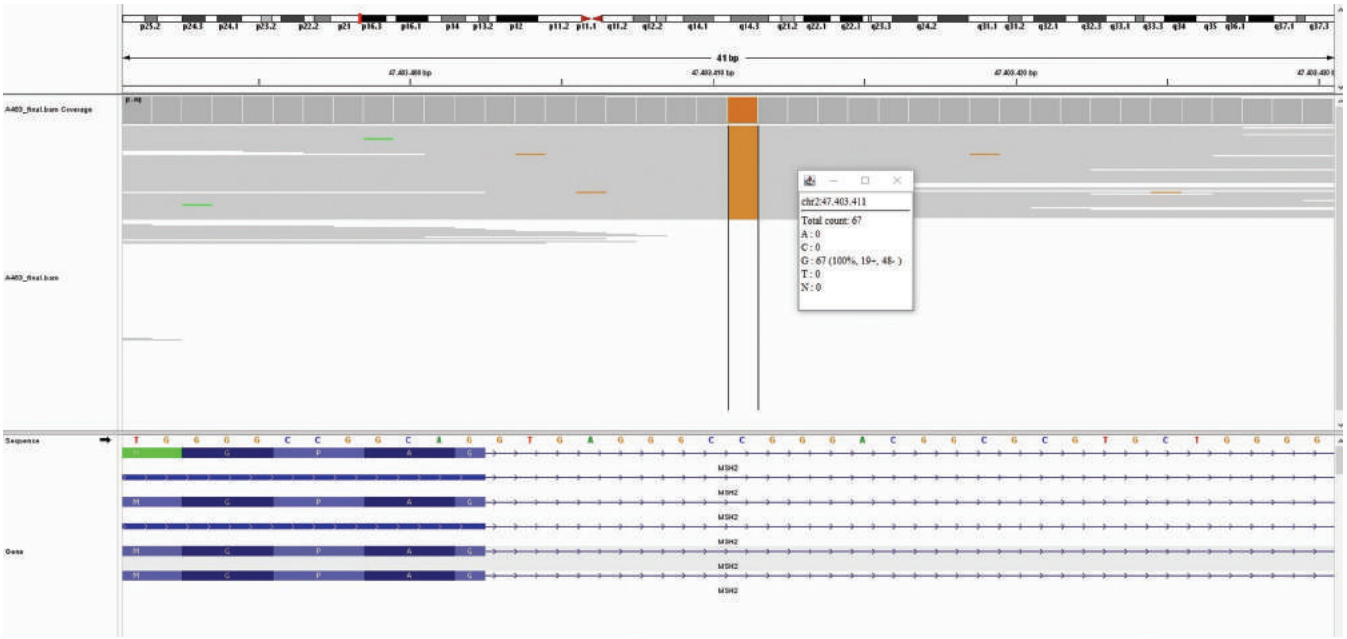

Fig. 1. Integrative Genomics Viewer image of next-generation sequencing data of MSH2 47403411 C>G variant detected.

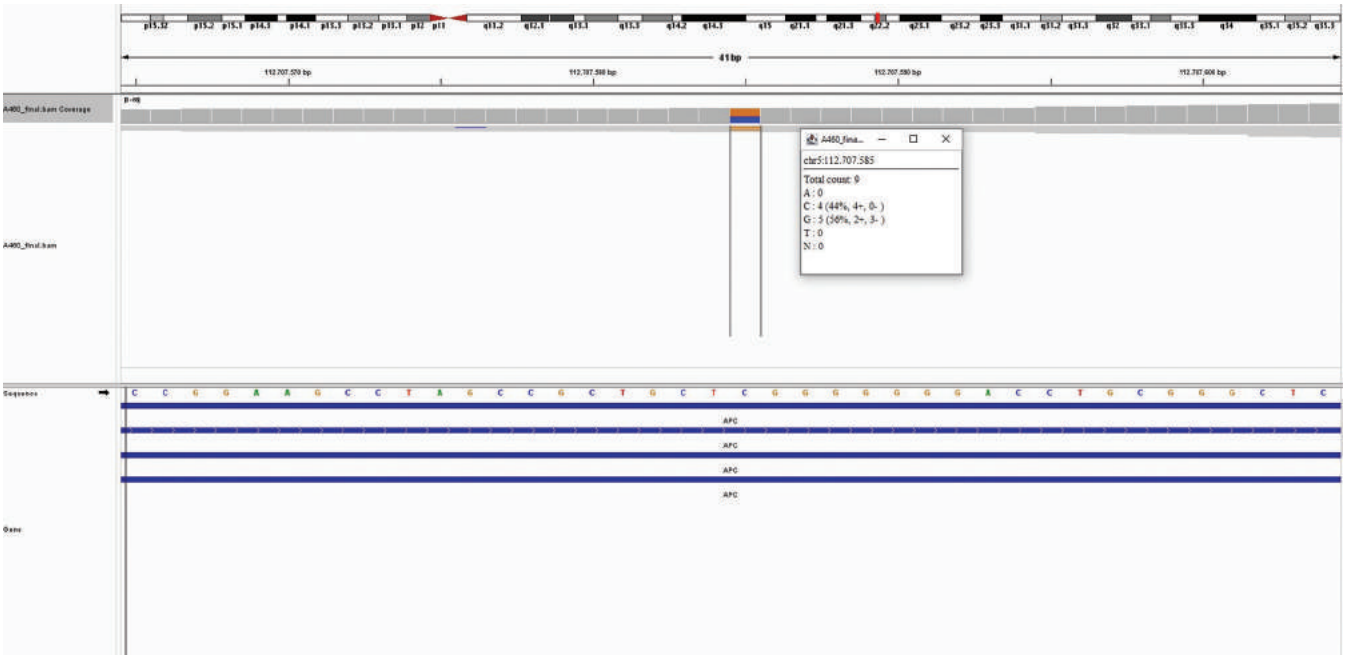

Fig. 2. Integrative Genomics Viewer image of next-generation sequencing data of Adenomatous Polyposis Coli 112707585 C>G variant detected.

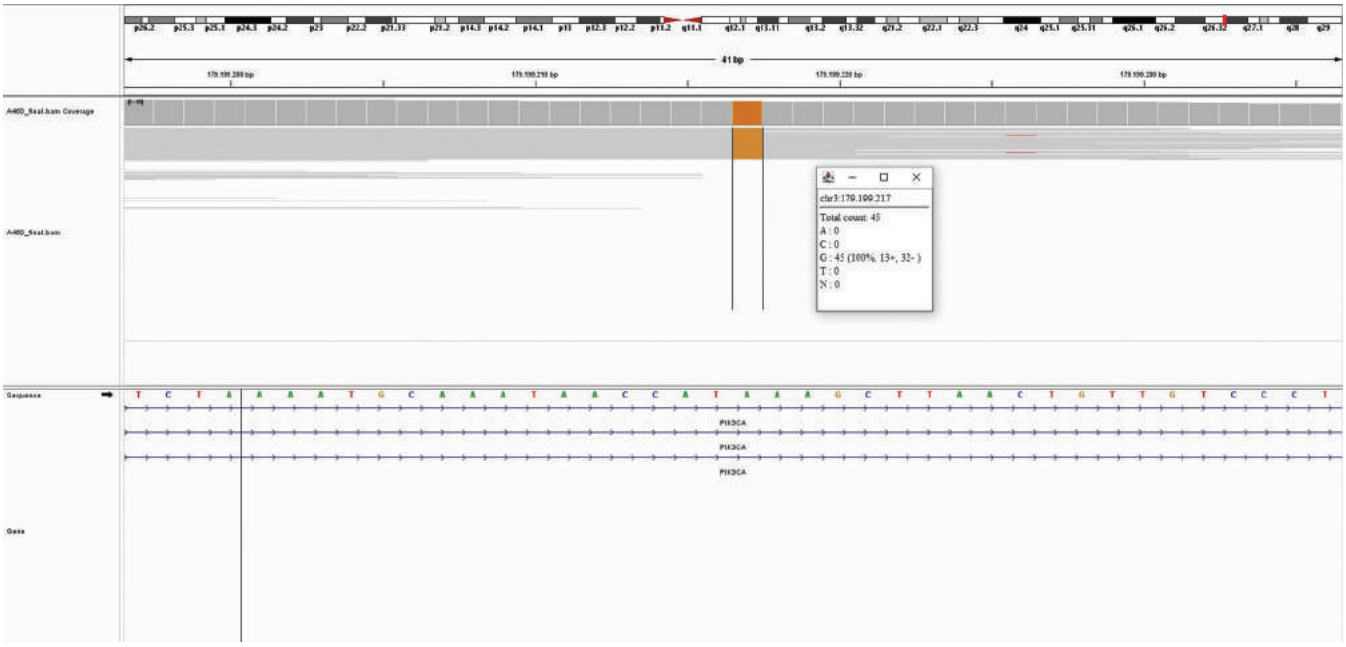

Fig. 3. Integrative Genomics Viewer image of next-generation sequencing data of PIK3CA 179199217 A>G variant detected.

to be tolerated, and a score less than 0.05 is predicted to be deleterious. SIFT predicted tolerated effects in a variant of APC and BRAF as well as the deleterious effects in a variant of MSH6, PIK3CA, and PMS2.

Mutation Taster evaluates mutation effect on protein function and structure. It considers the effect of mRNA expression or splicing (Malińska, et al., 2020). It predicts the disease potential of an alteration as disease causing which is probably deleterious, disease-causing automatic which is deleterious, polymorphism which is probably harmless, and polymorphism automatic which is harmless. The results predicted disease causing in a variant of MSH6, APC, and A variant of PIK3CA (Perne, et al., 2021). In many cases, the first mutation occurs in the APC gene. This leads to an increased growth of colorectal cells because of the loss of this "brake" on cell growth. Further mutations may then occur in other genes, which can lead the cells to grow and spread uncontrollably.

The roles of these genes were known in the literature.

- MutS Homolog 6 (MSH6): MSH6 is a crucial component of the DNA mismatch repair (MMR) system. Mutations in MSH6 can lead to microsatellite instability (MSI), a hallmark of CRC. MSI can result in the accumulation of errors during DNA replication, contributing to tumorigenesis (Boland and Goel, 2010)
- MutS Homolog 2 (MSH2): MSH2 is an essential component of the DNA mismatch repair system. Mutations in MSH2

http://dx.doi.org/10.14500/aro.11495

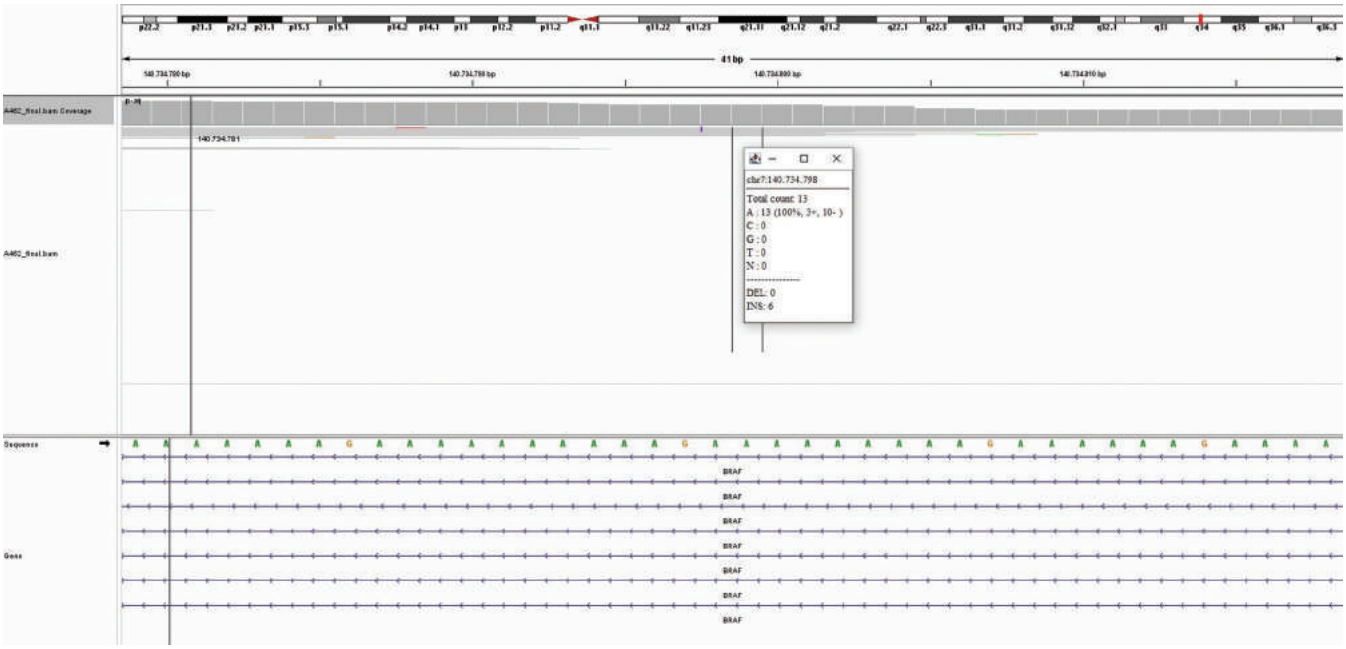

Fig. 4. Integrative Genomics Viewer image of next-generation sequencing data of BRAF 140734797 ?>A variant detected.

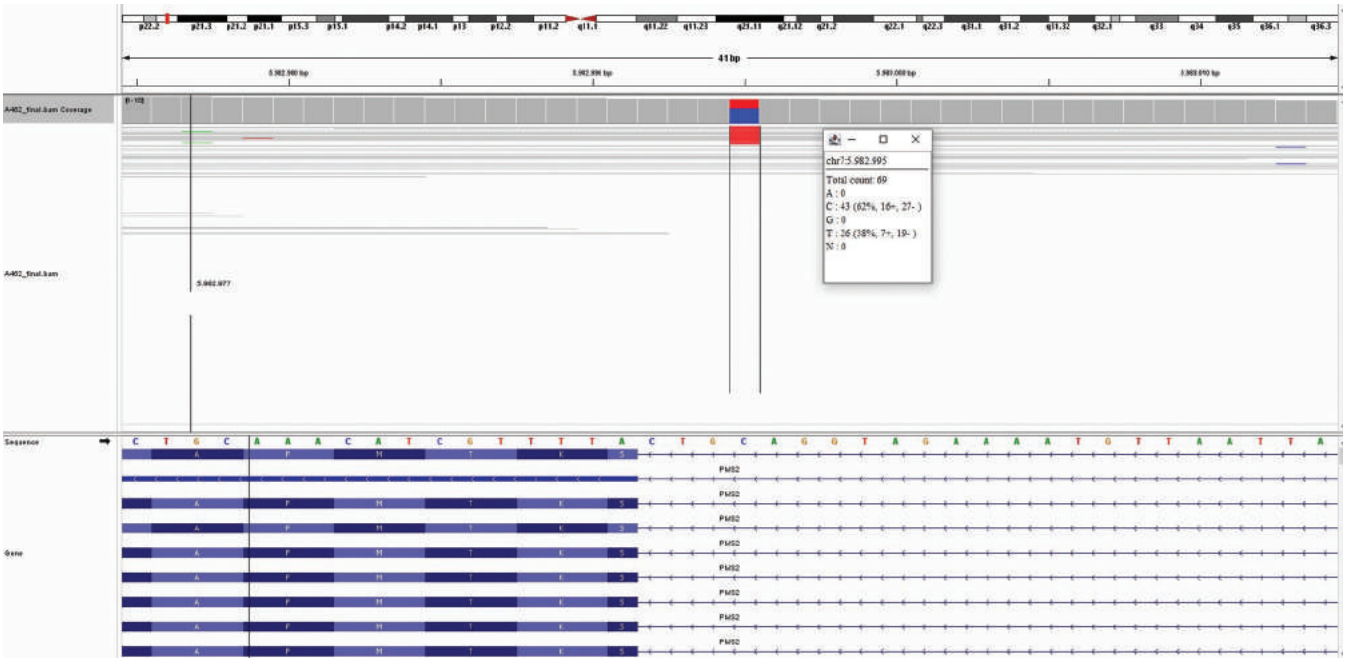

Fig. 5. Integrative Genomics Viewer image of next-generation sequencing data of PMS2 5982995 C>T variant detected.

can impair the correction of DNA replication errors, leading to MSI and an increased risk of CRC (Lynch and De la Chapelle, 1999)

- Protein Tyrosine Phosphatase, Receptor Type J (PTPRJ): PTPRJ is a receptor-type protein tyrosine phosphatase involved in cell adhesion and signaling. In CRC, mutations in PTPRJ may disrupt cellular communication and adhesion, contributing to cancer progression (Li, et al., 2022)
- PMS2 (PMS1 Homolog 2, Mismatch Repair System Component): PMS2 is a key player in the DNA mismatch repair system. Mutations in PMS2 can compromise the repair of DNA errors, leading to MSI and an increased susceptibility to CRC (Ten Broeke, et al., 2015)
- Tumor Protein P53 (TP53): TP53 is a tumor suppressor gene crucial for cell cycle regulation and DNA repair. Mutations in TP53 are common in CRC and can result in the loss of its tumor-suppressing function, leading to uncontrolled cell growth (Olivier, Hollstein and Hainaut, 2010)
- B-Raf Proto-Oncogene, Serine/Threonine Kinase (BRAF): BRAF is a proto-oncogene involved in the RAS/RAF/MEK/ERK signaling pathway. Mutations in BRAF, particularly the V600E mutation, are associated with a subset of CRCs, leading to increased cell proliferation (Davies, et al., 2002)
- Adenomatous Polyposis Coli (APC): APC is a critical tumor suppressor gene that regulates the Wnt signaling pathway. Mutations in APC are early events in colorectal

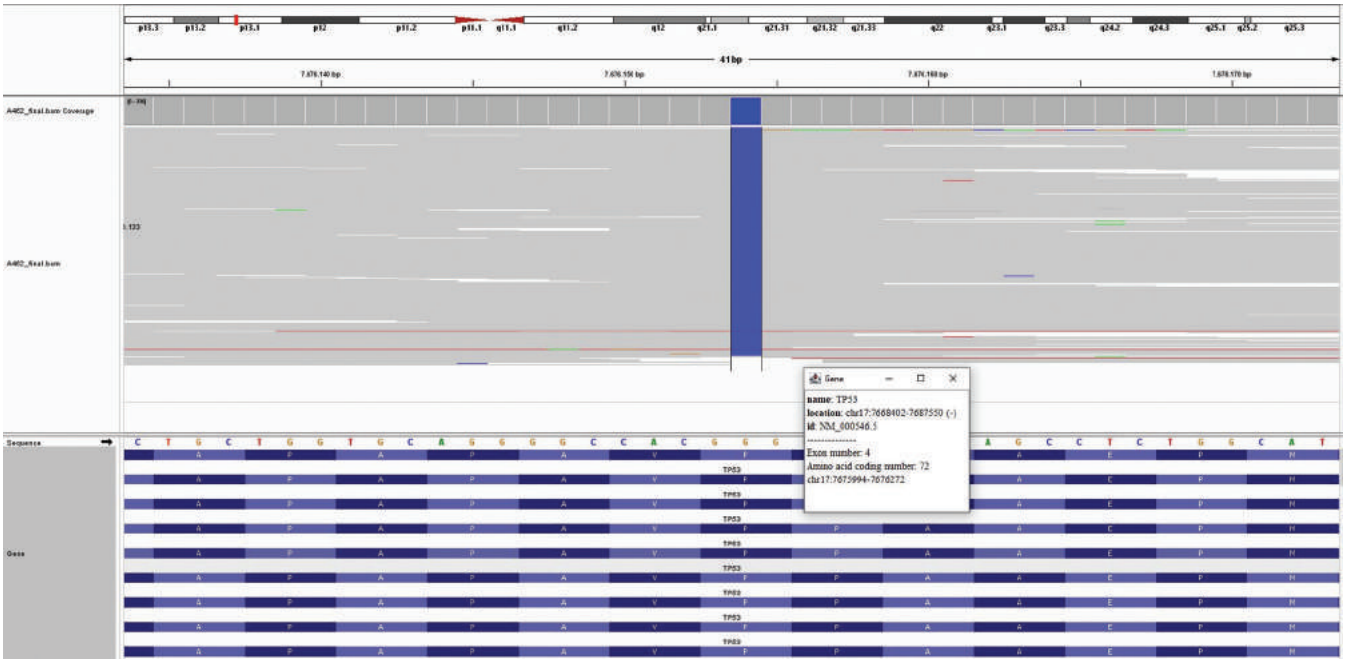

Fig. 6. Integrative Genomics Viewer image of next-generation sequencing data of TP53 ENST00000359597.8 c.215C>G variant detected.

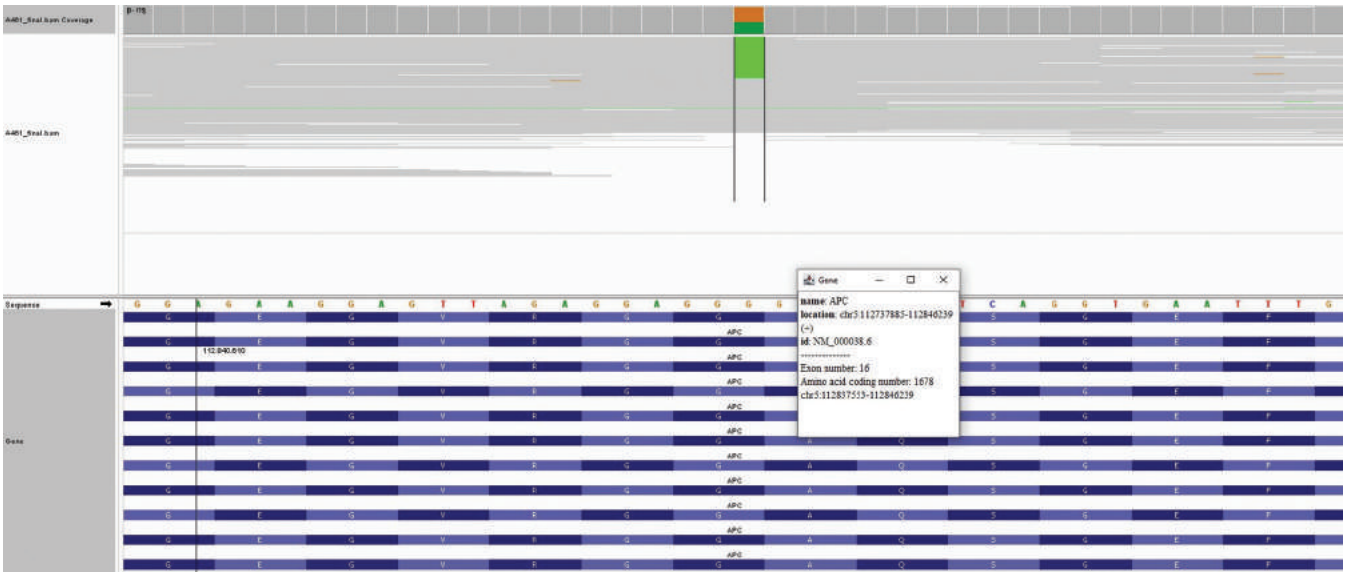

Fig. 7. Integrative Genomics Viewer image of next-generation sequencing data of Adenomatous Polyposis Coli ENST00000257430.9 c.5034G>A variant detected.

carcinogenesis, leading to uncontrolled cell proliferation and the formation of adenomas (Segditsas and Tomlinson, 2006)

- Phosphatidylinositol-4,5-Bisphosphate 3-Kinase Catalytic Subunit Alpha (PIK3CA): PIK3CA is involved in the PI3K/AKT/mTOR signaling pathway, regulating cell survival and growth. Mutations in PIK3CA can lead to increased PI3K activity, promoting CRC development (Janku, et al., 2012).

The initial discovery of a pathogenic MSH6 variant occurred in 1997 within a family afflicted by multiple LS-spectrum tumors, and subsequent investigations have consistently demonstrated that individuals with pathogenic MSH6 variants exhibit a reduced risk and delayed onset of colorectal cancer when compared to those with MLH1 and MSH2 variants as shown in Fig. 1, (Frederiksen, et al., 2021). For instance, when individuals with MSH6 variants reach the age of 70, they face a CRC risk of 20% for males and 12% for females. In contrast, male and female carriers of MLH1 variants have a higher risk (Dominguez-Valentin, et al., 2020).

According to the genetic analysis study of the present work, the HOMOZYGOTE splicing site was detected at 47403411 C>G which was classified as uncertain significance as shown in Fig. 2. The MSH2 variant exhibits the second-highest CRC risk, closely trailing MLH1, with an impact more pronounced

http://dx.doi.org/10.14500/aro.11495

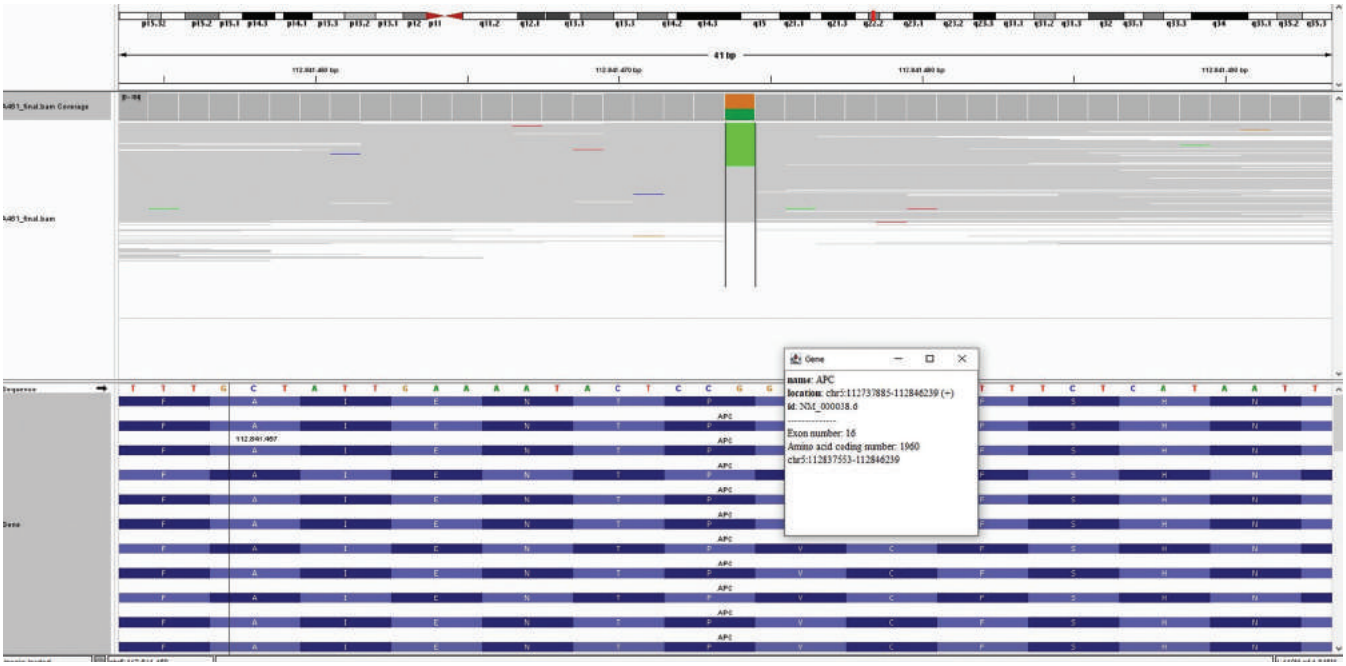

Fig. 8. Integrative Genomics Viewer image of next-generation sequencing data of Adenomatous Polyposis Coli ENST00000257430.9 c.5880G>A variant detected.

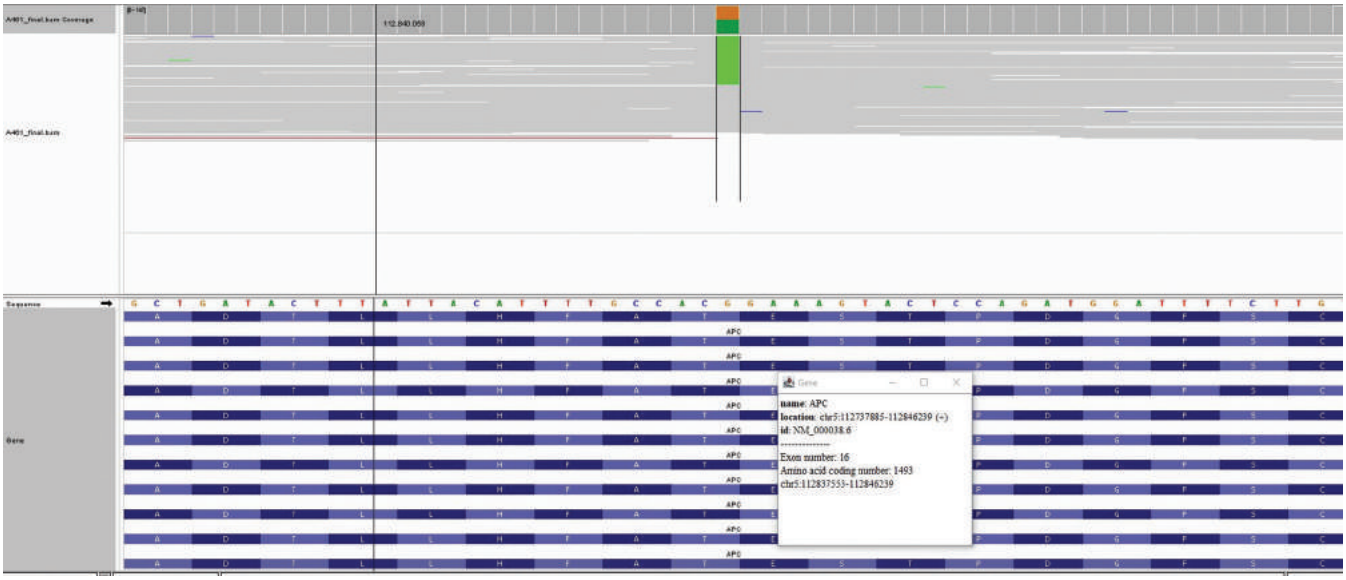

Fig. 9. Integrative Genomics Viewer image of next-generation sequencing data of Adenomatous Polyposis Coli ENST00000257430.9 c.4479G>A variant detected.

in individuals aged over 75, affecting 46.6% of women and 51.4% of men carrying this genetic variation (Dominguez-Valentin, et al., 2020; Fatemi, et al., 2023).

Our examination in Fig. 3 underscores the identification of the heterozygous variant c.827A>C within the tumor suppressor gene PTPRJ, which has been classified as having pathogenic significance. Protein tyrosine phosphatase receptor type J (PTPRJ) is a gene known for its tumor-suppressing properties, as it exerts a negative regulatory influence on critical processes like angiogenesis, cell proliferation, and migration that make it a crucial player in the context of tumor formation and development (Laczmanska and Sasiadek, 2019). A prior investigation verified that the presence of c.827A>C markedly elevates the risk of developing colon cancer (Mita, et al., 2010).

Fig. 4 shows that HETEROZYGOTE PMS2 is observed at the splicing site (5982995 C>T). Usually, PMS2 mutations are implicated in lynch syndrome (LS) associated colorectal cancer in approximately 8 to 15% of cases, with variable incidence rates and depending on diagnostic methods such as PCR, microsatellite instability, IHC, or DNA sequencing (Poaty et al., 2023). Heterozygous PMS2 mutations were identified in 90.16% (55/61) of cases, while homozygous PMS2 mutations were observed in 9.83% (6/61) of LS cases (Senter, et al., 2008).

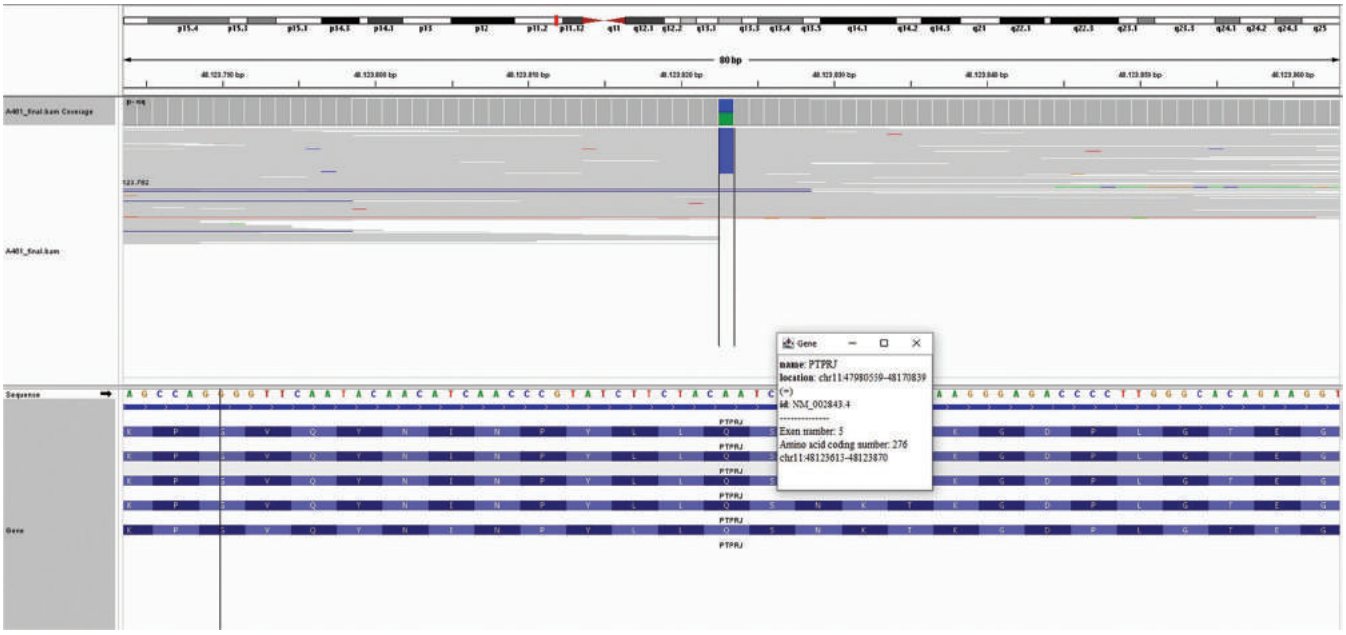

Fig. 10. Integrative Genomics Viewer image of next-generation sequencing data of PTPRJ ENST00000418331.7 c.827A>C variant detected.

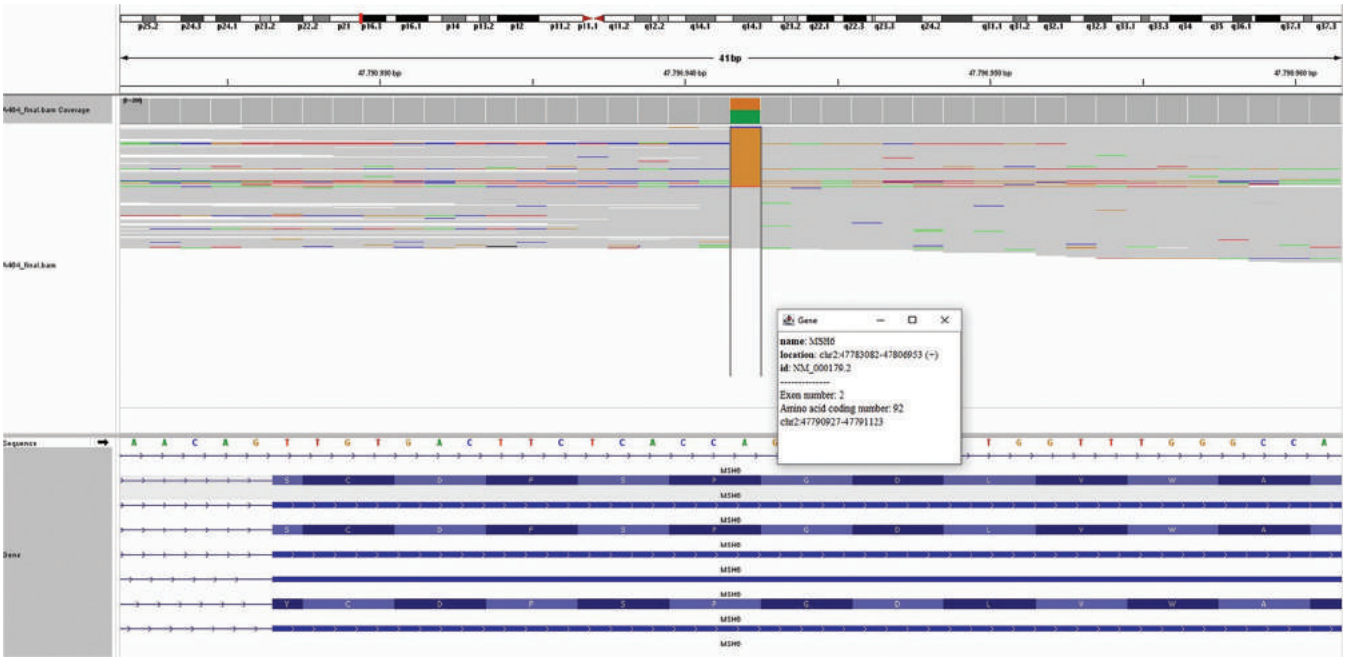

Fig. 11. Integrative Genomics Viewer image of next-generation sequencing data of MSH6 ENST00000234420.11 c.276A>G variant detected.

According to the NGS results in the present study, HOMOZYGOTE (c.215C>G) TP53 was detected as shown in Fig. 5. TP53 gene undergoes alterations considered hallmarks of tumors, and its mutation status is linked to the progression and prognosis of sporadic CRC, with a prevalence rate of 52.5% in the Arab population compared to 47.5% in a matched Western population (Youssef, et al., 2020). In addition, it has been observed that PMS2 deficiency is also linked to an increased risk of other cancers (Roberts, et al., 2018; Raza, et al., 2020).

Fig. 6 shows BRAF functions as a serine/threonine protein kinase within the mitogen-activated protein kinase (MAPK) pathway, orchestrating critical cellular processes such as proliferation, survival, differentiation, migration, and angiogenesis, and disruptions in this pathway are a fundamental driver in the development of numerous types of cancer (Caputo et al., 2019) and (Morgan et al., 2022). Based on the genomic and transcriptomic study, a BRAF mutation is found in roughly 10% of individuals diagnosed with colon cancer (Caputo, et al., 2019).

In the present study, likely pathogenic and uncertain significance mutations in the APC gene were identified as indecated in the Figs. 7-10. APC gene mutation in CRC initiates early activation of the Wnt/β-catenin pathway. Mutant APC, along with Axin2 and AMER1, disrupts the β-catenin destruction complex, leading to the accumulation

of β-catenin. This abnormal activation promotes cancer cell proliferation, invasion, and metastasis (Sanz-Pamplona, et al., 2015; Nguyen and Duong, 2018; Youssef, et al., 2020). The APC protein serves as a tumor suppressor, playing a pivotal role in both the canonical (β-catenin-dependent) Wnt signaling pathways and additional functions (Zhang, et al., 2023). Apart from its role in canonical Wnt signaling, APC contributes to the prevention and progression control of colorectal tumors (Keum and Giovannucci, 2019) and (Giannopoulou and Constantinou, 2023). It is actively participated in tasks such as chromosome segregation, the establishment of cellular polarity, migration, and the suppression of DNA replication (Stefanski and Prosperi, 2020). Most CRCs (70–80%) occur spontaneously, predominantly in individuals aged 70–75, lacking genetic predisposition or a family history. It is thought that a significant number of these sporadic cases involve somatic mutations in both alleles of the APC gene during early stages. However, about 20% of CRC patients exhibit familial aggregation, indicating a hereditary form with a family history of CRC in at least one other relative (Aghabozorgi, et al., 2019).

Fig. 11 presents the phosphatidylinositol-3-kinase (PI3K) is part of a lipid kinase family characterized by its heterodimeric structure composed of both regulatory and catalytic subunits (Cathomas, 2014). PI3K operates by phosphorylating phosphatidylinositol, a critical component of the cell membrane and a pivotal second messenger in cellular signaling pathways (He, et al., 2022). This versatile kinase plays a central role in modulating a wide array of cellular processes, encompassing proliferation, survival, apoptosis, migration, and metabolism regulation (Rakesh, et al., 2022). A prior investigation established that PIK3CA is responsible for encoding the catalytic component of phosphatidylinositol 3-kinase α (PI3Kα), which undergoes mutations in a broad spectrum of human malignancies, comprising approximately 30% of cases in CRC (Zhao, et al., 2019).

IV. Conclusions

Utilization of NGS technology in the sequencing platform has enabled to acquisition of extensive data on genetic alterations and specific gene mutations within colorectal tumor samples. This valuable information holds the potential to significantly inform clinical decision-making, aiding in the development of treatment strategies to optimize patient outcomes in the clinical setting.

References

Abid, M.N., Qadir, F.A., and Salihi, A., 2021. Association between the serum concentrations and mutational status of IL8, IL27 and VEGF and the expression levels of the hERG potassium channel gene in patients with colorectal cancer. *Oncology Letters,* 22, p.665.

Aghabozorgi, A.S., Bahreyni, A., Soleimani, A., Bahrami, A., Khazaei, M., Ferns, G.A., Avan, A., and Hassanian, S.M., 2019. Role of adenomatous polyposis coli (APC) gene mutations in the pathogenesis of colorectal cancer; current status and perspectives. *Biochimie*, 157, pp.64-71.

Ali Hama, H., 2019. Evaluation of p53 expression among colorectal cancer patients. *Zanco Journal of Pure and Applied Sciences*, 31, pp.131-134.

Arbyn, M., Weiderpass, E., Bruni, L., De Sanjose, S., Saraiya, M., Ferlay, J., and Bray, F., 2020. Estimates of incidence and mortality of cervical cancer in 2018: A worldwide analysis. *The Lancet Global Health*, 8, pp.e191-e203.

Baglietto, L., Lindor, N.M., Dowty, J.G., White, D.M., Wagner, A., Gomez Garcia, E.B., Vriends, A. H., Dutch Lynch Syndrome Study Group, Cartwright, N.R., and Barnetson, R.A., 2010. Risks of lynch syndrome cancers for MSH6 mutation carriers. *Journal of the National Cancer Institute*, 102, pp.193-201.

Bardhan, K., and Liu, K., 2013. Epigenetics and colorectal cancer pathogenesis. *Cancers* (*Basel*), 5, pp.676-713.

Barrasa, J.I., Olmo, N., Lizarbe, M.A., and Turnay, J., 2013. Bile acids in the colon, from healthy to cytotoxic molecules. *Toxicology in Vitro,* 27, pp.964-977.

Berends, M.J.W., Wu, Y., Sijmons, R.H., Mensink, R.G.J., Van Der Sluis, T., Hordijk-Hos, J.M., De vries, E.G., Hollema, H., Karrenbeld, A., and Buys, C.H.C.M., 2002. Molecular and clinical characteristics of MSH6 variants: An analysis of 25 index carriers of a germline variant. *The American Journal of Human Genetics*, 70, pp.26-37.

Boland, C.R., and Goel, A., 2010. Microsatellite instability in colorectal cancer. *Gastroenterology,* 138, pp.2073-2087.e3.

Caputo, F., SantinI, C., Bardasi, C., Cerma, K., Casadei-Gardini, A., Spallanzani, A., Andrikou, K., Cascinu, S., and Gelsomino, F., 2019. BRAF-mutated colorectal cancer: Clinical and molecular insights. *International Journal of Molecular Sciences,* 20, p.5369.

Carneiro Da Silva, F., Ferreira, J.R.D.O., Torrezan, G.T., Figueiredo, M.C.P., Santos, É.M.M., Nakagawa, W.T., Brianese, R.C., Petrolini de oliveira, L., Begnani, M.D., and Aguiar-Junior, S., 2015. Clinical and molecular characterization of Brazilian patients suspected to have Lynch syndrome. *PLoS One*, 10, p.e0139753.

Cathomas, G., 2014. PIK3CA in colorectal cancer. *Frontiers in Oncology*, 4, p.35.

Cossio, S.L., Koehler-Santos, P., Pessini, S.A., Mónego, H., Edelweiss, M.I., Meurer, L., Errami, A., Coffa, J., Bock, H., and Saraiva-Pereira, M.L., 2010. Clinical and histomolecular endometrial tumor characterization of patients at-risk for Lynch syndrome in South of Brazil. *Familial Cancer*, 9, pp.131-139.

Da Silva, F.C., De Oliveira, L.P., Santos, E.M., Nakagawa, W.T., Aguiar Junior, S., Valentin, M.D., Rossi, B.M., and De Oliveira Ferreira, F., 2010. Frequency of extracolonic tumors in Brazilian families with Lynch syndrome: Analysis of a hereditary colorectal cancer institutional registry. *Familial Cancer*, 9, pp.563-570.

Davies, H., Bignell, G.R., Cox, C., Stephens, P., Edkins, S., Clegg, S., Teague, J., Woffendin, H., Garnett, M.J., and Bottomley, W., 2002. Mutations of the BRAF gene in human cancer. *Nature*, 417, pp.949-954.

Dominguez-Valentin, M., Nilbert, M., Wernhoff, P., López-Köstner, F., Vaccaro, C., Sarroca, C., Palmero, E.I., Giraldo, A., Ashton-Prolla, P., and Alvarez, K., 2013. Mutation spectrum in South American Lynch syndrome families, *Hereditary Cancer in Clinical Practice*, 11, p.18.

Dominguez-Valentin, M., Sampson, J.R., Seppälä, T.T., Ten Broeke, S.W., Plazzer, J.P., Nakken, S., Engel, C., Aretz, S., Jenkins, M.A., and Sunde, L., 2020. Cancer risks by gene, age, and gender in 6350 carriers of pathogenic mismatch repair variants: Findings from the prospective lynch syndrome database. *Genetics in Medicine*, 22, pp.15-25.

Fatemi, N., Tu, S.J., Chung, C.C., Moghadam, P.K., Mojarad, E.N., Sadeghi, A., Totonchi, M., Aghdaei, H.A., and Chang, J.G., 2023. Whole exome sequencing identifies MAP3K1, MSH2, and MLH1 as potential cancer-predisposing genes in familial early-onset colorectal cancer. *The Kaohsiung Journal of Medical Sciences*, 39, pp.896-903.

Frederiksen, J.H., Jensen, S.B., Tumer, Z., and Hansen, T.V.O., 2021. Classification of MSH6 variants of uncertain significance using functional assays. *International Journal of Molecular Sciences*, 22, p.8627.

Fuchs, C.S., Giovannucci, E.L., Colditz, G.A., Hunter, D.J., Speizer, F.E., and Willett, W.C., 1994. A prospective study of family history and the risk of colorectal cancer. *New England Journal of Medicine*, 331, pp.1669-1674.

Giannopoulou, N., and Constantinou, C., 2023. Recent developments in diagnostic and prognostic biomarkers for colorectal cancer: A narrative review. *Oncology,* 101, pp.675-684.

Hause, R.J., Pritchard, C.C., Shendure, J., and Salipante, S.J., 2016. Classification and characterization of microsatellite instability across 18 cancer types. *Nature Medicine*, 22, pp.1342-1350.

He, X., Li, Y., Deng, B., Lin, A., Zhang, G., Ma, M., Wang, Y., Yang, Y., and Kang, X., 2022. The PI3K/AKT signalling pathway in inflammation, cell death and glial scar formation after traumatic spinal cord injury: Mechanisms and therapeutic opportunities. *Cell Proliferation*, 55, p.e13275.

Hendriks, Y.M., Wagner, A., Morreau, H., Menko, F., Stormorken, A., Quehenberger, F., Sandkuijl, L., Møller, P., Genuardi, M., and Van Houwelingen, H., 2004. Cancer risk in hereditary nonpolyposis colorectal cancer due to MSH6 mutations: Impact on counseling and surveillance. *Gastroenterology*, 127, pp.17-25.

Janku, F., Wheler, J.J., Westin, S.N., Moulder, S.L., Naing, A., Tsimberidou, A.M., Fu, S., Falchook, G.S., Hong, D.S., and Garrido-Laguna, I., 2012. PI3K/AKT/mTOR inhibitors in patients with breast and gynecologic malignancies harboring PIK3CA mutations. *Journal of Clinical Oncology*, 30, p.777.

Kamal, L.A., and Jalal, J.A., 2019. Immunohistochemical expression of HER2/neu in colorectal carcinoma in Erbil city, Kurdistan region. *Zanco Journal of Medical Sciences* (*Zanco J Med Sci*), 23, pp.421-428.

Keum, N., and Giovannucci, E., 2019. Global burden of colorectal cancer: Emerging trends, risk factors and prevention strategies. *Nature Reviews Gastroenterology and Hepatology*, 16, pp.713-732.

Kontomanolis, E.N., Koutras, A., Syllaios, A., Schizas, D., Mastoraki, A., Garmpis, N., Diakosavvas, M., Angelou, K., Tsatsaris, G., and Pagkalos, A., 2020. Role of oncogenes and tumor-suppressor genes in carcinogenesis: A review. *Anticancer Research*, 40, pp.6009-6015.

Laczmanska, I., and Sasiadek, M.M., 2019. Meta-analysis of association between Arg326Gln (rs1503185) and Gln276Pro (rs1566734) polymorphisms of PTPRJ gene and cancer risk. *Journal of Applied Genetics*, 60, p.57-62.

Li, H., Zhang, P., Liu, C., Wang, Y., Deng, Y., Dong, W., and Yu, Y., 2022. The structure, function and regulation of protein tyrosine phosphatase receptor type J and its role in diseases. *Cells*, 12, p.8.

Lynch, H.T., and De La Chapelle, A., 1999. Genetic susceptibility to non-polyposis colorectal cancer. *Journal of Medical Genetics*, 36, pp.801-818.

Lynch, H.T., and Lynch, J.F., 1985. Hereditary nonpolyposis colorectal cancer (Lynch syndromes I and II): A common genotype linked to oncogenes? *Medical Hypotheses*, 18, pp.19-28.

Malińska, K., Deptuła, J., Rogoża-Janiszewska, E., Górski, B., Scott, R., Rudnicka, H., Kashyap, A., Domagała, P., Hybiak, J., and Masojć, B., 2020. Constitutional variants in POT1, TERF2IP, and ACD genes in patients with melanoma in the Polish population. *European Journal of Cancer Prevention*, 29, pp.511-519.

Mathe, E., Olivier, M., Kato, S., Ishioka, C., Hainaut, P., and Tavtigian, S.V., 2006. Computational approaches for predicting the biological effect of p53 missense mutations: A comparison of three sequence analysis based methods. *Nucleic Acids Research*, 34, pp.1317-1325.

Mita, Y., Yasuda, Y., Sakai, A., Yamamoto, H., Toyooka, S., Gunduz, M., Tanabe, S., Naomoto, Y., Ouchida, M., and Shimizu, K., 2010. Missense polymorphisms of PTPRJ and PTPN13 genes affect susceptibility to a variety of human cancers. *Journal of Cancer Research and Clinical Oncology,* 136, pp.249-259.

Morgan, D., Berggren, K.L., Spiess, C.D., Smith, H.M., Tejwani, A., Weir, S.J., Lominska, C.E., Thomas, S.M., and Gan, G.N., 2022. Mitogen-activated protein kinase-activated protein kinase-2 (MK2) and its role in cell survival, inflammatory signaling, and migration in promoting cancer. *Molecular Carcinogenesis,* 61, pp.173-199.

Murphy, N., Moreno, V., Hughes, D.J., Vodicka, L., Vodicka, P., Aglago, E.K., Gunter, M.J., and Jenab, M., 2019. Lifestyle and dietary environmental factors in colorectal cancer susceptibility. *Molecular Aspects of Medicine*, 69, pp.2-9.

Nguyen, H.T., and Duong, H.Q., 2018. The molecular characteristics of colorectal cancer: Implications for diagnosis and therapy. *Oncology Letters,* 16, pp.9-18.

Olivier, M., Hollstein, M., and Hainaut, P., 2010. TP53 mutations in human cancers: Origins, consequences, and clinical use. *Cold Spring Harbor Perspectives in Biology,* 2, p.a001008.

Peltokallio, P., and Peltokallio, V., 1966. Relationship of familial factors to carcinoma of the colon. *Diseases of the Colon and Rectum,* 9, pp.367-370.

Perne, C., Peters, S., Cartolano, M., Horpaopan, S., Grimm, C., Altmuller, J., Sommer, A.K., Hillmer, A.M., Thiele, H., and Odenthal, M., 2021. Variant profiling of colorectal adenomas from three patients of two families with MSH3-related adenomatous polyposis. *PLos One*, 16, p.e0259185.

Poaty, H., Bouya, L.B., Lumaka, A., Mongo-Onkouo, A., and Gassaye, D., 2023. PMS2 Pathogenic variant in lynch syndrome-associated colorectal cancer with polyps. *Global Medical Genetics*, 10, pp.1-5.

Rakesh, R., Priyadharshini, L.C., Sakthivel, K.M., and Rasmi, R.R., 2022. Role and regulation of autophagy in cancer. *Biochimica et Biophysica Acta (BBA)-Molecular Basis of Disease*, 1868, p.166400.

Rao, C.V., and Yamada, H.Y., 2013. Genomic instability and colon carcinogenesis: From the perspective of genes. *Frontiers in Oncology,* 3, p.130.

Raza, Y., Ahmed, A., Khan, A., Chishti, A.A., Akhter, S.S., Mubarak, M., Bernstein, C., Zaitlin, B., and Kazmi, S.U., 2020. Helicobacter pylori severely reduces expression of DNA repair proteins PMS2 and ERCC1 in gastritis and gastric cancer. *DNA Repair* (*Amst*), 89, p.102836.

Roberts, M.E., Jackson, S.A., Susswein, L.R., Zeinomar, N., Ma, X., Marshall, M.L., Stettner, A.R., Milewski, B., Xu, Z., and Solomon, B.D., 2018. MSH6 and PMS2 germ-line pathogenic variants implicated in Lynch syndrome are associated with breast cancer. *Genetics in Medicine*, 20, p.1167-1174.

Sanz-Pamplona, R., Lopez-Doriga, A., Pare-Brunet, L., Lázaro, K., Bellido, F., Alonso, M.H., Aussó, S., Guinó, E., Beltrán, S., and Castro-Giner, F., 2015. Exome sequencing reveals AMER1 as a frequently mutated gene in colorectal cancer. *Clinical Cancer Research,* 21, pp.4709-4718.

Schwarz, J.M., Cooper, D.N., Schuelke, M., and Seelow, D., 2014. MutationTaster2: Mutation prediction for the deep-sequencing age. *Nature Methods*, 11, pp.361-362.

Segditsas, S., and Tomlinson, I., 2006. Colorectal cancer and genetic alterations in the Wnt pathway. *Oncogene*, 25, pp.7531-7537.

Senter, L., Clendenning, M., Sotamaa, K., Hampel, H., Green, J., Potter, J.D., Lindblom, A., Lagerstedt, K., Thibodeau, S.N., and Lindor, N.M., 2008. The clinical phenotype of Lynch syndrome due to germ-line PMS2 mutations. *Gastroenterology*, 135, pp.419-428.

Sinicrope, F.A., 2018. Lynch syndrome-associated colorectal cancer. *New England Journal of Medicine,* 379, pp.764-773.

Stefanski, C.D., and Prosperi, J.R., 2020. Wnt-independent and Wnt-dependent effects of APC loss on the chemotherapeutic response. *International Journal of Molecular Sciences*, 21, p.7844.

Tariq, K., and Ghias, K., 2016. Colorectal cancer carcinogenesis: A review of mechanisms. *Cancer Biology and Medicine*, 13, p120.

Tavtigian, S.V., Deffenbaugh, A.M., Yin, L., Judkins, T., Scholl, T., Samollow, P.B., De Silva, D., Zharkikh, A., and Thomas, A., 2006. Comprehensive statistical study of 452 BRCA1 missense substitutions with classification of eight recurrent substitutions as neutral. *Journal of Medical Genetics*, 43, p.295-305.

Ten Broeke, S.W., Brohet, R.M., Tops, C.M., Van der Klift, H.M., Velthuizen, M.E., Bernstein, I., Capellá Munar, G., Gomez Garcia, E., Hoogerbrugge, N., and Letteboer, T., 2015. Lynch syndrome caused by germline PMS2 mutations: Delineating the cancer risk. *Journal of Clinical Oncology*, 33, p.319-325.

Vaser, R., Adusumalli, S., Leng, S.N., Sikic, M., and NG, P.C., 2016. SIFT missense predictions for genomes. *Nature Protocols*, 11, p.1-9.

Winawer, S., Fletcher, R., Rex, D., Bond, J., Burt, R., Ferrucci, J., Ganiats, T., Levin, T., Woolf, S., and Johnson, D., 2003. Colorectal cancer screening and surveillance: Clinical guidelines and rationale-update based on new evidence. *Gastroenterology*, 124, p.544-560.

Youssef, A., Abdel-Fattah, M.A., Touny, A.O., Hassan, Z.K., Nassar, A., Lotfy, M.M., Moustafa, A., Eldin, M.M., Bahnassy, A., and Zekri, A.R.N., 2020. Deep Next Generation Sequencing Identifies Somatic Mutational Signature in Egyptian Colorectal Cancer Patients.

Zhang, X., Li, C., Wu, Y., and Cui, P., 2023. The research progress of Wnt/β-catenin signaling pathway in colorectal cancer. *Clinics and Research in Hepatology and Gastroenterology*, 47, p.102086.

Zhao, Y., Zhao, X., Chen, V., Feng, Y., Wang, L., Croniger, C., Conlon, R.A., Markowitz, S., Fearon, E., and Puchowicz, M., 2019. Colorectal cancers utilize glutamine as an anaplerotic substrate of the TCA cycle *in vivo*. *Scientific Reports*, 9, p.19180.

Deep Learning-Based Optical Music Recognition for Semantic Representation of Non-overlap and Overlap Music Notes

Rana L. Abdulazeez[1] and Fattah Alizadeh[2]

[1]Department of Software and Informatics Engineering, College of Engineering, Salahaddin University-Erbil, Kurdistan Region – F.R. Iraq

[2]Department of Computer Engineering, School of Science and Engineering, University of Kurdistan Hewler, Kurdistan Region – F.R. Iraq

***Abstract*—In the technology era, the process of teaching a computer to interpret musical notation is termed optical music recognition (OMR). It aims to convert musical note sheets presented in an image into a computer-readable format. Recently, the sequence-to-sequence model along with the attention mechanism (which is used in text and handwritten recognition) has been used in music notes recognition. However, due to the gradual disappearance of excessively long sequences of musical sheets, the mentioned OMR models which consist of long short-term memory are facing difficulties in learning the relationships among the musical notations. Consequently, a new framework has been proposed, leveraging the image segmentation technique to break up the procedure into several steps. In addition, an overlap problem in OMR has been addressed in this study. Overlapping can result in misinterpretation of music notations, producing inaccurate findings. Thus, a novel algorithm is being suggested to detect and segment the notations that are extremely close to each other. Our experiments are based on the usage of the Convolutional Neural Network block as a feature extractor from the image of the musical sheet and the sequence-to-sequence model to retrieve the corresponding semantic representation. The proposed approach has been evaluated on The Printed Images of Music Staves dataset. The achieved results confirm that our suggested framework successfully solves the problem of long sequence music sheets, obtaining SER 0% for the non-overlap symbols in the best scenario. Furthermore, our approach has shown promising results in addressing the overlapping problem: 23.12 % SER for overlapping symbols.**

***Index Terms*—Sequence-to-sequence, Long short-term memory network, Convolutional neural network, Segmentation, Semantic representation, Overlapping.**

I. Introduction

Musical notation is a visual representation of a musical sound heard or imagined or a sequence of visual instructions for playing music or performing it later by the musician. As such, it is a necessary approach toward conserving musical compositions and enabling the preservation of the music phenomenon. Despite the fact that musicians can read and interpret fairly sophisticated musical notation, no system can do so as of yet (Calvo-Zaragoza, et al., 2020; Castellanos, et al., 2020).

The digitalization process of musical score libraries is an essential initial step in different data-driven methods of musical analysis or other uses requiring the utilization of digital forms to modernize and enhance many facets of the music industry from performance and research to education and cooperation. Indeed, optical music recognition (OMR) aims to translate musical shapes from musical notation graphics. The outcome will be a new version of the score, which can be read by the computer, such as MusicXML and Musical Instrument Digital Interface. These forms would keep and maintain musical properties and stuff such as pitches, duration, dynamics, and notes (Shatri and Fazekas, 2020). Even though there is a great deal of research conducted in the literature, still some challenges are available that should be tackled to enhance their accuracy and performance. Problems such as segmentation, recognition accuracy, overlapping symbols, low-quality paper sheets, and process speed, are among the ones that attracted the researcher's attention.

In the field of OMR, some researchers in previous works tend to adopt Machine translation techniques such as the sequence-to-sequence (seq2seq) model, which is made up of two recurrent neural networks (RNN): an encoder and a decoder. Seq2seq models have a significant role in recent achievements in natural language processing (NLP) approaches such as machine translation and speech recognition. However, seq2seq models are unable to preserve global implicit information from a long sequence of words (Jang, Seo, and Kang, 2019) causing improper music note recognition and a high error rate in long sequence musical sheets. The OMR systems for converting images of music scores into another music notation format such as semantic representation produce a long sequence of words to tell their musical meaning. Furthermore, in the case of multiple-voice polyphonic staves (overlapping), various symbols

ARO-The Scientific Journal of Koya University
Vol. XII, No. 1 (2024), Article ID: ARO.11402. 9 pages
Doi: 10.14500/aro.11402
Received: 13 September 2023; Accepted: 01 March 2024
Regular research paper: Published: 11 March 2024
Corresponding author's e-mail: rana.abdulazeez@su.edu.krd

may occur at the same time (Shatri and Fazekas, 2020). The segmentation of complex notations is still a challenging problem in OMR given that proper segmentation is necessary to obtain correct symbol recognition.

In this study, a novel segmentation algorithm has been proposed to address the long sequence problem along with an OMR system. The presented OMR architecture includes two common deep learning models, convolutional neural networks (CNNs) and RNNs. The CNN block is used to learn the feature representation of the input image. The target tokens are then produced directly by the seq2seq model from the acquired representation learned by the CNN. The major advantage of this approach is the ability of the seq2seq model to be trained by pairs of inputs: The input images and their corresponding transcription, and it can handle variable lengths and capture context information. In addition, to engage with the complex notations issue, a sophisticated algorithm to detect and solve the overlap situation has been suggested. The following list summarizes the main contributions of this study:

- This study proposes a new segmentation algorithm, which is then applied to the (PrIMuS) dataset to generate a new version of it
- The previous OMR works used the VGG pre-trained model to extract the relevant features, whereas ResNet50, Xception, and VGG16, 19 pre-trained models were used in this work as feature extractors
- A novel method is proposed to detect and segment the overlapping music notes to solve the overlap issue.

The structure of the paper is as follows: Sec. II reviews the state-of-the-art methods relevant to this work. Sec. III detailed the proposed approach starting from the dataset preparation phase and model architecture design to the prediction phase. Sec. IV explains the usage of the image augmentation technique. Sec. V addresses the overlapping symbols. Sec. VI provides the results and discussions. Finally, Sec. VII gives the conclusion and future work.

II. Related Work

This section describes the most common OMR methodologies and the state-of-the-art methods relevant to this work. We first provide an overview of the traditional OMR approaches and then review the most current deep-learning-based available techniques.

Over the past few decades, the OMR problem has been tackled by computer vision and pattern recognition based on traditional techniques. Since the musical score follows a sequence, the Hidden Markov Model has been employed (Pugin, 2006; Pugin, Burgoyne, and Fujinaga, 2007). Although this method has shown promising results, there is room for more experimentation in the OMR field due to traditional approaches are unable to cover all challenges.

In recent years, the performance of OMR systems has been significantly enhanced thanks to deep learning models, and promising results on OMR problems were shown by deep learning algorithms. Calvo-Zaragoza, Valero-Mas and Pertusa (2017) have set the basis for the evolution of models that directly work with a major part of the OMR framework by submitting a system based on an end-to-end approach. The presented model is based on a recurrent CNNs architecture that accepts the image of the monophonic notes as input and the output is a sequence of music descriptions. Then, Calvo-Zaragoza and Rizo (2018) presented their dataset called Printed Images of Music Staves (PrIMuS) to train the suggested OMR deep-learning model based on (RCNN). However, the usage of this architecture might not offer the accuracy at the symbol level needed for musical content transcription. In addition, the current approach could not effectively capture long-range dependencies and global context.

There are attempts to adapt some machine translation techniques in the OMR field, such as the seq-to-seq model. In 2017, a novel convolutional seq2seq architecture model was presented by Van Der Wel and Ullrich (2017) in the direction of a trainable end-to-end OMR pipeline. Two common deep learning algorithms have been employed: First, the CNN block converts the input image window to feature vectors. Second, an encoder RNN encodes the feature vectors to the context vector representation. Followed by a decoder RNN decodes the context vector to the sequence of labels. The algorithm's image input is described as a series of image patches produced by sliding a window across the original input score. Then, an OMR system based on the seq2-seq model with an attention mechanism has been presented by Baró, Badal, and Fornés (2020). They tried to adapt the seq2seq model which is used in handwritten recognition and machine translation problems to recognize old music notations, and their study was inspired by the work submitted by Michael, et al. (2019) for handwritten text recognition. To decrease statistically improbable outcomes of Handwritten Music Recognition, Torras, et al. (2022) presented a study based on making use of a language model with the seq2seq model. The pipeline of the system started with giving the input image to the VGG 19 to extract the high-level features. The encoder was a stacked layer of bi-directional gated recurrent units to create the intermedium context vector. In the decoder phase, at each time step, an attention-weighted summary of the hidden state is computed and given the output token. The current output token and the final state are used as input for the next time step. To improve the OMR system performance, Language Model Integration has been employed with the seq2seq model. Furthermore, a novel sequence (Seq2Seq) framework, based on the transformer with a masked language model (ST-MLM) was submitted by Wen and Zhu (2022). This approach consists of five modules: Pre-processing, encoder, decoder, transformer with masked language model (T-MLM), and output. The encoder layer uses a multi-scale CNN and Bi-LSTM for music symbol information, whereas the T-MLM layer uses masked self-attention. Nevertheless, employing the attention mechanism with seq2seq models has limitations: First, increasing the computational cost and level of complexity of the model through needing to add more parameters. Second, Seq2seq

models might be influenced by noise and redundancy through generating unnecessary or repetitive input or output positions or by producing too uniform or sparse attention weights. Third, different structures lengths, vocabularies, domains, or languages between input and output sequences can cause alignment problems and mismatches in the domains that attention mechanisms process.

III. Proposed Approach

The general flow of the proposed framework includes the following three phases: Dataset preparation phase, model architecture design phase, and prediction phase, as depicted in Fig. 1. In the sequel, a complete explanation of each step will be presented.

A. Dataset Preparation phase

Segmentation of the music sheets is an important step of the proposed work by which each music symbol or several symbols connected by a beam will be extracted from the input music sheet. Since the music symbols are mainly stored in a sheet containing a long sequence of individual symbols, a robust and efficient segmentation algorithm can play a significant role in the recognition output. The PrIMS dataset (Calvo-Zaragoza and Rizo, 2018) which contains images of music scores and their musical meanings (semantic representation as a text file) is utilized as a basic material to generate our dataset. The musical meanings might have a large number of sequence words which makes the recognition process quite challenging by seq2seq models. The seq2seq model is a unique type of RNN architecture that is usually used in complex language problems such as machine translation (Jang, Seo, and Kang, 2019). Consequently, the suggested resolving, splitting the process into smaller steps which means dividing the image (its associated semantic representation) into several smaller pieces of images/ semantic representation. A segmentation algorithm inspired by the vertical projection concept in image processing has been designed. The starting and ending columns of each symbol or several symbols connected by a beam are found. Next, each sub-images between starting and ending pixels are cropped and saved, separately, as shown in Fig. 2. Around 100 images are randomly selected from the (PrIMS) dataset and they have been fed to the segmentation algorithm. The complete algorithm is shown in Algorithm 1. After applying the proposed segmentation algorithm on the selected sheet, a dataset of 800 images and their description file is generated.

Algorithm 1: Segmentation Algorithm.

Input: The music sheet contains several musical notes.
Output: Set of images of individual music symbols or a group of beaming music notes.

1- Read the input image, and convert it to the binary form
2- Apply staff lines removable.

Object detection part

1- Set the following variables with values:
start=[]
end=[]
s_flag=False
e_flag=True
t_flag=False
sum=0

2- Check every pixel, column-wise
For i in range(width)
Begin
For j in range(height)
Begin
If in_image[j][i]== 0 and s_flag==False and e_flag==True
(means: detecting the start/first column of the symbol)

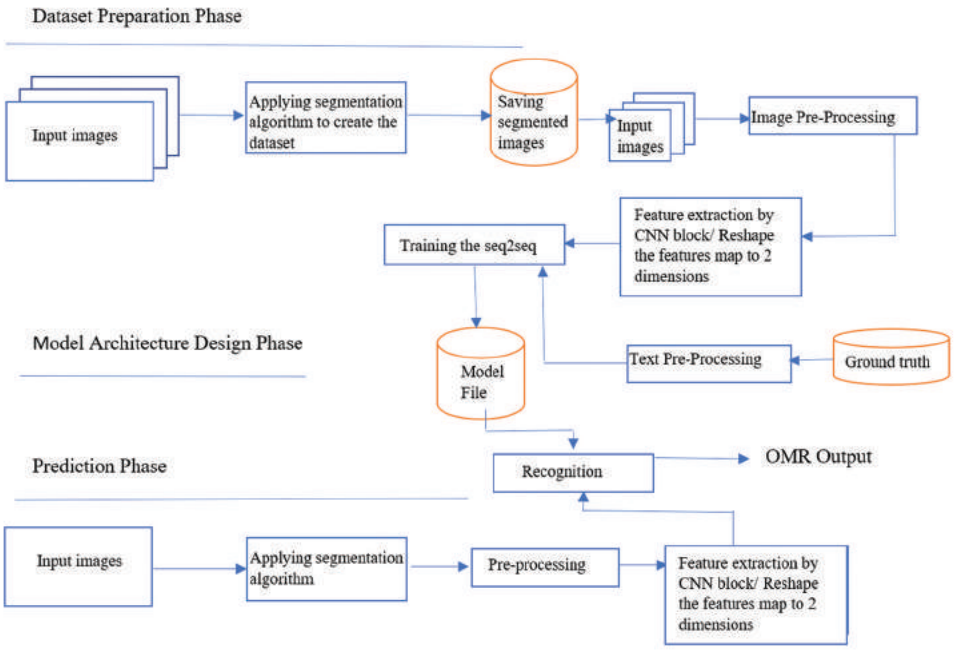

Fig. 1. Proposed approach.

 http://dx.doi.org/10.14500/aro.11402

```
        Then
        s_flag=True
        t-flag=True
        e_flag=Fals
        if in_image[j][i]==255 and s_flag==True and e_
        flag==True (seeking for the first white column after the
        symbol detection to get the end column)
        then
        sum+=1
    end
        if temp_f== True then
        start.append(column)
        if sum== height (means: getting the first white column
        after symbol detection to obtain the end column)
        then
        end.append(end)
    end
Segmentation part
    1. or_img=raw image (with five lines)
    2. for I in range (length(start))
        crop the raw image with a fixed height and variable
        width which is taken from start and end lists.
        Cropped=or_img[0:height,start[i]: end[i]
    3. save the cropped image
End of Algorithm
```

The suggested deep learning model requires two types of input data: Image (musical notes) and text (musical meaning). Thus, the image with its description should be encoded before being fed to the model. From the created corpus of music notes, each image is read from the defined path. The dimensions of every image are altered according to the architecture of the feature extractor that is used (block of CNN). It is extremely common to normalize the input images in computer vision tasks. As mentioned above, the text data are one of the inputs to the OMR system (semantic representation). Hence, a part of this work is related to NLP. The methods that are used in text pre-processing for NLP problems are followed. Because (PrIMuS) dataset is a clean one, the only step is needed to convert the words to numbers in an efficient manner to enable the machine to deal with them.

Every token or string of the semantic representation is read from the ground truth, and then, <start> and <end> tokens are added to the beginning and end of the string. Finally, each string or word is converted to an integer representation to be suitable for the embedding layer.

B. Model Architecture Design

The proposed OMR system pipeline consists of two main parts: A block of a CNN and a seq2seq model (an encoder and a decoder).

The variety of CNN block structures as a feature extractor has proven to be an effective method (Brownlee, 2019) among which two approaches are used in this study: CNN with transfer learning and CNN without transfer learning. Transfer learning is a machine-learning technique in which a pre-trained model is reused as a fundamental point in another task. High-performance models are trained on large datasets, such as ImageNet datasets, to detect common features and extract them. The output will be from the layer before the output layer of the model (Brownlee, 2019). In this study, the feature extractor has been implemented with some pre-trained models such as VGG19, ResNet50, and Xception. Then, the features are reshaped into a two-dimensional features map to be later input into the seq2seq model. Adding to the previous models, another deep learning model is suggested consisting of a block of CNN and the seq2seq model without employing the transfer learning technique to examine the role of transfer learning on the results. The CNN used in this experiment includes four convolutional layers with an increased number of filters starting with 32, 64, 128, and 256 to enhance its ability to learn complex and diverse features from input data, and kernel size (3 × 3), four batchnormalization layers; each batchnormalization layer transforms the inputs to maintain the mean output close to zero and the output standard deviation close to one, (2 × 2) first two max pooling layers and second two max-pooling layers with (2 × 1). The rectified linear unit activations have been used. All images are resized into (224,224,3). The configurations of the proposed CNN are depicted in Table I.

The second part of the proposed OMR system is a seq2seq model (encoder–decoder) which is used in the text recognition method and has been adapted to music scores. The aim rationale behind seq2seq which follows the encoder–decoder structure is to separate the decoding from the feature extraction. Two main components are available in the model: First, the encoder, which converts the entire input sequence to a fixed-size representation (context vector), then the decoder that produces the output sequence one token at each time step (Van Der Wel and Ullrich, 2017; Mondal, et al., 2022; Neubig, 2017; Baró, Badal, and Fornés, 2020). LSTM is simplified and represented in equation (1).

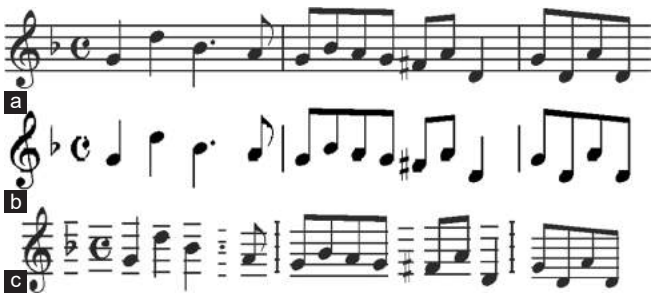

Fig. 2. Segmentation steps results, (a) the input image from (PrIMuS), (b) the image after applying the staff line removable function, and (c) the final segmented sub-images.

TABLE I
CNN Customized Model Structure

Input (224,224,3)
Convolutional block
Conv (32, 3×3, relu), Batch Normalization(), (Max Pooling (2×2))
Conv (64, 3×3, relu), Batch Normalization(), (Max Pooling (2×2))
Conv (128, 3×3, relu), Batch Normalization(), (Max Pooling (2×1))
Conv (256, 3×3, relu), Batch Normalization(), (Max Pooling (2×1))

$$ht,ct = LSTM\ (xt,ht-1,ct-1) \quad (1)$$

At each time step t, the encoder iteratively inputs the sequence $x_1,\ldots,x_T$ of length T and updates the hidden state vector h_t and cell memory state vector c_t.

In the following, the layers of the proposed network along with their functionality will be detailed.

1. Two input layers are available in seq2seq architecture: The input layer is used to feed the encoder with the features map of the input image takes the shape of two dimensions NumPy array and the input layer that used to supply the decoder with the target tokens to fulfill the teacher forcing training concept and takes the shape of the length of the input sequence
2. The encoder is a single LSTM layer, with 256 hidden units and 50% dropout, to avoid the vanishing gradients problem. In the encoder, the final hidden state and cell state are kept for further use as an initial state of the decoder, whereas the outputs of the encoder at each time step are discarded. The encoder produces a final encoded feature map (context vector). Formally, the feature map *X* of the input image *I* is generated by the CNN block, this is equivalent to a series of column vectors $X = (X1,\ldots, XM)$, where M is the length of the input sequence. Followed by this sequence's processing by the LSTM layer (encoder) to produce the final feature map $H=(h1,\ldots,hM)$
3. The decoder module is formed by a single LSTM layer with 256 hidden units and 50% dropout to generate the target token of the note that is present in the input image. As mentioned, the initial state of the decoder is set with the final cell and hidden states of the encoder, this helps the decoder to generate the target token. In the decoder, the output from each time step serves as the input for the following time step. The decoder determines the most likely token yt, at each time step t by computing a probability distribution over the vocabularies of potential tokens. dependent on its prior predictions (y1,…,yt-1) along with some context vector ct which involves details from the encoded features H. It determines the probability throughout the series of outputs Y=(y1,…,yT), dividing the combined probability into the ordered conditionals $p(Y)=\Pi^{T}_{t=1}p(yt \mid y1,\ldots,y-1,ct)$, where the output sequence length is represented by T
4. An embedding layer is a word embedding layer or word representation layer employed in the seq2seq model to represent the target tokens that feed into the decoder (Van Der Wel and Ullrich, 2017; Mondal, et al., 2022; Baró, Badal, and Fornés, 2020; Neubig, 2017). It is a class of approaches used for word representation, it represents each word in a fixed-size vector corresponding to particular words in the vocabulary (Sutskever, Vinyals, and Le, 2014; Brownlee, 2019)
5. Two dense layers exist. First, a dense layer with 256 neurons and a ReLU activation function to improve the performance of RNN (LSTM). ReLU activation function in the Dense layer efficaciously tackles the vanishing gradient problem (Matrenin, et al., 2020). Second, the dense layer of (vocab_size) and Softmax activation function. A Softmax to find a probability distribution to determine the final output (token) (Van Der Wel and Ullrich, 2017; Mondal, et al., 2022; Baró, Badal, and Fornés, 2020; Neubig, 2017). Fig. 3. shows the whole OMR system.

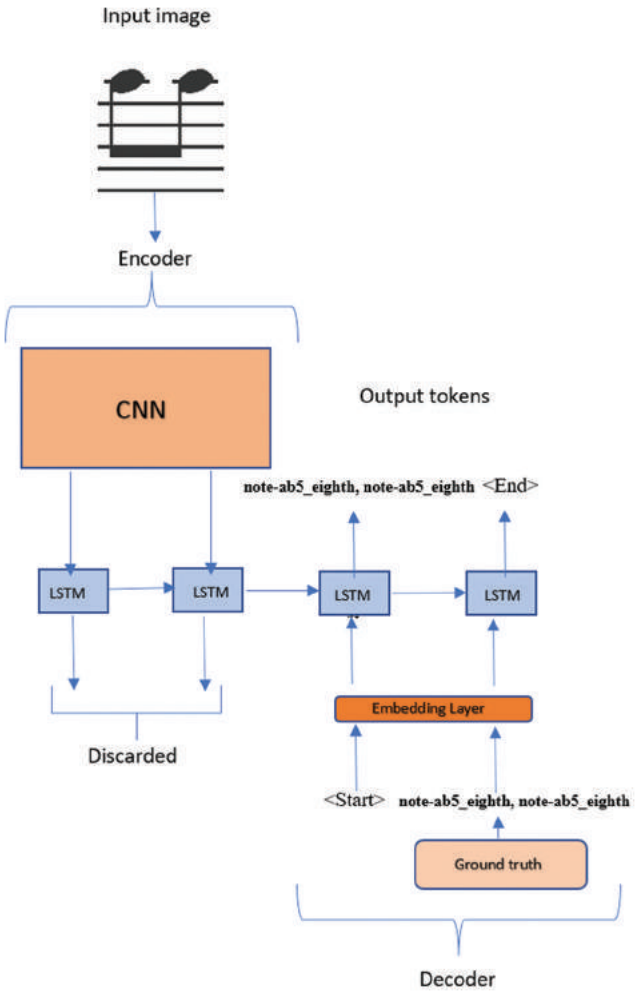

Fig. 3. Optical music recognition system.

The neural seq2seq model is trained to make a prediction of the probability distribution for the next token given the previous context. At each time step, the probability is maximized and assigned to the correct token by making use of the categorical_crossentropy loss function. For a given random variable or series of events, categorical_crossentropy is used for a multi-class classification model and the output will be assigned to an integer value (Brownlee, 2019). Training is done using the Adam optimizer to iteratively adjust network weights using training data. As mentioned before, the target tokens are expanded in pre-processing step adding two artificial tokens <start> and <end>. At training time, making use of the teacher force ensures that the decoder can see the correct tokens of the previous time step for rapidly and efficiently training the RNN model (Sutskever, Vinyals, and Le, 2014; Brownlee, 2019).

C. Prediction Phase

Once the defined seq2seq model is trained and saved, it can be used for the prediction. Nevertheless, the structure

http://dx.doi.org/10.14500/aro.11402

of the model is not engineered to be used recursively to generate one token at a time because the model is defined for the training phase to learn weights. Therefore, two models are required for the prediction phase. A model for encoding the features map, and a model gets the token generated so far and its encoding as inputs and predicts the next token in the sequence (Brownlee, 2019).

The pipeline of the prediction process in our experiment:

Input: The image of the music sheet (a long sequence of notes from [PrIMS] dataset).

Output: The musical meaning of all notes presented on the input image.

1. Applying a segmentation algorithm to split the input image into individual notes or grouped notes connected by beamline
2. Depending on the number of segmented images, the prediction operation is iterated

IV. Image Augmentation

Computer vision models frequently utilize image augmentation techniques to improve the accuracy of the model by increasing its ability to recognize new variants of the training data. In this work, the impacts of three types of image augmentation techniques have been explored in the results. The blurring technique is implemented with (5,5) kernel size, in the rotation technique the images are rotated at (−15,15) degrees, and the images are resized between 50% and 150% in the scale technique (Fig. 4).

V. Dealing with Overlapping Symbols

Shatri and Fazekas (2020) have addressed some of the major challenges such as overlapping and complexity of common Western music notation. The overlapping situation happens when various notes might be played at the same time. The OMR system should be able to recognize each symbol individually. As a consequence, a novel algorithm is designed to detect the overlap problem and segment the existing symbols in the input image. The presented algorithm was inspired by the set intersection concept in mathematics. The intersection is represented by $A \cap B$, more formally, $x \in A \cap B$ if $x \in A$ and $x \in B$. The intersection of two sets that include the same elements in both sets (Rosen, 2018). In the case of overlapping, after removing the staff lines, each image has two symbols that are overlapping vertically. All columns that the symbol passes through are considered a set. Thus, each of the two symbols is associated with a set of columns. Once overlapping occurs, the input image has two symbols: One above and one below. The two symbols can have some common columns which results in a segmentation problem. Algorithm 2 shows the steps to solve the overlapping case:

Algorithm 2: Overlap Detection Algorithm

1. Check the input image if contains one symbol or more by testing each pixel row by row
2. Find the start column and the end column of the upper symbol, then save them in variables
3. Find the start column and the end column of the lower symbol, then save them in variables
4. Create set 1 which contains numbers between the start and the end columns of the upper symbol:
   For example:
   If the first (upper) symbol starts in column 4 and ends in column 10 the set1 will be:
   Set1= {4,5,6,7,8,9,10}.
5. Create set 2 which contains numbers between the start and the end columns of the lower symbol:
   For example:
   If the second (lower) symbol starts in column 3 and ends in column 6 the set 2 will be:
   Set2= {3,4,5,6}.
   From set 1 and set 2, we can see that both symbols overlapped in columns 4, 5, and 6.

The overlapping can be determined when we apply the intersection concept.

After determining the overlapping input images, the available symbols are segmented into two images, as shown in Fig. 5.

However, after applying the above algorithm, each segmented image loses some staff lines. On the other hand, the deep learning model is trained using samples of notes with the staff lines. As a result, adding the missing lines of every segmented image is a crucial step to enable the model to recognize the music notes properly. To add the missing lines, the thickness of the staff line and the white space between every two lines are found. Then, the number of missing staff lines is calculated for each segmented image. Then, two plain white images are created, and then, a specified number of lines equal to the number of missing

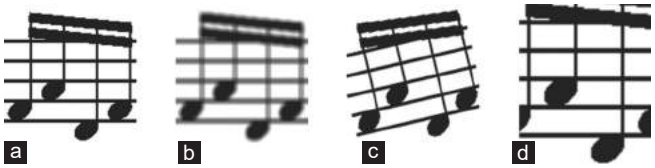

Fig. 4. Original image with its augmented images; (a) original image, (b) blurring image, (c) rotation image, and (d) scaling image.

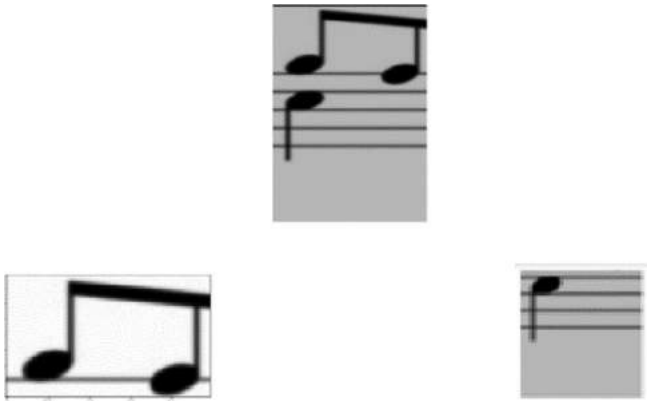

Fig. 5. The input image with its two segmented overlapped notes.

lines will be drawn in each generated image. Finally, each segmented image is concatenated with its corresponding created white image (the white image contains the staff lines) to form an output image containing a music note with five staff lines.

VI. Results and Discussion

A. Evaluation Metric

At present, the commonly used evaluation metric to assess OMR models is Symbol Error Rate (SER) as a substitute for the well-known character/word error rate which is utilized in text recognition tasks, due to the concern in the computational aspect (Baró, Badal and Fornés, 2020). The error rate is used to determine the extent of the difference between the OMR transcribed text and the ground truth text. The SER can be found by (2) equation.

$$SER = (S+D+1)/N \quad (2)$$

where S refers to the substitutions, D the deletions, I the insertions, and N the number of characters in the ground truth.

B. Dataset

To evaluate the proposed methodology, our generated dataset is used which consists of 800 images with its ground_ truth text file. The dataset is randomly divided into two sets: The training set and the unseen set of samples. Three strategies for splitting data are used in this study. Multiple scenarios are trained using data augmentation techniques including blurring, rotation, and scaling.

C. Training seq2srq Models

Diverse models are trained with the original dataset and using data augmentation depending on the learning method used in the feature extractor models: With the transfer learning concept, including VGG pre-trained model, ResNet50 pre-trained model, and Xception pre-trained model, and without the transfer learning concept, using the proposed customized model. The epochs number used in this study is up to 30, and batch sizes are 8,16, and 32.

Table II shows the SER % of a test set using VGG19 as a feature extractor and the best results values are in bold formatting to indicate the minimum SER %. In general, the ability of the model to learn was improved by increasing the batch size whereas applying data augmentation techniques badly affected SER. Likewise, as illustrated in Table III, the achieved SER from training the seq2seq model with Resnet50 has decreased through increasing the batch size, particularly in batch size 32, the best results have been bolded to draw attention to the minimum SER % in this experiment. However, the SER has been increased once data augmentation techniques are applied. Furthermore, the results of using Xception as a feature extractor as depicted in Table IV are sanguinely improved compared with VGG19 and Resnet50 in both batch sizes 16 and 32. Bold formatting has been used to emphasize the experiment's best results values which represent minimum SER %. To test, compare, and evaluate other available pre-trained models with CNN block without transfer learning, we trained the seq2seq model with the proposed CNN model as a feature extractor. The practical results are presented in Table V.

From the presented results, there is a considerable difference between the performance of the feature extractor pre-trained models and the proposed CNN block for feature extraction. The architecture of the feature extractor model plays a vital role in enhancing the performance of the seq2seq model. Based on the achieved SER, the usage of CNN block with very deep layers including VGG19, Resnet50, and Xception has decreased SER. It is also worth mentioning that the utilization of the Xception model to extract the relevant features reduced SER compared with VGG19 and ResNet50. The Xception model relies on both depthwise and pointwise convolution concepts, with its effective architecture, it can accurately and efficiently capture small details in the images.

Moreover, employing a pre-trained learning model is useful to speed up the training process (Fig. 6). Noticeably, Xception requires less training time compared with other pre-trained CNN models (VGG16,19 and ResNet50), that is because of the depthwise convolution and the pointwise convolutions concepts used in Xception. Depthwise convolution helps reduce the computational complexity of the convolutional layer by reducing the number of parameters and computations compared to traditional convolution. Pointwise convolution helps adjust the number of channels and perform feature fusion or dimensionality reduction. Due to the usage of the trained parameters to

TABLE II
Symbol Error Rate (%) in Different Scenarios using the Original dataset and Data Augmentation Employing the VGG19 Model as a Feature Extractor

Batch size	Splitting strategy (%)	Original dataset	Original dataset+blurring	Original dataset+rotation	Original dataset+scaling
8	(90/10)	1.30	24.43	9.04	11.24
	(80/20)	1.1	12.95	13.37	12.98
	(70/30)	0.98	80.32	18.42	56.74
16	(90/10)	**0**	5.25	6.76	1.6
	(80/20)	0.06	1.45	1.19	3.85
	(70/30)	**0.04**	1.28	2.42	1.92
32	(90/10)	**0.03**	1.03	0.81	0.79
	(80/20)	**0.04**	0.35	0.57	0.15
	(70/30)	0.05	0.32	0.51	0.29

 http://dx.doi.org/10.14500/aro.11402

TABLE III
SYMBOL ERROR RATE (%) IN DIFFERENT SCENARIOS USING THE ORIGINAL DATASET AND DATA AUGMENTATION EMPLOYING THE RESNET50 MODEL AS A FEATURE EXTRACTOR

Batch size	Splitting strategy (%)	Original dataset	Original dataset+blurring	Original dataset+rotation	Original dataset+scaling
8	(90/10)	6.04	20.65	16.81	48.67
	(80/20)	6.56	19.49	26.19	16.56
	(70/30)	1.44	24.64	19.69	12.42
16	(90/10)	0.18	6.93	7.23	23.18
	(80/20)	0.17	0.14	0.04	2.24
	(70/30)	0.21	2.99	2.04	3.2
32	(90/10)	**0.03**	2.47	1.76	1.97
	(80/20)	**0**	0.87	0.33	**0.02**
	(70/30)	**0**	0.11	0.11	0.16

TABLE IV
SYMBOL ERROR RATE (%) IN DIFFERENT SCENARIOS USING THE ORIGINAL DATASET AND DATA AUGMENTATION EMPLOYING THE EXCEPTION MODEL AS A FEATURE EXTRACTOR

Batch size	Splitting strategy (%)	Original dataset	Original dataset+blurring	Original dataset+rotation	Original dataset+scaling
8	(90/10)	**0**	1.03	0.81	0.79
	(80/20)	0.71	10.57	0.39	0.14
	(70/30)	**0**	1.21	32.88	1.44
16	(90/10)	**0**	0.35	0.81	0.34
	(80/20)	**0**	0.14	**0.04**	2.24
	(70/30)	**0**	0.05	**0.1**	**0**
32	(90/10)	**0**	**0**	**0.02**	**0**
	(80/20)	**0.04**	**0**	**0.04**	**0**
	(70/30)	**0**	**0.02**	**0**	**0**

TABLE V
SYMBOL ERROR RATE (%) OF THE CUSTOMIZED CNN MODEL

Splitting strategy (%)	Batch size	Original dataset	Original dataset+blurring
(80/20)	16	30.46	55.2
	32	5.22	26.63

TABLE VI
SYMBOL ERROR RATE (%) OF THE OVERLAPPING SET USING THE XCEPTION MODEL AS A FEATURE EXTRACTOR

Splitting strategy (%)	Batch size	Original dataset
(80/20)	32	23.12

TABLE VII
SYMBOL ERROR RATE (%) OF THE OVERLAPPING SET USING THE CUSTOMIZED CNN AS A FEATURE EXTRACTOR

Splitting strategy (%)	Batch size	Original dataset
(80/20)	32	28.34

extract features instead of starting from scratch, training the model with our customized CNN needs more time compared with the usage of pre-trained CNN models to get feature maps.

There might be reasons why using data augmentation for OMR activities leads to producing poor results in comparison to other computer vision tasks. Here are some potential justifications:

1. OMR requires accurate identification of musical symbols and notations; augmentation procedures can alter structural integrity, reducing the model's ability to detect and comprehend notation effectively
2. Musical symbols require precise alignment and regular spatial connections, but random transformations during augmentation can reduce system performance
3. Various musical symbols require different augmentation techniques to preserve distinctive characteristics and requirements effectively.

D. Overlapping Symbols Situation

This study focuses on addressing overlapping musical notes. Therefore, a set of widely available images that contain two overlapping symbols is used. This set consists of 20 images collected from the Internet in different conditions. Then, every image was segmented into two images of individual symbols and performed all necessary steps before being fed to the model to predict its musical meaning. By making a trade-off between all

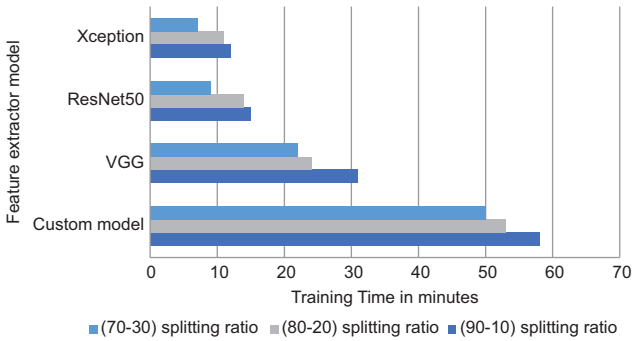

Fig. 6. The training time required for different feature extractor models and three various splitting ratios.

the previous models' architectures, the Xception feature extractor model is used in this experiment. Table VI shows the SER of testing the set of these segmented images. Then, our customized model has been involved in this experiment to earn more results for comparison and evaluation (Table VII). The original dataset was used to train the model.

As expected, the outcome of this experiment is below the desired result compared with testing non-overlapped symbols, because of the possible following reasons:

1. The images were collected from the Internet in different situations, conditions, and various numeric representations such as the thickness of the staff lines or the white space between them
2. Splitting the image which contains two overlapping symbols into two individual images and adding the missing lines might violate the image quality.

VII. Conclusion

In this study, an OMR system has been presented based on a deep learning approach including a CNN block to extract relevant features followed by seq2seq (encoder–decoder) to retrieve the semantic representation of a monophonic music sheet that is rendered on an image. It has been experimentally demonstrated that the suggested model can deal with long-sequence music notes by applying the proposed segmentation algorithm to the (PrIMS) dataset to create a new version of the dataset before being fed to the model. The achieved results indicate, that the usage of the Xception CNN block along with the seq2seq model outperformance other models with different CNN architectures (VGG, ResNet50, the customized CNN). Furthermore, the complexity of music notation has been addressed in this study, and a novel algorithm is proposed to detect and tackle the overlap problem on a set of images collected under different or non-identical conditions. It is worth mentioning that this work has some limitations, it is unable to handle polyphonic music sheets, and the overlapped symbols should be disjoint components and not have any touching pixels.

It has been proposed that the suggested framework might be used to challenges outside OMR that translates a spatial sequential representation to a set of labels, such as converting an auditory signal into a token sequence (an example of such a job would be optical character recognition).

Future work is suggested to create an OMR framework for converting polyphonic notes to musical meaning, addressing overlapping symbols including touching cases between the musical notes, and generating a training dataset for hand-written music symbols.

References

Baró, A., Badal, C., and Fornés, A., 2020. Handwritten Historical Music Recognition by Sequence-to-Sequence with Attention Mechanism. In: *2020 17th International Conference on Frontiers in Handwriting Recognition* (*ICFHR*). IEEE, United States, pp.205-210.

Brownlee, J., 2019. *Deep Learning for Computer Vision: Image Classification, Object Detection, and Face Recognition in Python*. Machine Learning Mastery, Vermont.

Calvo-Zaragoza, J., and Rizo, D., 2018. End-to-end neural optical music recognition of monophonic scores. *Applied Sciences*, 8(4), p.606.

Calvo-Zaragoza, J., Valero-Mas, J.J., and Pertusa, A., 2017. End-to-End Optical Music Recognition using Neural Networks. In: *Proceedings of the 18th International Society for Music Information Retrieval Conference*. ISMIR, Canada, pp.23-27.

Castellanos, F.J., Calvo-Zaragoza, J., and Inesta, J.M., 2020. A *Neural Approach for Full-Page Optical Music Recognition of Mensural Documents*. ISMIR, Canada, pp.558-565.

Jang, M., Seo, S., and Kang, P., 2019. Recurrent neural network-based semantic variational autoencoder for sequence-to-sequence learning. *Information Sciences*, 490, pp.59-73.

Matrenin, P.V., Manusov, V.Z., Khalyasmaa, A.I., Antonenkov, D.V., Eroshenko, S.A., and Butusov, D.N., 2020. Improving accuracy and generalization performance of small-size recurrent neural networks applied to short-term load forecasting. *Mathematics*, 8(12), p.2169.

Michael, J., Labahn, R., Grüning, T., and Zöllner, J., 2019. Evaluating Sequence-to-Sequence Models for Handwritten Text Recognition. In: *2019 International Conference on Document Analysis and Recognition. ICDAR*. IEEE, United States, pp.1286-1293.

Mondal, R., Malakar, S., Barney Smith, E.H., and Sarkar, R., 2022. Handwritten English word recognition using a deep learning based object detection architecture. *Multimedia Tools and Applications*, 81, pp.1-26.

Neubig, G., 2017. Neural Machine Translation and Sequence-to-Sequence Models: A Tutorial. [arXiv Preprint] arXiv:1703.01619.

Pugin, L., 2006. *Optical Music Recognitoin of Early Typographic Prints using Hidden Markov Models*. ISMIR, Canada, pp.53-56.

Pugin, L., Burgoyne, J.A., and Fujinaga, I., 2007. *MAP Adaptation to Improve Optical Music Recognition of Early Music Documents Using Hidden Markov Models*. ISMIR, Canada, pp.513-516.

Rosen, K.H., 2007. *Discrete Mathematics and Its Applications*. The McGraw Hill Companies, United States.

Shatri, E., and Fazekas, G., 2020. Optical Music Recognition: State of the Art and Major Challenges. Computer Science, Engineering. [arXiv preprint] arXiv:2006.07885.

Sutskever, I., Vinyals, O., and Le, Q.V., 2014. Sequence to Sequence Learning with Neural Networks. In: *Advances in Neural Information Processing Systems*. Vol. 27. The MIT Press, United States.

Torras, P., Baró, A., Fornés, A., and Kang, L., 2022. Improving Handwritten Music Recognition through Language Model Integration. In: *4th International Workshop on Reading Music Systems*, p.42.

Van Der Wel, E., and Ullrich, K., 2017. Optical Music Recognition with Convolutional Sequence-to-Sequence Models. [arXiv preprint] arXiv:1707.04877.

Wen, C., and Zhu, L., 2022. A sequence-to-sequence framework based on transformer with masked language model for optical music recognition. *IEEE Access*, 10, pp.118243-118252.

http://dx.doi.org/10.14500/aro.11333

Brain Tumor Segmentation Using Enhancement Convolved and Deconvolved CNN Model

Mohammed Al-Mukhtar[1], Ameer H. Morad[2], Hussein L. Hussein[3] and Mina H. Al-hashimi[4]

[1]Electronic Computer Center, University of Baghdad, Baghdad, Iraq

[2]Department of Software Engineering, Faculty of Engineering, Gilgamesh Ahliya University, Baghdad, Iraq

[3]Department of Computer Science, College of Education for Pure Science - Ibn Al Haitham, University of Baghdad, Baghdad, Iraq

[4]Department of Computer Science and Information System, Al-Mansour University College, Baghdad, Iraq

***Abstract*–The brain assumes the role of the primary organ in the human body, serving as the ultimate controller and regulator. Nevertheless, certain instances may give rise to the development of malignant tumors within the brain. At present, a definitive explanation of the etiology of brain cancer has yet to be established. This study develops a model that can accurately identify the presence of a tumor in a given magnetic resonance imaging (MRI) scan and subsequently determine its size within the brain. The proposed methodology comprises a two-step process, namely, tumor extraction and measurement (segmentation), followed by the application of deep learning techniques for the identification and classification of brain tumors. The detection and measurement of a brain tumor involve a series of steps, namely, preprocessing, skull stripping, and tumor segmentation. The overfitting of BTNet-convolutional neural network (CNN) models occurs after a lot of training time because training the model with a large number of images. Moreover, the tuned CNN model shows a better performance for classification step by achieving an accuracy rate of 98%. The performance metrics imply that the BTNet model can reach the optimal classification accuracy for the brain tumor (BraTS 2020) dataset identification. The model analysis segment has a WT specificity of 0.97, a TC specificity of 0.925914, an ET specificity of 0.967717, and Dice scores of 79.73% for ET, 91.64% for WT, and 87.73% for TC.**

***Index Terms*—Brain tumor, Magnetic resonance imaging, Image enhancement, Image segmentation, Convolutional neural network.**

I. Introduction

According to Gull, Akbar and Khan (2021), an estimated 29,000 individuals in the United States were diagnosed with primary brain tumors in 2015. In 2019, it was anticipated that there were 17,760 fatalities and 23,820 new cases of brain tumors in the United States. Based on the latest cancer data from 2021, there were projected to be a total of 24,530 reported instances of brain tumors in the United States. Among these cases, 13,840 were expected to be diagnosed in men, while 10,690 were anticipated in women (Siegel, et al., 2021). Magnetic resonance imaging (MRI) is a sophisticated medical imaging technique used to provide high-resolution images for the diagnosis and treatment of brain cancers. The commonly used multimodal imaging techniques for brain tumor detection in MRI include T1-weighted, T2-weighted, T1-weighted with contrast enhancement (T1CE), and fluid-attenuated inversion recovery. T1 images are capable of identifying different types of tissues, while T2 MR images provide positive signals in the image to address the presence of edema in the area. In T1CE images, the tumor edges are detected without the use of the high-intensity signal, namely, gadolinium particles, by specialists in the intricate cellular composition of tumor tissue.

Preprocessing methods and machine learning models have achieved great results in enhancing images (Taha, et al., 2021). The methodology used in this study involves using the least significant bits as a means of detecting the presence of concealed encrypted bits inside the dual-tree complex wavelet coefficient framework. Some other ML algorithms, such as the random forest (RF) algorithm, well recognized as a reliable and efficient classifier in the field of brain lesion segmentation, play a crucial role in our framework for segmenting lesions. Furthermore, our approach incorporates dense conditional random fields (CRF) as an optimizer, a commonly used technique for enhancing spatially contiguous segmentations in post-processing (Chen, et al., 2020).

The convolutional neural network (CNN)-based deep learning model demonstrates encouraging outcomes in the detection of cancers using magnetic resonance (MR) images (Ismael, et al., 2020). In the preceding automated methodologies, to optimize the performance of tumor size, position, and shape measurement

ARO-The Scientific Journal of Koya University
Vol. XII, No. 1 (2024), Article ID: ARO.11333. 12 pages
DOI: 10.14500/aro.11333
Received: 07 August 2023; Accepted: 08 March 2024
Regular research paper: Published: 30 March 2024
Corresponding author's email: mohammed.abdul@cc.uobaghdad.edu.iq

techniques, it is imperative to prioritize background subtraction, color visualization of the brain tumor region, fragmentation, size measurements, and classification. This approach will minimize complexity and enhance the segmentation process. According to the dataset that was used in the study (Bakas, S., et al. 2017), it is important to depict that the size, location and form of the tumors might vary, see Fig. 1.

It is noteworthy that tumor size, position, and shape may vary, as shown in Fig. 1. This approach is necessary to optimize segmentation and measurement efficacy. Subsequent to this stage, morphological filtering can be employed to eliminate any extraneous signals that may have arisen due to the segmentation procedure. The utilization of high-precision segmentation techniques has the potential to ascertain the benign or malignant characteristics of a tumor (Pedapati and Tannedi, 2017). The purpose of the paper is to develop a time-saving automated image processing system for appropriately segmenting and categorizing brain tumor and sub-tumor tissue from multimodal MR data. Due to its high soft-tissue contrast compared to other imaging modalities, such as computed tomography imaging (Ghadi and Salman, 2022), MRI is an effective and sensitive imaging modality for the purpose of tumor, lesion, tissue, and disease identification/characterization. The brain tumor segmentation procedure entails distinguishing brain tumor tissues from surrounding normal tissues.

Some researchers have created unique deep learning-based systems with highly enhanced automated brain tumor recognition and delineation by concentrating on brain tumor segmentation. Havaei, et al. (2017) suggested a complicated CNN architecture for brain tumor segmentation from MR images. The goal of this project is to create a deep learning model for automatic segmentation of brain tumors from various MR sequences. Fig. 1 shows some samples of the dataset with normal cases and brain tumor cases with each class related.

II. Literature Review

The identification of brain cancer and the automated categorization of brain tissue through the utilization of MRI scans hold significant value in the realm of investigating and diagnosing human mental health. Segmentation is a critical component of medical imaging operations for MR images. It involves the separation and identification of the constituent

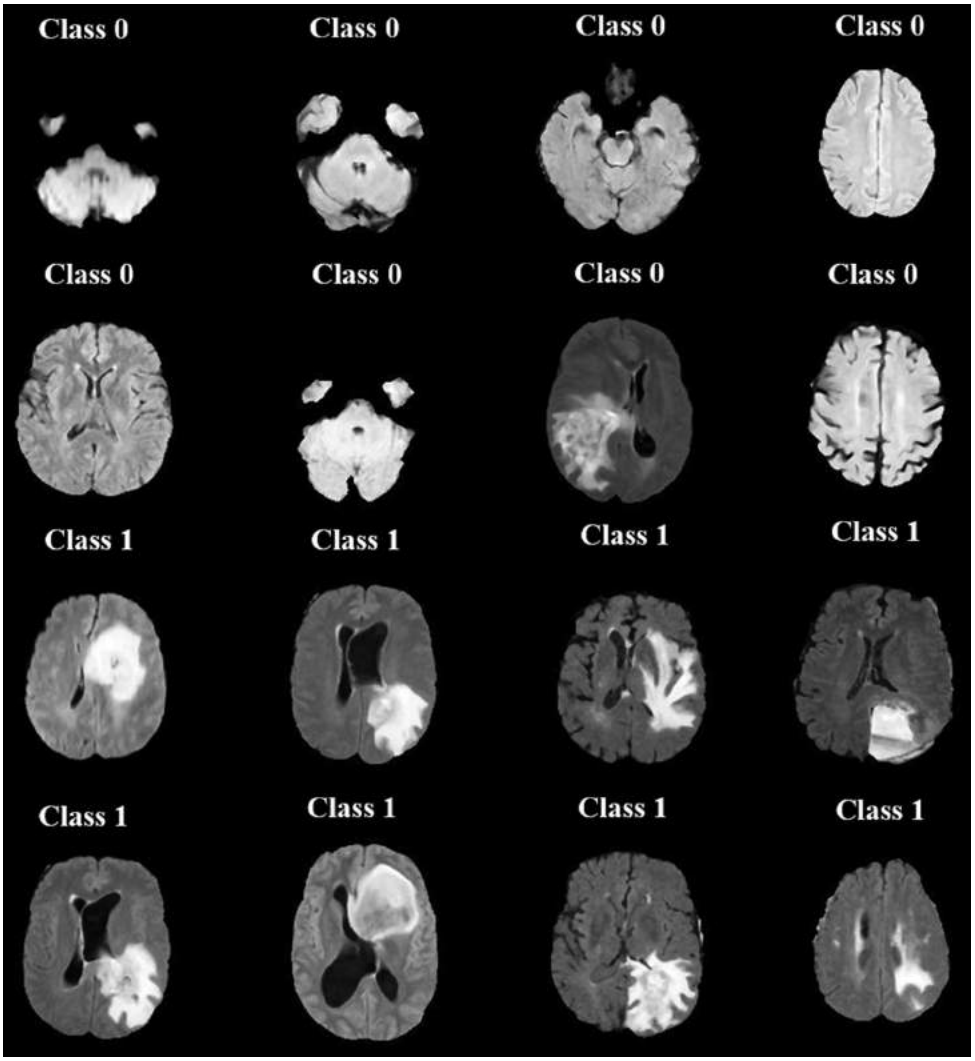

Fig. 1. Samples of brain tumor magnetic resource imaging.

parts of the image, enabling individual processing. The utilization of principal component analysis and discrete wavelet transform can facilitate the identification of the most salient characteristics of an image (El-Dahshan, Hosny and Salem, 2010). The suggested approach is useful for distinguishing between normal and abnormal human brains. MRI is considered to be the foremost diagnostic modality for the detection of brain tumors. The analysis of MR images through medical image processing has garnered significant interest in recent times (Morad and Al-Dabbas, 2020; Rao and Karunakara, 2021). Despite the diligent efforts of researchers studying brain tumors, it remains a formidable task to identify the most effective feature to target for elimination. The task of selecting suitable training and testing samples poses a significant challenge (Ortiz, et al., 2013).

The study employed a Gaussian filter to mitigate noise, followed by the acquisition of embedding, cyclic, contrast, and block appearance features for segmentation processing. The cross-validation method was utilized for classification to extract the features of the brain images. The utilization of a hybrid technique in conjunction with segmented supporting data renders this approach highly effective (Chen, et al., 2017). The utilization of particle swarm optimization and the rejection of outliers in conjunction with a level set were suggested (Huang, et al., 2020). The process of partitioning brain tumors in an MR database is frequently accomplished through the utilization of the fuzzy C-means (FCM) algorithm.

Another effective technique is to segment the lesion, and the well-known U-Net network design has met or exceeded the state-of-the-art performance standards for a variety of 2D and 3D semantic segmentation tasks as well as for a wide range of imaging modalities. When it comes to identifying patients and tracking the development of malignant entities over time, semantic segmentation of brain tumors using different MRI imaging modalities is an essential medical image processing field. The Swin UNET architecture is proposed as an innovative approach for the semantic segmentation of brain tumors, specifically using multimodal MRI data (Hatamizadeh, et al., 2021).

Wang (2021) introduced the use of the transformer model in conjunction with a 3D CNN for the purpose of MRI brain tumor segmentation. We offer a unique network architecture called TransBTS, which is built around an encoder-decoder structure. The decoder utilizes the characteristics included by the transformer model and employs a progressive upsampling technique to provide predictions for the precise segmentation map. Zhang, et al. (2017) proposed that multiple well-known fully CNNs (FCNNs) have been used for the purpose of brain tumor segmentation. These studies include conducting comparisons and modifying network designs in order to enhance performance, as assessed by metrics such as accuracy, recall, mean of intersection of union, and Dice score coefficient. The original convolutional layers of the FCNN and U-Net architectures are substituted with residual structures, along with the inclusion of batch normalization layers.

Chen (2020) proposed a two-stage automated framework for brain lesion segmentation. The system incorporates a cascaded RF algorithm and a dense CRF model, resulting in a combined approach referred to as RFDCR. The model was assessed on two segmentation tasks, namely, the segmentation of brain tumors and ischemic strokes. A two-stage supervised learning system is proposed for the purpose of automating brain lesion segmentation. In the first step, the training of the RF classifier involves the use of intensity-based statistical features, template-based asymmetric features, and GMM-based tissue probability maps (Cao, et al., 2022). This study introduces a context attention module, namely, the multiscale contextual attention, as a solution to address the issue of context information loss during feature extraction. The proposed module aims to effectively collect and filter high-level features by including spatial context information. The incorporation of the channel attention mechanism into the decoding structure facilitates the integration of high-level characteristics with low-level features.

A. Problem Statement

In Europe, approximately 60,000 individuals currently have a brain tumor, and an annual incidence of 18,000 new cases has been reported. As per the NHS (Cheng, 2017), there has been a surge in the occurrence of brain tumors in the United Kingdom, posing a significant cause for apprehension. Approximately 82% of all brain tumors, including normal brain tumors, are attributed to aggressive gliomas (Pedapati and Tannedi, 2017). The present study underscores the necessity of a meticulously planned therapeutic approach for this particular form of malignancy. Although brain tumors are prevalent globally, primary brain tumors are infrequent. The incidence of extracranial metastases originating from primary tumors in the brain and central nervous system is relatively low. Conversely, a significant proportion of brain tumors are classified as metastatic tumors, which have an extracranial origin and disseminate to the brain through the circulatory or lymphatic systems. A tumor's therapeutic response is influenced by various factors, such as its size, cellular composition, and stage. Tumor segmentation holds significant importance in the context of surgical and other therapeutic planning. Medical imaging techniques can be employed to detect and assess neoplasms. Selection of the optimal treatment modality for diverse clinical conditions aims to facilitate surgical intervention and coordinate radiation therapy (Rao and Karunakara, 2021).

B. Preprocessing Techniques

Preprocessing is a crucial step in enhancing the quality of MR images of a specific region of interest (ROI), such as brain tumors, to facilitate comprehensive analysis. In addition, Hamad, Mohammed and Simonov (2019), preprocessing produces the effect of enhancing some MRI characteristics. As demonstrated by Huang, et al. (2020), the application of preprocessing techniques has been observed to enhance certain features of MRI. In spite of the fact that, this technique makes use of a high-frequency emitter to improve the look of edges and finer details.

The grayscale image's intensity can be denoted by a set of K values ranging from 1 to K. The variable xi (i) represents the proportion of dots that exhibit a particular shade of gray, denoted by p (Shukla, 2016).

The summation of all feasible values is represented by the mathematical expression $X=x_1+x_2+\ldots.+x_L$. The frequency distribution of events is commonly used to interpret the distribution of a grayscale image. $(i)=x_i/X,\ x_i\geq 0,\quad \Sigma x_i=1$.

Every individual pixel within an image comprises two distinct components, namely, a foreground component (denoted as C_0) and a background component (denoted as C_1, which possesses a minimum value of t). The pixels that fall within the range of levels [1, 2,…,k] are denoted by the symbol C_0, while those that belong to the range of levels $[t + 1,\ldots,k]$ are represented by the symbol C_1 (Shukla, 2016). The formulas for defining the class occurrence probability W_{c0} and the median occurrence probability are as follows in Eq. (1):

$$W_{c0} = \sum_{i=1}^{t} p(i) \tag{1}$$

$$\mu_{c0} = \sum_{i=1}^{t} \frac{i.p(i)}{w_{c0}} = \frac{1}{w_{c0}} \tag{2}$$

The formula for calculating the expected value of a random variable is expressed as in Eq. (3):

$$\mu_T = \sum_{i=1}^{L} i.p(i) \tag{3}$$

Where: $\mu_T = w_{c0}\mu_{c0} + w_{c1}\mu_{c1}$ (4)

Subsequently, by utilizing this formula in Eq. (2) (3), we can determine the value of μ_T as the weighted sum of μ_{c0} and μ_{c1}, where w_0 and w_1 represent the respective weights. The variables and in Eq. (4) represent the probabilities of the foreground and background regions, respectively. Furthermore, it should be noted that μ_{c0} and μ_{c1} correspond to the mean gray value of the image foreground and background, respectively. The image's complete gray level is denoted as μ_T (Wala'a, and Rana, 2021).

C. Classification and Segmentation of Brain Tumors

Various imaging modalities, including computed tomography, MRI, and X-ray, have been employed to examine the brain's anatomy and identify malignant tumors (Zebari, et al., 2020; Zhang, 2010). The utilization of MRI is increasingly prevalent in the identification of brain cancer, as evidenced by scholarly literature (Wang, Cheng and Basu, 2009). The technique for segmenting brain tumors in computer vision involves partitioning an image into distinct components by categorizing the image's adjacent pixels according to specific predetermined pixel characteristics or properties (Faris, et al., 2019).

Segmentation is a critical operation in the domain of image processing, particularly in the context of extracting information from intricate medical scans. These data have the potential to aid in the identification and management of medical conditions in individuals. The fundamental aim of image segmentation is to partition a digital image into discrete regions that are mutually exclusive (Joseph, Singh and Manikandan, 2014).

There exist notable dissimilarities in the attributes of tumors and malignancies. Irrespective of its composition, a tumor represents an anomalous aggregation of tissues. Tumors can be categorized as either primary or secondary based on their specific type. The nervous system is a commonly observed source of nourishment for the gradual proliferation of primary tumors. Gliomas are a type of brain tumor characterized by the presence of glass cells as their predominant structural component. These tumors are frequently observed within the central nervous system (Al-Dabbas, et al., 2019; Al Mahmud, et al., 2020; Mohammed, et al., 2021).

The advancement of a cerebral neoplasm (cancer) mandates a meticulous evaluation of the individual's clinical manifestations. MRI is the preferred modality for detecting brain tumors. The task of exposing a tumor without causing harm to surrounding healthy tissue is a highly challenging endeavor.

III. Methodology

The present investigation entails the utilization of automated techniques for brain tumor segmentation, measurements, and classification, which are known to be time-intensive. Typically, MRI scans are utilized to examine the brain's anatomy.

This study aims to investigate feature representations that can improve the precision of brain tumor segmentation and size measurements. This will be achieved by combining handmade features, which account for local dependencies, with machine-learned features that provide global information.

This study's objective is to explore the optimal combination of features extracted from multimodal MR scans, with the aim of maximizing the informative content derived from particular MR modalities.

The objective is to devise an automated methodology for producing a tumor segment that is consistent with the delineation of experts across all grades of glioma, utilizing a single, commonly employed MRI technique. The proposed methodology involves using CNN for enhancement purposes, as shown in Fig. 2, and using machine learning techniques for classification subsequent to the extraction of features from a segmented tumor and its subsequent categorization, as shown in Fig. 3. The CNN-MRI architecture was developed with consideration of the aforementioned requirements. It consists of three parallel layers, each containing 16, 64, and 64 filters, respectively. The filters in each layer are of varying sizes, specifically 3 × 3, 5 × 5, and 9 × 9.

Subsequently, the images that have undergone coevolution are observed. The data underwent batch normalization and rectified linear unit activations, subsequently undergoing two distinct types of pooling operations, namely, average pooling and maximum pooling. The justification for utilizing varying filter dimensions is to discern regional characteristics through the implementation of 3-by-3 filters and relatively

http://dx.doi.org/10.14500/aro.11333

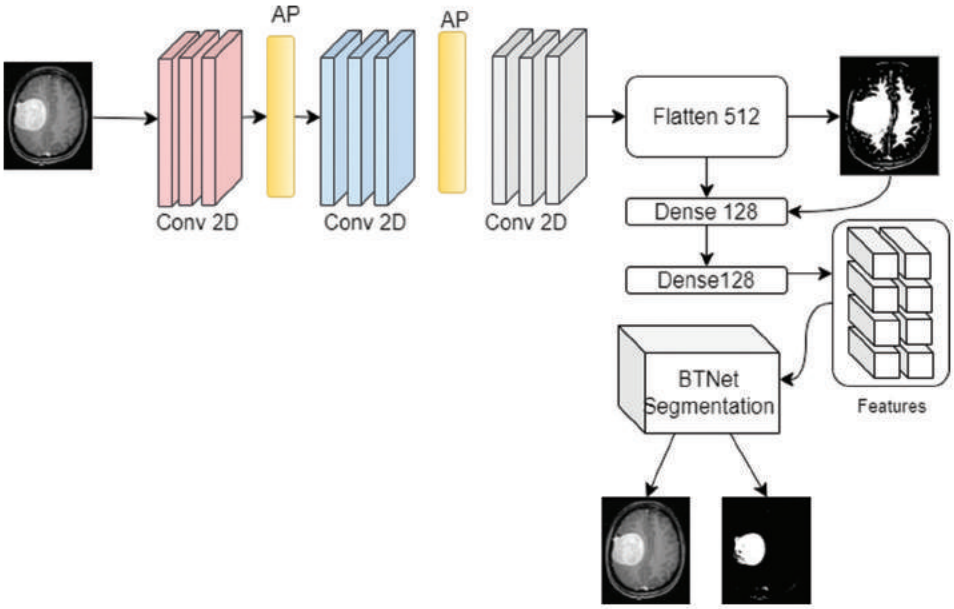

Fig. 2. Enhanced brain tumor convolutional neural network model.

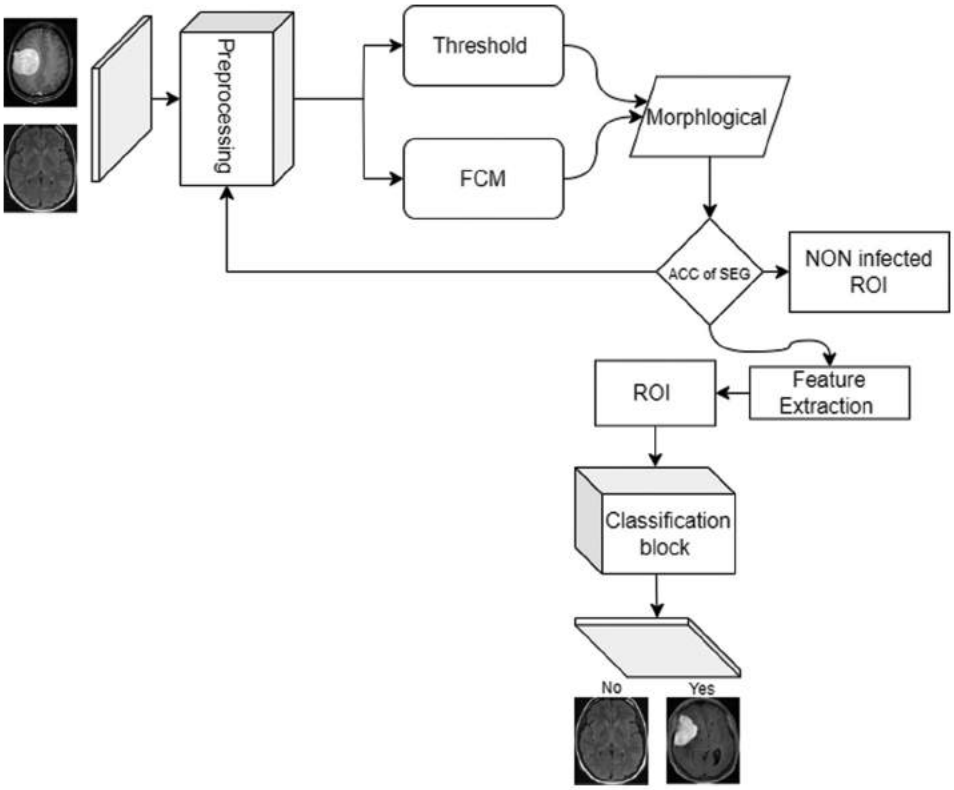

Fig. 3. Brain tumor classification model in magnetic resonance imaging.

broader features through 9-by-9 filters. The 5-by-5 filter size is employed to detect any features that may have been overlooked by the other two filters, as shown in Fig. 3.

Our study explores methods for classifying and segmenting MR images using an iterative approach and a methodology based on thresholds. The process of selecting an optimal starting contour for the purpose of FCM and thresholding is challenging due to the presence of gray-level variations in the pathological area of images, such as brain tumors. The process of delineating and characterizing the boundaries of regions of interest, such as the brain or pathological areas within it, as depicted in MR images, plays a crucial role in aiding medical practitioners in arriving at a diagnosis, such as the presence of gliomas or meningiomas. Segmentation enables precise delineation of the dimensions (contour) of said regions (neoplasms and healthy brain tissue).

A. Image Classification

The task of categorizing images was executed by utilizing manually designed features and advanced computational methods such as support vector machines or decision trees. CNNs have emerged as the predominant technique for image classification due to the progress made in deep learning and the accessibility of vast labeled image datasets (Abdulkareem, et al., 2019). The CNN training procedure entails inputting a vast labeled image dataset into the network, which then adapts its internal parameters (weights and biases) to minimize the disparity between its predicted class labels and the actual ground truth labels. After undergoing training, the neural network can subsequently be employed to categorize novel and unobserved images by conducting forward-propagation through the network and acquiring the probabilities or predictions for each class.

The block diagram in Fig. 3 illustrates a technique for enhancing the precision of diagnostic analysis of MR images, which has the following steps:

1. Preprocessing has been shown to enhance images' resolution.
2. Tumor segmentation is a technique utilized to quantify a tumor's size by demarcating the regions that are affected by the tumor from those that are not.
3. Morphological operations are utilized to eliminate undesirable regions from binary images and to smooth the boundaries of bulk objects.
4. The accuracy of tumor categorization can be improved by utilizing feature extraction techniques.
5. The process of classification involves categorizing segmented tumors into either malignant or non-cancerous groups.

In numerous cases, the region of the image that portrays the neoplasm exhibits greater visual prominence than the adjacent healthy tissue. The approach and code utilized in this particular scenario are based on the fundamental principles of an algorithm that has been developed to detect malignancies. At this juncture, the pertinent section of the document can be addressed as necessary during the data processing stage.

B. Threshold-based Segmentation and FCM

Pattern recognition was developed due to the importance of picture segmentation and its crucial role in object extraction within the field of image processing. The process involves partitioning the input image into multiple segments, thereby simplifying the identification and extraction of the desired region by locating the optimal matching data. A segmentation technique utilizing a localized threshold is employed to partition images containing multiple regions that correspond to distinct objects.

Pixels with a value of one denote the ROI, while pixels with a value of zero represent the background of the image. The present research utilizes a segmentation model based on thresholds, enabling the exploration of input images at different thresholds and maximum values to enhance the information obtained (Fig. 4a).

The FCM algorithm is widely acknowledged as a highly efficient technique for data clustering (Fig. 4b). The unsupervised technique known as FCM has the potential to perform various tasks, including but not limited to factor identification, grouping, and segmentation. This technology has potential applications in various fields such as horticulture construction, astronomy, biochemistry, image analysis, and medical evaluation. FCM employs multiple data regions to address the issue of partial volume impact. The method described is an iterative approach that solely analyzes the luminosity of the segmented image. The method involves

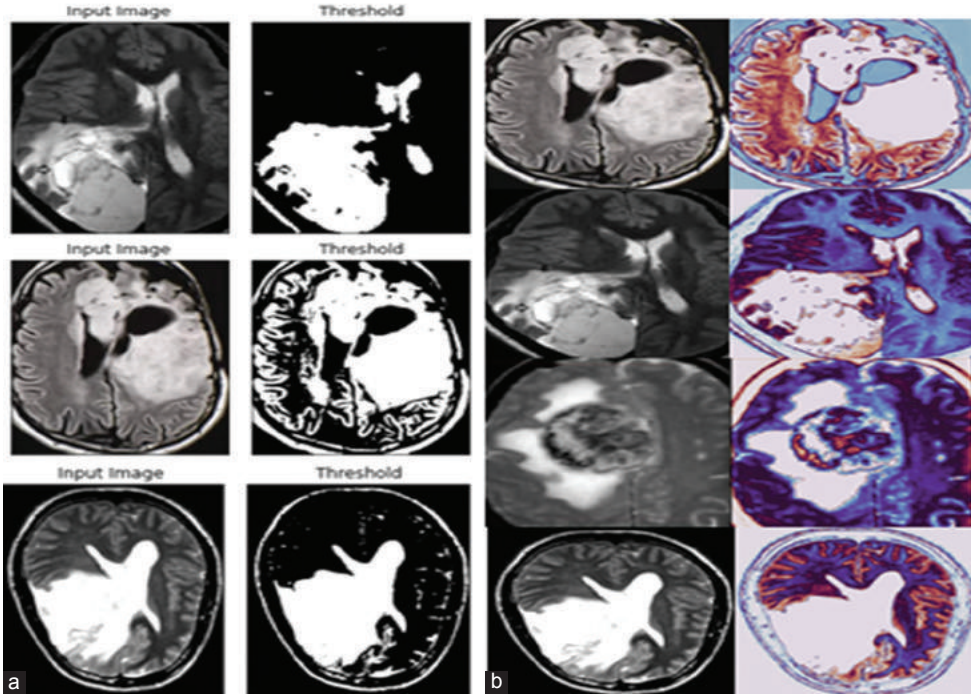

Fig. 4. Preprocessing techniques to enhance feature extraction: (a) Threshold and (b) fuzzy C-means segmentation.

http://dx.doi.org/10.14500/aro.11333

conducting an incremental search to identify a sequence of imprecise clusters and their corresponding cluster centers, with the aim of achieving the most precise clustering of the given data structure.

Tumor segmentation is a technique utilized to quantify the size of a tumor. Morphological operations are utilized to eliminate undesirable regions in binary images and refine the boundaries of bulk objects. The accuracy of tumor categorization can be enhanced through the implementation of feature extraction techniques.

The process of classification involves categorizing segmented tumors into either malignant or non-cancerous groups. The developed approach is expected to facilitate the cancer diagnosis process and enable the system to be trained with a reduced quantity of data. On the conclusion of the validation process, the gathered data will be incorporated into a comprehensive report detailing the patient's health status.

C. Brain Tumor Segmentation Method

Image segmentation is frequently employed to detect boundaries and objects, such as curves and lines. The initial stage in identifying a particular attribute in medical images involves the segmentation process. For instance, brain tumors can be detected by utilizing MR images or other medical imaging techniques. This suggests that the prompt initiation of therapy is crucial in identifying the optimal treatment approach. The objective of utilizing the aforementioned illustrations is to aid radiologists in prioritizing patients with gliomas or meningiomas for diagnostic testing and therapeutic interventions, contingent on their distinct etiology. The convolution operation is a fundamental process employed in CNNs to extract local features from an input image. The process entails the utilization of a diminutive matrix, commonly referred to as a kernel or filter, which is moved across the image. During this movement, element-wise multiplications are carried out between the kernel and the corresponding pixels of the image.

The summation of the products yields a solitary numerical output that signifies a localized feature or activation. Through the implementation of various filters, a CNN can acquire distinct characteristics at diverse spatial positions within an image. Fig. 5 illustrates the process of BTNet based on a convolved algorithm. The process of upsampling or decoding the feature maps derived from the convolutional layers of a CNN is commonly referred to as "deconvolution," as per the prevailing terminology. The BTNet model is a crucial process in the realm of medical imaging. The model creates four blocks of CONV as a convolution phase and four blocks as a deconvolution phase. Between the convolution and deconvolution phases, four FC-layers are used. Moreover, the utilization of certain architectures, such as convolutional autoencoders, variational autoencoders, and generative adversarial networks, involves the aforementioned technique. Deconvolution is a technique employed to reconstruct the initial image or produce novel images by utilizing the acquired features.

It is noteworthy that the usage of the term "deconvolution" may be somewhat deceptive. Within the realm of CNNs, it is important to note that deconvolution does not constitute a genuine mathematical inverse operation of convolution. The term in question pertains to transposed convolution or fractionally strided convolution, a technique employed to increase the resolution of feature maps by means of zero insertion or interpolation between the preexisting feature values. This enables the network to enhance the spatial resolution of the feature maps. Various techniques of image segmentation, which involves the extraction of an ROI from a larger image, have been employed to isolate specific organs and tissues for diagnostic testing. The utilization of this methodology encompasses a diverse range of fields, including but not limited to the identification of masses in mammographic images, the alignment of photographic data, the examination of cardiac imaging, and the partitioning of cardiac structures.

IV. Results

In this experiment, an MRI-scan grayscale database was employed, with each image having a size of 240*240 pixels. Preprocessing is critical in image analysis activities such as tumor identification in medical imaging. It emphasizes many major goals of image preprocessing. Fig. 6a illustrates the input image with three different preprocessing phases. We used a threshold technique after that to apply *contrast limited adaptive histogram equalization* CLAHE technology to enhance picture detail, which is important in medical imaging for improved visibility of things such as malignancies. By increasing local contrast, small details that may have been concealed by shifting lighting or noise become more visible, assisting in the accurate diagnosis of abnormalities such as tumors. However, the threshold value is determined locally for each section of the image based on the local attributes of the image. In image processing applications such as segmentation, object recognition, and feature extraction,

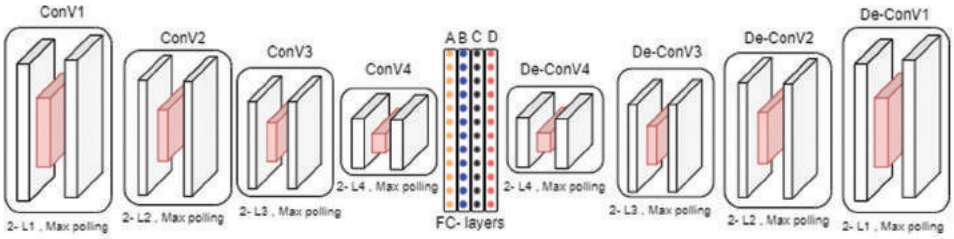

Fig. 5. BTNet convolved and deconvolved convolutional neural network model.

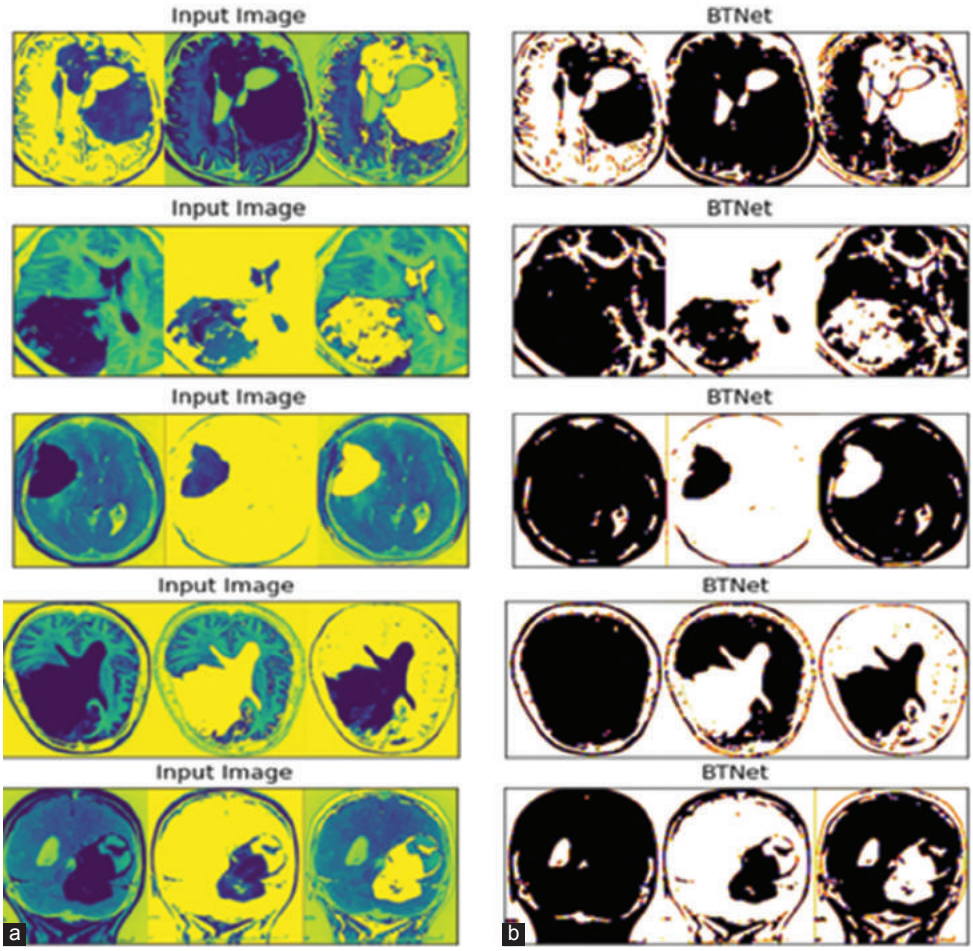

Fig. 6. (a) Input image thresholding and CLAHE and (b) brain tumor image classification phase.

thresholding is an effective strategy. It is especially useful when there is a clear divide between foreground and background intensities in the image.

Fig. 6-b shows the results of our BTNet for these three preprocessing input images in the first phase of the training model that is used to classify brain tumor lesions. The image undergoes grayscale conversion while it is being read. Next, the model retains the binary image for further training. Additionally, determine the aggregate quantity of white pixels inside the binary spectrum, and thereafter divide this figure by the overall pixel count in the image. While, CLAHE was used for the purpose of enhancing low-contrast medical photographs. Using the CLAHE approach, an input original image is segmented into non-overlapping contextual sections that are referred to as sub-images, tiles, or blocks.

The segmentation phase results are shown in Fig. 7, which depicts BTNet's segmentation of the ROI lesion. The receiver operating characteristic (ROC) curve shown in Fig. 8 is a visual depiction that illustrates the effectiveness of a binary classification model. The graph illustrates the relationship between the true positive rate and the false-positive rate across different classification thresholds. The utilization of the area under the ROC curve (AUC-ROC) is frequently employed as a metric to evaluate a model's predictive capability, where a greater AUC signifies superior performance. BTNet's ROC achieves accuracy of 0.98, as compared to the ROCs of the ResUNet model and ROC UNet++, which have both achieved accuracy of 0.97.

TABLE I
Comparison of the Proposed Framework with State-of-the-Art Approaches for Brain Tumor Segmentation.

Author	Technique	Dataset	Metrics
Wu, et al. (2021)	V-Net dropout 0.1	NTUH dataset	Sensitivity 0.66
Hu, et al. (2019)	MCCANN1 MCCANN2	BRATS 2013	Sensitivity 0.91 Sensitivity 0.89
Tustison, et al. (2015)	supervised brain tumor segmentation	BraTS 2013	Sensitivity 0.89 Dice Score 0.87
Zhao, et al. (2018)	FCNNs and CRFs	BraTS 2013	Sensitivity 0.83 Dice Score 0.87
Siar and Teshnehlab (2019)	Deep neural networks CNN+DT	BraTS 2013	Accuracy 0.9424
Havaei, et al. (2019)	LocalCascadeCNN	BraTS 2013	Sensitivity 0.84
Kamnitsas, et al. (2017)	DeepMedic	BraTS 2015	Sensitivity 0.88
Sharif, et al. (2020)	DRLBP	BraTS 2018	Accuracy 0.92
Gull, Akbar and Khan (2021)	FCNN and CRFs	BraTS 2020	Accuracy 0.980
Proposed Method	BTNet	BraTS 2020	Accuracy 0.9823 Sensitivity WT0.987 TC 0.986, ET 0.987

http://dx.doi.org/10.14500/aro.11333

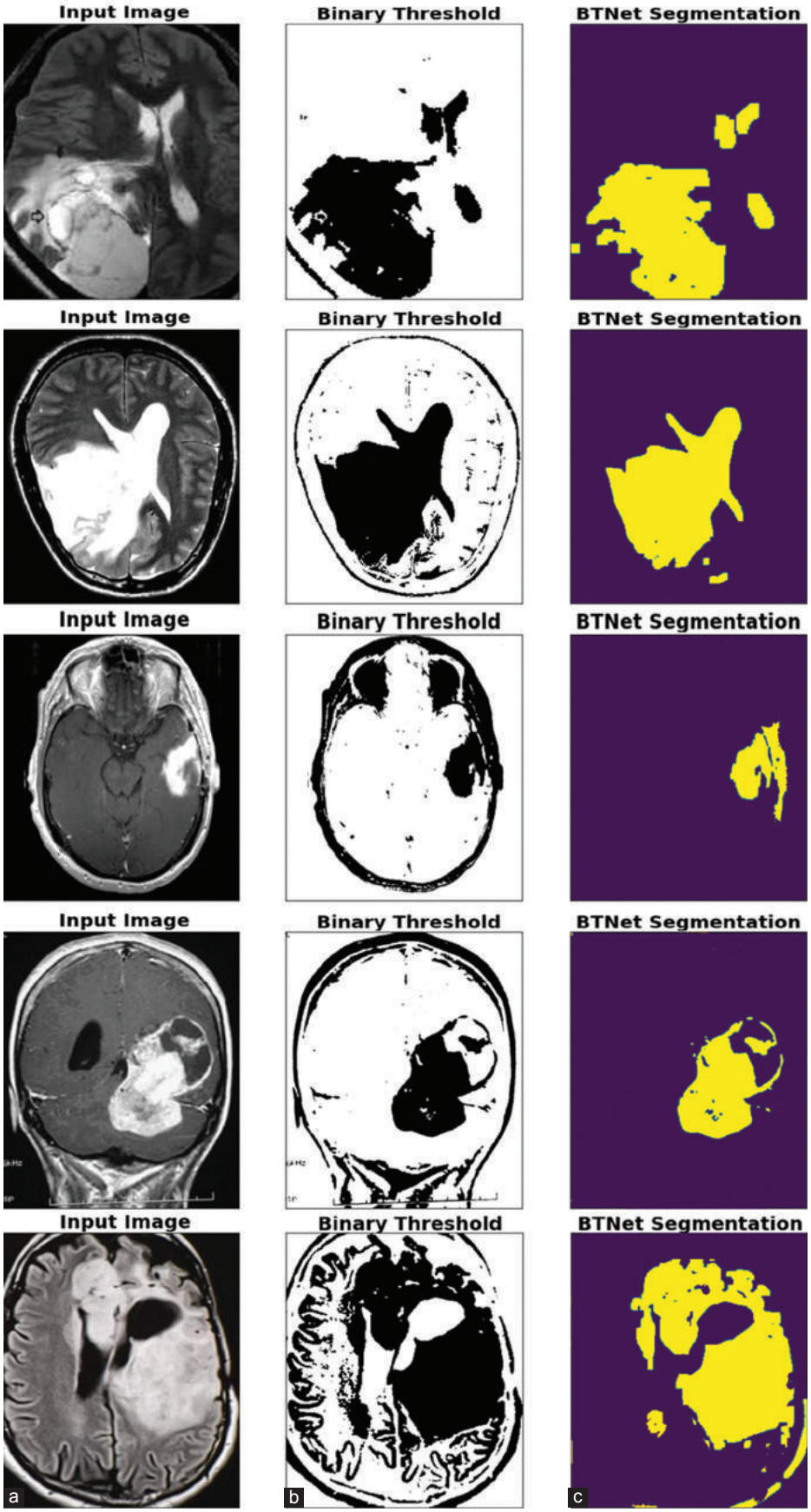

Fig. 7. (a) Input image; (b) binary threshold; and (c) ROI segmentation for brain tumor lesion.

To evaluate a model's efficacy, it is customary to calculate accuracy individually for both the training set and the test set. The training set is utilized to train the model, whereas the test set is employed to assess its performance on data that have not been previously encountered. The act of comparing the accuracy achieved on the training set and the test set offers valuable insights regarding the model's ability to effectively generalize its predictions to novel, previously unseen data. Fig. 9 illustrates the accuracy for the training and test phases of the UNet++ model, while (B) shows the training and test accuracy for the BTNet model.

Table I shows the results of other comparative methods that may discover that the axial view segmentation results are optimal in the coarse segmentation stage. Furthermore, of all the phases involved in the process of identifying malignancies, segmentation is the most important and advantageous.

Table II presents the results of an evaluation model that measures the modified CNN's efficiency in identifying tumors from the BraTS 2020 dataset. The best accurate results for 30 epochs, while the results achieved for Dice Score, Sensitivity, and Specificity. Fig. 10 depicts the assessment model employs for WT, TC, and ET to determine the efficacy of the modified CNN.

The Dice Score results for the proposed model are compared with existing techniques and shown in Table 3. which shows the ET score is 79.73, the WT score is 91.64, and the TC score is 87.73. Total number of images is 2470 MR images 70% for train and 30% for test as the divided datasets. For training phase, the model utilizes 1680 for training and feed 790 image for test phase. The initial learning rate is set at 0.001 at the minimum batch size of 30. The learning method used is Adam, and the optimizer used is Momentum. Accordingly, the use of a momentum optimizer leads to improved accuracy in achieving more precise results. Moreover, the value of the focal loss function is 10. However, the maximum epochs are 30 with number of

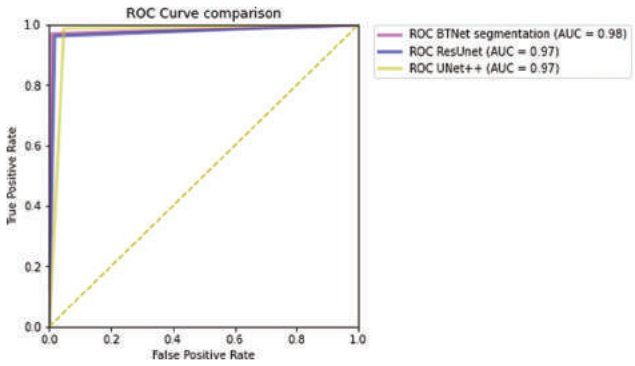

Fig. 8. Receiver operating characteristic curve comparative results.

TABLE II
THE RESULTS FOR BRATS 2020 DATASET FROM ALL THREE MRI MODALITIES ARE THE BASELINE RESULTS

Epoch No.	WT dice score	WT sensitivity	WT specificity
5	0.883095	0.784932	0.78306
10	0.838448	0.83322	0.844257
15	0.935524	0.92049	0.973394
20	0.970243	0.976846	0.963729
30	0.975987	0.9879	0.945358
Epoch No.	TC dice score	TC sensitivity	TC specificity
5	0.906776	0.89741	0.679755
10	0.769711	0.84817	0.704538
15	0.850613	0.885764	0.85922
20	0.967822	0.891602	0.945632
30	0.97548	0.986997	0.925914
Epoch No.	ET dice score	ET sensitivity	ET specificity
5	0.841533	0.813294	0.871802
10	0.547767	0.754954	0.429811
15	0.803296	0.918384	0.713841
20	0.83659	0.952891	0.75439
30	0.977399	0.987276	0.967717

TABLE III
COMPARATIVE ANALYSIS OF THE AVERAGE DICE SCORES OF OUR PROPOSED FRAMEWORK ON THE BRATS 2020 TRAINING DATASETS AND ALTERNATIVE APPROACHES

Study	Method	Dice score
Milletari, Navab and Ahmadi (2016)	Basic V-Net	ET 61.79 WT 84.63 TC 75.26
Wang, et al. (2021)	Residual 3D U-Net	ET 71.63 WT 82.46 TC 76.47
Wang, et al. (2021)	TransBTS	ET 78.73 WT 90.09 TC 81.73
Yang, et al. (2023)	ODE model	ET 0.775 TC 0.845 WT 0.773
Proposed Method	BTNet	ET 79.73 WT 91.64 TC 87.73

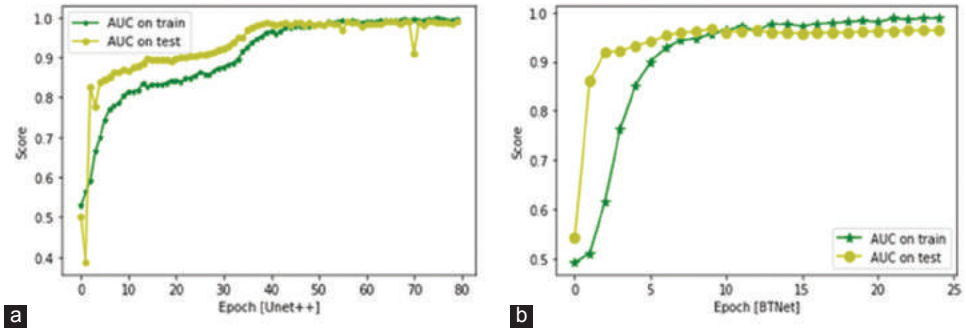

Fig. 9. Training and test accuracy for (a) UNet++ and (b) BTNet segmentation model.

http://dx.doi.org/10.14500/aro.11333

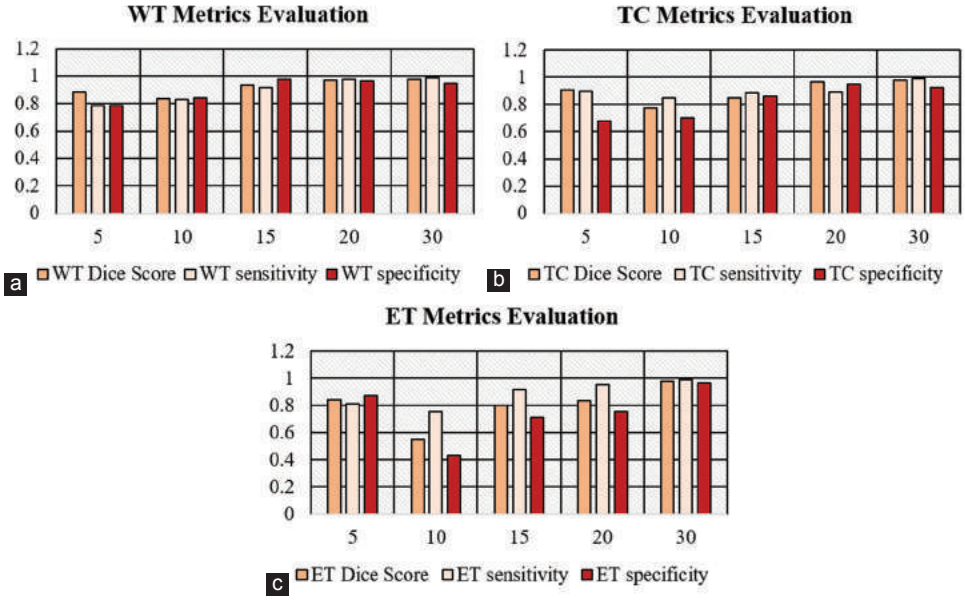

Fig. 10. (a-c) Metrics evaluation for three phases of BraTS 2020 dataset.

iterations 10,000. The presented approach obtains an overall classification accuracy of 98.23% for the BraTS 2020 dataset.

V. Conclusion

The domain of MRI-based segmentation and prediction of brain tumors has undergone significant advancements recently, primarily attributed to the utilization of machine learning algorithms. Notwithstanding this fact, MRI continues to be a complex topic that warrants further investigation. Our model combined classification and segmentation networks together for give the best accurate detection of the lesions. The central objective of this paper pertains to the utilization of deep learning techniques for the purpose of segmenting and classifying malignancies, specifically gliomas and meningiomas. The preprocessing technique used in this study shows the powerful effect to increase the accuracy of the training model. Our enhanced brain tumor CNN framework is adaptable and capable of detecting multiple types of cancer would be highly advantageous for medical professionals. BTNet used a CNN for segmentation, using both convolutional and deconvolutional layers. Improving the quality of this work may be achieved using ensemble classification methods, such as deploying a CNN with different layer configurations or a deep CNN. Future work, we want to assess the robustness of our Custom YOLO tool for use in various MRI images analysis applications. Furthermore, our goal is to enhance the model's accuracy by increasing training samples and optimizing hyper-parameters.

References

Abdulkareem, M., Islam, M.S., Aljoubory, A.D., and Nuoya, Z., 2019. Deep Fully Convolutional Networks for Mitosis Detection. In: *Proceedings of the 2019 4th International Conference on Robotics, Control and Automation*, pp.84-89.

Al Mahmud, M.A., Karim, A.Z., Miah, M.S., Kim, Y., Kim, J., and Bashar, S.S., 2020. Biomedical image processing: Spine tumor detection from MRI image using MATLAB. *The Journal of Contents Computing*, 2(2), pp.225-235.

Al-Dabbas, H.M., and Morad, A.H., 2019. Medical image enhancement to extract brain tumors from CT and MRI images. *Iraqi Journal of Science*, 60(8), pp.1820-1829.

Cao, T., Wang, G., Ren, L., Li, Y., and Wang, H., 2022. Brain tumor magnetic resonance image segmentation by a multiscale contextual attention module combined with a deep residual UNet (MCA-ResUNet). *Physics in Medicine and Biology*, 67(9), p.095007.

Chen, G., Li, Q., Shi, F., Rekik, I., and Pan, Z., 2020. RFDCR: Automated brain lesion segmentation using cascaded random forests with dense conditional random fields. *NeuroImage*, 211, p.116620.

Chen, M., Yan, Q., and Qin, M., 2017. A segmentation of brain MRI images utilizing intensity and contextual information by Markov random field. *Computer Assisted Surgery*, 22(Suppl 1), pp.200-211.

Cheng, J., 2017. Brain tumor dataset. In: *Dataset*. Figshare, London.

El-Dahshan, E.S.A., Hosny, T., and Salem, A.B.M., 2010. Hybrid intelligent techniques for MRI brain images classification. *Digital Signal Processing*, 20(2), pp.433-441.

Faris, M., Javid, T., Fatima, K., Azhar, M., and Kamran, R., 2019. Detection of Tumor Region in MR Image through Fusion of Dam Construction and K-mean Clustering Algorithms. In: *2019 2nd International Conference on Computing, Mathematics and Engineering Technologies (ICOMET)*. IEEE, Piscataway, pp.1-16.

Ghadi, N.M., and Salman, N.H., 2022. Deep learning-based segmentation and classification techniques for brain tumor MRI: A review. *Journal of Engineering*, 28(12), pp.93-112.

Gull, S., Akbar, S., and Khan, H.U., 2021. Automated detection of brain tumor through magnetic resonance images using convolutional neural network. *BioMed Research International*, 2021, p.3365043.

Hamad, Y., Mohammed, O.K.J., and Simonov, K., 2019. Evaluating of Tissue Germination and Growth Rate of ROI on Implants of Electron Scanning Microscopy Images. In: *Proceedings of the 9th International Conference on Information Systems and Technologies*, pp.1-7.

Hatamizadeh, A., Nath, V., Tang, Y., Yang, D., Roth, H.R., and Xu, D., 2021. Swin Unetr: Swin Transformers for Semantic Segmentation of Brain Tumors in Mri

Images. In: *International MICCAI Brainlesion Workshop*. Springer International Publishing, Cham, pp.272-284.

Havaei, M., Davy, A., Warde-Farley, D., Biard, A., Courville, A., Bengio, Y., Pal, C., Jodoin, P.M., and Larochelle, H., 2017. Brain tumor segmentation with deep neural networks. *Medical Image Analysis*, 35, pp.18-31.

Hu, K., Gan, Q., Zhang, Y., Deng, S., Xiao, F., Huang, W., Cao, C., and Gao, X., 2019. Brain tumor segmentation using multi-cascaded convolutional neural networks and conditional random field. *IEEE Access*, 7, pp.92615-92629.

Huang, Z., Xu, H., Su, S., Wang, T., Luo, Y., Zhao, X., Liu, Y., Song, G., and Zhao, Y., 2020. A computer-aided diagnosis system for brain magnetic resonance imaging images using a novel differential feature neural network. *Computers in Biology and Medicine*, 121, p.103818.

Ismael, S.A.A., Mohammed, A., and Hefny, H., 2020. An enhanced deep learning approach for brain cancer MRI images classification using residual networks. *Artificial Intelligence in Medicine*, 102, p.101779.

Joseph, R.P., Singh, C.S., and Manikandan, M., 2014. Brain tumor MRI image segmentation and detection in image processing. *International Journal of Research in Engineering and Technology*, 3(1), pp.1-5.

Kamnitsas, K., Ledig, C., Newcombe, V.F., Simpson, J.P., Kane, A.D., Menon, D.K., Rueckert, D., and Glocker, B., 2017. Efficient multi-scale 3D CNN with fully connected CRF for accurate brain lesion segmentation. *Medical Image Analysis*, 36, pp.61-78.

Milletari, F., Navab, N., and Ahmadi, S.A., 2016. V-net: Fully Convolutional Neural Networks for Volumetric Medical Image Segmentation. In: *2016 Fourth International Conference on 3D Vision (3DV)*. IEEE, Piscataway, pp.565-571.

Mohammed, E., Hassaan, M., Amin, S., and Ebied, H.M., 2021. Brain Tumor Segmentation: A Comparative Analysis. In: *The International Conference on Artificial Intelligence and Computer Vision.* Springer International Publishing, Cham, pp.505-514.

Morad, A.H., and Al-Dabbas, H.M., 2020. Classification of brain tumor area for MRI images. *Journal of Physics: Conference Series*, 1660(1), p.012059.

Ortiz, A., Gorriz, J.M., Ramírez, J., Salas-Gonzalez, D., and For the Alzheimer's Disease Neuroimaging Initiative., 2013. Improving MRI segmentation with probabilistic GHSOM and multiobjective optimization. *Neurocomputing*, 114, pp.118-131.

Pedapati, P., and Tannedi, R.V., 2017. Brain Tumour Detection Using Hog by SVM. Department of Applied Signal Processing. Master Thesis, Blekinge Institute of Technology SE-37179, Karlskrona, Sweden.

Rao, C.S., and Karunakara, K., 2021. A comprehensive review on brain tumor segmentation and classification of MRI images. *Multimedia Tools and Applications*, 80(12), pp.17611-17643.

Sharif, M.I., Li, J.P., Khan, M.A., and Saleem, M.A., 2020. Active deep neural network features selection for segmentation and recognition of brain tumors using MRI images. *Pattern Recognition Letters*, 129, pp.181-189.

Shukla, A.P., 2016. Training cellular automata for image edge detection. *Romanian Journal of Information Science and Technology*, 19(4), pp.338-359.

Siar, M., and Teshnehlab, M., 2019. Brain Tumor Detection Using Deep Neural Network and Machine Learning Algorithm. In: *2019 9th International Conference on Computer and Knowledge Engineering (ICCKE)*. IEEE, Piscataway, pp.363-368.

Siegel, R.L., Miller, K.D., Fuchs, H.E., and Jemal, A., 2021. Cancer statistics, 2021. *CA: A Cancer Journal for Clinicians*, 71(1), pp.7-33.

Taha, N.A., Qasim, Z., Al-Saffar, A., and Abdullatif, A.A., 2021. Steganography using dual tree complex wavelet transform with LSB indicator technique. *Periodicals of Engineering and Natural Sciences*, 9(2), pp.1106-1114.

Tustison, N.J., Shrinidhi, K.L., Wintermark, M., Durst, C.R., Kandel, B.M., Gee, J.C., Grossman, M.C., and Avants, B.B., 2015. Optimal symmetric multimodal templates and concatenated random forests for supervised brain tumor segmentation (simplified) with ANTsR. *Neuroinformatics*, 13, pp.209-225.

Wala'a, N.J., and Rana, J.M., 2021. A survey on segmentation techniques for image processing. *Iraqi Journal for Electrical and Electronic Engineering*, 17, pp.73-93.

Wang, T., Cheng, I., and Basu, A., 2009. Fluid vector flow and applications in brain tumor segmentation. *IEEE Transactions on Biomedical Engineering*, 56(3), pp.781-789.

Wang, W., Chen, C., Ding, M., Yu, H., Zha, S., and Li, J., 2021. Transbts: Multimodal Brain Tumor Segmentation Using Transformer. In: *Medical Image Computing and Computer Assisted Intervention–MICCAI 2021: 24th International Conference, Strasbourg, France, September 27-October 1, 2021, Proceedings, Part I 24*. Springer International Publishing, Cham, pp.109-119.

Wu, S., Wu, Y., Chang, H., Su, F.T., Liao, H., Tseng, W., Liao, C., Lai, F., Hsu,F., and Xiao, F., 2021. Deep learning-based segmentation of various brain lesions for radiosurgery. *Applied Sciences*, 11(19), p.9180.

Yang, Z., Hu, Z., Ji, H., Lafata, K., Vaios, E., Floyd, S., Yin, F.F., and Wang, C., 2023. A neural ordinary differential equation model for visualizing deep neural network behaviors in multi□parametric MRI□based glioma segmentation. *Medical Physics*, 50(8), pp.4525-4838.

Zebari, D.A., Zeebaree, D.Q., Abdulazeez, A.M., Haron, H., and Hamed, H.N.A., 2020. Improved threshold based and trainable fully automated segmentation for breast cancer boundary and pectoral muscle in mammogram images. *IEEE Access*, 8, pp.203097-203116.

Zhang, B., 2010. Computer Vision vs. Human Vision. In *9th IEEE International Conference on Cognitive Informatics (ICCI'10)*. IEEE, Piscataway, p.3.

Zhang, J., Shen, X., Zhuo, T., and Zhou, H., 2017. Brain tumor segmentation based on refined fully convolutional neural networks with a hierarchical dice loss. *arXiv preprint arXiv:1712.09093*.

Zhao, X., Wu, Y., Song, G., Li, Z., Zhang, Y., and Fan, Y., 2018. A deep learning model integrating FCNNs and CRFs for brain tumor segmentation. *Medical Image Analysis*, 43, pp.98-111.

 http://dx.doi.org/10.14500/aro.11519

Bridging the Gap: Enhancing Kurdish News Classification with RFO-CNN Hybrid Model

Soran S. Badawi

Charmo Center for Scientific Research and Consulting – Language and Linguistic Center, Charmo University Chamchamal, Sulaimani, Kurdistan region - F.R. Iraq

***Abstract*—Effective organization and retrieval of news content are heavily reliant on accurate news classification. While the mountainous research has been conducted in resourceful languages like English and Chinese, the researches on under-resourced languages like the Kurdish language are severely lacking. To address this challenge, we introduce a hybrid approach called RFO-CNN in this paper. The proposed method combines an improved version of red fox optimization algorithm (RFO) and convolutional neural network (CNN) for finetuning CNN's parameters. Our model's efficacy was tested on two widely used Kurdish news datasets, KNDH and KDC-4007, both of which contain news articles classified into various categories. We compared the performance of RFO-CNN to other cutting-edge deep learning models such as bidirectional long short-term memory networks and bidirectional encoder representations from transformers (BERT) transformers, as well as classical machine learning approaches such as multinomial naive bayes, support vector machine, and K-nearest neighbors. We trained and tested our datasets using four different scenarios: 60:40, 70:30, 80:20, and 90:10. Our experimental results demonstrate the superiority of the RFO-CNN model across all scenarios, outperforming the benchmark BERT model and other machine learning models in terms of accuracy and F1-score.**

***Index Terms*—News Classification, Kurdish Language, Red fox optimization-Convolutional neural network, Bidirectional long short-term memory, Bidirectional encoder representations from transformers.**

I. Introduction

With the rise of social media, journalism has shifted from traditional print media to digital platforms (Kaliyar, et al., 2021). While this has increased the speed of news dissemination, the editing process is not as strictly controlled as it is with traditional media. This has resulted in an overwhelming amount of news content across different topics. Regrettably, news agencies often neglect to categorize their content, particularly in languages with limited resources. The absence of automated tools for categorizing news in these languages has made it difficult to present viewers and readers with organized content. The categorization of news is a crucial component of natural language processing, as it enables the organization of articles and stories by subject matter. Precise news classification has the potential to enhance news recommendation systems, facilitate more effective article searches and indexing, and offer valuable insights into the latest news trends and public interest in various topics (Jing and Bailong, 2021). According to Jugovac, Jannach, and Karimi (2018), news recommendation systems aim to enhance human and machine relationships by offering users personalized and relevant news articles based on their preferences and attention (Jugovac, Jannach and Karimi, 2018).

Accurately categorizing news text is essential for various industries. First, it can aid in anticipating shifts in market conditions by classifying diverse internet news sources, obtaining economic and current political news, and analyzing such information (Dai and Wang, 2021). Second, it can benefit readers by organizing and analyzing previously read news to suggest additional articles that may pique their interest (Reddy, et al., 2019). Third, categorizing news texts plays a pivotal role in detecting rumors (Verma, et al., 2021), analyzing public sentiment, and filtering spam news (Zhang, Xu and Zhao, 2020). It can help to identify deceptive information and support making informed decisions. Nevertheless, creating news classification systems can be a difficult undertaking, particularly in languages with limited labeled datasets, lexical resources, and pre-trained models.

This article presents an innovative solution called RFO-CNN that employs a hybrid approach to automatically categorize news articles based on their headlines. By combining a convolutional neural network (CNN) with an improved Red Fox Algorithm (RFO), the CNN's parameters are fine-tuned for improved accuracy. This approach is particularly effective in handling the rapidly changing nature of news content and has outperformed existing methods in news classification, including the state-of-the-art BERT, across a range of evaluation metrics. To summarize, our article makes significant contributions to the field of news categorization.

II. Related Works

Over the past few years, an array of studies has been conducted to investigate the classification of news texts.

ARO-The Scientific Journal of Koya University
Vol. XII, No. 1 (2024), Article ID: ARO.11519. 8 pages
DOI: 10.14500/aro.11519
Received: 16 January 2024; Accepted: 26 March 2024
Regular research paper: Published: 03 April 2024
Corresponding author's e-mail: soran.sedeeq@charmouniversity.org

Before delving into an examination of the proposed approach, it would be worthwhile to briefly review the methods that were previously introduced in this context.

Xie, et al. (2019) employed LSTM to extract context and sequence characteristics from Chinese news text for classification purposes (Xie, et al., 2019), while Liu, et al. (2019) presented a hierarchical model that combined LSTM and temporal convolutional networks to extract context and information sequentially (Liu, et al., 2019). Chen, Cong and Lv (2022) introduced a local feature convolution network based on BERT to capture local features and address the characteristics of lengthy Chinese news texts with significant amounts of information (Chen, Cong and Lv, 2022). Furthermore, Zhu (2021) leveraged the VSM (vector space model) to calculate text weight, and information gain, and obtain text features (Zhu, 2021). In another research by Sergio Cleger-Tamayo, a recommender approach has been suggested. Its purpose is to provide users with a ranked list of news articles based on their previous visits, the terms found in articles, and the assigned categories. The authors of the study have proposed a model that identifies semantic relationships in user access to categorize news. The findings of this study suggest that incorporating news classification into the model significantly improves its ability to predict user interest in articles (Cleger-Tamayo, Fernandez-Luna and Huete, 2012). Moreover, an innovative algorithm developed by Bouras et al. has been introduced to provide personalized and succinct articles to users through the PeRSSonal communication channel (Bouras and Tsogkas, 2009). This algorithm was designed to cater to individual preferences and deliver high-quality content that was curated for each user. While the approach is primarily content based, it also employs collaborative filtering features that adapt to the user's evolving profile over time. The authors observed a marked improvement in the system's performance when tested with real users. However, it should be noted that evaluating a summarization system is a challenging and subjective task, as acknowledged by the authors. In a study conducted by Al-Tahrawi, the Alj-News corpus – a collection of 1500 Arabic news documents – was divided into five classes for categorization. Out of these, 240 documents were used for training and 60 for testing. The author utilized the Chi-square method for this task (Al-Tahrawi, 2015). In another study, Garrido, et al. (2011) proposed a system for categorizing media content. This system was specifically designed to accurately classify real newspaper articles that have been manually tagged. By refining the support vector machine and object-based information extraction systems through testing on actual news articles, the authors were able to achieve a high level of accuracy. The authors suggest that incorporating natural language processing and semantic tools can further improve accuracy, especially in situations where the SVM training set requires frequent updates. According to the authors, this approach is user-friendly, simple, and achieves almost 99% accuracy in labeling (Garrido, et al., 2011).

It is worth mentioning that many researchers have used red fox optimization (RFO) for classification purposes. Khorami, Mahdi Babaei, and Azadeh (2021) proposed an innovative approach to COVID-19 virus detection, using a hybrid RFO combined with a CNN. They utilized chest X-ray images and a machine vision-based system to deliver highly precise outcomes. The process involved pre-processing the input X-ray images and isolating the region of interest, followed by extracting a combination of gray-level co-occurrence matrix (GLCM) and discrete wavelet transform (DWT) features from the processed images. The results demonstrated that this method outperformed other methods in the literature, making it a more effective diagnostic tool for COVID-19 virus detection. Mahesh and Hemalatha (2022) proposed a CNN-ARFO approach based on a CNN to assist users in identifying malicious applications. Pugal Priya, Saradadevi Sivarani, and Gnana Saravanan (2021) developed a RFO algorithm that employs deep long short-term memory to classify mild, moderate, and severe stages of NPDR.

In the Kurdish language, there is limited research on news detection. The existing studies focus mainly on detecting fake news. Azad, et al. (2021) sought to identify fake news in the Kurdish language. The researchers created two sets of news, one with 5000 real and 5000 fake news from Facebook pages and Sorani Kurdish websites, and another with 5000 real news and 5000 fake news generated from the real news. The study employed five machine learning classification methods, including Logistic Regression (LR), Naive Bayes, Decision Tree (DT), SVM, and Random Forest (RF), to analyze the news. The SVM classifier achieved the highest accuracy rate of 88.71%, while Random Forest scored 79.08% accuracy for only one set of manipulated text data (Azad, et al., 2021). However, the study did not label the data based on the Kurdistan Journal Syndicate rules and regulations, and only a limited number of features were extracted from the dataset. Salih and Nalbi (2023) classified fake news articles using a framework developed from text data from Kurdish news articles. However, they utilized a dataset that comprises 100,962 news articles from various domains. Of these, 50,751 articles were real, while the other 50,211 were flagged as 1 and 0 for fake news. They analyzed the dataset using three classifiers – RF, SVM, and CNNs – employing machine learning and deep learning techniques. They also utilized various feature extraction techniques, including TF-IDF, count-vector, and word embedding, to obtain different textual features from the articles. Following pre-processing steps, they fed the feature set into the classifiers. Their multi-model approach resulted in a fake news detection system that employs various models to achieve more accurate results. Their findings indicated that the CNN architecture was the most effective in identifying the most erroneous articles, with fewer false negatives a higher accuracy rate of 91%, and a higher f1-score of 95% (Salh and Nabi, 2023).

There is a significant gap in the domain of Kurdish news detection models. To bridge this gap, we have developed the RFO-CNN model. This model incorporates the Modified RFO Algorithm into a CNN architecture to optimize parameters and improve text classification. Our goal is to contribute to the creation of a culturally sensitive and robust solution for news detection in the Kurdish language by addressing the limitations of previous studies. With the RFO-CNN

model, we aim to provide a more precise and effective way of determining the authenticity of news articles, thereby filling a crucial gap in the current Kurdish language research landscape.

III. Methodology

The overall RFO-CNN model is depicted in Fig. 1, which consists of several distinct phases. The first phase involves dataset collection. Phase 2 focuses on pre-processing, while Phase 3 concentrates on feature extraction and feature selection. Finally, the fourth phase is responsible for classification.

A. Dataset Collection

The experiment utilized two datasets obtained from GitHub and Mendeley. The first dataset, KDC4007, was chosen for its simplicity and well-documented nature, making it ideal for various text classification studies on Kurdish Sorani news and articles. The corpus consists of 4007 text files categorized into eight distinct categories, namely. Sports, Religion, Arts, Economics, Education, Socials, Styles, and Health, each containing 500 texts (Rashid, Mustafa and Saeed, 2017). Access to the dataset and documents is available at https://github.com/arazom/KDC-4007-Dataset/blob/master/Kurdish-Info.txt.

The second dataset, KNDH, is a massive collection of 50,000 news headlines from popular Kurdish news websites. Each category has an equal number of samples, including social, sport, science, health, and economy (Badawi, et al., 2023). This dataset is freely available to access at https://data.mendeley.com/datasets/kb7vvkg2th/2. These datasets are valuable resources for natural language processing and text classification studies, particularly in the Kurdish Sorani language.

B. Text Preprocessing

After gathering news articles, we begin the process of cleaning the datasets by eliminating irrelevant and noisy information. This involves removing unrelated words such as brackets, semicolons, full stops, and other unnecessary characters. We also remove frequent words that appear in the text, known as stop words (Badawi, 2023b). To do this, we use libraries such as KLPT, NumPy, Pandas, and Scikit-Learn. Moreover, we perform text tokenization on news headlines, which involves dividing text into smaller words or tokens. Each word in both the headlines and content is treated as a string and broken down into smaller tokens. These tokens are then used in text-mining processes. To form a vocabulary of words, the headlines are merged.

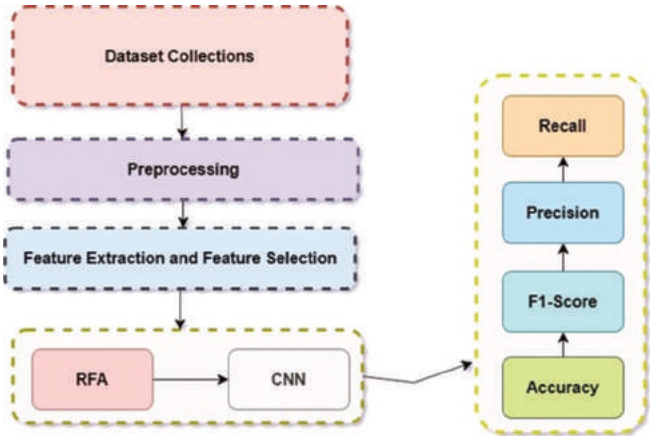

Fig. 1. The diagram of the proposed method.

We remove diacritics, using language-specific methods, and remove various punctuation marks, special characters, and brackets from words. We also identify and remove stop words, which are connecting or joining words in a text. These frequently occurring words have little impact on the overall meaning of the text. Finally, we employ word stemming to reduce words to their stem or root. It is important to note that the stemmed word may not always be the same as its dictionary root.

C. Feature Extraction

One widely used technique in natural language processing for identifying linguistic features is TFIDF, which stands for fequency-inverted document frequency. This method is particularly helpful in classifying news headlines, as it searches for specific tokens within news content. Tokens are assigned weights based on their frequency and the importance of the document. To apply TF-IDF, the Scikit-Learn library is commonly used with document pre-processing pipelines. In this approach, the product of term frequency (TF) is evaluated by measuring the occurrence of each topic within a document and weighing it by its importance value (IDF). Equation (1) provides the formula for calculating the TF, which represents the term frequency of each topic. The IDF, which measures the criticality of the topic, is then used to create a weight matrix for each case in the dataset. Finally, the TF-IDF values can be calculated using the formula provided in equation (2) (Zhang, et al., 2019), which displays the IDF formula:

$$\mathrm{TF}(\text{term, document}) = \frac{\text{No. of times term appears in a document}}{\text{Total words of the document}} \quad (1)$$

$$\mathrm{IDF}(\text{term}) = \frac{\text{Total number of documents}}{\text{Number of documents with term in it}} \quad (2)$$

The next step is to calculate the TF-IDF. TF-IDF is the product of the term frequency and inverse document frequency, which is shown in formula (3):

$$\text{TF}-\text{IDF (term, document)} = \text{TF (term, document)} \times \text{IDF (term)} \quad (3)$$

TF-IDF vectors can be generated using different input tokens, such as characters, words, and n-grams.

IV. Proposed Method

A. Improved RFO

The RFO algorithm is a cutting-edge optimization framework inspired by the foraging behavior of red foxes

(Połap and Wozniak, 2021). Similar to other nature-inspired algorithms, ´ RFO aims to harness the efficiency of biological systems to tackle complex problems. RFO employs a virtual population of "foxes" to represent potential solutions within a defined search space. These foxes emulate the foraging behavior of actual red foxes, skillfully balancing exploration and exploitation to discover optimal solutions. While the RFO Algorithm may offer a promising approach to optimization, traditional implementations may face challenges. Two primary issues are often associated with the conventional RFO.

B. Limited Exploration

In certain scenarios, the algorithm may face challenges in identifying the optimal solution as it only assesses a restricted segment of the search space. Such constraints can hinder the algorithm from discovering a wider range of potential and effective solutions. To address this limitation, we have introduced a novel operation that empowers exploration. This operation incorporates a transformative process that is influenced by a random gamma value, thereby introducing a stochastic element to the population of foxes. This adaptive mechanism enables the algorithm to avoid being trapped in local optima and promotes exploration of diverse regions within the search space as shown in equation (4).

$$X_i = (1 - \lambda) \bullet X_i + \lambda \bullet U(L,R) \quad (4)$$

In this equation, *Xi* represents the vector that signifies the present location of the *ith* fox in the search space. The process of updating this location involves a weighted combination of the current position and a new position. The parameter *(λ)* is a random value that is sampled from a uniform distribution between 0 and 1. This parameter adds an element of chance in the update process. The term *(1- λ). Xi* stands for the influence of the current position, where *(1-λ)* serves as a scaling factor. The term *λ.U(L,R)* signifies the influence of a randomly generated position within the specified range *[L,R]* and of the same dimension as foxes. Ultimately, this equation merges the current position of the *ith* fox with a new position determined by a random factor *(λ).* The incorporation of randomness in this way enriches exploration in the search space, addressing the issue of limited exploration. It empowers the algorithm to effect significant alterations to the fox positions, encouraging diversity and preventing premature convergence to suboptimal solutions.

C. Risk of Premature Convergence

Premature convergence occurs when an algorithm settles on a solution without fully exploring the search space, leading to less-than-optimal results. This is especially problematic for intricate optimization problems with rough terrain, where the algorithm may become stuck in local optima and fail to discover globally optimal solutions. To avoid premature convergence, we can modify the update rule by introducing diversity into the parameter updates. This can be accomplished by introducing an alpha value, which is calculated by determining the Euclidean distance between the current fox and the first fox in the population as shown in the equation. Furthermore, a beta value can be included to introduce randomness into the update process, preventing foxes from converging to similar positions.

$$a = \frac{1}{\sqrt{(X_{i[j]} - X_{0[j]})^2 + (X_{i[j+1]} - X_{0[j]})}} \quad (5)$$

To determine the value of *a*, a random selection is made from a uniform distribution that ranges between 0 and the Euclidean distance between the initial fox in the population and the *ith* fox. This means that a is determined by selecting a random value within the aforementioned range, which is determined by the distance between the position of the *ith* fox and the position of the first fox. The update rule for each dimension *j* of the *ith* fox's position is given by this equation:

$$X_{i[j]} = X_{i[j]} + a.b.\ (R - L) \quad (6)$$

This equation updates the *jth* dimension of the ith fox's position by adding a value. The value is calculated based on the product of a, b, and the range $(R - L)$. The a and b terms introduce randomness and exploration in the update process. b is a random number uniformly distributed in the range (0,1).

Overall, we developed an enhanced iteration of the RFO algorithm, specifically tailored for fine-tuning the parameters of CNNs. This modified algorithm tackles the challenges of early convergence and insufficient exploration encountered in the original version by incorporating adaptive exploration and diverse update rules. Our results indicate that these modifications effectively improve the optimization process and demonstrate the potential of the Modified RFO algorithm in optimizing CNN parameters. Ultimately, this algorithm presents a promising approach for optimizing problems, particularly in the realm of CNN parameter optimization.

D. Applying RFO to CNN Parameter Optimization

CNN is a powerful deep-learning model that has proven to be remarkably successful in computer vision applications. In recent years, it has also demonstrated impressive results in natural language processing, specifically text classification. The architecture employed in this study encompasses the following parameters as shown in Fig. 2.

- Input dimension: The parameter known as the "input dimension" plays a crucial role in establishing the input space for the CNN model and limiting the number of words that can be included within the input text. Its value is typically derived from the maximum length of sequences or documents in the dataset, making it a key factor to consider.
- Embedding dimension: The modified RFO algorithm offers a solution that yields an optimized embedding dimension. This dimension is subsequently employed to establish the dimensionality of the embedding space. The model must possess the appropriate dimensionality to effectively capture the semantic relationships among words, enabling the model to depict them in a seamless vector space.
- Convolutional layer: This particular layer is classified as a 1D convolutional layer within a neural network. It boasts

http://dx.doi.org/10.14500/aro.11519

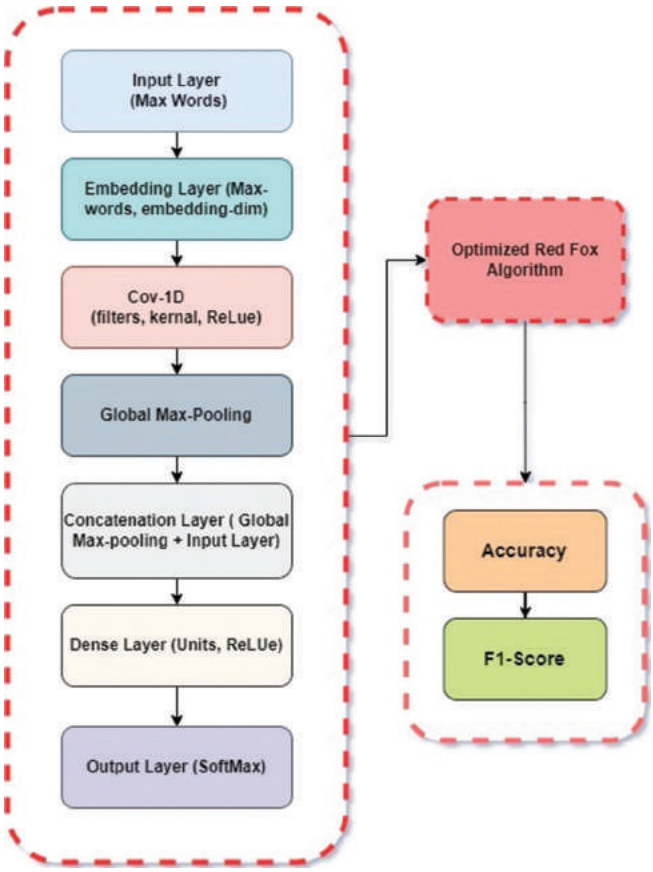

Fig. 2. The architecture of the proposed model.

numerous filters and utilizes a kernel size activated by ReLU. This layer carries out a majority of the network's computation by conducting the convolution operation, resulting in a fresh representation of the input data. During convolution, a kernel is slid over the input spectrum with a specific stride, generating a feature map that captures spatial information. Subsequently, the output feature map passes through an activation function (such as ReLU) to introduce nonlinearity to the network. This allows the network to grasp more intricate patterns found within the text data. The RFO algorithm is utilized to determine the number of filters and filter size present within the convolutional layers (Badawi, 2024).

- Global maxpooling layer: Following the convolutional layer, the architecture incorporates a Global Max Pooling layer. This layer effectively consolidates the most critical features throughout the entire sequence by extracting the maximum value from each feature map. This process condenses the spatial data into a single value for each channel. The *pool_size*, which determines the range over which the maximum value is extracted, is influenced by the RFO. The RFO is a parameter optimization technique that fine-tunes model hyperparameters, including the size of the pooling operation. The *pool_size* is dynamically adjusted based on the characteristics of the dataset to optimize the model's performance.
- Concatenation layer: In the neural network architecture, a concatenation layer follows the global max pooling layer to merge the extracted features from different branches. Specifically, this concatenation layer combines the output from the global max pooling layer with additional engineered features displayed by the input layer. Neural network architectures rely on concatenation as a crucial operation to integrate diverse information sources. By blending the high-level abstract features learned by convolutional layers with additional engineered features, the model gains a more comprehensive understanding of the input data. This enhances its capacity to capture intricate patterns and relationships. The incorporation of concatenation enriches the model's expressive power, allowing it to leverage both learned hierarchical features and domain-specific information, ultimately leading to improved overall performance and adaptability. This architectural element aligns with the holistic optimization approach facilitated by the red fox algorithm, which dynamically influences the neural network structure to achieve optimal outcomes.
- Dense layers: Our model comprises of fully connected layers, known as dense layers, at the fifth and sixth levels. With dense units neurons, these layers establish connections between neurons in the same layer and those in other layers. The activation function of the dense layer is set to Softmax to enable classification, and the model predicts class probabilities as a result. Our model has two dense layers. The first dense layer, optimized with the RFO optimization algorithm, has a variable number of units, C. The second dense layer, designed explicitly for classification, includes 11 units that correspond to the five and eight categories in the KNDH and KDC datasets, respectively.

The input dimension parameter plays a key role in defining the input space for the CNN model, as it determines the maximum number of words in the input text. Typically, this value is determined by the maximum allowable length of sequences or documents in the dataset. In addition, the optimized embedding dimension, which is derived from the RFO, is used to establish the dimensionality of the embedding space. This parameter is critical for the model to effectively capture semantic relationships between words and represent them in a continuous vector space. Finally, the total number of class parameters is used to specify the total number of distinct categories or labels that the CNN model needs to predict.

The initial step involves accessing the first fox in the population and retrieving its first element. To ensure that the embedding dimension remains a whole number. This refined embedding dimension is then utilized to configure the CNN model's architecture The RFO is used to fine-tune essential CNNs parameters. Its objective is to determine the optimal configuration for the CNN model by prioritizing significant factors such as the embedding dimension. The improved RFO returns the parameters of the first fox in the population as the optimized solution. The optimized solution is a vector of specific parameters, represented by the symbol θ. In this case, θ is a one-dimensional vector with the sole element corresponding to the embedding dimension. The embedding dimension determines the number of dimensions in the vector space in which words or tokens from the input text are embedded.

The RFO algorithm is a process that is repeated until a stopping criterion is met. This criterion can be a maximum number of iterations or a minimum fitness value. The final CNN model that is produced has the optimal values for each of its parameters. By using this process, CNN can be effectively tuned and applied for news classification in the Kurdish language. You can find the pseudocode for RFO-CNN in Algorithm.

Algorithm 1 RFO-CNN Algorithm

Begin
Initialize RFO-CNN parameters: population size, iterations, lower and upper bounds.
Generate an initial population of foxes with random values within the specified bounds. Equation (4)
Load the training data, including selected features and labels.
while num-search-iterations < stopping criteria **do**
for e **do**each fox in the population
Calculate a random value alpha based on the distance between the fox and the first fox in the population Equation (5).
Update each dimension of the fox using random value beta.
end for
Introduce a new operation:
for e **do**each fox
Calculate a random value gamma. Equation (6)
Update the fox position using a weighted combination of the current position and a new random position within the bounds.
end for
Evaluate the fitness function for each fox to select the best configuration of parameters.
if the new position > the old position. the old position == the new position.
end while
Extract the optimized parameters from the first fox in the population.
Build CNN model with the extracted parameters with predefined architecture.
Compile the CNN model with the specified loss function, optimizer, and metrics.
Train the CNN model using the selected features and the training dataset.
Evaluate the final model`s performance on the test set.
Return the optimized parameters and the trained CNN model.
end.

V. Experimental Results and Discussions

This section presents an evaluation of RFO-CNN using available datasets collected from online repositories. F-measure and accuracy are used as the metrics for comparison. To assess its performance, RFO-CNN is compared to two baseline deep learning classification models BLSTM (Badawi, 2023a) and BERT (Badawi, 2023b) and three baseline machine learning models (SVM [Saeed, et al., 2023], MNB [Saeed, et al., 2023], and K-nearest neighbors (KNN) [Tan, 2018]) that have been selected from state-of-the-art Kurdish classification. The same setup parameters configurations of the considered baseline models in the original papers are used. The experiments were conducted on Python 3.10 and Google Colab, utilizing Keras, TensorFlow, NumPy, Scikit-learn, Pandas, among other required libraries. Evaluations were carried out on a personal system with an Intel Core-i5 CPU, Windows 11, and 16 Gigabyte RAM. Preprocessing steps were performed using the KLPT Python package as proposed in (Ahmadi, 2020). The input dataset was divided into training and testing datasets and classified into four different scenarios - 90:10%, 80:20%, 70:30%, and 60:40%. To prevent overfitting, we have limited the number of epochs to two. The evaluation metrics were chosen to display the best performance of each method. Each implemented method was run N = 10 times to obtain an average value of each evaluation metric, and 5-fold cross-validation was adopted.

A. Discussion

Tables I and II offer a comprehensive analysis of diverse models utilized in the classification of Kurdish news headlines, tested under varying train-test split scenarios (90:10, 80:20, 70:30, and 60:40). The models evaluated include conventional approaches such as naïve Bayes, SVM, and KNN, as well as advanced deep learning techniques such as BLSTM, BERT, and the suggested RFO-CNN, providing a comprehensive view of their effectiveness.

Regarding KNDH dataset, it is important to mention that the RFO-CNN model consistently demonstrates superior

TABLE I
Performance Metrics for Different Models in Various Scenarios for KNDH Dataset

Scenarios		Performance metrics	
Training and test splitting	Models	Accuracy (%)	F1-score micro
90:10	Naïve Bayes	78.26	78.10
	SVM	74.71	74.69
	KNN	69.59	68.85
	BLSTM	87.50	87.50
	BERT	88.32	88.31
	RFO-CNN	89.25	89.36
80:20	Naïve Bayes	81.75	81.62
	SVM	75.89	75.88
	KNN	76.67	76.15
	BLSTM	87.80	87.85
	BERT	88.56	88.51
	RFO-CNN	89.47	89.49
70:30	Naïve Bayes	83.60	83.48
	SVM	75.19	75.18
	KNN	76.76	76.34
	BLSTM	87.32	87.36
	BERT	87.49	87.45
	RFO-CNN	88.6	88.7
60:40	Naïve Bayes	84.38	84.26
	SVM	75.99	76.02
	KNN	78.78	78.44
	BLSTM	86.27	86.29
	BERT	85.74	85.83
	RFO-CNN	87.4	87.64

SVM: Support vector machine, KNN: K-nearest neighbors, BERT: Bidirectional encoder representations from transformers, RFO-CNN: Red fox optimization-Convolutional neural network

http://dx.doi.org/10.14500/aro.11519

TABLE II
PERFORMANCE METRICS FOR DIFFERENT MODELS IN VARIOUS SCENARIOS FOR KDC-4007 DATASET

Scenarios		Performance metrics	
Training and test splitting	Models	Accuracy (%)	F1-score micro
90:10	Naïve Bayes	78.25	78.15
	SVM	73.53	73.60
	KNN	59.11	58.88
	BLSTM	81.53	81.57
	BERT	81.52	81.45
	RFO-CNN	91.62	91.54
80:20	Naïve Bayes	83.37	83.47
	SVM	80.56	80.58
	KNN	72.54	72.26
	BLSTM	80.76	81.25
	BERT	80.27	80.00
	RFO-CNN	91.12	91.11
70:30	Naïve Bayes	87.20	87.19
	SVM	82.93	82.90
	KNN	76.24	76.10
	BLSTM	76.40	74.68
	BERT	74.67	75.27
	RFO-CNN	88.40	88.42
60:40	Naïve Bayes	88.52	88.47
	SVM	84.78	84.78
	KNN	79.97	79.98
	BLSTM	71.93	72.33
	BERT	63.54	61.69
	RFO-CNN	84.14	83.19

SVM: Support vector machine, KNN: K-nearest neighbors, BERT: Bidirectional encoder representations from transformers, RFO-CNN: Red fox optimization-Convolutional neural network

performance compared to other models in all situations, showcasing its resilience and adaptability. Of particular significance is its ability to achieve accuracy scores of 89.25% and 89.47% in the 90:10 and 80:20 splits respectively, surpassing even the highly acclaimed BERT model which is recognized as a state-of-the-art in natural language processing. The F1-score micro, a metric that takes into account both precision and recall further emphasizes the exceptional performance of the RFO-CNN. It consistently exceeds 89%, and even outperforms BERT in select scenarios.

While traditional machine learning models such as Naïve Bayes, SVM, and KNN have proven effective in many scenarios, they struggle to handle the complexities of semantic analysis in Kurdish news headlines. On the other hand, the deep learning model BLSTM performs well, but it consistently falls short of the RFO-CNN's impressive results, highlighting the effectiveness of this approach. Even the highly regarded BERT, with its contextualized word embeddings and transformer architecture, is outperformed by the RFO-CNN in multiple scenarios in terms of accuracy and F1-score micro. This underscores the adaptability and optimization capabilities of the RFO-CNN, which benefits from the modified RFO algorithm's dynamic exploration and exploitation. The RFO-CNN has proven to be a successful model by leveraging the modified RFO algorithm and CNN architecture in a highly effective manner. The RFO algorithm has been designed to tackle common optimization challenges, giving it a competitive edge over traditional algorithms. In addition, the CNN's deep learning capabilities enable it to automatically extract hierarchical features from text, which significantly enhances its ability to classify news articles.

Similarly, the performance evaluation of the models trained on the KDC-4007 dataset yields valuable insights into their adaptability across various train-test split scenarios. By analyzing the accuracy and F1-score micro of the models in each scenario, we can identify distinct patterns and assess their performance on handling different data distributions. Our findings indicate that the RFO-CNN model consistently outperforms other models in the 90:10 and 80:20 splits, demonstrating its strength in managing imbalanced datasets. In these scenarios, the RFO-CNN achieves accuracy scores of 91.62% and 90.13%, respectively, showcasing its robustness and superiority. Notably, the F1-score micro for the RFO-CNN surpasses 91% in both cases, indicating its ability to balance precision and recall effectively. Several machine learning models, such as Naïve Bayes, SVM, and KNN, perform well in balanced datasets but struggle when there is a significant class imbalance, such as an 80:20 or 90:10 split. BERT is another popular model that uses contextualized embeddings, but it has lower performance in imbalanced datasets compared to the BLSTM. The RFO-CNN consistently outperforms BERT and shows adaptability and optimization capabilities. Even in datasets with class in different sizes, such as a 70:30 or 60:40 split, the RFO-CNN maintains high accuracy and F1-score. As the dataset distribution becomes more skewed, the RFO-CNN remains effective while other models struggle to maintain accuracy and F1-score. This suggests that the RFO-CNN's use of the modified RFO algorithm, combined with the CNN architecture, contributes to its adaptability and effectiveness in scenarios with varying class sizes. However, it is worth mentioning that Naive Bayes exhibits superior performance to RFO-CNN when the train-test split ratio is 60:0. This is due to the relatively small-size of the dataset containing KDC-4007, which results in fewer class numbers during the training phase. As a result, RFO-CNN is unable to identify the optimal score.

Overall, the RFO-CNN model has proven to be a highly effective solution for classifying Kurdish news headlines. It consistently outperforms both traditional and advanced models, including the state-of-the-art BERT, thanks to the integration of the modified RFO algorithm. This integration has significantly improved the model's accuracy and F1-score micro across various train-test split scenarios, making the RFO-CNN a reliable and robust tool for semantic analysis in natural language processing tasks for low-resourced languages. In particular, the RFO-CNN exhibits exceptional performance in the KDC-4007 dataset, surpassing other models in accuracy and F1-score micro across different train-test split scenarios. Its ability to perform well, especially in imbalanced datasets, makes the RFO-CNN a highly trustworthy and effective model other low-resourced language.

VI. CONCLUSION

In this study, we presented RFO-CNN, a novel approach for classifying Kurdish news. Our experimental results

demonstrated that RFO-CNN outperforms state-of-the-art models, such as BERT, as well as other baseline machine learning methods when experimenting them on two benchmark Kurdish datasets KNDH and KDC007. The red fox algorithm enhanced CNN's parameter configuration, enabling it to detect patterns more effectively in Kurdish news articles. Our findings highlight the importance of utilizing tailored algorithms for specific low-resourced languages. RFO-CNN presents exciting possibilities for optimizing deep learning architectures for underrepresented languages and domains. Future research could explore the interpretability of the RFO-CNN's decision-making processes and identify further linguistic features that could enhance its performance in the context of Kurdish news

References

Ahmadi, S., 2020. KLPT-Kurdish Language Processing Toolkit. *In Proceedings of the Second Workshop for NLP Open Source Software (NLP-OSS)*, pp.72-84.

Al-Tahrawi, M.M., 2015. Arabic text categorization using logistic regression. *International Journal of Intelligent Systems and Applications*, 7(6), pp.71-78.

Azad, R., Mohammed, B., Mahmud, R., Zrar, L., and Sdiqa, S.J., 2021. Fake news detection in low resourced languages "Kurdish language" using machine learning algorithms. *Journal of Computational Science Education*, 12(6), pp.4219-4225.

Badawi, S., 2023. Data augmentation for Sorani Kurdish news headline classification using back-translation and deep learning model. *Kurdistan Journal of Applied Research*, 8(1), pp.27-34.

Badawi, S., 2024. Deep learning-based cyberbullying detection in Kurdish language. *The Computer Journal*, p.bxae024.

Badawi, S., Saeed, A.M., Ahmed, S.A., Abdalla, P.A., and Hassan, D.A., 2023. Kurdish News Dataset Headlines (KNDH) through multiclass classification. *Data in Brief*, 48, p.109120.

Badawi, S.S., 2023. Using multilingual bidirectional encoder representations from transformers on medical corpus for Kurdish text classification. *ARO-The Scientific Journal of Koya University*, 11(1), pp.10-15.

Bouras, C., and Tsogkas, V., 2009. Personalization Mechanism for Delivering News Articles on the User's Desktop. In: *2009 Fourth International Conference on Internet and Web Applications and Services*, pp.157-162.

Chen, X., Cong, P., and Lv, S., 2022. A Long-text classification method of Chinese news based on BERT and CNN. *IEEE Access*, 10, pp.34046-34057.

Cleger-Tamayo, S., Fernandez-Luna, J.M., and Huete, J.F., 2012. Top-N news recommendations in digital newspapers. *Knowledge-Based Systems*, 27, pp.180-189.

Dai, Y., and Wang, T., 2021. Prediction of customer engagement behaviour response to marketing posts based on machine learning. *Connection Science*, 33(4), pp.891-910.

Garrido, A.L., Gomez, O., Ilarri, S., and Mena, E., 2011. NASS: News Annotation Semantic System. IN: *2011 IEEE 23rd International Conference on Tools with Artificial Intelligence*, pp.904-905.

Jing, W., and Bailong, Y., 2021. News Text Classification and Recommendation Technology Basedon Wide and Deep-Bert Model. In: *2021 IEEE International Conference on Information Communication and Software Engineering (ICICSE)*, pp.209-216.

Jugovac, M., Jannach, D., and Karimi, M., 2018. Streamingrec. In: *Proceedings of the 12th ACM Conference on Recommender Systems*, pp.269-273.

Kaliyar, R.K., Goswami, A., and Narang, P., 2021. FakeBERT: Fake news detection in social media with a BERT-based deep learning approach. *Multimedia Tools and Applications*, 80(8), pp.11765-11788.

Khorami, E., Mahdi Babaei, F., and Azadeh, A., 2021. Optimal diagnosis of COVID-19 based on convolutional neural network and red fox optimization algorithm. *Computational Intelligence and Neuroscience*, 2021, p.4454507.

Liu, J., Xia, C., Yan, H., Xie, Z., and Sun, J., 2019. Hierarchical Comprehensive Context Modeling for Chinese Text Classification. *IEEE Access*, 7, pp.154546-154559.

Mahesh, P.C.S., and Hemalatha, S., 2022. An efficient android malware detection using adaptive red fox optimization based CNN. *Wireless Personal Communications*, 126(1), pp.679-700.

Połap, D., and Wozniak, M., 2021. Red fox optimization algorithm. *Expert Systems with Applications*, 166, p.114107.

Pugal Priya, R., Saradadevi Sivarani, T., and Gnana Saravanan, A., 2022. Deep long and short term memory based Red Fox optimization algorithm for diabetic retinopathy detection and classification. *International Journal for Numerical Methods in Biomedical Engineering*, 38(3), p.e3560.

Rashid, T.A., Mustafa, A.M., and Saeed, A.M., 2017. Automatic Kurdish Text Classification Using KDC 4007 Dataset. In: *International Conference on Emerging Intelligent Data and Web Technologies*.

Reddy, S., Nalluri, S., Kunisetti, S., Ashok, S., and Venkatesh, B., 2019. *Content-Based Movie Recommendation System Using Genre Correlation*. Springer, Singapore, pp.391-397.

Saeed, A.M., Badawi, S., Ahmed, S.A., and Hassan, D.A., 2023. Comparison of feature selection methods in Kurdish text classification. *Iran Journal of Computer Science*, 7, pp.55-64.

Salh, D.A., and Nabi, R.M., 2023. Kurdish fake news detection based on machine learning approaches. *Passer Journal of Basic and Applied Sciences*, 5(2), pp.262-271.

Tan, Y., 2018. An Improved KNN Text Classification Algorithm Based on K-Medoids and Rough Set. In: *2018 10th International Conference on Intelligent Human-Machine Systems and Cybernetics (IHMSC)*, pp.109-113.

Verma, P.K., Agrawal, P., Amorim, I., and Prodan, R., 2021. WELFake: Word embedding over linguistic features for fake news detection. *IEEE Transactions on Computational Social Systems*,8(4), pp.881-893.

Xie, J., Chen, B., Gu, X., Liang, F., and Xu, X., 2019. Self-attention-based BiLSTM model for short text fine-grained sentiment classification. *IEEE Access*, 7, pp.180558-180570.

Zhang, C., Gupta, A., Kauten, C., Deokar, A.V., and Qin, X.J., 2019. Detecting fake news for reducing misinformation risks using analytics approaches. *European Journal of Operational Research*, 279(3), pp.1036-1052.

Zhang, Y., Xu, B., and Zhao, T., 2020. Convolutional multi-head self-attention on memory for aspect sentiment classification. *IEEE/CAA Journal of Automatica Sinica*, 7(4), pp.1038-1044.

Zhu, Y., 2021. Research on news text classification based on deep learning convolutional neural network. *Wireless Communications and Mobile Computing*, 2021, p.1508150.

 http://dx.doi.org/10.14500/aro.11486

Synthesis, Characterization, and Bioactivity Studies of the Schiff Base Ligand and its Zinc(II) Complex

Nabaz A. Muhammad Salih

Department of Chemistry, Faculty of Science, Soran University,
Kurdistan Region – F.R. Iraq

***Abstract*—One of the largest concerns to global health in recent decades has been identified as the growth of bacteria resistance to antibiotics. The Schiff base (SBs) and the zinc(II) SBs complex compounds category have attracted a lot of interest because of their function in chemical syntheses and their potential for bioactive and pharmacological effects. The present study includes the synthesis of various SBs with different substituents. Equimolar mixtures of benzaldehyde derivatives (1, 2) and aniline derivatives (3, 4) are used to carry out a series of condensation reactions to get compounds (5-7). By stoichiometrically combining Zn (II) acetate and $ZnCl_2$ separately with the SBs ligand (7) in ethanol, it has been possible to prepare the SBs zinc(II) complex (8). The structure of the ligand and its metal complex are analyzed using (Fourier-transform infrared spectroscopy, ^{1}H-NMR, ^{13}C-NMR) spectroscopy, scanning electron microscopy, and liquid chromatography–mass spectrometry. Moreover, the synthesized compounds are verified *in vitro* against *Escherichia coli* Gram negative, *Staphylococcus aureus* Gram positive, and fungi (*Candida albicans*). Compounds (5, 7, and 8) indicated significant growth inhibition against *E. coli* Gram negative and fungi (*C. albicans*) with different inhibition zones starting from 7 to 17.5 mm.**

***Index Terms*—Bioactive studies, Condensation reaction, Microorganism, Schiff base, Zinc(II) complex.**

I. Introduction

Schiff bases (SBs) and their metal complexes have been widely investigated because of their biological activity (Liang, et al., 2023), (Shammout, et al., 2021). It is an important class of compounds containing the azomethine (>C=N-) linkage as a functional group, nitrogen bonds to the aryl or alkyl group but not to the hydrogen atom, and are excellent ligands that can coordinate and stabilize metal ions with various oxidation states (Yousif, et al., 2017), (Shah, et al., 2020). Hugo Schiff, a German chemist, reported these chemicals in 1864 (Scheme 1), hence his name was used to refer to them (Omidi and Kakanejadifard, 2020). Most of the SBs are represented by the generic formula $R_1R_2C=NR_3$ (Muzammil K et al., 2015), whereas some of these have the general formula R1CH=NR2, wherein a hydrogen atom rather than an alkyl or aryl group attaches to the carbon (Kolapwar, 2017).

When carbonyl compounds, such as ketones or aldehydes, condense with primary amines (aliphatic, aromatic, or heteroaromatic), SBs are created. Because of conjugation, aromatic aldehyde-based SBs compounds are stable, whereas corresponding aliphatic aldehyde-based SBs compounds are unstable because they spontaneously polymerize. (Sadia, et al., 2021), (Mahdi and Ismail, 2022).

In literature, various techniques have been employed to prepare SBs: Gopalakrishnan et al., have reported CaO-catalyzed synthesis of SBs under microwave conditions (Gopalakrishnan et al., 2007). Devidas, et al., synthesized SBs catalyzed by P_2O_5 under free solvent conditions (Devidas et al., 2011). Furthermore, Bendale, Bhatt, and Narkhede reported the synthesis of SBs using mortar and pastel, sonicator bath (without catalyst or with a catalyst), and in the presence of U.V. Rays (Bendale, Bhatt, and Narkhede, 2011).

The SBs have been reported to be one of the most active classes of the compound possess remarkable biological activities such as antiviral, antibacterial, antifungal and anticancer, antitumor activities (Journal and Al-daffaay, 2022), (Jaber, 2023). SBs find many applications including reduction catalysts, oxidation catalysts, acid catalyst, and dye, and display a unique reactivity to metal ions (Vhanale, Deshmukh and Shinde, 2019).

Many metal complexes of SBs have been reported in literature possessing bioactivity including insecticides, pesticides antibacterial, antimalarial, antifungal, antiviral, anti-inflammatory, anticancer, antitumor, antioxidant, and anti-human immunodeficiency virus activity (Vhanale, Deshmukh and Shinde, 2019), (Pinchaipat, et al., 2021).

Zinc(II) is a component of many different enzymes and is involved in numerous physiological processes in living organisms, therefor zinc(II) is an essential element that is crucial to biological systems (Bazhina, et al., 2023), (Poole, 2017). Through research on Zn(II) coordination compounds with organic molecules, compounds with therapeutic (antifungal, antibacterial, anti-inflammatory, and anticancer) action can be obtained that may be used as building blocks for novel medications and chemo/biosensors (Slassi, et al., 2020). While some chemical compounds may be highly

ARO-The Scientific Journal of Koya University
Vol. XII, No. 1 (2024), Article ID: ARO.11486. 7 pages
DOI: 10.14500/aro.11486
Received: 26 November 2023; Accepted: 02 March 2024
Regular research paper: Published: 08 April 2024
Corresponding author's e-mail: nabaz.mohammad@soran.edu.iq

biologically active on their own, they may also be quite poisonous to the organism or have poor solubility. These compounds can be coordinated with transition metal ions, such Zn(II), to increase the therapeutic effect provided by the organic part and enhance the resultant molecules' bioavailability (Mathews, Begum and Kurup, 2020), (Bazhina, et al., 2023).

II. Experimental

Materials and Methods

All the starting materials compounds (1-4), reagents, as well as solvents, were obtained commercially and used without further purification. Thin layer chromatography (TLC) (*silica* gel on aluminum plates) was used to track the reactions' progress; ethyl acetate with toluene (1:9) was used as a solvent system, and the result was observed by UV light. The purification of the products was done by recrystallization in ethanol.^{1}H and the ^{13}C-NMR spectrum was observed by 400 and 100 MHz (Ascend) respectively. Fourier-transform infrared spectroscopy (FT-IR) Affinity-1S spectrometer Shimadzu), and melting points were taken by Stuart Scientific melting point apparatus 3. Mol.Wt.where taken by liquid chromatography–mass spectrometry Shimadzu UFLC-AB Sciex 3200 QTRAP. Finally, scanning electron microscopy (SEM) where taken by SEM Quanta agent 450.

General procedure A: Preparation of the SBs ligand (5-7) (Hajiashrafi, Zekriazadeh and Kubicki, 2020)

In a flask with a flat bottom, an equimolar mixture of benzaldehyde and aniline derivatives was added. In an acidic medium, the reaction mixture was refluxed for 7 h. TLC was used to keep track of the reaction's development. After a reaction has been completed, the solvent is slightly evaporated, the precipitate is washed with ethanol, filtered out, and the product is recrystallized in warm ethanol.

General procedure B: Preparation of the complex (8)

To a flask with a flat bottom, an equimolar mixture of compound (7) (0.0013 mol and 0.0006 mol) respectively, and zinc salt (0.0013 mol and 0.0006 mol) was added. The mixture was then heated at 78°C under reflux in ethanol for 3 h to produce a colored precipitate (8). The precipitates were afterward removed by filtering, rinsed with distilled water, and then crystallized again from ethanol.

(*E*)-1-(4-(2-nitrostyryl)phenyl)ethan-1-one (5)

General procedure A: 2-nitrobenzaldehyde 3 (0.72 g, 0.0099 mol, 1 equivalent), glacial acetic acid (2 drops) was dissolved in EtOH (20 mL), then compound 1 (0.65 g, 0.0048 mol, 1.0 equivalent) was added; gave the product 5 as a yellow color, (72%) yield, m.p./154–156°C. ^{1}H-NMR (400 MHz, DMSO-d^{6}) δ ppm: 2.52 (quintet, *J* = 1.9 Hz, DMSO), 2.6 (s, CH_3CO, 3H), 3.41 (H_2O), 6.58 (d, *J* = 7.7 Hz, 2Ar-H), 7.36 (d, *J* = 7.6 Hz, 2Ar-H), 7.79 (t, *J* = 12.3 Hz, 1Ar-H), 7.86–7.92 (m, 1Ar-H), 8.05 (d, *J* = 7.6 Hz, 1Ar-H), 8.19 (d, *J* = 7.3 Hz, 1Ar-H), 8.9 (s, CH=N); ^{13}C-NMR (100 MHz, DMSO-d^{6}) δ ppm: 22.7, 124.7, 130.3, 130.9, 131, 132, 134.3, 134.6, 134.7, 137, 148.9, 155.9, and 190.4; FT-IR (cm^{-1}): 1697 (C=N) stretching, 1651 (C=O) stretching, 1517, 1338 (NO_2) stretching (symmetric and asymmetric), *m/z* (ES+) found: MH+ 269.

(*E*)-1-(4-(4-methylstyryl)phenyl)ethan-1-one (6)

General procedure A: 4-methylbenzaldehyde 4 (0.57 g, 0.0048 mol, 1 equivalent), glacial acetic acid (2 drops) was dissolved in EtOH (20 mL), then compound 1 (0.65 g, 0.0048 mol, 1.0 equivalent) was added; gave the product 6 as a light orange, (65%) yield, m.p./139–140°C. ^{1}H-NMR (400 MHz, DMSO-d^{6}) δ ppm: 2.5 (quintet, *J* = 1.9 Hz, DMSO), 2.39 (s, Ar-CH_3, 3H), 2.58 (s, CH_3CO, 3H), 3.38 (H_2O), 7.32 (d, *J* = 8.6 Hz, 2Ar-H), 7.35 (d, *J* = 7.35 Hz, 2Ar-H), 7.87 (d, *J* = 8 Hz, 2Ar-H), 8 (d, *J* = 8.5, 2Ar-H), 8.59 (s, CH=N), 9.95 (impurities); ^{13}C-NMR (100 MHz, DMSO-d^{6}) δ ppm: 21.5, 26.9, 121.5, 129.5, 129.9, 131, 133.6, 134.4, 142.5, 156.34, 162.4, and 197.3; FT-IR (cm^{-1}): 1699 (C=N) stretching, 1670 (C=O) stretching, *m/z* (ES+) found: M+ 237.

(*E*)-2-(2-nitrostyryl)phenol (7)

General procedure A: 2-nitrobenzaldehyde 3 (2.72 g, 0.018 mol, 1 equivalent), glacial acetic acid (2 drops) was dissolved in EtOH (20 mL), then compound 2 (2 g, 0.018 mol, 1.0 equivalent) was added; gave the product 7 as a dark yellow solid, (76%) yield, m.p./106–108°C. ^{1}H-NMR (400 MHz, DMSO-d^{6}) δ ppm: ^{1}H-NMR (400 MHz, DMSO-d^{6}) δ ppm: 2.51 (quintet, *J* = 1.9 Hz, DMSO), 3.4 (H_2O), 6.87 (t, *J* = 7.5 Hz, 1Ar-H), 6.94 (d, *J* = 8 Hz, 1Ar-H), 7.14 (t, *J* = 7.7 Hz, 1Ar-H), 7.18 (d, *J* = 7.8 Hz, 1Ar-H), 7.76 (t, *J* = 7.7 Hz, 1Ar-H), 7.87 (t, *J* = 7.5 Hz, 1Ar-H), 8.11 (d, *J* = 8.1 Hz, 1Ar-H), 8.43 (d, *J* = 7.8 Hz, 1Ar-H), 8.98 (s, CH=N), 9.26 (s, =COH); ^{13}C-NMR (100 MHz, DMSO-d^{6}) δ ppm: 116.8, 120, 120.3, 124.8, 128.7, 130.2, 130.8, 132, 134, 137.8, 149.7, 151.8, 155.5; FT-IR (cm^{-1}): 3388 (OH) stretching, 1699 (C=N) stretching, 1514, 1336 (NO_2) stretching (symmetric and asymmetric), *m/z* (ES+) found: MH+ 243.

Bis(2-(((*Z*)-2-nitrobenzylidene)amino)phenoxy)zinc (8)

General procedure B: Compound 7 (0.15 g, 0.0006 mol, 1 equivalent), was dissolved in EtOH (10 mL), then zinc acetate (0.11 g, 0.0006 mol, 1.0 equivalent) was added; gave product 8 as a mustard color, (80%) yield. ^{1}H-NMR (400 MHz, DMSO-d^{6}) δ ppm: 2.51 (quintet, *J* = 1.9 Hz, DMSO), 3.41 (H_2O), 6.68 (bro.s, 1Ar-H), 6.85 (t, *J* = 7.4 Hz, 1Ar-H), 7.1 (t, *J* = 7.1 Hz, 1Ar-H), 7.27 (bro.s,1Ar-H), 7.77 (t, *J* = 8.3 Hz, 1Ar-H), 7.87 (t, *J* = 7.4 Hz, 1Ar-H), 8.18 (d, *J* = 7.8 Hz, 1Ar-H), 8.27 (bro.s,1Ar-H), 9.1 (s, CH=N); ^{13}C-NMR (100 MHz, DMSO-d^{6}) δ ppm: 113.6, 117.8, 120.4, 124.7, 124.9, 130.3, 130.9, 131.2, 132.2, 134.5, 134.7, 148.7, 164.5; FT-IR (cm^{-1}):1590 (C=N) stretching, 1516, 1334 (NO_2) stretching (symmetric and asymmetric).

General procedure B: Compound 7 (0.3 g, 0.0013 mol, 1 equivalent), KOH (0.07 g, 0.0013 mol) was dissolved in EtOH/H_2O (10 mL, 3 mL), then zinc chloride (0.17 g, 0.0013 mol, 1.0 equivalent) was added; gave the product 8 as a dark mustard color, (77%) yield. ^{1}H-NMR (400 MHz, DMSO-d^{6}) δ ppm: 2.51 (quintet, *J* = 1.9 Hz, DMSO), 3.41 (H_2O), 6.4 (bro.s, 1Ar-H), 6.6 (bro.s, 1Ar-H), 7.05

http://dx.doi.org/10.14500/aro.11486

(bro.s, 1Ar-H), 7.4 (bro.s,1Ar-H), 7.7–7.9 (m, 2Ar-H), 8.2 (bro.s, 1Ar-H), 8.4 (bro.s, 1Ar-H), 9.26 (s, CH=N); FT-IR (cm^{-1}):1589 (C=N) stretching, 1517, 1338 (NO_2) stretching (symmetric and asymmetric).

III. Results and Discussion

One of the largest risks to world health in recent decades has been the evolution of germ resistance to antibiotics. Therefore, we decided to synthesize some new expected bioactive SB derivatives.

In the present work, SBs were synthesized by the condensation of different substituted aromatic amines with a series of aromatic aldehydes (Scheme 2):

The synthesis of SBs undergoes according shown mechanism below (Scheme 3):

Furthermore, the synthesized SB (7) utilized in the creation of Zn (II) complex (8) by stoichiometrically Zn (II) acetate and $ZnCl_2$ separately (Scheme 4):

FT-IR Spectroscopy

The IR spectra of the SB and the Zn (II) complex are shown in Figs. 1 and 2. The IR stretching frequencies of free SB and SB Zn-complex have been reported in Table I. Distinct bands appear at (1651, 1670) and (1690, 1699) cm^{-1} were attributed to (C=O) stretching and azomethine (CH=N) group in compounds (5 and 6), respectively. The IR spectrum of compound (7) indicated a band at (3388) cm^{-1} for the (O-H) group, but when compound (7) was used to make complex (8a and 8b) (OH) peak disappeared and this shows that the zinc ion is coordinated over oxygen of (OH) group. The azomethine (CH=N) group in compound 7 also produces a unique band at 1699 cm^{-1}, but in the complex (8a and 8b), this peak is displaced to lower frequencies (1590, 1589) cm^{-1} respectively, demonstrating that the nitrogen atom of the azomethine group is coordinated to the metal ion too.

TABLE I
IR Spectra for Synthesized Compounds in (Cm^{-1}). 8A, When $Zn(CH_3CO_2)_2$ and 8B When $ZnCl_2$ Used

Compounds	(OH) str.	(C=N) str.	(C=O) str.	(C=C) Str.		(NO_2) str. assym. and symm.	
5	---	1690	1651	1485	1560	1338	1517
6	---	1699	1670	1512	1589	---	---
7	3388	1699	---	1480	1581	1336	1514
8a	---	1590	---	1485	1570	1516	1334
8b	---	1589	---	1485	1570	1517	1334

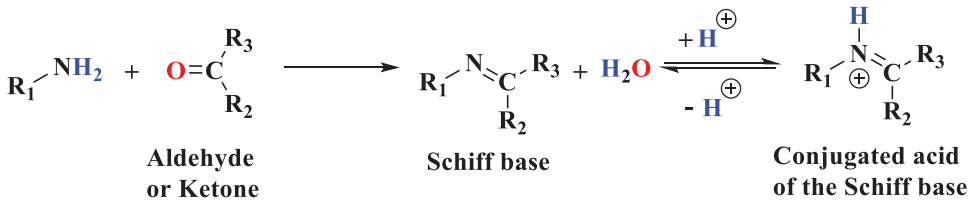

Scheme 1. General route for synthesis Schiff base (Pooja et al., 2018).

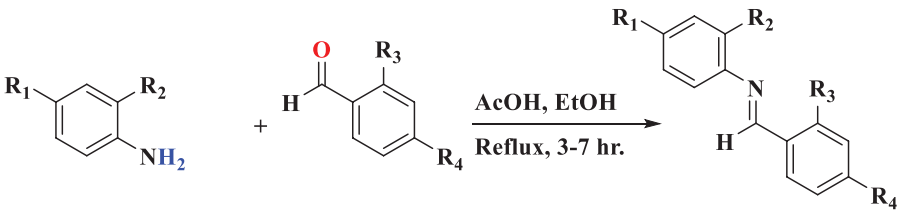

In compound 1 = R_1= CH_3CO, R_2= H
In compound 2 = R_1= H, R_2= OH
In compound 3 = R_3 = NO_2, R_4 = H
In compound 4 = R_3 = H, R_4 = Me

In compound 5 = R_1 = CH_3CO, R_2 = H, R_3 = NO_2 , R_4 = H
In compound 6 = R_1 = CH_3CO, R_2 = H, R_3 = H , R_4 = Me
In compound 7 = R_1 = H, R_2 = OH, R_3 = NO_2 , R_4 = H

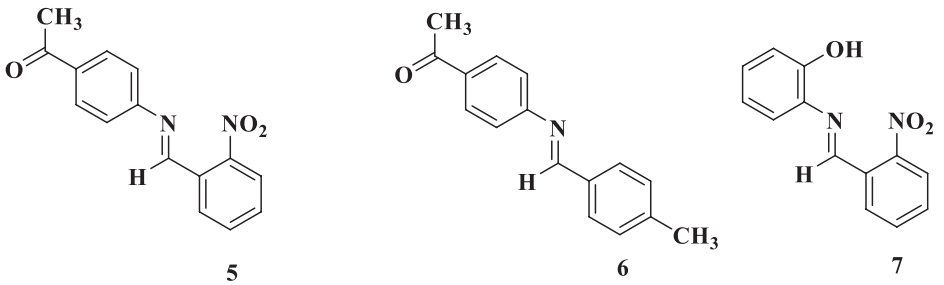

Scheme 2. Synthesis of Schiff base.

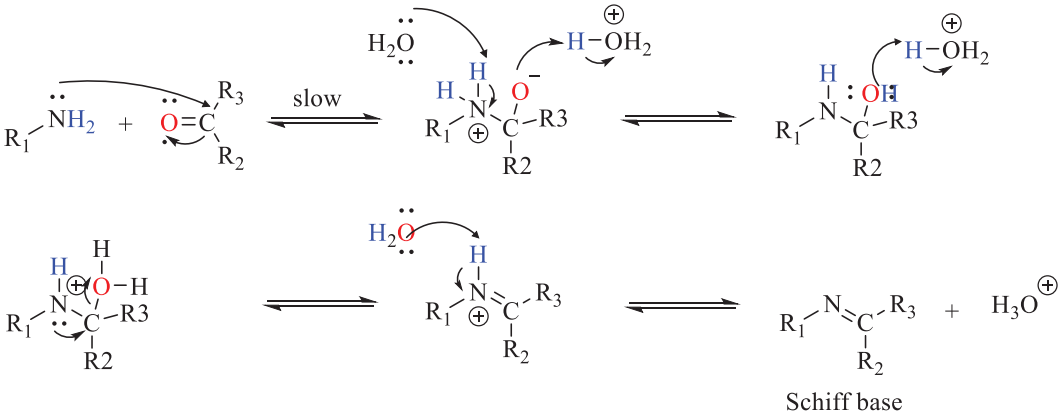

Scheme 3. Suggested mechanism for synthesis of Schiff base.

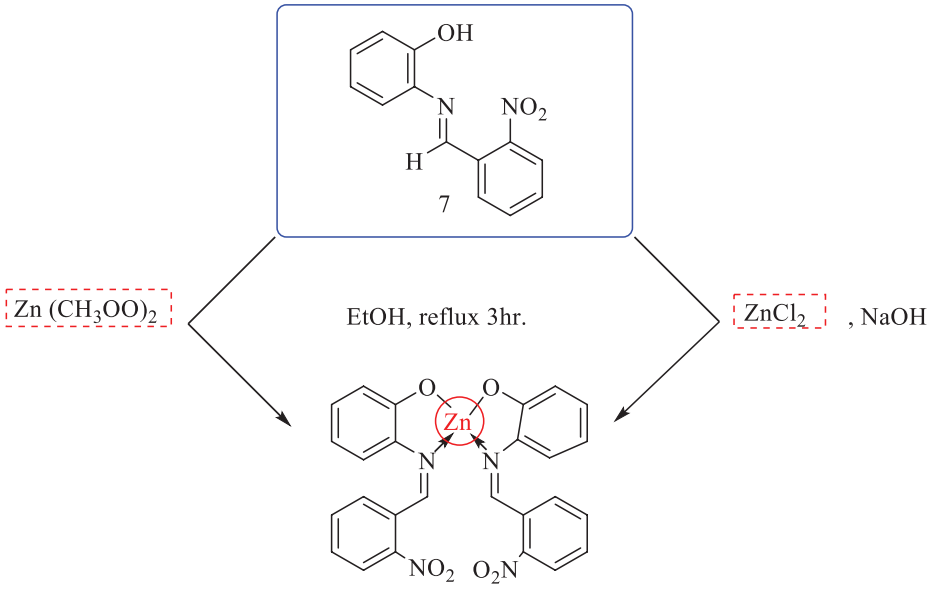

8

Scheme 4. Synthesis of Schiff base zinc complexes.

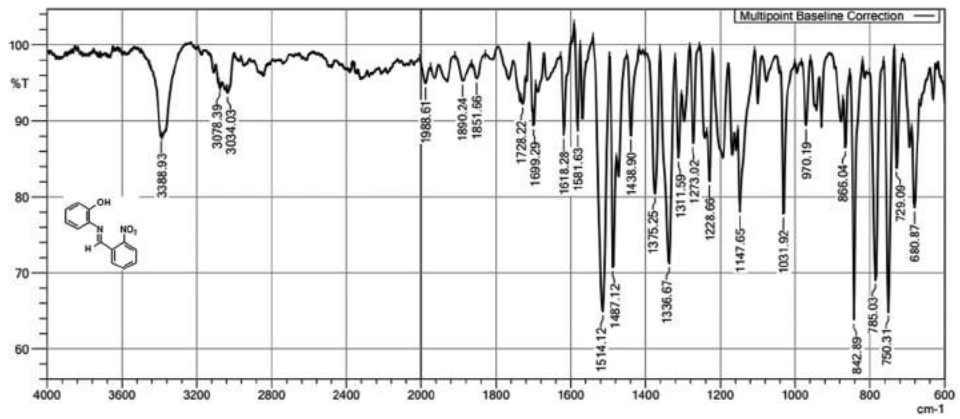

Fig. 1. Fourier-transform infrared spectroscopy for Schiff base 7.

The structures of the compounds (5-8) were evaluated by ^{1}H-NMR spectra Figs. 3 and 4. Imine protons (CH=N) in ^{1}H-NMR spectra of compounds (5 and 6) appeared as a singlet at (8.9) and (8.59) ppm, respectively. Furthermore, the imine proton in the compound (7) appears at (8.98) ppm, while the azomethine proton of the zinc complex

http://dx.doi.org/10.14500/aro.11486

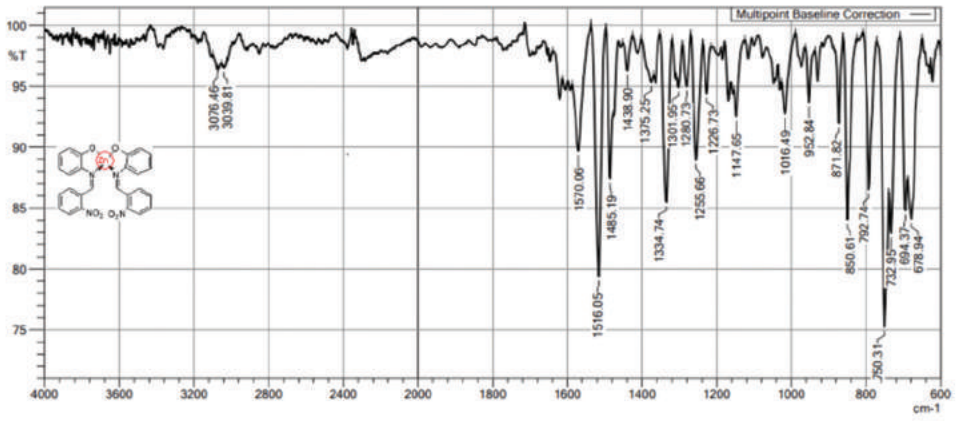

Fig. 2. Fourier-transform infrared spectroscopy of Schiff base zinc complex 8 When $Zn(CH_3CO_2)_2$ used as the reagent.

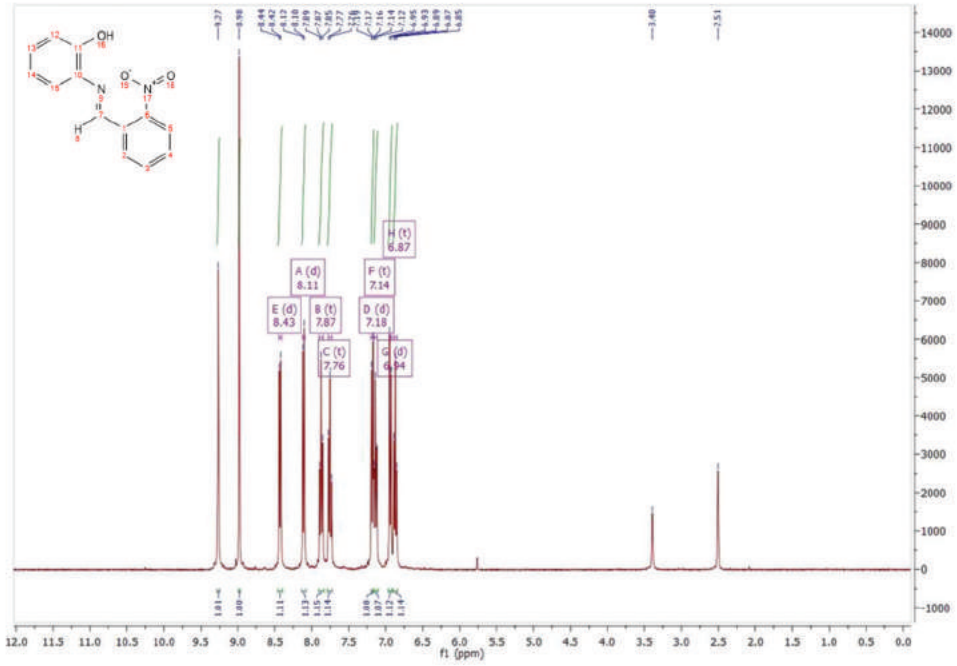

Fig. 3. ^{1}H-NMR spectroscopy for Schiff base 7.

TABLE II
ILLUSTRATES THE PHYSICAL PROPERTIES AND YIELDS OF THE SYNTHESIZED COMPOUNDS

Yield %	Color	m.p. in °C	Compounds
72	Yellow color onion	154–156	5
65	Light orang	139–140	6
76	Dark yellow-solid	106–108	7
80	Mustard color	---	8a
77	Dark Mustard color	---	8b

TABLE III
BIOLOGICAL ACTIVITY OF SYNTHESIZED COMPOUNDS IN MM

Bacterial species			10 mg/1 mL CH_2Cl
Candida albicans	*Escherichia coli*	*Staphylococcus aureus*	Samples
-	10	-	5
-	-	-	6
15	7	-	7
17.5	8	-	8

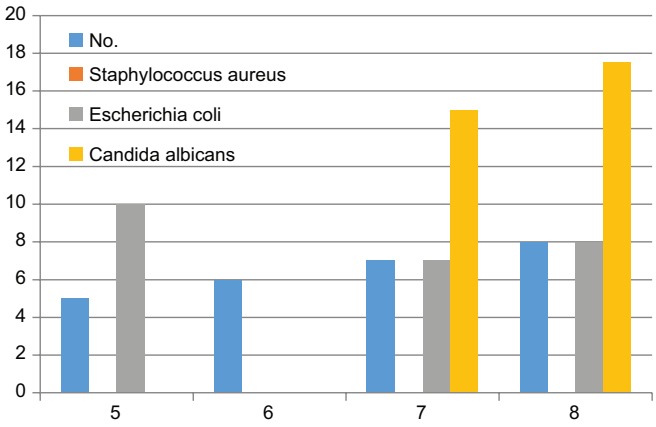

Diagram 1. Biological activity of synthesized compounds.

appears at (9.1) ppm. The predicted range of (6.4–8.4) ppm is where the aromatic ring protons are found.

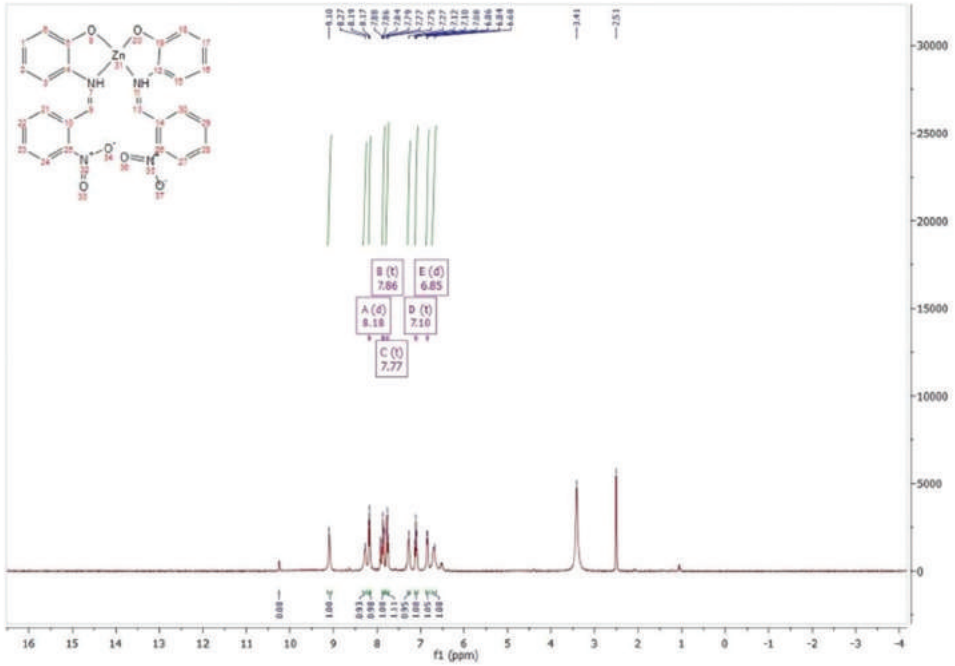

Fig. 4. ^{1}H-NMR of Schiff base zinc complex 8 When $Zn(CH_3CO_2)_2$ used.

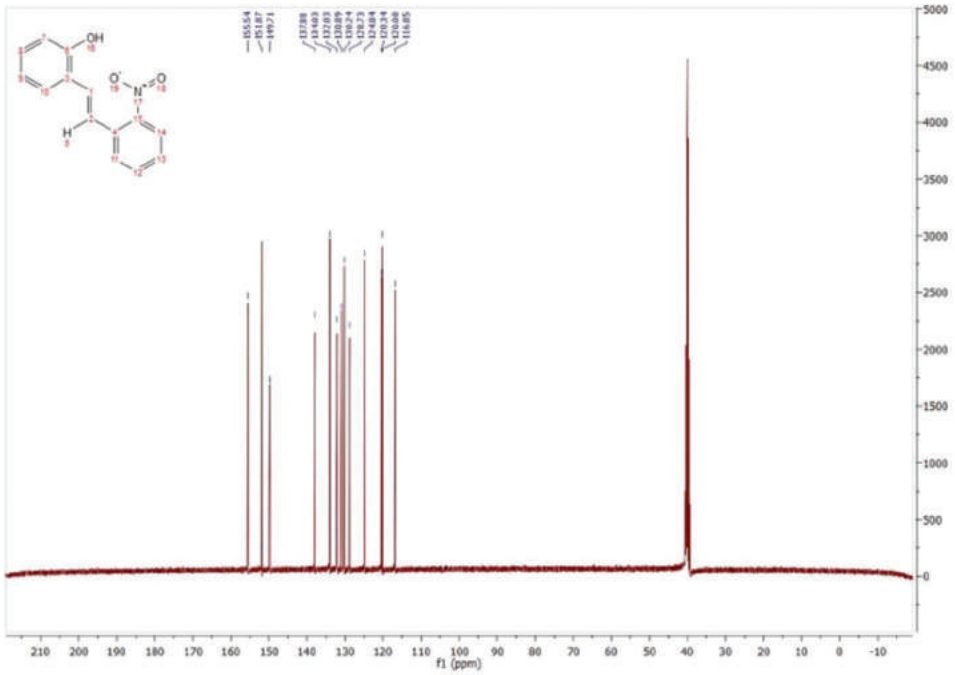

Fig. 5. ^{13}C-NMR spectroscopy for Schiff base 7.

Furthermore, using ^{13}C-NMR the signal at (155.9), (162.4) and (155.5) were attributed to azomethine carbon in compounds (5-7) Fig. 5 for compound 7.

Table I IR spectra for synthesized compounds in (cm^{-1}). 8a, when $Zn(CH_3CO_2)_2$ and 8b when Zn used

Table II illustrates the physical properties and yields of the synthesized compounds.

B. SEM Analysis

The SEM method was employed to examine the morphology of the SB no. 7 and zinc(II) complex no. 8. The SEM picture of the SB (7) has a sheet mass structure; however, Zn(II) complex (8) has appeared as a sphere on a sheet is shown in Fig. 6.

Table III shows the results of the study on the antibacterial and antifungal properties of synthetic compounds against *Staphylococcus aureus*, *Escherichia coli* bacteria and *Candida albicans* fungus.

Diagram 1 clarifies the inhibition activity of the compounds (5, 7, and 8) against *S. aureus*, *E. coli* bacteria, and *C. albicans* fungus with different inhibition zones starting from 7 to 17.5 mm.

http://dx.doi.org/10.14500/aro.11486

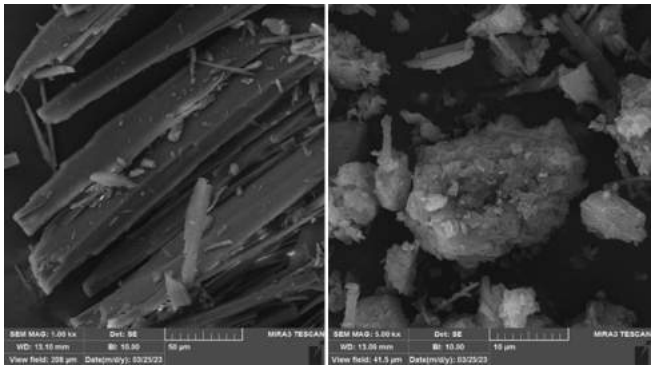

Fig. 6. Scanning electron microscopy of compounds 7 and 8.

IV. Conclusion

The study has demonstrated a straightforward method for synthesizing biologically active and non-toxic SB compounds and zinc(II) SB complexes. These newly developed chemicals exhibited inhibitory effects against *E. coli* and *C. albicans*. Furthermore, the ligand was found to coordinate with the metal ion via phenolic oxygen and azomethine nitrogen.

V. Acknowledgment

The cooperation of the Faculty of Science staff at the Soran University in Soran, Erbil Kurdistan Region, Iraq, is appreciated.

References

Bazhina, E.S., Bovkunova, A.A., Shmelev, M.A., Korlyukov, A.A., Pavlov, A.A., Hochvaldov, L., Kopel, P., Eremenko, L., and Kiskin, M.A., 2023. Inorganica chimica acta zinc(II) and copper(II) complexes with N-substituted imines derived from 4-amino-1, 2, 4-triazole : Synthesis, crystal structure, and biological activity. *Inorganica Chimica Acta*, 547, p.121359.

Bekdemir, Y., and Efil, K., 2014. Microwave assisted solvent-free synthesis of some imine derivatives. *Organic Chemistry International*, 2014, pp.816487.

Bendale, A.R., Bhatt, R., and Narkhede, S., 2011. Scholars research library. *Der Pharma Chemica*, 3(2), pp.34-38.

Devidas, S.M., Quadri, S.H., Kamble, S.A., Syed, F.M., and Vyavhare, D.Y., 2011. Novel one-pot synthesis of Schiff base compounds derived from different Diamine and aromatic aldehyde catalyzed by P_2O 5/SiO_2 under free-solvent condition at room temperature. *Journal of Chemical and Pharmaceutical Research*, 3, pp. 489-495.

Gopalakrishnan, M., Sureshkumar, P., Kanagarajan, V., and Thanusu, J., 2007. New environmentally-friendly solvent-free synthesis of imines using calcium oxide under microwave irradiation. *Research on Chemical Intermediates,* 33(6), pp. 541-548.

Hajiashrafi, T., Zekriazadeh, R., and Kubicki, M., 2020. Synthesis, characterization, and crystal structure analysis of group IIB coordination compounds containing N,N'-bidentate chelating Schiff-base ligand. *Journal of Coordination Chemistry*, 73(20-22), pp.3044-3061.

https://doi.org/10.1080/00958972.2020.1830072

Jaber, Z.A., 2023. Synthesis, Theoretical study, and Biological evaluation of some metal ions with ligand "Methyl-6-[2-(4-hydroxyphenyl) -2-((1-phenylethylidene) amino) acetamido]-2,2-dimethyl-5-oxo-1-thia-4-azabicyclo [3.2.0] heptane-3-carboxyylate. *Baghdad Science Journal*, 20, pp.102-113.

Journal, B.S., and Al-Daffaay, R.K., 2022. Preparation-and spectroscopic characterization of transition metal complexes with schiff base 2-[1-(1H-indol-3-yl) ethylimino)methyl. *Baghdad Science Journal*, 19, pp.1036-1044.

Kolapwar, B.G., 2017. Study of schiff base compounds and its derivatives. *Anveshana's International Journal of Research in Pharmacy and Life Sciences*, 2(1), pp.15-18.

Liang, X., Zhao, X., Guo, A., Wang, X., Rong, M., Chang, L., Sun, Z., and Jin, X., 2023. Synthesis, crystal structure and antibacterial activity of zinc(II) complexes with Schiff bases derived from 5-fluorosalicylaldehyde. *Journal of Coordination Chemistry*, 76(2), pp.307-321.

Mahdi, A.S., and Ismail, A.H., 2022. New tetra-dentate schiff base ligand N2O2 and its complexes with some of metal ions : Preparation, identification, and studying their enzymatic and biological activities. *Baghdad Science Journal*, 19, pp.155-167.

Mathews, N.A., Begum, P.M.S., and Kurup, M.R.P., 2020. Synthesis, characterization, biological screening and molecular docking of Zn(II) and Cu(II) complexes of 3,5-dichlorosalicylaldehyde-N4-cyclohexylthiosemicarbazone. *Applied Organometallic Chemistry*, 34(1), pp.1-14.

Murhekar, M.M., and Khadsan, R.E., 2011. Synthesis of schiff bases by organic free solvent method. *Journal of Chemical and Pharmaceutical Research*, 3(6), pp.846-849.

Muzammil, K., Trivedi, P., and Khetani, D., 2015. Synthesis and characterization of Schiff base m-nitro aniline and their complexes. *Research Journal of Chemical Sciences*, 5(5), pp. 52-55.

Omidi, S., and Kakanejadifard, A., 2020. A review on biological activities of Schiff base, hydrazone, and oxime derivatives of curcumin. *RSC Advances*, 10(50), pp.30186-30202.

Pinchaipat, B., Khudkham, T., Wongsuwan, S., and Chotima, R., 2021. The novel zinc(II) complex with dibromo substituted Schiff base and its biological activity. *Materials Letters*, 293, p.129749.

Pooja, B., Lalit, M., Richa, G., and Pramanik, T., 2018. Microwave assisted green synthesis of Schiff bases in lemon juice medium. *Research Journal of Chemistry and Environment*, 22(8), pp. 19-23.

Poole, K., 2017. At the nexus of antibiotics and metals: The impact of Cu and Zn on antibiotic activity and resistance. *Trends in Microbiology*, 25(10), pp.820-832.

Sadia, M., Khan, J., Naz, R., Zahoor, M., Wadood Ali Shah, S., Ullah, R., Naz, S., Bari, A., Majid Mahmood, H., Saeed Ali, S., Ansari, S.A., and Sohaib, M., 2021. Schiff base ligand L synthesis and its evaluation as anticancer and antidepressant agent. *Journal of King Saud University-Science*, 33(2), p.101331.

Shah, S.S., Shah, D., Khan, I., Ahmad, S., Ali, U., and Rahman, A.U., 2020. Synthesis and antioxidant activities of schiff bases and their complexes: An updated review. *Biointerface Research in Applied Chemistry*, 10(6), pp.6936-6963.

Shammout, M.J.A., Jazzazi, T.M.A., Alomari, M., Daoud, S., and Talib, W.H., 2021. Synthesis, computational, anticancerous and antiproliferative effects of some copper, manganese and zinc complexes with ligands derived from symmetrical 2,2'-diamino-4,4'-dimethyl-1,1'-biphenyl-salicylaldehyde. *Polish Journal of Chemical Technology*, 10(4), pp.7-15.

Slassi, S., El-Ghayoury, A., Aarjane, M., Yamni, K., and Amine, A., 2020. New copper(II) and zinc(II) complexes based on azo schiff base ligand: Synthesis, crystal structure, photoisomerization study and antibacterial activity. *Applied Organometallic Chemistry*, 34(4), pp.1-10.

Vhanale, B.T., Deshmukh, N.J., and Shinde, A.T., 2019. Synthesis, characterization, spectroscopic studies and biological evaluation of schiff bases derived from 1-hydroxy-2-acetonapthanone. *Heliyon*, 5(11), p.e02774.

Yousif, E., Majeed, A., Al-Sammarrae, K., Salih, N., Salimon, J., and Abdullah, B., 2017. Metal complexes of schiff base: Preparation, characterization and antibacterial activity. *Arabian Journal of Chemistry*, 10, pp.S1639-S1644.

Oxidative Stress Assessment in Colorectal Cancer Patients: Erbil Population Study

Vyan A. Qadir[1,*] and Kamaran K. Abdoulrahman[2]

[1]Department of Chemistry, Faculty of Science and Health, Koya University, Koya KOY45, Kurdistan Region - F.R. Iraq

[2]Department of Chemistry, College of Science, Salahaddin University-Erbil, Kurdistan Region - F.R. Iraq

***Abstract*—Colorectal cancer (CRC), a global health challenge, exhibits rising incidence in low-income nations due to lifestyle changes. Oxidative stress, indicated by reactive oxygen species imbalance and Malondialdehyde (MDA), is linked to CRC. This study investigates oxidative stress markers, antioxidant enzymes, genetic markers, cellular regulation markers, and Vitamin E in CRC patients in Erbil. Ninety CRC patients and 30 healthy controls provided blood samples, processed and stored at –20°C. Enzyme-linked immunosorbent assay kits quantified oxidative stress, antioxidant markers, and Vitamin E. Oxidative stress markers showed significant differences, with elevated MDA and 8-hydroxy-2'-deoxyguanosine levels in patients. Nitrotyrosine exhibited lower expression in patients. Antioxidant enzymes glutathione peroxidase and superoxide dismutase were enhanced in patients, while glutathione (GSH), glutathione reductase and catalase levels were significantly lower in patients. The genetic marker KRAS showed a substantial decrease in patients (<0.0001) but both adenomatous polyposis coli (APC) and CRC antigen (CCA) were higher. Serum vitamin E levels were significantly lower in patients (71.78 ± 6.368) compared to controls (142.3 ± 4.828, $p < 0.0001$). Elevated oxidative stress, altered enzymatic activity, significantly lower expression of KRAS, and higher expression of APC and CCA in the patient group. Furthermore, reduced Vitamin E levels were observed in the patient group, highlighting potential challenges in antioxidant defense.**

***Index Terms*—Colorectal cancer, Colorectal cancer patients, Erbil city, Oxidative stress markers, Vitamins.**

I. Introduction

Colorectal cancer (CRC) is one of the most common malignancy in the world which poses a significant global health challenge, prompting extensive exploration into the molecular intricacies underlying its development (Zińczuk, et al., 2019a; Janion, et al., 2020a), and (Beniwal, et al., 2023). Over 50% of cases are diagnosed in countries with a high or very high human development index. The rising incidence in low-income countries is linked to urbanization (Western lifestyles) or a shift in dietary habits, marked by increased consumption of animal fat and simple sugars (Fedacko, et al., 2019, Janion, et al., 2020a), and (Lewandowska, et al., 2022). In 2017, there were 1.8 million global CRC cases, with an age-standardized incidence rate of 23.2/100,000 person-years, marking a 9.5% increase from 1990 to 2017 (Lewandowska, et al., 2022). The precise causes of colorectal neoplasms remain unclear, though extensive research has identified various risk factors (Wong, et al., 2019). These include nonmodifiable elements such as age and heredity, along with modifiable factors linked to lifestyle and the environment (Wang, et al., 2019). Early diagnosis is crucial in detecting CRC during its development, which typically spans from several to numerous years (Sawicki, et al., 2021).

Oxidative stress is characterized by an imbalance between reactive oxygen species (ROS) and antioxidant defenses (Zińczuk, et al., 2020) and (Basak, Uddin, and Hancock, 2020). A substantial and compelling body of evidence indicates a robust association between oxidative stress and its role in the development and progression of CRC, marked by elevated levels of ROS in chronic gastrointestinal tract diseases (Basak, Uddin, and Hancock, 2020) and (Rasool, et al., 2021). Malondialdehyde (MDA), a prominent and deleterious byproduct arising from lipid peroxidation, represents a common and harmful consequence capable of causing cellular damage by interacting with free amino groups in proteins and nucleic acids (Rašić, et al., 2018). Particularly noteworthy is its mutagenic activity (Chatterjee and Walker, 2017). Elevated MDA levels serve as a recognized marker of oxidative stress, providing reliable indicators of damage to cellular membranes and offering valuable insights into the extent of oxidative stress in cancer (Marrocco, Altieri and Peluso, 2017) and (Janion, et al., 2022). Deoxyribonucleic acid (DNA) Damage 8-hydroxy-2'-deoxyguanosine (8-OHdG), serves as a crucial marker of oxidative damage to DNA (Borrego, et al., 2013). Marked elevation in oxidative stress is a prominent feature across diverse cancer types, substantiated by the presence of heightened levels of oxidized DNA base 8-OHdG and lipid peroxidation products in clinical specimens (Demirci-Cekic,

ARO-The Scientific Journal of Koya University
Vol. XII, No. 1 (2024), Article ID: ARO.11526, 9 pages
DOI: 10.14500/aro.11526
Received: 25 January 2024; Accepted: 24 April 2024
Regular research paper: Published: 10 May 2024
Corresponding author's e-mail: vyan.asad@koyauniversity.org

et al., 2022). Nitrotyrosine (NT) is a marker of oxidative stress resulting from the reaction between reactive nitrogen species (RNS), such as peroxynitrite and tyrosine residues in proteins (Kreutzmann, et al., 2023). The existence of NT within proteins indicates a heightened level of oxidative modifications to proteins, promoting processes that lean toward pro-oxidation (Demasi, et al., 2021) and (Bartesaghi and Radi, 2018). Examination of human biopsies from individuals with colitis and colon cancer indicated heightened protein expression levels of inducible nitric oxide synthase, with a corresponding marked increase in NT expression (Gochman, et al., 2012). This occurs as NT serves as an indicator of oxidative stress arising from the interaction between RNS, including peroxynitrite, and tyrosine residues present in proteins (Bandookwala and Sengupta, 2020).

On the other hand, in response to elevated levels of ROS induced by environmental factors, cells deploy a variety of antioxidants, thereby establishing antioxidative systems to counteract oxidative stress (Gochman, et al., 2012). This intricate balance between oxidants and antioxidants is essential for maintaining cellular homeostasis (He, et al., 2017). The GSH system represents a pivotal cellular antioxidant network, actively collaborating to both uphold and synergize the redox balance (Lv, et al., 2019). This intricate system plays a crucial role in neutralizing ROS and maintaining the cellular redox equilibrium, highlighting its significance in cellular defense against oxidative stress (Lv, et al., 2019) and (Kennedy, et al., 2020). Moreover, deviations in the levels of ROS-scavenging enzymes, including superoxide dismutase (SOD), glutathione peroxidase (GPx), and peroxiredoxin, serve as markers of disrupted redox homeostasis within tumor cells (Mohan, et al., 2022). Elevated GPX1 levels may indicate an increased antioxidant response, suggesting a cellular attempt to counteract oxidative stress (Nalkiran, et al., 2015). SOD is a primary defense against oxidative stress, catalyzing the breakdown of superoxide radicals (Zińczuk, et al., 2019b). Higher SOD levels may suggest an enhanced cellular response to oxidative stress, potentially reflecting an adaptive mechanism against ROS (Irawan, et al., 2020). Excessive free radicals in cells can induce damage to DNA, proteins, and cell membranes, with antioxidants such as Vitamins A, C, and E, β-carotene, and selenium playing a crucial role in reducing oxidative stress by neutralizing these harmful free radicals (Katona and Weiss, 2020). Glutathione reductase (GR) is an enzyme that plays a crucial role in maintaining the cellular antioxidant defense by reducing oxidized glutathione (GSSG) back to its reduced form (GSH), in living cells (Raj Rai, et al., 2021). Conversely, the quantity of GSH and its ratio to the oxidized form plays a crucial role in regulating the activity of other redox-sensitive proteins, implying a fundamental role in controlling cellular function (Lorestani, et al., 2018). Given the impact of oxidative stress on the development of malignancies, alterations in the expression and activity of the GR enzyme may be pivotal in cancer progression (Cecerska-Heryć, et al., 2021). Catalase (CAT) (natural antioxidant) is an enzyme that catalyzes the breakdown of hydrogen peroxide (H_2O_2) into water and oxygen, playing a crucial role in protecting cells from oxidative damage (Bratovcic, 2020). CAT is advantageous for breaking down hydrogen peroxide and generating oxygen in solid cancers like CRC (Najafi, et al., 2023).

KRAS is a proto-oncogene that, when mutated, can become an oncogene and contribute to the development of various cancers, including CRC (Arrington, et al., 2012) and (Zhu, et al., 2021). In addition, the majority of studies conducted in Western nations explore the correlation between the risk of CRC and both Vitamin A and Vitamin E (Luo, et al., 2019) and (Alves Ribeiro, et al., 2022). The adenomatous polyposis coli (APC) protein functions as a tumor suppressor and plays a crucial role in the canonical (β-catenin-dependent) (Aghabozorgi, et al., 2019). Beyond its canonical functions, APC has the capacity to independently inhibit the initiation and progression of colorectal tumors (Hankey, Frankel, and Groden, 2018). In addition, APC contributes to various cellular processes, including chromosome segregation, establishment of cellular polarity and migration, and repression of DNA replication, highlighting its multifaceted roles in maintaining cellular homeostasis and preventing tumorigenesis (Daly, 2013) and (Aghabozorgi, et al., 2019). CRC antigen (CCA) is a marker associated with CRC, this antigen is often used as a diagnostic tool in assessing the presence and progression of CRC (Li, et al., 2018).

This study aims to investigate various markers in CRC patients in Erbil city, focusing on assessing key parameters, markers of oxidative stress: Such as 8-OHdG, NT, and MDA, antioxidant enzymes: Such as GSH, GPX1, SOD, CAT, GR, and genetic factors including: (KRAS oncogene), APC, and CCA. Furthermore, the levels of Vitamin E (VIT E).

II. Materials and Methods

A. Patients and Sample Collection

A total of 90 patients diagnosed with CRC were recruited for this study from Rezgari Hospital and Nanakali Hospital in Erbil city. Employing a case–control design, blood samples were systematically collected from CRC patients between April 15, 2022, and April 1, 2023. In addition, 30 healthy subjects were included as a control group for comparative analysis. The inclusion criteria for all patients involved the initial suspicion of diagnosis based on endoscopic observations, followed by confirmation through histopathological examination of colonic biopsies obtained during endoscopy. All enrolled patients were ultimately diagnosed with adenocarcinoma, presenting with varying degrees of differentiation.

B. Sample Processing and Storage

Briefly, after an overnight fast, blood samples were obtained using an ethylenediaminetetraacetic acid vacutainer for the separation of plasma specifically for MDA measurement. Following sample collection, the blood samples underwent centrifugation at 3.000 rpm for 10 min. In post-centrifugation, samples were meticulously processed and subsequently stored at –20°C. This cryopreservation step

ensured the preservation of sample integrity for subsequent analysis.

C. Analytical Techniques

The determination of carcinoembryonic antigen (CEA) levels was conducted using a Roche kit (Roche Company, Germany). Serum levels of oxidative stress markers, including: 8-OHdG, MDA, and NT. Furthermore, the concentration of the antioxidant markers was determined including: GPX1, SOD, CAT, and GR. Finally, the concentration level of both genetic markers and Vitamin E (VIT E) was reported.

D. Enzyme-linked Immunosorbent Assay (ELISA) Analysis

For the quantitative assessment of each enzyme and antigen, specific ELISA kits were employed. These kits were sourced from SunLong Biotech Co., Ltd, Zhejiang, China, ensuring a standardized and precise approach to biomarker quantification. The microplate reader utilized for ELISA analysis was sourced from BioTek Company, USA.

E. Statistical Analysis

Analysis of the data was performed utilizing Statistical Package for the Social Sciences software version 24 (IBM Corp., Armonk, NY, USA). For the comparison of unpaired data, the Student's t-test was employed to assess the uptake values. A significance level of $p < 0.05$ was applied, ensuring a stringent criterion for determining the statistical significance of observed differences (Giovanni and Francesco, 2020).

III. Result and Discussion

A. Demographic and Clinical Characteristics

In Table I, the results reveal that the mean age for the CRC group was 55.65 years, slightly higher than the control group at 50.10 years, showing no significant difference ($p = 0.154$). Gender distribution indicated a higher percentage of females in the CRC group (56.41%) compared to the control group (42.86%), (Fig. 1a). The average body mass index for individuals with CRC was 26.12 kg/m². Regarding cancer staging, the majority of CRC cases were in Stage IV (67.95%), followed by Stage III (29.48%), and a small percentage in Stage II (2.564%), (Fig. 1b). The current study uncovered a higher incidence of CRC in females. This result contradicts previous findings that indicated an age-related increase in the prevalence of CRC, which is typically higher in males (Arnold, et al., 2017), (Patel, et al., 2018), and (Janion, et al., 2020b). Furthermore, our results do not align with those of another study conducted in Iraq, which asserted a male predominance in CRC (Ibrahem, Ahmed and Zangana, 2022). Another study in Iraq similarly noted a slight male predominance (Alrubaie, Alkhalidi, and Abd-Alhusain, 2019).

TABLE I
Demographic and Clinical Characteristics of Colorectal Cancer Patients Compared to the Control Group

Characteristics	Study groups		p-value
	Colorectal cancer (n=90)	Control group (n=30)	
Age (yrs.) Mean±SE	55.65±1.752	50.10±3.656	0.154
Geneder distribution No. (%)			
Male	43 (43.59%)	27 (57.14%)	
Female	57 (56.41%)	23 (42.86%)	
BMI (kg/m²) Mean±SE	26.12±0.815		
TNM stage of cancer			
Stage (IV) 67.95%			
Stage (III) 29.48			
Stage (II) 2.564			
CEA at the time of case diagnosis mean±SEM	35±10.38 (ng/mL)		
CA19.9 at the time of case diagnosis mean±SEM	78.13±16.67 (ng/mL)		

CEA: Carcinoembryonic antigen, BMI: Body mass index

This study used CEA and CA19-9 for the diagnosis and monitoring of CRC in patients of Erbil city. The levels of CEA at the time of case diagnosis were 35 ± 10.38 ng/mL, while carbohydrate antigen 19–9 (CA19.9) levels were 78.13 ± 16.67 ng/mL. CEA and CA19-9 have been extensively investigated for their utility in screening, post-diagnosis follow-up, and treatment monitoring in CRC patients; current guidelines have traditionally endorsed the exclusive use of CEA for prognosis determination, surveillance post-curative resection, and treatment monitoring (Lakemeyer, et al., 2021). Despite CA19-9 not being officially recommended as a valuable marker in CRC patients, assessing pre-operative CEA and CA19-9 levels remains crucial for ongoing monitoring and treatment, with CEA specifically acknowledged as a valuable predictor of overall survival according to guidelines (Hidaka, et al., 2019) and (Lakemeyer, 2023).

B. Oxidative Stress Markers

MDA, the ultimate product of lipoperoxidation, reacts with several nucleic acids, resulting in MDA-DNA oxidation products with pro-mutagenic properties that induce mutations in oncogenes/tumor suppressor genes in human tumors (Zińczuk, et al., 2019b). Oxidative DNA damage, pivotal in the onset and advancement of diseases such as CRC, is closely tied to ROS (Kang, et al., 2023). The inherent instability of ROS hinders precise measurements, leading to the utilization of stable metabolites like 8-OHdG as reliable indicators of oxidative stress and cancer, commonly

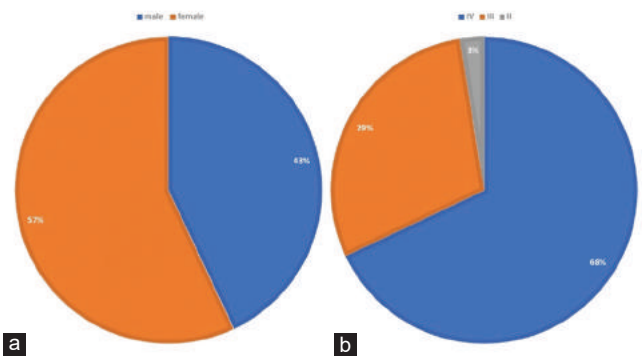

Fig. 1. (a) Represents gender distribution, (b) Represents stages of cancer.

http://dx.doi.org/10.14500/aro.11526

employed to assess DNA damage in individuals exposed to carcinogens like cigarettes and asbestos (Jelic, et al., 2021).

MDA: MDA levels were significantly elevated in the patient group (1179 ± 74.38 ng/mL, n = 32) compared to the control group (844.1 ± 75.92 ng/mL, n = 40) with a p = 0.0028, suggesting increased lipid peroxidation and oxidative stress, as shown in (Fig. 2).

8-OHdG: The patient group (5682 ± 133.1 ng/mL, n = 32) showed significantly higher (8-OHdG) levels compared to the control group (4783 ± 196.7 ng/mL, n = 39) with a p = 0.0006, as shown in (Fig. 3).

NT: as presented in (Fig. 4), NT showed significant differences (p = 0.0313) between the patient group (19.59 ± 1.339 pg/mL, n = 32) and the control group (25.34 ± 2.301 pg/mL, n = 32). These differences, as indicated by the respective p-values, show lower expression parameters in the patient group.

According to the results, CRC patients exhibited significantly elevated oxidative stress markers including MDA levels and 8-OHdG. Furthermore, it indicates a significant difference in NT levels between the control group (25.34 ± 2.301 pg/mL) and the patient group (19.59 ± 1.339 pg/mL), with a p = 0.0313. These findings align with those of other studies, indicating significantly higher levels of MDA in colorectal patients compared to the control group (Zińczuk, et al., 2019b). Conversely, in a study conducted in Iraq by (Balaky, 2023), the increase in 8-OHdG was non-significant (p = 0.054). The previous study concluded that concentrations of peroxynitrite, and NT were considerably higher in CRC tissue than in normal mucosa, (p < 0.0009) and p = 0.0004, respectively (Zińczuk, et al., 2021).

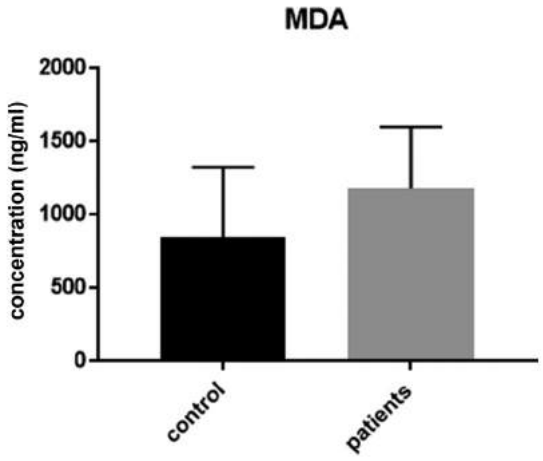

Fig. 2. Malondialdehyde levels in colorectal cancer patients versus control.

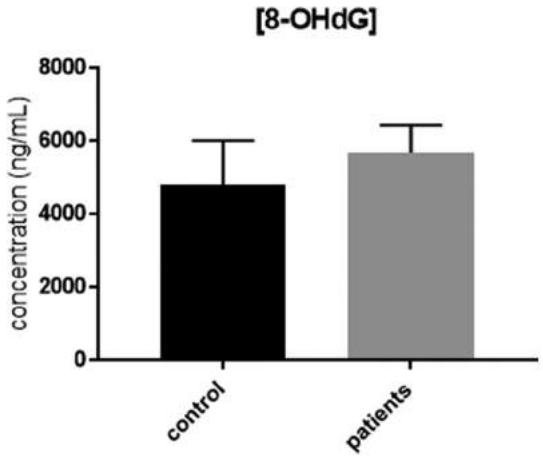

Fig. 3. Circulating concentration of 8-hydroxy-2'-deoxyguanosine.

C. Antioxidant Enzymes

Gpx-1, an antioxidant enzyme, is implicated in cancer development and progression, regulating various cellular processes. The previous study revealed that the first to assess Gpx-1 in European colon adenocarcinoma patients, found high Gpx-1 expression in 78% of specimens, primarily in the cytoplasm, associated with distinct cellular compartments (Zhao, et al., 2022). Statistical analysis revealed significant correlations between elevated Gpx-1 levels and tumor characteristics, suggesting its potential as a prognostic biomarker (Wei, et al., 2020). Specifically, high Gpx-1 expression was significantly associated with tumor histological grade, depth of invasion, angioinvasion, and PCNA immunohistochemical expression (Brzozowa-Zasada, et al., 2023). Notably, Gpx-1 levels varied across tumor grades and stages, emphasizing its diverse roles in different cancer contexts (Borkowska, et al., 2022) and (Brzozowa-Zasada, et al., 2023). SOD, a crucial antioxidant enzyme, showed significantly increased activity in CRC patients, suggesting an adaptive response to elevated ROS formation (Gopčević, et al., 2013) and (Bardelčíková, Šoltys and Mojžiš, 2023). In addition, patients with CRC displayed higher concentrations of uric acid, a key non-enzymatic antioxidant, emphasizing the reinforcement of the antioxidant barrier as a fundamental defense mechanism against heightened free radical production and oxidative stress (Bardelčíková, Šoltys, and Mojžiš, 2023).

Table II and Figs. 5-9 highlight significant distinctions between the control and patient groups, particularly concerning

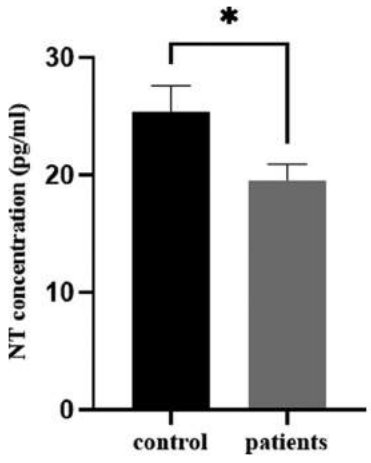

Fig. 4. Comparison of oxidative stress-related parameter between control and patient groups in (Nitrotyrosine).

antioxidant enzymes and key parameters. Specifically, GSH levels were lower in the patient group (66.84 ± 5.072) compared to the control group (89.11 ± 5.226), with a p = 0.0034. The patient group exhibited significantly higher GPX1 levels (3.395 ± 1.129 ng/mL, n = 16) compared to the control group (1.783 ± 0.1248 ng/mL, n = 48) with a p = 0.0203, indicating an enhanced antioxidant response. SOD levels were significantly higher in the patient group (2.099 ± 0.2936 ng/mL, n = 47) compared to the control group (0.9832 ± 0.06143 ng/mL, n = 24) with a p = 0.0089, indicating an enhanced response to oxidative stress. Noteworthy differences were observed in the levels of GR and CAT between the control and patient groups. The control

TABLE II
Comparison of Oxidative Stress-Related Enzymes in Control and Colorectal Cancer Groups

Parameters	Control group Mean±SEM	Patient group Mean±SEM	p-value
GSH	89.11±5.226, n=35	66.84±5.072, n=31	0.0034
GPX1 (ng/mL)	1.783±0.1248, n=48	3.395±1.129, n=16	0.0203
SOD (ng/mL)	0.9832±0.06143, n=24	2.099±0.2936, n=47	0.0089
GR (pg/mL)	388.9±75.87	145.5±19.13	<0.0001
CAT (pg/mL)	0.6282±0.06614	0.4272±0.01397	<0.0001

GPX1: Glutathione peroxidase, SOD: Superoxide dismutase, CAT: Catalase, GR: Glutathione reductase

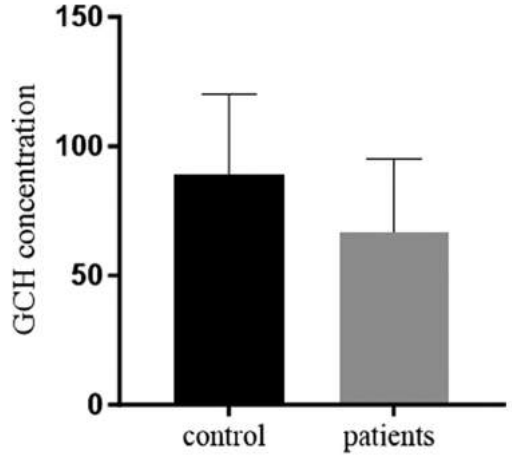

Fig. 5. Displays the concentrations of GSH in both control and patient groups.

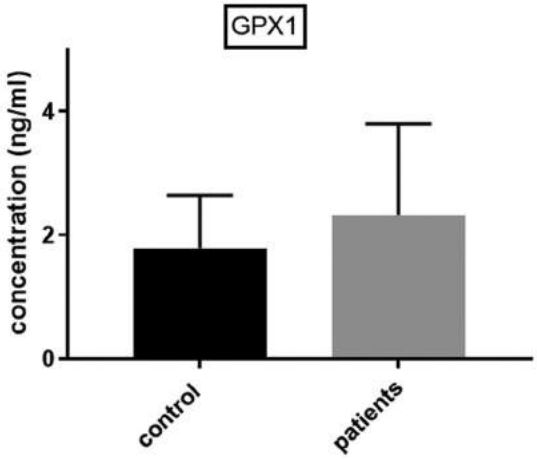

Fig. 6. Depicts the concentrations of glutathione peroxidase in both control and patient groups.

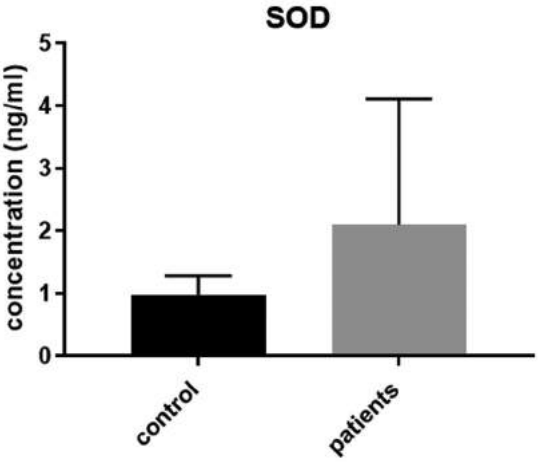

Fig. 7. The levels of superoxide dismutase in both control and patient groups.

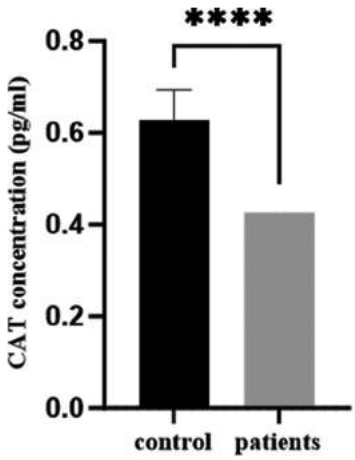

Fig. 8. The levels of catalase in both control and patient groups.

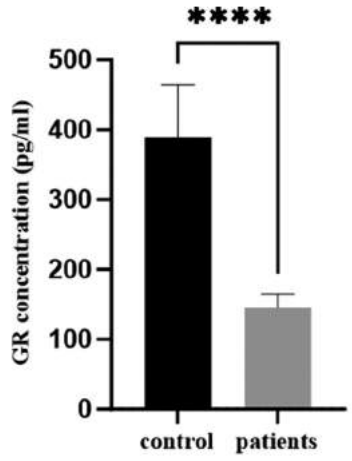

Fig. 9. The levels of glutathione reductase in both control and patient groups.

http://dx.doi.org/10.14500/aro.11526

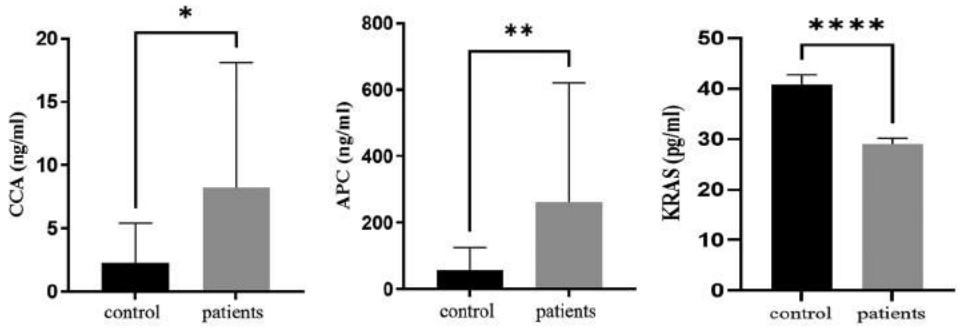

Fig. 10. Genetic markers colorectal cancer antigen, adenomatous polyposis coli, and KRAS concentration in Control and Patient groups.

group exhibited a mean GR level of 388.9 ± 75.87 pg/mL, while the patient group showed a significant decrease at 145.5 ± 19.13 pg/mL ($p < 0.0001$). Similarly, CAT levels displayed a significant decrease in the patient group compared to the control group (0.6282 ± 0.06614 pg/mL vs. 0.4272 ± 0.01397 pg/mL, $p < 0.0001$).

The findings of the present study suggest that GSH levels are significantly lower in the patient group compared to the control group, indicating a potential association between reduced GSH levels and CRC. The finding regarding the serum level of the GSH in CRC patients agree with previous findings (Acevedo-León, et al., 2021) and (Acevedo-León, et al., 2022). Upregulated GPX1 and SOD enzymes compared to controls, which collectively indicating heightened oxidative stress, DNA damage, and altered antioxidant response. The increased concentrations of antioxidant enzymes, such as GPX-1 and SOD, in the serum of cancer patients can be attributed to various factors, including ROS that led to oxidative stress and damage to cellular components. In response, the body upregulates antioxidant enzymes (Zhao, et al., 2022). On the other hand, chronic inflammation, a common feature in many cancers, also contributes to ROS production, prompting an increased expression of antioxidant enzymes (Wang, et al., 2021). In addition, the metabolic changes in cancer cells influence ROS production, and the body's adaptive response involves elevating GPX-1 and SOD levels (Kennedy, et al., 2020) and (Irazabal and Torres, 2020).

These findings agree with studies that concluded significantly elevation of SOD in colorectal patients compared to the control group (Zińczuk, et al., 2019b) and (Balaky, 2023). A study by (Al-Ansari, Al-Gebori, and Sulaiman, 2020) concluded that values of all the tested (GPx) in blood samples were significantly lower in all CRC patient groups as compared to healthy subjects. A study carried out at the Medical University in Łódź affirmed a notable rise in GPx and SOD ($p < 0.05$) among patients in comparison to the healthy control group (Malinowska, et al., 2015).

The results for GR levels show a substantial difference between the control group (388.9 ± 75.87 pg/mL) and the patient group (145.5 ± 19.13 pg/mL), with a highly significant $p < 0.0001$. This significant decrease in the mean concentration of GR in CRC patients compared to the control group suggests potential alterations in redox homeostasis associated with cancer development. Research conducted by (Gopčević, et al., 2013) and (Zińczuk, et al., 2019b), determined that the activity of GR is diminished in all colorectal carcinoma groups when compared to the control. The data for CAT levels indicates a significant difference between the control group (0.6282 ± 0.06614 pg/mL) and the patient group (0.4272 ± 0.01397 pg/mL), with a highly significant $p < 0.0001$. This finding may contribute to the understanding of oxidative stress dynamics in CRC and could be relevant for therapeutic considerations. Results regarding CAT consistent with findings from other studies (Zińczuk, et al., 2019b) and (Acevedo-León et al., 2022).

D. Genetic Markers

The substantial decrease in KRAS concentration in the patient group (<0.0001) indicates a lower expression of the KRAS oncogene in CRC patients (29.03 ± 1.184 pg/mL) compared to the control group (40.85 ± 1.963 pg/mL). APC levels exhibited a substantial increase in the patient group (262.6 ± 52.22 ng/mL) compared to the control group (55.68 ± 13.94 ng/mL), with a $p = 0.0057$. CCA levels were also markedly higher in the patient group (8.255 ± 1.28 ng/mL) compared to the control group (2.255 ± 0.87 ng/mL), with a $p = 0.0338$, as shown in (Fig. 10). The data for all parameters showed significant differences, both APC and CCA levels demonstrate significant increases in the patient group with the $p = 0.0057$ and 0.0338, respectively. Suggesting their potential relevance as markers or indicators associated with CRC. KRAS levels (pg/mL) show that there is a significant difference ($p < 0.0001$) between the patient group (29.03 ± 1.184) and the control group (40.85 ± 1.963). This substantial decrease in the mean concentration of KRAS in CRC patients compared to the control group suggests a potential association between KRAS levels and the presence of CRC. A prior investigation conducted in the same geographical region of Iraq affirmed the presence of APC protein expression in CRC, whereas it was absent in histologically normal-looking colorectal tissue (Altoriah, et al., 2020). As per the findings, the KRAS gene exhibited markedly elevated expression at 15.6 ± 1.82 ($p = 0.001$) in Stage IV CRC cases in comparison to the early stages (Jafri, Mushtaq, and Baig, 2021).

E. Serum Vitamin E

(Fig. 11), Vitamin E levels were significantly lower in the patient group (71.78 ± 6.368, $n = 59$) compared to the

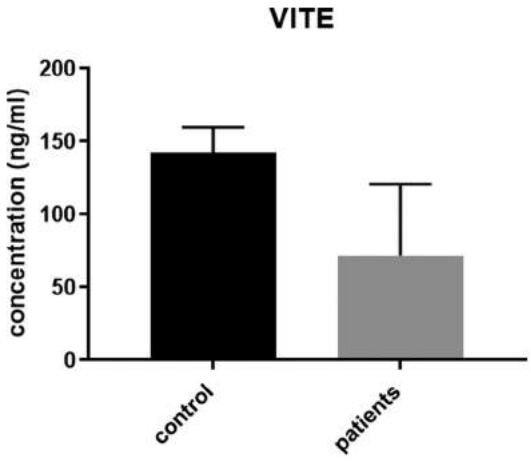

Fig. 11. Serum Vitamin E concentration level.

control group (142.3 ± 4.828, n = 13) with a $p < 0.0001$. Vitamin E levels in the patient group (71.78 ± 6.368 ng/mL, n = 59) were significantly lower than those in the control group (142.3 ± 4.828 ng/mL, n = 13) with a $p < 0.0001$, indicating a potential deficiency or altered metabolism. This observation aligns with another study's results, which reported significantly reduced serum concentrations of Vitamins C and E in the study group compared to the control group ($p < 0.01$) (Chang, et al., 2008).

IV. Conclusion

The present study concluded the following:

- CRC patients exhibited elevated levels of MDA and (8-OHdG), indicating increased oxidative stress, while the concentration of NT was lower in CRC group
- The study identified higher GPX1 and SOD levels in patients, suggesting altered enzymatic activity, while GSH levels are significantly lower
- Notably, oxidative stress-related parameters, including GR, CAT, and the KRAS Oncogene, demonstrated significantly lower expression in patients, while APC and CCA levels demonstrate significant increases in the patient group
- Vitamin E levels were significantly reduced in the patient group.

These findings collectively underscore distinct differences in oxidative stress markers and related enzymes in CRC patients.

V. Conflicts of Interest

The authors have no conflicts of interest to declare.

References

Acevedo-León, D., Monzó-Beltrán, L., Gómez-Abril, S.Á., Estañ-Capell, N., Camarasa-Lillo, N., Perez-Ebri, M.L., Escandón-Álvarez, J., Alonso-Iglesias, E., Santaolaria-Ayora, M.L., Carbonell-Moncho, A., Ventura-Gayete, J., Pla, L., Martínez-Bisbal, M.C., Martínez-Máñez, R., Bagán-Debón, L., Viña-Almunia, A., Martínez-Santamaría, M.A., Ruiz-Luque, M., Alonso-Fernández, J., Bañuls, C., and Sáez, G., 2021. The effectiveness of glutathione redox status as a possible tumor marker in colorectal cancer. *International Journal of Molecular Sciences*, 22, p.6183.

Acevedo-León, D., Monzó-Beltrán, L., Perez-Sánchez, L., Naranjo-Morillo, E., Gómez-Abril, S.Á., Estañ-Capell, N., Bañuls, C., and Sáez, G., 2022. Oxidative stress and DNA damage markers in colorectal Cancer. *International Journal of Molecular Sciences*, 23, p.11664.

Aghabozorgi, A.S., Bahreyni, A., Soleimani, A., Bahrami, A., Khazaei, M., Ferns, G.A., Avan, A., and Hassanian, S.M.J.B., 2019. Role of adenomatous polyposis coli (APC) gene mutations in the pathogenesis of colorectal cancer; current status and perspectives. *Biochimie*, 157, pp.64-71.

Al-Ansari, R.F., Al-Gebori, A.M., and Sulaiman, G.M., 2020. Serum levels of zinc, copper, selenium and glutathione peroxidase in the different groups of colorectal cancer patients. *Caspian Journal of Internal Medicine*, 11, p.384.

Alrubaie, A., Alkhalidi, N., and Abd-Alhusain, S., 2019. A clinical study of newly-diagnosed colorectal cancer over 2 years in a gastroenterology center in Iraq. *Journal of Coloproctology*, 39, pp.217-222.

Altoriah, K.M.J., Jumaah, A., Abdulhussein, A.A., Aljanabi, A.A.H., Al-Haddad, H.S., Al-Quzweni, A., and Hadi, N., 2020. Immunohistochemical study of adenomatous polyposis coli protein in colorectal carcinoma and its precursor lesions in Iraq. *Systematic Reviews in Pharmacy*, 11, pp.75-79.

Alves Ribeiro, R.R., Rolim De Brito, I., Andrade Souza, K., De Castro Souza, L., Almeida De Oliveira, T., and Weller, M., 2022. Risk of colorectal cancer in a brazilian population is differentially associated with the intake of processed meat and vitamin E. *Nutrition and Cancer*, 74, pp.820-829.

Arnold, M., Sierra, M.S., Laversanne, M., Soerjomataram, I., Jemal, A., and Bray, F., 2017. Global patterns and trends in colorectal cancer incidence and mortality. *Gut*, 66, pp.683-691.

Arrington, A.K., Heinrich, E.L., Lee, W., Duldulao, M., Patel, S., Sanchez, J., Garcia-Aguilar, J., and Kim, J., 2012. Prognostic and predictive roles of KRAS mutation in colorectal cancer. *International Journal of Molecular Sciences*, 13, pp.12153-12168.

Balaky, H.M., 2023. Potential role of 8-hydroxyguanosine and some pro inflammatory cytokines as biomarkers in colorectal cancer Iraqi patients. *Baghdad Science Journal*, 20, p.0082.

Bandookwala, M., and Sengupta, P., 2020. 3-Nitrotyrosine: A versatile oxidative stress biomarker for major neurodegenerative diseases. *International Journal of Neuroscience*, 130, pp.1047-1062.

Bardelčíková, A., Šoltys, J., and Mojžiš, J., 2023. Oxidative stress, inflammation and colorectal cancer: An overview. *Antioxidants* (*Basel*), 12, p.901.

Bartesaghi, S., and Radi, R., 2018. Fundamentals on the biochemistry of peroxynitrite and protein tyrosine nitration. *Redox Biology*, 14, pp.618-625.

Basak, D., Uddin, M.N., and Hancock, J., 2020. The role of oxidative stress and its counteractive utility in colorectal cancer (CRC). *Cancers* (*Basel*), 12, p.3336.

Beniwal, S.S., Lamo, P., Kaushik, A., Lorenzo-Villegas, D.L., Liu, Y., and Mohanasundaram, A., 2023. Current status and emerging trends in colorectal cancer screening and diagnostics. *Biosensors* (*Basel*), 13, p.926.

Borkowska, A., Olszewska, A., Skarzynska, W., Marciniak, M., Skrzeszewski, M., Kieda, C., and Was, H., 2022. High hemin concentration induces escape from senescence of normoxic and hypoxic colon cancer cells. *Cancers* (*Basel*), 14, p.4793.

Borrego, S., Vazquez, A., Dasí, F., Cerdá, C., Iradi, A., Tormos, C., Sánchez, J.M., Bagán, L., Boix, J., Camps, J., Sáez, G., and Zaragoza, C., 2013. Oxidative stress and DNA damage in human gastric carcinoma: 8-Oxo-7'8-dihydro-2'-deoxyguanosine (8-oxo-dG) as a possible tumor marker. *International Journal of Molecular Sciences*, 14, pp.3467-3486.

Bratovcic, A.J.A.S., 2020. Antioxidant enzymes and their role in preventing cell damage. *Acta Scientific Nutritional Health*, 4, pp.1-7.

Brzozowa-Zasada, M., Ianaro, A., Piecuch, A., Michalski, M., Matysiak, N., and Stęplewska, K., 2023. Immunohistochemical expression of glutathione peroxidase-2 (Gpx-2) and its clinical relevance in colon adenocarcinoma patients. *International Journal of Molecular Sciences*, 24, p.14650.

Cecerska-Heryć, E., Surowska, O., Heryć, R., Serwin, N., Napiontek-Balińska, S., and Dołęgowska, B., 2021. Are antioxidant enzymes essential markers in the diagnosis and monitoring of cancer patients-a review. *Clinical Biochemistry*, 93, pp.1-8.

Chang, D., Wang, F., Zhao, Y.S., and Pan, H.Z., 2008. Evaluation of oxidative stress in colorectal cancer patients. *Biomedical and Environmental Sciences*, 21, pp.286-289.

Chatterjee, N., and Walker, G.C., 2017. Mechanisms of DNA damage, repair, and mutagenesis. *Environmental and Molecular Mutagenesis*, 58, pp.235-263.

Daly, C.S., 2013. *The Roles of the Apc Proteins in Homeostasis and Tumourigenesis.* Cardiff University, Cardiff.

Demasi, M., Augusto, O., Bechara, E.J., Bicev, R.N., Cerqueira, F.M., Da Cunha, F.M., Denicola, A., Gomes, F., Miyamoto, S., Netto, L.E.S., Randall, L.M., Stevani, C.V., and Thomson, L., 2021. Oxidative modification of proteins: From damage to catalysis, signaling, and beyond. *Antioxidants and Redox Signaling*, 35, pp.1016-1080.

Demirci-Cekic, S., Özkan, G., Avan, A.N., Uzunboy, S., Çapanoğlu, E., and Apak, R.J., 2022. Biomarkers of oxidative stress and antioxidant defense. *Journal of Pharmaceutical and Biomedical Analysis*, 209, p.114477.

Fedacko, J., Takahashi, T., Singh, R.B., Pella, D., Chibisov, S., Hristova, K., Pella, D., Elkilany, G.N., Tomar, R.S., and Juneja, L.R., 2019. Globalization of diets and risk of noncommunicable diseases. In: *The Role of Functional Food Security in Global Health.* Elsevier, Netherlands.

Giovanni, D.L., and Francesco, S., 2020. Statistical significance: P Value, 0.05 threshold, and applications to radiomics-reasons for a conservative approach. *European Radiology Experimental*, 4, p.18.

Gochman, E., Mahajna, J., Shenzer, P., Dahan, A., Blatt, A., Elyakim, R., and Reznick, A.Z., 2012. The expression of iNOS and nitrotyrosine in colitis and colon cancer in humans. *Acta Histochemica*, 114, pp.827-835.

Gopčević, K.R., Rovčanin, B.R., Tatić, S.B., Krivokapić, Z.V., Gajić, M.M., and Dragutinović, V.V., 2013. Activity of superoxide dismutase, catalase, glutathione peroxidase, and glutathione reductase in different stages of colorectal carcinoma. *Digestive Diseases and Sciences*, 58, pp.2646-2652.

Hankey, W., Frankel, W.L., and Groden, J., 2018. Functions of the APC tumor suppressor protein dependent and independent of canonical WNT signaling: Implications for therapeutic targeting. *Cancer and Metastasis Reviews*, 37, pp.159-172.

He, L., He, T., Farrar, S., Ji, L., Liu, T., and Ma, X., 2017. Antioxidants maintain cellular redox homeostasis by elimination of reactive oxygen species. *Cellular Physiology and Biochemistry*, 44, pp.532-553.

Hidaka, E., Maeda, C., Nakahara, K., Wakamura, K., Ishiyama, Y., Shimada, S., Seki, J., Takano, Y., Oae, S., and Enami, S.E., 2019. High serum CA19-9 concentration predicts poor prognosis in elderly patients with stage IV Colorectal cancer. *Gastrointestinal Tumors*, 5, pp.117-124.

Ibrahem, S., Ahmed, H., and Zangana, S., 2022. Trends in colorectal cancer in Iraq over two decades: Incidence, mortality, topography and morphology. *Annals of Saudi Medicine*, 42, pp.252-261.

Irawan, B., Labeda, I., Lusikooy, R.E., Sampetoding, S., Kusuma, I.M., Uwuratuw, J.A., Syarifuddin, E., Warsinggih, Prihantono, and Faruk, M., 2020. Association of superoxide dismutase enzyme with staging and grade of differentiation colorectal cancer: A cross-sectional study. *Annals of Medicine and Surgery* (*Lond*), 58, pp.194-199.

Irazabal, M.V., and Torres, V.E., 2020. Reactive oxygen species and redox signaling in chronic kidney disease. *Cells*, 9, p.1342.

Jafri, H.S.M.O., Mushtaq, S., and Baig, S., 2021. Detection of kras gene in colorectal cancer patients through liquid biopsy: A cost-effective method. *Journal of College of Physicians and Surgeons Pakistan,* 31, pp.1174-1178.

Janion, K., Strzelczyk, J.K., Walkiewicz, K.W., Biernacki, K., Copija, A., Szczepańska, E., and Nowakowska-Zajdel, E., 2022. Evaluation of Malondialdehyde level, total oxidant/antioxidant status and oxidative stress index in colorectal cancer patients. *Metabolites*, 12, p.1118.

Janion, K., Szczepańska, E., Nowakowska-Zajdel, E., Strzelczyk, J., and Copija, A., 2020a. Selected oxidative stress markers in colorectal cancer patients in relation to primary tumor location-a preliminary research. *Medicina* (*Kaunas*), 56, p.47.

Janion, K., Szczepańska, E., Nowakowska-Zajdel, E., Strzelczyk, J., and Copija, A., 2020b. Selected oxidative stress markers in colorectal cancer patients in relation to primary tumor location-a preliminary research. *Medicina* (*Kaunas*), 56, p.47.

Jelic, M.D., Mandic, A.D., Maricic, S.M., and Srdjenovic, B.U., 2021. Oxidative stress and its role in cancer. *Journal of Cancer Research and Therapeutics*, 17, pp.22-28.

Kang, M., Jeong, S., Park, S., Nam, S., Chung, J.W., Kim, K.O., An, J., and Kim, J.H., 2023. Significance of 8-OHdG expression as a predictor of survival in colorectal cancer. *Cancers* (*Basel*), 15, p.4613.

Katona, B.W., and Weiss, J.M., 2020. Chemoprevention of colorectal cancer, *Gastroenterology*, 158, pp.368-388.

Kennedy, L., Sandhu, J.K., Harper, M.E., and Cuperlovic-Culf, M., 2020. Role of glutathione in cancer: From mechanisms to therapies. *Biomolecules*, 10, p.1429.

Kreutzmann, M., Kraus, B.J., Christa, M., Störk, S., Jansen, E.H., Stopper, H., and Schupp, N., 2023. Differential modulation of markers of oxidative stress and DNA damage in arterial hypertension. *Antioxidants* (*Basel*), 12, p.1965.

Lakemeyer, L., Sander, S., Wittau, M., Henne-Bruns, D., Kornmann, M., and Lemke, J., 2021. Diagnostic and prognostic value of CEA and CA19-9 in colorectal cancer. *Diseases*, 9, p.21.

Lakemeyer, L.E., 2023. *Colorectal Cancer: Impact of CEA and CA19-9.* Universität Ulm, Ulm.

Lewandowska, A., Rudzki, G., Lewandowski, T., Stryjkowska-Gora, A., and Rudzki, S., 2022. Risk factors for the diagnosis of colorectal cancer. *Cancer Control*, 29, p.1-15.

Li, T., Qian, Y., Li, H., and Deng, J., 2018. Combination of serum lipids and cancer antigens as a novel marker for colon cancer diagnosis. *Lipids in Health and Disease*, 17, p.261.

Lorestani, S., Hashemy, S.I., Mojarad, M., Keyvanloo Shahrestanaki, M., Bahari, A., Asadi, M., and Zahedi Avval, F.Z., 2018. Increased glutathione reductase expression and activity in colorectal cancer tissue samples: An investigational study in Mashhad, Iran. *Middle East Journal of Cancer*, 9, p.99-104.

Luo, H., Fang, Y.J., Lu, M.S., Pan, Z.Z., Huang, J., Chen, Y.M., and Zhang, C.X., 2019. Dietary and serum vitamins A and E and colorectal cancer risk in Chinese population: A case-control study. *European Journal of Cancer Prevention*, 28, p.268-277.

Lv, H., Zhen, C., Liu, J., Yang, P., Hu, L., and Shang, P., 2019. Unraveling the potential role of glutathione in multiple forms of cell death in cancer therapy. *Oxidative Medicine and Cellular Longevity*, 2019, p.3150145.

Malinowska, K., Mik, M., Dziki, Ł., Dziki, A., and Majsterek, I.J., 2015. Evaluation of antioxidant defense in patients with colorectal carcinoma. *Polish Journal of Surgery*, 87, pp.357-361.

Marrocco, I., Altieri, F., and Peluso, I., 2017. Measurement and clinical significance of biomarkers of oxidative stress in humans. *Oxidative Medicine and Cellular Longevity*, 2017, p.6501046.

Mohan, M., Rafi, S.T.M., Muthusami, S., Muthusami, S., Ramalingam, S., Sambandam, Y., Selvendiran, K., Ramachandran, I., and Kumaran, R.I., 2022. Targeting the metabolism in cancer cells for cancer therapy. In: *Handbook of Oxidative Stress in Cancer: Therapeutic Aspects.* Springer, Germany.

Najafi, A., Keykhaee, M., Kazemi, M.H., Karimi, M.Y., Khorramdelazad, H., Aghamohamadi, N., Bolouri, M.R., Ghaffari-Nazari, H., Mirsharif, E.S., Karimi, M., Dehghan Manshadi, H.R., Mahdavi, S.R., Safari, E., Jalali, S.A., Falak, R., and Khoobi, M., 2023. Catalase-gold nanoaggregates manipulate the tumor microenvironment and enhance the effect of low-dose radiation therapy by reducing hypoxia. *Biomedicine and Pharmacotherapy*, 167, p.115557.

Nalkiran, I., Turan, S., Arikan, S., Kahraman, Ö.T., Acar, L., Yaylim, I., and Ergen, A., 2015. Determination of gene expression and serum levels of MnSOD and GPX1 in colorectal cancer. *Anticancer Research*, 35, pp.255-259.

Patel, M., Mcsorley, S.T., Park, J.H., Roxburgh, C.S.D., Edwards, J., Horgan, P.G., and Mcmillan, D.C., 2018. The relationship between right-sided tumour location, tumour microenvironment, systemic inflammation, adjuvant therapy and survival in patients undergoing surgery for colon and rectal cancer. *British Journal of Cancer*, 118, pp.705-712.

Raj Rai, S., Bhattacharyya, C., Sarkar, A., Chakraborty, S., Sircar, E., Dutta, S., and Sengupta, R., 2021. Glutathione: Role in oxidative/nitrosative stress, antioxidant defense, and treatments. *ChemistrySelect*, 6, pp.4566-4590.

Rašić, I., Rašić, A., Akšamija, G., and Radović, S., 2018. The relationship between serum level of malondialdehyde and progression of colorectal cancer. *Acta Clinica Croatica*, 57, pp.411-416.

Rasool, M., Malik, A., Waquar, S., Ain, Q.T., Rasool, R., Asif, M., Anfinan, N., Haque, A., Alam, H., Ahmed, S., and Hamid Hamdard, M., 2021. Assessment of clinical variables as predictive markers in the development and progression of colorectal cancer. *Bioengineered*, 12, pp.2288-2298.

Sawicki, T., Ruszkowska, M., Danielewicz, A., Niedźwiedzka, E., Arłukowicz, T., and Przybyłowicz, K.E., 2021. A review of colorectal cancer in terms of epidemiology, risk factors, development, symptoms and diagnosis. *Cancers* (*Basel*), 13, p.2025.

Wang, X., O'Connell, K., Jeon, J., Song, M., Hunter, D., Hoffmeister, M., Lin, Y., Berndt, S., Brenner, H., Chan, A.T., Chang-Claude, J., Gong, J., Gunter, M.J., Harrison, T.A., Hayes, R.B., Joshi, A., Newcomb, P., Schoen, R., Slattery, M.L., Vargas, A., Potter, J.D., Le Marchand, L., Giovannucci, E., White, E., Hsu, L., Peters, U., and Du, M., 2019. Combined effect of modifiable and non-modifiable risk factors for colorectal cancer risk in a pooled analysis of 11 population-based studies. *BMJ Open Gastroenterology,* 6, p.e000339.

Wang, Y., Qi, H., Liu, Y., Duan, C., Liu, X., Xia, T., Chen, D., Piao, H.L., and Liu, H.X., 2021. The double-edged roles of ROS in cancer prevention and therapy. *Theranostics*, 11, p.4839.

Wei, R., Qiu, H., Xu, J., Mo, J., Liu, Y., Gui, Y., Huang, G., Zhang, S., Yao, H., Huang, X., and Gan, Z., 2020. Expression and prognostic potential of GPX1 in human cancers based on data mining. *Annals of Translational Medicine*, 8, p.124.

Wong, M.C., Ding, H., Wang, J., Chan, P.S., and Huang, J., 2019. Prevalence and risk factors of colorectal cancer in Asia. *Intestinal Research,* 17, pp.317-329.

Zhao, Y., Wang, H., Zhou, J., and Shao, Q.J.C., 2022. Glutathione peroxidase GPX1 and its dichotomous roles in cancer. *Cancers* (*Basel*), 14, p.2560.

Zhu, G., Pei, L., Xia, H., Tang, Q., and Bi, F., 2021. Role of oncogenic KRAS in the prognosis, diagnosis and treatment of colorectal cancer. *Molecular Cancer*, 20, pp.1-17.

Zińczuk, J., Maciejczyk, M., Zaręba, K., Pryczynicz, A., Dymicka-Piekarska, V., Kamińska, J., Koper-Lenkiewicz, O., Matowicka-Karna, J., Kędra, B., Zalewska, A.J.C., and Guzińska-Ustymowicz K., 2020. Pro-oxidant enzymes, redox balance and oxidative damage to proteins, lipids and DNA in colorectal cancer tissue. Is oxidative stress dependent on tumour budding and inflammatory infiltration? *Cancers (Basel)*, 12, p.1636.

Zińczuk, J., Maciejczyk, M., Zaręba, K., Romaniuk, W., Markowski, A., Kędra, B., Zalewska, A., Pryczynicz, A., Matowicka-Karna, J., and Guzińska-Ustymowicz, K., 2019a. Antioxidant barrier, redox status, and oxidative damage to biomolecules in patients with colorectal cancer. Can malondialdehyde and catalase be markers of colorectal cancer advancement? *Biomolecules,* 9, p.637.

Zińczuk, J., Maciejczyk, M., Zaręba, K., Romaniuk, W., Markowski, A., Kędra, B., Zalewska, A., Pryczynicz, A., Matowicka-Karna, J., and Guzińska-Ustymowicz, K., 2019b. Antioxidant barrier, redox status, and oxidative damage to biomolecules in patients with colorectal cancer. Can malondialdehyde and catalase be markers of colorectal cancer advancement? *Biomolecules*, 9, p.637.

Zińczuk, J., Zaręba, K., Kamińska, J., Koper-Lenkiewicz, O.M., Dymicka-Piekarska, V., Pryczynicz, A., Guzińska-Ustymowicz, K., Kędra, B., Matowicka-Karna, J., Żendzian-Piotrowska, M., Zalewska, A., and Maciejczyk, M., 2021. Association of tumour microenvironment with protein glycooxidation, DNA damage, and nitrosative stress in colorectal cancer. *Cancer Management and Research*, 13, pp.6329-6348.

http://dx.doi.org/10.14500/aro.11393

Analysis and Design of a Box Culvert Using Bentley Culvert Master Software: Qoshtapa Culvert as a Case Study

Anwer H. Dawood[1,*] and Dana K. Mawlood[1,2]

[1]Department of Civil Engineering, College of Engineering, Salahaddin University, Erbil, Kurdistan Region – F.R. Iraq

[2]Department of Civil Engineering, University of Kurdistan Hawler (UKH), Erbil, Kurdistan Region – F.R. Iraq

***Abstract*—Box culverts are utilized in situations where natural stream flow intersects with roads and railway lines. This research utilizes a digital elevation model and the water Modeling System software to assess the catchment area of the primary valley and identify the factors contributing to flooding in Qoshtapa City. The study involves an analysis of the existing culvert and generated the necessary data for the design of a new culvert. Despite the presence of the existing culvert, floodwater levels rose to over 1 m above the roadway elevation of Erbil-Kirkuk during the last flood event in 2021–2022. The research collected hydrological and climatic data for the study area, conducted soil type analysis using the Harmonized World Soil Database software, and performed hydraulic calculations to estimate the maximum flood discharge of the valley using the Hydrological Engineering Center-Hydrological Modeling System software for flood return periods of 50, 100, and 200 years, for design, to select the best economic alternative. The new culvert design was executed using Bentley Culvert Master software to ensure that floodwaters can flow through the culvert without rising to street level. The results indicated that the new culvert design surpasses the capacity of the existing one. The results show that the best economic alternative hydraulic design is the first alternative capacity of 201 m^3/s of a 100-year return period; the new design cross-section area of the culvert is 52.5 m^2.**

***Index Terms*—Bentley software, Culvert design, Flood level, Hydrological Engineering Center-Hydrological Modeling System, Hydraulic modeling.**

I. Introduction

Floods present significant challenges to urban areas, and Erbil city in Iraq is not an exception. The city is susceptible to flood hazards, particularly in low-lying topographical areas. In this specific case study, Qoshtapa city, located to the south of Erbil, has experienced extensive flooding, resulting in comprehensive damage encompassing human, economic, and environmental impacts. As a rapidly growing city in a developing country, Erbil faces additional challenges due to inadequate drainage systems, further exacerbating flood risk. To address flood mitigation in Erbil, this research focused on culvert design as a potential solution. Culverts play a critical role in managing stormwater runoff by providing a conduit for water to flow beneath roadways and other structures. Proper culvert design can mitigate flooding by efficiently conveying water and reducing the risk of infrastructure damage (Sissakian, et al., 2022).

This study leverages the Bentley Culvert Master software, a powerful engineering tool for culvert design and analysis. The design and analysis of box culverts hold immense significance in hydraulic engineering, especially in areas prone to flooding. Culverts are typically constructed from materials such as concrete, metal, or plastic and come in various shapes and sizes, depending on the specific requirements of the location. Culvert design factors include the volume of expected water flow, water velocity, the area to be spanned, and potential environmental impacts. Culverts play a crucial role in preventing flooding, erosion, and damage to transportation infrastructure by diverting water away from roadways and other structures (Brinley, 2010).

For road designers, the primary concern revolves around understanding surface water movement to acquire data used in designing hydraulic structures, such as culverts. These structures serve the purpose of mitigating flood damage on roads. Culverts serve both hydraulic and non-hydraulic functions. Hydraulic function involves facilitating the passage of floodwater through stream channels, while non-hydraulic functions include serving as crossings for human or animal traffic, equipment, etc., during droughts (Moore, et al., 1999), designing these hydraulic structures optimally necessitates a meticulous study of various factors, including catchment area, natural stream patterns, intersection points with roadways, soil characteristics, climate in the study area, and land use. This comprehensive understanding aids in accurately selecting the best economic alternative design by determining peak flood flows to avoid the utilization of

ARO-The Scientific Journal of Koya University
Vol. XII, No. 1 (2024), Article ID: ARO.11393, 11 pages
DOI: 10.14500/aro.11393
Received: 09 September 2023; Accepted: 25 April 2024
Regular research paper: Published: 10 May 2024
Corresponding author's email: anwer.hazim@koyauniversity.org

oversized hydraulic structures, which would inflate road construction costs unnecessarily. Conversely, employing undersized structures could lead to flooding and consequent road and infrastructure damage, causing significant material and potential human losses, as observed in the disaster during the rainy season in 2021–2022 (Deutsche Welle Newsletter, 2021; News, 2021) in the study area. Culverts remain instrumental in averting flooding, erosion, and damage to transportation infrastructure by efficiently directing water away from roadways and other structures, particularly in regions prone to heavy rainfall or requiring effective water flow management.

According to Software (2022), OpenFlows CulvertMaster software is a comprehensive tool designed specifically for efficiently generating well-structured culvert designs that are ready for reporting. This user-friendly software leverages input provided by users to deduce crucial design parameters, such as headwater depth, discharge, and culvert dimensions. Its ease of use ensures a straightforward operation, enabling users to assess existing culverts and seamlessly compare various design alternatives.

Several studies have investigated the application of Bentley Culvert Master software in the hydraulic analysis and design of box culverts. These studies have focused on parameters such as flow velocity, slope, headwater, and tailwater to assess the hydraulic performance of box culverts under different conditions of flood. For example, Daniel (2001) conducted a master's study on the rating system for rural culvert crossing repair and maintenance at Montana State University in Bozeman, Montana. Utilizing an ordered probit statistical model in conjunction with Culvert Master, Baker analyzed nine parameters to classify culverts into conditions ranging from 1 to 5, with 5 representing the best condition and 1 the worst. The identification of specific parameters contributing to the culvert condition is deemed highly valuable, and the versatility of the numerical model is seen as a key asset, making it applicable across a wide range of situations. Rowley, et al. (2007) conducted a study on the numerical modeling of culvert hydraulics, utilizing several computer programs including HY-8, Culvert Master, and the Hydrologic Engineering Center River Analysis System (HEC-RAS) that this paper aimed to compare the hydraulic features provided by these programs and assess their accuracy. Test cases were developed to evaluate the accuracy of the program results, particularly in terms of flow controls, headwater depths, and outlet velocities. These results were compared to calculations based on the theory outlined in the Federal Highway Administration publication Hydraulic Design Series 5. Popovska (2010) conducted a study in Kosovo focusing on frequent flooding, hydrological analysis, and hydraulic modeling of the existing storm sewer system at Prishtina Airport. The study utilized the Culvert Master Program, which facilitates the design and analysis of culvert hydraulics. Yoo and Lee (2012) conducted a study focusing on the direct determination of the width and height of a box culvert by applying Culvert Master software. Their research aimed to determine the appropriate method for culvert section design. Altuwaijri (2019) conducted a morphometric network drainage analysis for railway locations in Saudi Arabia, and he recommended using Culvert Master software to calculate the culvert size. Abdelkarim (2019) conducted a study focusing on the assessment of expected flood hazards along the Jizan–Abha Highway in the Kingdom of Saudi Arabia and also utilized Culvert Master Software to evaluate the efficiency and capabilities of the existing floodwater drainage facilities, such as bridges, culverts, and dry communication infrastructure located below the Jizan–Abha Highway, to accommodate peak flows. The research aimed to assist decision makers in Jizan City and various areas of Saudi Arabia by providing insights into alternative solutions that can be studied and implemented to protect roads from anticipated future floods. Adeogun, et al. (2019) conducted a study to evaluate the hydraulic analysis of selected culverts along Ilorin-Jebba Road in Kwara State, Nigeria. In their research, they utilized HY-8 and Culvert Master Software. They concluded that these software tools were developed to aid engineers in designing and analyzing culverts within road projects.

While each program for culvert analysis possesses unique characteristics, they all offer automated solutions to culvert analysis and design challenges. Ramadan, et al. (2022) conducted a study on the flood protection system in Aswan under current and future climate conditions. The assessment of culverts using Culvert Master revealed that they are unsafe in a 100-year event with the existing dimensions of two vents measuring 5 × 2.5 m. Therefore, a proposal was made to add three additional vents to the culvert with the same dimensions. Regarding the existing channel, assessment results indicated that it cannot accommodate the incoming flow, prompting a proposed rehabilitation plan with a constant bed width of 18 m and a total depth of 2.0 m. Mamoon, et al. (2022) employed various computer programs, including THYSYS and Culvert Master, to carry out a performance analysis of culverts in Bangladesh. They conducted hydrologic-hydraulic analyses of selected culverts using the rational formula, *in situ* site data. The study revealed that all selected culverts were vulnerable under future climate scenarios, necessitating the design of new culverts. Consequently, it can serve as a significant tool in mitigating water congestion or flooding scenarios on or around any highway project, ensuring a smooth flow of transportation. Alqreai and Altuwaijri (2023) conducted a study in Wadi Malham (Saudi Arabia), using Culvert Master software to perform calculations related to the hydraulic analysis and design of culverts under the highway and railway track for a 100-year return period.

This software effectively addresses various hydraulic variables, such as culvert size, flow, and headwater. In addition, Culvert Master software provides options for different culvert barrel shapes, including circular pipes, arches, and boxes.

The hydraulic design of box culverts necessitates the determination of key parameters, including flow rates, water levels, and culvert dimensions, to ensure effective water conveyance while preventing flooding and structural issues. Culvert Master, a prominent software solution in this domain,

offers a comprehensive platform for efficiently performing these tasks.

The gap in the study is that most culverts are designed without a hydrologic study, resulting in designs that either exceed the required specifications (meaning a considerable amount of money is spent without any benefit, making them uneconomical) or fall short of the required specifications (meaning they cannot handle the flow of floodwater and will result in overflow, as seen in several culverts, including the one in the present study). This study enhances culvert infrastructure effectiveness by improving design methodologies through conducting hydrological studies and integrating cutting-edge tools and technologies for effective culvert design according to Engineering standards.

This research aims to leverage Bentley Culvert Master software for the design and analysis of the box culvert, taking into account the hydraulic behavior of the surrounding area, Qoshtapa City, located at the intersection of the primary valley and the Erbil–Kirkuk main roadway. The objective of the study involves a comparison between the results of the best economic culvert design and the existing culvert's performance during the last flood event. The importance of this study lies in safeguarding human lives, minimizing highway damage, protecting against collapses, minimizing culvert construction costs, and preserving soil layers. Poor culvert design without hydrological study has led to road collapses and substantial material and potential human losses, as evidenced in Fig. 1.

II. Description of Study Area

The Qoshtapa district is situated to the south of Erbil City, approximately 20 km from the city center. This district plays a critical role as a strategic roadway connecting Erbil and Kirkuk cities. It serves as an economic lifeline, facilitating the connection between Turkey and southern Iraq through Iraqi Kurdistan, and vice versa (Fig. 2). The focal point of this research is the design of a culvert at the intersection of the main valley in Qoshtapa and the Erbil–Kirkuk main road, specified by the coordinate's latitude: 36° 0'1.52" N, longitude: 44° 2'30.41" E. This location already has an existing culvert. However, during the last flood, water overtopped the roadway about 1 m above the street level, resulting in material and human losses and road blockages.

Fig. 1. Study area material losses in the last flood event, December 17, 2021.

The primary pieces of physical evidence used in this study include high water marks and road elevations concerning canal banks. Multiple site visits confirmed that the existing culvert capacity was inadequate for passing the flood flow during the last flood. The main valley extends over a catchment area of about 71 km² at the city center, reaching 68.5 km² at the intersection of the Erbil–Karkuk roadway, basin slope of 5.8%, maximum flow distance of about 27 km; the highest elevation in the catchment area was 840 m (a.s.l.), the elevation of the street above the existing culvert was 400 m (a.s.l.), and the ground elevation in the bed of the valley at the same point was 396 m (a.s.l.) (Fig. 3).

The climate in the Qoshtapa district resembles that of Erbil City, which is characterized by a transition between a Mediterranean climate and a desert environment. It experiences lower humidity and temperatures in winter and moderate weather in summer. The research area's climate is categorized as arid and semi-arid. Mean annual rainfall was 350 mm, and the study area was exposed to sudden floods like the one that happened in the last season on December 17, 2021. The necessary rainfall data were collected from the General Directorate of Meteorology and Seismic Monitoring (Kurdistan Regional Government, Ministry of Transport and Communications, 2021). The maximum daily rainfall data for the Erbil station are presented in Table I. The intensity–duration–frequency (IDF) curve used in this study was obtained from the work of Dawood and Mawlood (2023) (Fig. 4).

III. Methodology

To carry out the present study on flood mitigation in the study area through culvert design, rainfall design depth, intensity, and duration estimated through the IDF curve for Erbil station (Fig. 4). Watershed delineation was carried out using the watershed modeling system (WMS) with a digital elevation model (DEM) of 30 × 30 m to find hydraulic parameters of the catchment area, as presented in Table II.

Soil classification was performed using the Harmonized World Soil Database (HWSD) to estimate the soil conservation service curve number (SCS-CN) (Table III). In the next step, runoff hydrograph calculations were performed utilizing the HEC-HMS, with the determination of peak flow according to SCS-CN principles. The HEC-HMS model, developed by the Center for Hydrological Engineering of the US Army Corps of Engineers, is a widely adopted hydrological model. It is particularly well suited for arid and semi-arid regions and serves as a valuable tool for simulating rainfall-runoff processes in sub-catchments within the study area. This model excels in calculating various hydrological parameters, allowing users to define reference intervals based on historical rainfall data. Key parameters encompass the computation of flood hydrographs, estimation of losses, soil infiltration rates, surface runoff volumes, time to reach peak flow, and other critical factors. The model's accuracy hinges on the precision and quality of input data, including rainfall design depths of rainfall for specific return periods according to the IDF curve, as detailed in Table IV. The HEC-RAS

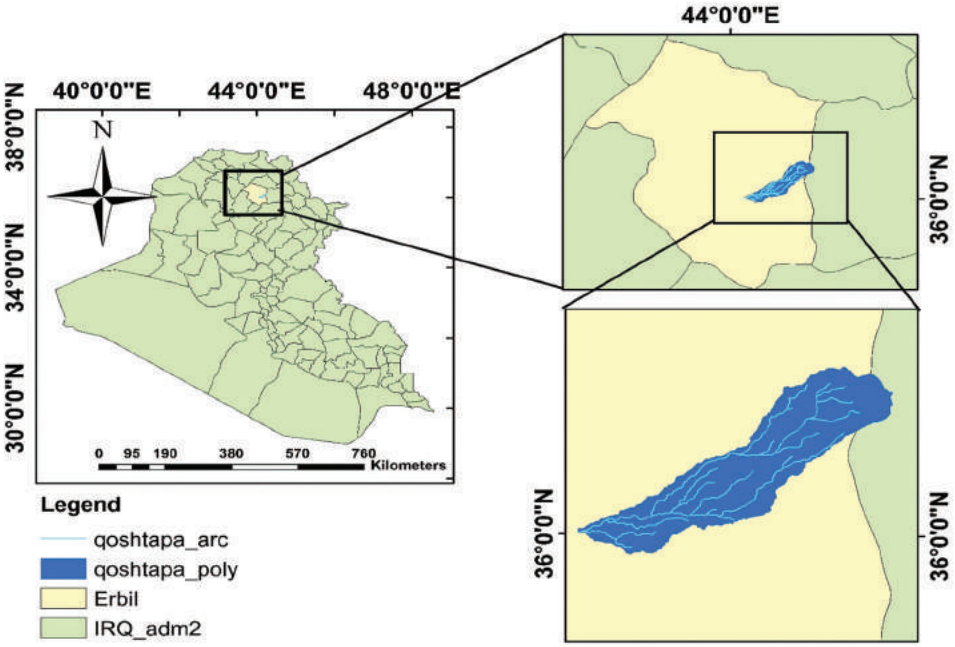

Fig. 2. Location of study area.

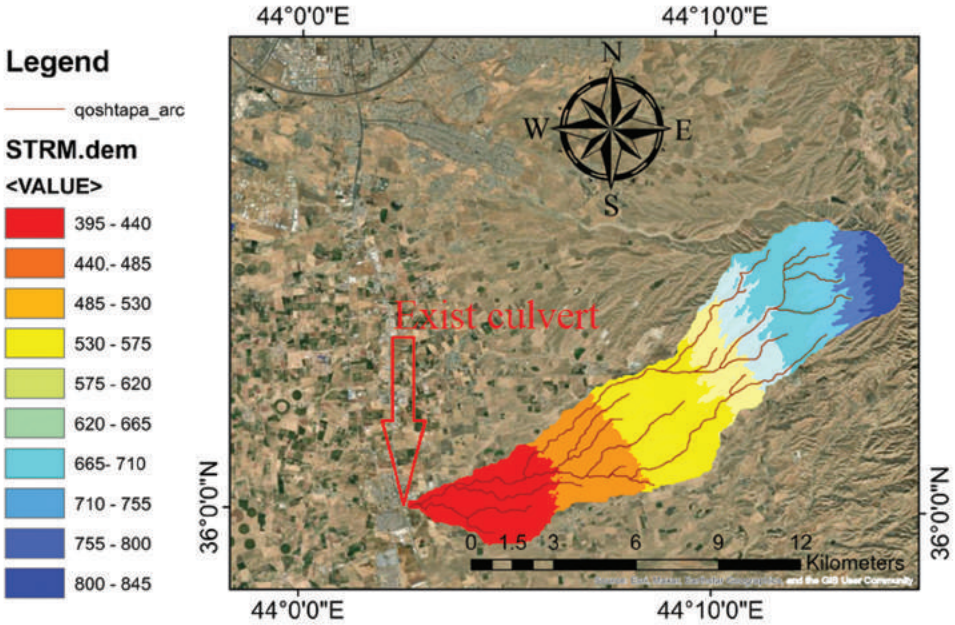

Fig. 3. Study area catchment contour map showing the location of the existing culvert.

model was then employed to delineate the floodplain, and Culvert Master software was utilized for the analysis and design of the box culvert. Finally, economic analysis was used to select the optimal economical design that meets all the technical and economic standards for culvert design.

IV. Results and Discussion

A. Water Shed Delineation

Watershed delineation was conducted using the WMS software with a DEM 30 × 30 m resolution, and the results are presented in Fig. 3 and Table II.

B. Land Cover and Land Use Data

The SCS-CN method is widely employed to estimate runoff in hydrologic analysis. Soil groups, as defined by the SCS, determine the curve number (CN) for a given catchment area. In this study, the catchment area was analyzed using the Harmonized World Soil Database HWSD Viewer (Nachtergaele, Van Velthuizen and Batjes, 2012) (Table III), revealing in the catchment area D-type soil, which is characterized by low infiltration and a high runoff CN. The study area included barley cultivation, brush weed grass, and urbanized areas. Due to delayed rainfall in the 2021–2022 season, farmers did not plow the area, resulting

TABLE I
MAXIMUM DAILY RAINFALL DATA IN THE ERBIL STATION

Year	Max daily rainfall mm	Year	Max daily rainfall mm	Year	Max daily rainfall mm	Year	Max daily rainfall mm
1980	57.6	1991	62.4	2002	32.3	2013	71.8
1981	40.9	1992	15.7	2003	59.2	2014	51
1982	38.1	1993	79	2004	41.4	2015	37.6
1983	32.9	1994	41.7	2005	34	2016	55.8
1984	42.7	1995	75.7	2006	103.9	2017	36.4
1985	72.7	1996	22.3	2007	38	2018	51.1
1986	73.6	1997	35.8	2008	37.8	2019	59.5
1987	31.8	1998	36.8	2009	41	2020	36.8
1988	37.2	1999	25.8	2010	33.8	2021	16
1989	48.4	2000	46.4	2011	67		
1990	35.8	2001	48.3	2012	21		

TABLE II
MAIN PARAMETERS OF THE QOSHTAPA CATCHMENT AREA

No.	Catchment name	Basin area (km^2)	CN	Basin slope (m/m)	Basin length (km)	Mean basin elevation (m)	Maximum stream length (km)	Maximum stream slope (m/m)
1	Qoshtapa	68.5	81	0.058	20.06	570.96	21.635	0.0156

TABLE III
STUDY AREA SOIL CLASS PROPERTIES BY HWSD VIEWER HARMONIZED WORLD SOIL DATABASE, UNITED NATIONS (NACHTERGAELE, VAN VELTHUIZEN AND BATJES, 2012).

Properties	Dominant	Associated
Soil Unit Name (FAO74)	Calcic xerosols	Chromic vertisols
Topsoil Texture	Medium	Fine
Reference Soil Depth (cm)	100	100
Topsoil Sand Fraction (%)	40	16
Topsoil Silt Fraction (%)	37	29
Topsoil Clay Fraction (%)	23	55
Topsoil USDA Texture Classification	Loam	Clay (light)
Topsoil Reference Bulk Density (kg/dm^3)	1.39	1.21
Topsoil Bulk Density ($kg/d\ m^3$)	1.31	1.65
Topsoil Gravel Content (%)	4	4
Topsoil Organic Carbon (% weight)	0.56	0.75
Topsoil Gypsum (% weight)	0.4	0
Subsoil Sand Fraction (%)	37	15
Subsoil Silt Fraction (%)	36	28
Subsoil Clay Fraction (%)	27	57
Subsoil USDA Texture Classification	Clay loam	Clay (light)
Subsoil Reference Bulk Density ($kg/d\ m^3$)	1.36	1.21
Subsoil Bulk Density ($kg/d\ m^3$)	1.33	1.76
Subsoil Gravel Content (%)	4	5
Subsoil Organic Carbon (% weight)	0.33	0.45
Subsoil Gypsum (% weight)	0.3	0

in decreased infiltration, an increased CN, and a transition to sagebrush with grass understory, brush weed, and grass mixture with brush land. The estimated CN is 80.42, with a value of 81 used in the study (United States Department of Agriculture, Natural Resources Conservation Service and Conservation Engineering Division, 1986). The SCS-CN method is widely used to predict storm runoff for hydraulic design purposes, such as sizing culverts and detention basins. The method takes into account various factors, including rainfall, soil properties, and land-use type. The SCS-CN method is sensitive to the value of CN, which represents the

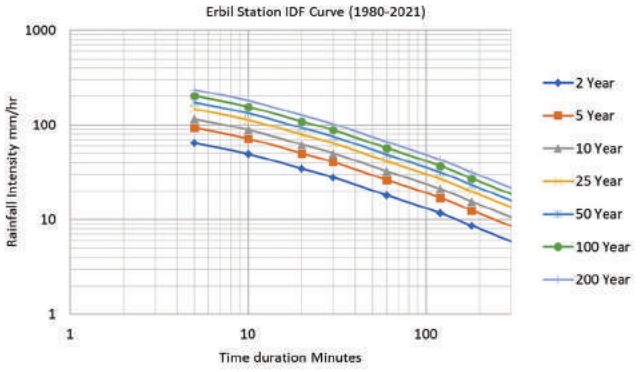

Fig. 4. Intensity–duration–frequency curves for Erbil station (Dawood and Mawlood, 2023).

runoff potential based on hydrological soil class and land cover, as shown in Table V.

C. Hydrologic Modeling by HEC-HMS

The HEC-HMS model, a valuable asset for hydrological analysis (rainfall-runoff process), serves as a reference for both researchers and practitioners in the field (US Army Corps of Engineers, 2018). The rainfall-runoff process using HEC-HMS typically involves several key steps, as follows:

Define watershed characteristics, including its size, shape, land use, and soil types.

Design rainfall for certain return periods.

Estimate soil SCS CN.

Land surface processes, including infiltration, evapotranspiration, and surface detention within the watershed.

By following these steps, practitioners can effectively use HEC-HMS to simulate the rainfall-runoff process and understand the hydrological behavior of watersheds under different conditions (US Army Corps of Engineers, 2018).

This study conducted a comprehensive analysis, encompassing a morphological study of the drainage network,

TABLE IV
AVERAGE REOCCURRENCE INTERVAL (ARI) AND CHARACTERISTICS OF THE FLOOD WATER OF QOSHTAPA SUB-CATCHMENT FOR DIFFERENT RETURN PERIODS

Return period year	Max daily rainfall mm	Losses rainfall mm	Excess rainfall mm	Runoff vol. *1000 m^3	Peak Q m^3/s
2	41.2	31.6	9.6	660	20.6
5	59.8	38.5	21.3	1460	48.9
10	74.1	42.3	31.8	2174	74.8
25	94.4	46.5	47.9	3279	115
50	111	49.1	61.9	4237	150
100	130	51.5	78.5	5375	191.3
200	151	53.6	97.4	6669	238

TABLE V
ESTIMATION SCS-CN FOR THE CASE STUDY CATCHMENT AREA

No.	Matrix calculating CN	CN	Area (km^2)	% Area	Weighted CN
1	Barley cultivation	68	12.33	18	12.24
2	Brush weed grass	77	39.73	58	44.66
3	Urbanized area	98	16.44	24	23.52
	Total		68.5	100	80.42

SCS-CN: Soil conservation service-curve number

TABLE VI
COMPARISON BETWEEN MODELED RESULTS AND THE OBSERVATIONS OF WATER DEPTHS THROUGH SITE VISITS ALONG THE QOSHTAPA FLOOD

Location	100 years modeled (m)	Observed (m)
Water depth in the center of Qoshtapa	4.5	3.9
Water depth in western Qoshtapa	3.6	3.4
Water depth in eastern Qoshtapa	3.5	3.3

ground cover characteristics, utilization of a CN value of 81, soil classification, and Manning coefficient. Flood hydrographs and peak flow calculations were performed for return periods of 2, 5, 10, 25, 50, 100, and 200 years using the SCS-CN method. The network comprises drainage lines (valleys) that converge near the urban area, although their surface features have been altered due to urban expansion.

The results derived from hydrologic modeling are instrumental in evaluating the effectiveness of various mitigation measures, such as the construction of culverts. This evaluation involves a comparison of the results from different scenarios to determine which measures are most efficient in reducing flood risk. Furthermore, hydrologic modeling results play a crucial role in calibrating and validating the model to ensure its accurate representation of the watershed system's behavior. This validation process entails comparing the modeled results to observed data to ascertain the model's accuracy. Furthermore, the accuracy of the model's results hinges on various factors including the precision and quality of the utilized data, design depth of rainfall, morphological study of the drainage network, ground cover assessment, CN analysis, soil classification, Manning coefficient determination for assessing flood hydrograph, and peak flow at return period by HEC-HMS (Scharffenberg, 2013). The calibrated simulation results of the HEC-HMS model, including the hydrograph in the catchment area, are presented in Fig. 5 and Table IV.

The results of the characteristics of the flood water of the Qoshtapa sub-catchment for different return periods are shown in Table IV.

D. Hydraulic Modeling (Flood Inundation by HEC-RAS)

The Hydrological Engineering Center River Analysis System (HEC-RAS) model is a software tool employed for flood inundation modeling. This model conducts hydraulic calculations for unsteady flow based on the Saint Venant equations governing water flow. The flood hydrograph generated by the HEC-HMS model serves as input data for the HEC-RAS model, allowing it to define the catchment and

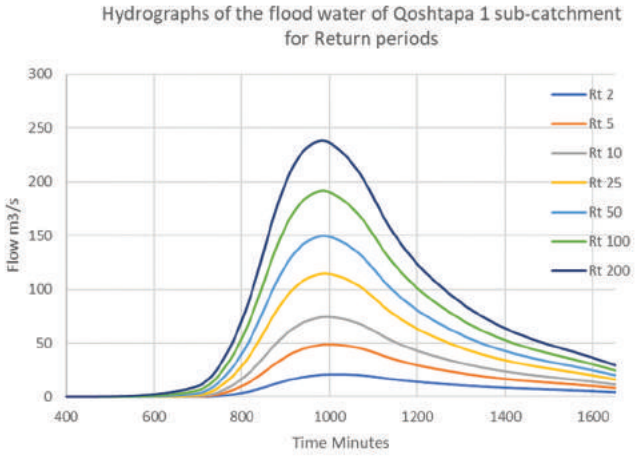

Fig. 5. Results of simulation hydrograph model for Qoshtapa sub-catchment for return period (2–200 years) by HEC-HMS model.

simulate flood inundation. To facilitate modeling, the flood area is subdivided into a network of small mesh cells with dimensions of 10 × 10 m. Fig. 6 displays the inundation map, including depth and flow velocity. HEC-RAS is widely used for hydraulic analyses of river systems, encompassing tasks such as floodplain mapping, bridge and culvert design, and levee analysis. The model's capabilities extend to steady flow water surface profile calculations, 2D unsteady flow simulations, and sediment transport modeling (Kinyanjui, et al., 2011).

To validate the modeling results for Qoshtapa City, real-world data from a flood event that occurred on December 17, 2021, were utilized. Validation involved a comparative analysis between modeled outcomes for a 100-year return period and on-site observations collected during the Qoshtapa flood event. The results of this validation are outlined in Table VI.

E. Design and Analysis of Culvert using Bently Culvert Master Software

This section focuses on the utilization of the Culvert Master software for culvert design. The Qoshtapa case study

http://dx.doi.org/10.14500/aro.11393

addresses the inadequacy of culvert waterway crossings on the roadway, necessitating sizing to effectively handle flood runoff. This process also accounts for the interaction between generated headwater, which refers to the increase in the water level upstream of the culvert due to flow restrictions (Systems, 2007).

On December 17, 2021, an unprecedented flood disaster occurred, resulting in the overtopping of the culvert and subsequent road flooding. Notably, floodwaters surged to a height of approximately 1.0 m above the roadway, particularly at the culvert's central location along the Erbil–Kirkuk route (latitude: 36.000589°, longitude: 44.041706°), as shown in Fig. 7. The existing culvert boasts a cross-sectional area measuring 3 × 3 × 3.5 m^2, as illustrated in Fig. 8, which served as the conduit for water flow. An analysis of this existing culvert section, as elucidated in Fig. 9, reveals that its capacity to accommodate floodwater is approximately 119 m^3/s. However, according to modeling conducted for the flood event of December 17, 2021, corresponding to a 100-year return period, the peak flow reached 191.3 m^3/s as

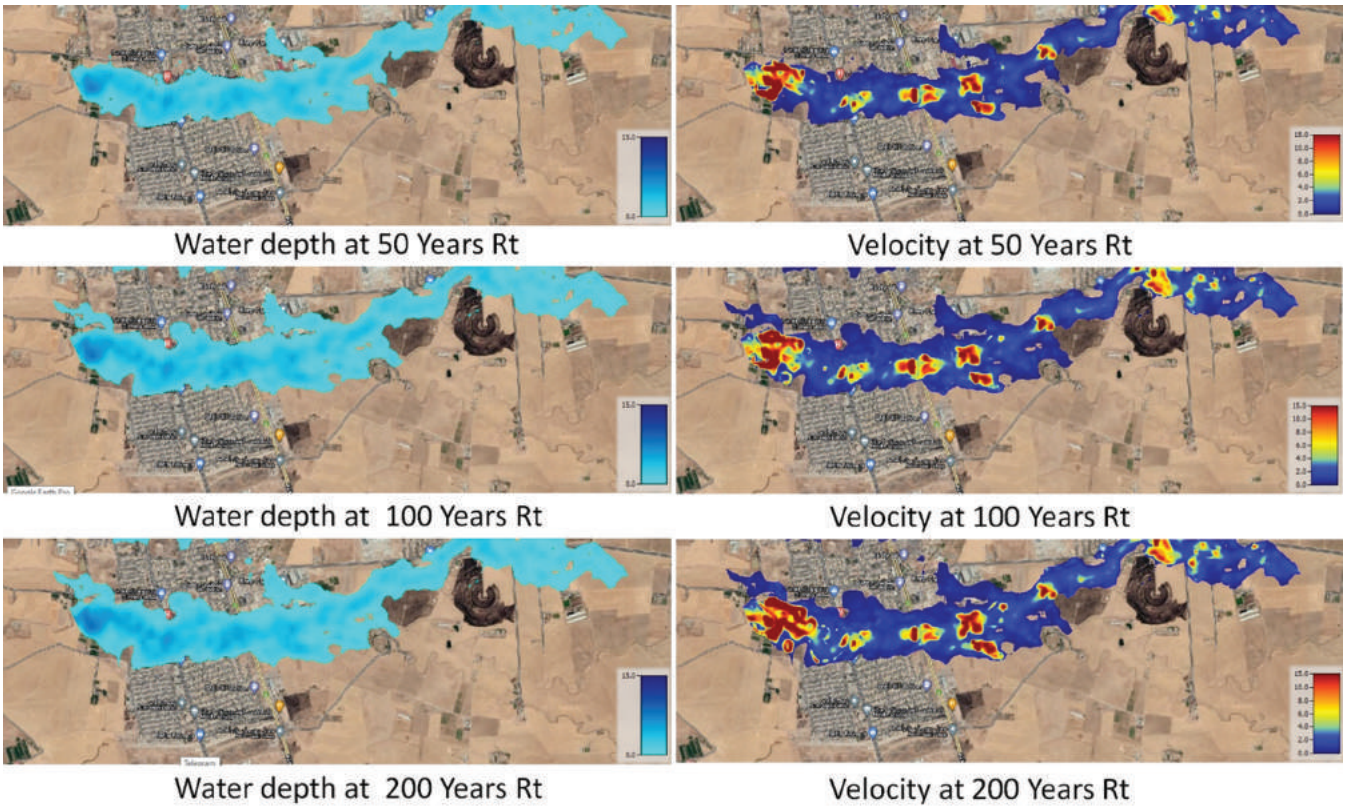

Fig. 6. Flood surface area depth and velocity of hydraulic modeling using HEC-RAS software in the Qoshtapa Sub-Catchment area for 50, 100, and 200-year return periods.

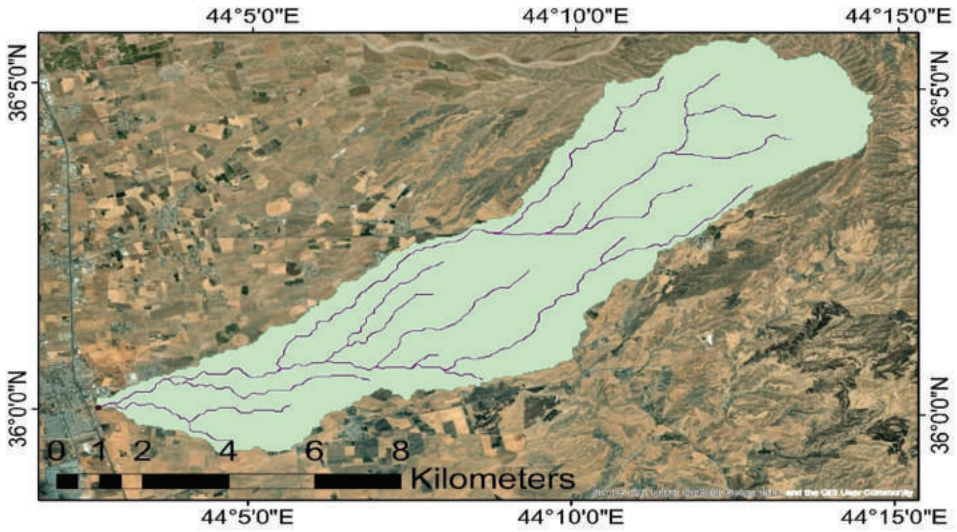

Fig. 7. Location of case study Qoshtapa sub-catchment.

illustrated in Table IV, surpassing the culvert's capacity and leading to overtopping.

Table IV provides a comprehensive overview of floodwater characteristics within the Qoshtapa sub-catchment for varying return periods.

The essential data required for the culvert design using Culvert Master software encompasses parameters such as headwater elevation, Manning's roughness coefficient for the concrete box culvert (0.013), upstream invert level (395 m), downstream invert level (394.7 m), length of conduit 30 m, slope (1%), and the peak discharge for a 100 and 200-year return period or higher. The results of the culvert design alternatives are presented in Fig. 10a and b.

Fig. 8. Existing culvert cross-section, in case study Qoshtapa1 sub-catchment.

In comparing the inundated areas caused by both the existing culvert (Fig. 6) and the proposed new culvert (Figs. 11a and b), it becomes evident that the inundation area has decreased.

For effective conveyance of floodwaters with a first alternative design for a 100-year return period (ranging from 191 to 201.4 m^3/s) as illustrated in Table IV and Fig. 10a, the culvert design necessitates specific dimensions, including a 5-cell configuration, a 3-m span, a 3.5-m riser, and a cross-sectional area measuring $5 \times 3 \times 3.5 = 52.5$ m^2, as exemplified in Fig. 12.

The second alternative design has a 200-year return period (ranging from 238 to 241 m^3/s) as illustrated in Table IV and Fig. 10b. The culvert design necessitates specific dimensions, including a 6-cell configuration, a 3-m span, a 3.5-m riser, and a cross-sectional area measuring $6 \times 3 \times 3.5 = 63$ m^2.

F. Economical Analysis

Culverts are constructed from a variety of materials. Factors considered when selecting a culvert include roadway profiles, channel characteristics, hydraulic performance, construction and maintenance costs, and the estimated service life of the culvert project.

A reinforced concrete box culvert is typically a drainage structure with a square or rectangular opening. It consists of two horizontal and two vertical slabs built monolithically, with some or all sides of the structure reinforced. A box culvert can have one or more cells (boxes). The selection of the best economic hydraulic section is determined using the scenario of cell dimension ratio (CDR) (Kalyanshetti and Gosavi, 2014; Shreedhar and Shreedhar, 2013). These studies demonstrate that multi-celled box culverts prove to be more cost-effective for larger spans when compared to single-cell

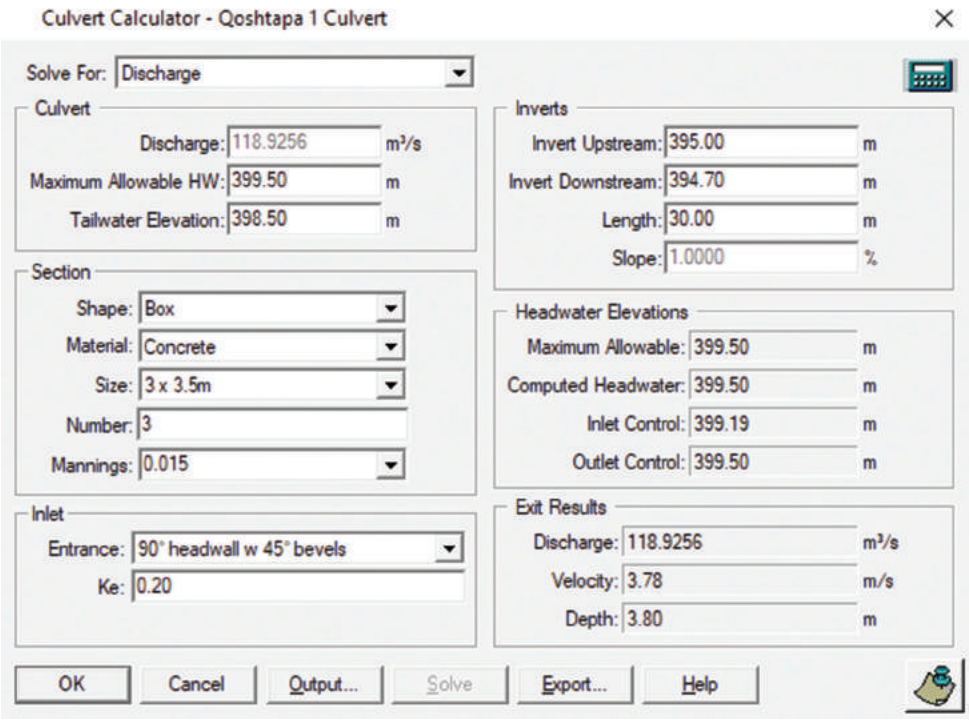

Fig. 9. Analysis of flood passing for existing culvert Qoshtapa1.

http://dx.doi.org/10.14500/aro.11393

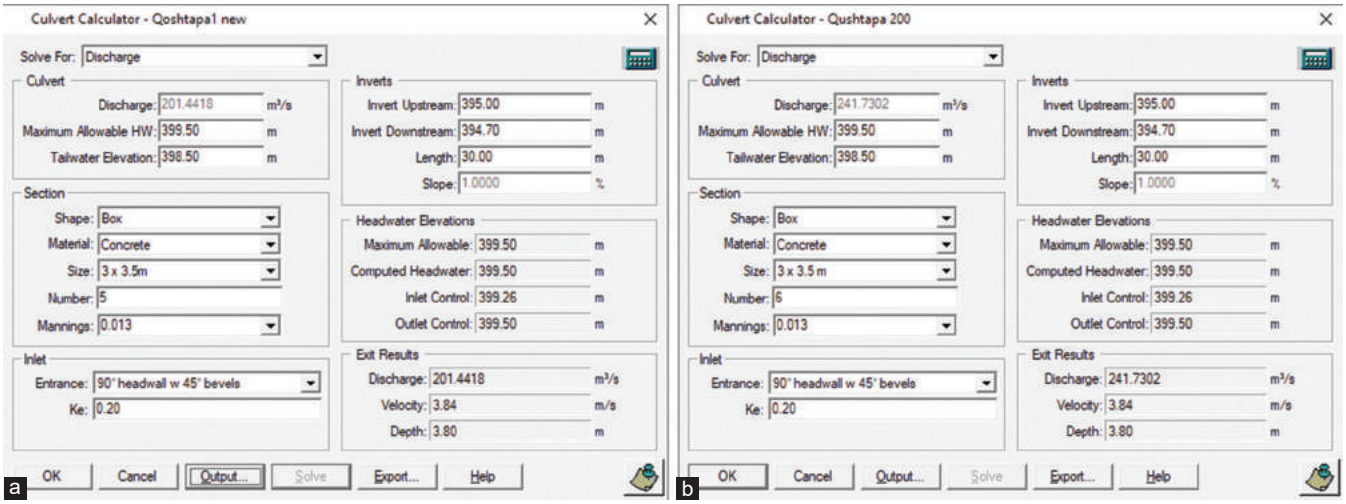

Fig. 10. (a) Culvert design results from Culvert Master for a 100-year flood return period. (b) Culvert design results from Culvert Master for 200-year flood return period.

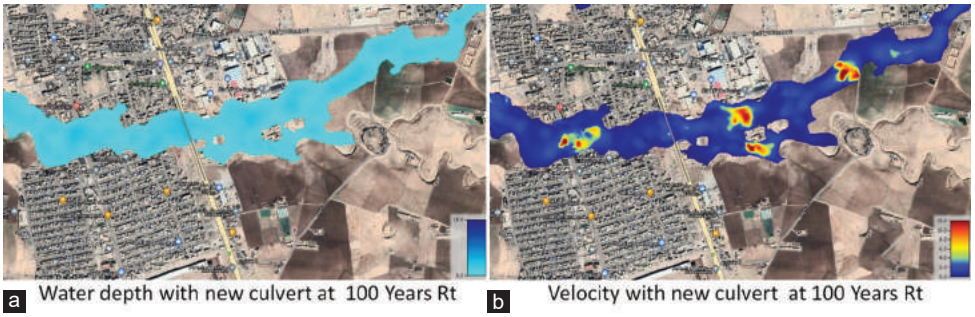

Fig. 11. Hydraulic modeling using HEC-RAS software at Qoshtapa sub-catchment area for a 100-year return period with a new culvert cross section (5 × 3 × 3.5) m^2. (a) Flood (inundation) surface area depth and (b) velocity of flood.

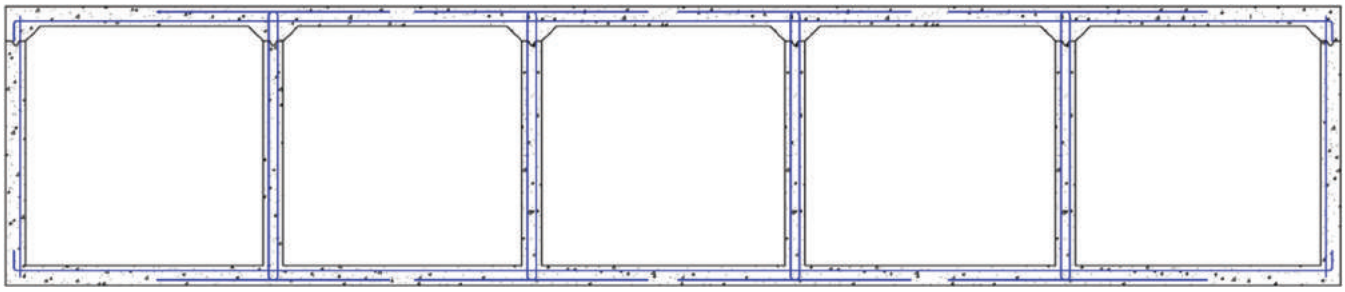

Fig. 12. Detailed cross-section of the culvert design depicting a 5-cell box culvert.

box culverts. This is because the maximum bending moment and shear force values decrease significantly, necessitating thinner sections.

The economic analysis for the 100-year return period and cross-section area of 52.5 m^2 is presented in Tables VII and VIII. The CDR used is 1.9–0.85.

Practically, according to the stream section in Fig. 13, the best selection is 0.85 for the cell dimension span and a height of 3 × 3.5m. Choosing other options would alter the road profile due to the addition of slab thicknesses, freeboard, and depth of earth fill. The rectangular reinforced concrete box culvert with inside dimensions of 3 × 3.5 m is used, with a slab and wall thickness of 0.25–0.35 m, averaging at 0.3 m, as per the standard box culvert (Qasim, 2020). The roadway asphalt thickness is 0.2 m, the depth of earth filling is 1 m, the road level is 400 m, as shown in Fig. 14, and the invert level is 395 m, as shown in Figs. 9,13,14.

The criteria used for the CDR cost assessment in Table VIII are based on the shear and moment diagram of the structure, as well as the maximum compressive strength of reinforced concrete required to support the ultimate dead load and ultimate live load of the culvert design (according to Shreedhar and Shreedhar, 2013).

The criteria include the following: CDR value: CDR; different ratios of width to height are considered. Material Costs: The relative cost of materials required for design and construction. Construction Costs: The estimated structure construction expenses associated with the respective CDR

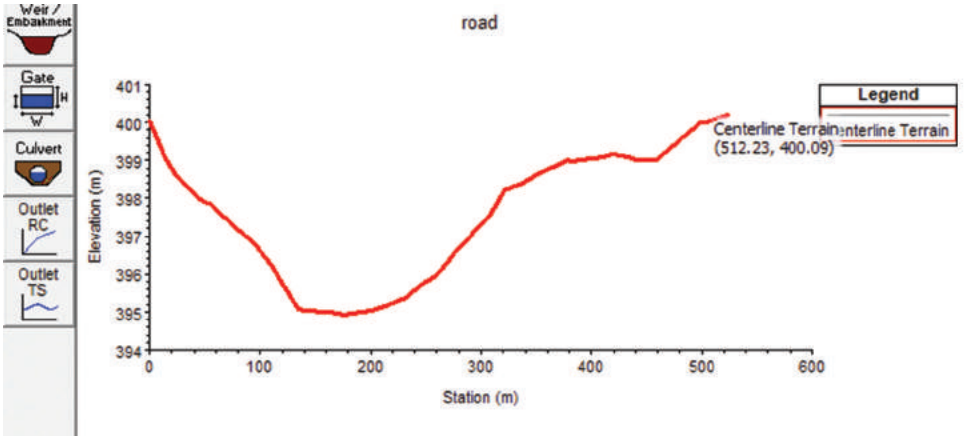

Fig. 13. Stream cross-section at the roadway–stream intersection.

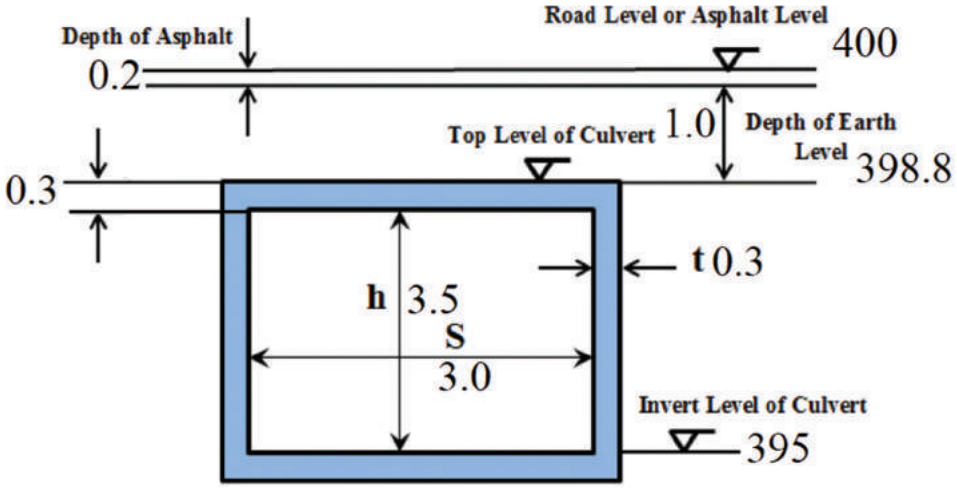

Fig. 14. Culvert cell design cross-section of selected aspect ratio 0.85 and dimension 3.0 × 3.5 m.

TABLE VII
Analysis of Cell Ratio Aspect

Configuration of cell	Channel length m	Span m	Size of cell m	Cell no.	Total section area m²	Aspect ratio
	30	10	10×5.25	1	52.5	1.9
	30	6.6	6.6×4	2	52.8	1.65
	30	5	4.5×4	3	54	1.1
	30	3	3×3.5	5	52.5	0.85

values. Maintenance Costs: The anticipated maintenance expenses over the culvert's lifespan. Long-term Durability: The expected durability and structural integrity of the culvert design.

Top level of road = Invert culvert level + Height of culvert + Top slab thickness + Depth of earth filling + Asphalt thickness.

Top level of the road = 395 + 3.5 + 0.3 + 1.0 + 0.2 = 400 m, as illustrated in Fig. 14. This dimension satisfies the standard culvert design (Shreedhar and Shreedhar, 2013).

Conducting an economic analysis based on CDR, and considering material costs, construction costs, maintenance costs, and durability, is crucial for selecting the optimum culvert section cell design. By balancing these factors, engineers can achieve cost-effective designs that meet both technical and economic requirements for infrastructure projects.

TABLE VIII
Economic Analysis of Cell Ratio Aspect

CDR value	Material costs	Construction costs	Maintenance costs	Long-term durability
1.9	High	High	High	Low
1.65	Moderate	Moderate	Moderate	Moderate
1.1	Moderate	Moderate	Moderate	High
0.85	Low	Low	Moderate	High

V. Conclusion

The research focused on the hydraulic analysis and design of a box culvert in Qoshtapa City, utilizing Bentley Culvert Master software. This study yielded significant insights and practical solutions for the efficient management of urban water drainage systems. The integration of advanced software

tools, such as Bentley Culvert Master, has emerged as a pivotal resource in optimizing the design and functionality of box culverts, thereby ensuring the secure and dependable conveyance of water through these structures at minimum cost.

The analysis unequivocally indicates that the existing culvert, with a cross-sectional area of 31.5 m^2 and a total of 3 cells in Qoshtapa1, falls short of meeting the requirements. Conversely, the designed culvert, with a cross-sectional area of 52.5 m^2 and a total of 5 cells, proves to be adequate for accommodating floods with the first alternative design a 100-year return period. When comparing the inundated areas caused by both the existing culvert and the proposed new culvert, the inundation area has decreased because the existing culvert makes a barrier in front of flood water drainage.

Through economic analysis, the best economic design that satisfies hydraulic standards (freeboard, invert level, top road level, and minimum quantity of cut and fill) is multi-celled box culverts, with cell sizes of 3 × 3.5 m and a total of 5 cells.

Fig. 14 and Tables VII and VIII provide a comparative analysis of the economic and durability associated with different CDR values in box culvert design, aiding decision making in infrastructure projects. Selecting the optimal culvert section through economic analysis ensures that transportation infrastructure (road way and culverts) projects achieve a balance between functionality, cost-effectiveness, and long-term sustainability, meeting the needs of both present and future generations.

It is easy to add two cells to the three-cell existing culvert, and the cross-section of the stream is suitable for absorbing flood waves and conserving human life and materials in the study area.

VI. Acknowledgments

The author would like to thank Dr. Ihsan Hamawand, Wide Bay Water and Waste Services, FCRC, QLD 4655, Australia. And London Proof readers, for English Grammar Review, they support is highly appreciated.

References

Abdelkarim, A., 2019. Assessment of the expected flood hazards of the Jizan-Abha Highway, Kingdom of Saudi Arabia by integrating spatial-based hydrologic and hydrodynamic modeling. *Global Journal of Research in Engineering*, 19(4), p.92.

Adeogun, A.G., Akinpelu, M.A., Yusuf, M.A., and Animashaun, R.A., 2019. Evaluation of HY-8 modeling tool for hydraulic analysis of selected culverts along Ilorin-Jebba Road, Kwara State, Nigeria. *Arid Zone Journal of Engineering, Technology and Environment*, 15, pp.133-141.

Alqreai, F.N., and Altuwaijri, H.A., 2023. Hydrological modeling and evaluation of the efficiency of culverts in drainage basins affecting the north railway in Wadi Malham. *Sustainability*, 15(19), p.14489.

Altuwaijri, H.A., 2019. Morphometric network drainage analysis for railway location: Case study of Saudi Railway Company's project. *Arabian Journal of Geosciences*, 12(16), p.508.

Brinley, J.C., 2010. *Practical Application of Hydraulic Tools in Urban Stormwater Design* [Thesis].

Daniel, W.B., 2001. *Rating System for Rural Culvert Crossing Repair and Maintenance*. Montana State University-Bozeman Bozeman, Montana.

Dawood, A.H., and Mawlood, D.K., 2023. Derivation of the rainfall intensity-duration-frequency curve for Erbil city, using SCS II method. *Zanco Journal of Pure and Applied Sciences*, 35, pp.1-10.

Deutsche Welle Newsletter, 2021. *Deadly Floods hit Iraqi Kurdistan*. Available from: https://koqihqmvkv.oedi.net/en/deadly-floods-hit-iraqi-kurdistan/a-60171223 [Last accessed on 2024 May 09].

Kalyanshetti, M.G., and Gosavi, S.A., 2014. Analysis of box culvert-cost optimization for different aspect ratios of cell. *IJRET: International Journal of Research in Engineering and Technology*, 3, pp.508-514.

Kinyanjui, M.N., Tsombe, D.P., Kwanza, J.K., and Gaterere, K., 2011. Modeling fluid flow in open channel with circular cross-section. *Journal of Agriculture, Science and Technology*, 13(2), pp.78-89.

Mamoon, W.B., Islam, A.K.M.S., Kaiser, S., Islam, G.M.T., and Bala, S.K., 2022. Performance Analysis of Culverts Along The N105 Bypass Road Using Hy-8 Software for Future Climate Scenario. In: *6th International Conference on Civil Engineering for Sustainable Development.* KUET, Bangladesh.

Moore, K., Furniss, M.J., Flanagan, S., and Love, M.A., 1999. *A Guide to Computer Software Tools for Culvert Design and Analysis*. U.S. Department of Agriculture Forest Service, United States.

Nachtergaele, F., Van Velthuizen, H., and Batjes, N.H., 2012. *Harmonized World Soil Database Version 1.0*. Food and Agriculture Organization, Austria.

News, R., 2021. *Death Toll Rises to 11 in Erbil Floods, New Wave of Rain to Hit the Region*. Available from: https://www.rudaw.net/english/kurdistan/171220211 [Last accessed on 2024 May 09].

Popovska, C., 2010. *Storm Sewer System Analysis in Urban Areas and Flood Risk Assessment*. *Modeling in Civil*, pp.1-7. Available from: https://search.ebscohost.com/login.aspx?direct=true&profile=ehost&scope=site&authtype=crawler&jrnl=20666926&an=60014793&h=hyr6jgspevtz4o2u9uh1w08pdukpg3pic3wsfkmruskchlfhiwa%2blfaxxuj%2fq8oxqrv17wf%2fgovrh1w9ynyvcw%3d%3d&crl=c [Last accessed on 2024 May 09].

Qasim, O.A., 2020. *Design of a Box Culvert*. Scribd, Inc., United States.

Ramadan, H., El Gindy, H., Gomaa, A., Ayman, A., Fouda, M., and Abdallah, A., 2022. Flood Protection System to Aswan Under Current and Future Climate Conditions. In: *6th IUGRC International Undergraduate Research Conference*. Military Technical College, Cairo, Egypt.

Rowley, B.J., Thiele, E.A., Hotchkiss, R.H., and Nelson, E.J., 2007. Numerical modeling of culvert hydraulics: Modernization of existing HY8 software. In: *Examining the Confluence of Environmental and Water Concerns-Proceedings of the World Environmental and Water Resources Congress 2006*, p.40856.

Scharffenberg, W.A., 2013, *Hydrologic Modeling System User's Manual*. Hydrologic Engineering Center, California.

Shreedhar, S., and Shreedhar, R., 2013. Design coefficients for single and two cell box culvert. *International Journal of Civil and Structural Engineering*, 3(3), pp.475-494.

Sissakian, K.V., Al-Ansari, N., Adamo, N., Abdul Ahad, I.D., and Abed, A.S., 2022. Flood hazards in Erbil City Kurdistan Region Iraq, 2021: A case study. *Engineering*, 14(12), pp.591-601.

Software, 2022. *Open Flows Culvert Master*. Available from: https://www.bentley.com/software/openflows-culvertmaster [Last accessed on 2024 May 09].

Systems, B. 2007. *Bentley Culvert Master User's Guide*. Bentley Systems, United States.

United States Department of Agriculture, Natural Resources Conservation Service, and Conservation Engineering Division, 1986. *Urban Hydrology for Small Watersheds TR-55*. *Soil Conservation*, *Technical Release 55* (*TR-55*), p.164. Available from: https://scholar.google.com/scholar?hl=en&btng=search&q=intitle: urban+hydrology+for+small+watersheds#1 [Last accessed on 2024 May 09].

US Army Corps of Engineers, 2018. *Hydrologic Modeling System HEC-HMS. User's Manual*. *Version 4.3*. Hydrologic Engineering Centre, Davis, CA, p.640. Available from: https://www.hec.usace.army.mil/software/hec-hms/documentation/hec-hms_users_manual_4.3.pdf [Last accessed on 2024 May 09].

Yoo, D.H., and Lee, S., 2012. Direct determination of the width or the height for a box culvert applying dimensionless equations. *KSCE Journal of Civil Engineering*, 16(7), pp.1302-1307.

Efficient and Simplified Modeling for Kerosene Processing Quality Detection Using Partial Least Squares-Discriminant Analysis Regression

Hayder M. Issa* and Rezan H. Hama Salih

Department of Chemistry, University of Garmian, Kalar, Sulaymaniyah Province, 46021, Kurdistan Region – F.R. Iraq

***Abstract*—Kerosene from various refineries and crudes is used for heating and other purposes in many countries like Iraq; therefore, it is important to identify its source to recognize and tax any adulteration. In this study, a fast classification technique for kerosene marketed in Iraq was developed with the goal of identifying its quality. The samples were categorized using a supervised partial least squares discriminant analysis (PLS-DA) approach. Multivariate analyses using agglomerative hierarchal clustering and principal component analysis were utilized to identify outliers and sample dissimilarities. The dataset was divided into calibration and prediction sets. The prediction set was used to evaluate the model's separation performance. The Q^2 cross-validation was applied. The PLS-DA models achieved significant accuracy, sensitivity, and specificity, showing strong segregation ability, notably for the calibration set (100% accuracy and 1.00 sensitivity). It was found that kerosene processing can be classified rapidly and non-destructively without the need for complicated analyses, demonstrating the best results for classification even when compared with the classification outcomes of other fuels. This PLS-DA approach has never been looked at before for process quality detection, and the results are comparable to direct kerosene classification with soft independent modeling of class analogy and support vector machines.**

***Index Terms*—Supervised discrimination technique, Modeling, Kerosene processing, Quality control, PLS-DA, Machine learning tool.**

I. Introduction

Kerosene is a mixture of hydrocarbons with carbon atom counts ranging from 6 to 16, and kerosene can be utilized in a variety of applications, including as an aviation fuel and a home heating fuel. It is isolated as a straight-chain component of petroleum; kerosene is produced primarily through fractional distillation of crude oil (Lam, et al., 2012). N-alkane, alkyl benzene, and naphthalene are the main components of kerosene (Kaltschmitt and Deutschmann, 2012). Its volatility is between that of gasoline and diesel fuel, and its boiling point range is between 150 and 350°C.

The refineries at Bazian and Kirkuk are the main sources of kerosene for the region of study in north-eastern Iraq. A total of 34,000 barrels/day is produced at the 2009-founded Bazian refinery, which uses only atmospheric distillation and hydrotreating equipment. The Taq-Taq oil field is the principal source of crude oil for the Bazian refinery (Ali and Khodakarami, 2015). The Kirkuk oil field supplies the crude for the Kirkuk refinery, which began operations in 1938 and has seen its capacity rise over the years to the current 30,000 barrels/day. Atmospheric distillation, vacuum distillation, catalytic reforming, and hydrotreating are just some of the process units in the Kirkuk refinery (Abdullah and Daij, 2021). Both Taq-Taq and Kirkuk crudes can be refined into kerosene at about the same rate (25.6% for Taq-Taq and 23.6% for Kirkuk), but Taq-Taq crude has a higher API (47.52) and is more expensive (Karim, Khanaqa and Shukur, 2017, Naman, et al., 2019). When comparing the Bazian refinery to the Kirkuk refinery, the Nelson complexity index, which is used to define the sophistication of a refinery (Kaiser, 2017), for the former is 2.26 whereas the latter is 2.03 (Abdullah and Daij, 2021).

Therefore, there must be a method to categorize and identify the source of locally produced kerosene because each type has a distinct composition, which affects performance as well as the possibility of adulteration and taxation. Several standards can be used to control the quality of middle distillates like kerosene. They are time-consuming, require many samples, and have expensive measurement equipment. It has proven possible to identify sources, detect adulteration, or classify fuels using chemometrics analysis with spectral or property input data (Barra, et al., 2020, De Paulo, et al., 2014, Comesaña-García, et al., 2013, Dago Morales, et al., 2008). The principle component analysis (PCA) and hierarchical cluster analysis (HCA) multivariate calibration techniques have been used by Tanaka, et al. (2011) to detect solvent traces in gasoline. They found 83.8% and 77.1% sensitivity results for calibration and external sets, respectively, by

ARO-The Scientific Journal of Koya University
Vol. XII, No. 1 (2024), Article ID: ARO.11515. 8 pages
Doi: 10.14500/aro.11515
Received: 08 January 2024; Accepted: 21 March 2024
Regular research paper: Published: 10 May 2024
Corresponding author's e-mail: hayder.mohammed@garmian.edu.krd

adopting the soft independent modeling of class analogy (SIMCA) algorithm. Dadson, Pandam, and Asiedu (2018) have looked at the possibility of classifying gasoline based on four added adulterants using the same approach except for HCA. The SIMCA classification model has a sensitivity of 100% for the calibration set and 75% for the external set.

Furthermore, Mohammadi, et al. (2020) employed attenuated total reflectance-Fourier transform infrared (ATR-FTIR) spectroscopy with partial least squares discriminant analysis (PLS-DA) to sort crude oil samples into groups. This created a model that was 100% accurate in terms of both sensitivity and specificity. Mazivila, et al. (2015) used the mid-infrared spectroscopy (MIR) data to sort biodiesel samples into groups based on their types and routes. They did this using a PLS-DA-based classification algorithm. The PLS-DA classification model yielded identical accuracy values of 100%.

Kerosene is relatively understudied compared to gasoline and biodiesel. Innovatively, this work categorizes kerosene by source conformance using a multivariate method. This method handles heterogeneous and uncalibrated kerosene samples with optimal spectral profiles, which goes beyond quality assurance to target tax avoidance and adulteration at local filling stations and reduce refining process and crude oil source uncertainty by establishing effective kerosene compositional classification algorithms. These categorization algorithms ensure kerosene integrity, reliability, and regulatory compliance for industrial and home consumers.

Kerosene has been classified in only a few studies in the literature. To check for adulteration in kerosene samples, Pontes, et al. (2011) used PLS-DA and the successive projections method (SPA-LDA) in conjunction with near-infrared NIR data with an optical path of 10 mm. When it came to classifying a subset of the input data, PLS-DA produced the greatest results, with a 100% accuracy rate in the external set.

In regard to taxation and identification of kerosene adulteration at local fueling stations, the current study tested the multivariate methods (PLS-DA with HCA and PCA) for the direct classification of kerosene, which is a novel strategy never tried previously for kerosene, based on their conformance to the refining source, where different crude oil and refinery processes were used, from its optimized spectra profile. These classification models are necessary to overcome the difficulties of anomalous conditions generated from different kerosene samples; those were not previously included in calibration sets of existing prediction models.

II. Materials And Methods

A. Kerosene Sampling and Analysis

During a 6-month period, 60 kerosene samples were gathered from service stations in the eastern Iraqi city of Kalar to consider time-dependent variation in crude oil's chemical structure. The crude oil for these samples comes from Kirkuk and Bazian (Classes K and R, respectively), two of the largest local refineries with different process specifications. Their crude oil comes from different sources. Additional 10 kerosene samples were tested, obtained from a different source, outside the study area, for model verification (external validation). Polyethylene containers containing specimens for FTIR analysis were maintained at a temperature below 8°C in accordance with the usual procedure of the standard test method (ASTM D4057 - 19, 2019).

In this study, a spectrophotometer (Model: IRAffinity-1S: SHIMADZU) was used. The spectral resolution power was 4.0 cm^{-1}. For each sample, three absorbance spectra in the 4000–400 cm^{-1} wavenumber region were taken and averaged. Three spectra were multivariate calibrated to (ASTM E1655-17, 2018). Testing on the used spectrophotometer is being done using a routine quality assessment system developed according to standard procedure (ISO 4259-3, 2020). These measurement methods were evaluated for repeatability and reproducibility (accuracy) in accordance with (ISO 5725-2, 2019).

B. Multivariate Statistical Analysis and Model Development

The obtained FT-Mid IR spectral data was first pretreated for curve smoothing and baseline correction by applying the Savitzky-Golay first derivative method of a 21-point window and a second-order polynomial using OriginLab software (free trial version), resulting in 448 variables. The data were also preprocessed by changing the values to mean-centered – variance set to be 1. The results of each class were arranged into a matrix of samples as rows and spectra as columns. Kerosene samples were then subjected to statistical analysis using agglomerative hierarchal cluster analysis (AHC), which uses Euclidean distances and Ward linkage measures, to show that the samples were indeed grouped together. PCA analysis has been applied to each class to segregate the dataset into main groups (Issa, 2024). To further purify component scores, a varimax rotation of the PCs with significant eigenvalues was conducted. This allowed us to maximize the distribution of the components by minimizing the number of small coefficients whereas maintaining a high level of detail in the original data, as illustrated in Fig. 1a.

Next, samples have been divided into a calibration set after removing outliers, and a validation set using the Kennard-Stone algorithm (Kennard and Stone, 1969). The PLS-DA multivariate calibration method was used to establish the classification model with a threshold between 0 and 1. To verify an appropriate number of latent variables (LV) for the PLS-DA classification model, the cross-validated (leave one out) predictive relevance (Q^2) of the model that each LV manages to accomplish has been taken into account. A higher Q^2 value means a higher predictive ability for the model, as reported by Roy and Roy (2008).

$$Q^2 = 1 - \frac{\sum\left(Y_{meas} - Y_{pred.}\right)^2}{\sum\left(Y_{meas} - \bar{Y}\right)^2} \quad (1)$$

Outliers were detected using high leverage values and Q residuals at a 95% level of confidence. Sensitivity (Sens), specificity (Spec), precision (Pre), and accuracy (Acc), Equations 2–5, evaluations for PLS-DA model quality have been employed as reported by Mohammadi, et al. (2020) and presented in the following equations (2–5), where TP,

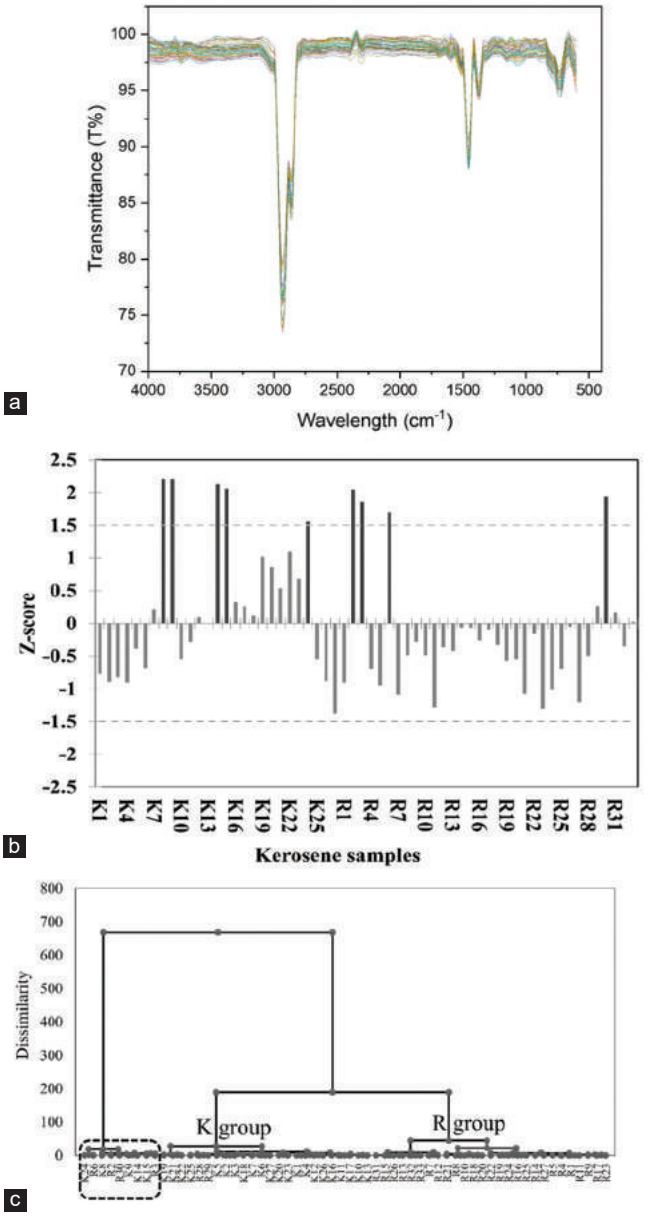

Fig. 1. (a) Mid-infrared spectrum of 60 kerosene samples in the range of 600–4000 cm^{-1}, (b) Results of Grubb's test for outlier detection at a significance level of 95%, and (c) Dendrogram of agglomerative hierarchal cluster for the 60 kerosene samples.

FN, TN, and FP represent the statistical parameters of true positive, false negative, true negative, and false positive, respectively.

$$\text{Sens} = \frac{\text{TP}}{\text{TP} + \text{FN}} \quad (2)$$

$$\text{Spec} = \frac{\text{TN}}{\text{TN} + \text{FP}} \quad (3)$$

$$\text{Pre} = \frac{\text{TP}}{(\text{TP} + \text{FP})} \quad (4)$$

$$\text{Acc} = \frac{\text{TN} + \text{TP}}{(\text{TN} + \text{TP} + \text{FN} + \text{FP})} \quad (5)$$

III. Results and Discussion

A. Characteristics of Kerosene Samples

Fig. 1a presents the FT-Mid IR spectra analysis of kerosene samples after applying curve smoothing and baseline correction. It is apparent from Fig. 1a that kerosene samples are composed of several main hydrocarbon compounds. Several typical band vibrations within the FT-Mid IR range (4000–600 cm^{-1}) are presented. According to the existing vibration types in Fig. 1a, different stretching and bending of various functional groups for diagnostic and fingerprint regions have occurred within the tested range. The stretching vibrations of aliphatic and aromatic C-H, C=C, and C-C groups are presented. Bending vibration related to C-H also existed in tested samples around 730 cm^{-1} and 1035 cm^{-1}. In general, samples contain aliphatic compounds, with a considerable proportion of long linear types of absorption range around 730 cm^{-1}, and aromatic compounds with an absorption range of 1400–1600 cm^{-1} (Coates, 2000). Results of Grubb's test for outlier detection at a significance level of 95% are shown in Fig. 1b.

The AHC method was applied to determine if the unidentified outliers in Grubb's test should be rejected or kept in the dataset. According to the AHC method, results displayed in Fig. 1c, the questionable outlier samples existing in the dataset are clearly identified. These samples have demonstrated a high degree of dissimilarity when compared to the rest of the samples. These outliers, which are shared by both the R and K sample sets, were excluded in the next classification calculations. For the remaining dataset, the spectra of the samples that were measured within the FT-Mid IR range are correctly classified into two main clusters, which reflect the origin of the samples at the moment of sampling.

PCA was used to look at and sort samples of kerosene into different groups based on how they were refined and where they came from. As can be seen from the score plot of PCA results in Fig. 2a, Varimax rotation of the principal components (PCs) of significant eigenvalues was performed to explain more than 99.76% of the total variation in the IR spectra, which was represented by two main components, PC1 and PC2. PC1 (accounts 50.15%) and PC2 (accounts 49.61%) recognized two groups in the dataset corresponding to different sources and refining processes of kerosene samples.

A PLS-DA model has been established on the basis of two groups, R and K that were previously defined by PCA and AHC for FT-Mid IR spectral analysis of kerosene samples after excluding outliers, given that 36 samples were for the calibration set and 15 samples were for the prediction set. Of the 36 samples in the calibration set, 21 are of class R and 15 are of class K.

The 15 samples in the prediction set are comprised of 8 of R and 7 of K. The number of latent variables, for the supervised technique of PLS-DA, the term discriminant factor is also used for the spectral dataset was chosen on the basis of the maximum predictive ability explained for the dependent variable of the kerosene group classifier (Y) and FT-Mid IR explanatory variables Xi and using cross-validated Q^2.

http://dx.doi.org/10.14500/aro.11515

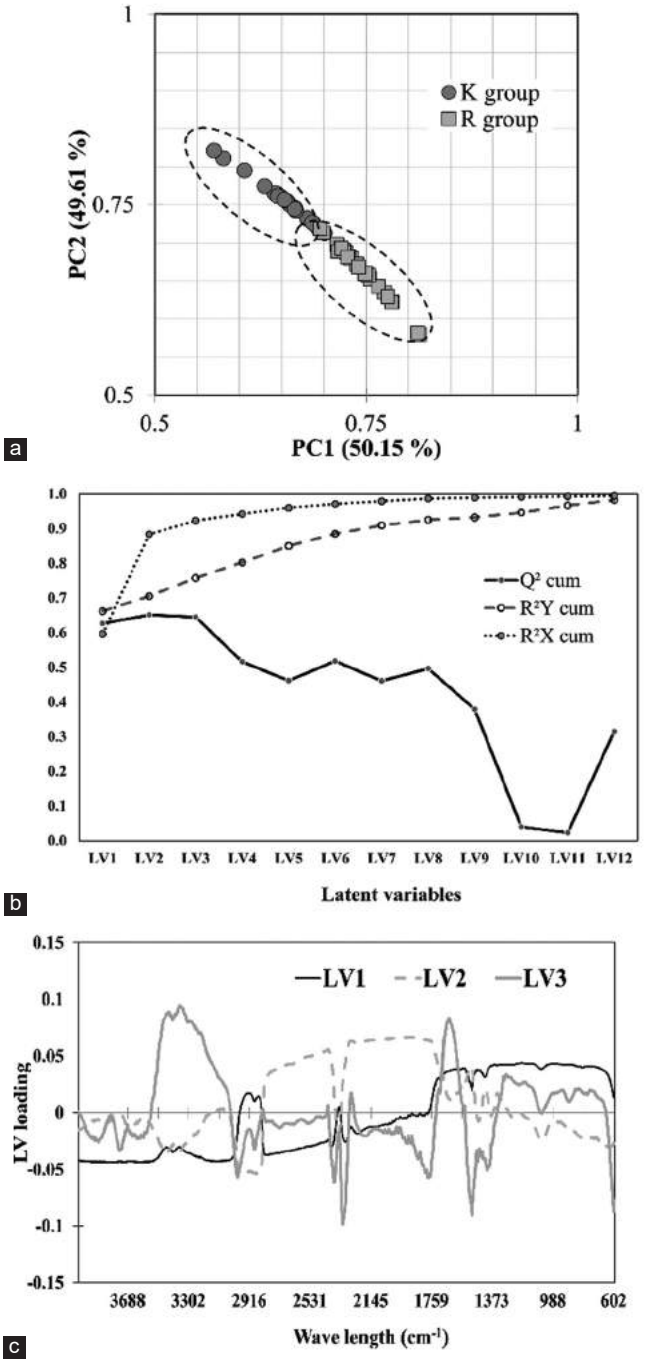

Fig. 2. (a) Principle component analysis score plots (PC1 and PC2) account 99.76% of the total variation in FT-Mid IR spectra for the kerosene dataset after Varimax rotation, (b) Plot of cross-validated Q2, R2Y, and R2X and number of LVs in partial least squares-discriminant analysis, (c) line loading plot for the three LVs for FT-Mid IR explanatory variables.

Fig. 2b shows that the cumulative Q^2 has been maximized when considering three LVs (Q^2 equals 65.13%) and that after this point, Q^2 values give lower predictive relevance for the model, despite the fact that a larger number of LVs succeeds in explaining a larger total variance of Y and Xi, as shown by the cumulative values of the regression coefficient (R^2). The total variance explained by three LVs for Y was 75.75% and for Xi was 92.29%.

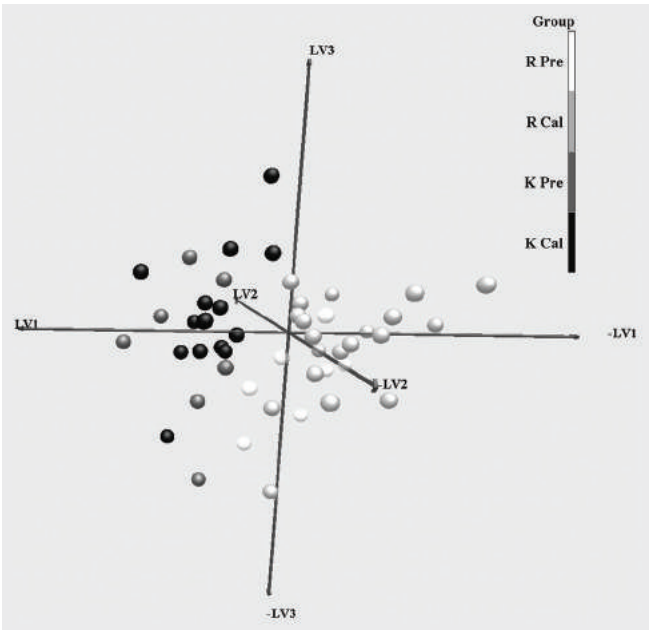

Fig. 3. Three-dimensional score plot of the LV1, LV2, and LV3 for calibration and prediction sets in partial least squares-discriminant analysis model.

The loading line for the LVs is depicted in Fig. 2c. It can be seen that the spectral transmission bands at wavenumbers between 600 and 1700 cm^{-1}, involving C-H and C-C bending and CH_3 stretch, are the sections that had the most impact on LV1. The absorption peaks at 2990–2400 and 2300–1650 cm^{-1}, which may have been caused by CH3 and C=C stretches, had a greater impact on LV2. In addition, the primary absorption peaks that characterized the LV3 are located between 3550 and 3028 cm^{-1}, 2450 and 2300 cm^{-1}, and 1700 and 1400 cm^{-1}, respectively, where these frequencies correlate to stretches in the CH_2 and CH_3 bonds, as well as aromatic C=C bonds.

The FT-Mid IR spectra shown in Fig. 2c, that the fingerprint region is the most significant for LV1. Using the PLS-DA model for three latent variables and leaving one out cross-validation technique, the data set was classified into two main groups. In Fig. 3, adequate separation performance for the samples is depicted by the 3D score plot of LV1, LV2, and LV3 (accounting for 59.63%, 28.74%, and 3.92% of the variances in the FT-Mid IR spectra, respectively). The figure shows that the PLS-DA model can correctly divide the kerosene samples into two Groups, K and R, based on how they were refined and where they came from, for the calibration and prediction sets.

Table I displays the results of a classification analysis of the PLS-DA model. The results demonstrate that 100% of the samples in the calibration set were correctly identified, whereas 86.67% of the samples in the prediction set were correctly classified. To further evaluate the efficacy of the PLS-DA model, the Sens, Spec, Pre, and Acc were computed for both the calibration and prediction sets, as shown in Table I. Sens and Spec are statistical parameters for measuring the dependability of any classification model, whereas Acc and Pre can be estimated to help with the realization of the model's specifications. The suggested

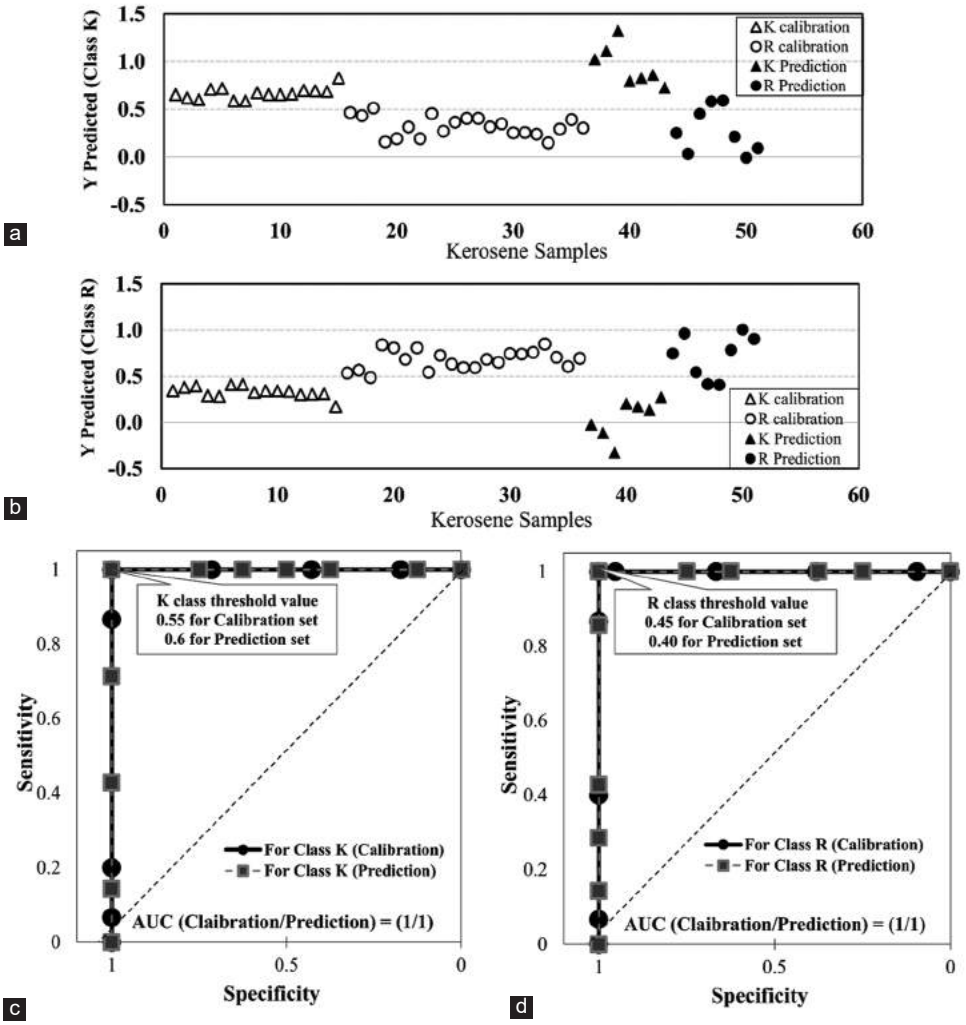

Fig. 4. (a) Class values estimation plots of calibration and prediction sets using partial least squares-discriminant analysis (PLS-DA) models for class K, (b) for class R, (c) ROC curve using PLS-DA models for classification of the kerosene samples for class K; and (d) for class R.

TABLE I
The Confusion Matrix And Classification Characterization of Kerosene Groups Classification using the PLS-DA Model for Calibration and Prediction Sets

Calibration set				
From/to	K	R	Total	% correct
K	15	0	15	100.00%
R	0	21	21	100.00%
Total	15	21	36	100.00%
Prediction set				
From/to	K	R	Total	% correct
K	7	0	7	100.00%
R	2	6	8	75.00%
Total	9	6	15	86.67%
Calibration set				
Class	Sens.	Spec.	Pre.	Acc.
K	1.00	1.00	1.00	1.00
R	1.00	1.00	1.00	1.00
Prediction set				
Class	Sens.	Spec.	Pre.	Acc.
K	1.00	0.75	0.78	0.78
R	0.75	1.00	1.00	0.87

PLS-DA: Partial least squares discriminant analysis

model's sensitivity measures the fraction of true positives and its specificity measures the fraction of false negatives for correctly classified data (Khanmohammadi, et al., 2013). Table I also shows that the model's quality evaluation demonstrates its dependability in classifying kerosene samples into their respective categories, with a Sens of 1.00 for class K and a Spec of 1.00 for class R in both the calibration and prediction sets. Model performance is slightly lower for the prediction set compared to the calibration set class for some defining parameters, which may be due to the relatively limited number of samples employed.

Fig. 4a and b display an analysis of the discrimination of kerosene samples using the PLS-DA model. The goal of this analysis is to determine the differences in refining procedures and crude oil origin that exist between the classes K and R that have been allocated to the FT-Mid IR spectral data set. The sample classification procedure appears to have been carried out satisfactorily, as evidenced by the accurate segregation of the class values for both the calibration and prediction sets. Fig. 4 demonstrates quite clearly how the two sets of kerosene samples, denoted as K and R, can be distinguished from one another.

The receiver operating characteristic (ROC) curve, which is utilized for the examination of classification abilities, has been applied to illustrate the performance, in terms of Sens and Spec, of an existing model as a function of varying the discrimination threshold (Hanley, 1998).

The ROC curves for the groups K and R that were examined are shown in Fig. 4c and d. It is clear that a threshold value of 0.55 or 0.6 for the K class will result in a sensitivity and specificity value of 100 percent. The same result has also been achieved for the R class, with threshold values of 0.45 and 0.4 for the calibration and prediction sets, respectively. This indicates that the two groups for K and R classes have been entirely separated from one another. Because the area under the curve (AUC) is always equal to 1.00, the p value is always less than 0.05, which indicates that the PLS-DA model diagnostic is significant. Since the PLS-DA model screening is significant, the null hypothesis H_o is rejected in this scenario. According to H_o, the area under the curve (AUC) is equal to 0.5, which indicates that the separation performance of the model is completely a matter of chance (Mallick, et al., 2022).

Before comparing the results of the PLS-DA model derived in this work to those of related previous studies, it is important to state that the results obtained by the PLS-DA model and those raised by PCA and AHC analysis methods are highly consistent, confirming the difference between the K and R classes of kerosene samples. This finding suggests that the differences in hydrocarbon composition between these two groups are the result of differences in refining processing and crude oil origin.

The external validation for the PLS-DA model was made up of validation samples of the classes R and K and 10 foreign samples (F) collected from a different source of kerosene samples, to check the model capability to discriminate the F samples as not belonging to any of the classes. Fig. 5 shows the observation chart, showing the distances of the F samples from the validation set of K and R classes. It can easily be seen that classes R and K are correctly classified and F samples are outside the boundaries of the studied classes K and R.

The PLS-DA model's verification was independently validated by an external source by distinguishing the 10 foreign samples (F), collected from a different source of kerosene, as not belonging to any of the classes was tested. Observation chart depicting F samples distances from the K and R classes in the validation set within the 5% confidence

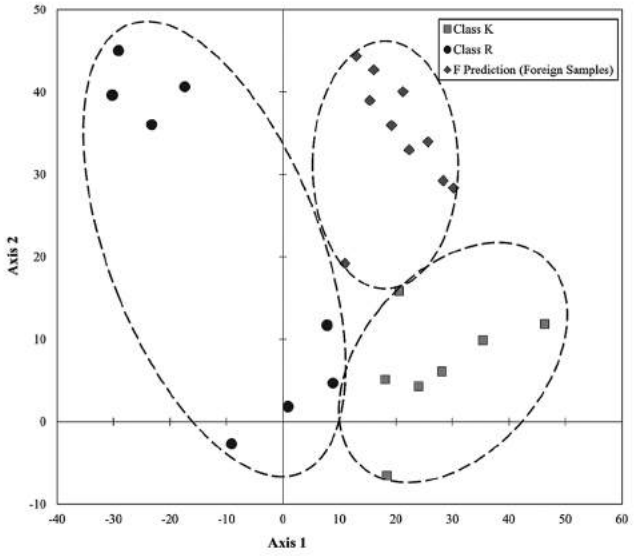

Fig. 5. Three classes observation chart with confidence ellipses for the partial least squares-discriminant analysis model external verification over the first two LVs (with a significance level of 5%).

TABLE II
Sens and Spec of PLS-DA Model for Kerosene Screening Compared to Previous Studies.

Investigation approach	Ave. Sens[1]	Ave. Spec*	No. of LVs	No. of classes (NC)	NS [9]/NC
PLS-DA, IR (calib. set in this work)	1.00	1.00	3	2	18
PLS-DA, IR (pred. set in this work)	0.88	0.88			7.5
PLS-DA, IR for crude oil (calib. set)[2]	1.00	1.00	2	3	23.33
PLS-DA, IR for crude oil (pred. set)[2]	1.00	1.00			10
PLS-DA, GC-MS for gasoline (calib. set)[3]	0.97	0.99	3	4	16
PLS-DA, GC-MS for gasoline (pred. set)[3]	0.97	0.93			4
PLS-DA, IR for gasoline (calib. set)[3]	1.00	0.99	3	4	16
PLS-DA, IR for gasoline (pred. set)[3]	1.00	1.00			4
QDA, IR for gasoline (calib. set)[4]	0.90	0.90	3	2	20
QDA, IR for gasoline (pred. set)[4]	0.85	0.88			22.5
PLS2-DA, IR for biodiesel (calib. set)[5]	1.00	1.00	3	4	15
PLS2-DA, IR for biodiesel (pred. set)[5]	1.00	1.00			7
PLS-DA, FE for gasoline (calib. set)[6]	0.87	0.89	3	3	16.66
PLS-DA, FE for gasoline (pred. set)[6]	1.00	1.00			8.33
SIMCA, Phys Prop for kerosene (calib. set)[7]	0.79	0.29	2	2	16
SVM Phys Prop for kerosene (calib. set)[7]	1.00	1.00	-	2	20
SVM, Phys Prop for kerosene (pred. set)[7]	1.00	1.00			12.5
SIMCA, IR for kerosene (calib. set)[8]	1.00	1.00	2	2	20
SIMCA, IR for kerosene (pred. set)[8]	1.00	1.00			15

[1]Average of Sens and Spec values for classes were taken into account; [2]adopted from (Mohammadi, et al., 2020); [3]adopted from (Barra, et al., 2020); [4]adopted from (Khanmohammadi, et al., 2013); [5]adopted from (Mazivila, et al., 2015); [6]adopted from (De Paulo, et al., 2014); [7]adopted from (Comesaña-García, et al., 2013); [8]adopted from (Dago Morales, et al., 2008); 9NS is a number of samples. PLS-DA: Partial least squares discriminant analysis, SIMCA: Soft independent modeling of class analogy, SVM: Support vector machine

limits, Fig. 5 shows that over the latent variables LV1 and LV2. It is clear that classes R and K have been appropriately identified and that the F samples lie outside of the boundaries of the classes K and R that have been examined.

Table II displays a comparative analysis of the current study with different methods in the literature used to classify various fuels such as crude oil, gasoline, biodiesel, and kerosene. The models were established using techniques such as PLS-DA, quadratic discriminant analysis (QDA), support vector machine (SVM), and SIMCA, along with analytical methods such as infrared spectroscopy (IR), gas chromatography-mass spectrometry (GC-MS), and Physical properties (Phys Prop). Performance indicators such as Average Sensitivity (Ave. Sens) and Average Specificity (Ave. Spec) are provided for both calibration and prediction sets to demonstrate the models' capacity to generalize to new data. Some methods consistently perform well on both calibration and prediction sets, such as PLS-DA with IR for gasoline, crude oil, and biodiesel or SIMCA with IR and Phys Prop for kerosene. However, other methods show variability or lower performance on prediction sets compared to calibration sets. The outcomes obtained from this study, the developed PLS-DA model, for kerosene process detection indicate a potential model robustness and generalization. Despite differences, the comparison with previous models, the model here for kerosene has a promising accuracy in categorizing the samples, offering vital insights into their usefulness in fuel classification tasks.

The classification assessment presented in Table II reveals that despite the fact that chemometrics and spectral analysis have been utilized in numerous attempts to differentiate between crude oil and petroleum products, relatively little work has been done in this area with regard to the categorization of kerosene as it can be drawn from the researches in the literature. In the investigations conducted by (Comesaña-García, et al., 2013, Dago Morales, et al., 2008), the distinction between kerosene sample was achieved through the utilization of several modeling approaches. These approaches included SIMCA coupled with physical parameters and SVM coupled with IR spectra, there results were close to those obtained here, especially for the calibration data set.

This work utilizes a unique modeling strategy that combines PLS-DA with FT-Mid IR spectrum analysis to differentiate between two groups of kerosene based on their origins and refining processes. Throughout the investigation, it was shown that PLS-DA models can effectively do the task, leading to the highly satisfactory findings described earlier. The classification performance was promising despite the small sample size employed for the prediction set. The study used a limited number of samples, but the results demonstrate that PLS-DA is a valuable, statistically significant, straightforward, and cost-effective method for distinguishing kerosene, similar to its application for other petroleum products.

IV. Conclusions

- Utilizing the supervised pattern detection method PLS-DA and multivariate analyses of AHC and PCA on the FT-Mid IR dataset can aid in sorting kerosene from different refineries and sources efficiently for quality and taxation purposes.
- Kerosene samples from various routes can be effectively classified using PLS-DA.
- AHC has been applied professionally to classify kerosene samples and detect outliers.
- Outliers identified by Grubb's test were discarded.
- PCA with the varimax rotation method easily distinguished the sample distribution into two main classes.
- Three LVs from cross-validated PLS-DA models were utilized in the calibration set, resulting in successful discrimination.
- Compared to SIMCA and SVM models, PLS-DA demonstrated significant discrimination capability.
- The supervised PLS-DA discrimination model significantly improved the classification of kerosene samples into clear groups, achieving 100% accuracy in the calibration set and 86.7% accuracy in the prediction set.
- The study highlights the effectiveness of using supervised PLS-DA for sorting kerosene samples based on their origin and processing methods, facilitating quality control and fraud detection.
- Further research is needed to explore the combination effect of PLS-DA with SIMCA on classification accuracy.
- Other methodologies such as artificial neural networks and classification and regression trees could be promising for kerosene categorization and warrant investigation.

V. Acknowledgment

The authors express their gratitude to Lox-Agency Laboratories, Kalar-Garmian Region, for providing the required laboratories and facilities to complete the experimental portion of this study.

References

Abdullah, Z.F., and Daij, M.A., 2021. Analytical study of oil refining in the North refineries company for the period 2013-2019. *Journal of Al-Frahedis Arts*, 13(46), pp.131-159.

Ali, J.A., and Khodakarami, L., 2015. Optimal oil pipeline route in Kurdistan Region Taq Taq-Bazian refinery as case study. *International Journal of Engineering Trends and Technology*, 23(5), pp.257-262.

ASTM D4057 - 19, 2019. *Standard Practice for Manual Sampling of Petroleum and Petroleum Products*. ASTM International, West Conshohocken, PA.

ASTM E1655-17, 2018. *Standard Practices for Infrared Multivariate Quantitative Analysis*. ASTM International, West Conshohocken, PA.

Barra, I., Kharbach, M., Bousrabat, M., Cherrah, Y., Hanafi, M., Qannari, E.M., and Bouklouze, A., 2020. Discrimination of diesel fuels marketed in Morocco using FTIR, GC-MS analysis and chemometrics methods. *Talanta*, 209, p.120543.

Coates, J., 2000. Interpretation of infrared spectra, a practical approach. In: *Encyclopedia of Analytical Chemistry.* John Wiley and Sons Ltd., Chichester, UK.

Comesaña-García, Y., Cavado-Osorio, A., Linchenat-Dennes, E., and Dago-Morales, Á., 2013. Classification of kerosene using physicochemical data and multivariate techniques. *Revista CENIC Ciencias Químicas*, 44, pp.13-22.

Dadson, J., Pandam, S., and Asiedu, N., 2018. Modeling the characteristics and quantification of adulterants in gasoline using FTIR spectroscopy and chemometric calibrations. *Cogent Chemistry*, 4(1), p.1482637.

Dago Morales, Á., Cavado Osorio, A., Fernández Fernández, R., and Dennes, E.L., 2008. Development of a SIMCA model for classification of kerosene by infrared spectroscopy. *Química Nova*, 31, pp.1573-1576.

De Paulo, J.M., Barros, J.E.M., and Barbeira, P.J.S., 2014. Differentiation of gasoline samples using flame emission spectroscopy and partial least squares discriminate analysis. *Energy and Fuels*, 28(7), pp.4355-4361.

Hanley, J.A., 1998. Receiver operating characteristic (ROC) curves. In: Armitage, P., and Colton, Y., (eds.). *Encyclopedia of Biostatistics.* Wiley, Chichester.

ISO 4259-3, 2020. *Petroleum and Related Products - Precision of Measurement Methods and Results - Part 3: Monitoring and Verification of Published Precision data in Relation to Methods of Test*. ISO - International Organization for Standardization, Geneve.

ISO 5725-2, 2019. *Accuracy* (*Trueness and Precision*) *of Measurement Methods and Results - Part 2: Basic Method for the Determination of Repeatability and Reproducibility of a Standard Measurement Method*. ISO - International Organization for Standardization, Geneve.

Issa, H.M., 2024. Prediction of octane numbers for commercial gasoline using distillation curves: A comparative regression analysis between principal component and partial least squares methods. *Petroleum Science and Technology*, 42(10), pp.1233-1249.

Kaiser, M.J., 2017. A review of refinery complexity applications. *Petroleum Science*, 14(1), pp.167-194.

Kaltschmitt, T., and Deutschmann, O., 2012. Chapter 1 - Fuel processing for fuel cells. In*:* Sundmacher, K., (ed.). *Advances in Chemical Engineering.* Academic Press, Cambridge.

Karim, A.R., Khanaqa, P., and Shukur, D.A., 2017. Kurdistan crude oils as feedstock for production of aromatics. *Arabian Journal of Chemistry*, 10, pp.S2601-S2607.

Kennard, R.W., and Stone, L.A., 1969. Computer aided design of experiments. *Technometrics*, 11(1), pp.137-148.

Khanmohammadi, M., Garmarudi, A.B., Ghasemi, K., and De La Guardia, M., 2013. Quality based classification of gasoline samples by ATR-FTIR spectrometry using spectral feature selection with quadratic discriminant analysis. *Fuel*, 111, pp.96-102.

Lam, N.L., Smith, K.R., Gauthier, A., and Bates, M.N., 2012. Kerosene: A review of household uses and their hazards in low- and middle-income countries. *Journal of Toxicology and Environmental Health, Part B*, 15(6), pp.396-432.

Mallick, J., Talukdar, S., Alsubih, M., Ahmed, M., Islam, A.R.M.T., Shahfahad, and Thanh, N.V., 2022. Proposing receiver operating characteristic-based sensitivity analysis with introducing swarm optimized ensemble learning algorithms for groundwater potentiality modelling in Asir region, Saudi Arabia. *Geocarto International*, 37(15), pp.4361-4389.

Mazivila, S.J., Mitsutake, H., Santana, F.B.D., Gontijo, L.C., Santos, D.Q., and Borges Neto, W., 2015. Fast classification of different oils and routes used in biodiesel production using mid infrared spectroscopy and PLS2-DA. *Journal of the Brazilian Chemical Society*, 26(4), pp.642-648.

Mohammadi, M., Khanmohammadi Khorrami, M., Vatani, A., Ghasemzadeh, H., Vatanparast, H., Bahramian, A., and Fallah, A., 2020. Rapid determination and classification of crude oils by ATR-FTIR spectroscopy and chemometric methods. *Spectrochimica Acta Part A: Molecular and Biomolecular Spectroscopy*, 232, p.118157.

Naman, S., Jamil, L.A., Al-Gulami, F., Simo, S., and Ali, M.K., 2019. Evaluation of crude oils and natural gases of Kurdistan-Iraq by catalytic improvements to lighter oils using local clays. *WIT Transactions on Ecology and the Environment*, 222, pp.81-91.

Pontes, M.J.C., Pereira, C.F., Pimentel, M.F., Vasconcelos, F.V.C., and Silva, A.G.B., 2011. Screening analysis to detect adulteration in diesel/biodiesel blends using near infrared spectrometry and multivariate classification. *Talanta*, 85(4), pp.2159-2165.

Roy, P.P., and Roy, K., 2008. On some aspects of variable selection for partial least squares regression models. *QSAR and Combinatorial Science*, 27(3), pp.302-313.

Tanaka, G.T., De Oliveira Ferreira, F., Ferreira Da Silva, C.E., Flumignan, D.L., and De Oliveira, J.E., 2011. Chemometrics in fuel science: Demonstration of the feasibility of chemometrics analyses applied to physicochemical parameters to screen solvent tracers in Brazilian commercial gasoline. *Journal of Chemometrics*, 25(9), pp.487-495.

A Review on Adverse Drug Reaction Detection Techniques

Ahmed A. Nafea[1,*], Manar AL-Mahdawi[2], Mohammed M AL-Ani[3] and Nazlia Omar[3]

[1]Department of Artificial Intelligence, College of Computer Science and IT, University of Anbar, Ramadi, Iraq

[2]Department of Medical Physics, College of Science, Al-Nahrain University, Jadriya, Baghdad, 10072, Iraq

[3]Center for Artificial Intelligence Technology, Faculty of Information Science and Technology, Universiti Kebangsaan Malaysia, Bangi, Selangor, Malaysia

***Abstract*—The detection of adverse drug reactions (ADRs) is an important piece of information for determining a patient's view of a single drug. This study attempts to consider and discuss this feature of drug reviews in medical opinion-mining systems. This paper discusses the literature that summarizes the background of this work. To achieve this aim, the first discusses a survey on detecting ADRs and side effects, followed by an examination of biomedical text mining that focuses on identifying the specific relationships involving ADRs. Finally, we will provide a general overview of sentiment analysis, particularly from a medical perspective. This study presents a survey on ADRs extracted from drug review sentences on social media, utilizing and comparing different techniques.**

***Index Terms*—Adverse drug reactions, Detection, Machine learning, Deep learning, Sentiment analysis, Trigger terms.**

I. Introduction

Adverse drug reactions (ADRs) are unintended negative effects that occur as a result of taking a medication. They can range from minor side effects, such as a headache, to severe and life-threatening reactions, such as anaphylaxis. ADRs are important for both patients and health-care workers, as they can be a precedent for increased disease, hospitalization, and even death. The World Health Organization (WHO) estimates that ADRs are responsible for around 6.5% of hospital charges worldwide and that about 1 in 10 hospital admissions are related to ADRs. Early detection of ADR is important in reducing its impact on patients and health-care systems (Edwards and Aronson, 2000).

Detection of ADRs is a main step in reducing the problem of these reactions in patients and health-care systems. A common method for ADR is natural reporting, in which health-care professionals and patients report ADR to supervisory groups or pharmaceutical companies. Natural reporting is known to be underreported and not fully typical of the true incidence of ADRs (Yadesa, et al., 2021).

The growth of social networks has led to a significant increase in the amount of text-based information available in recent years. This has allowed common users to freely share their thoughts and opinions on a category of topics like product reviews (Kiritchenko, Zhu and Mohammad, 2014). In these reviews, users can offer evaluations of a specific product, detailing both its positive and negative sides based on their personal experience with it (Liu, Bi and Fan, 2017).

In the last year, researchers have become interested in a novel form of product evaluation known as medical reviews. These reviews concern users sharing their personal experiences with specific medications to evaluate their efficiency. They often mention several side effects and other medically relevant information. As a result, a new task has arisen, namely, the identification of these mentions, referred to as ADR detection (Ebrahimi, et al., 2016).

Several studies in the literature have focused on detecting ADR by crawling data from social media like drug websites or Twitter (Sarker and Gonzalez, 2015; De Rosa, et al., 2021). Comments and reviews from regular users are analyzed to identify ADR mentions. The statement "It made me very dizzy" is an example of dizziness, where the user is describing a side effect of a specific medication.

In the literature, a lot of researchers have been utilizing ML techniques to detect ADR (Ebrahimi, et al., 2016; Kiritchenko, et al., 2018; Yousef, Tiun and Omar, 2019; Pain, et al., 2016; and Plachouras, Leidner and Garrow, 2016). To detect ADR, researchers use annotated medical data to train classification models. The model is trained to recognize features, such as trigger terms, that are frequently associated with ADR. These trigger terms are selected keywords that have been determined to have a high likelihood of showing the presence of ADRs. Different classification methods are utilized in combination with trigger-term features to train the

ARO-The Scientific Journal of Koya University
Vol. XII, No. 1 (2024), Article ID: ARO.11388. 11 pages
Doi: 10.14500/aro.11388
Received: 06 September 2023; Accepted: 16 May 2024
Regular review paper: Published: 07 June 2024
Corresponding author's email: ahmed.a.n@uoanbar.edu.iq

model. However, numerous complex challenges persist in the field of ADR extraction.

This study is important because it has applications in the mining of medical opinion, a process that can be utilized to evaluate medications and gather feedback from patients. This can be beneficial to both patients, who can make other informed decisions about their medication, and doctors and drug manufacturers, who can use the feedback to make better decisions about the development, regulation, and prescribing of medications. The objectives of this work include understanding ADR detection, characterizing the key concepts of ADR, and presenting a classification of various methods used for ADR extraction.

II. Literature Review

In the past, ADR was described as major, dangerous, or bad reactions resulting from the use of a medication. These reactions required warning, immediate medical attention, dosage adjustments, or discontinuation of the product to prevent potential risks associated with its administration (Edwards and Aronson, 2000). ADR is a universal issue of importance, as it can impair patients' medical conditions and contribute to increased morbidity rates, even leading to fatalities. According to a prior investigation, there were approximately 100,000 deaths resulting from medical errors in the United States in 2000, with approximately 7,000 of those deaths attributed to drug reactions (Pouliot, Chiang and Butte, 2011).

ADR is extremely dangerous for patients around the world and is one of the leading causes of death for patients (Pirmohamed, et al., 2004). Traditional ADR surveillance systems are often ineffective in detecting ADR that occurs after long-term exposure or under specific conditions. These systems are prone to underreporting, a lack of complete data, and delayed detection. Due to these limitations, many ADRs may go undetected (Sarker, et al., 2015). Latest medical reports (Gurulingappa, Mateen-Rajpu and Toldo, 2012) and data on the social network (Ginn, et al., 2014; Nikfarjam, et al., 2015) about ADRs abound and are rapidly generated. Furthermore, machine learning (ML) and advanced natural language processing (NLP) algorithms help automatically detect large numbers of ADRs of unstructured data.

Pharmacovigilance strategies face a critical obstacle in identifying early identification of ADR in their post-approval times. Pharmacovigilance is described as the research and practices related to the identification, evaluation, awareness, and prevention of adverse effects or any other drug problem (WHO, 2002). A research has shown that ADR is a major public health concern after a drug is released. These reactions can cause hospitalizations, emergency visits, and even deaths, with numbers in the millions and resulting in costs of around $75–180 billion annually (Hacker, 2009). However, pre-approved clinical trials have various limitations; therefore, it is difficult to measure the true effects of a medication until it has been released and used by a larger population (Ahmad, 2003; Lazarou, Pomeranz and Corey, 1998). For example, through volunteer reporting systems and electronic health records (EHRs), various resources have been used to monitor ADR. The exponential development of electronically accessible health information and the ability to process vast amounts of it automatically, using ML algorithms and NLP, opened new opportunities for pharmacovigilance. Annotated companies have recently become available to identify ADR, enabling data-centric NLP algorithms and supervised ML techniques to automatically help detect ADR (Harpaz, et al., 2012).

One field in which data have grown and continue to grow tremendously in recent years is social media (Ginn, et al., 2014). Individuals share their personal health experiences in online communities each day. The strength of this study includes information about the utilization of prescription medications, side effects, and treatments discussed in social networks. Those that focus on health issues, in particular, attract significant user interest. These social networks are a valuable and credible source of information for people dealing with similar health issues. In recent years, a research on the detection of ADR has shifted to the utilization of data from these social media platforms due to the wealth of information available on them (Leaman, et al., 2010).

A. Terminology of ADRs

This study (Edwards and Aronson, 2000) proposed new terminology for ADRs by analyzing the definitions provided by the WHO and other sources. ADR was defined as a detrimental or unpleasant reaction caused by a medical product that needs prevention, specific treatment, dosage adjustment, or discontinuation of the product. The definition of "adverse event" refers to an outcome occurring during drug use but not necessarily directly linked to it. These definitions were distinguished from an "adverse event," which refers to an outcome occurring, while a patient is using a drug but may not necessarily be directly attributed to it. The terms "adverse drug reaction" and "drug side effect" were considered interchangeable, with the latter being more commonly utilized by non-health-care professionals and incorporating unintended beneficial reactions.

B. Biomedical Text Mining and Information Extraction (IE)

IE refers to the automatic extraction of structured data from semistructured or unstructured text. The purpose of a lot of biomedical text mining tasks is the extraction of some specific information from domain resources (Simpson and Demner-Fushman, 2012). To achieve this goal, the IE task falls into three subtasks: named entity recognition (NER), relation extraction, and event extraction. The following sections provide a brief overview of some of this area's tasks and their current state-of-the-art techniques and open issues (Cohen and Hersh, 2005).

Biomedical text mining resources

The main exchequer for biomedical text mining is text, either annotated or non-annotated (Simpson and Demner-Fushman, 2012). It can be divided into many different categories based on various portions, such as EHRs and published papers. Medical social media are a big group of

medical texts and the topic of much biomedical text mining research.

Medical social media and drug reviews

Medical Question and Answer portals, medical reviews, medical weblogs, and Wiki are a sample of social networks in the medical domain. The basic difference between these resources and other more formal texts, such as published research articles, is that their contents usually contain both experience and medical information. Processing these sources, which can be written by patients, doctors, physicians, and nurses considering this difference, is crucial. In a good step toward taking this problem into account, the authors (Denecke and Nejdl, 2009) classified content on social networks into two groups: affective content and informative content. To do this task, they used ML. Based on this observation, the extensive use of adjectives is an effective sign of content, and medical terminology is an indicator of informative content. Then, they applied this classifier to a comprehensive comparison of existing social media on the web based on their informativeness. This approach, similar to subjectivity classification, is unable to evaluate opinionated and unelected sentences in the medical domain due to the side effects, which typically imply unfavorable opinions.

As a result, more research is needed in this direction. This study focuses on ADR detection techniques in drug reviews. There are vast numbers of social networking platforms where people can share, experience, or gain awareness of one drug. These websites may be dedicated to drugs or may overlay different types of products. From a structural point of view, most of these drug reviews, such as Drugratingz.com and Druglib.com, are semistructured.

The study by Goeuriot et al., (2011) analyzes drug reviews on three websites, analyzing user-generated information based on view terms, medical terminology frequency, article length, sentence length, and specific POS proportions. They also deduce from the linguistic observation that drug reviews are much more like spoken language than survey papers, while both are full of medical terminology. However, in spite of the existence of some drug side effects such as anxiety, insomnia, headaches, and nausea in some of the opinion lexicons as opinion words, some other side effects such as sweating and impulsiveness are typically assigned to neutral words.

In addition, it is valuable to imply another special feature of drug review and its effect on opinion mining. You can see this phenomenon in the comment section of semistructured reviews and in unstructured reviews. Many patients cover their experiences in reviews. They talk about their disease and their condition before taking the drug or even after stopping the drug. As a result, the existence of sentimental words or symptoms in a sentence cannot indicate that the sentence is opinionated.

This section includes some special characteristics of drug reviews investigated, particularly from the perspective of opinion mining. Further details on the opinion mining concepts discussed here will be given in section on Relation extraction.

NER

The word “named entity” was coined for the Sixth Message Understanding Conference (MUC-6) and is now commonly used in NLP (Grishman and Sundheim, 1996). During that period, MUC primarily focused on IE tasks that involved extracting structured information about client operations and associated security measures from unstructured text sources, such as newspaper articles. In the process of defining these tasks, it became evident that the identification of information entities, such as personal, organizational, and geographical names, as well as numerical expressions, such as time, date, monetary values, and percentages, was crucial.

The task of NER involves identifying specific entities within the text, such as individuals, locations, organizations, drugs, time expressions, clinical procedures, and biological proteins. NER systems are commonly employed as an initial step in various tasks, including question answering, information retrieval, coreference resolution, and topic modeling.

NER is the process of identifying terms in biomedical texts. It was also used in biomedical texts. This task consists of three stages: (1) term recognition, (2) term mapping, and (3) term classification (Li, 2011). For example, in the sentence “Methadone works very well for chronic pain,” methadone and chronic pain should be known in the first phase. In the classification stage, they are classified into pre-defined groups, which are the name and symptoms of the drug in this case. A final step is to map these meanings to medical definitions using lexicons such as the Unified Medical Language System (UMLS) Metathesaurus.

Although this task appears simple on the surface, there are many challenging issues in the biomedical domain that should be considered, including name variation, extensive use of acronyms and abbreviations, lack of a complete dictionary, and context-dependence of language. However, NER systems exhibit high accuracy in their results, as recent community-wide evaluations have shown (Simpson and Demner-Fushman, 2012). Nevertheless, existing systems are not sufficient to address all long-term extraction problems. Therefore, it would be helpful to know the NER approaches and their limitations. The following includes discussing NER.

Dictionary-based algorithm

The dictionary-based algorithm uses exact or partially matching terms with words or phrases in a given biomedical lexicon. This algorithm is sensitive to spelling mistakes, homonymy, and morphological variants. Although some schemes are applied to resolve these problems, this method is often used in combination with the other methods.

Rule-based approach

The earliest NER systems used common rule-based methods (Zweigenbaum, et al., 2007). These systems define some rules to show the patterns of medical target terms and their contexts. Rule-based approaches outperform dictionary-based approaches in many cases due to the consideration of context and the definition of detailed rules for extraction. However, the manual generation of these rules takes time but is a one-time effort, and they are very specific and are not extensible to other entity extractions.

ML-based approach

With the growth of available annotated corpora, ML-based approaches have been converted into a common approach in the NER problem, either as a standalone solution or in combination with other techniques in a supervised or semisupervised manner and classification-based (using NB and SVM) or sequence-based Hidden Markov Model (HMM), Maximum Entropy (ME), and Conditional Random Fields (CRF). (Cohen and Hersh, 2005; Simpson and Demner-Fushman, 2012; Simpson and Demner-Fushman, 2012).

Side effect extraction

Defining side effect extraction is a common NER issue that is used in biomedical literature for pharmacovigilance and recently in biomedical opinion analysis for drug reviews. Some works cited by Li (2011) show the importance of patient-reported side effects in pharmacovigilance. On the basis of these observations, Li proposes a statistical algorithm to identify adverse reactions to cholesterol-lowering drugs taken from five websites in drug reports. To do so, he compares the word distributions of reviews of statin drugs with those of non-statin drugs using statistical NLP techniques such as pointwise mutual information and log likelihood. Having a distinction will assess the side effects that are more associated with statin drugs than other reducing cholesterol medications. In fact, this method also discriminates patient pre-condition from special drug side effects, since patient pre-condition is common in all cholesterol-reducing drugs and will be eliminated. For example, in the sentence 'I took Lipitor because I had high cholesterol, but it caused muscle aches', this system does not detect 'high cholesterol' as a side effect because it is often reviewed in other reviews of cholesterol-lowering drugs. However, this work has some limitations. First, it should focus on two types of drugs for one disease. Second, it omits the common side effects of one disease drug, so it is not applicable to discovering all the side effects of one particular drug. In another work, Skentzos, et al. (2011) used TextMiner to find an adverse reaction to statin drugs in the electronic medical records of patients.

In another work, Yalamanchi (2011) developed a query-based side effect extraction system from drug reviews at the site "www.askapatient.com" called Sideffective. In this system, they use a BigHugeLabs thesaurus service to recursively build a complete side effect lexicon from small training data. This system's main drawback is that it does not discriminate between drug side effects and symptoms of the disease.

Relation extraction

The objective of the extraction relationship is to determine the presence of a relationship between a couple of entities. Although the type of entity is typically very specific (that is, drugs), the relationship type can be very general (that is, any biomedical association) or very specific (that is, a regulatory relationship) (Cohen and Hersh, 2005). Most of the work in this field focuses on relational extraction between genes, proteins, and other kinds of relationships (Cohen and Hersh, 2005). Approaches to relational extraction fall into four categories: statistically based, rule-based, classification-based, and NLP-based methods.

In the first, it will include insight into some types of relations that are more related to side effect extraction in the next two sections, and then it will discuss relation extraction methods in the following sections.

Drug–symptom relation

The drug–symptom relation is an example of many associations between entities in the medical domain, such that its detection is essential for many biomedical systems such as pharmacovigilance and, in particular, for drug review sentiment analysis systems.

In a medical text, drug–symptom association is subdivided into 3 categories as follows (Wang, Tsujii and Ananiadou, 2010):

1. Treat relation: A drug is taken to cure a disease or symptom (that is, methadone and pain).
2. Cause relation: A drug causes a symptom (that is, methadone and nausea).
3. Indirect treatment relationship: A drug treats a disease (that is, rosiglitazone, diabetes, and polyuria).

In short, a drug and symptom are related to each other in a treatment or cause relationship. A side effect is a symptom that participates in a causal relationship with a particular drug, that is, nausea for methadone.

Disease–symptom relation

Similarly, this researcher can see the problem from the perspective of the disease and its relationship with the symptom (Wang, Tsujii and Ananiadou, 2010) and divide this relation into 3 groups as follows:

1. Manifestation relation: A symptom is a direct sign of disease (that is, migraine and headache).
2. Indirect manifestation relationship refers to the scenario where a symptom serves as an indication of a disease that has a strong association with the target disease. For example, chest pain can be considered a symptom that is closely linked to diseases like diabetes and heart disease.
3. Treatment-induced relationship: The sign is caused by a procedure or treatment (that is, clinical depression, imipramine, and fever).

Among these three groups, the first two groups show disease symptoms and should not be considered drug side effects. The third relationship can show drug side effects in some situations in which the drug has performed the treatment procedure. For example, in the above example, 'fever' is the side effect of 'Imipramine' (an antidepressant drug). Therefore, the symptoms in the last case should be considered a side effect.

Statistical methods

The essence of these methods is using the co-occurrence degree of two entities to detect the relationship between them. The research in Cao, Hripcsak and Markatou (2007) is an example of using co-occurrence measures to detect the association between clinical entities.

The main advantage of this technique is its simplicity. However, in most cases, it is not possible to use this method alone to detect the type and direction of the association. In fact, the high co-occurrence of two entities just shows the existence of a relationship and nothing more. An additional problem inherent in this method is the lack of equivalency between statistical and medical associations in some cases.

These two drawbacks make these methods inconvenient for detecting a special type of disease symptom or drug symptom.

Classification

These types of algorithms use supervised ML to detect the association between entities using lexical, syntactic, and semantic features. This approach can be used to detect a special relationship between a drug or disease and symptoms by defining the appropriate features for the training phase.

NLP based

Large progress in terms of extraction techniques has been made (Zweigenbaum, et al., 2007). In these techniques, the syntactic structure of the biomedical text, which can be made of a dependency analyzer, is utilized to find the grammatical relationship among two biomedical entities.

Event extraction

Event extraction is a task of text mining in the biomedical scope. It is the process of extracting interactions between biomedical entities and their consequences. Simple verbs are typically utilized to detect events. For example, in the sentence "In E. Coli, glnAP2 can be activated by NifA", the verb 'activated' is the event, and the event cases are 'In E. Coli", "glnAP2", "NifA" (Ananiadou, et al., 2010).

Knowledge of resources and tools

The main difference between the biomedical field and other areas is the broad scale of knowledge, resources, and methods. The UMLS is a set of biomedical lexicons and instruments that have been created by the US National Library of Medicine (NLM) (Li, 2011). This collection, which is extensively used by researchers, provides a Metathesaurus, a semantic network, and a lexicon that contains biomedical terms and common English words (Simpson and Demner-Fushman, 2012). The UMLS Metathesaurus, the most extensive biomedical thesaurus, contains about 1.7 million biomedical terms, and each of the 134 semantic categories is assigned to at least one. Such semantic types are grouped into 15 semantic groups (Denecke and Nejdl, 2009).

The mapping of words or phrases to UMLS concepts is very common in biomedical literature. To achieve this goal, most medical systems, such as SeReMeD, use MetaMap. MetaMap is an NLM-configurable program that automatically maps biomedical text to Metathesaurus concepts (Aronson, 2001).

Detection using a combined approach

The extraction of some meaningful, specific associations is a challenging issue in the biomedical research area. Few studies have been conducted on clinical texts, and drug reviews have remained almost unexplored in this research direction until now.

Discrimination of disease (magnetic resonance spectroscopy) and drug (adverse drug event [ADE]): Methods and applications

Recommend a combination of approaches to NLP and approaches to statistics (Wang, Tsujii and Ananiadou, 2010). For electronic health reports, they use co-occurrence to track two signs of disease and an ADE. They use the EHR structural function to resolve the limitations of statistical methods and assess the form of relationships based on the section in which they occur. Although performance improvements are demonstrated using section-by-section filtering, the unstructured narrative analysis of drugs does not apply to this method. In a different statistical way (Li, 2011), they extract non-statin and statin cholesterol side effects by reducing the drug, taking into account the difference between the pre-condition of the patient and the side effects. They filter the pre-conditions of patients by removing symptoms that occur in both statin and non-statin drug reviews. In addition, another study (Weeber, et al., 2000) developed a system called the DAD, which uses the rules of association to detect adverse reactions to drugs.

III. ADR Detection Techniques

A. ML Techniques

ML plays a vital role in accurately categorizing text through the use of supervised or unsupervised methods. The challenge lies in choosing the most suitable approach for a given sentiment analysis task. For example, when the objective is to classify opinionated documents into positive or negative categories, supervised learning is more effective as it can handle pre-defined class labels. Conversely, if the task involves analyzing text and classifying nouns, adjectives, and adverbs, unsupervised learning is more suitable. This section will explore recently proposed techniques for sentiment analysis, utilizing both supervised and unsupervised learning techniques.

Supervised learning

Supervised learning is aimed at training the data to identify specific patterns during the testing phase. In the context of sentiment analysis, this becomes highly useful as the data can be trained to identify patterns that show whether an opinion is positive or negative. Several supervised learning techniques, such as NB, SVM, and K-nearest neighbor, can be applied efficiently in sentiment analysis.

NB

This is one of the commonly used classifiers for SA (Tan, et al., 2009), which mimics statistics to build a probabilistic model (Thabtah, et al., 2009) for the individual examination of each feature. This can be represented through the identification of the presence and absence of each character in a given case (Huang, Lu and Ling, 2003). Referring to SA, this classifier searches a document for the presence or absence of words (Govindarajan, 2013).

The Naive Bayes classifier exists in two forms: multinomial model and the multivariate Bernoulli model. The aim of the multinomial model is to address the existence of opinion words with respect to their presence or absence in the considered text, while the multivariate Bernoulli model examines the frequency of occurrence of the opinion words in a text. As per Huang, Lu and Ling (2003), the multivariate Bernoulli model handles relatively small data more efficiently than the multinomial model.

The study by Yu and Hatzivassiloglou (2003) presented an NB-based subjectivity identification approach for the classification of opinionated sentences. They used the NB classifier to classify such sentences as positive or negative. Similarly, Zhang, et al. (2011) comparatively studied the

performance of NB and SVM classifiers in the classification of opinions into classes (positive and negative). From the analysis, they reported better performance of the NB classifier compared to the SVM classifier. Another study by Moghaddam and Ester (2012) compared the performance of KNN, NB, and SVM classifiers for sentiment analysis and reported that the SVM classifier outperformed the NB and KNN classifiers.

SVM

The SVM is basically a classifier that relies on labels for linear data classification (Joachims, 1998). This is not an indication of the inability of SVM to handle more than two classes; rather, its training phase is based on two classes (Lee, et al., 2012). In this study, the SVM training will be based on the '1' class label, 'not-1' class label, '2' class label, and not-5 class label. Then, the testing phase will involve mapping new instances to the most similar class label (most proximal to the hyperplane). This hyperplane is a margin that divides the data into two linear groups (Zhang, Yoshida and Tang, 2008). SVM can handle a huge number of features efficiently (Huang, Lu and Ling, 2003).

A study by Somasundaran, et al. (2007) presented an SVM-based subjectivity identification approach for the classification of answers to opinion questions into subjective and objective classes. The proposed method relies on a keyword feature and question type to classify the answers into subjective and objective classes. Another study by Xu, et al. (2011) focused on the identification of comparative correlations between products based on the product's reviews. The authors succeeded in establishing a comparison between SVM and CRF, even though the performance of CRF was reported to be superior to that of SVM. Furthermore, Prabowo and Thelwall (2009) presented the approach of combining a rule-based approach and SVM for the classification of movie reviews into positive and negative classes. The study found a competitive performance of the approach compared to the performance of the baseline study.

Logistic regression (LR)

The LR model defines the linear equation for class probability (Montgomery, Peck and Vining, 2021).

Unsupervised learning

The unsupervised learning techniques show an alternative for ADR detection. These techniques do not require labeled data and instead aim to identify relationships in the data that can be utilized to detect ADRs. There are a lot of unsupervised learning techniques utilized for ADR detection, including clustering, association rule mining, and anomaly detection.

Clustering is a technique that group's similar data points together based on their characteristics. In the context of ADR detection, clustering can be utilized to identify subgroups of patients who are more likely to experience ADRs. In this study, Roitmann, Eriksson and Brunak (2014) utilized clustering to identify subgroups of patients with different patterns of ADRs caused by antibiotics. They found that the clustering approach was able to accurately identify patients who were at high risk for ADRs and that these patients could be trained for closer monitoring or preventive interventions.

Another unsupervised learning technique is association rule mining, which can be utilized for ADR detection. This technique is used to detect patterns in the data, like the association between a drug and an ADR. This study (Sangma, Anal and Pal, 2020) proposed association rule mining to identify associations between drugs and ADRs in a large EHR dataset. They found that the association rule mining method was able to identify various previously unknown drug-ADR associations, which could be used to improve the safety of drug prescribing.

Anomaly detection is utilized to detect data points that turn from the model. In the context of the detection of ADR, anomaly detection can be used to detect patients who have experienced unusual or unexpected ADRs. For example, a study by Bijlani, Nilforooshan and Kouchaki (2022) used anomaly detection to identify patients who experienced ADRs that were not listed in the package inset for a particular drug. They found that the anomaly detection method was able to identify a number of previously unknown ADRs, which could be used to improve the safety of drug prescribing.

B. Deep Learning (DL) Techniques

DL techniques are an important field in medical informatics, particularly for their ability to analyze large volumes of unstructured data, such as EHRs and social media posts, to identify ADRs. ADRs are defined as unintended and harmful effects of drugs, and they are a major public health concern, leading to hospitalization and even death.

Conventionally, ADR detection has been done through methods such as spontaneous reporting systems and clinical trials. However, these methods are often time-consuming and have low sensitivity, leading to the underreporting of ADRs. With the advent of digital health and the increasing availability of large amounts of data, there is an opportunity to use DL techniques to improve ADR detection.

One of the most popular DL techniques used in ADR detection is convolutional neural networks (CNNs). CNNs are particularly useful for analyzing text data, such as EHRs, and have been shown to be effective in identifying ADRs from free text notes. A study by Shen, et al. (2019) used CNN to identify ADRs.

Another DL technique that has been used in ADR detection is recurrent neural networks (RNNs). RNNs are particularly useful for analyzing sequential data, such as social media posts, and have been used to identify ADRs from social media data. In a study by Zhang and Geng (2019), RNNs analyzed social media posts and identified ADRs.

In addition to CNNs and RNNs, other DL techniques such as deep belief networks, deep neural networks, and long short-term memory networks have also been used in ADR detection. These techniques have been shown to be effective in identifying ADRs from various types of data, such as EHRs, social media posts, and clinical trial data.

To further improve the performance of ADR detection, some studies have used DL techniques in combination with other methods, such as NLP and feature engineering. For

example, a study by Zhang, et al. (2020) used a combination of NLP and a DL model to extract ADR-related information from EHRs.

C. NLP

Clinical information is not accessible for pharmacovigilance applications in narrative reports, and it is buried either in the scientific literature or in clinical narrative studies. High-throughput technology, NLP, has been applied for decades in biomedicine. The NLP systems were developed for the identification, extraction, and encoding of biomedical literature and then clinical narratives (Davis, 1965). Some NLP techniques have also been applied to identify ADE from EHR systems (Aronson, 2001; Bates, et al., 2003; Honigman, et al., 2001; and Rindflesch and Fiszman, 2003). However, these concentrate on ADE identification and patient protection, not on information discovery and pharmacovigilance.

An increasing number of researchers are focusing on establishing links and extracting between entities from textual data, and NLP has become an essential part of the automatic extraction of relations and entities during documents (Rebholz-Schuhmann, et al., 2007). Co-occurrence statistics are most commonly used to determine entity relationships and have been shown to be effective in acquiring associations between biological and clinical entities (Cohen and Hunter, 2008; Narayanasamy, et al., 2004).

Latent semantic analysis (LSA) is a technique used to detect ADRs in EHRs. LSA is a type of NLP method that is used to analyze unstructured text data and extract useful information. It works by identifying patterns and relationships between words in a text and grouping similar words together. This allows LSA to identify ADRs by detecting patterns in patient EHRs. LSA can be used to identify ADRs that may have been missed by traditional detection methods such as spontaneous reporting or active surveillance. In addition, LSA can help identify potential ADRs that may be associated with new medications by analyzing the literature and clinical trial data (Nafea, Omar and Al-Ani, 2021).

D. Data mining

This study (Roddick, Fule and Graco, 2003) presented observations on the application of exploratory data mining techniques to scientific and clinical data. This enabled the authors to raise a number of general issues and provide indicators from a broad perspective of possible future research areas in data mining and knowledge discovery (Hanauer, 2007). This study discusses the difficulties and resolutions encountered in conducting research and providing patient care through the analysis of electronic data. The figures from the Michigan health statistics system were used for their study, but the author was concerned and focused on the challenges involved in text mining alone. The challenges the author inferred included asserting accurate diagnosis and processing EHRs in the natural language (Hanauer, 2007).

IV. Challenges in ADR Detection

ADRs are a significant concern in the health-care industry, as they often lead to patient harm, increased health-care costs, and regulatory burdens. Detecting ADR with a timely approach is important for ensuring patient safety and efficiently observing the use of drugs. The process of ADR detection comes with various challenges that require the implementation of innovative approaches and techniques. This study shows the primary challenges in ADR detection techniques.

One major problem in ADR detection is the underreporting of adverse events. Health-care professionals frequently fail to report ADRs due to reasons like a lack of awareness, time constraints, fear of liability, or the observation that ADRs are expected outcomes. Consequently, this leads to incomplete and biased data, which hampers the detection process. Addressing underreporting requires initiatives to improve reporting systems, enhance awareness among health-care professionals, and foster a culture of reporting ADRs.

Another challenge in ADR detection is the heterogeneity and integration of the data. ADRs can be reported from many sources, including spontaneous reporting systems, EHRs, social media, scientific literature, and clinical trials. Each data source has its own limitations, biases, and data formats. Effectively integrating heterogeneous data from multiple sources when considering data quality, reliability, and standardization is a significant challenge. Advanced techniques such as data integration, NLP, and ML approaches are being developed to overcome this challenge.

Signal detection and noise present a fundamental challenge in ADR detection. It is difficult to identify meaningful signals from large volumes of noisy data due to the abundance of unrelated events, confounding factors, and background noise. Distinguishing true ADRs from coincidental associations becomes challenging. To address this, various signal detection methods, such as disproportionality analysis, data mining algorithms, and statistical modeling, are employed to improve the signal-to-noise ratio and accurately identify potential ADRs.

Establishing a temporal relationship and assessing causality between drug exposure and ADR occurrence is crucial in ADR detection. However, real-world data often present complex relationships due to factors such as delayed ADR onset, multiple drug exposures, and confounding variables. Differentiating between ADRs, pre-existing conditions, and other events becomes a challenge, making causality assessment difficult. Robust methods for analyzing temporal relationships and assessing causality are essential for accurate ADR detection.

The detection of rare and long-term ADRs poses additional challenges. Many ADRs are rare or occur after prolonged drug exposure, making their detection challenging. Traditional ADR detection methods may not adequately capture these events due to limited sample sizes or short monitoring periods. Innovative techniques, such as data mining algorithms, predictive modeling, and active surveillance systems are being explored to improve the

detection of rare and long-term ADRs.

Ethical and privacy concerns are integral to ADR detection. ADRs involve sensitive patient health information, raising ethical and privacy considerations. Striking a balance between the need for ADR detection and patient privacy and confidentiality is a significant challenge. Strict data anonymization and de-identification techniques, secure data sharing frameworks, and adherence to regulatory guidelines are necessary to ensure patient privacy when facilitating ADR detection research.

V. Discussion

As shown in Table I, a comparison between the techniques utilized to discover the side effect of a drug through our study shows that many studies rely on ML and DL to extract the side effect of a drug (Yates and Goharian, 2013; Emadzadeh, et al., 2018; Akhtyamova, Alexandrov and Cardiff, 2017; andCocos, Fiks and Masino, 2017; and Lee, et al., 2017). This review shows that the identification of adverse drug effects relies on

TABLE I
A Comparison between ADR Techniques

Author	Year	Method	Features	Data	F-measure
Yates and Goharian (2013)	2013	Rule-based	Trigger terms	Benchmark dataset	0.78
Pain, et al. (2016)	2016	SVM	Trigger terms	Twitter data	0.94
Ebrahimi, et al. (2016)	2016	SVM	Trigger terms+Medical Concepts	Drug websites	0.55
Plachouras, Leidner and Garrow (2016)	2016	SVM	Trigger terms+Gazetteers	Twitter data	0.60
Emadzadeh, et al. (2018)	2017	SVM	HAS	Twitter data	0.62
Akhtyamova, Alexandrov and Cardiff (2017)	2017	CNN	word2vec embedding	Twitter data	0.54
Cocos, Fiks and Masino (2017)	2017	RNN	Word-embedding vectors	Twitter data	0.75
Lee, et al. (2017)	2017	CNN	word2vec	Twitter data	0.64
Wang, et al. (2018)	2018	WSVM	combination of synthetic oversampling techniques and under-sampling performs	Twitter	0.42
Kiritchenko, et al. (no date)	2018	SVM	Domain-specific trigger terms	Twitter data	0.43
Yousef, Tiun and Omar (2019)	2019	SVM, LR, NB	Syntactic trigger terms	Dataset from Yates and Goharian (2013) updated by Yousef, Tiun and Omar (2019)	0.69
Wang, et al. (2019)	2019	DNN	Word-embedding	SIDER	0.84
Dai and Wang (2019)	2019	Vote-based undersampling (VUE) and random under-sampling boosting	WESMOTE	Imbalanced social media	0.49
Odeh and Taweel (2019)	2019	CNN	domain and semantic	Twitter posts ADE data	0.60 0.76
Yousef, et al. (2020)	2020	RNN	document embedding	medical sentiments data	0.90
Zhang, et al. (2020)	2020	CNN	GICN	TwiMed- Twitter	0.83
Yousef, et al. (2020)	2020	SVM, LR, NB	Lexicon replacement	medical review	0.87
Li, et al. (2020)	2020	Adversarial transfer learning	Private CNN	TwiMed	0.67
Fan, Fan and Smith (2020)	2020	BERT	Word-embedding	WebMD and Drugs.com	0.97
Zhang, Cui and Gao (2020)	2020	SVM, LR, NB, RF	The shallow linguistic feature set and a deep linguistic feature	Twitter	0.94
Zhang, et al. (2021)	2021	Adversarial transfer learning	Bi-LSTM	Twitter	0.68
Shen, et al. (2021)	2021	GAR framework	Word-embedding	TwitterADR	0.74
Nafea, Omar and AL-Ani (2021)	2021	SVM, LR, NB	LSA	Dataset from Yates and Goharian (2013) updated by Yousef, Tiun and Omar (2019)	0.82
Nafea, Omar and Al-qfail (2023)	2023	ANN	LSA	Dataset from Yates and Goharian (2013) updated by Yousef, Tiun and Omar (2019)	0.85
Nafea, et al. (2024)		Ensemble model	Point-wise mutual information	Dataset from Yates and Goharian (2013) updated by Yousef, Tiun and Omar (2019)	0.89

ADR: Adverse drug reactions, SVM: Support vector machine, CNN: Convolutional neural networks, RNN: Recurrent neural networks, WSVM: Wavelet support vector machine, LR: Logistic regression, NB: Naive Bayes, RF: Random forest, GICN: Gated Iterative Capsule Network, BERT: Bidirectional encoder representations from transformers, GAR: Graph adversary representation, ANN: Artificial neural networks, LSA: Latent semantic analysis, WESMOTE: Word embedding-based synthetic minority oversampling technique, SIDER: Data from side effect resource, ADE: Adverse drug event, HAS: Hybrid semantic analysis, LSTM: long short-term memory, DNNs: Deep neural networks

the use of ML and DL (Zhang, Cui and Gao, 2020; Wang, et al., 2018; Wang, et al., 2019; and Dai and Wang, 2019). The results varied depending on the data, and various methods were used to address them. This review particularly focused on the application of these methods to the task of extracting ADR and highlighted which methods might be suitable for this purpose. Despite the diversity, there are several common elements among the systems (Pain, et al., 2016; Ebrahimi, et al., 2016; Plachouras, Leidner and Garrow, 2016; Emadzadeh, et al., 2018; and Kiritchenko, et al., no date).

According to this study, DL techniques have shown a great approach to the detection of ADR and have been shown to improve the performance of ADR detection methods (Fan, Fan and Smith, 2020). However, more research is needed to address the challenges with DL-based ADR detection, such as the lack of labeled data and the interpretability of models (Zhang, et al., 2021; Li, et al., 2020). The DL techniques for ADR detection are still in the early stages of development, and there are various challenges that need to be addressed. One of the major challenges is the lack of labeled data, which is necessary to train DL models (Shen, et al., 2021), while another challenge is the interpretability of DL models, which is important for understanding the underlying mechanisms of ADRs and making decisions based on the results of the models (Wang, et al., 2019; Odeh and Taweel, 2019; Yousef, et al., 2020; and Zhang, et al., 2020) (Li, et al., 2020; Nafea, Omar and Al-qfail, 2023).

ML is utilized to predict ADRs with various algorithms such as SVM, NB, and LR (Yousef, Tiun and Omar, 2019; Rami Naim Mohammad Yousef, et al., 2020; and Nafea, Omar and Al-Ani, 2021). This study shows that the algorithms can be trained on large datasets of ADRs and drug information to detect patterns and relationships among drugs and ADRs. The results can be utilized to develop predictive models that can help detect patients at risk for ADRs, allowing for earlier intervention and potentially reducing the incidence of ADRs. By utilizing these techniques, ML can assist health-care professionals in detecting ADRs more effectively and efficiently, leading to improved patient outcomes. However, there are several challenges with using ML for ADR detection. The first challenge is that the quality of the data used for training and testing ML models can impact the accuracy of ADR predictions. This includes issues with data completeness, accuracy, and consistency. The second challenge is limited data availability. The availability of high-quality, comprehensive data on ADRs is limited, making it challenging to train ML models with sufficient data to accurately predict ADRs.

Unsupervised learning techniques show alternatives for ADR detection. These techniques do not require labeled data and rather aim to identify patterns and relationships in the data that can be used to detect ADRs. Clustering, association rule mining, and anomaly detection are some of the most common unsupervised learning techniques used for ADR detection. These techniques have been shown to be effective in identifying patients at high risk of ADRs and identifying previously unknown drug-ADR associations.

VI. Conclusion

This review delves into text mining and IE algorithms within the biomedical field, specifically focusing on the detection of ADRs from social media drug reviews. By examining previous research and addressing the challenges integral to ADR detection, as well as discovering biomedical sentiment analysis, this study has gained valuable insights into the complexities of this field. This study shows a comprehensive survey of ADRs extracted from drug review sentences on social networks, employing various techniques and methodologies. Looking ahead, there are promising avenues for future research. This research proposes the utilization of active learning and transfer learning methodologies to augment the performance of ADR detection models. These advanced techniques offer the potential to enhance the accuracy and reliability of ADR detection within medical opinion-mining systems. By addressing these challenges and incorporating sophisticated methodologies, we anticipate significant improvements in the accuracy and efficiency of ADR detection. This will contribute to enhancing patient safety and health-care outcomes by providing timely and reliable information on drug reactions.

References

Ahmad, S.R., 2003. Adverse drug event monitoring at the Food and Drug Administration. *Journal of General Internal Medicine*, 18(1), pp.57-60.

Akhtyamova, L., Alexandrov, M., and Cardiff, J., 2017. Adverse Drug Extraction in Twitter Data using Convolutional Neural Network. In: *2017 28th International Workshop on Database and Expert Systems Applications (DEXA)*. IEEE, pp.88-92.

Ananiadou, S., Pyysalo, S., Tsujii, J., and Kell, D.B., 2010. Event extraction for systems biology by text mining the literature. *Trends in Biotechnology*, 28(7), pp.381-390.

Aronson, A.R., 2001, Effective mapping of biomedical text to the UMLS Metathesaurus: The MetaMap program. In: *Proceedings of the AMIA Symposium*. American Medical Informatics Association, p.17.

Bates, D.W., Scott Evans, R., Murff, H., Stetson, P.D., Pizziferri, L., and Hripcsak, G., 2003. Detecting adverse events using information technology. *Journal of the American Medical Informatics Association*, 10(2), pp.115-128.

Bijlani, N., Nilforooshan, R., and Kouchaki, S., 2022. An unsupervised data-driven anomaly detection approach for adverse health conditions in people living with dementia: Cohort study. *JMIR Aging*, 5(3), p.e38211.

Cao, H., Hripcsak, G., and Markatou, M., 2007. A statistical methodology for analyzing co-occurrence data from a large sample. *Journal of Biomedical Informatics*, 40(3), pp.343-352.

Cocos, A., Fiks, A.G., and Masino, A.J., 2017. Deep learning for pharmacovigilance: Recurrent neural network architectures for labeling adverse drug reactions in Twitter posts. *Journal of the American Medical Informatics Association*, 24(4), pp.813-821.

Cohen, A.M., Hersh, W.R., 2005. A survey of current work in biomedical text mining. *Briefings in Bioinformatics*, 6(1), pp.57-71.

Cohen, K.B., and Hunter, L., 2008. Getting started in text mining. *PLoS Computational Biology*, 4(1), p.e20.

Dai, H.J., and Wang, C.K., 2019. Classifying adverse drug reactions from imbalanced twitter data. *International Journal of Medical Informatics*, 129, pp.122-132.

Davis, J.M., 1965. Efficacy of tranquilizing and antidepressant drugs. *Archives*

of General Psychiatry, 13(6), pp.552-572.

De Rosa, M., Fenza, G., Gallo, A., Gallo, M., and Loia, V., 2021. Pharmacovigilance in the era of social media: discovering adverse drug events cross-relating Twitter and PubMed. *Future Generation Computer Systems*, 114, pp.394-402.

Denecke, K., and Nejdl, W., 2009. How valuable is medical social media data? Content analysis of the medical web. *Information Sciences*, 179(12), pp.1870-1880.

Ebrahimi, M., Yazdavar, A., Salim, N., and Eltyeb, S., 2016. Recognition of side effects as implicit-opinion words in drug reviews. *Online Information Review*, 40(7), pp.1018-1032.

Edwards, I.R., and Aronson, J.K., 2000. Adverse drug reactions: Definitions, diagnosis, and management. *The Lancet*, 356(9237), pp.1255-1259.

Emadzadeh, E., Sarker, A., Nikfarjam, A., and Gonzalez, G., 2018. Hybrid semantic analysis for mapping adverse drug reaction mentions in tweets to medical terminology. *The AMIA Annual Symposium*, 2017, pp.679-688.

Fan, B., Fan, W., and Smith, C., 2020. Adverse drug event detection and extraction from open data: A deep learning approach. *Information Processing and Management*, 57(1), p.102131.

Ginn, R., Pimpalkhute, P., and Nikfarjam, A., 2014. Mining Twitter for Adverse Drug Reaction Mentions: A Corpus and Classification Benchmark. In: *Proceedings of the Fourth Workshop on Building and Evaluating Resources for Health and Biomedical Text Processing*. Citeseer, pp.1-8.

Goeuriot, L., Na, J.C., Kyaing, W.Y.M., Foo, S., Khoo, C., Theng, Y.L., and Chang, Y.K., 2011. Textual and informational characteristics of health-related social media content: A study of drug review forums, p. 548-557.

Govindarajan, M., 2013. Sentiment analysis of movie reviews using hybrid method of naive bayes and genetic algorithm. *International Journal of Advanced Computer Research*, 3(4), p.139.

Grishman, R., and Sundheim, B.M., 1996. Message Understanding Conference-6: A Brief History. In: *COLING 1996 Volume 1: The 16th International Conference on Computational Linguistics*.

Gurulingappa, H., Mateen-Rajpu, A., and Toldo, L., 2012. Extraction of potential adverse drug events from medical case reports. *Journal of Biomedical Semantics*. *Journal of Biomedical Semantics*, 3(1), pp.15.

Hacker, M., 2009. Adverse drug reactions. In: *Pharmacology*. Elsevier, Netherlands, pp.327-352.

Hanauer, D., 2007. *Mining Clinical Electronic Data for Research and Patient Care: Challenges and Solutions*. Clinical Assistant Professor University of Michigan, USA.

Harpaz, R., DuMouchel, W., Shah, N.H., Madigan, D., Ryan, P., and Friedman, C., 2012. Novel data-mining methodologies for adverse drug event discovery and analysis. *Clinical Pharmacology and Therapeutics*, 91(6), pp.1010-1021.

Honigman, B., Lee, J., Rothschild, J., Light, P., Pulling, R.M., Yu, T., Bates, D.W., 2001. Using computerized data to identify adverse drug events in outpatients. *Journal of the American Medical Informatics Association*, 8(3), pp.254-266.

Huang, J., Lu, J., and Ling, C.X., 2003. Comparing Naive Bayes, Decision Trees, and SVM with AUC and Accuracy. In: *Third IEEE International Conference on Data Mining*. IEEE, pp.553-556.

Joachims, T., 1998. Text Categorization with Support Vector Machines: Learning with Many Relevant Features. In: *European Conference on Machine Learning*. Springer, Berlin, pp.137-142.

Kiritchenko, S., Mohammad, S.M., Morin, J., and de Bruijn, B., 2018. NRC-Canada at SMM4H shared task: Classifying Tweets mentioning adverse drug reactions and medication intake. *arXiv preprint arXiv:1805.04558*.

Kiritchenko, S., Zhu, X., and Mohammad, S.M., 2014. Sentiment analysis of short informal texts. *Journal of Artificial Intelligence Research*, 50, pp.723-762.

Lazarou, J., Pomeranz, B.H., and Corey, P.N., 1998. Incidence of adverse drug reactions in hospitalized patients: A meta-analysis of prospective studies. *JAMA*, 279(15), pp.1200-1205.

Leaman, R., Wojtulewicz, L., Sullivan, R., Skariah, A., Yang, J., and Gonzalez, G., 2010. Towards Internet-Age Pharmacovigilance: Extracting Adverse Drug Reactions from User Posts to Health-Related Social Networks. In: *Proceedings of the 2010 Workshop on Biomedical Natural Language Processing*, pp.117-125.

Lee, K., Qadir, A., Hasan, S.A., Datla, V., Prakash, A., Liu, J., and Farri, D., 2017. Adverse Drug Event Detection in Tweets with Semi-Supervised Convolutional Neural Networks. In: *Proceedings of the 26th International Conference on World Wide Web*, pp.705-714.

Lee, L.H., Wan, C.H., Rajkumar, R., and Isa, D., 2012. An enhanced support vector machine classification framework by using Euclidean distance function for text document categorization. *Applied Intelligence*, 37(1), pp.80-99.

Li, Y.A., 2011. *Medical Data Mining: Improving Information Accessibility Using Online Patient Drug Reviews*. Massachusetts Institute of Technology, Cambridge.

Li, Z., Yang, Z., Luo, L., Xiang, Y., and Lin, H., 2020. Exploiting adversarial transfer learning for adverse drug reaction detection from texts. *Journal of Biomedical Informatics*, 106, p.103431.

Liu, Y., Bi, J.W., and Fan, Z.P., 2017. Ranking products through online reviews: A method based on sentiment analysis technique and intuitionistic fuzzy set theory. *Information Fusion*, 36, pp. 149-161.

Moghaddam, S., and Ester, M., 2012. Aspect-Based Opinion Mining from Online Reviews. In: *Tutorial at SIGIR Conference*.

Montgomery, D.C., Peck, E.A., and Vining, G.G., 2021. *Introduction to Linear Regression Analysis*. John Wiley & Sons, United States.

Nafea, A.A., Ibrahim, M.S., Mukhlif, A.A., AL-Ani, M.M., and Omar, N., 2024. An ensemble model for detection of adverse drug reactions. *ARO-The Scientific Journal of Koya University*, 12(1), pp.41-47.

Nafea, A.A., Omar, N., and AL-Ani, M.M., 2021. Adverse drug reaction detection using latent semantic analysis. *Journal of Computer Science*, 17(10), pp.960-970.

Nafea, A.A., Omar, N., and Al-Qfail, Z.M., 2024. Artificial neural network and latent semantic analysis for adverse drug reaction detection. *Baghdad Science Journal*, 21, pp.226-233.

Narayanasamy, V., Mukhopadhyay, S., Palakal, M., and Potter, D.A., 2004. TransMiner: Mining transitive associations among biological objects from text. *Journal of Biomedical Science*, 11(6), pp.864-873.

Nikfarjam, A., Sarker, A., O'Connor, K., Ginn, R., and Gonzalez, G., 2015. Pharmacovigilance from social media: Mining adverse drug reaction mentions using sequence labeling with word embedding cluster features. *Journal of the American Medical Informatics Association*, 22(3), pp.671-681.

Odeh, F., and Taweel, A., 2019. A Deep Learning Approach to Extracting Adverse Drug Reactions. In: *2019 IEEE/ACS 16th International Conference on Computer Systems and Applications (AICCSA)*. IEEE, pp.1-6.

Pain, J., Levacher, J., Quinquenel, A., and Belz, A., 2016. Analysis of Twitter Data for Postmarketing Surveillance in Pharmacovigilanc. In: *Proceedings of the 2nd Workshop on Noisy User-generated Text (WNUT)*, pp.94-101.

Pirmohamed, M., James, S., Meakin, S., Green, C., Scott, A.K., Walley, T.J., Farrar, K., Park, B.K., and Breckenridge, A.M., 2004. Adverse drug reactions as cause of admission to hospital: Prospective analysis of 18 820 patients. *BMJ*, 329(7456), pp.15-19.

Plachouras, V., Leidner, J.L., and Garrow, A.G., 2016. Quantifying Self-Reported Adverse Drug Events on Twitter: Signal and Topic Analysis. In: *Proceedings of the 7th 2016 International Conference on Social Media and Society*, pp.1-10.

Pouliot, Y., Chiang, A.P., and Butte, A.J., 2011. Predicting adverse drug reactions using publicly available PubChem BioAssay data. *Clinical Pharmacology and Therapeutics*, 90(1), pp.90-99.

Prabowo, R., and Thelwall, M., 2009. Sentiment analysis: A combined approach. *Journal of Informetrics*, 3(2), pp.143-157.

Rebholz-Schuhmann, D., Kirsch, H., Arregui, M., Gaudan, S., Riethoven, M., and Stoehr, P., 2007. EBIMed-text crunching to gather facts for proteins from Medline. *Bioinformatics*, 23(2), pp.e237-e244.

Rindflesch, T.C., and Fiszman, M., 2003. The interaction of domain knowledge and linguistic structure in natural language processing: Interpreting hypernymic propositions in biomedical text. *Journal of Biomedical Informatics*, 36(6), pp.462-477.

Roddick, J.F., Fule, P., and Graco, W.J., 2003. Exploratory medical knowledge discovery: Experiences and issues. *ACM SIGKDD Explorations Newsletter*, 5(1), pp.94-99.

Roitmann, E., Eriksson, R., and Brunak, S., 2014. Patient stratification and identification of adverse event correlations in the space of 1190 drug related adverse events. *Frontiers in Physiology*, 5, p.332.

Sangma, J.W., Anal, S.R.N., and Pal, V., 2020. Clustering-based hybrid approach for identifying quantitative multidimensional associations between patient Attributes, drugs and adverse drug reactions. *Interdisciplinary Sciences: Computational Life Sciences*, 12, pp.237-251.

Sarker, A., and Gonzalez, G., 2015. Portable automatic text classification for adverse drug reaction detection via multi-corpus training. *Journal of Biomedical Informatics*, 53, pp.196-207.

Sarker, A., Ginn, R., Nikfarjam, A., O'Connor, K., Smith, K., Jayaraman, S., Upadhaya, T., and Gonzalez, G., 2015. Utilizing social media data for pharmacovigilance: A review. *Journal of Biomedical Informatics*, 54, pp.202-212.

Shen, C., Li, Z., Chu, Y., and Zhao, Z., 2021. GAR: Graph adversarial representation for adverse drug event detection on Twitter. *Applied Soft Computing*, 106, p.107324.

Shen, C., Lin, H., Guo, K., Xu, K., Yang, Z., and Wang, J., 2019. Detecting adverse drug reactions from social media based on multi-channel convolutional neural networks. *Neural Computing and Applications*, 31, pp.4799-4808.

Simpson, M.S., and Demner-Fushman, D., 2012. Biomedical text mining: A survey of recent progress. In: *Mining Text Data*. Springer, Berlin, pp.465-517.

Skentzos, S., Shubina, M., Plutzky, J., and Turchin, A., 2011. Structured vs. unstructured: Factors affecting adverse drug reaction documentation in an EMR repository. *AMIA Annual Symposium Proceedings*, 2011, p.1270.

Somasundaran, S., Wilson, T., Wiebe, J., and Stoyanov, V., 2007. QA with Attitude: Exploiting Opinion Type Analysis for Improving Question Answering in On-line Discussions and the News. In: *The International AAAI Conference on Web and Social Media*.

Tan, S., Cheng, X., Wang, Y., and Xu, H., 2009. Adapting Naive Bayes to Domain Adaptation for Sentiment Analysis. In: *European Conference on Information Retrieval*. Springer, Berlin, pp.337-349.

Thabtah, F., Eljinini, M.A.H., and Hadi, W.M., 2009. Naïve Bayesian Based on Chi SQUARE to Categorize Arabic Data. In: *Proceedings of the 11th International Business Information Management Association Conference (IBIMA) Conference on Innovation and Knowledge Management in Twin Track Economies, Cairo, Egypt*, pp.4-6.

Wang, C.K., Dai, H., Su, E.C.Y., and Wang, F.D., 2018. Adverse Drug Reaction Post Classification with Imbalanced Classification Techniques. In: *2018 Conference on Technologies and Applications of Artificial Intelligence (TAAI)*. IEEE, pp.5-9.

Wang, C.S., Lin, P.F., Cheng, C.L., Tai, S.H., Yang, Y.H.K., and Chiang, J.H., 2019. Detecting potential adverse drug reactions using a deep neural network model. *Journal of Medical Internet Research*, 21(2), p.e11016.

Wang, X., Tsujii, J., and Ananiadou, S., 2010. Disambiguating the species of biomedical named entities using natural language parsers. *Bioinformatics*, 26(5), pp.661-667.

Weeber, M., Klein, H., Aronson, A.R., Mork, J.G., de Jong-van den Berg, L.T., and Vos, R., 2000. Text-Based Discovery in Biomedicine: The Architecture of the DAD-System. In: *Proceedings of the AMIA Symposium*. American Medical Informatics Association, p. 903.

WHO., 2002. *The Importance of Pharmacovigilance*. WHO, Geneva.

Xu, K., Liao, S.S., Li, J., and Song, Y., 2011. Mining comparative opinions from customer reviews for competitive intelligence. *Decision Support Systems*, 50(4), pp.743-754.

Yadesa, T.M., Kitutu, F.E., Deyno, S., Ogwang, P.E., Tamukong, R., and Alele, P.E., 2021. Prevalence, characteristics and predicting risk factors of adverse drug reactions among hospitalized older adults: A systematic review and meta-analysis. *SAGE Open Medicine*, 9, p. 20503121211039100.

Yalamanchi, D., 2011. *Sideffective-System to Mine Patient Reviews: Sentiment Analysis*. Rutgers University-Graduate School-New Brunswick, New Jersey.

Yates, A., and Goharian, N., 2013. ADRTrace: Detecting Expected and Unexpected Adverse Drug Reactions from User Reviews on Social Media Sites. In: *Advances in Information Retrieval: 35th European Conference on IR Research, ECIR 2013, Moscow, Russia. Proceedings 35.* Springer Berlin Heidelberg, pp.816-819.

Yousef, R.N.M., Tiun, S., and Omar, N., 2019. Extended trigger terms for extracting adverse drug reactions in social media texts. *Journal of Computer Science*, 15(6), pp.873-879.

Yousef, R.N.M., Tiun, S., Omar, N., and Alshari, E.M., 2020. Enhance medical sentiment vectors through document embedding using recurrent neural network. *International Journal of Advanced Computer Science and Applications*, 11(4).

Yousef, R.N.M., Tiun, S., Omar, N., and Alshari, E.M., 2020. Lexicon replacement method using word embedding technique for extracting adverse drug reaction. *International Journal of Technology Management and Information System*, 2(1), pp.113-122.

Yu, H., and Hatzivassiloglou, V., 2003. Towards Answering Opinion Questions: Separating Facts from Opinions and Identifying the Polarity of Opinion Sentences. In: *Proceedings of the 2003 Conference on Empirical Methods in Natural Language Processing*, pp.129-136.

Zhang, M., and Geng, G., 2019. Adverse drug event detection using a weakly supervised convolutional neural network and recurrent neural network model. *Information*, 10(9), p.276.

Zhang, T., Lin, H., Ren, Y., Yang, Z., Wang, J., Duan, X., and Xu, B., 2021. Identifying adverse drug reaction entities from social media with adversarial transfer learning model. *Neurocomputing*, 453, pp.254-262.

Zhang, T., Lin, H., Xu, B., Ren, Y., Yang, Z., Wang, J., and Duan, X., 2020. Gated Iterative Capsule Network for Adverse Drug Reaction Detection from Social Media. In: *2020 IEEE International Conference on Bioinformatics and Biomedicine (BIBM)*. IEEE, pp.387-390.

Zhang, W., Peissig, P., Kuang, Z., and Page, D., 2020. Adverse Drug Reaction Discovery from Electronic Health Records with Deep Neural Networks. In: *Proceedings of the ACM Conference on Health, Inference, and Learning*, pp.30-39.

Zhang, W., Yoshida, T., and Tang, X., 2008. Text classification based on multi-word with support vector machine. *Knowledge-Based Systems*, 21(8), pp.879-886.

Zhang, Y., Cui, S., and Gao, H., 2020. Adverse drug reaction detection on social media with deep linguistic features. *Journal of Biomedical Informatics*, 106, p.103437.

Zhang, Z., Ye, Q., Zhang, Z., and Li, Y., 2011. Sentiment classification of Internet restaurant reviews written in Cantonese. *Expert Systems with Applications*, 38(6), pp.7674-7682.

Zweigenbaum, P., Demner-Fushman, D., Yu, H., and Cohen, K.B., 2007. Frontiers of biomedical text mining: Current progress. *Briefings in Bioinformatics*, 8(5), pp.358-375.

http://dx.doi.org/10.14500/aro.11477

Optimizing Emotional Insight through Unimodal and Multimodal Long Short-term Memory Models

Hemin F. Ibrahim[1]*, Chu K. Loo[2], Shreeyash Y. Geda[3] and Abdulbasit K. Al-Talabani[4]

[1]Department of Information Technology, Tishk International University, Erbil, Kurdistan Region - F.R. Iraq

[2]Department of Artificial Intelligence, Faculty of Computer Science and Information Technology, Universiti Malaya, Kuala Lumpur, Malaysia

[3]Indian Institute of Technology Roorkee, Roorkee, Uttarakhand, India

[4]Department of Software Engineering, Faculty of Engineering, Koya University, Danielle Mitterrand Boulevard, Koya KOY45, Kurdistan Region – F.R. Iraq

***Abstract*—The field of multimodal emotion recognition is increasingly gaining popularity as a research area. It involves analyzing human emotions across multiple modalities, such as acoustic, visual, and language. Emotion recognition is more effective as a multimodal learning task than relying on a single modality. In this paper, we present an unimodal and multimodal long short-term memory model with a class weight parameter technique for emotion recognition on the CMU-Multimodal Opinion Sentiment and Emotion Intensity dataset. In addition, a critical challenge lies in selecting the most effective fusion method for integrating multiple modalities. To address this, we applied four different fusion techniques: Early fusion, late fusion, deep fusion, and tensor fusion. These fusion methods improved the performance of multimodal emotion recognition compared to unimodal approaches. With the highly imbalanced number of samples per emotion class in the MOSEI dataset, adding a class weight parameter technique leads our model to outperform the state of the art on all three modalities — acoustic, visual, and language — as well as on all the fusion models. The challenges of class imbalance, which can lead to biased model performance, and using an effective fusion method for integrating multiple modalities often result in decreased accuracy in recognizing less frequent emotion classes. Our proposed model shows 2–3% performance improvement in the unimodal and 2% in the multimodal over the state-of-the-art achieved results.**

***Index Terms*—Multimodal emotion recognition, Long short-term memory model, Class weight technique, Fusion techniques, Imbalanced data handling.**

ARO-The Scientific Journal of Koya University
Vol. XII, No. 1 (2024), Article ID: ARO.11477. 7 pages
Doi: 10.14500/aro.11477
Received: 25 January 2024; Accepted: 25 May 2024
Regular research paper: Published: 09 June 2024
Corresponding author's e-mail: hemin.ibrahim@tiu.edu.iq

I. Introduction

Technology in the 21st century has become widespread, dramatically transforming and significantly revolutionizing our way of life. Artificial intelligence (AI) has the potential to perform complex tasks that humans cannot do as quickly or as precisely as machines. However, adopting soft skills such as empathy, creativity, kindness, and caring for one another is just beginning (Paiva, et al., 2017).

Furthermore, emotions can significantly play an important role in various aspects of human daily life, including communication, comprehension, mutual assistance, and sometimes even decision-making. However, real human emotions are challenging to categorize, recognize, and analyze due to the differences among situations, cultures, and individuals (Angelov, et al., 2017).

The vocal modulations (speech) and facial expressions as visual data from the videos, in addition to textual data, provide significant cues to better identify emotions. Nonetheless, managing heterogeneous data in multimodal analysis necessitates a robust fusion strategy (Vijayaraghavan, et al., 2024) (Chen, et al., 1998).

The heterogeneity of multimodal data makes it challenging to build models that achieve information and not only capture complementary information. This explains why implementing proper fusion techniques is necessary to increase accuracy, learn the importance of each modality, and increase the reliability of estimation. This multimodal approach helps close the gap between technology and human interaction, potentially improving applications in customer satisfaction, mental health, and human-computer interfaces that utilize different modalities. By combining different data sources, this approach enhances the ability to understand and respond to complex emotional cues.

In this work, we present four different multimodal fusion techniques and evaluate their performance in detecting

binary-class-based emotion recognition, using the CMU-Multimodal Opinion Sentiment and Emotion Intensity (CMU-MOSEI) dataset. To the best of our knowledge, the investigation of these three models under the proposed fusions has not been investigated for the emotion recognition application. In addition, we present the results from each modality separately and compare them with one another. The analysis aims to identify which fusion technique is most effective for this specific dataset. Our findings provide valuable insights for researchers and practitioners interested in multimodal emotion recognition.

Most classifications are facing difficulties in getting efficient accuracy and performing poorly when the training dataset is significantly imbalanced (Crangle, et al., 2019). Classification of binary imbalanced data, such as the CMU-MOSEI dataset, is a significant challenge in the field of machine learning (Yang and Wu, 2006).

Emotion classes in the CMU-MOSEI dataset used in this work are highly imbalanced; for example, the surprise emotion has a ratio of 1:10 (true class: false class), indicating that classification accuracy may not be efficient. To address this issue, we used the class weight parameter in our model, which assigns weight to the imbalanced classes during training by multiplying the loss of each sample by a specific factor depending on the class. The class weight technique helps focus the model's attention on samples from an underrepresented class. The use of class weights in the long short-term memory (LSTM) model demonstrated considerable efficacy, facilitating the model's ability to learn from underrepresented class samples without overly penalizing them, consequently improving performance across all classes.

II. Related Work

Over the last few years, the use of a multimodal approach has increased. In their review, (Jiang, et al., 2020) indicate that feature-level fusion is a common approach in multimodal models, where features from different types of data, such as text, audio, and images, are combined to create a single, unified representation. The processing of fusion between heterogeneity data and the variety of signals to support different channels through supplementary information fusion are significantly improved (Huang, et al., 2017). The survey paper by (Gladys and Vetriselvi, 2023) offers a detailed summary of emotion recognition that focuses on unimodal, such as visual, auditory, and linguistic, as well as multimodal emotion recognition. The paper examines the different ways to combine and represent information from multiple modalities.

Most previous works have primarily focused on combining features (concatenate features) from different channels into a single input to the network, which is called early fusion (EF) (Churamani, et al., 2018). In their research work, (Zadeh, et al., 2017) proposed a tensor fusion (TF) method to combine speech, facial expressions, and text, using a supervised learning method on the CMU-MOSI sentiment analysis dataset. In addition, the authors have proposed an end-to-end fusion method for sentiment analysis that explicitly represents unimodal, bimodal, and trimodal interactions between different channels. In their work, (Zhang, et al., 2024) investigate the current multimodal datasets for emotion recognition, looking into both hand-crafted and deep learning-based algorithms for extracting features from audio, visual, and text data. In addition, they discuss different methods for combining features, in addition to approaches that fuse at the feature level, decision level, or model level.

Majority voting, classification scores, and Borda count fusion have been used by Griol et al. in different multimodal approaches for both acoustic and language channels, using a multilayer perceptron for the acoustic modality and an extreme learning machine for the language modality (Griol, Molina and Callejas, 2019).

Comparing late fusion (LF) and EF (as called by features-level and decision-level fusion) is studied in (Busso, et al., 2004) by using a dataset that has been recorded from an actress. The study showed that the performance of the multimodal emotion classifier was better than each of the unimodal systems. In addition, the study concluded that both fusion techniques have similar performance.

Some datasets have skewed class distributions, and most classifiers perform poorly on highly unbalanced datasets. Therefore, researchers are addressing this problem by oversampling and using the Synthetic Minority Oversampling Technique (Lotfian and Busso, 2019). Furthermore, other studies proposed Cycle Generative Adversarial Networks to generate extra data for minority classes in the training set for solving the imbalanced data (Zhu, et al., 2018). Another technique, that can be used for the same purpose is the class weight, which helps improve domain classification performance (Ahmed and Green II, 2024; Kim and Kim, 2018).

As a summary of the literature, studies have exposed that the performance of emotion recognition can be developed by using multimodal information fusion. Various techniques for fusion modalities refer to having different performances. Furthermore, there are numerous methods for addressing imbalanced data, which normally improve accuracy results in a more efficient manner.

III. Methods

A. Dataset

For our experiments, the CMU-MOSEI dataset (Zadeh, et al., 2018) has been adopted, which contains 23,453 annotated video segments from 1,000 distinct speakers and 250 topics that were all collected from different channels on YouTube.

The CMU-MOSEI dataset was annotated for both sentiment and six different emotions. The dataset is gender balanced by using the data provided by the judges (57% male to 43% female) and contains different topics from different personalities. The dataset contains the following emotion

categorical labels: happiness, sadness, anger, fear, disgust, and surprise.

The dataset itself is split into a train and test set, where the train contains 15290 utterances and the test contains 4832 utterances and provides the {0,1} binary labels for each emotion class. However, all emotion classes in CMU-MOSEI except happiness are highly imbalanced. Table I shows that the emotion class labels are imbalanced, which affects efficiency and accuracy. That is why calculating the unweighted accuracy (UA) is necessary.

B. Feature Extraction

We adopted the same features for acoustic, visual, and language modalities that were provided in (Zadeh, et al., 2018). The extracted features for channels are as follows:

- Acoustic: The COVAREP software (Degottex, et al., 2014) has been used to extract 74 rich acoustic features. For each utterance, a set of acoustic features is extracted, including 12 Mel-frequency cepstral coefficients, pitch, energy, peak slope, maxima dispersion quotients (Kane and Gobl, 2011), and glottal source parameters (Drugman, et al., 2012).
- Visual: facial expression is one of the most important sources for detecting emotions (Ekman, Friesen, and Ancoli, 1980). The library Emotient Facet (Krosschell, 2017) is used to extract 35 visual features, including facial action units, facial landmarks, head pose, eye gaze, and head orientation features (Zhu, et al., 2006).
- Language: The Glove word embeddings (Pennington, Socher, and Manning, 2014) are used to extract word vectors from transcripts. The timing of word utterances is extracted and aligned with audio at a sound level using P2FA (Yuan and Liberman, 2008), which enables alignment between audio, video, and text.

C. LSTM and Class Weight

LSTM, as a deep learning model for supporting time series data is applied to both proposed unimodal and multimodal approaches to learning and predicting emotions. The LSTM technique is one of the most popular and powerful deep learning methods for time-series data, and unlike the traditional RNN, it can capture long-term dependencies (Sherstinsky, 2020). LSTM gets better performance as a part of recurrent neural networks (RNNs) by having memory cells and gates that protect the information for the long term (Li, Abdel-Aty, and Yuan, 2020).

The main advantages of the LSTM are the memory cells in its hidden layers, which are organized into memory blocks rather than traditional neuron nodes. A memory cell has four main elements: An input gate (i_t), forget gate (f_t), self-connected memory cells (g_t), and an output gate (O_t), as shown in Fig. 1 (Li, Abdel-Aty and Yuan, 2020). The cell state at time is computed using the following equations:

$$i_t=\sigma(W_{xi}x_t+W_{hi}h_{t-1}+W_{ci}c_{t-1}+b_i)$$

$$f_t=\sigma(W_{xf}x_t+W_{hf}h_{t-1}+W_{cf}c_{t-1}+b_f)$$

$$o_t=\sigma(W_{xo}x_t+W_{ho}h_{t-1}+W_{co}c_t+b_o)$$

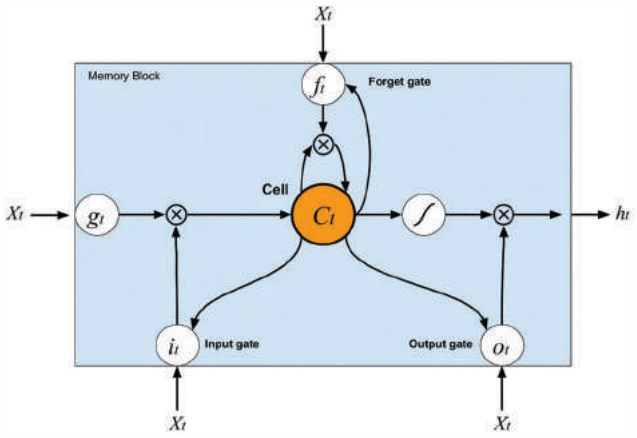

Fig. 1. The structure of long short-term memory cell (Li, Abdel-Aty, and Yuan, 2020).

$$g_t=tanh(W_{xc}x_t+W_{hc}h_{t-1}+b_c)$$

$$c_t=f_t\odot c_{t-1}+i_t\odot g_t$$

$$h_t=o_t\odot tanh(c_t)$$

Where σ is the gate activation function by using the sigmoid function, W represents weight matrices, c_{t-1} is the previous cell state, and $\odot$ denotes element-wise multiplication. However, the CMU-MOSEI dataset has some levels of class imbalance, except happiness class, as shown in Table I. To solve this issue, we used class weight as an additional parameter for weighting the loss function, which gives a weight to imbalanced classes by multiplying the loss of each sample by a certain factor based on their class. Class weights will be given by the following equation:

$$wi=\frac{n}{k\times ni}$$

Where w_i is the weight to class i, n is the number of samples, ni is the number of samples in class i, and k is the total number of classes.

This dictionary weight can be used directly to modify the loss function during the training time, by giving more class weights to the minority class and less class weights to the majority class, so that the learning dynamics of both classes remain the same. If we are assuming that L_1 and L_2 represent losses for the true and false classes, respectively, the total loss (L) can be calculated as follows:

$$L=\alpha\times L_1+\beta\times L_2$$

Where

$$L_1=-y\times log(f(x))$$

$$L_2=-(1-y)\times log(1-f(x))$$

$f(x)$ is the output of the final prediction in the dense layer and y is the class label. Binary cross entropy was used as loss for binary emotion classification. σ and β are class weights of the true and false classes, respectively.

TABLE I
HIGHLY EMOTION CLASSES IMBALANCED IN CMU-MOSEI DATASET, ONLY HAPPY CLASS IS BALANCED.

Emotions	Train set		Test set	
	True	False	True	False
Happy	53.3%	46.7%	52.2%	47.8%
Angry	22.5%	77.5%	20.1%	79.9%
Sad	25.5%	74.5%	27.6%	72.4%
Fear	8.6%	91.4%	6.9%	93.1%
Disgust	17.8%	82.2%	19.1%	80.9%
Surprise	10.2%	89.8%	9.9%	90.1%

In the validation label, we used UA (Tong, et al., 2017) which represents the actual performance, especially when the data areimbalanced in terms of sample sizes per emotion class. UA is computed as follows:

$$\text{Unweighted accuracy} = \frac{1}{|C|}\sum_{i=1}^{|C|}\frac{TP_i}{TP_i + FN_i}$$

Where i = 1,2,…, C introduces the number of emotion classes used, true positive refers to the number of positive samples that were recognized correctly as positive samples from the classification model.

IV. UNIMODAL AND MULTIMODAL

In this work, unimodal and multimodal approaches are proposed and evaluated using the specified dataset. First, we tried to check all the modalities, acoustic, visual, and language, separately and input their features into a specified LSTM for each modality, as shown in Fig. 2. In this study, we adopted various fusion approaches for multimodal emotion recognition using acoustic, visual, and language, such as EF, LF, deep fusion (DF), and TF.

EF: EF (Churamani, et al., 2018) as shown in Fig. 3, refers to the simple concatenation of acoustic (A), visual (V), and language (L) features and feeding them to the deep learning model. Features are fused at an early stage, hence the name EF. Concatenation was performed, on feature dimensions (35+74+300 = 409) and then the 409 features were used as input to the LSTM model. The training procedure was kept consistent with the unimodal approach to enable a comparison of the relative strengths of the models.

LF: LF (Busso, et al., 2004) as shown in Fig. 4, refers to the concatenation of 32 features that are extracted from the last layer of each LSTM unimodal for acoustic, visual, and language channels. The concatenated features feed two fully connected layers with several neurons equal to 32 and 1, respectively, which is shown in Fig. 4. This proposed fusion makes unimodal learn intramodal relations, while dense learns intermodal relations. The class weight is used for weighting the loss function during the training model.

DF: The DF approach (Fig. 5) is applied based on the work of (Nojavanasghari, et al., 2016). First, the pre-trained features from all three channels are used to give final prediction values, which are combined with their complementary values, then fed to the new dense, and classification is performed. Furthermore, the class weight used to tell the model takes more attention to these samples from an underrepresented population.

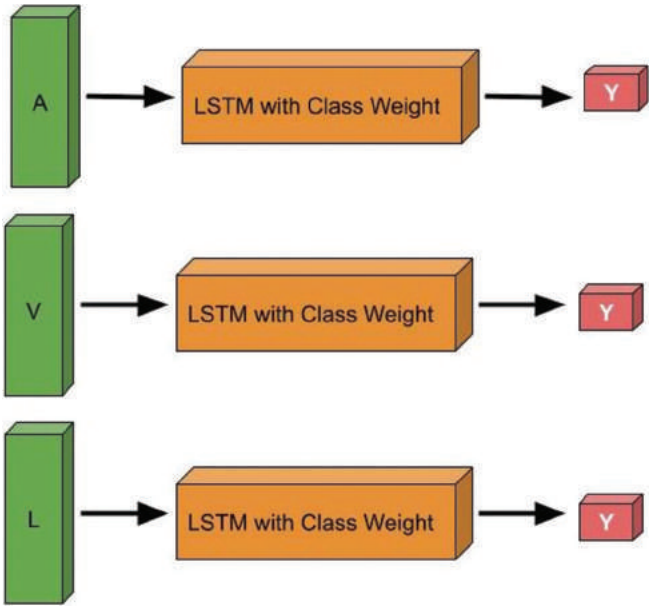

Fig. 2. The features from each unimodal (Acoustic [A], Visual [V] and Language [L]) are fed to the long short-term memory (LSTM)+CW using a 3-layer LSTM model with 1 dense layer and prediction.

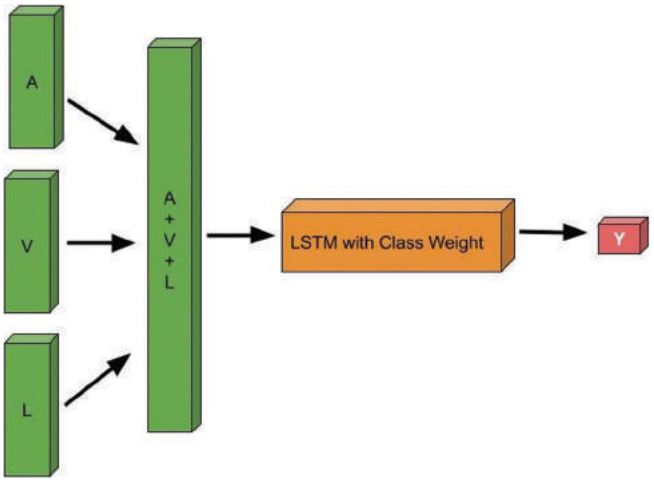

Fig. 3. Early fusion technique which refers to the direct concatenation of acoustic (A), visual (V) and language (L) features and feeding them to the long short-term memory+CW model.

After pre-training A, V, and L channels are represented as confidence scores of unimodal classifiers, and 1-A, 1-V, and 1-L are complementary values.

TF: Most of the fusion methods discussed so far use concatenation for fusion, but TF Network (Zadeh, et al., 2017) presents a new type of fusion method where they use the outer product of unimodally extracted features instead of direct concatenation, as shown in Fig. 6.

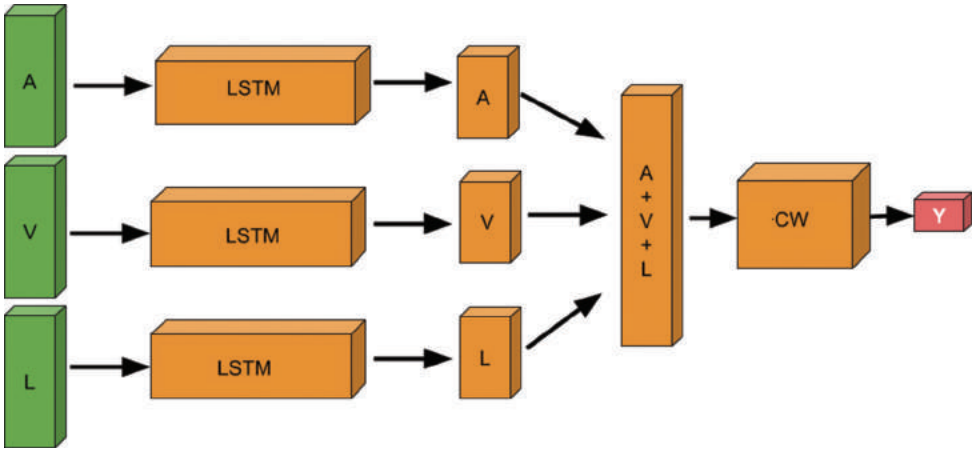

Fig. 4. Late fusion of the concatenation of features extracted from unimodal models for acoustic (A), visual (V) and language (L) and utilized a dense layer using these features for classification.

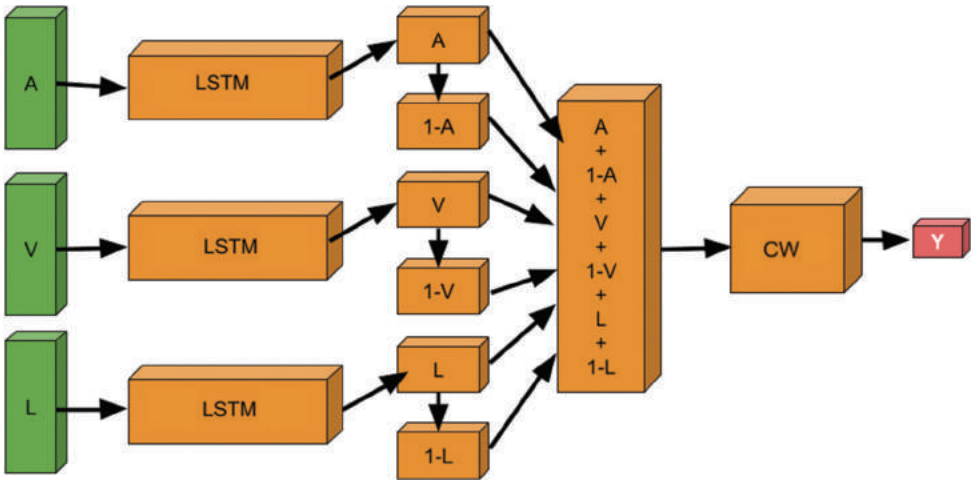

Fig. 5. Deep fusion, final prediction values from unimodal and complementary values are fed to dense.

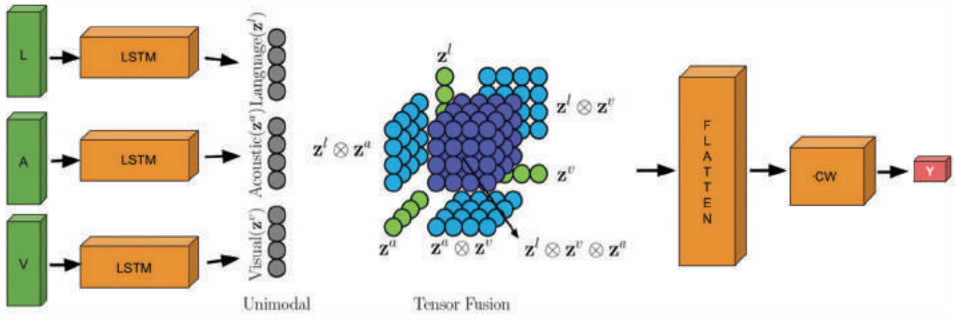

Fig. 6. Tensor fusion.

In Fig. 6, z^v, z^a, and z^l are the pre-trained unimodal and they used the outer product between these features to find a correlation according to the formula:

$$z^m = \begin{bmatrix} z^l \\ 1 \end{bmatrix} \otimes \begin{bmatrix} z^v \\ 1 \end{bmatrix} \otimes \begin{bmatrix} z^a \\ 1 \end{bmatrix}$$

Where z^m is flattened and fed to a dense layer for the classification task. This way, they argue to learn better correlation among different modalities. Furthermore, class weight is used in the loss function to assign a higher value to these instances that are smaller.

V. Results and Discussion

In this section, we present the results of our model for both unimodal and multimodal approaches with different fusion approaches. In addition, to evaluate our results and have valid accuracy, we use UA as our metric. Our model outperforms

many baselines and state-of-the-art (SOTA) methods for emotion recognition on the CMU-MOSEI dataset.

A. Unimodal

On the unimodal part, we trained and tested each channel separately, and our binary classification results for different emotions demonstrate better performance compared to SOTA methods. Table II shows the results for all three modalities, indicating that only the sad emotion class in the acoustic modality and the fear class in the visual modality did not outperform the SOTA (Zadeh, et al., 2018) with a difference of 1.55%, and 0.35%, respectively. However, all the other classes and the average of all modalities outperform the SOTA. The last row shows the average value over the six emotion classes, indicating that the proposed LSTM+CW outperforms the work of (Zadeh, et al., 2018) in the unimodal approach.

B. Multimodal and Fusion Approaches

As mentioned in Section III, we used four different fusion approaches with the LSTM and the class weight parameter to address the issue of imbalance. Our model, across all the different fusion approaches, was able to achieve better performance than the SOTA (Zadeh, et al., 2018). However, as shown in Table III, one can see that the EF approach outperforms other models in three emotions in addition to the average of all emotions.

Table III shows that our multimodal (acoustic [A], visual [V], and language [T]) UA using the four suggested fusions for binary classification of different emotions outperforms the SOTA (Zadeh, et al., 2018). The average of EF is higher than that of SOTA and the other approaches; also, TF performs competitively with EF. Three emotion classes, such as happiness, disgust, and surprise, in TF produce better results. The last row shows the average value over six emotion classes. We can clearly observe that DF and LF outperform SOTA, but they are still not performing as well as tensors and EF. Overall, for all three modalities (acoustic, visual, and language), LSTM and class weight for giving weight to the loss function, outperformed SOTA. Furthermore, all comparisons are based on UA metrics, because we handle imbalanced data directly.

TABLE II
Unweighted Accuracy (in Percentage) of CMU-MOSEI Dataset for Each Modality Based on Different Emotion Classes, the SOTA Refers to the SOTA from the CMU Multimodal Data SDK GitHub (Zadeh, et al., 2018)

Emotions	Acoustic		Visual		Language	
	SOTA	LSTM+CW	SOTA	LSTM+CW	SOTA	LSTM+CW
Happy	61.5	62.73	57.4	64.11	54	63.12
Angry	56.4	61.46	60	62.27	56.6	62.64
Sad	62	60.45	57.7	59.38	54	59.49
Fear	62.7	63.91	64.2	63.85	58.8	63.98
Disgust	60.9	71.26	60.3	70.52	64	68.61
Surprise	54.3	53.81	51.8	53.11	54.3	59.13
Avg	59.63	62.27	58.57	62.21	56.95	62.83

LSTM: Long short-term memory, SOTA: State-of-the-art

TABLE III
Unweighted Accuracy (in Percentage) of CMU-MOSEI Dataset Multimodal for 4 Different Fusion Approaches, such as DF, TF, LF, and EF Compared with the SOTA (Zadeh, et al., 2018)

Emotions	SOTA	DF	TF	LF	EF
Happy	66.3	64.43	67.57	66.48	67.44
Angry	62.6	63.32	64.15	63.71	66.46
Sad	60.4	59.78	61.52	61.61	62.68
Fear	62	64.29	61.87	58.43	65.14
Disgust	69.1	69.54	72.92	71.68	70.53
Surprise	53.7	57.41	58.99	58.45	56.64
AVG	62.35	63.13	64.5	63.39	64.82

DF: Deep fusion, TF: Tensor fusion, LF: Late fusion, EF: Early fusion, SOTA: State-of-the-art

VI. Conclusion and Future Work

In this paper, we present a deep learning architecture using LSTM to introduce an additional parameter, which is the class weight parameter, in the loss function that deals with the class distribution to handle the imbalance from the CMU-MOSEI dataset. LSTM and class weight parameters are used during training the model for unimodal and multimodal approaches with different fusion approaches.

Our model achieves better results in language modality compared to the other modalities, and the average of unimodal outperforms the SOTA UA.

Our study shows that EF in multimodal emotion recognition performs the best compared to other fusion approaches. The difference between all the fusion approaches is 1.5%, and the best-proposed fusion approaches outperform the SOTA by 2.47%. A limitation of this work that needs to be mentioned is that the proposed models have been validated on the binary version of emotions rather than the multiclass approach. For the next step in this work, different methods will be proposed to deal with imbalanced data, such as creating an end-to-end model. Furthermore, our model can be applied to sentiment analysis in the MOSEI dataset, and using more than one multimodal emotion dataset. A more advanced model can be tried (with class weights), such as unsupervised or semi-supervised learning methods, which may help in dealing with the problem of manual labeling of emotional data.

Acknowledgment

This study was supported by the Grand Challenge Grant-HTM (Wellness): GC003A-14HTM from the University of Malaya, IIRG Grant (IIRG002C-19HWB) from the University of Malaya and funding from the International Interfaculty Initiative in Computational Systems Care at Tokyo Metropolitan University, Japan.

References

Ahmed, J., and Green 2nd, R.C., 2024. Cost aware LSTM model for predicting hard disk drive failures based on extremely imbalanced S.M.A.R.T. sensors data. *Engineering Applications of Artificial Intelligence*, 127, 107339.

Angelov, P., Gu, X., Iglesias, J., Ledezma, A., Sanchis, A., Sipele, O., and Ramezani, R., 2017. Cybernetics of the mind: Learning individual's perceptions autonomously. *IEEE Systems, Man, and Cybernetics Magazine*, 3(2), pp.6-17.

Busso, C., Deng, Z., Yildirim, S., Bulut, M., Lee, C.M., Kazemzadeh, A., Lee, S., and Neumann, U., 2004. Analysis of Emotion Recognition Using Facial Expressions, Speech and Multimodal Information. In: *Proceedings of the 6th International Conference on Multimodal Interfaces*.

Chen, L., Huang, T., Miyasato, T., and Nakatsu, R., 1998. Multimodal Human Emotion/Expression Recognition. In: *Proceedings 3rd IEEE International Conference on Automatic Face and Gesture Recognition.* Nara, Japan.

Churamani, N., Barros, P., Strahl, E., and Wermter, S., 2018. Learning Empathy-Driven Emotion Expressions using Affective Modulations. In: *Proceedings of the 2018 International Joint Conference on Neural Networks* (*IJCNN*).

Crangle, C.E., Wanga, R., Perreau-Guimaraesa, M., Nguyena, M.U., Nguyena, D.T., and Suppes, P., 2019. *Machine learning for the recognition of emotion in the speech of couples in psychotherapy using the Stanford Suppes Brain Lab Psychotherapy Dataset*. Available from: https://arxiv.org/abs/1901.04110v1

Degottex, G., Kane, J., Drugman, T., Raitio, T., and Scherer, S., 2014. COVAREP - A Collaborative Voice analysis Repository for Speech Technologies. In: *IEEE International Conference on Acoustics, Speech and Signal Processing* (*ICASSP*). Florence, Italy.

Drugman, T., Thomas, M., Gudnason, J., Naylor, P., and Dutoit, T., 2012. Detection of glottal closure instants from speech signals: A quantitative review. *IEEE Transactions on Audio Speech and Language Processing*, 20, pp.994-1009.

Ekman, P., Friesen, W.V., and Ancoli, S., 1980. Facial signs of emotional experience. *Journal of Personality and Social Psychology*, 39, pp.1125-1134.

Geetha, A.V., Mala, T., Priyanka, D., and Uma, E., 2024. Multimodal emotion recognition with deep learning: Advancements, challenges, and future directions. *Information Fusion*, 105, 102218.

Gladys, A.A., and Vetriselvi, V., 2023. Survey on multimodal approaches to emotion recognition. *Neurocomputing*, 556, p.126693.

Griol, D., Molina, J.M., and Callejas, Z., 2019. Combining speech-based and linguistic classifiers to recognize emotion in user spoken utterances. *Neurocomputing*, 326, pp.132-140.

Huang, Y., Yang, J., Liao, P., and Pan, J., 2017. Fusion of Facial Expressions and EEG for Multimodal Emotion Recognition. *Computational Intelligence and Neuroscience*, 2017, p.2107451.

Jiang, Y., Li, W., Hossain, MS., Chen, M., Alelaiwi, A., and Al-Hammadi, M., 2020. A snapshot research and implementation of multimodal information fusion for data-driven emotion recognition. *Information Fusion*, 53, pp.209-221.

Kane, J., and Gobl, C., 2011. Identifying Regions of Non-modal Phonation Using Features of the Wavelet Transform. In: *Proceedings of the Annual Conference of the International Speech Communication Association*.

Kim, J.K., and Kim, Y.B., 2018. Joint Learning of Domain Classification and Out-of-Domain Detection with Dynamic Class Weighting for Satisficing False Acceptance Rates. In: *Proceedings of the Annual Conference of the International Speech Communication Association.*

Stöckli, S., Schulte-Mecklenbeck, M., Borer, S., and Samson, A.C., 2018. Facial expression analysis with AFFDEX and FACET: A validation study. *Behavior Research Methods*, 50, pp. 1446-1460.

Li, P., Abdel-Aty, M., and Yuan, J., 2020. Real-time crash risk prediction on arterials based on LSTM-CNN. *Accident Analysis and Prevention*, 135, p.105371.

Lotfian, R., and Busso, C., 2019. Over-sampling emotional speech data based on subjective evaluations provided by multiple individuals. *IEEE Transactions on Affective Computing*, 12, pp.870-882.

Nojavanasghari, B., Gopinath, D., Koushik, J., Baltrušaitis, T., and Morency, L.P., 2016. Deep Multimodal Fusion for Persuasiveness Prediction. In: *Proceedings of the 18th ACM International Conference on Multimodal Interaction*. New York.

Paiva, A.M., Leite, I., Boukricha, B., and Wachsmuth, I., 2017. Empathy in virtual agents and robots: A survey. *ACM Transactions on Interactive Intelligent Systems*, 7, pp.1-40.

Pennington, J., Socher, R., and Manning, C.D., 2014. GloVe: Global Vectors for Word Representation. In: *Proceedings of the 2014 Conference on Empirical Methods in Natural Language Processing* (*EMNLP*).

Sherstinsky, A., 2020. Fundamentals of Recurrent Neural Network (RNN) and Long Short-Term Memory (LSTM) network. *Physica D: Nonlinear Phenomena*, 404, p.132306.

Tong, E., Zadeh, A., Jones, C., and Morency, L.P., 2017. Combating Human Trafficking with Multimodal Deep Models. In: *Proceedings of the 55th Annual Meeting of the Association for Computational Linguistics* (*Volume 1: Long Papers*).

Yang, Q., and Wu, X., 2006. 10 challenging problems in data mining research. *International Journal of Information Technology and Decision Making*, 5, pp.597-604.

Yuan, J., and Liberman, M., 2008. Speaker identification on the SCOTUS corpus. *The Journal of the Acoustical Society of America*, 123, p.3878.

Zadeh, A., Chen, M., Poria, S., Cambria, E., and Morency, LP., 2017. Tensor Fusion Network for Multimodal Sentiment Analysis. Copenhagen, Denmark. In: *Proceedings of the 2017 Conference on Empirical Methods in Natural Language Processing*.

Zadeh, A.B., Liang, P.P., Poria, S., Cambria, E., and Morency, L.P., 2018. Multimodal Language Analysis in the Wild: CMU-MOSEI Dataset and Interpretable Dynamic Fusion Graph. In: *Proceedings of the 56th Annual Meeting of the Association for Computational Linguistics* (*Volume 1: Long Papers*). Melbourne, Australia.

Zhang, S., Yang, Y., Chen, C., Zhang, X., Leng, Q., and Zhao, X., 2024. Deep learning-based multimodal emotion recognition from audio, visual, and text modalities: A systematic review of recent advancements and future prospects. *Expert Systems with Applications*, 237, p.121692.

Zhu, Q., Yeh, M.C., Cheng, K.T., and Avidan, S., 2006. Fast Human Detection Using a Cascade of Histograms of Oriented Gradients. In: *2006 IEEE Computer Society Conference on Computer Vision and Pattern Recognition* (*CVPR'06*).

Zhu, X. Liu, Y., Li, J., Tao, W., and Qin, Z., 2018. *Emotion Classification with Data Augmentation Using Generative Adversarial Networks*. Springer, Cham.

Microstrip Passive Components for Energy Harvesting and 5G Applications: A Comprehensive Review

Leila Nouri[1,2,*], Salah I. Yahya[3,4], Abbas Rezaei[5], Sohrab Majidifar[5]

[1]Institute of Research and Development, Duy Tan University, Da Nang, Vietnam

[2]School of Engineering and Technology, Duy Tan University Da Nang, Vietnam

[3]Department of Communication and Computer Engineering, Cihan University-Erbil, Erbil, Kurdistan region – F.R. Iraq

[4]Department of Software Engineering, Faculty of Engineering, Koya University, Koya KOY45, Kurdistan region – F.R. Iraq

[5]Department of Electrical Engineering, Kermanshah University of Technology, Kermanshah, Iran

***Abstract*—This paper provides a comprehensive overview of microstrip passive components for energy harvesting and 5G applications. The paper covers the structure, fabrication, and performance of various microstrip passive components such as filters, couplers, diplexers, and triplexers. The size and performance of several 5G and energy harvester microstrip passive devices are compared and discussed. The review highlights the importance of these components in enabling efficient energy harvesting and high-speed communication in 5G networks. In addition, the paper discusses the latest advancements in microstrip technology and identifies key research challenges and future directions in this field. Overall, this review serves as a valuable resource for researchers and engineers working on microstrip passive components for energy harvesting and 5G applications.**

***Index Terms*—5G, Diplexer, Energy harvesting, Filter, Microstrip, Passive component, Triplexer.**

I. Introduction

Microstrip passive devices are fundamental components in the realm of microwave and RF engineering, offering a versatile and efficient means of implementing essential functions such as filtering (Yahya, et al., 2024; Capstick, 1994; Chen, et al., 2015; Feng, Zhang and Che, 2017), coupling (Arriola, Lee and Kim, 2021; Yahya, et al., 2023; Abouelnaga and Mohra, 2017; Alhalabi, et al., 2018; Kim, et al., 2004), matching (Salehi, Noori and Abiri, 2016), and power division (Chi, 2012; Chen, et al., 2019). With applications spanning across communication systems, radar systems, satellite communications, and more, microstrip passive devices play a pivotal role in enabling the development of high-performance and reliable electronic systems operating at microwave and millimeter-wave frequencies (Shukor and Seman, 2020; Shukor and Seman, 2016; Shi, et al., 2016; Rezaei and Noori, 2018). In recent years, the demand for efficient and high-performance communication systems has driven the development of advanced technologies in the field of microstrip passive devices. These devices, including couplers (Kim and Kong, 2010; Rezaei, Yahya and Nouri, 2023; Lai and Ma, 2013; Li, Qu and Xue, 2007), diplexers (Nouri, Yahya and Rezaei, 2020; Rezaei, Noori and Mohammadi, 2019; Bukuru, Song and Xue, 2015; Capstick, 1999), filters (Nouri, et al., 2024; Feng, Zhang and Che, 2017; Rezaei, et al., 2022), and triplexers (Nouri, et al., 2024; Nouri, et al., 2023; Jamshidi, et al., 2023), play a crucial role in various applications such as energy harvesting and 5G networks. By leveraging the unique properties of microstrip technology, these passive devices offer compact size, low cost, and excellent performance characteristics (Rezaei, Yahya and Nouri, 2024; Yahya, et al., 2023). In the context of energy harvesting, microstrip passive devices are utilized to efficiently capture and convert ambient energy sources such as solar, thermal, and kinetic energy into usable electrical power. Couplers are commonly employed to split or combine power signals (Liou, et al., 2009), whereas diplexers and triplexers enable the simultaneous transmission and reception of multiple frequency bands (Chen, et al., 2006; Nouri, et al., 2023). Filters are also essential components for ensuring the

ARO-The Scientific Journal of Koya University
Vol. XII, No. 1 (2024), Article ID: ARO.11620. 9 pages
Doi: 10.14500/aro.11620
Received: 01 May 2024; Accepted: 01 June 2024
Regular review paper: Published: 10 June 2024
Corresponding author's e-mail: leilanouri@duytan.edu.vn

purity and stability of harvested energy signals (Salehi and Noori, 2015; Zakaria, et al., 2013). Moreover, in the rapidly evolving landscape of 5G networks, microstrip passive devices are indispensable for enabling high-speed data transfer, low latency communication, and increased network capacity (Nouri, et al., 2023; Jamshidi, et al., 2023; Yahya, et al., 2023). Overall, the application of microstrip passive devices in energy harvesting and 5G networks represents a promising avenue for advancing communication technologies and addressing the growing demand for efficient and reliable wireless systems (Nouri, et al., 2023). Passive microstrip devices that have less losses are suitable for energy-harvesting applications such as the proposed structures in (Rezaei and Noori, 2018). On the other hand, several passive microstrip structures which work at 1GHz up to 6GHz are appropriate for 5G mid-band applications (Chinig, et al., 2015; Chinig, et al., 2015; Heshmati and Roshani, 2018).

In this paper, we will examine the structure of passive microstrip devices suitable for 5G and energy harvesting users. Furthermore, their performance and advantages and disadvantages will be examined. The paper is organized as follows: First, the structure and performance of some 5G passive microstrip devices will be studied, and then, the structure and performance of microstrip passive devices suitable for energy harvesting will be reviewed. Finally, the importance of microstrip passive devices in 5G and energy harvesting is investigated. These studied devices are diplexers, filters, couplers, and triplexers.

II. Structures and Performance of 5G Passive Microstrip Devices

The 5G frequencies are divided into three frequency bands, which are low, mid, and high. Each band has different capabilities. The low band frequencies are <1 GHz. This frequency band has greater coverage but lower speeds. The mid band covers from 1 GHz up to 6 GHz and offers a balance of both. The high band is from 24 GHz up to 40 GHz offers higher speeds but a smaller coverage radius. The operating frequencies of most of the microstrip devices can be tuned at low and mid bands. However, the design of a microstrip passive device for high band 5G is difficult. Because to set an operating frequency in this band, the dimensions should be very small, which makes the fabrication process difficult. For example, the GSM association describes spectrum in the 3.3 GHz-3.8 GHz range as ideal because many countries worldwide have already designated it for 5G. However, other mid-band spectrum is also being used. Table I shows a comparison between some of 5G microstrip passive devices. In Table I, the parameters band-pass filter (BPF), low-pass to band-pass (LP-BP), and band-pass-band-pass (BP-BP) are band-pass filter, LP-BP, and BP-BP, respectively. Moreover, λg is the guided wavelength calculated at the first operating frequency of each device.

As depicted in this Table, only the designed microstrip coupler in (Shukor and Seman, 2020) is suitable for High-Band 5G applications. Its passband is from 22.55 GHz up to 30 GHz. This branch-line coupler (BLC) has a traditional simple structure presented in Fig. 1. Furthermore, Fig. 2 shows its simulated and measured frequency responses. As shown in Fig. 2, the S_{21} and S_{31} of this BLC are better than −4.6 dB within the passbands. The phase difference between S_{21} and S_{31} from 22 GHz to 30 GHz fluctuates in the range of 86°-94° in (Shukor and Seman, 2020). Fig. 3 illustrates the isolation factor (S_{41}) and return loss (S_{11}) of this coupler.

It can be seen that from 20 GHz to 30 GHz, the isolation is better than −10 dB, but the in-band return loss is not well. The LP-BP triplexers in (Yahya, et al., 2024), (Zhu, et al., 2017), and (Xu, Chen and Wan, 2020) are designed for 5G Mid-Band and Low-Band applications. The proposed structures in (Yahya, et al., 2024) and (Zhu, et al., 2017) are implemented only on a microstrip substrate but in (Zhu, et al., 2017), in addition to microstrip transition lines, lumped elements are used too. The introduced 4-Chanel BPF in (Rezaei, et al., 2022) occupies a very compact area of 0.0012 λg^2, which is suitable for 5G Mid-Band and Low-Band applications. The layouts of some 5G microstrip devices are presented in (Fig. 4a-d). The frequency responses of these devices are depicted in (Fig. 5a-d). The coupled meandrous microstrip lines presented in (Fig. 4a) are implemented on Taconic RF-35 (tm) substrate with thickness of 0.508 mm, dielectric constant of 3.5, and loss tangent of 0.0018. Using this structure leads to suppressed harmonics up to 15 GHz, which is presented in (Fig. 5a). Meanwhile, the illustrated structure in (Fig. 4b) is fabricated on a RT/duroid® 5880 substrate with ε_r = 2.22, h = 31 mil, and a loss tangent of 0.0009. It has four narrow channels as shown in (Fig. 5b). The height of the substrate of the simple microstrip band-pass filter which is presented in (Fig. 4c) is 1.524 mm, whereas it has a relative permittivity of 3.38, conductor thickness of 0.07 mm, and loss tangent of 0.0025. As shown in (Fig. 5c), it works at 5.4 GHz which makes it suitable for 5G networks. To obtain the switchable triplexer in (Fig. 4d), in addition to microstrip structure, p-i-n diode and some resistances are used. This BP-BP triplexer has some harmonics, which are depicted in (Fig. 5d).

Due to the complex design process, the number of reported microstrip multiplexers is few. Meanwhile, reducing the loss level in multiple channels simultaneously is a difficult process. However, the resonance frequencies can be tuned for 5G applications. A switchable eight-channel microstrip multiplexer is proposed by (Chen, et al., 2018). The resonance frequencies of this multiplexer are located at 0.85, 1.05, 1.3, 1.5, 1.65, 1.85, 2.05, and 2.3 GHz. Therefore, it is suitable for low-band and mid-band 5G applications. A quadruplexer is designed by (Zeng, Wu and Tu, 2011) using microstrip structure. This multiplexer operates at 2.3, 3.7, 5, and 6.1 GHz. The 1st, 2nd and 3rd channels of this device can be used for 5G applications. Another microstrip quadruplexer is reported by (Rezaei and Noori, 2018) which works at 3.211, 3.276, 3.38, and 3.491 GHz for IEEE 802.16 WiMAX and 5G mid-band applications. This multiplexer is designed using four semicircular microstrip resonators and its overall size is 0.36 λg^2.

TABLE I
A Comparison between 5G Microstrip Passive Devices

References	Operating frequencies (GHz)	Type	FBWs%	Size (λg^2)	5G application
(Yahya, et al., 2024)	0.87, 1.33, 2.05	LP-BP Triplexer	14.1, 25.5	0.0038	Low & Mid Bands
(Chen, et al., 2015)	3.967	BPF	5	---	Mid-Band
(Abouelnaga and Mohra, 2017)	2.5	Coupler	---	---	Mid-Band
(Shukor and Seman, 2020)	26	Coupler	32	---	High-Band
(Shukor and Seman, 2016)	From 2.9 to 4.1	Coupler	34.4	---	Mid-Band
(Rezaei and Noori, 2018)	2.82	Coupler	---	0.0754	Mid-Band
(Lai and Ma, 2013)	2.4	Coupler	18.8	0.0231	Mid-Band
(Bukuru, Song and Xue, 2015)	3.65, 5.2	BP-BP Diplexer	8.2, 7.69	0.0506	Mid-Band
(Rezaei, et al., 2022)	0.7, 2.2, 3.8, and 5.6	4-Chanel BPF	---	0.0012	Low & Mid Bands
(Chen, et al., 2006)	1.35, 1.76	BP-BP Diplexer	3.4, 3.4	---	Mid-Band
(Zakaria, et al., 2013)	5.4	BPF	---	---	Mid-Band
(Yahya, et al., 2023)	5.2	Coupler	---	0.04	Mid-Band
(Chen, et al., 2015)	1.1, 1.3	BP-BP Diplexer	8, 9.2	0.705	Mid-Band
(Rezaei, Yahya and Nouri, 2023)	1.65, 2.57	LP-BP Diplexer	14	0.037	Mid-Band
(Deng and Tsai, 2013)	1.5, 2.4	LP-BP Diplexer	8	---	Mid-Band
(Feng, Gao and Che, 2014)	1.84, 2.42	BP-BP Diplexer	6, 5.8	---	Mid-Band
(Zhu, et al., 2017)	0.85, 1.6, 2.1	LP-BP Triplexer	13.9, 12.7	0.048	Low & Mid Bands
(Chen, et al., 2015)	1, 2.4, 5.8	LP-BP Triplexer	10, 7	---	Mid-Band
(Xu, Chen and Wan, 2020)	0.95, 1.58, 2.8	LP-BP Triplexer	17, 8.1	0.018	Low & Mid Bands
(Noori and Rezaei, 2017)	2.62, 2.88, 4.34, 4.67	4-Chanel BPF	5.3, 5.5, 3.2, 3.6	0.079	Mid-Band
(Noori and Rezaei, 2018)	1.67, 2.54, 3.45, 4.57	4-Chanel Diplexer	1.2, 1.96, 1.15, 1.09	0.029	Mid-Band
(Hsu, Hung and Tu, 2016)	0.9, 1.5, 2.4, 3.5	4-Chanel Diplexer	4.3, 4.6, 3.3, 4	0.041	Low & Mid Bands
(Rezaei and Noori, 2018)	1.8, 2.4	BP-BP Diplexer	11, 7.1	0.022	Mid-Band
(Salehi and Noori, 2015)	2.39	BPF	46	0.0045	Mid-Band
(Salehi and Noori, 2014)	2.4	Coupler	---	0.023	Mid-Band
(Salehi, et al., 2016)	2.3, 2.55	BP-BP Diplexer	3.6, 3.4	---	Mid-Band
(Xu and Zhu, 2017)	1.21, 1.8, 2.41	BP-BP Triplexer	14.4, 14, 13.6	0.0553	Mid-Band

BPF: Band band-pass filter, LP-BP: Low-pass to band-pass, BP-BP: Band-pass-band-pass

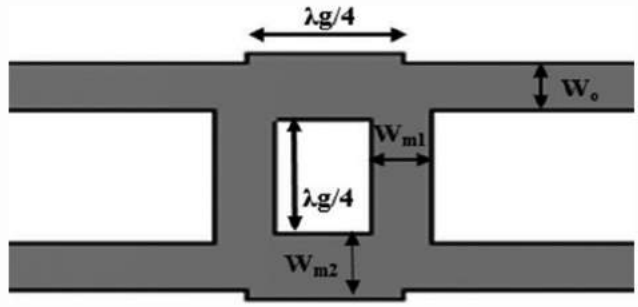

Fig. 1. Layout of a 5G high-band branch-line coupler in (Shukor and Seman, 2020).

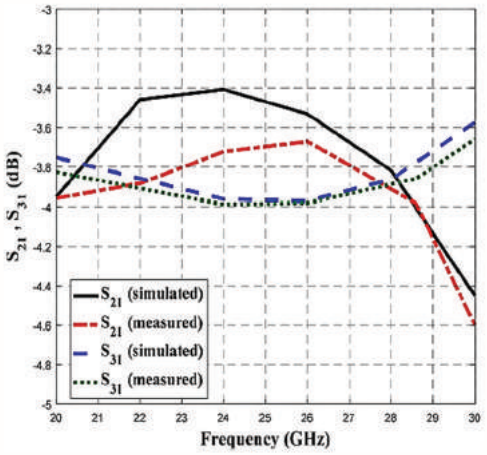

Fig. 2. Frequency response of the 5G high-band branch-line coupler in (Shukor and Seman, 2020).

III. Structures and Performance of Passive Microstrip Devices for Energy Harvesting

Passive microstrip devices designed for energy harvesting are essential components in the field of wireless power transfer and autonomous sensor systems. These devices are used to efficiently capture and convert ambient electromagnetic or RF energy into electrical power for various applications. By leveraging the principles of electromagnetic induction and resonance, passive microstrip devices enable the extraction of energy from the surrounding environment without the need for an external power source. This technology has gained significant interest due to its potential to provide sustainable and autonomous power solutions for IoT devices, wearable electronics, and other low-power applications (Jamshidi, et al., 2023). Several types of passive microstrip devices are commonly used for energy harvesting applications. RF filters with low losses are used to filter out unwanted noise and interference from the RF signal before it is converted into electrical power. These filters help improve the overall efficiency of the energy harvesting system by reducing signal distortion and improving signal quality. Consequently, diplexers, triplexers, and filtering couplers (Shi, et al., 2016) with low insertion losses are suitable for energy harvesting. Overall, a combination of these passive microstrip devices is often

http://dx.doi.org/10.14500/aro.11620

used in energy harvesting systems to efficiently capture and convert ambient RF energy into electrical power for various applications. The size and performance of some microstrip passive devices useful for energy harvesting are depicted in Table II. In this Table, Fo, ILs, and RLs are operating frequencies, insertion losses, and return losses.

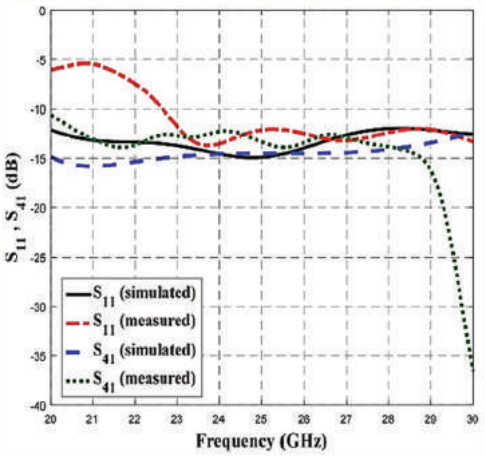

Fig. 3. Simulated and measured S_{11} and S_{41} of the proposed 5G high-band branch-line coupler in (Shukor and Seman, 2020).

Usually, triplexers have higher losses than filters and diplexers. Because, controlling three channels are more difficult. However, the LP-BP triplexer designed in (Yahya, et al., 2024) has very low losses, with the most compact size in comparison with the introduced structures in Table II. Furthermore, in (Yahya, Rezaei and Nouri, 2021), the insertion losses are very low and the size is small. The reported devices in Table II are designed based on various types of microstrip structures. (Fig. 6a-d) illustrates the layouts of some energy harvester microstrip passive devices. Meanwhile, the frequency responses of these devices are shown in (Fig. 7a-d). As shown in (Fig. 6a), two open loops are coupled to port 1 to obtain a BP-BP diplexer with a frequency response presented in (Fig. 7a). This diplexer is suitable for energy harvesting, but it has several problems in terms of low selectivity, large size, and narrow channels. The layouts of two energy harvester lowpass filters are depicted in (Fig. 6b and c).

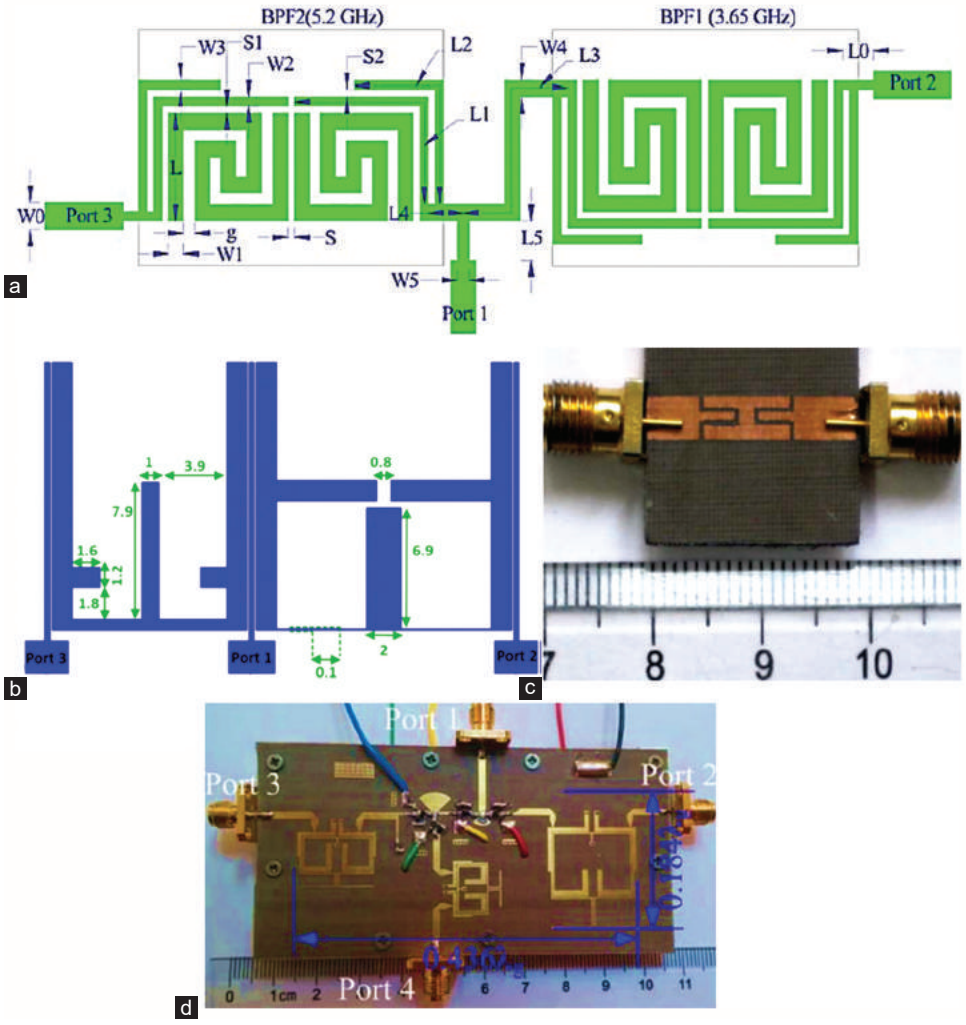

Fig. 4. Geometrical structures of the 5G microstrip (a) BP-BP diplexer in (Bukuru, Song and Xue, 2015), (b) 4-channel diplexer (unit: mm) in (Noori and Rezaei, 2018), (c) fabricated band band-pass filter in (Zakaria, et al., 2013), (d) fabricated BP-BP triplexer in (Xu and Zhu, 2017). BP-BP: Band-pass-band-pass.

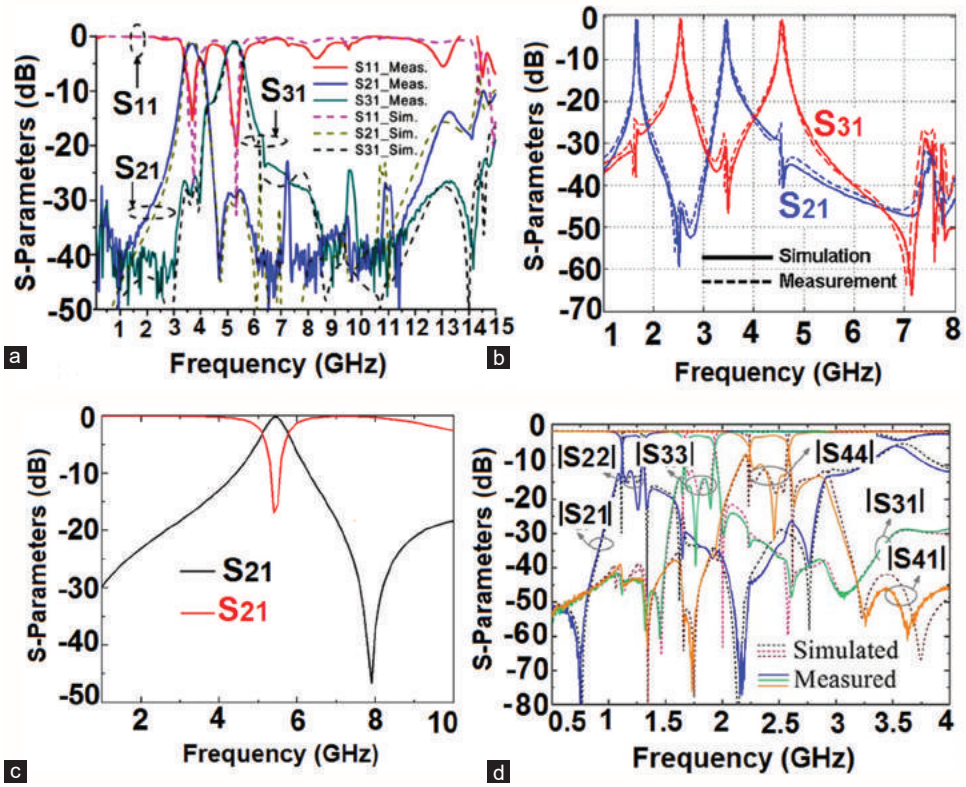

Fig. 5. Frequency responses of the 5G microstrip (a) BP-BP diplexer in (Bukuru, Song and Xue, 2015), (b) 4-channel diplexer (unit: mm) in (Noori and Rezaei, 2018), (c) fabricated band-pass filter in (Zakaria, et al., 2013), (d) fabricated BP-BP triplexer in (Xu and Zhu, 2017). BP-BP: Band-pass-band-pass.

TABLE II
A Comparison between Energy Harvester Microstrip Passive Devices

References	Type	F_o (GHz)	ILs (dB)	RLs (dB)	Size (λg^2)
(Yahya, et al., 2024)	LP-BP Triplexer	0.87, 1.33, 2.05	0.2, 0.09, 0.04	25.6, 19.4, 25.1	0.0038
(Yahya, et al., 2023)	Coupler	1.61	0.45, 0.75	19.76	0.014
(Alhalabi, et al., 2018)	Coupler	2.45	0.6, 0.8	70	---
(Shi, et al., 2016)	Coupler	1.87	1.4*	20	0.1386
(Majdi and Mezaal, 2023)	BP-BP Diplexer	2.84, 4.08	0.7, 0.9	21.2, 17	---
(Yahya, Rezaei and Nouri, 2021)	BP-BP Diplexer	1.4, 3	0.06, 0.07	28.6, 20	0.004
(Rezaei and Nouri, 2020)	BP-BP Diplexer	1, 1.3	0.21, 0.21	32, 25	0.018
(Majidifar and Hayati, 2017)	Lowpass Filter	1.76	0.42	11	0.0215
(Majidifar, 2016)	Lowpass Filter	1.71	0.1	18	0.02
(Khajavi, AL-Din Makki and Majidifar, 2015)	Dual-band BPF	2.45, 3.7	0.458, 0.672	23.57, 17.2	---
(Fadaee, et al., 2023)	Lowpass Filter	2.42	0.1	22	0.042
(Afzali, et al., 2021)	BPF	2.4	1.2	---	0.037
(Heng, et al., 2014)	Multiplexer	2.8, 2.809, 2.81,2.82	0.4, 0.3, 0.3, 0.4	19,19,19, 20	1.114
(Elden and Gorur, 2021)	LP-BP Diplexer	2, 3.5	0.3, 1.28	Better than 15	0.095
(Deng and Tsai, 2013)	LP-BP Diplexer	1.5, 2.4	0.25, 2.42	---	---
(Heshmati and Roshani, 2018)	LP-BP Diplexer	1, 2.4	0.25, 0.58	15, 30	0.046

*The maximum IL within -3dB passband. BPF: Band band-pass filter, LP-BP: low-pass to band-pass, BP-BP: Band-pass-band-pass

Both of them are designed by loading some patch stubs on a thin transmission line. Theses filters could suppress the harmonics well, whereas they have high selectivity (Fig. 7b and c). However, a filter design is easier than the diplexer design. (Fig. 6a) presents a layout configuration of a BP-BP diplexer with compact size. Its frequency response is illustrated in (Fig. 7d). As shown, this diplexer can select the desired frequencies better than the proposed design in (Majdi and Mezaal, 2023).

IV. Importance of Microstrip Passive Devices in 5G Networks and Energy Harvesting

Microstrip passive devices play a crucial role in enabling efficient energy harvesting and high-speed communication in 5G networks due to several key reasons:

1. Compact Size: Microstrip passive components are inherently compact and can be integrated into small form factors, making them ideal for energy harvesting systems and miniaturized 5G devices where space is limited.

2. Low Cost: Microstrip components are cost-effective to manufacture compared to other technologies, making them attractive for mass production of energy harvesting systems and 5G devices.
3. High Efficiency: Microstrip passive components, such as filters and couplers, can be designed with high efficiency, enabling optimal energy transfer and signal reception in energy harvesting systems and 5G networks.
4. Frequency Selectivity: Microstrip filters provide frequency selectivity, allowing for the isolation of specific frequency bands in 5G communication systems, which is essential for efficient spectrum utilization and interference mitigation.
5. Low Insertion Loss: Microstrip components can be designed with low insertion loss, minimizing signal attenuation in communication systems and maximizing energy conversion efficiency in energy harvesting applications.
6. Versatility: Microstrip technology offers flexibility in design and fabrication, allowing for the customization of passive components to meet the specific requirements of energy harvesting systems and 5G networks.
7. Integration: Microstrip passive components can be easily integrated with active components, such as amplifiers and transceivers, to create complete energy harvesting systems and 5G communication modules.

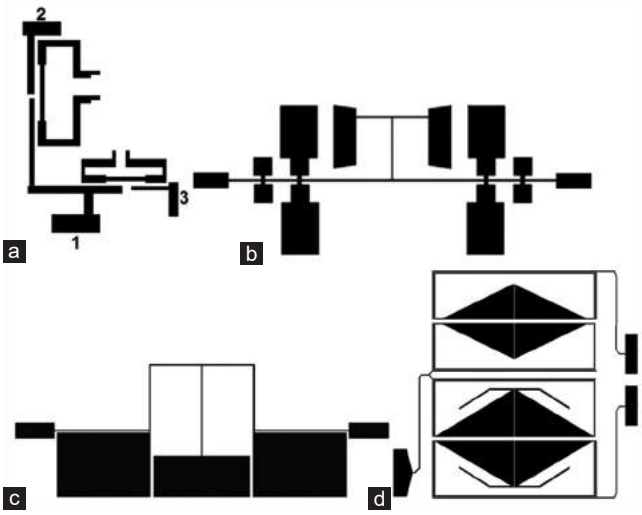

Fig. 6. Geometrical structures of the energy harvester microstrip (a) BP-BP diplexer in (Majdi and Mezaal, 2023), (b) lowpass filter in (Majidifar, 2016), (c) lowpass filter in (Fadaee, et al., 2023), (d) BP-BP diplexer in (Rezaei and Nouri, 2020). BP-BP: Band-pass-band-pass.

Overall, the importance of microstrip passive devices lies in their ability to provide efficient, cost-effective, and compact solutions for energy harvesting and high-speed communication applications in 5G networks. Their performance characteristics make them essential building blocks for enabling the next generation of wireless technologies.

Microstrip passive devices such as diplexers, triplexers, and multiplexers are essential components in modern communication systems. Diplexers are commonly used to combine or separate signals in two different frequency bands, allowing for efficient use of the available spectrum. Triplexers, on the other hand, can combine or separate signals in three different frequency bands. Multiplexers are used to combine multiple signals onto a single transmission line, enabling simultaneous transmission of different data streams. These components find wide applications in various communication systems, such as radar systems, satellite communication, wireless networks, and cellular base stations. They play a crucial role in managing signal interference,

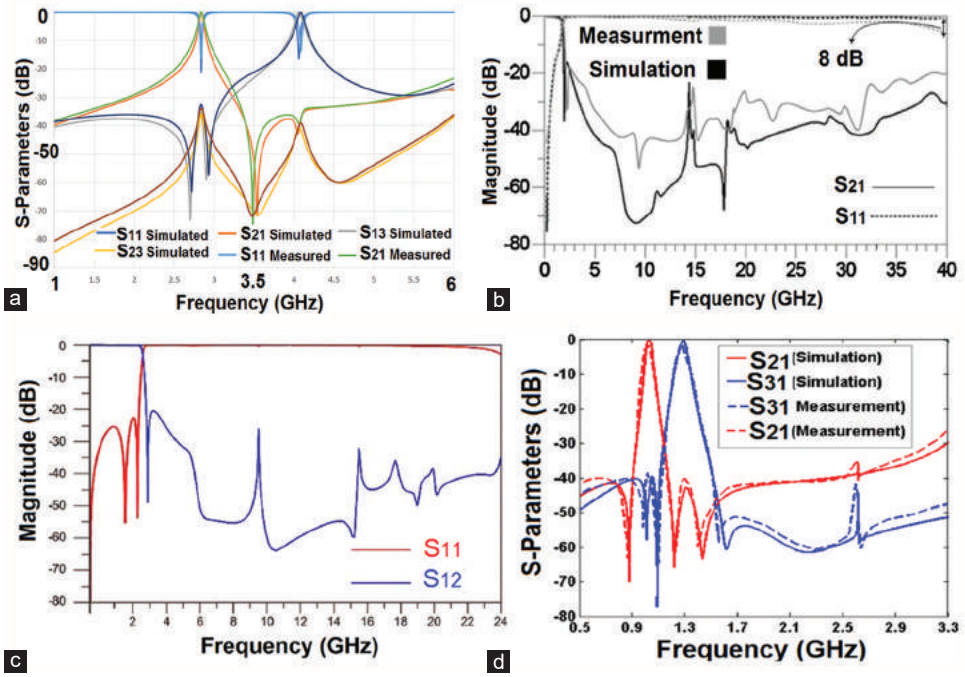

Fig. 7. Frequency responses of the energy harvester microstrip (a) BP-BP diplexer in (Majdi and Mezaal, 2023), (b) lowpass filter in (Majidifar, 2016), (c) lowpass filter in (Fadaee, et al., 2023), (d) BP-BP diplexer in (Rezaei and Nouri, 2020). BP-BP: Band-pass-band-pass.

improving system efficiency, and increasing bandwidth utilization. Using microstrip technology, these devices offer compact size, lightweight design, and cost-effective solutions for high-frequency applications.

V. Conclusion

This paper highlights the significance of microstrip passive components in enabling efficient energy harvesting and high-speed communication in 5G networks. The compact size, low cost, high efficiency, frequency selectivity, low insertion loss, versatility, and integration capabilities of microstrip devices make them essential building blocks for energy harvesting systems and 5G communication modules. By leveraging the unique characteristics of microstrip technology, researchers and engineers can develop innovative solutions that drive the advancement of wireless technologies, paving the way for a more connected and sustainable future.

References

Abouelnaga, T.G., and Mohra, A.S., 2017. Reconfigurable 3/6 dB Novel branch line coupler. *Open Journal of Antennas and Propagation*, 5, pp.7-22.

Afzali, B., Abbasi, H., Shama, F., and Heydari, R.D., 2021. A microstrip bandpass filter with deep rejection and low insertion loss for application at 2.4 GHz useful wireless frequency. *AEU-International Journal of Electronics and Communications*, 138, p.153811.

Alhalabi, H., Issa, H., Pistono, E., Kaddour, D., Podevin, F., Baheti, A., Abouchahine, S., and Ferrari, P., 2018. Miniaturized branch-line coupler based on slow-wave microstrip lines. *International Journal of Microwave and Wireless Technologies*, 10(10), pp.1103-1106.

Arriola, W.A., Lee, J.Y., and Kim, I.S., 2021. Wideband 3 dB branch line coupler based on λ/4 open circuited coupled lines. *IEEE Microwave and Wireless Components Letters,* 21(9), pp.486-488.

Bukuru, D., Song, K., and Xue., 2015. Compact wide-stopband planar diplexer based on rectangular dual spiral resonator. *Microwave and Optical Technology Letters*, 57(1), pp.174-178.

Capstick, M.H., 1994. Simple fast synthesis method for microstrip lowpass filters. *Electronics Letters*, 30(18), pp.1496-1497.

Capstick, M.H., 1999. Microstrip lowpass-bandpass diplexer topology. *Electronics Letters*, 35(22), pp.1958-1960.

Chen, C.F., Huang, T.Y., Chou, C.P., and Wu, R.B., 2006. Microstrip diplexers design with common resonator sections for compact size, but high isolation. *IEEE Transactions on Microwave Theory and Techniques*, 54(5), pp.1945-1952.

Chen, C.F., Tseng, B.H., Wang, G.Y., and Li, J.J., 2018. Compact microstrip eight-channel multiplexer with independently switchable passbands. *IET Microwave, Antennas and Propagation*, 12(6), pp.1026-1033.

Chen, C.F., Zhou, K.W., Chen, R.Y., Wang, Z.C., and He, Y.H., 2019. Design of a microstrip diplexer-integrated filtering power divider. *IEEE Access*, 7, pp.106514-106520.

Chen, D., Zhu, L., Bu, H., and Cheng, C.H., 2015. A novel planar diplexer using slot line-loaded microstrip ring resonator. *IEEE Microwave and Wireless Components Letters*, 25(11), pp.706-708.

Chen, F.C., Qiu, J.M., Hu, H.T., Chu, Q.X., and Lancaster, M.J., 2015. Design of microstrip lowpass-bandpass triplexer with high isolation. *IEEE Microwave and Wireless Components Letters*, 25(12), pp.805-807.

Chen, J.X., Zhan, Y., Qin, W., Bao, Z.H., and Xue, Q., 2015. Novel narrow-band balanced Bandpass filter using rectangular dielectric resonator. *IEEE Microwave and Wireless Components Letters*, 25(5), pp.289-291.

Chi, P.L., 2012. Miniaturized ring coupler with arbitrary power divisions based on the composite right/left-handed transmission lines. *Microwave and Wireless Component Letters*, 22(4), pp.170-172.

Chinig, A., Zbitou, J., Errkik, A., Elabdellaoui, L., Tajmouati, A., Tribak, A., and Latrach, M., 2015. A new microstrip diplexer using coupled stepped impedance resonators. *International Journal of Electronics and Communication Engineering*, 9(1), pp.41-44.

Chinig, A., Zbitou, J., Errkik, A., Tajmouati, A., Abdellaoui, L.E., and Latrach, M., 2015. Microstrip diplexer using stepped impedance resonators. *Wireless Personal Communications*, 84(4), pp.2537-2548.

Deng, P.H., and Tsai, J.T., 2013. Design of microstrip lowpass-bandpass diplexer. *IEEE Microwave and Wireless Components Letters*, 23(7), pp.332-334.

Elden, S., and Gorur, A.K., 2021. Design of a compact lowpass-bandpass diplexer with high isolation. *Progress in Electromagnetics Research Letters*, 97, pp.21-26.

Fadaee, M.D., Shama, F., Feali, M.S., and Gilan, M.S., 2023. A miniaturized wide stopband low-pass filter using T and modified L shapes resonators. *ARO-the Scientific Journal of Koya University*, 11, pp.116-120.

Feng, W., Gao, X., and Che, W., 2014. Microstrip diplexer for GSM and WLAN bands using common shorted stubs. *IET Electronics Letters*, 50(20), pp.1486-1488.

Feng, W., Zhang, Y., and Che, W., 2017. Tunable dual-band filter and diplexer based on folded open loop ring resonators. *IEEE Transactions on Circuits and Systems*, 64(9), pp.1047-1051.

Heng, Y., Guo, X., Cao, B., Wei, B., Zhang X., Zhang, G., and Song, X., 2014. A narrowband superconducting quadruplexer with high isolation. *IEEE Trans Applied Superconductivity*, 24(2), pp.21-26.

Heshmati, H., and Roshani, S., 2018. A miniaturized lowpass bandpass diplexer with high isolation. *AEÜ International Journal of Electronics and Communications*, 87, pp.87-94.

Hsu, K.W., Hung, W.C., and Tu, W.H., 2016. Design of four-channel diplexer using distributed coupling technique. *Microwave and Optical Technology Letters*, 58(1), pp.166-170.

Jamshidi, M., Yahya, S.I., Nouri, L., Dezaki, H.H., Rezaei, A., and Chaudhary, M.A., 2023. A super-efficient GSM triplexer for 5G-enabled IoT in sustainable smart grid edge computing and the metaverse. *Sensors*, 23(7), p.3775.

Jamshidi, M., Yahya, S.I., Nouri, L., Dezaki, H.H., Rezaei, A., and Chaudhary, M.A., 2023. A high-efficiency diplexer for sustainable 5G-enabled IOT in metaverse transportation system and smart grids. *Symmetry*, 15(4), p.821.

Khajavi, N., AL-Din Makki, S.V., and Majidifar, S., 2015. Design of high performance microstrip dual-band bandpass filter. *Radioengineering*, 24(1), pp.32-37.

Kim, C.S., Lim, J.S., Kim, D.Y., and Ahn, D., 2004. A design of single and multi-section microstrip directional coupler with the high directivity. *IEEE MTT-S International Microwave Symposium Digest*, 3, pp.895-1898.

Kim, J.S., and Kong, K.B., 2010. Compact branch-line coupler for harmonic suppression. *Progress in Electromagnetics Research,* 16, pp.233-239.

Lai, C.H., and Ma T.G., 2013. Miniaturised rat-race coupler with second and third harmonic suppression using synthesised transmission lines. *Electronics Letters,* 49(22), pp.1394-1396.

Li, J.L., Qu, S.W., and Xue, Q., 2007. Microstrip directional coupler with flat coupling and high isolation. *Electronics Letters*, 43(4), pp.228-229.

Liou, C.Y., Wu, M.S., Yeh, J.C., Chueh, Y.Z., and Mao, S.G., 2009. A novel triple-band microstrip branch-line coupler with arbitrary operating frequencies. *IEEE Microwave and Wireless Components Letters*, 19(11), pp.683-685.

Majdi, K.A., and Mezaal, Y.S., 2023. New miniature narrow band microstrip diplexer for recent wireless communications. *Electronics*, 12, p.716.

Majidifar, S., 2016. High performance microstrip LPFs using dual taper loaded resonator. *Optik*, 127(6), pp.3484-3488.

Majidifar, S., and Hayati, M., 2017. Design of a sharp response microstrip lowpass filter using taper loaded and radial stub resonators. *Turkish Journal of Electrical Engineering and Computer Sciences*, 5, pp.4013-4022.

Noori, L., and Rezaei, A., 2017. Design of microstrip wide stopband quad-band bandpass filters for multi-service communication systems. *AEU-International Journal of Electronics and Communications*, 81, pp.136-142.

Noori, L., and Rezaei, A., 2018. Design of a compact narrowband quad-channel diplexer for multi-channel long-range RF communication systems. *Analog Integrated Circuits and Signal Processing*, 94(1), pp.1-8.

Nouri, L., Nkenyereye, L., Hafez, M.A., Hazzazi, F., Chaudhary, M.A., and Assaad, M., 2024. A simplified and efficient approach for designing microstrip bandpass filters: Applications in satellite and 5G communications. *AEU-International Journal of Electronics and Communications*, 177, p.155189.

Nouri, L., Yahya, S.I., and Rezaei, A., 2020. Design and fabrication of a low-loss microstrip lowpass-bandpass diplexer for WiMAX applications. *China Communications*, 17(6), pp.109-120.

Nouri, L., Yahya, S.I., Rezaei, A., Chaudhary, M.A., and Nhu, B.N., 2023. A novel configuration of microstrip coupler with low loss and suppressed harmonics. *AEU-International Journal of Electronics and Communications*, 165, p.154653.

Nouri, L., Yahya, S.I., Rezaei, A., Hazzazi, F., Chaudhary, M.A., Assaad, M., and Nhu, B.N., 2023. Microstrip lowpass-bandpass triplexer with flat channels and low insertion losses: Design and fabrication for multi-service wireless communication systems. *AEU-International Journal of Electronics and Communications*, 170, p.154807.

Nouri, L., Yahya, S.I., Rezaei, A., Hazzazi, F.A., and Nhu, B.N., 2023. A compact negative group delay microstrip diplexer with low losses for 5G applications. *ARO-The Scientific Journal of Koya University*, 11(2), pp.17-24.

Nouri, L., Zubir, F., Nkenyereye, L., Rezaei, A., Hafez, M.A., Hazzazi, F., Chaudhary, M.A., Assaad, M., and Yusoff, Z., 2024. Novel ultra-compact wide stopband microstrip lowpass-bandpass triplexer for 5G multi-service wireless networks. *IEEE Access*, 12, pp.2926-2940.

Nouri, L., Zubir, F., Yahya, S.I., Rezaei, A., Hazzazi, F., Chaudhary, M.A., Assaad, M., Yusoff, Z., and Le, B.N., 2023. A high-performance microstrip triplexer with compact size, flat channels and low losses for 5G applications. *IEEE Access*, 11, pp.78768-78777.

Rezaei, A., and Noori, L. 2020. Miniaturized microstrip diplexer with high performance using a novel structure for wireless L-band applications. *Wireless Networks*, 26, pp.1795-1802.

Rezaei, A., and Noori, L., 2018. Compact low-loss microstrip diplexer using novel engraved semi-patch cells for GSM and WLAN applications. *AEU-International Journal of Electronics and Communications*, 87, pp.158-163.

Rezaei, A., and Noori, L., 2018. Microstrip hybrid coupler with a wide stop-band using symmetric structure for wireless applications. *Journal of Microwaves, Optoelectronics and Electromagnetic Applications*, 17, pp.23-31.

Rezaei, A., and Noori, L., 2018. Novel low-loss microstrip triplexer using coupled lines and step impedance cells for 4G and WiMAX applications. *Turkish Journal of Electrical Engineering and Computer Sciences*, 26(4), pp.1871-1880.

Rezaei, A., and Noori, L., 2018. Novel microstrip quadruplexer with wide stopband for WiMAX applications. *Microwave and Optical Technology Letters*, 60(6), pp.1491-1495.

Rezaei, A., Noori, L., and Mohammadi, H., 2019. Design of a miniaturized microstrip diplexer using coupled lines and spiral structures for wireless and WiMAX applications. *Analog Integrated Circuits and Signal Processing*, 98, pp.409-415.

Rezaei, A., Yahya, S.I., and Nouri, L., 2023. A high-performance microstrip bandpass filtering coupler with low-loss and compact size. *Microwave and Optical Technology Letters*, 65(9), pp.2483-2487.

Rezaei, A., Yahya, S.I., and Nouri, L., 2023. Design and analysis of a compact microstrip lowpass–bandpass diplexer with good performance for wireless applications. *International Journal of Microwave and Wireless Technologies*, 15(7), pp.1099-1107.

Rezaei, A., Yahya, S.I., and Nouri, L., 2024. An ultra-compact diplexer based on simple microstrip coupled lines for GSM and wideband wireless applications. *Wireless Networks*, 30(2), pp.857-865.

Rezaei, A., Yahya, S.I., Noori, L., and Jamaluddin, M.H., 2022. Designing high-performance microstrip quad-band bandpass filters (for multi-service communication systems): A novel method based on artificial neural networks. *Neural Computing and Applications*, 34(10), pp.7507-7521.

Salehi, M., and Noori, L., 2015. Miniaturized microstrip bandpass filters using novel stub loaded resonator. *Applied Computational Electromagnetics Society Journal*, 30(6), pp.692-697.

Salehi, M.R., and Noori, L., 2014. Novel 2.4 Ghz branch-line coupler using microstrip cells. *Microwave and Optical Technology Letters*, 56(9), pp.2110-2113.

Salehi, M.R., Keyvan, S., Abiri, E., and Noori, L., 2016. Compact microstrip diplexer using new design of triangular open loop resonator for 4G wireless communication systems. *AEU International Journal of Electronics and Communications*, 70(7), pp.961-969.

Salehi, M.R., Noori, L., and Abiri, E., 2016. Prediction of matching condition for a microstrip subsystem using artificial neural network and adaptive neuro-fuzzy inference system. *International Journal of Electronics*, 103(11), pp.1882-1893.

Shi, J., Qiang, J., Xu, K., Wang, Z.B., Lin, L., Chen, J.X., Liu, W., and Zhang, X.Y., 2016. A balanced filtering branch-line coupler. *IEEE Microwave and Wireless Components Letters*, 26(2), pp.119-121.

Shukor, N.A.M., and Seman, N., 2016. Enhanced design of two-section microstrip-slot branch line coupler with the overlapped λ/4 open circuited lines at ports. *Wireless Personal Communications*, 88, pp.467-478.

Shukor, N.A.M., and Seman, N., 2020. 5G planar branch line coupler design based on the analysis of dielectric constant, loss tangent and quality factor at high frequency. *Scientific Reports*, 10, p.16115.

Xu, J., and Zhu, Y., 2017. Microstrip triplexer and switchable triplexer using new impedance matching circuits. *International Journal of RF and Microwave Computer-Aided Engineering*, 27, p.e21057.

Xu, J., Chen, Z.Y., and Wan, H., 2020. Lowpass-bandpass triplexer integrated switch design using common lumped-element triple-resonance resonator technique. *IEEE Transactions on Industrial Electronics*, 67(1), pp.471-479.

Yahya, S.I., Rezaei, A., and Nouri, L., 2021. The use of artificial neural network to design and fabricate one of the most compact microstrip diplexers for broadband L-band and S-band wireless applications. *Wireless Networks*, 27, pp.663-676.

Yahya, S.I., Zubir, F., Nkenyereye, L., Hafez, M.A., Nouri, L., Assaad, M., Chaudhary, M.A., and Jizat, N.M., 2024. A lowpass-bandpass triplexer with a new microstrip configuration and compact size for 5G and energy harvesting applications. *IEEE Access*, 12, pp.60264-60275.

Yahya, S.I., Zubir, F., Nouri, L., Hazzazi, F., Yusoff, Z., Chaudhary, M.A., Assaad, M., Rezaei, A., and Le, B.N., 2023. A balanced symmetrical branch-line microstrip coupler for 5G applications. *Symmetry*, 15(8), p.1598.

Yahya, S.I., Zubir, F., Nouri, L., Yusoff, Z., Chaudhary, M.A., Assaad, M., Rezaei, A., and Le, B.N., 2023. A new compact and low phase imbalance

microstrip coupler for 5G wireless communication systems. *PLoS One*, 18(12), p.e0296272.

Yahya, S.I., Zubir, F., Nouri, L., Yusoff, Z., Hazzazi, F., Chaudhary, M.A., Assaad, M., Rezaei, A., and Le, B.N., 2023. Design and optimization of a compact microstrip filtering coupler with low losses and improved group delay for high-performance RF communication systems. *IEEE Access*, 11, pp.103976-103985.

Zakaria, Z., Mutalib, M.A., Isa, M.S.M., Zainuddin, N.A., Yik, S.W., and Othman, A., 2013. Design of microstrip bandpass filter with defected microstrip structure (DMS). *Australian Journal of Basic and Applied Sciences*, 7(11), pp.263-269.

Zeng, S.J., Wu, J.Y., and Tu, W.H., 2011. Compact and high-isolation quadruplexer using distributed coupling technique. *IEEE Microwave and Wireless Component Letters,* 21(4), pp.197-199.

Zhu, C., Xu, J., Kang, W., and Wu, W., 2017. Design of balun-integrated switchable low-pass-bandpass triplexer. *IEEE Microwave and Wireless Components Letters*, 27(4), pp.353-355.

 http://dx.doi.org/10.14500/aro.11618

Encryption of Color Images with a New Framework: Implementation Using Elzaki Transformation

Mardan A. Pirdawood[1*], Shadman R. Kareem[1,2] and Omar Al-Rassam[1]

[1]Department of Mathematics, Faculty of Science and Health, Koya University, Danielle Mitterrand Boulevard, Koya KOY45, Kurdistan Region – F.R. Iraq

[2]Department of Computer Science, College of Information Technology and Computer Sciences, Catholic University in Erbil, Kurdistan Region – F.R. Iraq

***Abstract*— The significance of image encryption has risen due to the widespread use of images as a key means of sharing data across different applications. Encryption methods are crucial in defending the confidentiality and integrity of valuable image data. This work proposes a novel method of image encryption technique based on the Elzaki transformation and substitution process, which is made possible by the extension of the Maclaurin series coefficients. The image is encrypted using an infinite series of hyperbolic functions and the Elzaki transform; the inverse Elzaki transform is then used to decrypt the image. Using modular arithmetic, the coefficients that result from the transformation are keyed.**

***Index Terms*—Cryptography, Elzaki Transformations, Image Encryptions, Maclaurin Series**.

I. Introduction

The widespread use of image data in various multimedia applications highlights the crucial need to secure such data for communication and storage purposes. In the realm of protecting private information, image encryption emerges as an effective technique, with several methods proposed for communication purposes (Yang and Wang, 2021; Kaur and Jindal, 2019; Sui, Duan and Liang, 2015). Image encryption presents notable differences compared to text encryption, due to several important factors, including the large amount of data that images contain and the intricate correlations between pixel values. This complexity arises from the multidimensional character of images, where each pixel contributes to the overall composition and visual content. Unlike text, which is typically represented as a linear sequence of characters, images contain rich spatial and color information, requiring encryption methods that can effectively preserve these attributes while ensuring security. Thus, image encryption methods must navigate the intricacies of image representation and processing, making them distinct from traditional text-based encryption approaches. Traditional encryption methods such as advanced encryption standard (AES), data encryption standard (DES), and Rivest-Shamir-Adleman (RSA) are considered inappropriate for image encryption due to their higher processing time requirements. In recent work, non-standard encryption techniques have mostly been used to encrypt digital media to improve both speed and security requirements. These unconventional methods employ techniques for changing and rearranging (substitution and permutation). The image encryption algorithm described combines several techniques to enhance security and reduce confusion in the encryption process. Based on the algorithm of complete shuffling and the transformation of a substitution box, this proposed algorithm presents extra confusion (Hamad and Farhan, 2020).

To achieve crucial encryption characteristics, namely, confusion and diffusion, image encryption algorithms manipulate the pixel values of the image. Confusion refers to the complex and nonlinear transformation of pixel values, making it challenging for adversaries to discern any patterns or relationships within the encrypted image. This ensures that even small changes in the input image result in significant alterations in the encrypted output. Derived from the wavelet transform (Wei and Liu, 2023; An and Liu, 2019), chaos theory (Elshamy, et al., 2019; Liu, Sun and Zhu, 2016), and discrete cosine transform (DCT) (Wang, Liu and Jiang, 2021; Liang and Xiao, 2020). These investigations have significantly enriched the literature in the field, showcasing the wide array of approaches adopted to secure digital images. A novel strategy grounded in multi-chaotic theory is put forth. To create an effective encryption that is challenging to crack, the study also employed two distinct dimensions to build S-box. Process using a single keystream generator, shift process (based on 3D Lorenz map) related diffusion operations, and produce S-box (based on 2D Henon map) related confusion operations (Nasry, et al., 2022, August.)

ARO-The Scientific Journal of Koya University
Vol. XII, No. 1 (2024), Article ID: ARO.11618. 11 pages
Doi: 10.14500/aro.11618
Received: 04 October 2023; Accepted: 16 May 2024
Regular research paper: Published: 14 June 2024
Corresponding author's e-mail: mardan.ameen@koyauniversity.org

Amitava Nag, et al. introduced an innovative encryption approach centered on location transformation. Their strategy involved employing the method of the affine transform and utilizing four 8-bit keys for dispersing pixel data across the entire image. Subsequently, the image was divided into 2 × 2-pixel chunks, with each block being encrypted using the XOR algorithm and the four 8-bit keys (Nag, et al., 2011, July; Priya, et al.). Another study introduced a groundbreaking methodology for the encryption and decryption of color images, wherein the researchers presented an innovative solution based on the "SEE transform." The study extensively delved into encryption technology, offering comprehensive insights into the proposed approach (Kuffi, Mehdi and Mansour, 2022, August).

Integrating various cryptographic techniques has become pivotal in enhancing the robustness and versatility of security measures. The amalgamation of multiple methodologies in cryptography aims to address the evolving challenges posed by diverse data types and security requirements (Hamad and Farhan, 2020). Noteworthy among these integrated approaches is the fusion of symmetric and asymmetric encryption algorithms, leveraging the strengths of both for heightened security.

The fusion of various methodologies enables the creation of enhanced security modules that address security concerns and yield more dependable outcomes in image processing. This amalgamation of techniques is exemplified in Al-Khazraji, Abbas and Jamil (2022), wherein they introduced an innovative model amalgamating deep dreaming with neural style transfer (NST). In their research, the authors constructed a model that merges deep dreaming and NST to generate novel images. The utilization of VGG-19 and Inception-v3 pre-trained networks was employed for NST and deep dream, respectively. The study revealed that varying images result in distinct loss values, contingent on the clarity levels inherent in each of those images. Subsequent to this development, numerous alternative methodologies for image encryption have been proposed through the integration of diverse techniques. Manisekaran, the proponent, advocates for the adoption of an innovative methodology wherein enhancements are made to both the key space and the encryption process. The encryption process involves subjecting the DCT of the image to encryption through a generalized logistic equation. This innovative approach facilitates simultaneous compression and encryption. Before the application of the DCT, an Arnold cat map is employed to shuffle the image. The efficacy of the proposed compression and encryption method is substantiated through the examination of various chaotic metrics, including bifurcation diagrams and mutual information (Pradheep, 2021).

The Elzaki transformation, a mathematical technique known for its efficacy in cryptographic applications, was strategically applied to transform the information into a secure format, rendering it less susceptible to unauthorized access. Concurrently, the congruence modulo operator played a pivotal role in preserving the integrity of the encrypted information during the encryption and decryption processes. The researchers employed the Elzaki transformation in conjunction with the congruence modulo operator to ensure the security and subsequent decipherment of a concealed piece of information (Salim and Ashruji, 2016). Furthermore, the Laplace integral transforms and their inverses represent pivotal counterparts within the domain of cryptographic techniques, having a critical impact on the security and functionality of cryptographic processes. Laplace integral transforms application in cryptography and underscores the utilization of advanced mathematical methods to enhance data security (Shivaji and Hiwarekar, 2021), for instance. This study examines the prerequisites for developing an encryption method based on the Laplace transform. In addition, it explores strategies aimed at fortifying the identified vulnerabilities inherent in said cryptographic process. A proposed modification to the initial step of the encryption scheme is presented, resulting in the generation of two distinct passwords for a singular iteration. This modification serves the dual purpose of enhancing the overall security of the encryption process while addressing potential sources of weakness. The amalgamation of diverse techniques yields the capacity to formulate additional security modules within the domain of security. Concurrently, such integration enhances the dependability of outcomes in the context of image processing, particularly concerning security considerations. This multifaceted approach to security not only broadens the repertoire of available protective measures but also ensures a heightened level of reliability in addressing security concerns, specifically in the realm of image processing applications. In Pirdawood, Kareem and Zahir (2023), the researchers articulate a novel encryption methodology tailored for real-time audio applications. The encryption process involves the application of hyperbolic functions and the Laplace transform to secure the audio data. Subsequently, the decryption of the encrypted sound is executed through the inverse Laplace transformation process (Wang et al., 2015). Key generation, crucial for the establishment of a set of coefficients derived from the transformation, is systematically conducted by employing a modular arithmetic rule. The other transformation to encrypt the audio was introduced. Farsana, Devi and Gopakumar (2023) introduce an audio encryption algorithm predicated on the permutation of audio samples, achieved through the utilization of a discrete modified Henon map, followed by a substitution operation employing a key stream generated from the modified Lorenz-hyperchaotic system. The methodology commences with the application of the fast Walsh–Hadamard transform to compress the initial audio file, thereby eliminating residual intelligibility in the transformed domain. Subsequently, the encrypted file undergoes a two-phase encryption process.

In this research, we developed a novel mathematical transformation for cryptography that involves the integration of hyperbolic functions, specifically, the Elzaki transform, for encrypting digital image data and its corresponding inverse Elzaki transforms for decryption purposes. The transformation, defined over a finite field, is recursively applied to blocks of samples extracted from a non-compressed digital image input, with the secret key determining the number of iterations of the transformation

 http://dx.doi.org/10.14500/aro.11618

applied to each block. Confusion is achieved through the manipulation of power series coefficients. The approach that we have chosen has been previously utilized across various disciplines by numerous researchers. For instance, Elzaki (2011) innovatively employed power series transformations in a creative way to encrypt a certain text in cryptography. This was achieved through the utilization of the extended Elzaki transform of an exponential function. The construction of the key involved applying the principles of modular arithmetic to the transformation coefficients. Furthermore, we utilize this technique to encrypt digital picture data by combining the Elzaki transformation, which is applied to the Maclaurin series coefficients, with the Maclaurin series of the cosine hyperbolic transform.

II. The Elzaki Transform

The Elzaki transforms, introduced by Elzaki in 2011, have garnered considerable prominence in both the applied mathematics and engineering domains. This transformative mathematical tool has found widespread utility, demonstrating its efficacy in various applications. Its introduction has significantly influenced the resolution of mathematical problems and engineering challenges.

The application of the Elzaki transforms in digital image processing extends its reach beyond its origins in applied mathematics and engineering. In the realm of digital image processing, the Elzaki transform emerges as a valuable mathematical tool with the potential to contribute to various aspects of image analysis and manipulation. In digital image processing, the Elzaki transform's adaptability and unique characteristics make it an intriguing choice for certain applications; see the reference (Elzaki, 2011). The designated functions within set A are contemplated as follows.

$$A=\left\{f(t):\exists M,k_1,k_2>0,\left|f(t)\right|<Me^{\frac{|t|}{k_j}},\text{if } t\in(-1)^j\times[0,\infty)\right\}$$

For a specific function within the set, M should be a finite value, whereas k_1 and k_2 could be either finite or infinite. The Elzaki transformation can be expressed as follows:

$$E[f(t)]=T(s)=s\int_0^{\infty}f(t)e^{\frac{-t}{s}}dt,\ k_1\le s\le k_2,t\ge 0 \tag{1}$$

The Elzaki transformation exhibits linearity, meaning that it follows the principles of a linear transformation, that is,

$$E\{f_1(t)\}=F_1(s),E\{f_2(t)\}=F_2(s),\ldots,E\{f_n(t)\}=F_n(s),$$

if then

$$E\{c_1f_1(t)+c_2f_2(t)+\ldots+c_nf_n(t)\}=c_1F_1(s)+c_2F_2(s)+\ldots+c_nF_n(s), \tag{2}$$

Where $c_1,c_2,\ldots,c_n$ represent constant values (Elzaki, 2011). Below are the descriptions of the Elzaki transformation and the inverse Elzaki transform for several elementary functions:

- $E(a)=au^2$ where a is constant,
- $E(t^n)=n!s^{n+2}$,
- $E^{-1}(s^2)=1$,
  $E^{-1}(s^{n+2})=t^n/n!$.

III. Proposed Method

The following steps outline the application procedures that enhance data security and privacy in the proposed hybrid mode Elzaki transformation through the integration of cryptography and encryption technology. The encryption of the color image is accomplished through the utilization of the Elzaki transform, while the corresponding inverse Elzaki transform is employed for the decryption process.

A. Encryption

The encryption procedure is delineated into three distinct phases, each integral to the overarching process. These phases include

(i) Key Generation

The initial phase of the encryption process involves the generation of cryptographic keys. These keys play a pivotal role in ensuring the security and confidentiality of the data.

(ii) Color Change

The subsequent phase introduces a transformative step known as color alteration. This facet of the encryption process focuses on modifying the color attributes of the data, contributing to obfuscation, and adding a layer of security to the encrypted information.

(iii) Maclaurin Series Application (t cosh t)

The final phase incorporates the utilization of the Maclaurin series, specifically pertaining to t cosh t. This mathematical series is invoked as a crucial component in the encryption algorithm, contributing to the intricate transformation of the data. The Maclaurin series expansion involving hyperbolic cosine functions is employed to achieve a nuanced and effective encryption strategy.

The Maclaurin series expansion of t cosh t is mathematically expressed as:

$$t\cosh t=\sum_{i=0}^{\infty}\frac{t^{2i+1}}{2i!} \tag{3}$$

It intended for encryption as input to conduct simulation studies. The implementation of this proposed approach was realized through the utilization of MATLAB. In this phase, the dynamic original image undergoes a transformative process, resulting in an encrypted image. Notably, within the Maclaurin series of t cosh t stage, pixel values undergo simultaneous alterations, whereas the color modification is facilitated through the application of the Elzaki transform.

Step 1: Choose the color plain image P (M,N,3), where M×N is the size of the RGB components of the plain image.

Step 2: Make the entries P_{ij} of the matrix P for the RGB components as the coefficients of the Maclaurin series of t

cosh t as follows:

$$\text{Pt}\cosh t = \sum_{j=0}^{\infty} \frac{P_{ij}}{2j!} t^{2j+1}, \text{ where i=1,2,…M and } P_{ij}=0, \text{ for j > N} \quad (4)$$

Step 3: Utilizing the Elzaki transformation for Equation (4), we derive the transformed expression, as follows:

$$E\left[\sum_{j=0}^{\infty} \frac{P_{ij}}{2j!} t^{2j+1}\right] = s\int_0^{\infty}\sum_{j=0}^{\infty} \frac{P_{ij}}{2j!} t^{2j+1} e^{\frac{-t}{s}} dt = \sum_{i=0}^{\infty} P_{ij}(2j+1)s^{2j+3}$$

$$= \sum_{i=0}^{\infty} q_{ij} s^{2j+3} \quad (5)$$

Where $q_{ij}=P_{ij}(2j+1)$, for i=0,1,2,…,N, and j=1,2,…,N.

Step 4: Find C_{ij} such that $q_{ij} \cong C_{ij}$ mod 256, for i=0,1,2,…,N, and j=1,2,…,N, for all of the three RGB-image components. Thus, the RGB-encoded image C become "M×N×3".

Note that, the plain image P(M,N,3) in terms of i and j, for i=0,1,2,…M and j=1,2,…,N under the Elzaki transform of Pt cosh t can be converted to cipher image C, where the components of this matrix are given by

$$C_{ij} = q_{ij} - 256K_{ij} \quad (6)$$

and

$$q_{ij} = (2j+1)P_{ij} \quad (7)$$

with key

$$K_{ij} = \frac{q_{ij} - C_{ij}}{256} \quad (8)$$

Consequently, the key matrix will assume dimensions of K(M,N,3). To illustrate, Fig. 1 presents a visual representation of the key within the histogram diagram during the RGB encryption process applied to the Lena image.

A. Decryption Algorithm

The decryption process serves as the inverse operation to encryption. During decryption, the input is the RGB-encrypted image represented as a Vector C, as depicted in Fig. 2 for illustrative purposes. The secret key, denoted as K(M,N,3) in accordance with Equation (8), is employed in this process, ultimately resulting in the generation of the decrypted image. The ensuing decryption procedure encompasses a series of sequential steps aimed at reconstructing the original image from its encrypted form.

Step 1: Choose the RGB-encrypted image C(M,N,3), where M×N is the size of the RGB components of the RGB-encrypted image.

Step 2: Find q_{ij} such that $q_{ij} \cong C_{ij}$ mod 256 for i=0,1,2,…,M and j=1,2,…,N, for all of the three components of the RGB-image. Then, make it as the coefficient of the follow series:

$$T(s) = \sum_{i=0}^{\infty} q_{ij} s^{2j+3} \quad (9)$$

Step 3: Utilizing the Elzaki inverse transformation for Equation (9), we derive the transformed expression, as follows:

$$E^{-1}\left[\sum_{i=0}^{\infty} q_{ij} s^{2j+3}\right] = E^{-1}\left[\sum_{i=0}^{\infty} P_{ij}(2j+1)s^{2j+3}\right] = \sum_{j=0}^{\infty} \frac{P_{ij}}{2j!} t^{2j+1}$$

$$= \text{Pt}\cosh t \quad (10)$$

where $P_{ij} = \frac{q_{ij}}{(2j+1)}$, for i=0,1,2,…,M and j=1,2,…,N

Step 4: The matrix P(M,N,3) become the RGB-decrypted image.

IV. Results and Simulation Analysis

A comprehensive assessment was conducted on a multitude of color images, and the outcomes demonstrated uniform consistency. Specifically, images featuring Lena, Baboon, and Sailboat on Lake, sourced from the USC-SIPI image database (Weber, 2006), as well as Lya, were considered as original experimental photographs for simulation purposes. The proposed RGB photo encryption technique incorporates the application of the Elzaki transformation, employing the following key components:

- Red component only (R-Encryption),
- Green component only (G-Encryption),
- Blue component only (B-Encryption),
- The concurrent integration of both elements is associated with the red and green components (RG-Encryption),
- The concurrent integration of both elements is associated with the red and blue components (RB-Encryption),
- The concurrent integration of both elements is associated with the green and blue components (GB-Encryption),
- All the red, green, and blue components together (RGB-Encryption).

As depicted in Fig. 1, our experimental results based on

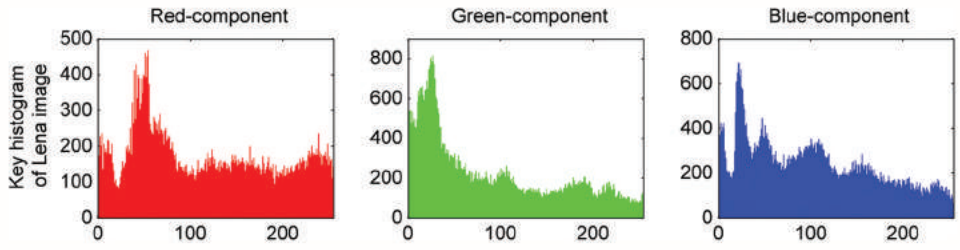

Fig. 1. The histogram embodies the key matrix *K* (*M*, *N*, 3) for the Lena image.

http://dx.doi.org/10.14500/aro.11618

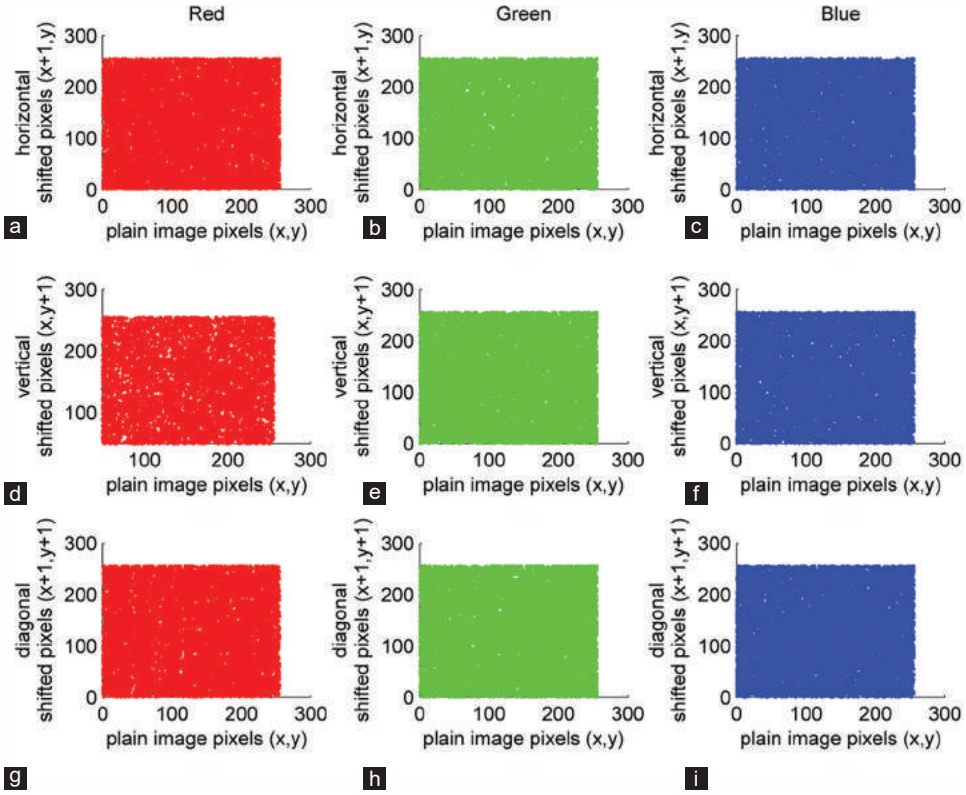

Fig. 2. Correlation analysis was conducted on the RGB-encrypted image of Lena, involving the examination of horizontally, vertically, and diagonally correlated pixels. The analysis specifically centered on three components of the RGB-encrypted image, denoted as the red, green, and blue components (a, d, g), (b, e, h), and (c, f, i), respectively.

the proposed approach are showcased using the reference image, denoted as "Lena 256 × 256 × 3," serves as the unaltered basis and is visually represented in Fig. 3 in the RGB format. The proposed methodology is to be executed using MATLAB R2016a. The implementation transpired on an individual computing system, featuring an Intel(R) Core(TM) i5-1135G7 central processing unit operating at a clock speed of 2.42 GHz. The computational unit is equipped with a capacious 1 TB hard disk drive for storage and a substantial 8 GB of RAM to facilitate efficient memory operations. The operating environment for this implementation was Windows 11 Pro.

A. Statistical Analysis

Numerous statistical evaluations on the generated procedures are carried out to assess the dependability of the suggested encryption cryptosystem. To determine the efficacy and resilience of the encryption technique, we offer comprehensive insights into the findings of these investigations in this part. In addition, the statistical studies explore the analysis of encryption outputs, including pixel value distributions, correlation coefficients, and error metrics like peak signal-to-noise ratio (PSNR) and mean squared error (MSE). These evaluations give important insights into the integrity and dependability of the encrypted data, as well as useful details on how to maintain image security and quality throughout the encryption and decryption procedures.

Histogram analysis

The representation of pixel intensity levels within an image is effectively captured by a histogram, a significant metric that could be exploited by malicious entities to devise potential attacks, particularly if they possess knowledge about pixel frequency patterns across different intensity levels. In the context of encrypted images, it becomes imperative to guarantee that the histograms of these images do not reveal any information derived from the statistical analysis of the original image pixels. The scrutiny of histogram distribution is exemplified in Fig. 3. Specifically, Fig. 3 presents the histograms corresponding to the red, green, and blue components of the unencrypted Lena image, respectively. This examination underscores the importance of mitigating any potential leakage of information through the careful handling of histograms during the encryption process.

The histograms corresponding to the encrypted portions of the image are illustrated in Fig. 3. It is evident that the encrypted image histograms do not reveal any insights into the distribution of intensity levels found in the original image. Nonetheless, prior research underscores that the histogram derived from the fractional domain tends to be constrained to a narrow range of pixel values due to the concentration of transform energy at the center. To mitigate this concern and guarantee a more equitable distribution of energy within the cryptographic framework, achieving a flat or uniform histogram becomes of paramount importance. As depicted in Fig. 3, the histograms of the encrypted image demonstrate a

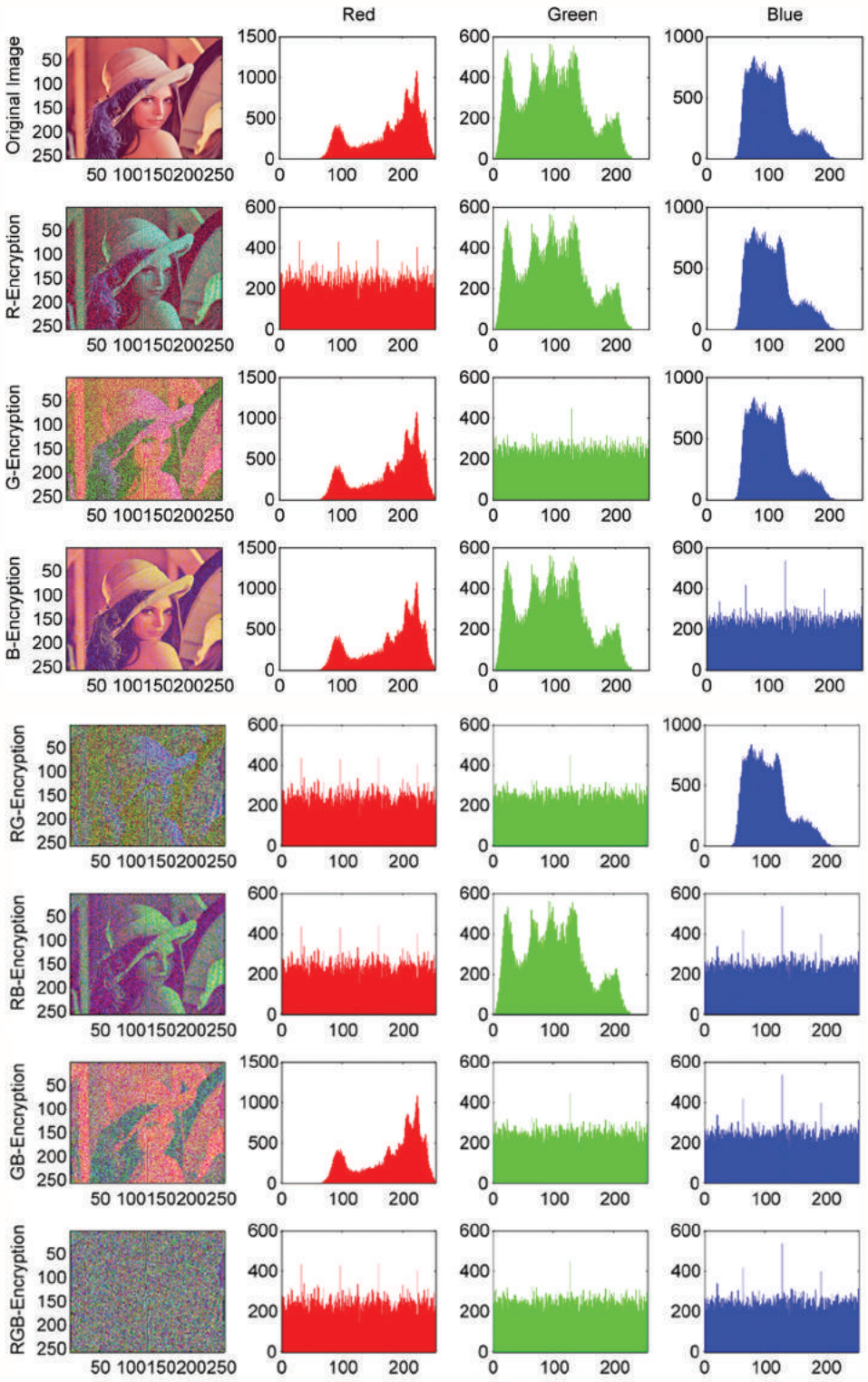

Fig. 3. The observed distribution of correlations distinctly underscores a noteworthy separation among pixel values in the encrypted image, emphasizing the successful accomplishment of decorrelation.

markedly flatter and more uniform pattern when juxtaposed with methodologies documented in recent studies. This observation emphasizes the effectiveness of the proposed approach in attaining a desirable histogram characteristic, contributing to enhanced security in the cryptographic context (Kang, et al., 2017, September; Lang, 2012; Sui, Duan and Liang, 2015; Wu, et al., 2014).

Correlation coefficient analysis

An effective encryption method should have the ability to disrupt the connection between neighboring pixels. The relationship between adjacent pixels in an encrypted image should be minimized. Thus, ensuring the uniform distribution of pixel values across the entire intensity spectrum in both dimensions becomes a crucial factor

http://dx.doi.org/10.14500/aro.11618

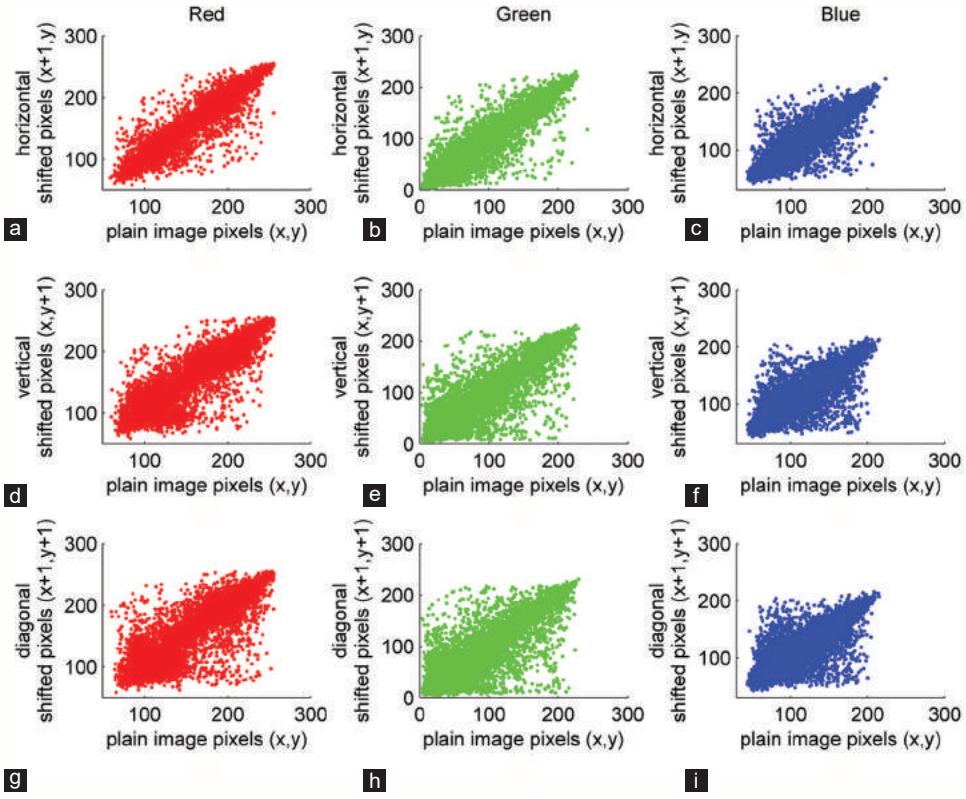

Fig. 4. Correlation analysis was performed on the Lena image, investigating the horizontal, vertical, and diagonal correlations among pixels. The analysis specifically concentrated on the three components of the RGB-original image: The red, green, and blue components denoted as (a, d, g), (b, e, h), and (c, f, i), respectively.

for encrypted image integrity. The distributions of these values have been visually represented in Fig. 4, using the Lena image as an illustrative example. Our analysis predominantly focuses on the individual components of red, green, and blue, delving into the pixel distributions of neighboring elements. The initial column of Fig. 4 showcases the distributions of diagonally, vertically, and horizontally adjacent pixels within the unencrypted source image. In the subsequent column, we present the corresponding correlation patterns for the encrypted image, followed by a third column depicting the same for the decrypted version.

The observed distribution of correlations distinctly underscores a noteworthy separation among pixel values in the encrypted image, emphasizing the successful accomplishment of decorrelation. For a more quantitative evaluation, we calculated correlation coefficients for diverse test images, and the specific outcomes are detailed in Table I.

The calculation of the correlation coefficient will be performed as follow:

$$\rho(x,y)=\frac{cov(x,y)}{\sqrt{D(x)}\sqrt{D(y)}} \tag{11}$$

$$cov(x,y)=\frac{1}{N}\sum_{i=1}^{N}\left((x_i-\bar{x})(y_i-\bar{y})\right),$$

$$D(x)=\frac{1}{N}\sum_{i=1}^{N}(x_i-\bar{x})^2,\ D(y)=\frac{1}{N}\sum_{i=1}^{N}(y_i-\bar{y})^2,$$

$$\bar{x}=\frac{1}{N}\sum_{i=1}^{N}x_i,\ \bar{y}=\frac{1}{N}\sum_{i=1}^{N}y_i$$

TABLE I

THE COMPUTATION OF CORRELATION COEFFICIENTS WAS UNDERTAKEN TO SCRUTINIZE THE RELATIONSHIPS BETWEEN ADJACENT PIXELS WITHIN DIFFERENT UNENCRYPTED IMAGES. THIS COMPREHENSIVE ANALYSIS EXTENDED TO VERTICALLY, HORIZONTALLY, AND DIAGONALLY ADJACENT PIXEL PAIRS. FURTHERMORE, THE IDENTICAL CORRELATION COEFFICIENTS WERE CALCULATED FOR THEIR CORRESPONDING RGB-ENCRYPTED IMAGES

Images	Direction	Plain-image correlation coefficients			RGB-encrypted-image correlation coefficients		
		Red	Green	Blue	Red	Green	Blue
Lena	Horizontal	0.9704	0.9553	0.9126	0.1026	0.0616	0.0482
	Vertical	0.9448	0.9204	0.8746	−0.0145	−0.0102	−0.0029
	Diagonal	0.9218	0.8994	0.8548	−0.0219	0.0056	−0.0093
Baboon	Horizontal	0.8183	0.6609	0.8075	0.0338	0.0128	0.0127
	Vertical	0.8626	0.7251	0.8162	8.8268e-4	−0.0040	−0.0085
	Diagonal	0.8090	0.6430	0.7772	−7.5326e-5	−0.0028	−0.0088
Sailboat on Lake	Horizontal	0.9201	0.9272	0.9401	0.0390	0.0546	0.0832
	Vertical	0.9234	0.9354	0.9377	−0.0069	0.0010	−0.0259
	Diagonal	0.8886	0.8943	0.9099	−0.0148	−0.0132	−0.0258
Lya	Horizontal	0.9813	0.9449	0.9295	0.1093	0.1013	0.0976
	Vertical	0.9799	0.9423	0.9259	−0.0123	0.0032	−0.0195
	Diagonal	0.9742	0.9279	0.9078	−0.0141	0.0017	−0.0171

The range of ρ(x,y) values spans from −1 to 1. A value of ρ(x,y)≈1 denotes a robust correlation between adjacent pixels, while of ρ(x,y)≈0 suggests no correlation. Negative values indicate an inversion in one of the series. Table I provides the correlation coefficients for both plain and encrypted image. To demonstrate the efficacy of the proposed approach with respect to correlation coefficients, a comparative evaluation is presented in Table I, employing the Lena image as a reference point.

The secret key $K(M_0,N_0,3)$ is derived during the RGB-encryption process for the Lena image, as illustrated in Fig. 1.

To enhance our comprehension and gain further insights into this technique, we have the opportunity to conduct additional experiments on various other images, as shown in Fig. 5. By exploring its performance on different types of images, we can deepen our understanding of how this technique functions across diverse scenarios.

In comparing the proposed method with the results presented in Table II, it's important to note that correlation coefficients measure the linear relationship between two variables. Our scheme generally demonstrates commendable correlation coefficients with the original Lena image and its encrypted versions image across the horizontally, vertically, and diagonally correlated pixels. However, a notable discrepancy arises in the vertical direction. Furthermore, an intriguing aspect pertains to the divergent behavior of distinct color channels within our scheme. Variability in correlation preservation among these channels warrants further investigation into underlying mechanisms. While our proposed scheme generally upholds competitive standing in comparison to its counterparts, nuances in correlation outcomes across different spatial orientations and color domains underscore the need for comprehensive analysis and potential refinement. Tackling these intricacies is expected to improve our method's effectiveness and applicability.

Table III presents the correlation coefficients comparing unencrypted images with their encrypted counterparts across various color images. The findings reveal exceedingly low correlation coefficients, approximately approaching zero, indicative of a lack of correlation between the encrypted and unencrypted images. Moreover, the correlation coefficient consistently registers as "1" between the original and decrypted images, providing conclusive evidence of their identical nature. The algorithm's performance was systematically evaluated using diverse images, including Lena, Baboon, Sailboat on Lake, and Lya, thereby affirming its efficacy across a spectrum of image types.

B. Perceptual Security

This section delves into the visual comparison between encrypted data and the original plain image. Two distinct

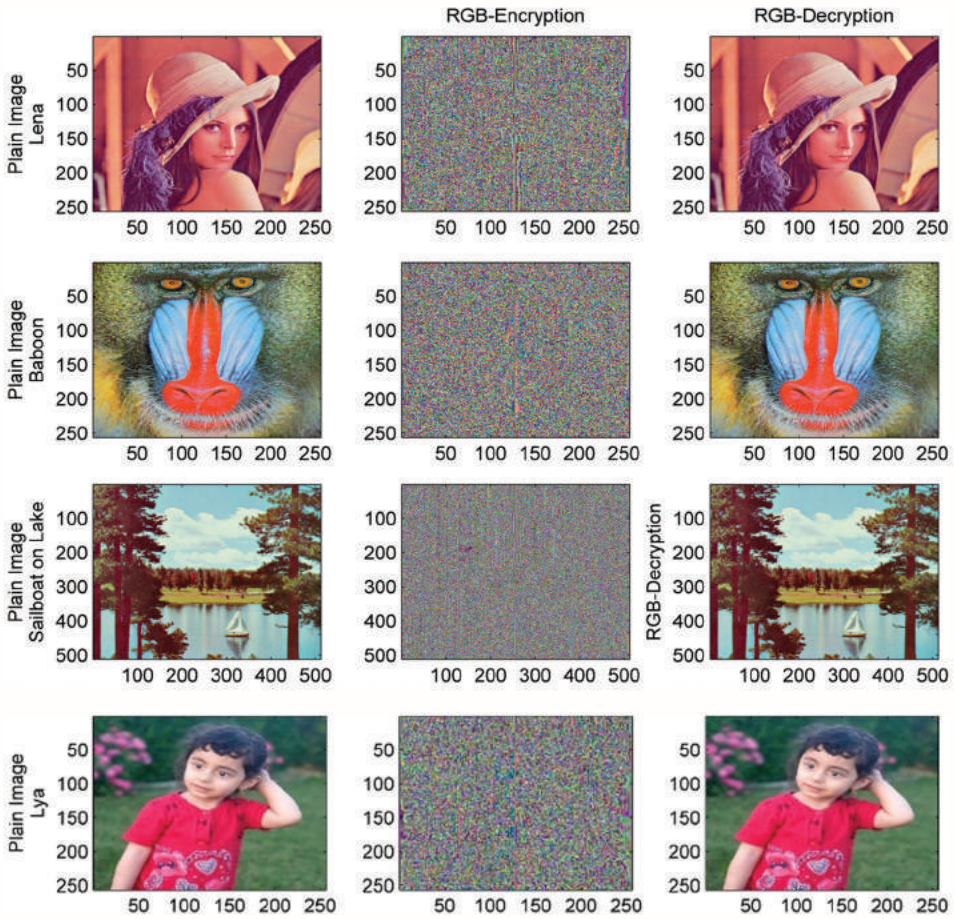

Fig. 5. Plain, RGB-encrypted, and RGB-decrypted images of Lena, Baboon, and Sailboat on Lake and Lya.

examinations are undertaken to assess the extent to which the proposed encryption method preserves visual quality. These evaluations encompass both subjective and objective analyses, collectively offering a comprehensive assessment of the visual security of the encryption process (Lian, 2008).

Visual evaluation

Fig. 3 provides a comprehensive visual representation of our analysis. The original RGB color presentation of Lena is exhibited in Fig. 3. We systematically explored various potential encryption methods for the RGB components of the Lena image, considering combinations such as {ϕ, R, G, B, RG, RB, GB, RGB}, with ϕ representing exclusion. Among the seven conceivable combinations, the RGB-encryption method yielded the most favorable outcomes, as illustrated in Fig. 3.

This preference is grounded in the efficacy of RGB-encryption, which effectively eradicates any visually identifiable connections to the original Lena image. This underscores the robust transformative capability inherent in our encryption technique.

Assessing perceptual quality through objective measures

An alternative method of assessment entails the scrutiny of impartial criteria employed to assess excellence, as illustrated in Table IV. The subsequent section provides a mathematical elucidation of these specific measures of inaccuracies. Readers are encouraged to delve into the details presented in Table IV to acquire a comprehensive understanding of the outcomes.

TABLE II
Analysis of Correlation Coefficients in Comparison (Lena Image)

Lena image	The encrypted image's correlation coefficients		
	Horizontal	Vertical	Diagonal
Zhou, et al. (2014)	0.0864	0.0583	0.0931
Pan, et al. (2016)	0.0249	0.0505	0.0280
Kaur and Jindal (2019)	0.5051	0.0020	−0.0010
Faragallah, et al. (2019)	−6.6700e-5	0.0367	0.0247
Proposed scheme			
Red	0.1026	-0.0145	−0.0219
Green	0.0616	-0.0102	0.0056
Blue	0.0482	-0.0029	−0.0093

1) MSE: An alternative approach to assess the dissimilarity between visually distinct images involves the utilization of the mean square error (MSE). This metric will be applied to compute disparities between images, where a higher MSE value signifies greater dissimilarity between the compared images. Ideally, in the context of comparing two highly similar images, the MSE should yield a value approaching zero.

$$MSE = \frac{\sum_{i=1}^{M}\sum_{j=1}^{N}\left(P_{ij}-C_{ij}\right)^2}{M\times N} \tag{12}$$

In the equation, P_{ij} and C_{ij} denote the pixel values situated at the (i,j) coordinates within the plain and decoded images, respectively. The dimensions of the image are determined by the product of M and N. When conducting comparisons between encrypted photographs and their corresponding original images, the MSE results presented in Table IV reveal significant values, approximately around 10,000. These values indicate a discernible visual distinction between the two sets of images.

2) PSNR measurement: The PSNR quantifies spectral information and mirrors the likeness between a pair of images. Elevated PSNR values suggest greater The PSNR serves as a quantitative measure of spectral information and reflects the resemblance between a pair of images. Higher PSNR values indicate a greater similarity, with this parameter approaching infinity when dealing with two entirely identical pictures. In practical terms, an image is deemed visually meaningful when the PSNR ≥28. The subsequent expression represents its mathematical representation:

$$PSNR = 10\times\log_{10}\left(\frac{\left(L-1\right)^2}{MSE}\right) \tag{13}$$

For an *n* -bit image, where, *L* typically equals 2^n, representing the maximum pixel intensity value, the average squared difference between the plain and encrypted images is quantified by the MSE. Given the notably low PSNR values ((<< 28) observed in the encoded image, it can be inferred

TABLE III
Correlation Coefficients for Certain Images

Images	Size	Component	Evaluating the correlation coefficients between original and RGB-encrypted images.	Evaluating the correlation coefficients between original and RGB-decrypted images.
Lena		Red	−0.0049	1
	256×256	Green	−5.0293e-4	1
		Blue	−0.0026	1
Baboon		Red	5.4068e-4	1
	256×256	Green	−0.0042	1
		Blue	−0.0079	1
Sailboat on Lake		Red	0.0013	1
	256×256	Green	0.0202	1
		Blue	0.0098	1
Lya		Red	−0.0217	1
	256×256	Green	0.0042	1
		Blue	−0.0044	1

TABLE IV
QUANTITATIVE MEASURES EVALUATING THE PERCEPTUAL EXCELLENCE OF THE PLAIN IMAGE COMPARED TO THE ENCRYPTED IMAGE AND DECRYPTED IMAGE

Images	Size	Component	Original plain image with encrypted image		Original plain image with decrypted image.	
			MSE	*PSNR*	*MSE*	*PSNR*
Lena	256×256	Red	1.0627e+4	7.8668	0	∝
		Green	8.9963e+3	8.5902	0	∝
		Blue	7.0973e+3	9.6199	0	∝
Baboon	256×256	Red	8.5137e+3	8.8296	0	∝
		Green	7.6851e+3	9.2743	0	∝
		Blue	9.4692e+3	8.3677	0	∝
Sailboat on Lake	256×256	Red	7.2657e+3	9.5180	0	∝
		Green	1.1333e+4	7.5875	0	∝
		Blue	1.1449e+4	7.5430	0	∝
Lya	256×256	Red	1.1513e+4	7.5188	0	∝
		Green	8.2606e+3	8.9607	0	∝
		Blue	7.6799e+3	9.2773	0	∝

TABLE V
RGB-ENCRYPTION/DECRYPTION TIME

Image	Size	Extension	RGB-Encryption and Decryption time (S)
Lena	256×256	PNG	0.5174
Baboon	256×256	PNG	0.4293
Sailboat on Lake	256×256	TIFF	0.5095
Lya	256×256	JPEG	0.3746

that these images fail to convey any meaningful details from the original image.

In the comparison of encrypted photographs with their corresponding original images, the PSNR results in Table IV reveal significant values ((<< 28), indicating the absence of additional context in the encrypted photos concerning the plain image. Furthermore, the mean square error between the decrypted and plain images consistently registers as zero across all tested images, as evidenced in Table IV. This outcome underscores the absence of errors resulting from the application of our technique. Consequently, the decrypted counterparts align perfectly with the original images, preserving every single data detail intact.

C. Execution Time

Time emerges as a pivotal consideration when formulating an encryption strategy. The efficacy of an encryption algorithm in maintaining its security level is maximized when its execution time is minimized. The proposed method, leveraging the Elzaki transformation for color image encryption and decryption, guarantees a harmonious balance between speed and security. Comprehensive findings pertaining to the duration of the color images utilized in the encryption and decryption processes are elucidated in Table V.

V. CONCLUSION

In the present study, a framework for encryption ensures the security of color image applications. The design framework encrypts the color image to safeguard confidentiality. The proposed work suggests a novel cryptographic technique for the encryption of digital images by combining an infinity series of specific hyperbolic functions with Elzaki transforms for encryption and corresponding inverse Elzaki transforms for decryption. The private key in this technique is the sum of multiples of the mod. This makes it extremely difficult for an eyedropper to use a brute-force attack or any other kind of attack to discover the secret key. The process's performance and recorded results unequivocally show that our approach was effective in accomplishing its main goal of sound data encryption. In-depth statistical analyses, comprising evaluations of histograms and correlation coefficients, in addition to metrics such as MSE and PSNR, were utilized to determine how effective the suggested security measure was. The process's execution time was also carefully tracked.

REFERENCES

Al-Khazraji, L.R., Abbas, A.R., and Jamil, A.S., 2022. Employing neural style transfer for generating deep dream images. *Aro-The Scientific Journal of Koya University*, 10(2), pp.134-141.

An, F.P., and Liu, J.E., 2019. Image encryption algorithm based on adaptive wavelet chaos. *Journal of Sensors*, 2019, pp.1-12.

Elshamy, A., Hussein, A., Hamed, H.F.A., Abdelghany, M.A., and Kelash, H.M., 2019. Color image encryption technique based on chaos. *Procedia Computer Science*, 163, p.49-53.

Elzaki, T., 2011. The new integral transform "Elzaki transform". *Global Journal of Pure and Applied Mathematics*, 7(1), pp.57-64.

Faragallah, O.S., Alzain, M.A., El-Sayed, H.S., Al-Amri, J.F., El-Shafai, W., Afifi, A., Naeem, E.A., and Soh, B., 2018. Block-based optical color image encryption based on double random phase encoding. *IEEE Access*, 7, pp.4184-4194.

Farsana, F.J., Devi, V.R., and Gopakumar, K., 2023. An audio encryption scheme based on Fast Walsh Hadamard Transform and mixed chaotic keystreams. *Applied Computing and Informatics*, 19, pp.239-264.

Hamad, A.S., and Farhan, A.K., 2020. Image encryption algorithm based on substitution principle and shuffling scheme. *Journal of Engineering Technology*, 38(3B), pp.98-103.

Kang, X., Han, Z., Yu, A., and Duan, P., 2017. Double Random Scrambling Encoding in the RPMPFrHT Domain. In: *2017 IEEE International Conference on Image Processing* (*ICIP*), pp.4362-4366.

Kaur, J., and Jindal, N., 2019. A secure image encryption algorithm based on fractional transforms and scrambling in combination with multimodal biometric keys. *Multimedia Tools and Applications*, 78, pp.11585-11606.

Kuffi, E.A., Mehdi, S.A., and Mansour, E.A., 2022. Color image encryption based on new integral transform SEE. *Journal of Physics: Conference Series*, 2322(1), p.012016.

Lang, J., 2012. Image encryption based on the reality-preserving multiple-parameter fractional Fourier transform and chaos permutation. *Optics and Lasers in Engineering*, 50(7), pp.929-937.

Lian, S., 2008. *Multimedia Content Encryption: Techniques and Applications*. CRC Press, United States.

Liang, Y.R., and Xiao, Z.Y., 2020. Image encryption algorithm based on compressive sensing and fractional DCT via polynomial interpolation. *International Journal of Automation and Computing*, 17(2), pp.292-304.

Liu, W., Sun, K., and Zhu, C., 2016. A fast image encryption algorithm based

on chaotic map. *Optics and Lasers in Engineering*, 84, p.26-36.

Nag, A., Singh, J.P., Khan, S., Ghosh, S., Biswas, S., Sarkar, D., and Sarkar, P.P., 2011. Image Encryption using Affine Transform and XOR Operation. In: *International Conference on Signal Processing, Communication*, *Computing and Networking Technologies*.

Nasry, H., Abdallah, A.A., Farhan, A.K., Ahmed, H.E., and El Sobky, W.I., 2022. Multi chaotic system to generate novel S-box for image encryption. *Journal of Physics: Conference Series*, 2304(1), p. 012007.

Pan, S.M., Wen, R.H., Zhou, Z.H., and Zhou, N.R., 2017. Optical multi-image encryption scheme based on discrete cosine transform and nonlinear fractional Mellin transform. *Multimedia Tools and Applications*, 76, pp.2933-2953.

Pirdawood, M.A., Kareem, S.R., and Zahir, D.C., 2023. Audio encryption framework using the laplace transformation. *Aro-the Scientific Journal of Koya University*, 11(2), pp.31-37.

Pradheep, M., 2021. *Image Encryption by Using ACGLML*. Munich, GRIN Verlag, p.130.

Priya, S.S.S., KarthigaiKumar, P., Mangai, N.S., and Vanathi, P.T., 2012. Survey on efficient, Low-Power, AES image encryption and bio-cryptography schemes. *SmartCR*, 2, pp.379-390.

Salim, S.J., and Ashruji, M.G., 2016. Application of El-Zaki transform in cryptography. *International Journal of Modern Sciences and Engineering Technology*, 3, pp.46-48.

Shivaji, J.S., and Hiwarekar, A.P., 2021. Cryptographic method based on Laplace-Elzaki transform. *Journal of the Maharaja Sayajirao University of Baroda*, 55(1), pp.187-191.

Sui, L., Duan, K., and Liang, J., 2015. Double-image encryption based on discrete multiple-parameter fractional angular transform and two-coupled logistic maps. *Optics Communications*, 343, pp.140-149.

Wang, X., Liu, C., and Jiang, D., 2021. A novel triple-image encryption and hiding algorithm based on chaos, compressive sensing and 3D DCT. *Information Sciences*, 574, p.505-527.

Wang, Z.Y., Zhang, Y.Q., and Bao, X.M., 2015. A novel chaotic image encryption scheme using DNA sequence operations. *Optics and Lasers in Engineering*, 73, p.53-61.

Weber, A.G., 2006. The USC-SIPI Image Database: Version 5. Available from: http://sipi.usc.edu/database [Last accessed on 2023 Oct 01].

Wei, L., and Shi, H., 2023. Chaotic image encryption algorithm based on wavelet transform. *Journal of Applied Mathematics and Computation*, 7(3), pp.359-364.

Wu, J., Guo, F., Liang, Y., and Zhou, N., 2014. Triple color images encryption algorithm based on scrambling and the reality-preserving fractional discrete cosine transform. *Optik*, 125(16), pp.4474-4479.

Yang, J., and Wang, X., 2021. A privacy image encryption algorithm based on piecewise coupled map lattice with multi dynamic coupling coefficient. *Information Sciences*, 569, p.217-240.

Zhou, N., Zhang, A., Zheng, F., and Gong, L., 2014. Novel image compression-encryption hybrid algorithm based on key-controlled measurement matrix in compressive sensing. *Optics and Laser Technology*, 62, pp.152-160.

Geotechnical Assessment of the Slopes of Hamamok Dam, NE of Koya, Kurdistan Region of Iraq

Bahra Dh. Ghafour[1*], Mohammed J. Hamawandy[1], and Varoujan K. Sissakian[2]

[1]Department of Geotechnical Engineering, Faculty of Engineering, Koya University,
Koya KOY45, Kurdistan Region - F.R. Iraq

[2]Department of Petroleum Engineering, Komar University of Science and Technology,
Sulaymaniyah, Kurdistan Region – F.R. Iraq

***Abstract*—The Hamamok Dam is an earthfill dam with a height of 25 m and a length of 125 m, constructed in 2011, located northwest of Koya town on a deep canyon-like valley that flows along the southeastern plunge of the Bana Bawi anticline, which forms Bawagi Mountain. The exposed rocks at the site belong to the Pila Spi and Gercus Formations; however, rocks from the Khurmala and Kolosh formations are exposed upstream from the dam's reservoir. The difference in the hardness of the carbonate rocks of the Pila Spi formation, which forms the uppermost parts of the cliffs surrounding the dam site, and those of the soft reddish brown clastics of the Gercus Formation caused steep slopes that suffered from slope instability problems. To perform a geotechnical study of slopes at the dam site, we have collected different field data to perform a kinematic assessment method using DipAnalyst 2.0 software and drawn the stereographic projections for the studied 10 stations using Stereonet v11 software. Besides, Bejerman's method, which is based on field data, is used to indicate the landslide possibility index (LPI). The results showed that the LPI values range between 23 and 27, whereas the results of the kinematic analysis showed that the right bank (stations 1–5) suffers from plane sliding, whereas the left bank (stations 6–10) suffers from toppling. In both cases, Joint 2 has the main role in the developed failures.**

***Index Terms*—Bejerman's method, Factor of safety, Hamamok Dam, Kinematic analysis, Landslide possibility index.**

I. Introduction

The Ministry of Agricultural and Water Resources in the Kurdistan Regional Government has planned to construct tens of dams of different sizes at different places in the Kurdistan Region of Iraq. Among those dams is the Hamamok Dam, it is an earth fill dam, constructed in 2011 with a height of 25 m, a length of 120 m, and a reservoir capacity of 250,000 m^3. The dam is constructed on a deeply incised valley that flows along the southeastern plunge of the Bana Bawi anticline, and it is represented by Bawagi Mountain, which is the western continuation of the Haibat Sultan Range Fig. 1.

ARO-The Scientific Journal of Koya University
Vol. XII, No. 1 (2024), Article ID: ARO.11553. 10 pages
DOI: 10.14500/aro.11553
Received: 25 February 2024; Accepted: 25 May 2024
Regular research paper: Published: 17 June 2024
Corresponding author's e-mail: bahra.dhahir@koyauniversity.org

II. Hamamok Dam

Hamamok Dam is an earthfill dam with a length of 120 m, and a height of 25 m, and the surface area of the lake at an elevation of about 800 m (a.s.l.) is 18,044 m^2. Both upstream and downstream sides are paved by limestone blocks up to 0.3 m^3 as rip-rap, and the spillway is built on the right side of the dam at an elevation of 803 m (a.s.l.). On the left and right banks of the dam and the lake, and more upstream and downstream sides very steep slopes and cliffs are developed, and the slopes suffer from different types of failures.

The slope failures are developed due to the existence of the soft clastic rocks of the Gercus Formation overlain by hard carbonate rocks of the Pila Spi Formation (Sissakian and Fouad, 2014). The average gradients of the left and right banks of the lake are 53.51% and 23.62%, respectively. Whereas, the maximum heights on the left and right banks of the lake are 1300 m and 950 m, respectively, Fig. 2.

III. Geological Setting

Hamamok Dam is located in the High Folded Zone. It is a part of the Zagros-Fold-Thrust Belt (Fouad, 2015). The dam is constructed in a deep valley that flows along the southeastern plunge of the Bana Bawi anticline and a few hundred meters west of the Koisanjaq syncline Fig. 1. The northwestern hanging plunge of the Koisanjaq syncline forms an elevated area; called Bawaji Mountain. Some of the carbonate rocks of the Pila Spi Formation show microfolding with an amplitude of (1–5) m. These micro folds have accelerated the deformation of the beds and their break down into small pieces, accordingly, increasing the slope failure phenomenon. Both abutments of the dam are constructed within the clastic rocks of the Gercus Formation (Eocene age), which consists of reddish-brown fine clastics; mainly claystone and sandstone. In general, the beds are soft forming steep slopes. The thickness of the formation is about 80 m. The Gercus Formation is overlain by the Pila Spi Formation

http://dx.doi.org/10.14500/aro.11553

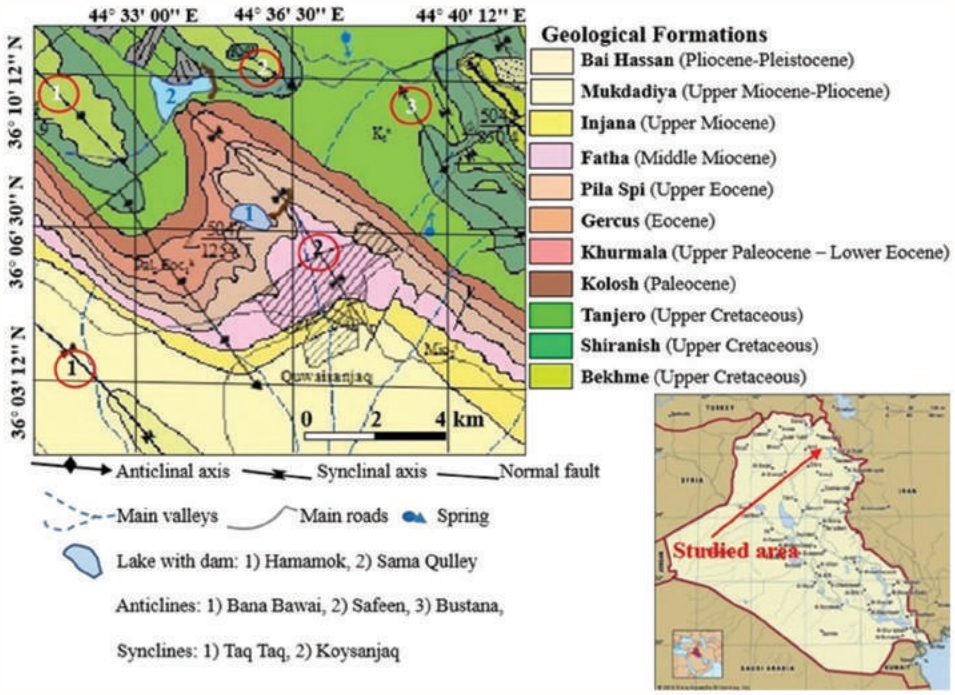

Fig. 1. Location and geological map of Hamamok Dam and surroundings, modified from (Sissakian and Fouad, 2014).

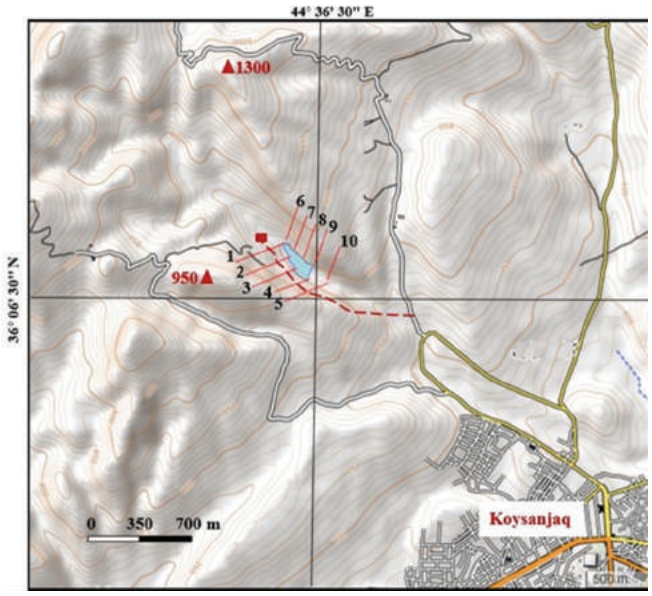

Fig. 2. Contour map of the studied area with the location of the studied 10 stations. The approximate coordinates, scale, and the unpaved road to the dam site (red dashed line) and guard house (red rectangle) are added by the authors after (Inkatlas, 2023).

(Upper Eocene age) Fig. 1. It consists of hard to very hard limestone and dolostone, and cliff-forming. The thickness of the formation is about 60 m (Sissakian and Fouad, 2014).

The most well-developed geomorphological form in the studied area is the giant flat irons Fig. 3. The average values of the width, height, and elevation difference between the top and bottom are 1.8 km, 1.3 km, and 305 m, respectively.

The steep slopes and cliffs are also well-developed at the dam site. These are attributed to the soft clastic rocks of the Gercus Formation, which are overlain by hard carbonate rocks of the Pila Spi Formation Fig. 3.

IV. Methodology and Work Procedure

We have reviewed many published scientific articles, which dealt with (Bejerman, 1994) and Kinematic analysis for geotechnical assessment of slope stability. We also used a geological map at a scale of 1:250,000 (Sissakian and Fouad, 2014; Esriimage, 2023; Inkatlas, 2023) to find relevant data relevant to Hamamok Dam site. For the geotechnical assessment of the slopes around the Hamamok Dam and the lake, we used two different methods, (1) the (Bejerman, 1994) Method, and (2) the Kinematic Method using DipAnalyst 2.0 software, and drawing the stereographic projection for the 10 studied stations using Stereonet v11 software.

We have used both methods because (1) Bejerman's Method is a quick and easy field method without the need for special laboratories, equipment, and specialized personnel, (2) We have used the Kinematic Method based on data from an abandoned tunnel, which is near the dam site, and (3) No field sampling and rock coring equipment is available.

A. Bejerman Method

This is a simple and quick field method through which any artificial or natural slope can be assessed geotechnically (Bejerman, 1994), (Bejerman, 1988). The method depends on 10 attributes Fig. 4. All can be measured and/or estimated in the field directly. Therefore, it is a very quick method.

We have selected 10 stations (five on each side of the dam site and reservoir) (Fig. 2) to represent the stability status on the slopes of both sides, each station is opposite to the other

one on the other side. Moreover, the last station on each side (numbers 5 and 10) is on the downstream of the dam. This was done to indicate the difference in the stability of the slopes upstream and downstream sides.

The height of the slope was measured from the Google Earth image. The slope angle and gradient of discontinuities were measured using Ferrybridge Compass. The grade of weathering, fracture, gradient of discontinuities, vegetation cover, and existing landslides were estimated directly in the field by personal observation. The spacing of discontinuities was measured using measuring tape. The orientation of discontinuities was indicated based on the dip direction of the rocks and the slope direction. The water infiltration was indicated directly in the field based on the presence of water among the slopes and the type of rocks.

B. Kinematic Analysis

The Kinematic analysis is the second analysis method, which we applied to assess the slopes of the Hamamok Dam site. This method is used to analyze the potential for the different modes of rock slope failures (plane, wedge, and toppling failures), which take place due to the presence of discontinuities that have unfavorable orientations. We found it to be a kind of block failure through the stereonet. The direction in which the block will slide can be detected using the same diagram; moreover, the stability condition can be detected (Goodman, 1976; Hoek and Bray, 1977; Wyllie and Mah, 2005). The software used was DipAnalyst 2.0, which is designed for both new quantitative kinematic analysis and stereonet-based analysis. To determine whether a dip direction or value has the potential to cause a plane or toppling failure, the software compares it with the slope angle and friction angle. There is a chance of a plane failure if the dip vector (middle point of the great circle) of the great circle, which represents a discontinuity set, lies inside the shaded region where the friction angle is greater than the slope angle. However, if the dip vector (the great circle's midpoint) falls inside the triangle-shaped shaded area, there is a chance that the structure will topple over.

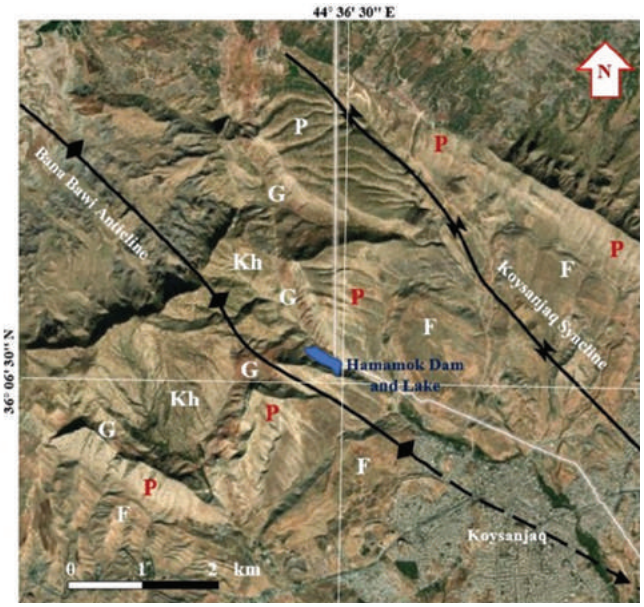

Fig. 3. Giant flat irons on the southeastern plunge of the Bana Bawi Anticline and Koysanjaq Syncline. Geological Formations: Kh=Khurmala, G=Gercus, P=Pila Spi, and F=Fatha (Esriimage, 2023).

V. Results

A. Bejerman Method

The obtained field data for (Bejerman, 1994) Method Table I were used to indicate the grade, category of the landslide possibility index (LPI) and hazard zones. The results are shown in Table II; based on (Bejerman, 1994) Method Table III. The obtained LPI values showed that the Category ranges between High (7 stations) and Very high (3 stations). Hazard zones range between Moderate (8 stations) and High (2 stations), whereas the Failure possibility ranges between High (8 stations) and Very high (2 stations).

B. Kinematic Analysis

The stereographic projections and Dip analysis 2.0 diagrams are presented in (Figs. 4 and 5) for the right and left banks' stations, respectively. By DipAnalyst 2.0 software the factor of safety can be calculated for plane and wedge failure but we cannot obtain it for toppling failure. Therefore, the values of the factor of safety were obtained only for stations 1, 2, 3, 4, and 5, which are presented in Table IV. The values of Friction angle, Cohesion and rock density were acquired from the geotechnical study of the Haibat Sultan tunnel (Bosphorus Technical Consulting Corporation, 2012), which is located about 1.5 km east of the study area within the same rocks and same geological condition (Sissakian and Fouad, 2014). Whereas, the results of the Kinematic analysis of the studied 10 stations using Dip analysis 2.0 are presented in (Tables V and VI).

For all stations, in stereographic (Figs. 4 and 5) (1B, 2B, 3B, 4B, 5B, 6B, 7B, 8B, 9B, and 10B), the slope face with the daylight window (envelope) and two lateral limit lines are in blue. Joint 2 is pink in color, joint1 is in orange color, the bedding plane is brown and the internal friction angle is in green color. For Dip Analyst (Figs. 4 and 5) (1A, 2A, 3A, 4A, 5A, 6A, 7A, 8A, 9A, and 10A), the slope face is in red and joints 1 and 2 are in orange and pink color, respectively. The bedding plane is in brown and the internal friction angle is in green color, whereas the critical area is determined by the Dip Analyst software.

VI. Discussion

A. Bejerman's Method

The high values of LPI and failure possibilities in the banks of the Hamamok Dam site (Tables III and IV) indicate that the slopes on both banks are unstable (Figs. 6 and 7). The unstable slopes are attributed to: (1) the Steep slopes of both banks of the valley, which form the lake of the dam (Fig. 2) have gradients of 53.51% and 23.62% of the left and right banks, respectively, (2) the well bedded and jointed hard carbonate rocks of the

Pila Spi Formation, which suffer from toppling (Figs. 6 and 7), (3) the presence of soft claystone beds of the Gercus Formation underlying the carbonate rocks of the Pilea Spi Formation act as a lubricant for sliding and toppling, and (4) the high rates of weathering and erosion in the site.

B. Kinematic Analysis

Based on (Markland, 1972; Hocking, 1976; Hoek and Bray, 1981; Wyllie and Mah, 2005) the modes of failure are analyzed. A potentially unstable planar block needs to meet the following conditions in order to occur:

- The bedding plane, which is referred to as a "daylight" on the face, dips at a flatter angle than the slope face ($\psi A < \psi f$)
- Considering that every discontinuity strikes nearly parallel to the slope face, the poles of the slope face and the discontinuity sets (symbol P) are plotted on the stereonet and displayed in (Figs. 4 and 5). These poles' positions with respect to the slope face demonstrate that all planes' poles are daylight, potentially unstable and located inside the slope face's pole. The daylight envelope, also known as the "Daylight Window," is this region that can be used to rapidly identify blocks that may be unstable
- -The stability will also be impacted by the discontinuity sets' dip direction. Only when the discontinuity's dip direction and the slope face's dip direction diverge by <20ϕ, or $|\alpha A - \alpha f| < 20\phi$, can plane sliding be achieved. In stations Nos. 1, 2, 3, 4, and 5 (Fig. 4), this is the situation, and Joint 2 plays a major part in the plane siding
- Two lines (Slope limits in the plane) defining the dip directions of ($\alpha f + 20\ \phi$) and ($\alpha f - 20\ \upsilon$) on the stereonet illustrate this restriction on the dip direction of the planes. The lateral boundaries of the daylight envelope in (Fig. 9) are indicated by these two lines.

Goodman and Bray (1976) and Wyllie and Mah (2005) state that the following conditions must be met for toppling failure to occur:

- In order to form a series of slabs parallel to the slope face, the discontinuities dipping into it must have a dip direction that is within approximately 10¸ of the slope face's dip direction. Two lines (Slope limits in the plane) that define the dip directions of ($\alpha f + 10\acute{r}$) and ($\alpha f - 10\acute{r}$) on the stereonet illustrate this restriction on the dip direction of the planes. The lateral boundaries of the daylight envelope in (Fig. 8) are indicated by these two lines. As shown in Fig. 6, this

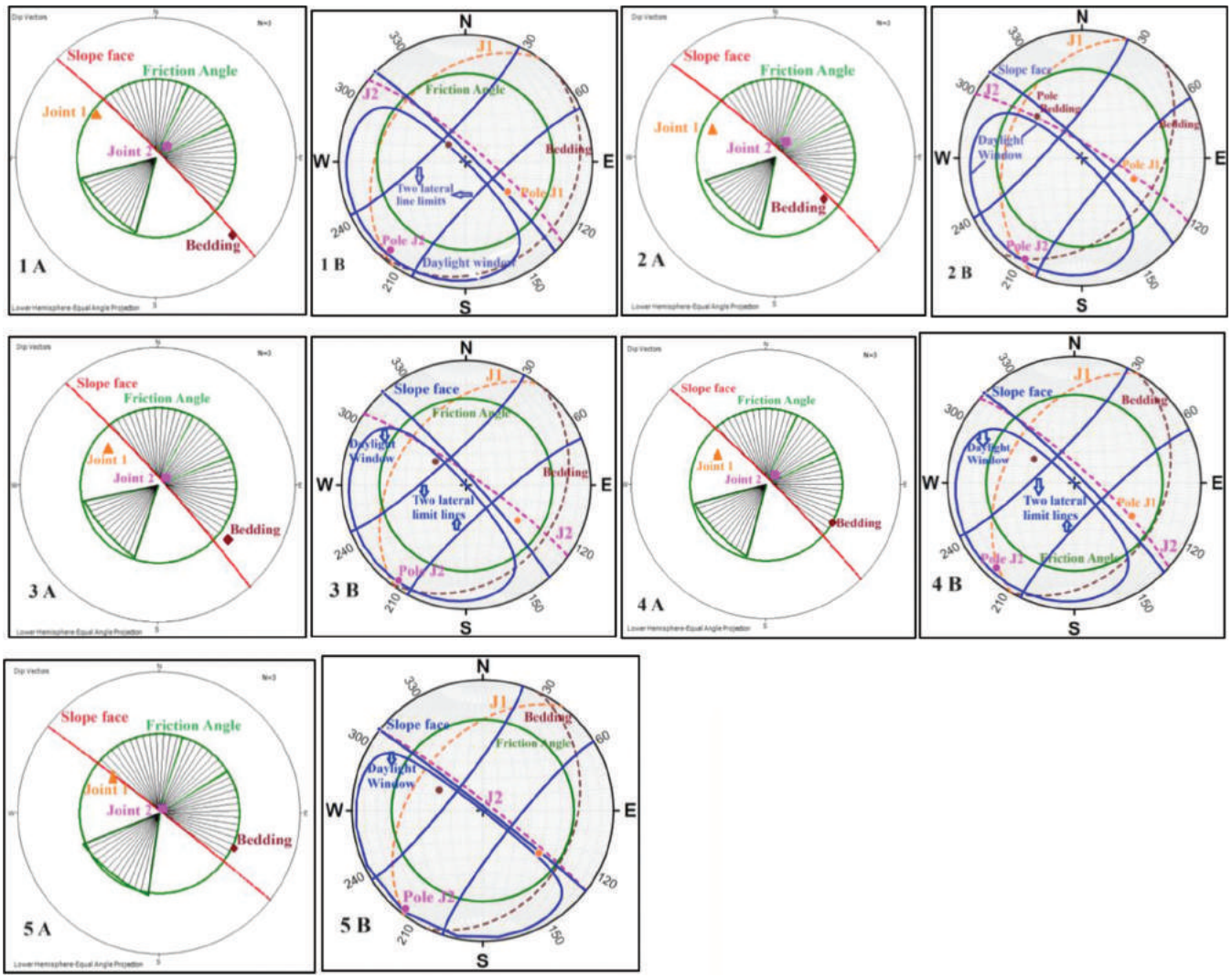

Fig. 4. Stereographic projections and Dip analysis diagrams of stations 1, 2, 3, 4, and 5 of the Hamamok Dam.

TABLE I
FIELD DATA OF THE 10 STUDIED STATIONS AT THE HAMAMOK DAM SITE

Station No.	Numbers of the attributes used in LPI from (Bejerman, 1994)										Rating LPI	Coordinates		Elevation (m, a.s.l.)	Figure No. in the text
	1	2	3	4	5	6	7	8	9	10					
	Slope		Grade of		Discontinuities			Vegetation cover (%)	Water infiltration (%)	Previous land slide volume					
	Height (m)	Angle (°)	Fracture	Weathering	Gradient (°)	Spacing (m)	Orientation					Latitude (N)	Longitude (E)		
1	121	85	H	H	34	0.3–1.0	Unf	Void	Inexist	High	24	36°06.183'	44°35.847'	840	7.1
	5	4	2	3	2	2	4	0	0	2					
2	125	83	H	H	38	0.3–1.0	Unf.	Scarce	Inexist.	High	25	36°06.143'	44°35.183'	838	7.2
	5	4	2	3	2	2	4	1	0	2					
3	110	85	H	H	62	0.3–1.0	Unf	Scrace	Inexist	H	27	36°06.100'	44°35.957'	828	7.3
	5	4	2	3	4	2	4	1	0	2					
4	72	85	H	H	44	0.3–1.0	Unf	Scrace	Inexist	H	25	36°06.079'	44°36.146'	815	7.4
	5	4	2	3	2	2	4	1	0	2					
5	70	88	H	H	45	0.3–1.0	Unf	Void	Inexist	Small	24	36°06.137'	44°36.037'	824	7.5
	5	4	2	3	3	2	4	0	0	1					
6	141	60	H	H	55	0.3–1.0	Unf	Void	Inexist	Small	23	36°06.140'	44°35.183'	830	8.6
	5	3	2	3	3	2	4	0	0	1					
7	98	65	H	H	50	1–3	Unf	Void	Inexist	Small	23	36° 06. 142'	44°35.180'	822	8.7
	5	4	2	3	3	1	4	0	0	1					
8	87	80	H	H	62	0.3–1.0	Unf	Void	Inexist	High	26	36°06.140'	44°35.957'	810	8.8
	5	4	2	3	4	2	4	0	0	2					
9	72	82	H	H	64	0.3–1.0	Unf	Void	Inexist	Small	25	36°06.137'	44°36.037'	784	8.9
	5	4	2	3	4	2	4	0	0	1					
10	68	85	H	H	57	0.3–1.0	Unf	Void	Inexist	High	25	36°06.135'	44°36.041'	824	8.10
	5	4	2	3	3	2	4	0	0	2					

LPI: Landslide possibility index

http://dx.doi.org/10.14500/aro.11553

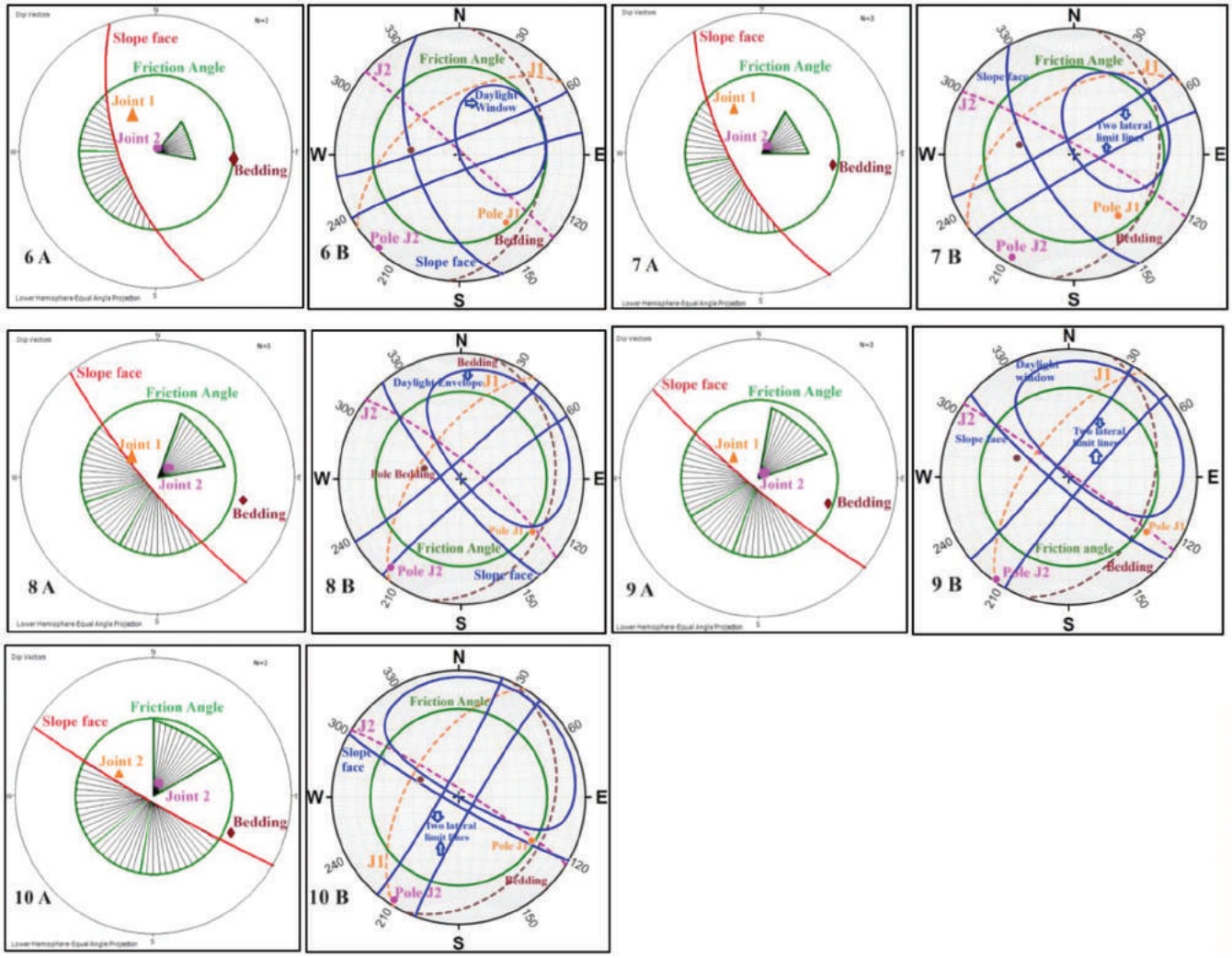

Fig. 5. Stereographic projections and Dip analysis diagrams of stations 6, 7, 8, 9, and 10 of the Hamamok Dam.

TABLE II
LPI Scored Values, Hazard Zones and Failure Possibility (After Bejerman, 1994) at 10 Stations

Station No.	LPI Value	LPI		Hazard Zone	Failure possibility
		Grade	Category		
1	24	V	High	Moderate	High
2	25	V	High	Moderate	High
3	27	VI	Very High	High Hazard	Very High
4	25	V	High	Moderate	High
5	24	V	High	Moderate	High
6	23	V	High	Moderate	High
7	23	V	High	Moderate	High
8	26	VI	Very High	High Hazard	Very High
9	25	V	High	Moderate	High
10	25	V	High	Moderate	High

LPI: Landslide possibility index

TABLE III
Landslides Hazard Categories, Hazard Zones, and Failure Possibility Range after (Bejerman, 1994; Bejerman, 1998)

Landslide possibility index (LPI)			Hazard Zone		Failure possibility	
Grade	Category	Estimation				
I	Small	0–5	<10	Low hazard	0–5	Small
II	Very Low	6–10			6–10	Very Low
III	Low	11–15	11–25	Moderate hazard	11–15	Low
IV	Moderate	16–20			16–20	Moderate
V	High	21–25	<25	High hazard	20–25	High
VI	Very High	<25			>25	Very High

is the situation at stations Nos. 6, 7, 8, 9, and 10. Joint 2 is primarily responsible for the toppling.

- The planes' dip needs to be sufficiently steep for interlayer slip to happen. Slip will only happen if the direction of the applied compressive stress is at an angle larger than ϕj with a normal direction to the layers if the friction angle on the layers' faces is ϕj. When the following circumstances are met, interlayer slip and toppling failure will occur on planes with dip ψp, as the major principal stress in the cut is oriented parallel to the cut face (dip angle ψf) (Goodman and Bray, 1976).
- The dip of the planes must be steep enough for interlayer slip to occur. If the faces of the layers have a friction angle ϕj, then slip will only occur if the direction of the

TABLE IV
NUMERICAL USED DATA IN THE CALCULATION OF THE FACTOR OF SAFETY.

Station No.	Slope face (Direction/ Inclination amount)	Discontinuity Dip direction/Dip amount	Slope height (m)	Cohesion (Kn/m^2)	Friction Angle (°)	Rock Density (Kn/m^3)	Tension Cracks (Depth/ height of water) (cm)	Factor of safety
1	045/85	040/80	121	61	31	25	50/2	0.57
2	042/83	030/81	125	61	31	25	60/4	0.97
3	048/85	035/83	110	61	31	25	65/4	0.99
4	045/85	042/80	72	61	31	25	55/3	0.89
5	038/88	038/85	70	61	31	25	50/3	0.64

TABLE V
RESULTS OF KINEMATIC ANALYSIS OF THE 5 STUDIED STATIONS ON THE RIGHT BANK SLOPE OF THE HAMAMOK DAM

Station No.	Kinematic analysis		DipAnalyst 2.0 software and Stereographic projection results
	Angles relationship between Joint 2 and Slope face ($\psi A<\psi f$)	Relation between the direction of discontinuities and slope face $\lvert\alpha A-\alpha f\rvert <20^\circ$	
1	The dip of joint 2 and its relation with the slope angle has a minor to moderate effect on the sliding failure because there is almost less difference between them. (80° <85°).	The dip direction of Joint 2 has a main role in sliding as the difference in their direction to the direction of the slope face is <20°. |310–315|=5 <20°	The stereographic projection for this station shows that the friction angle is greater than the slope angle and pole of the Joint 2 lies in the critical area for planar failure (between two lateral limit lines on the edge of the daylight window area) Fig. 5. 1B. The analysis by Dip Analysis 2.0 shows that the dip vector point of Joint 2 lies within the critical area for plane sliding criteria Fig. 5. 1A and the numerical analysis by DipAnalyst 2.0 software shows that the value of the factor of safety is 0.57 Table IV. Therefore, the potentiality for plane sliding is high.
2	The slope angle is almost equal to the dip of Joint 2, thus it has a minor to moderate effect on sliding failure in this station. (81° <83°)	The direction of Joint 2 has a significant role in sliding as the difference in their direction to the direction of the slope face is <20°. |300–312|=12 <20°	As is clear in Fig. 5. 2B the friction angle is greater than the slope angle, and the pole of Joint 2 lies within a critical area (between two lateral limit lines in the daylight window area). For DipAnalyst 2.0 software, the analysis shows that there is a medium possibility for sliding by joint 2 which lies on the edge of the critical zone for plane sliding Fig. 5. 2A. The numerical analysis by DipAnalyst 2.0 software shows that the value of the factor of safety for this station is 0.97 Table IV which indicates that the possibility of sliding failure is low.
3	The dip of the slope is almost equal to the dip of Joint 2, thus it has a minor to moderate effect on sliding failure in this station. (83°<85°)	Joint 2 has a significant role in sliding failure in this station as the difference of its direction to the direction of the slope face is <20°. |305–318|=13 <20	At this station, Joint 2 has the main effect on sliding failure as it is clear in (Fig. 5. 3B) that its pole lies on the edge of the line of the critical area between two lateral limits planes of the daylight window zone for sliding failure. The Analysis by DipAnalyst 2.0 software shows that the probability for sliding failures on the Joint 2 surfaces is potential as it lies within the critical area (Fig. 5. 3A). Therefore, the potentiality of plane sliding exists. The factor of safety for this station is 0.99 (Table IV) therefore the sliding possibility is low.
4	The dip of joint 2 and its relation with the slope angle has a minor to moderate effect on the sliding failure because there is almost less difference between them. (80° <85°)	In this station, the difference between the dip direction of Joint 2 and the slope face is<20o. Thus it has a main role in sliding failure|312–315|=3<20	(Fig. 5. 4B) shows that joint 2 has the main effect on sliding failure where it lies within a critical area between two slope limit planes in the daylight window zone. (Fig. 5. 4A) for The DipAnalyst 2.0 software shows that Joint 2 lies on the edge within the critical plane sliding zone. Therefore, the type of failure in this station is plane sliding. Numerical Analysis by DipAnalyst 2.0 software shows that the value of the factor of safety for this station is 0.89 (Table IV).
5	The dip of joint 2 and its relation with the slope angle has a minor to moderate effect on the sliding failure because there is almost less difference between them. (85° <88°)	The dip direction of Joint 2 has a main role in sliding as the difference in their direction to the direction of the slope face is <20°. |307–308|=1 <20	At this station, joint 2 has the main effect on sliding failure as it's clear in (Fig. 5. 5B) its pole lies within the area between two lateral slope limits planes of the daylight window zone (critical area) for sliding failures. (Fig. 5. 5A) for analysis by DipAnalyst 2.0 software shows that the probability for sliding failures on the Joint 2 surfaces is high, as it lies within the critical area zone for plane sliding failure. Numerical analysis shows that the factor of safety for this station is 0.64 (Table IV). Therefore, the potentiality of plane sliding is high.

applied compressive stress is at an angle greater than ϕj with a normal direction to the layers. The direction of the major principal stress in the cut is parallel to the face of the cut (dip angle ψf), so interlayer slip and toppling failure will occur on planes with dip ψp; when the following conditions are met (Goodman and Bray, 1976):

http://dx.doi.org/10.14500/aro.11553

Fig. 6. Right bank station Nos. 1, 2, 3, 4, and 5. Nos. 1 and 4: Active erosion areas indicating unstable slopes. No. 2: Bulged mass in the middle of the slope indicating an unstable slope. No. 3: Recent slid blocks as indicated from the fresh color of the blocks; indicating unstable slope. No. 5: The slope below the cliff is gentler as compared to the other stations; therefore, the amount of slid blocks is smaller and lesser. The reddish brown clastics of the Gercus Formation are overlain by the carbonates of the Pila Spi formation

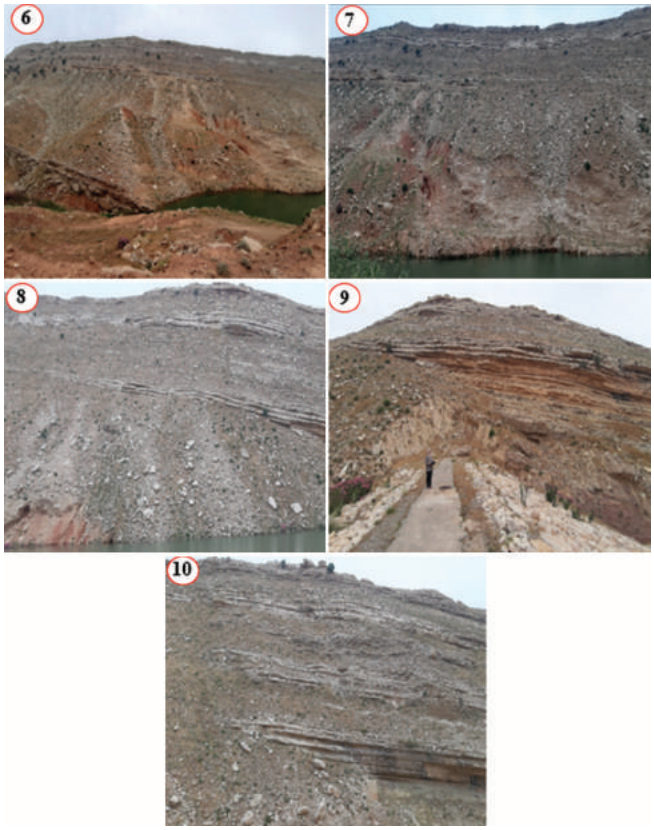

Fig. 7: Left bank station Nos., 6, 7, 8, 9, and 10. Nos. 6, 7, and 8: Active erosion areas and groves within the slopes indicating unstable slopes. No. 9: Bulged mass on the left of the slope indicating unstable slope. No. 10: Microfolds in the beds of the Pila Spi Formation, they deformed the beds and increased the instability of the slopes. Note the amount of the accumulated scree in the left side of the slope. The reddish brown clastics of the Gercus Formation are overlain by the carbonates of the Pila Spi Formation.

TABLE VII
The Attitude of Bedding Planes, Joints, (1 and 2), and Slope Face in the Hamamok Dam Site

Station		Bedding plane			Joint No. 1			Joint No. 2			Slope face		
No.	Location	Strike (°)	Dip (°)		Strike (°)	Dip (°)		Strike (°)	Dip (°)		Strike (°)	Inclination Dip (°)	
			Direction	Angle		Direction	Angle		Direction	Angle		Direction	Angle
1	Right Bank	N 45 E	135	15	N 35 E	305	34	N 50 W	40	80	315	45	85
2		N 42 E	132	40	N 22 E	292	38	N 60 W	30	81	312	42	83
3		N 32 E	128	25	N 35 E	305	42	N 55 W	35	83	318	48	85
4		N 30 E	120	30	N 30 E	300	44	N 48 W	42	80	315	45	85
5		N 25 E	115	30	N 37 E	307	45	N 53 W	38	85	308	38	88
6	Left Bank	N 05 E	95	32	N 53 E	325	55	N 49 W	41	88	340	250	60
7		N 10 E	100	35	N 55 E	325	50	N 60 W	30	84	330	240	65
8		N 15 E	105	25	N 36 E	306	62	N 51 W	39	80	320	230	80
9		N 20 E	110	35	N 35 E	305	64	N 62 W	28	88	310	220	82
10		N 25 E	115	27	N 31 E	301	57	N 58 W	32	85	300	210	85

$(90°–\psi f)+\phi j<\psi p$

To perform the Dip analysis 2.0, the strike and dip direction of the exposed beds and existing joint sets at each station were measured, besides the direction and inclination amount of the slope face. The results are presented in (Table VII). The data of rock properties from (Bosphorus Technical Consulting Corporation, 2012), which belongs to an abandoned tunnel that is 1.2 km east of the dam site and dug within the same rocks (the Pila Spi Formation) were adopted. The adopted data include (1) static friction angle, (2) rock density, and (3) cohesion for the construction of the stereonet projections, the adopted data are shown in (Table IV). To illustrate the relation

TABLE VI
RESULTS OF KINEMATIC ANALYSIS OF THE 5 STUDIED STATIONS ON THE LEFT BANK OF THE HAMAMOK DAM

Station	Kinematic analysis	Stereographic and Dip analysis 2.0 projection results
6	-The Kinematic analysis in this station shows that the dip direction of Joint 2 is about N41°E dipping into the slope face (S70°W) and for toppling failure to occur it must be within about 10°, but in this station is more than 10° where the pole of Joint 2 lies outside the critical area (Fig. 5. 6B). - Numerical analysis by (Goodman and Bray, 1976): *(90°– ψf) + φj < ψp* (90–60)+31 <88=(61 <88) indicates that the potentiality of toppling failure is high.	The stereo net's slope stability analysis in (Fig. 6. 6B) shows that the pole of Joint 2 lies outside of the critical area (Daylight window) area. The analysis by DipAnalyst 2.0 software shows that Joint 2, lies on the edge of the shaded area Fig. 6. 6A). Therefore, toppling failure is possible and is increased by the activity of differential weathering and/or erosion of the claystone layer that underwent various degrees of weathering and/or erosion inward for the claystone slope face with a decrease in bearing capacity toward the slope.
7	-The Kinematic analysis in this station shows that the dip direction of joint 2 is about N30° E dipping into the slope face (S60°W) and for toppling failure to occur it must be within about 10°, but in this station is more than10°. -According to numerical analysis by (Goodman and Bray, 1976). (90-65)+31 <84=(56 <84)	Slope stability analysis by Stereo nets (Fig, 6. 7B) indicates that the toppling failure possibility is low by Joint 2 as the pole of joint 2 lies outside the critical area (Daylight window). The analysis by DipAnalyst 2.0 software shows that Joint 2, lies on the edge of the shaded area (Fig. 6. 7A). This means that the possibility for toppling failure is low because the activity of differential weathering and/or erosion of rock masses below the slopes leads to gradation in weathering, the blocks move gradually and then topple.
8	The Kinematic analysis in this station shows that the dip direction of joint 2 is about N39°E dipping into the slope face (S50°W) and for toppling failure to occur it must be within about 10°, but in this station, it is <10° and as it is clear in (Fig. 5. 8B) the pole of Joint 2 lies in the critical area (between two lateral limit lines within the daylight envelope area). Therefore, the potentiality of toppling failure is high. - According to equation analysis. (90-80)+31 <80=(41 <80)	The stereographic projection in this station (Fig. 6. 8B) shows that the possibility of toppling failure is high where the pole of Joint 2 lies in the critical area (Daylight window) on the edge of the two lateral limit lines for toppling failure. This means the blocks in this station are more prone to toppling failure than sliding where the pole of Joint 2 is far and out of the sliding failure criteria. The analysis by DipAnalyst 2.0 software shows that Joint 2, lies on the edge of the shaded area (Fig. 6. 8A), where toppling failure is possible and is increased by the activity of differential weathering and/or erosion of rock masses below the slopes.
9	The Kinematic analysis shows that the dip direction of joint 2 has a main effect on toppling failure to occur in this station as it is about N28°E dipping into the slope face (S40°W) within about 10°. -Numerical analysis according to equations by (Goodman and Bray, 1976) shows that (90-82)+31=88=(39<88) Therefore, in this station potentiality of toppling failure is high.	The stereo net's slope stability calculation for station 9 (Fig. 6. 9B) shows that the possibility for toppling failure in this station is high, where the pole of Joint 2 lies inside the critical area (Daylight window) and between the two lateral limit lines. This means that blocks in this station are more prone to toppling failure than sliding where the pole of joint 2 is far and out of the sliding failure criteria. The analysis by DipAnalyst 2.0 software shows that Joint 2, lies within the triangular shaded area (area for toppling failure) (Fig. 6. 9A)
10	The Kinematic analysis shows that the attitude of joint 2 has a main effect on toppling failure to occur in this station as it is about N32°E dipping into the slope face has attitude (S30°W) within about 10°. - According to equation analysis (90-85)+31=85=(36<85). Therefore, the potentiality of toppling failure is almost high.	The stereographic analysis for this station (Fig. 6. 10B) shows that the possibility of Toppling failure is high, where the pole of joint 2 lies inside the critical area (Daylight window) This means the blocks in this station are more prone to toppling failure than sliding where the pole of Joint 2 is far and out of the sliding failure criteria. The analysis by DipAnalyst 2.0 software shows that Joint 2, lies on the edge of the triangular shaded area (Figure 6. 10A), where toppling failure is possible.

between the slope face direction and the orientation (dip and strike) of the joints and bedding planes of the exposed rocks at all 10 stations, stereographic projections were constructed by Stereonet v11 software.

VII. Conclusions

To evaluate the stability of the banks of the Hamamok Dam site, two methods have been applied. Bejerman's Method, based on 10 attributes, which were measured and/or estimated directly in the field. The results showed that the LPI values range between 23 and 27, which means High to Very high failure possibility. The second method is the Kinematic method; based on DipAnalyst 2.0 software, and drawing the stereographic projection using Stereonet v11 software showed that the right bank (Stations 1–5) suffers from plane sliding, whereas the left bank (Stations 6–10) suffers from toppling. In both banks, Joint 2 has the main role in the developed unstable slopes. This is attributed to its strike direction and dip amount.

VIII. Recommendations

Based on the acquired data on the stability of both banks and landslide possibility and their type, and because the hard carbonate rocks of the Pila Spi Formation form the top slope part, the main reasons for the possible failure are the orientation and dip amount of the bedding and joint planes; therefore, the protection measures which can be recommended are: (1) Digging a ditch on the top slope and line it by concrete to decrease the infiltration of rainwater to the rocks, (2) the ditch will also decrease the infiltrated water to the soft red claystone, which will form as a lubricant to the overlying hard carbonate rocks of the Pila Spi Formation, (3) to increase

http://dx.doi.org/10.14500/aro.11553

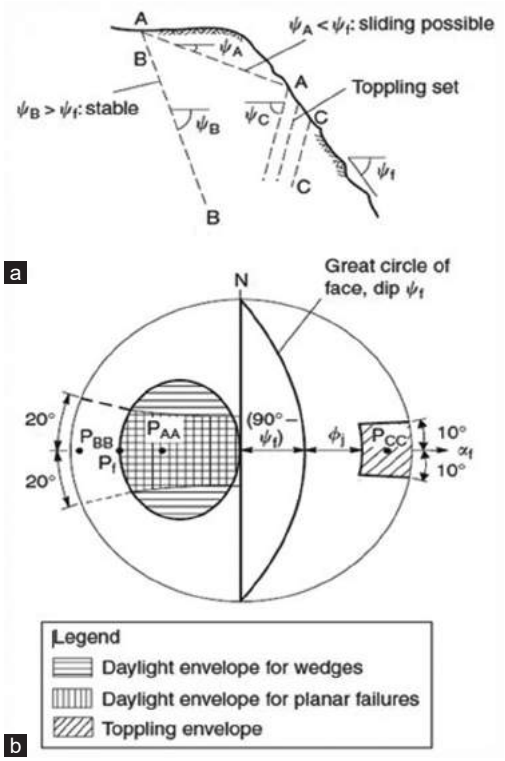

Fig. 8. Kinematic analysis of blocks of rock in slope: (a) discontinuity sets in slope; and (b) daylight envelopes on equal area stereonet.

the vegetation cover on the slopes of red soft rocks of the Gercus Formation to decrease the weathering and erosion of the soft clastic rocks which accelerate the toppling and sliding of the hard carbonate rocks, and (4) although we could not recognize very large blocks on the top slope, a detailed check should be done to check if such blocks exist or otherwise. If yes, then bolting to the bedrock should be done.

References

Bejerman, N., 1994. Landslide Possibility Index System. In: *7th International Congress International Association of Engineering Geology*. Balkema, Rotterdam, pp.1303-1306.

Bejerman, N.J., 1988. Evaluation of Landslide Susceptibility along a Sector of State Road E-5. In: *8th International Congress of IAEG*. Vancouver, Canada, Balkima, Rotterdam.

Bosphorus Technical Consulting Corporation, 2012. (*Bosphorus Technical Consulting and Corporation*) *Design of Haibat Sultan Tunnel and Approach Roads Report*. The Ministry of Housing and Constructions, Erbil, Iraq.

Esriimage, 2023. Available from: https://earthexplorer.usgs.gov [Last accessed on 2023 Jun 05].

Fouad, S.F.A., 2015. Tectonic Map of Iraq, Scale 1: 1000000. *Iraqi Bulletin of Geology and Mining,* 11(1), pp.1-8.

Goodman, R.E., 1976. *Methods of Geological Engineering in Discontinuous Rocks.* West Publishing Co., St.Paul.

Goodman, R.E., and Bray, J., 1976. Toppling of Rock Slopes. In: *Proceedings of the Specialty Conference on Rock Engineering for Foundations and Slopes*. ASCE, pp.201-234.

Hocking, G., 1976. Amethod for distinguishing between single and double plane sliding of tetrahedral wedges. *International Journal of Rock Mechanics and Mining Sciences*, 13, pp.225-226.

Hoek, E., and Bray, J., 1977. *Rock Slope Enginering.* 1st ed., IMM, London.

Hoek, E., and Bray, J., 1981. *Rock Slope Engineering.* 3rd ed., Institution of Mining and Metallurgy, London, UK.

Inkatlas, 2023. *Inkatlas.* Available from: https://inkatlas.com/create [Last accessed on 2023 Jun 04].

Markland, J., 1972. *A Useful Technique for Estimating the Stability of Rock Slopes when the Rigid Wedge Slide Type of Failure is Expected*. Imperial College Rock Mechanics Research Report No 19.

Sissakian, V.K., and Fouad, S.F., 2014. *The Geology of Erbil and Mahabad quadrangles, scale 1:250,000*. Iraq Geological Survey Publications, Baghdad, Iraq.

Sissakian, V.K., Ghafur, A.A., Ibrahem, F.I., Abdulhaq, H.A., Hamoodi, D.A., and Omer, H.O., 2022. Suitability of the carbonate rocks of the bekhme formation for cement industry, Hareer Mountain, North Iraq, Kurdistan Region. *Iraqi Geological Journal*, 54(2c), pp.59-67.

Sissakian, V.K., Hamoudi, D.A., Omer, H.O., and Niazi, S.A., 2019. Assessment of the carbonate rocks of the Pila Spi formation for cement industry, in Permam Mountain, Erbil, Iraqi Kurdistan Region. *UKH Journal of Science and Engineering*, 3(1), pp.1-9.

Wyllie, D., and Mah, C., 2005. In: Hoek, E., and Bray, J.W., editors. *Rock Slope Engineering: Civil and Mining*. 4th ed., Spon Press, Taylor and Francis Group, London, New York.

A Comprehensive Framework for Integrating Robotics and Digital Twins in Façade Perforation

Ahmed K. Ali

Department of Architectural Engineering, College of Engineering, University of Duhok,
Kurdistan region – F.R. Iraq

***Abstract*—In contemporary design practices, the conflict between initial design approaches and subsequent manufacturing and construction stages presents a notable challenge. To address this disparity, our study aims to establish a comprehensive digital design workflow, bridging these gaps. The authors introduce a conceptual framework that seamlessly integrates the imperatives of LEED with the realm of robotic manufacturing, specifically tailored for construction sites. The proposed methodology encompasses four distinct iFOBOT modules: iFOBOT-environment, iFOBOT-design, iFOBOT-construct, and iFOBOT-monitor. The integration of these modules allows for a holistic approach to design and construction, fostering efficient collaboration between multidisciplinary teams. To validate the efficacy of the author's approach, we conducted an empirical study involving the creation of a double-skin facade panel perforation using this integrated process. Initial findings emphasize the enhanced constructability achieved through simulated robotic interventions utilizing a heuristic function. Moreover, this research presents a functional prototype as a tangible embodiment of the method's practical application and potential impact on the field of architectural design and construction.**

***Index Terms*—Architectural design, Digital workflow, Integrated technology, Perforated facades, Robotic fabrication.**

I. Introduction

The contemporary construction industry has undergone a profound transformation, driven by the ascendancy of automated systems and robotics, resulting in a departure from traditional practices. This paradigm shift holds the potential to address entrenched profitability challenges while concurrently enhancing operational efficiency (Kontovourkis, Tryfonos, and Georgiou, 2020; Kurtser, et al., 2020). Within this dynamic context, the realm of on-site robotics has emerged as a focal point of both scholarly and industrial exploration, obtaining considerable attention. The applications of on-site robotics encompass a diverse spectrum, ranging from tasks such as milling, perforation, and inspection (Rea and Ottaviano, 2018) to the intricate oversight of structural safety monitoring. The rapid advancements of digital design methodologies have seamlessly integrated into modern manufacturing and construction frameworks, liberating architects from the constraints of conventional Fordist standardization. This transformative shift has ushered in a post-Fordist era, characterized by uncharted design possibilities (Abbasnejad, et al., 2021; Babatunde, et al., 2020; Yang, et al., 2020).

Embedded within architectural discourse, building information modeling (BIM) occupies a pivotal role, acting as a catalyst that unfolds architectural arrangements and many design possibilities, tailored to both pre- and post-rationalization design paradigms (Abbasnejad, et al., 2021; Babatunde, et al., 2020). This capacity to foster careful decision-making, resonating with an intrinsic harmony essential within the dynamic realms of dynamic and synthetic design, is seamlessly imparted to designers through simulations, thereby enhancing their computational ability (Ali, Lee, and Song, 2020b).

The seamless transmission of design attributes and limitations from upstream to downstream is hindered by the lack of anticipatory provisions within existing design methodologies and analytical resources (Babatunde, et al., 2020). The management of multiple robots under specialized semi-automated construction conditions remains constrained by the scarcity of robust and efficient programming techniques (Kontovourkis, Tryfonos, and Georgiou, 2020; Zied, 2007). Challenges inherent in such programming tasks include the constant evolution of the construction environment, significantly lower production volumes in building projects, and the diverse array of tasks involved (Hook, 2016).

This study advances the field by introducing and validating an integrated system, encompassing four integral modules: iFOBOT-environment, iFOBOT-design, iFOBOT-construct, and iFOBOT-monitor. These modules establish an end-to-end digital design workflow merging architectural creativity with robotic precision. The empirical exploration substantiates enhanced constructability and a transformative shift in how architectural design and construction synchronize. Amidst these imperatives, an integrated architectural robotics workflow is meticulously constructed, evading the limitations of proprietary software systems. The objective

ARO-The Scientific Journal of Koya University
Vol. XII, No. 1 (2024), Article ID: ARO.11351. 12 pages
Doi: 10.14500/aro.11351
Received: 14 August 2023; Accepted: 23 May 2024
Regular research paper: Published: 19 June 2024
Corresponding author's e-mail: ahmed.khairadeen@uod.ac

is a comprehensive framework unifying double-skin façade panel perforation following LEED (Leadership in Energy and Environmental Design), integrating architectural, climatic, construction, and quality assurance considerations.

II. Literature Review

A. Automation, Robotics, and Design Complexity in Architecture

(Kreig, 2022) stated that the computational design and robotic manufacture of segmented wood shells are well-suited to illustrate the performative possibilities at the intersection of complex geometry (Krieg, 2022). This research explored the use of robotics in building-scale projects. Three examples of this type of work were built using robotically milled planar shell segments, scanned and milled natural tree forks (Keating, et al. 2017), and robotically stapled timber slats (Willmann, et al., 2016).

This study offers a thorough summary of earlier investigations into automated building progress monitoring using 3D scanning and extended reality (XR) technologies. This compilation serves as a valuable reference, offering insights into the evolution of this field, the strengths and limitations of different methodologies, and the existing gaps that warrant further investigation for more robust and effective automated progress monitoring solutions as depicted in Table I.

B. 3D Scanning and Virtual Reality Integration for Automated Construction Progress Monitoring

In the context of automated building progress monitoring, this section critically assesses the integration of 3D scanning technologies with extended reality (XR) applications. The examination encompasses the implications and advancements resulting from the convergence of these technologies, offering a comprehensive analysis of their transformative role in reshaping the field.

Production monitoring (Ali, Lee, and ParkAli et al., 2020a), tracking hardware and inventory (Bosché, et al., 2014), and progress measurements (Rebolj, et al., 2017) all primarily rely on manual visual assessments and traditional progress reports. However, these practices are neither commonplace nor efficient, often demanding significant time investment and being susceptible to errors (Rahimian, et al., 2020). Expounding on this notion, Park, et al. (2013) outline a comprehensive three-stage framework for implementing augmented reality (Park, et al., 2013). The exploration of the utilization of BIM and AR/VR has accumulated extensive attention within various studies. Zied (2007) delves into mobile augmented reality software, wherein users capture screenshots from the web and previously collected images (Zied, 2007).

Despite all the developments, it is still difficult to create a practical workflow that allows designers to smoothly use simulation results as guiding parameters and restrictions throughout the early stages of design. A thorough and accurate construction monitoring system that covers the complete building, including both its interior and exterior domains, during the construction timetable is also lacking, according to prior studies.

III. Methodology

Expanding on previous research focused on the picking and placing of facade panels using a robot arm in the construction site optimization (Ali, Lee, and Song, 2021), the primary aim of this study is to introduce a methodology for constructing facades using a robotic arm integration with the design process, real-time monitoring, and environmental awareness, directly on the construction site. This expanded framework offers the idea of double-skin facade perforation as a cutting-edge construction method, building on the capabilities of the prior iFOBOT system, which included environmental analysis in the design phase and real-time monitoring during construction.

This study addresses several central research inquiries. First, it endeavors to develop a user-friendly facade design tool aligned with the environmental analysis criteria stipulated by LEED. Second, the study explores the combining of environmental analysis and robotic constraints into simulation-based performance assessments, thereby enhancing designers' decision-making processes. Finally, the research probes the feasibility of integrating iFOBOT technology to seamlessly synchronize the design phases of a

TABLE I
Technology, Solutions, Methodologies, and Gaps in Previous Research on 3D Scanning and Extended Reality Integration for Automated Construction Progress Monitoring

Study	Technology used	Solution	Methodology	Gap
Jenny, et al., (2023)	Mobile AR, Screenshots	Real-time progress tracking	Capture screenshots from the web and previous images to provide virtual information based on the user's role	Limited focus on mobile AR's potential for comprehensive progress monitoring
Kwon, Park and Lim (2014)	BIM, Augmented Reality	Enhanced inspection models	Integrating precise BIM data into AR markers for defect detection and quality control	Emphasis on inspection lacks exploration of broader automated progress monitoring
Hashemi (2021)	Augmented Reality	Fusion of physical environment with virtual elements	Three-tiered AR implementation: item identification, virtual object projection, and physical-virtual fusion	Primarily discusses AR framework, minimal focus on 3D scanning integration
Current Study	3D Scanning, Extended Reality	Comprehensive automated progress monitoring	Integrating 3D scanning for spatial accuracy and XR for real-time visualization	Investigates combining 3D scanning with XR for comprehensive automatic monitoring of construction site

wall in the construction site, relegating human involvement to the selection of design parameters and the supervision of the robotic arm's perforation activities. The proposed approach involves using an arm alongside analysis to carry out the perforation of a double-skin facade directly at the construction site. This system is called the iFOBOT, which stands for its components; "i" represents human involvement "F" signifies facade design and fabrication, and "OBOT" highlights the integration of the robotic arm, within the system's framework.

The proposed system architecture consists of four modules: (1) The iFOBOT-environment module is responsible, for conducting environmental analysis tasks to determine the foundational parameters of the double-skin façade, (2) the iFOBOT-design module generates a layer for the double-skin facade based on specifications obtained from the previous module, (3) the iFOBOT-construct module controls the movements of robot arms during the on-site perforation process and the iFOBOT-monitor module supervises the process, and (4) The iFOBOT-monitor module oversees the process. It is important to note that the graphical algorithm editor Grasshopper, a pivotal tool within the iFOBOT system, is seamlessly integrated into the commercially available 3D modeling software Rhinoceros 3D ("Fologram," 2018) all visually depicted in Fig. 1.

- iFOBOT-environment module
  The iFOBOT-environment module aims to provide a comprehensive understanding of the construction site and its contextual factors. This involves the integration of Building Information Modeling (BIM) data and environmental parameters. The module's key steps include: (1) BIM integration: Importing the BIM model of the building project into the Grasshopper environment for subsequent analysis, (2) Environmental data incorporation: Introducing relevant environmental data, such as sun path analysis, weather conditions, and shading factors, to ensure accurate simulation outcomes, (3) Contextual analysis: Generating an iFOBOT-environment heat map that highlights areas of potential interest and impact on the construction site, (4) Data integration: Combining BIM and environmental data to create a comprehensive virtual representation of the construction site.
- iFOBOT-design module
  The iFOBOT-design module is responsible for generating optimal facade perforation designs based on defined criteria and constraints. The following steps outline its methodology: (1) Input parameters: Specifying parameters such as daylight requirements, thermal comfort thresholds, and LEED compliance criteria, (2) Facade perforation generation: Utilizing computational algorithms within Grasshopper to generate various facade perforation designs that meet the input parameters, (3) Heat map analysis: Employing the iFOBOT-environment heat map to evaluate the performance of each design in terms of daylight penetration and environmental impact, and (4) Optimization process: Iteratively refining the designs based on feedback from the heat map analysis to converge on an optimal perforation design.
- iFOBOT-construct module
  The iFOBOT-construct module translates the optimized design into physical construction actions through robotic

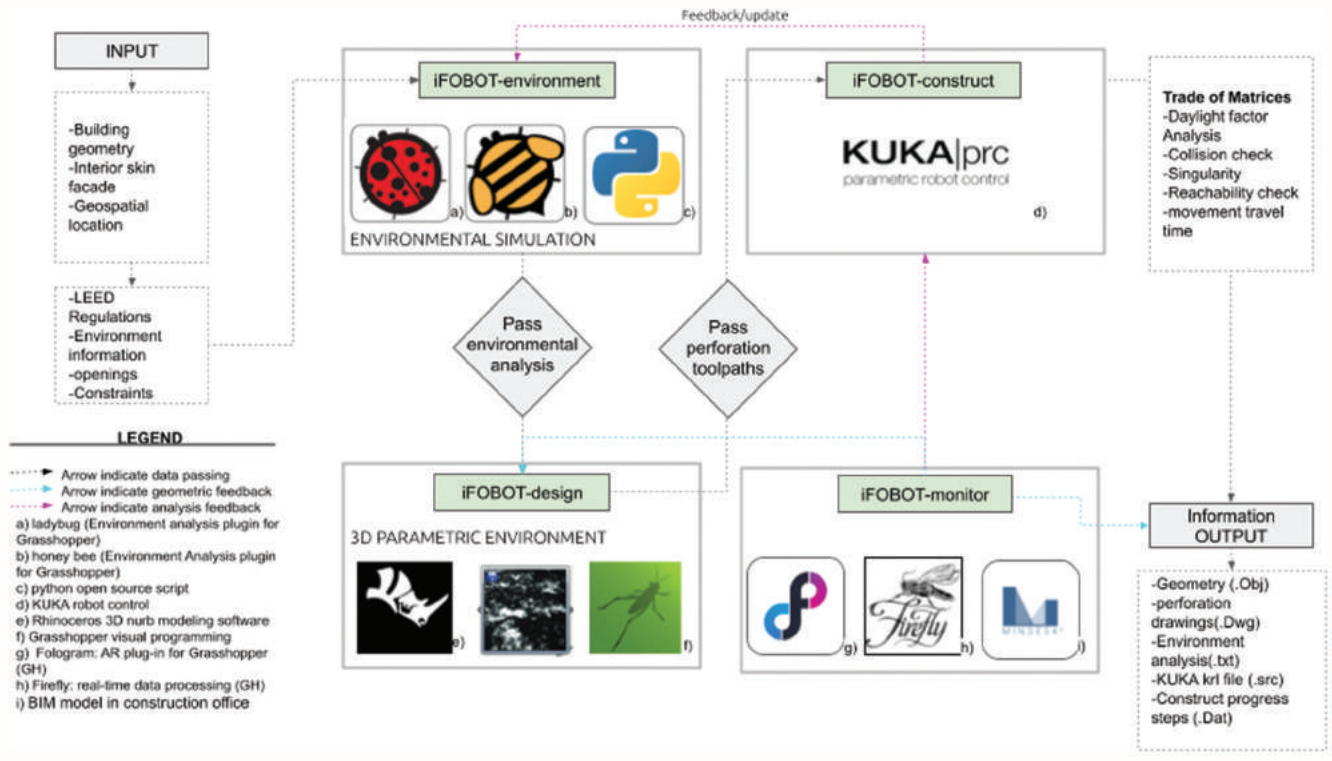

Fig. 1. The iFOBOT system's internal structure and the technique for transferring data between its many components.

perforation. The methodology comprises the following steps: (1) Geometry translation: Converting the finalized facade perforation design from the iFOBOT-design module into machine-readable commands for the robotic arm, (2) Robotic Path Planning: Developing a precise toolpath for the robotic arm to execute the perforation process efficiently and accurately, (3) real-time adjustment: Monitoring the robotic perforation process and making real-time adjustments based on environmental conditions and unforeseen obstacles, and (4) Quality assurance: Ensuring the quality and accuracy of the perforation process by validating the physical outcome against the digital design.

- iFOBOT-monitor module
  The iFOBOT-monitor module focuses on overseeing the robotic perforation process and facilitating communication between the construction site and the office. The methodology encompasses these steps: (1) Data acquisition: Capturing 3D point cloud data of the robotic perforation activity using a 3D camera, such as Kinect, (2) Data transformation: Converting the point cloud data into a 3D mesh representation for further analysis and inspection, (3) Data transmission: Transmitting the 3D mesh geometry from the construction site to the office for inspection and quality control, (4) Virtual reality inspection: Utilizing virtual reality interfaces, such as Oculus Rift, to enable inspectors to review and assess the as-built model in an immersive environment, and (5) Augmented reality feedback: Providing on-site workers with augmented reality feedback and reports for efficient communication and collaboration. Environment rule compliance and heat map generation (iFOBOT-environment Module)

The iFOBOT-environment module constitutes a sophisticated tool aimed at evaluating the adherence of facade designs to environmental regulations. Its primary function is to produce a heat map that identifies optimal areas for facade perforation, based on environmental considerations. Central to the iFOBOT-environment module's methodology is the meticulous evaluation of the annual solar exposure (ASE). This pivotal parameter serves as a cornerstone in assessing potential visual discomfort within the interior spaces of the building and contributes to determining the LEED v4 daylight credit. The approach involves constraining direct sunlight exposure beyond 1000 lux to no more than 250 h annually, ensuring it accounts for no less than 10% of the interior space ($ASE_{1000,250}$). This assessment operates at a specific work plane height of 750 mm above the finished floor, with the ASE grid size confined to dimensions below 600 mm^2 as visualized in Fig. 2.

The iFOBOT-construct module uses the KUKA|prc plugin ("KUKA|prc – parametric robot control for Grasshopper," 2011) to perform its tasks within the Grasshopper framework. This plugin enables the building of a parametric model for the trajectory of the robot arm as well as the production of a kinematic simulation of the robot's movements. Notably, the module creates 3D models of the workstation that include the robot arm, the outer facade wall, building limitations, and the perforation toolpath from the perforation process as shown in Fig. 3.

A. Augmented Reality and 3D Scanning Integration for Construction Oversight (iFOBOT-monitor)

Within the overarching iFOBOT framework, the iFOBOT-monitor module assumes a pivotal role in employing

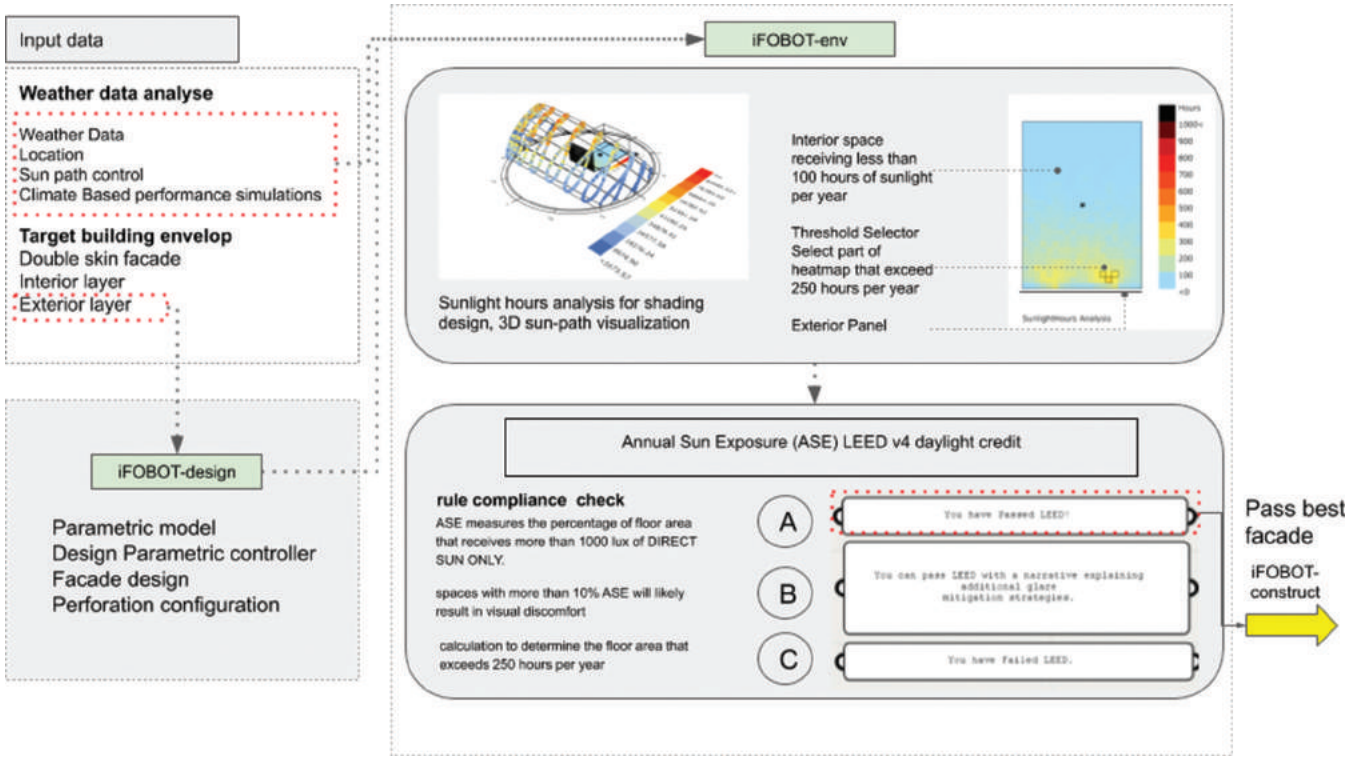

Fig. 2. Workflow and data interaction of iFOBOT-environment module with other modules.

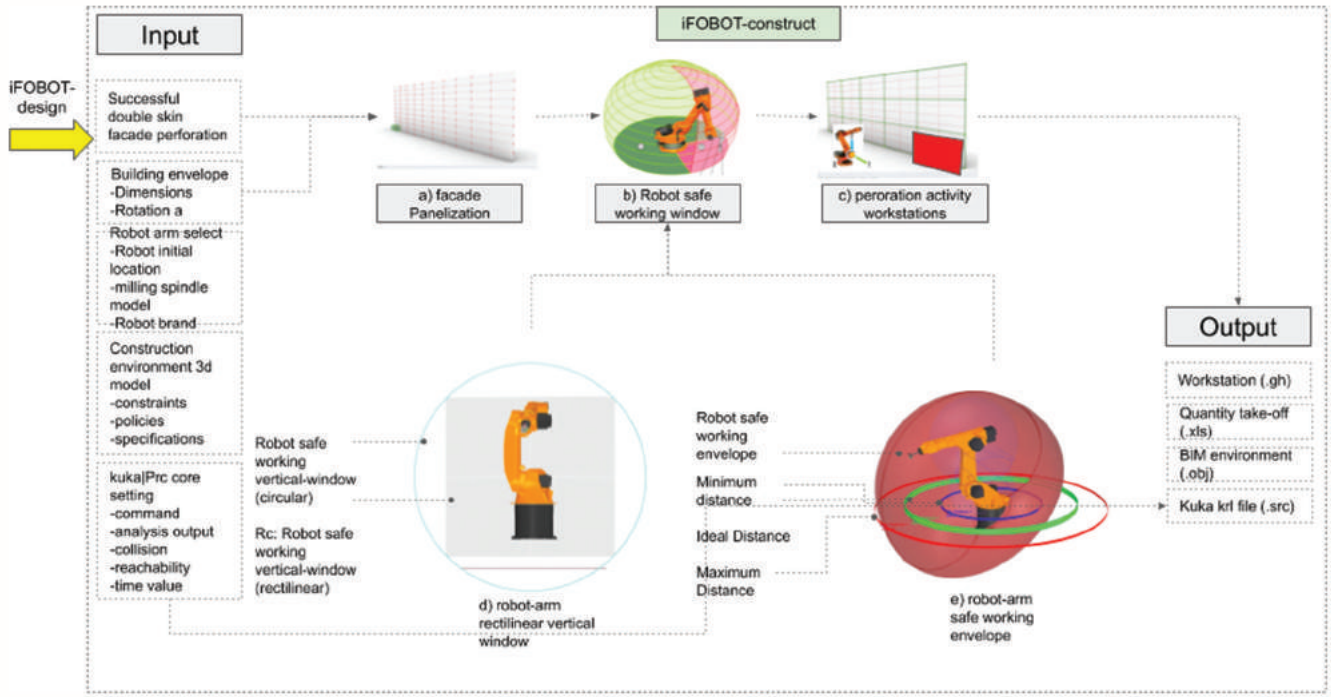

Fig. 3. Illustrates the workflow of the iFOBOT-construct module, focusing on robot simulation and the process of facade perforation.

augmented reality and 3D camera scanning to monitor the actions of the robotic arm within the construction site. Recognizing the dynamic and potentially hazardous nature of construction environments, the integration of a robust monitoring tool to capture and relay real-time data from the robotic arm's operations to the site office becomes indispensable during on-site perforation tasks. As a response to this imperative, the iFOBOT-monitor subsystem was seamlessly integrated into the broader iFOBOT system.

At its core, the iFOBOT-monitor strategy revolves around the continuous generation of 4D point clouds, achieved through the utilization of accessible and cost-effective on-site 3D scanning instruments, exemplified by the Kinect (Ali, Lee and Park, 2020a; Caruso, Russo and Savino, 2017; Weerasinghe, et al., 2012). At the construction job site (Location 1), the workflow commences with step 1, involving the utilization of a 3D LASER SCAN (c) employing the Xbox Kinect V2 laser scanning camera, connected to a dedicated computer (d). This initial step captures the physical environment in three dimensions, generating essential data for further analysis.

In step 2, this captured data undergoes a sequence of processing stages, encompassing POINT CLOUD MODELING. The process starts with Quokka (e), a tool for Kinect data processing within Grasshopper (GH), followed by real-time data processing facilitated by Firefly (f) within the Grasshopper environment. Tarsier (g) is then employed for point cloud management, and Speckle (h) handles real-time broadcasting of the collected data. Additionally, a 3D PARAMETRIC ENVIRONMENT (i) is established using Grasshopper, a graphical algorithm editor. Within this, step 3, engineers have the capability to remotely inspect the construction site from their office, facilitated by the Mindesk library integrated into Grasshopper (i). Rhinoceros (j), a 3D Nurbs modeling software, plays a pivotal role by converting the point cloud data from (i) into 3D geometry and subsequently feeds it into (i) for viewing in virtual reality. The building information modeling (BIM) model, represented in (k), serves as a crucial reference point in the construction office.

Finally, in Step 4, feedback is relayed to the workers on the job site. This feedback process is facilitated through the deployment of Fologram (a), an augmented reality plug-in integrated within Grasshopper (GH). Workers on the construction site receive this feedback on their smartphones (b). The feedback is presented in multiple layers, comprising the BIM model, a point cloud, and a BIM overlay model, as well as notes and drawings, providing a comprehensive and real-time insight into the project's status as shown in Fig. 4.

IV. Case Study

This section outlines the fundamental setup of the thermal model. It adopts a single-zone layout, representing a solitary room within a larger structure while treating the glass façade as non-adiabatic. Various shading techniques were applied to the model's external surfaces to facilitate comprehensive simulations of thermal properties, daylighting, and glare. The specific case study took place at the address 471-080 Galmae-dong Guri-si, Gyeonggi-do Seoul, South Korea, as depicted in Fig. 5.

Exploring the effectiveness of conventional shading strategies under stringent constraints involved an examination of four distinct facade design alternatives. The

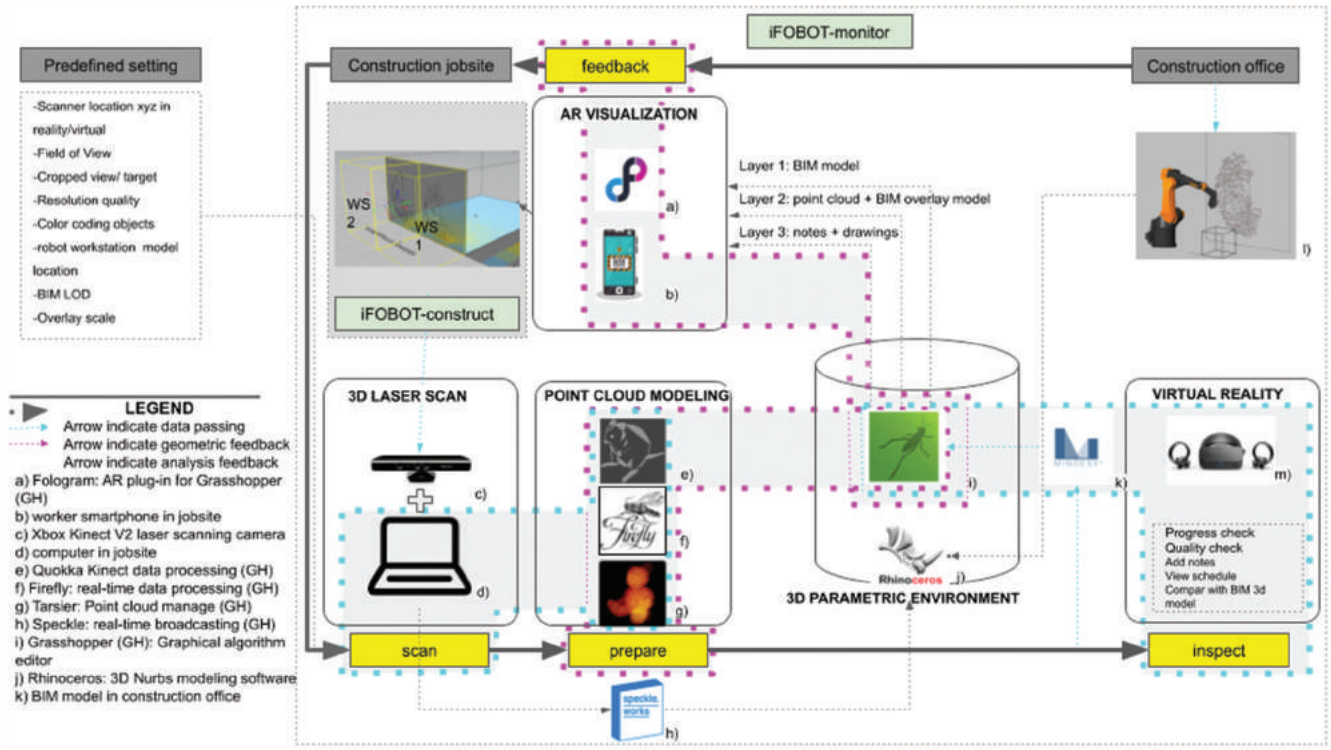

Fig. 4. The iFOBOT-monitor module utilizes 3D laser scanning and extended reality technologies for visual progress assessment.

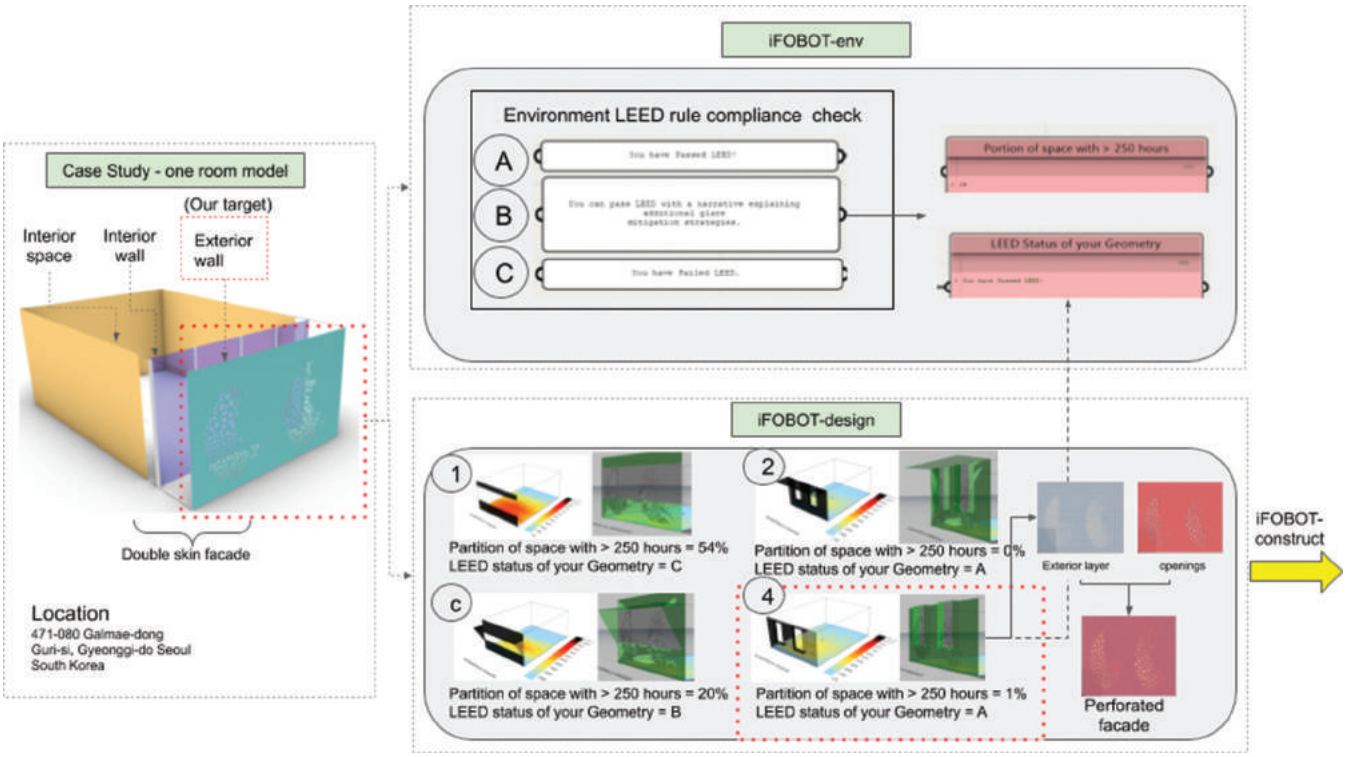

Fig. 5. Illustration of iFOBOT environment and design tool in a building's single room case study.

iFOBOT process was initiated by simulating these exterior configurations within the iFOBOT-environment, focusing on areas exposed to over 250 h of daylight and evaluating their compliance with LEED standards.

The initial design encompassed a partition of space with daylight exposure exceeding 250 h, accounting for 54% of the area; however, it did not meet LEED v4 requirements. In contrast, the second design achieved a partition with no daylight exposure beyond 250 h, aligning with LEED v4 criteria. The third design featured a partition of space with over 250 h of daylight, constituting 20% of the area, with a Geometry classification of "B" according to LEED standards. The fourth

design achieved a partition with only 1% of the space exposed to more than 250 h of daylight and successfully complied with the LEED v4 index. These distinct facade designs are visually depicted in Fig. 5, labeled as designs 1, 2, 3, and 4.

The integration of the model into the Rhino simulation environment facilitated an understanding of how building constraints impact the shading system's efficiency. This iterative feedback process informed the generation of robotic code for subsequent production, resulting in a comprehensive study that harmonized design performance and constraints. The case study is presented in a series of steps:

1. Initial Setup and Design Conceptualization:
   - Define the scope of the case study, focusing on the design and robotic fabrication of a double-skin facade system
   - Develop the preliminary design concepts for the double-skin facade, considering architectural esthetics and environmental performance
   - Identify the facade's perforation requirements and its alignment with the LEED v4 daylighting index.
2. iFOBOT-Environment Simulation:
   - Utilize the iFOBOT-environment module to simulate the environmental performance of various facade perforation configurations
   - Generate heat maps and daylighting simulations to assess the impact of different perforation patterns on interior illumination levels and energy efficiency.
3. iFOBOT-Design and Optimization:
   - Employ the iFOBOT-design module to translate the environmental simulation results into specific perforation designs
   - Utilize parametric modeling tools to generate intricate and visually appealing facade perforation patterns while meeting the LEED v4 criteria.
4. Robotic Path Generation and Simulation:
   - Implement the iFOBOT-construct module to generate robotic toolpath trajectories for on-site perforation using a 6-axis robotic arm
   - Simulate the robotic path and verify its accuracy in a virtual environment, considering factors such as material thickness and fabrication constraints.
5. On-Site Robotic Perforation:
   - Deploy the generated robotic toolpath on the actual construction site using a KUKA HA 30/60 robotic arm
   - Monitor the robotic perforation process, ensuring alignment with the pre-simulated path and precise execution of perforations.
6. Data Capture and iFOBOT-Monitor Integration:
   - Employ the iFOBOT-monitor module to capture 3D point cloud data of the perforation process using a Kinect V2 camera
   - Convert the captured point cloud data into a 3D mesh representation and transmit it to the construction office for inspection.
7. Virtual Reality Inspection and Feedback:
   - Utilize augmented reality technologies and the iFOBOT-monitor module to conduct a virtual reality inspection of the as-built facade
   - Enable inspectors to review the perforation quality, make annotations, and assess adherence to design specifications.
8. Evaluation and Comparison:
   - Evaluate the performance and effectiveness of the robotic fabrication process based on the physical outcome and the alignment with design intent
   - Compare the as-built facade with the initial design and simulation results, highlighting areas of success and potential improvements.
9. Iterative Refinement and Future Considerations:
   - Use the insights gained from the case study to refine and optimize the iFOBOT workflow for future projects
   - Consider the integration of outdoor depth sensing sensors for improved data capture in outdoor environments.
10. Conclusion and Contribution:
    - Summarize the case study findings, emphasizing the efficacy of the integrated iFOBOT workflow in achieving a harmonious synergy between design and robotic fabrication
    - Highlight the broader implications of the study's contribution to the field of architecture, automation, and sustainable design.

By following these steps, the case study effectively demonstrates the practical application and benefits of the iFOBOT platform in the context of designing and fabricating a double-skin facade system

A. Verification of iFOBOT-environment and iFOBOT-design through a Practical Case Study

In the pursuit of validating the efficacy of iFOBOT-environment and iFOBOT-design, a comprehensive case study was undertaken. Leveraging the capabilities of the Grasshopper framework, the iFOBOT-design module employed an image collection tool to generate perforations aligned with the initial facade openings. This process was guided by the heat map derived from the optimal facade design, designated as Façade Design 4 for this analysis. The resulting perforated facade apertures seamlessly transitioned from iFOBOT-design and iFOBOT-environment to the iFOBOT-construct module, facilitating a streamlined on-site construction process, as visually demonstrated in Fig. 5.

B. Case Study for iFOBOT Construct Validation

The validation process for iFOBOT-construct involved the utilization of a commercial 6-axis KUKA HA 30/60 robotic arm for the intricate perforation task. Employing a systematic approach, a series of specialized Grasshopper definitions was meticulously crafted to translate the meticulously optimized geometry positioning commands from earlier stages. This painstaking calibration ensured the attainment of stringent tolerances, further enhancing the quality and accuracy of the perforation process. Moreover, the enhanced manufacturing process incorporated robotic post-processing in its raw state, guaranteeing uniform thickness and meticulous shaping of components, thereby culminating in a cohesive and exacting outcome, as vividly depicted in Fig. 6.

http://dx.doi.org/10.14500/aro.11351

C. Case Study Validating iFOBOT-Monitor: Monitoring and Data Exchange Workflow

This case study scrutinizes the effectiveness of iFOBOT-monitor in supervising perforation activities and delivering real-time updates to the construction office. The module's operation commences with the acquisition of 3D point cloud data through a comprehensive scene scan conducted by a 3D camera. Subsequent to data collection, a transformation process ensues, transitioning from point cloud modeling to the creation of a 3D mesh representation.

The pivotal role of the iFOBOT-monitor module within the iFOBOT framework becomes evident through its efficient and rapid data exchange between the project site and the construction office. Integration of diverse technologies onto a single platform facilitates seamless communication, exemplified by an average 17-min data exchange cycle. Visual comparison between the digital model and the job site point cloud offers a definitive means of assessing the accuracy of robotic movements and perforation processes, as demonstrated in Fig. 7.

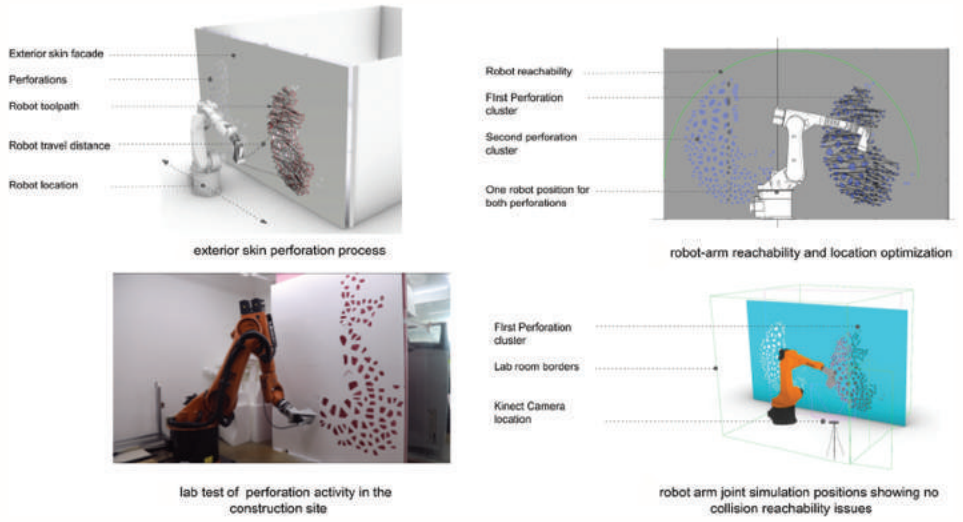

Fig. 6. Implementation of perforation process at the construction site utilizing robotic arm technology.

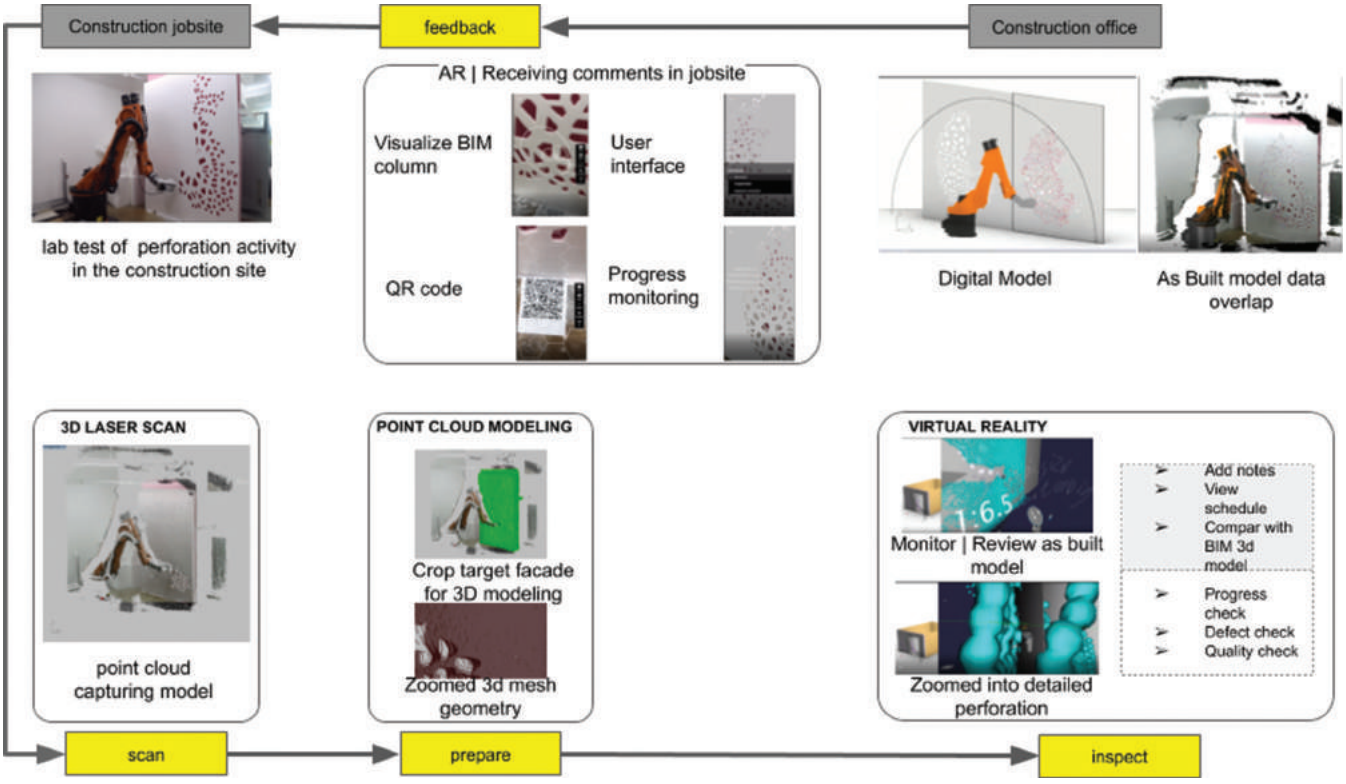

Fig. 7. The case study for the iFOBOT-monitor module involves the examination of point cloud generation and the utilization of extended reality technologies.

In the iFOBOT-monitor module's "Inspect" phase, virtual reality functionalities are facilitated through the Mindesk library, enabling remote inspection by engineers situated in the office. In the ensuing "Feedback" stage, the worker leverages augmented reality technology managed by the Fologram library within the iFOBOT-monitor module. Here, the worker can: employ QR codes to superimpose the digital model onto the actual wall; access comments provided by the inspector; and explore the BIM digital model through layered visualization. The amalgamation of mixed reality technologies enhances visual communication between the office and the construction site throughout the construction process as shown in Fig. 8.

This research provides a comprehensive depiction of the quantifiable workflow and the corresponding advantages realized during the validation of iFOBOT-Monitor in Case Study C. Quantitative metrics within the table highlight the average duration of data exchange between the construction site and office, effectively showcasing the remarkable efficiency gains achieved. Furthermore, the table underscores the module's intrinsic capability to visually assess the precision of robotic movements and the accuracy of the perforation process by superimposing the digital model onto the point cloud. This detailed analysis underscores the robustness and efficacy of iFOBOT-monitor in enhancing and optimizing construction procedures as shown in Table II.

V. Discussion

This study introduces an enhanced iFOBOT system, specifically tailored for the on-site perforation of dual skin surfaces, and provides a comprehensive assessment of its capabilities. The case study elucidated the profound influence of design parameters and perforation angles on design evolution and system dynamics. The precision of perforation scale and arrangement within the double skin façade is effectively regulated through the intricate interplay between iFOBOT-design and iFOBOT-environment, ensuring adherence to the LEED v4 index criteria. Empirical trials

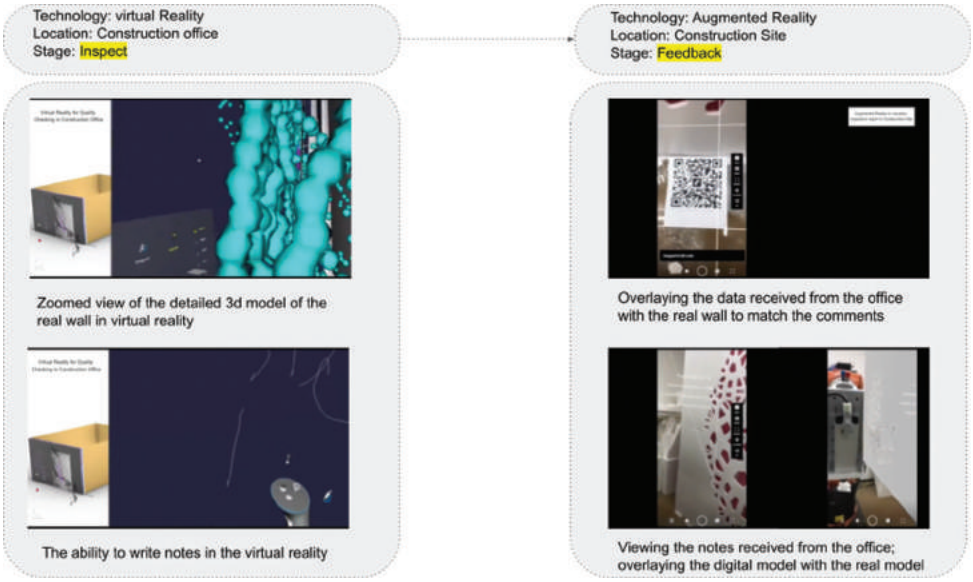

Fig. 8. Virtual reality and augmented reality technology tools are used in the inspection and feedback section.

TABLE II
The Information Presented in a Quantifiable Table Format

Case Study C: iFOBOT-Monitor Validation	
Monitoring and Data Exchange Workflow	
Step	Average time (min)
Acquisition of 3D Point Cloud Data	12
Point Cloud to 3D Mesh Transformation	5
Data Transmission to Construction Office	2
Virtual Reality Inspection and Report Generation	10
Feedback Report Communication to On-site Worker	5
Data Exchange Cycle	Average: 17
Benefits and Outcomes	
Real-time Monitoring and Reporting	Efficient oversight of perforation operations and instant status updates
Data Exchange Efficiency	Rapid data exchange between the project site and construction office
Visual Inspection in Virtual Reality	Detailed assessment and annotation of the as-built model
Accuracy Assessment	Comparison of digital model and job site point cloud for precise evaluation

yielded promising outcomes, with approximately 1.5 h expended to complete half of the perforation task.

While the Kinect camera employed in this study demonstrated optimal performance within controlled indoor lighting environments, its efficacy is constrained when deployed outdoors. As a future enhancement, we envisage the integration of outdoor depth sensing sensors such as ZED 2 ("ZED 2 – AI Stereo Camera | Stereolabs," n.d.) into the iFOBOT system, catering to a broader range of environmental conditions. Furthermore, data collection and assessment will be pursued to refine the heuristic methodology and facilitate module optimization. The seamless integration of geometry and data flow throughout the various iFOBOT modules remains a focal point for future endeavors. Enhancing dataflow to incorporate essential feedback gleaned from building inputs and simulations represents a pivotal stride toward fortifying the efficacy of the iFOBOT framework as illustrated in Table III.

Finally, the iFOBOT-monitor module plays a pivotal role in real-time oversight and management of the perforation process. Facilitating remote monitoring and data collection, this module ensures quality control and collaboration between on-site teams and the construction office. Its real-time insights provide numerous benefits, allowing for timely adjustments, quality assessments, and effective issue resolution. However, the module's efficacy may be contingent on stable communication networks and robust data acquisition, with potential limitations arising from data quality and resolution as shown in Table IV.

To comprehensively evaluate the performance and usability of the iFOBOT platform and its individual modules, a thorough assessment was conducted involving 30 experienced engineers from diverse backgrounds. In the assessment process, each module (iFOBOT-environment, iFOBOT-design, iFOBOT-construct, iFOBOT-monitor) and the iFOBOT platform as a whole are evaluated based on various survey questions. Engineers provide their rankings on a scale of 1–5, with 1 being the lowest and 5 being the highest satisfaction level. The table provides an overview of the survey results, allowing for a quick comparison of the user evaluation for each module and the overall platform as shown in Table V.

TABLE III
Comparison of iFOBOT with Other Platforms and Previous Research

Aspect	iFOBOT	Platform A (Kim, Konstantzos and Tzempelikos, 2007)	Platform B (Keating and Oxman, 2013)	Platform C (Kim, Konstantzos and Tzempelikos, 2020)
Perforation Task	On-site dual skin perforation with augmented reality feedback and monitoring	Exterior facade perforation with digital simulation and visualization	Robotic fabrication of building envelope using the multi-axis robotic arm	Single-layer facade perforation with low-cost robotic manipulation
Design Integration	Integrating design, simulation, and production processes in a seamless manner on a single platform	One software environment for the design and manufacturing processes	Separate design and fabrication processes	Integrated design and fabrication processes within a single platform
Robotic Arm Capability	6-axis KUKA HA 30/60 with efficient tool path generation and perforation control	4-axis robotic arm with limited tool path generation and perforation control	Multi-axis robotic arm with adaptable tool path generation and control	Multi-axis robotic arm with adaptable tool path generation and control
Data Exchange	Rapid and efficient data exchange between design, fabrication, and construction processes	Limited data exchange between design and fabrication processes	Data exchange with remote operation site and construction processes	Real-time data exchange and monitoring capabilities
Strengths	Real-time monitoring with augmented reality feedback, seamless design integration, rapid data exchange, and efficient robotic perforation control	Efficient design and fabrication processes within a unified environment	Multi-axis robotic arm with adaptable tool path generation and control	Integration of design, simulation, fabrication, and monitoring processes within a single platform
Weaknesses	Limited outdoor use, potential camera limitations, manual adjustments for optimal scanning	Limited capabilities for complex designs, limited tool path generation, no augmented reality feedback	Limited adaptability to varying designs, limited structural adaptability	Limited adaptability to complex designs, limited tool path generation, no real-time monitoring

TABLE IV
Comparison of Objectives, Benefits, and Limitations of iFOBOT Modules

iFOBOT Module	Objectives	Benefits	Limitations
iFOBOT-environment	Create an integrated digital workspace for architectural designs with environmental considerations	Real-time feedback, informed design decisions, performance metrics	Environmental simulation accuracy influenced by input data
iFOBOT-design	Automate facade design generation adhering to performance criteria	Efficient design exploration, streamlined decision-making	Potential constraints in addressing esthetics and complexities
iFOBOT-construct	Generate precise robotic tool paths and control commands for on-site fabrication	Enhanced fabrication accuracy, error minimization	Calibration and environmental variations affecting accuracy
iFOBOT-monitor	Provide real-time oversight and data management for perforation operations	Quality control, remote collaboration, timely adjustments	Dependence on stable communication, data quality, and resolution

TABLE V
User Assessment Results for iFOBOT Modules

Survey Question	iFOBOT-Environment	iFOBOT-Design	iFOBOT-Construct	iFOBOT-Monitor	iFOBOT Platform
Interface design	4.3	4.1	3.9	4.2	4.1
System flexibility	3.9	4.2	3.7	4.0	4.0
User friendliness	4.2	4.3	3.8	4.1	4.1
Learning curve	4.0	4.2	3.6	4.0	4.0
Efficiency in design process	4.1	4.3	3.8	4.2	4.1
Precision of generated design	3.8	4.2	3.9	4.1	4.0
Integration with existing software/tools	4.0	4.1	3.9	4.2	4.1
Real-time data exchange	4.1	4.0	3.7	4.3	4.1
Monitoring accuracy	3.9	4.0	3.8	4.2	4.0
Data visualization quality	4.2	4.3	3.9	4.1	4.1
Overall user satisfaction	4.1	4.2	3.8	4.2	4.1

The assessment outcomes from 30 engineers provide valuable insights into the usability and effectiveness of each iFOBOT module. Notably, iFOBOT-environment received high praise for its intuitive interface and efficient parameter input, resulting in an average ranking of 4.6 out of 5. iFOBOT-design, though positively received (average ranking of 4.3), was noted for a slight learning curve, suggesting the need for improved guidance. iFOBOT-construct, with an average ranking of 4.5, impressed users with its ability to generate accurate milling paths for robotic arms.

In conclusion, the comprehensive user assessment of the iFOBOT platform, involving a diverse group of 30 engineers, has provided valuable insights into the practical usability and effectiveness of each module. The obtained rankings, ranging from 1 (Low) to 5 (High), offer a quantifiable measure of the user experience, ease of use, and perceived benefits of the iFOBOT-environment, iFOBOT-design, iFOBOT-construct, and iFOBOT-monitor modules. The overall positive feedback indicates that the platform holds significant promise for enhancing efficiency and precision in robotic-assisted construction tasks. This assessment serves as a crucial step in validating the real-world applicability and user-centric design of the iFOBOT system, paving the way for further refinements and broader adoption in the construction industry.

VI. Conclusion

This study introduces a comprehensive and integrated methodology for robotic manufacturing, showcasing its adaptability to diverse material systems. Although specifically tailored to a high-performance ceramic facade system, the proposed framework demonstrates its potential applicability across various architectural contexts. The consolidation of crucial operations within a unified software framework, facilitated by custom Grasshopper scripts and components, serves as a catalyst for enhanced collaboration among key stakeholders involved in conceiving specialized and high-performance facade designs. Moreover, the automated workflow streamlines the production process, allowing for iterative exploration of building geometry and validation of its alignment with design intent during the early design phases.

Environmental optimization emerges as a pivotal contributor, enabling the generation of highly customized facade patterns that exhibit both complexity and esthetic appeal. The pragmatic dimension of this approach transcends performance-driven objectives, responding to a growing interest in meticulous parametric design representations that foster demand for optimization in their own right. The fusion of intricate geometries with established manufacturing practices, underpinned by digital design methodologies, underscores the feasibility of translating diverse design visions into tangible architectural realities.

Within the discourse of architectural discourse, the perpetual dichotomy between cost-effective, high-volume industrial manufacturing and bespoke, design-driven architecture has been an ongoing deliberation. This study suggests that the convergence of robotic technologies and design automation presents a potential reconciliation, offering a compelling third perspective. The coexistence of these attributes underscores that prioritizing environmental efficiency as a guiding principle need not eclipse the fundamental essence of architectural creativity. This synthesis of technological advancement and artistic expression opens avenues for design solutions that resonate with both economic considerations and design aspirations, thus contributing to the evolution of architectural practice.

References

Abbasnejad, B., Nepal, M.P., Ahankoob, A., Nasirian, A., and Drogemuller, R., 2021. Building Information Modelling (BIM) adoption and implementation enablers in AEC firms: A systematic literature review. *Architectural Engineering and Design Management*, 17, pp.411-433.

Ali, A.K., Lee, O.J., and Park, C., 2020a. Near real-time monitoring of construction progress: Integration of extended reality and kinect V2. In: *Proceedings of the International Symposium on Automation and Robotics in Construction*. IAARC Publications, pp.24-31.

Ali, A.K., Lee, O.J., and Song, H., 2020b. Generic design aided robotically facade pick and place in construction site dataset. *Data in Brief*, 31, p.105933.

Ali, A.K., Lee, O.J., and Song, H., 2021. Robot-based facade spatial assembly optimization. *Journal of Building Engineering*, 33, p.101556.

Babatunde, S.O., Ekundayo, D., Adekunle, A.O., and Bello, W., 2020. Comparative analysis of drivers to BIM adoption among AEC firms in developing countries: A case of Nigeria. *Journal of Engineering Design and Technology*, 18, pp.1425-1447.

Bosché, F., Guillemet, A., Turkan, Y., Haas, C.T., and Haas, R., 2014. Tracking the built status of MEP works: Assessing the value of a Scan-vs-BIM system. *Journal of Computing in Civil Engineering*, 28, p.05014004.

Caruso, L., Russo, R., and Savino, S., 2017. Microsoft Kinect V2 vision system in a manufacturing application. *Robotics and Computer-Integrated Manufacturing*, 48, pp.174-181.

Fologram, 2018. Food4Rhino. Available from: https://www.food4rhino.com/en/app/fologram [Last accessed on 2023 Aug 14].

Hashemi, M., 2021. *Human-Robot Collaborative Design (HRCoD): Real-Time Collaborative Cyber-Physical HMI Platform for Robotic Design and Assembly through Augmented Reality* (PhD Thesis). Kent State University.

Hook, J., 2016. *Automated Digital Fabrication Concept for Composite Facades.* Honours Thesis. The University of Queensland.

Jenny, S.E., Pietrasik, L.L., Sounigo, E., Tsai, P.H., Gramazio, F., Kohler, M., Lloret-Fritschi, E., and Hutter, M., 2023. Continuous mobile thin-layer on-site printing. *Automation in Construction*, 146, p.104634.

Keating, S., and Oxman, N., 2013. Compound fabrication: A multi-functional robotic platform for digital design and fabrication. *Robotics and Computer-Integrated Manufacturing*, 29, pp.439-448.

Keating, S.J., Leland, J.C., Cai, L., and Oxman, N., 2017. Toward site-specific and self-sufficient robotic fabrication on architectural scales. *Science Robotics*, 2, p.eaam8986.

Kim, M., Konstantzos, I., and Tzempelikos, A., 2020. Real-time daylight glare control using a low-cost, window-mounted HDRI sensor. *Building and Environment*, 177, p.106912.

Kim, Y.S., Jung, M.H., Cho, Y.K., Lee, J., and Jung, U., 2007. Conceptual design and feasibility analyses of a robotic system for automated exterior wall painting. *International Journal of Advanced Robotic Systems*, 4, p.49.

Kontovourkis, O., Tryfonos, G., and Georgiou, C., 2020. Robotic additive manufacturing (RAM) with clay using topology optimization principles for toolpath planning: The example of a building element. *Architectural Science Review*, 63, pp.105-118.

Krieg, O.D., 2022. *Architectural Potentials of Robotic Manufacturing in Timber Construction: Strategies for Interdisciplinary Innovation in Manufacturing and Design*. Institute for Computational Design and Construction, University, Stuttgart.

KUKA. Prc- Parametric Robot Control for Grasshopper, 2011. Food4Rhino. Available from: https://www.food4rhino.com/en/app/kukaprc-parametric-robot-control-grasshopper [Last accessed on 2023 Aug 14].

Kurtser, P., Ringdahl, O., Rotstein, N., Berenstein, R., and Edan, Y., 2020. In-field grape cluster size assessment for vine yield estimation using a mobile robot and a consumer level RGB-D camera. *IEEE Robotics and Automation Letters*, 5, pp.2031-2038.

Kwon, O.S., Park, C.S., and Lim, C.R., 2014. A defect management system for reinforced concrete work utilizing BIM, image-matching and augmented reality. *Automation in Construction*, 46, pp.74-81.

Park, C.S., Lee, D.Y., Kwon, O.S., and Wang, X., 2013. A framework for proactive construction defect management using BIM, augmented reality and ontology-based data collection template. *Automation in Construction*, 33, pp.61-71.

Rahimian, F.P., Seyedzadeh, S., Oliver, S., Rodriguez, S., and Dawood, N., 2020. On-demand monitoring of construction projects through a game-like hybrid application of BIM and machine learning. *Automation in Construction*, 110, p.103012.

Rea, P., and Ottaviano, E., 2018. Design and development of an inspection robotic system for indoor applications. *Robotics and Computer-Integrated Manufacturing*, 49, pp.143-151.

Rebolj, D., Pučko, Z., Babič, N.Č., Bizjak, M., and Mongus, D., 2017. Point cloud quality requirements for Scan-vs-BIM based automated construction progress monitoring. *Automation in Construction*, 84, pp.323-334.

Weerasinghe, I.T., Ruwanpura, J.Y., Boyd, J.E., and Habib, A.F., 2012. Application of Microsoft Kinect sensor for tracking construction workers. In: *Construction Research Congress 2012: Construction Challenges in a Flat World*. American Society of Civil Engineers, Reston, pp.858-867.

Willmann, J., Knauss, M., Bonwetsch, T., Apolinarska, A.A., Gramazio, F., and Kohler, M., 2016. Robotic timber construction-Expanding additive fabrication to new dimensions. *Automation in Construction*, 61, pp.16-23.

Yang, D., Li, Y., Li, T., Zhang, T., Han, M., and Yan, H., 2020. The system design of external cladding installation robot. *International Journal of Advanced Robotic Systems*, 17.

ZED 2 - AI Stereo Camera, n.d. Stereolabs. Available from: https://www.stereolabs.com/zed-2 [Last accessed on 2023 Aug 14].

Zied, K., 2007. An augmented framework for practical development of construction robots. *International Journal of Advanced Robotic Systems*, 4, p.43.

Upright Pyramid Surface Textures for Light Trapping and MoOx Layer in Ultrathin Crystalline Silicon Solar Cells

Halo D. Omar

Department of Physics, Faculty of Science and Health, Koya University,
Koya KOY45, Kurdistan Region - F.R. Iraq

***Abstract*—In this work, ray tracing is used to investigate the optical characteristics of various surface structures in ultrathin crystalline silicon (c-Si) for solar cells. Ultrathin c-Si with a thickness of 20 μm is used as the substrate. The light trapping includes front upright pyramids with a molybdenum oxides (MoOx) anti-reflection (AR) layer. Planar ultrathin c-Si (without a MoOx AR layer and upright pyramids) is used as a reference. The wafer ray tracer was developed by a photovoltaic (PV) lighthouse to model the MoOx AR layer to reduce the front surface reflectance and impacts of the AR layer on ultrathin Si solar cells. The optical properties are calculated on the AM1.5 global solar energy spectrum across the 200–1200 nm wavelength region. From the absorbance profile, the photogenerated current density (J_{ph}) in the substrate is also calculated with various surface structures. The front upright pyramids with the MoOx layer result in the largest absorbance enhancement due to the enhanced light scattering by the pyramids and MoOx AR layer. The J_{ph} of 37.41 mA/cm² is improved when compared to the planar ultrathin c-Si reference. This study is significant as it illustrates the potential of ultrathin c-Si as a promising PV module technology in the future.**

***Index Terms*—Absorbance, Crystalline silicon, Light trapping, MoOx, Solar Cells**

I. Introduction

Crystalline silicon (c-Si) solar cells have been dominating the photovoltaic (PV) market for more than 90% of the PV market share due to the high efficiency of c-Si, a non-toxic material, potentially lower manufacturing costs, and being naturally abundant on the earth crust (Zhou, et al., 2024). Today, 180 μm-thick c-Si is usually used for solar cell production (Li, et al., 2024). Reducing the c-Si thickness is an attractive solution to reduce the fabrication cost of the solar cells (Xue, et al., 2020). However, ultrathin c-Si solar cells suffer poor photogenerated current density (J_{ph}) due to their reduced absorbance at long wavelengths of light (Huang, et al., 2024, Li, et al., 2024). Light trapping strategies, such as microtextured surfaces and anti-reflection (AR) layers, have been commonly studied to increase effective light absorbance and reduce surface reflectance losses (Kanda, et al., 2016; Macco, 2015). In the literature, various materials have been used as AR layers on c-Si solar cells, such as silicon nitride (SiNx), aluminum oxide (Al_2O_3), silicon dioxide (SiO_2) magnesium fluoride (MgF_2), titanium dioxide (TiO_2), and zinc oxide (ZnO) (Shanmugam, et al., 2020, Zin, et al., 2018). This study aims to evaluate the MoOx AR layer with various surface structures in the ultrathin c-Si solar cells to observe several optical effects. The AR layer, such as ZnO and SiO_2/Si_3N_4, is used on the front c-Si surface (Chee, et al., 2018). By coating the Si surface with various thicknesses of AR layers of ZnO and SiO_2/Si_3N_4, the average reflectance shows about zero at the wavelength of 525 nm. Without the AR layer, the Si substrate achieves an average reflectance of about 40% at the same wavelength. The AR layer cells give a 1.15% efficiency improvement on Si when compared to the solar cells without the AR layer. In addition, the surface texture of a c-Si solar cell with an AR layer shows a conversion of 15.5% when compared to the surface texture of a c-Si solar cell without an AR layer (efficiency of 13.8%), due to the lower reflectance and improved light absorbance in the c-Si solar cell (Kanda, et al., 2016). However, the incident photon into the ultrathin c-Si is grading effect by the refractive index (n) within the molybdenum oxides (MoOx, n = 2) AR layer that is enclosed between air (n = 1) and ultrathin c-Si (n = 3.94 at 600 nm) (Macco, 2015, Lu, et al., 2018). Besides, microscale random upright pyramids have a suitable geometry for ultrathin c-Si with a thickness of 20 μm. Due to the enhanced scattering of incident light by pyramids at oblique angles, it leads to enhanced light absorbance in the ultrathin c-Si cells since the dimensions of the random pyramids are larger than the wavelength of the light (Garín, et al., 2023). In the conventional strategy used for industrial c-Si, solar cells are combined with an AR layer and upright pyramids to minimize surface reflectance losses on the front surface (Valiei, et al., 2022, Tahir, et al., 2024). Omar et al. have also studied the thin

ARO-The Scientific Journal of Koya University
Vol. XII, No. 1 (2024), Article ID: ARO. 11586. 4 pages
Doi: 10.14500/aro.11586
Received: 27 March 2024; Accepted: 05 June 2024
Regular research paper: Published: 25 June 2024
Corresponding author's e-mail: halo.dalshad@koyauniversity.org

http://dx.doi.org/10.14500/aro.11586

c-Si solar cell with different light-trapping schemes by ray tracing simulation. The highest J_{ph} of 39.1 mA/cm^2 is calculated by the SiNx layer on the inverted pyramids presented by (Omar Hashim and Pakhuruddin, 2020).

This study utilizes ray tracing simulation to investigate various surface structures in ultrathin c-Si cells. Ultrathin c-Si with a thickness of 20 μm is used to simulate the performance of upright pyramids for light trapping in c-Si. Ray tracing is used to investigate the MoOx AR layer and the light-trapping performance of upright pyramids in ultrathin c-Si for application in solar cells. Wafer ray tracing simulation studies the transmittance, reflectance, and absorbance of each substrate over a wavelength range of 200 nm to 1200 nm. The photogenerated current density (J_{ph}) can be calculated from the absorbance result. Planar ultrathin c-Si (without a MoOx layer and upright pyramids) is shown as a reference.

II. Methodology

PV Lighthouse is used with Wafer Ray Tracer software for light trapping in ultrathin c-Si with 20 μm thickness. The angle of the incidence is at zero degrees, and the AM 1.5 global solar spectrum is selected across the 200–1200 nm wavelength region (with an interval of 10 nm). The ray tracing uses a maximum total ray of 50,000 with 5,000 numbers of rays per run. The optical properties of ultrathin c-Si with different surface structures are designed with a front random upright pyramid (texture angle of 54.7°, width of 5.6 μm, and height of 4 μm) and 75 nm MoOx as AR layer (by atomic layer deposition ALD) as considered to cover the 200–1200 nm spectral region. Fig. 1 illustrates cross-sectional schematic diagrams of ultrathin c-Si with 20-μm thickness and various surface structures. Fig. 1a illustrates planar ultrathin c-Si, which is used as a reference. The planar ultrathin c-Si does not have a front MoOx AR layer or upright pyramids on either surface. Fig. 1b shows the front MoOx AR layer on planar ultrathin c-Si. Fig. 1c and d demonstrates two light traps with and without the front MoOx AR layer.

The potential photogenerated current density (J_{ph}) is calculated by integrating the absorbance result; EQE is the external quantum efficiency (EQE = IQE x A) of the cell; q is the elementary charge; and the solar spectrum S(λ) is calculated from the AM1.5 global solar energy spectrum across the 200–1200 nm wavelength region (Pakhuruddin, 2020; Pakhuruddin, et al., 2016). In equation (1), the carrier collection is assumed to be one (i.e., internal quantum efficiency, IQE = 1).

$$J_{ph} = q\int EQE(\lambda).S(\lambda)d\lambda \quad \text{(I)}$$

III. Results and Discussion

Reflectance, transmittance, and absorbance profiles of four surface types are depicted in Fig. 2. The planar ultrathin c-Si (without MoOx and pyramids) measures a surface reflection of about 0.35 for incident light at a wavelength of 600 nm and decreases to around zero after the 75 nm MoOx AR layer (Hu, et al., 2022). The reflectance appears from the difference in the refractive index of air (n = 1) and c-Si (n = 3.94 at 600 nm) (Macco, 2015; Lu, et al., 2018). The transmittance is about 0.5 at a wavelength of 1200 nm. The transmittance loss is high because of the low thickness of the ultrathin c-Si absorber. The planar ultrathin c-Si shows weak light absorbance across the 200–1200 nm wavelength region. The MoOx AR layer on planar ultrathin c-Si leads to reduced surface reflectance from the ultrathin c-Si. As a result, the surface reflectance improves significantly. The front pyramid illustrates a reflectance of 0.1 at the 600 nm wavelength. By using the MoOx layer on randomly upright pyramids with an ultrathin c-Si surface, the reflectance is decreased significantly to a minimum of 0.03 at wavelength regions between 450 and 850 nm. The light absorbance increases up to 0.95 at the same wavelength. As a result, the transmittance drops to 0.3 due to the enhanced scattering at the surface of the ultrathin c-Si. The transmittance values of the planar and MoOx AR layers on the planar surface are 0.5 and 0.6, respectively, above the 1100 nm region. A transmittance spectrum does not change with the MoOx layer on pyramids or without the AR layer on pyramids (OmarHashim and Pakhuruddin, 2020).

Table I depicts the resulting J_{ph} of ultrathin c-Si with various surface structures. Planar ultrathin c-Si is also included as a reference. Planar ultrathin c-Si demonstrates a J_{ph} of 21.12 mA/cm^2. For a MoOx layer on planar ultrathin c-Si, the calculated J_{ph} is about 29.57 mA/cm^2, due to the improved light coupling into the ultrathin c-Si absorber. With front upright pyramids on ultrathin c-Si, the J_{ph} is increased to 35.26 mA/cm^2. In addition, using 75 nm MoOx on upright pyramids, the J_{ph} is increased to 37.41 mA/cm^2 compared to the ultrathin c-Si with pyramids (with AR effect). This leads to increased light absorbance, as illustrated in Fig. 2c.

Fig. 1. Schematic diagram of ultrathin crystalline silicon (c-Si) (with 20 μm thickness) substrate (a) Planar ultrathin c-Si (without MoOx and upright pyramids) (b) MoOx AR layer on planar ultrathin c-Si; (c) front random upright pyramids (without MoOx) (d) front random upright pyramids with a front MoOx AR layer. The drawings are not to scale.

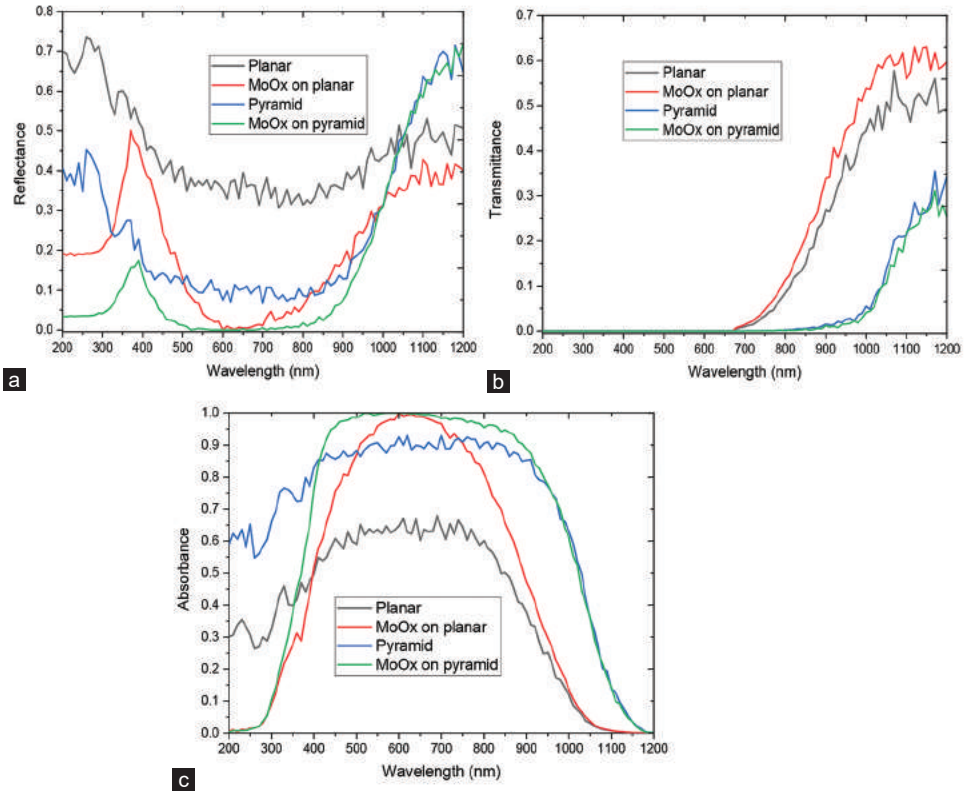

Fig. 2. (a-c) The light reflectance, transmittance, and absorbance spectra of the ultrathin crystalline silicon (c-Si) with various surface structures. Planar ultrathin c-Si (without MoOx layer and upright pyramids) is shown as a reference.

TABLE I
THE POTENTIAL J_{PH} OF ULTRATHIN C-SI WITH VARIOUS SURFACE STRUCTURES, AS DEPICTED IN FIG. 1. PLANAR ULTRATHIN C-SI IS USED AS A REFERENCE

Surface structures	J_{ph} (mA/cm^2)
Planar	21.12
MoOx on planar	29.57
Front pyramid	35.26
MoOx on pyramid	37.41

c-si: Crystalline silicon, J_{ph}: Photogenerated current density

IV. CONCLUSION

This study utilizes ray tracing simulation to investigate various surface structures in ultrathin c-Si cells. Ultrathin c-Si with a thickness of 20 μm is used as a substrate. The optical characteristics of ultrathin c-Si with different surface structures (with or without a 75 nm MoOx layer and randomly upright pyramids) are measured across the spectral region of 200–1200 nm. Planar ultrathin c-Si (without MoOx and upright pyramids) is used as a reference. The reflectance of ultrathin c-Si is about 0.35 at a wavelength of 600 nm. In the MoOx layer on ultrathin c-Si, the front surface reflectance reduces to zero at a wavelength of 600 nm due to its low refractive index (MoOx, n = 2 at 600 nm). With front upright pyramids, the reflectance drops to 0.1 at the same wavelength due to the enhanced scattering at the surface of the ultrathin c-Si. Using the MoOx layer on randomly upright pyramids with an ultrathin c-Si surface, lower reflectance and the highest J_{ph} of 37.41 mA/cm^2 are achieved.

REFERENCES

Chee, K.W.A., Tang, Z., Lü, H., and Huang, F., 2018. Anti-reflective structures for photovoltaics: Numerical and experimental design. *Energy Reports*, 4, 266-273.

Garín, M., Pasanen, T.P., López, G., Vähänissi, V., Chen, K., Martín, I., and Savin, H., 2023. Black ultra-thin crystalline silicon wafers reach the $4n^2$ absorption limit-application to IBC solar cells. *Small*, 19, 2302250.

Hu, Q., Wang, J., Lu, Y., Tan, R., Li, J., and Song, W., 2022. Sputtering-deposited thin films on textiles for solar and heat managements: A mini-review. *Physica Status Solidi (a)*, 219, 2100572.

Huang, S., Xu, C., Wang, G., Du, J., Yu, J., Zhang, L., Meng, F., Zhao, D., Li, R., Huang, H., Liu, Z., and Liu, W., 2024. Smaller texture improves flexibility of crystalline silicon solar cells. *Materials Letters,* 357, 135768.

Kanda, H., Uzum, A., Harano, N., Yoshinaga, S., Ishikawa, Y., Uraoka, Y., Fukui, H., Harada, T., and Ito, S., 2016. Al_2O_3/TiO_2 double layer anti-reflection coating film for crystalline silicon solar cells formed by spray pyrolysis. *Energy Science and Engineering*, 4, 269-276.

Li, Y., Ru, X., Yang, M., Zheng, Y., Yin, S., Hong, C., Peng, F., Qu, M., Xue, C., Lu, J., Fang, L., Su, C., Chen, D., Xu, J., Yan, C., Li, Z., Xu, X., and Shao, Z., 2024. Flexible silicon solar cells with high power-to-weight ratios. *Nature*, 626, 105-110.

Lu, C., Rusli, Prakoso, A.B., and Li, Z., (2018). Aqueous Solution Deposited Molybdenum oxide Crystalline Silicon Heterojunction Solar Cells. In: *2018 IEEE 7th World Conference on Photovoltaic Energy Conversion (WCPEC) (A Joint Conference of 45th IEEE PVSC, 28th PVSEC and 34th EU PVSEC)*, pp.2155-2157.

Macco, B., Vos, M., Thissen, N.F.W., Bol, A.A., and Kessels, W.M.M., 2015. Low-temperature atomic layer deposition of MoOx for silicon heterojunction solar cells. *Physica Status Solidi*, 9, 393-396.

Omar, H.D., Hashim, M.R., and Pakhuruddin, M.Z., 2020. Ray tracing of

inverted pyramids for light-trapping in thin crystalline silicon for solar cells. *Optik*, 219, 165279.

Pakhuruddin, M.Z., 2020. *Ray tracing of light trapping schemes in thin crystalline silicon for photovoltaics. Solid State Phenomena*. Trans Tech Publications, Switzerland, pp.183-191.

Pakhuruddin, M.Z., Huang, J., Dore, J., and Varlamov, S., 2016. Enhanced absorption in laser-crystallized silicon thin films on textured glass. *IEEE Journal of Photovoltaics,* 6, 852-859.

Shanmugam, N., Pugazhendhi, R., Madurai Elavarasan, R., Kasiviswanathan, P., and Das, N., 2020. Anti-reflective coating materials: A holistic review from PV perspective. *Energies*, 13, 2631.

Tahir, S., Saeed, R., Ashfaq, A., Ali, A., Mehmood, K., Almousa, N., Shokralla, E.A., Macadangdang, R.R. Jr., Soeriyadi, A.H., and Bonilla, R.S., 2024. Optical modeling and characterization of bifacial SiNx/AlOx dielectric layers for surface passivation and antireflection in PERC. *Progress in Photovoltaics: Research and Applications,* 32, 63-72.

Valiei, M., Shaibani, P.M., Abdizadeh, H., Kolahdouz, M., Asl Soleimani, E., and Poursafar, J., 2022. Design and optimization of single, double and multilayer anti-reflection coatings on planar and textured surface of silicon solar cells. *Materials Today Communications*, 32, 104144.

Xue, M., Nazif, K.N., Lyu, Z., Jiang, J., Lu, C.Y., Lee, N., Zang, K., Chen, Y., Zheng, T., Kamins, T.I., Brongersma, M.L., Saraswat, K.C., and Harris, J.S., 2020. Free-standing 2.7 μm thick ultrathin crystalline silicon solar cell with efficiency above 12.0%. *Nano Energy*, 70, 104466.

Zhou, Y., Wen, J., Zheng, Y., Yang, W., Zhang, Y., and Cheng, W., 2024. Status quo on recycling of waste crystalline silicon for photovoltaic modules and its implications for China's photovoltaic industry. *Frontiers in Energy*.

Zin, N., Mcintosh, K., Bakhshi, S., Vázquez-Guardado, A., Kho, T., Fong, K., Stocks, M., Franklin, E., and Blakers, A., 2018. Polyimide for silicon solar cells with double-sided textured pyramids. *Solar Energy Materials and Solar Cells,* 183*,* 200-204.

High-Resolution Biostratigraphic Zonation across the Cretaceous/Paleogene (K/Pg) Boundary from Sulaymaniyah Area, Kurdistan Region, Northeastern Iraq

Imad M. Ghafor[1], Asaad I. Mustafa[1*], Ibrahim M. Mohialdeen[1] and Howri Mansurbeg[2,3]

[1]Department of Earth Sciences and Petroleum, College of Science, University of Sulaimani, Sulaymaniyah, Kurdistan Region – F.R. Iraq

[2]Department of Geology, Palacký University, 17, listopadu 12, Olomouc 77146, Czechia

[3]General Directorate of Scientific Research Center, Salahaddin University-Erbil, Erbil 44002, Kurdistan Region – F.R. Iraq

***Abstract*—*The* present study interprets the high resolution of the biostratigraphy across the Cretaceous/Paleogene (K/Pg) boundary from Sulaymaniyah, Kurdistan Region, and north-east Iraq, based on planktic foraminifera. The Dartw section was selected for this study, within the High Folded Zone. The biozone contact consists of lithostratigraphic resemblance and is represented by the upper part of the Tanjero Formation (late Maastrichtian) with the overlying Kolosh Formation (Danian). Four late Maastrichtian planktic foraminiferal biozones have been recorded from the Tanjero Formation: *Racemiguembelina fructicosa* Interval Zone (CF4), *Pseudoguembelina hariaensis* Concurrent Range Zone (CF3), *Pseudoguembelina palpebra* Partial Range Zone (CF2), and Plummerita hantkeninoides Total Range Zone (CF1), while three Danian planktic foraminiferal biozones and two subzones have been recorded from the Kolosh Formation: (*Guembelitria cretacea* (P0) Interval Zone, *Parvularugoglobigerina eugubina* (Pα) Total Range Zone, and *Parasubbotina pseudobulloides* (P1) Partial-Range Zone (*Globoanomalina archaeocompressa* (P1a) Partial Range Subzone, and *Subbotina triloculinoides* (P1b) Interval Subzone). High biostratigraphic resolution indicates a complete K/Pg transition with no hiatus at the studied section in the Sulaymaniyah area. The ranges of the species recognized in this study are given. Correlations with other sections in Iraq and other parts of the world, including the type Maastrichtian and Danian areas, are discussed and represented in correlation charts, together with the ranges of the important Upper Maastrichtian and Paleocene species.**

***Index Terms*—High Resolution, K/Pg boundary, Kurdistan region of Iraq, Planktic Foraminifera.**

ARO-The Scientific Journal of Koya University
Vol. XII, No. 1 (2024), Article ID: ARO.11587. 17 pages
DOI: 10.14500/aro.11587
Received: 27 March 2024; Accepted: 16 May 2024
Regular research paper: Published: 26 June 2024
Corresponding author's e-mail: asaad.mustafa@univsul.edu.iq

I. Introduction

Mass extinctions have occurred many times throughout the Earth's history, one of the greatest and biggest extinctions was at the K/Pg boundary (end of Cretaceous 66 Ma) (Renne, et al., 2013). It is one of the best known for the impact triggered extinction at the Yucatan peninsula in Mexico and is known as the Chicxulub impact (Fig. 1) (Hildebrand, et al., 1991). Meteor impact theory was firstly only detected from the enrichment of platinum group elements especially Iridium, later the location of the impact was found (Alvarez, et al., 1980; Smit and Hertogen 1980; Bonté, et al., 1984; Alvarez, Claeys and Kieffer, 1995; Schulte, et al., 2010; Belza, et al., 2017). Environmental crises of the impact such as sunlight shielding, sulfuric and nitric acid rain, CO_2-induced global warming, ultraviolet penetration, and toxic effects of ground-level ozone made harsh situations across the Earth (Maruoka, 2019). Besides the impact of environmental catastrophe, another theory of the driving mechanism of the extinction is linked to Deccan volcanism in India by recording enrichment of mercury in sediments from the time of the extinction (Fig. 1) (Courtillot, et al., 1984; Hildebrand, Boynton and Zoller, 1984; Madhavaraju and Yong 2010; Font, et al., 2016; Keller, et al., 2020; Mateo, et al., 2020). The controversy between abrupt (meteoric impact) and gradual mass extinction (long-lasting volcanic activity) of which mechanisms had a great effect is still ongoing (Koeberl, 1989; Keller, 2014; Arenillas, et al., 2022). Planktic foraminifera's species suffered mass extinction from the consequences of the catastrophes, and most of the works on the boundary accepted the extinction (Smit and Ten Kate, 1982; Keller, 1988; Arenillas, et al., 2002). The K/Pg boundary in the Kurdistan Region of Iraq, which is a part of the Zagros Foreland Basin (ZFB), was recorded in sedimentary rocks between various lithostratigraphic units (Shiranish/Kolosh Formations, Shiranish/Aaliji formations, Tanjero Formation/

http://dx.doi.org/10.14500/aro.11587

Red bed series, and Tanjero/Kolosh Formations) (Bellen, et al., 1959; Ghafor, 1988; Al-Shaibani, Al-Hashimi and Ghafor, 1993; Bakkhal, et al., 1993; Ghafor, 2000; Al-Barzinjy, 2005; Jassim and Goff, 2006; Sharbazheri, Ghafor and Muhammed, 2009; 2011; Hammoudi, 2011; Al-Nuaimy, et al., 2020; Salih, Al-Mutwali and Aldabbagh, 2015; Al-Qayim, Kharajiany and Wise, 2020; Kharajiany, Wise and Al-Qayim, 2020; Bamerni, et al., 2021, Sahib and Al-Dulaimi, 2022; Lawa and Qadir, 2023). Basin configuration at the time of the late Cretaceous and early Paleogene resulted in the deposition of different facies at the same time (Jassim and Goff, 2006). As a consequence of this variation a discussion occurred about the boundary between different lithostratigraphic units shows that the occurrence of a complete K/Pg transition in Iraq (Sharbazheri, Ghafor and Muhammed, 2009; 2011; Salih, Al-Mutwali and Aldabbagh, 2015; Al-Nuaimy, et al. 2020; Mousa, Al-Dulaimi, and Mohammed, 2020; Bamerni, et al., 2021).

The research on the boundary between the Tanjero and Kolosh Formations and, the Shiranish and Kolosh Formations was mostly focused on biostratigraphy (Kassab, 1972; Ghafor, 2000; Kharajiany, Al-Qayim and Wise, 2019). The studies conducted on the boundary in particular shed light on the nature of sedimentation across the boundary and whether the boundary itself represents an unconformity or a hiatus surface. Most of the recent studies use planktic foraminifera, palynomorphs (Spores and Pollen), and nannofossils emphasizing that the Early Danian sediments exist between Tanjero and Kolosh Formations and mark the boundary as a conformable surface (i.e., without a break in sedimentation) (Al-Qayim and Al-Shaibani, 1989; Ghafor, 2000; Sharbazheri, Ghafor and Muhammed, 2009, 2011; Kharajiany, Al-Qayim and Wise, 2019; Al-Nuaimy, et al., 2020; Al-Qayim, Kharajiany and Wise, 2020; Kharajiany, Wise and Al-Qayim, 2020; Bamerni, et al., 2021), while many other studies mark the boundary as an unconformable surface (Kassab, 1972; Ghafor, 1988; Al-Shaibani, Al-Hashimi and Ghafor, 1993; Jassim and Goff, 2006; Sissakian and Al-Jubouri, 2014; Lawa and Qadir, 2023). One of the prominent works conducted on the contact between Tanjero and Kolosh Formations by Bellen, et al. (1959), concluded that in some areas of Northern Iraq, the boundary could represent conformable surfaces. These authors unfortunately did not specify the localities of these conformable surfaces. Thus, high-resolution biostratigraphic zonation will help to determine the nature of the boundary. Research works on the boundary continue to optimize the best result of recording biozones. This paper presents the high-resolution biostratigraphy of the K/Pg boundary interval to delineate the boundary in a section namely the Dartw section (Kurdistan Region, NE Iraq) between Tanjero and Kolosh Formations, by recognition of planktic foraminifera in thin sections. It is historical usage to determine the ages of marine sequences across the boundary (Sarigül, et al., 2017) and to compare these records with other areas available in the region and across Iraq.

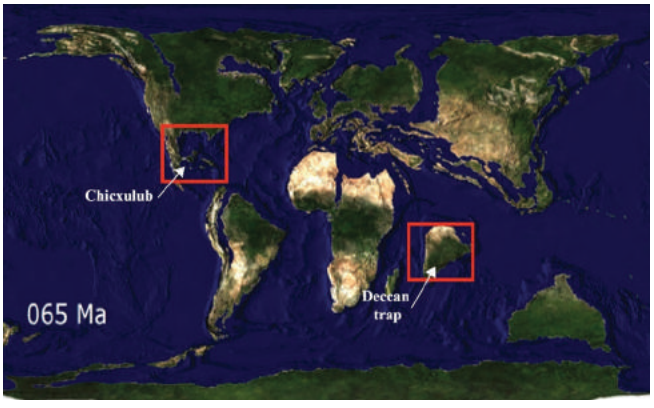

Fig. 1. Paleogeographic map at 65 Ma, showing the location of the meteorite impact and the Deccan volcanism (Scotese, 2011).

II. Geological Setting

In Sulaymaniyah Governorate, the Cretaceous and Paleocene succession is well exposed. This succession is exposed in almost all outcrops of the High Folded Zone of the Zagros Thrust-Fold around Sulaymaniyah city in the western part of the Zagros Thrust Fold Belt. The facies variation of K/Pg sections in areas around the Dartw section is between marine marl and argillaceous limestone (marly limestone), while in the furthest NE part (Imbricated Zone) of Sulaymaniyah the variation is between marine and terrestrial sediments (Tanjero and Red Bed Series) (Lawa and Qadir, 2023). At the time of the K/Pg boundary event(s), the study section was located in the ZFB, as a consequence of the convergence of the Arabian Plate with the Iranian Plate (Al-Qayim, Omer and Koyi, 2012). Structurally Dartw section is in a part of the southwestern limb of a small anticline (Yakhyan anticline) which is a part form a larger piramagrun anticline, more specifically the section is in the SE plunge of the anticline (Fig. 2). Structures around the section are striking SE-NW, parallel to the main trend of ZMB. The section is located at 35° 38’ 55.12” N and 45° 16’ 18.15”E in NE Iraq about 18.5 Km from N60W of the center of Sulaymaniah city, the coordination represents the exact boundary. In the Dartw section, the exposed outcrop of the boundary is between the Tanjero and Kolosh Formations as shown in (Fig. 2). The K/Pg boundary sequence is deposited on a carbonate platform at the northeastern margin of the Arabian Plate. The outcrop of the studied section is subdivided into two formations; based on the lithology, and stratigraphic position, these are Tanjero and Kolosh Formations. The latest Cretaceous unit is the Tanjero Formation, which was deposited by turbidite currents in the deep marine environment (Jaza, 1992; Karim, 2004). It was first described by Dunnington (1952), its type locality is in the Sirwan Valley, near Halabja Governorate, in the Kurdistan Region of Iraq, the Lithology of the Tanjero Formation is mainly composed of alternations between dark grey or olive green clastics (Sandstone and siltstone) marlstones, and argillaceous limestone with a massive conglomerate part in the proximal turbidite (Bellen, et al., 1959; Karim, 2004; Ahmed, Qadir and Müller, 2015). The depositional basin of this unit was

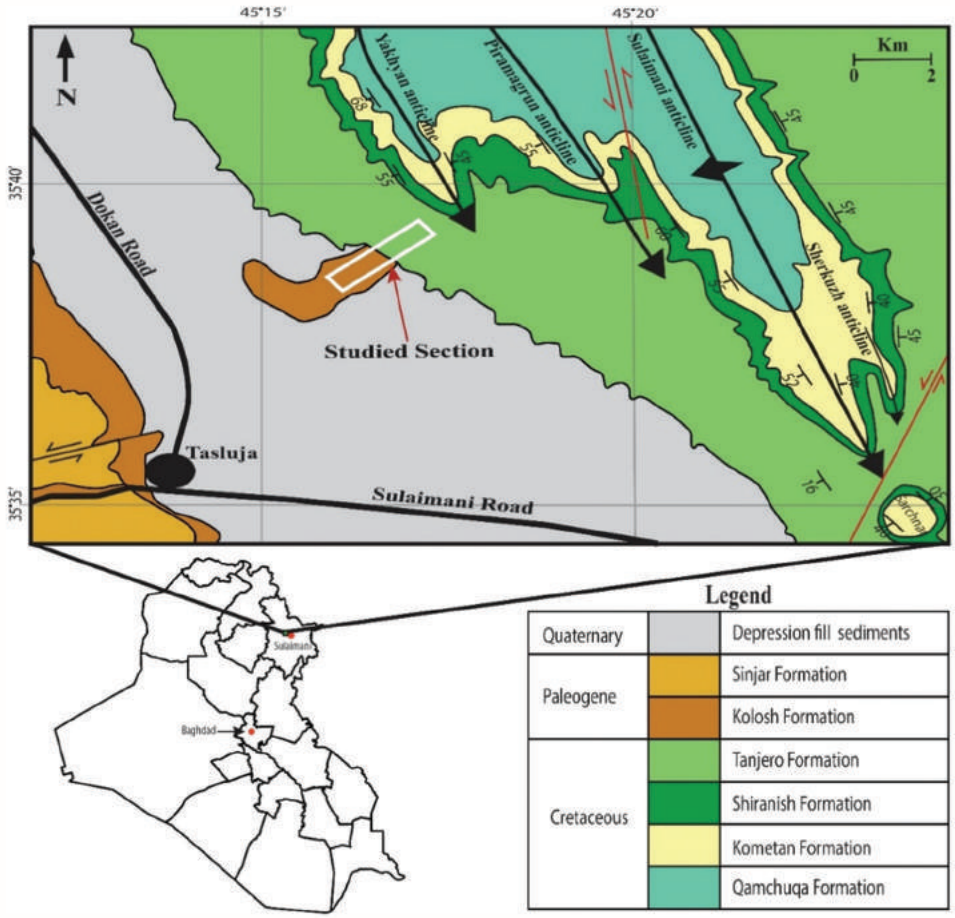

Fig. 2. Geological and location map of the studied section (after Mustafa, Mansurbeg, and Mohialdeen, 2022).

parallel to the convergence suture between the Arabian and Iranian plates in a Narrow northwest-southeast direction (Jassim and Goff, 2006). The lower part of the section could be misinterpreted lithologically as the Shiranish Formation since the strata are similar in appearance to the Shiranish Formation. However, in contrast to the Shiranish Formation, this lower part has unique thin beds of sandstone (Fig. 3). Jaza (1992) and Ismael, et al. (2011) in the Sulaymaniyah area have highlighted the problem of differentiating between Tanjero and Shiranish formations since Tanjero Formation contains intervals similar to Shiranish Formation lithologies. Both Tanjero and Shiranish formations were deposited in a single basin at the initial stage of the Zagros Foreland Basin development (Karim, 2004).

In the earliest time of the Paleogene, the basin was nearly the same as at the time of deposition of the Tanjero Formation, the Kolosh Formation started deposition. This formation was first described by Dunnington (1952; in Bellen et al., 1959) and the type locality of the formation is located in the north of Koya Town near Kolosh Village. This unit is a low-density turbidite with rhythmic alternation of sandstone and shale with beds of argillaceous limestone, limestone, and conglomerate (Bellen, et al., 1959; Al-Mashaikie Sa'ad and Mohammed, 2018; Karim and Hamza, 2023). These two formations both have a flysch deposit character deposited in the upper bathyal environment, outer shelf environment, and middle shelf area from bottom to top respectively (Jaza, 1992; Jassim and Goff, 2006; Al-Khalaif and Al-Mutwali, 2020). In the Dartw section, both formations have approximately similar lithological characteristics; the two formations are composed of interbedding between marlstone, argillaceous limestone, and sandstone. The consistency of lithology (no abrupt change) across the section makes a determination of the boundary by the field evidence impossible, especially in narrow intervals (centimeters scale) (Figs. 3 and 4). Color variation is noted in Kolosh Formation as it is darker compared to the Tanjero Formation.

III. Materials and Methods

Sixty-three rock samples for this study were taken from the Dartw section outcrop in four carried-out field trips. Intervals between individual samples are based on proximity to the boundary, at boundary transition, sample intervals are much smaller compared to distant samples (Fig. 4). Samples were collected in four stages, and especially near the boundary, samples were taken at 10cm intervals. (Fig. 3). Between each stage of field sampling, thin sections of samples were made in the workshop of the Department of Earth Sciences and Petroleum/University of Sulaimani to study planktic foraminifera, this would help us to concentrate samples at strata near the boundary. The samples are representative

 http://dx.doi.org/10.14500/aro.11587

Fig. 3. Field photograph showing sample interval near the K/Pg boundary transition in Dartw section.

of the lithology variation of turbidite cycles. Thin sections from all samples for petrographic study were prepared at the workshop of the Department of Geology/University of Sulaimani. The biozonal schemes of Li and Keller (1998a; 1998b) and Coccioni and Premoli Silva (2015) for the late Maastrichtian were followed and the biochronology of Wade, et al. (2011) was used for the Danian.

IV. Results and Discussion

A. Biostratigraphic Analysis

The studied section has the highest diversity of late Maastrichtian/Danian planktic foraminifera with a total identification of 71 species from 28 genera of planktic foraminifera (46 species of Maastrichtian from eighteen genera of planktic foraminifera and 25 species of Danian from ten genera of planktic foraminifera). The biozonation of the Dartw section was found on the apportionment of the planktic foraminifera that applied to the Tanjero and Kolosh Formations (Figs. 5-7), seven biozones have been recognized from Maastrichtian - Paleocene age (Fig. 8). For the late Maastrichtian, the biozonation of Li and Keller (1998a; 1998b), was used, which subdivides the *Abathomphalus mayaroensis* zone is subdivided into four Cretaceous Foraminiferal (CF) subzones (CF1, CF2, CF3 and CF4), four for the earliest Danian, the biozonation of Keller, et al. (1995) was subdivided into three biozones (P0, P*a* and P1) and 2 subzones (P1a, and P1b) have been recognized. These biozonal schemes are shown in Fig. 9 in comparison with other commonly used biozones.

B. Biostratigraphy of the Tanjero Formation (late Maastrichtian)

Forty-six species from eighteen genera of planktic foraminifera have been identified in the Tanjero Formation (Figs. 5 and 6). Based on the stratigraphic ranges of the recognized species, four subzones of the *A. mayaroensis* zone have been recognized in the Maastrichtian.

Total Range Zone of the nominated by taxon *Abathomphalus mayaroensis*. The *A. mayaroensis* was defined previously as the interval from the first appearance datum (FAD) to the last appearance datum (LAD) of *A. mayaroensis*, which spans the entire late Maastrichtian interval (Caron, 1985; Toumarkine and Lutherbacher, 1985). It is important to mention that the zonal scheme of CF proposed by Li and Keller (1998a; 1998b), which replaces the *A. mayaroensis* Zone, with four subzones (*Racemiguembelina fructicosa* subzone, *Pseudoguembelina hariaensis* subzone, *Pseudoguembelina palpebra* subzone, and *Plummerita hantkeninoides* subzone), for much-improved age estimation for the late Maastrichtian, This zone is coeval with the standard zonation of Caron (1985) and Berregren, et al. (1995), it also coincides with the zones CF4, CF3, CF2, of Li and Keller (1998). The upper and lower boundaries were drawn with the first and last occurrences of the nominate taxon. In the Dartw section of the studied area, the *A. mayaroensis* zone encompasses 19-m thick Maastrichtian limestone with marly limestone, which can be subdivided into the four CF subzones (Li and Keller, 1998a), and were arranged from older to younger (Fig. 8):

R. fructicosa interval subzone (CF4)

This zone is defined as the interval from the FAD of *R. fructicosa* and the FAD of *A. mayaroensis* to the FAD of *P. hariaensis* (Li and Keller, 1998). The lower boundary is not covered by this section and the upper boundary is defined by the first appearance of the *A. mayaroensis*. In the Dartw section, subzone CF4 extends from 0 m to 9 m (with a 9 m thick) of the alternation of calcareous shale (Occasionally siltstone) with a 0.5 m thick argillaceous limestone bed. A bed of sandstone 2-cm thick is present at the top. This zone is recognized at the base of the Tanjero Formation and is represented in the Dartw section by an interval extending from the samples DT-9, and DT-15.

The zone is characterized by these species of Planktic foraminifera: *Abathomphalus intermedius*, *A. mayaroensis, Gansserina gansseri, Globotruncana bulloides, Globotruncana pettersi, Globotruncana arca, Contusotrancana contusa., Contusotrancana walfischensis, Globotruncanita conica,*

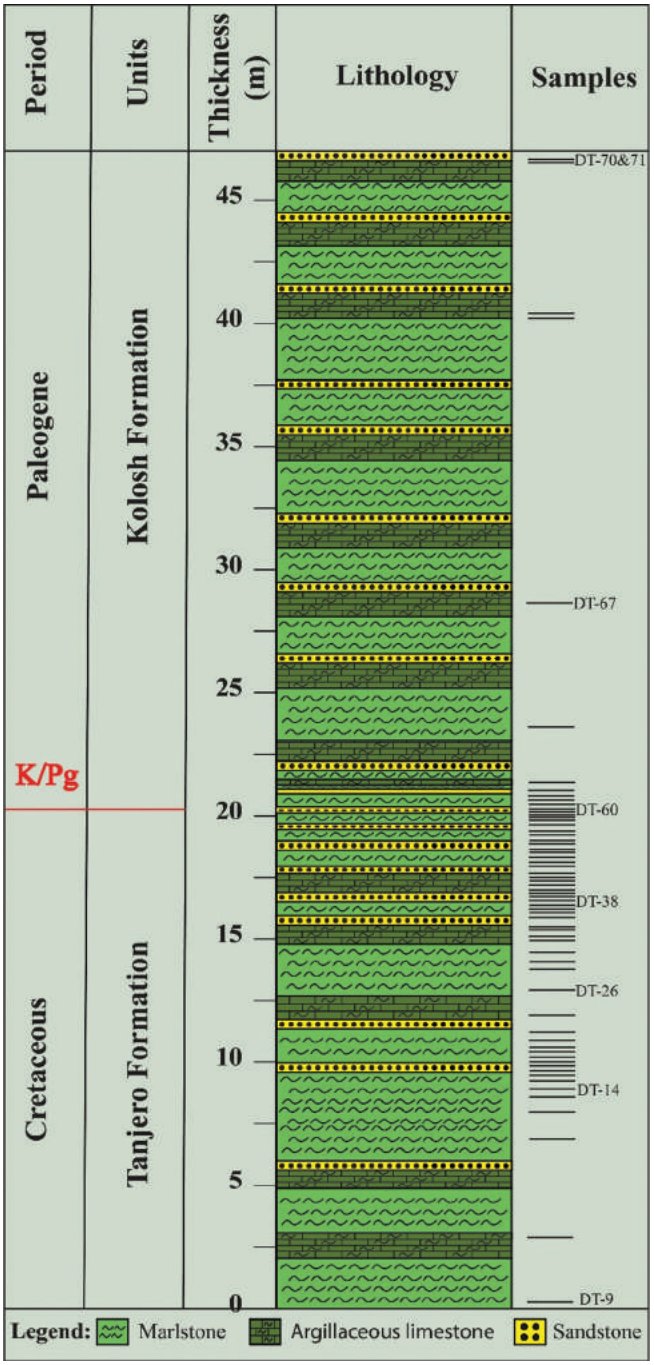

Fig. 4. Stratigraphic column of a Dartw section across the K/Pg boundary near Sulaymaniyah city, Kurdistan region, Iraq.

Globotruncanita stuarti, Hedbergella monmouthensis, Heterohelix globulosa, Heterohelix planata, Heterohelix punctulata R. fructicosa, *Rugoglobigerina rugosa, Rugoglobigerina macrocephala* and *Rugoglobigerina reicheli.* The *R. fructicosa* zone. (CF4) was introduced by Li and Keller (1998a; 1998b) as a biostratigraphic interval between the FAD of *R. fructicosa* at the base and the FAD of *P. hariaensis* at the top. according to most of the biozonation works this zone placed *R. fructicosa* zone at the lower late Maastrichtian (Abramovich and Keller, 2002) at DSDP Site 525A, Keller, et al. (1995) from Tunisia, Obaidalla (2005) and Samir (2002) from Egypt, Sharbazheri, Ghafor and Muhammed, (2009; 2011) and Al Nujaimy, et al., (2020) from Iraq. As defined above, the present subzone (CF4) of the studied section is correlatable with the lower part of *A. mayaroensis* (Abawi, Kireem and Yousef, 1982; Abdel-Kareem, 1986) from Iraq. Premoli Silva and Sliter (1999) from Italy. Caron (1985) and Robaszynski, et al. (1984) in some other localities. Sharbazheri, Ghafor and Muhammed (2009; 2011), Al-Nujaimy, et al. (2020), recorded this zone from the Dokan, Sirwan valley, Smaquli area, and they documented these planktic foraminiera *(Heterohelix navarroensis, Heterohelix globulosa. Heterohelix striata, Heterohelix punctulats, Planoglobulina carseyae, Planoglobulina brazoensis, Planoglobulina acervulinoides, Rugoglobigerina rugosa, Rugoglobigerina scotti, Rugoglobigerina hexacamerata, Rugoglobigerina macrocephala, Gansserina gansseri, Globotruncanita stuarti, Globotruncanita stuartiformis, Globotruncanita conica, Globotruncana aegyptiaca, Globotruncana falsostuarti, Globotruncana dupeublie, Globotruncana gagnebini, Globotruncana lapparenti Globotruncana arca, Globotruncana. bulloides, Contusotruncana contusa, Contusotruncana fornicate, Contusotruncana plicata, Rugotruncana circumnodifer, Rugotruncana. subcircumnodifer, Globotruncanella petaloidea, Globotruncanella havanensis, Globigerinelloides volutes, Globigerinelloides multispinata, Globigerinelloides subcarinate, Globigerinelloides prairiehillensis, Globigerinelloides bolli, Pseudotextularia elegans, Pseudotextularia deformis, Pseudotextularia intermedia, Racemiguembelina fructicosa, Racemiguembelina poweli, Pseudoguembelina costulata, Pseudoguembelina hariaensis, Pseudoguembelina palpebra, Pseudoguembelina excolata, Hedbergella monmothensis Hedbergella holmdelensis, Abathomphalus mayaroensis).*

The age calculation of this biozone by Li and Keller (1998a) recorded the time span between 68.33 Ma and 66.83 Ma. In the studied section, estimating absolute ages based on magnetochron age between a time span between 68.35 Ma and 67.25 Ma, and a high rate of deposition. Its age is early late Maastrichtian with 9-m thick.

P. hariaensis concurrent range subzone (CF3)

This zone defines the interval from the FAD of *P. hariaensis* at the base to the LAD of *G. gansseri* at the top (Li and Keller, 1998a; 1998b). This biozone spans 1 m of olive-green calcareous shale (Fig. 8). This zone is recognized at the Tanjero Formation and is represented in the Dartw section by an interval extending from the samples DT-16 to DT-22. It is characterized by these species of Planktic foraminifera: - *A. intermedius*, *A. mayaroensis, G. arca, Globotruncana calcarata, Contusutruncanita contusa, G. conica, G. stuarti, H. holmdelensis, H. monmouthensis, H. globulos*a, *H. navarroensis, Pseudoguembelina harensis, R. rugosa, R. reicheli.* The *P. hariaensis* (CF3) Zone was introduced by Li and Keller (1998a). This zone is equivalent to the middle part of the *A. mayaroensis* zone as recorded by Abawi, Kireem and Yousef (1982) and Abdel-Kireem (1986) in the northeast of Iraq. It is also correlated with the same zone that was recorded by Al-Mutwali and Al-Doori (2012), they recorded this zone as an interval zone of the zonal

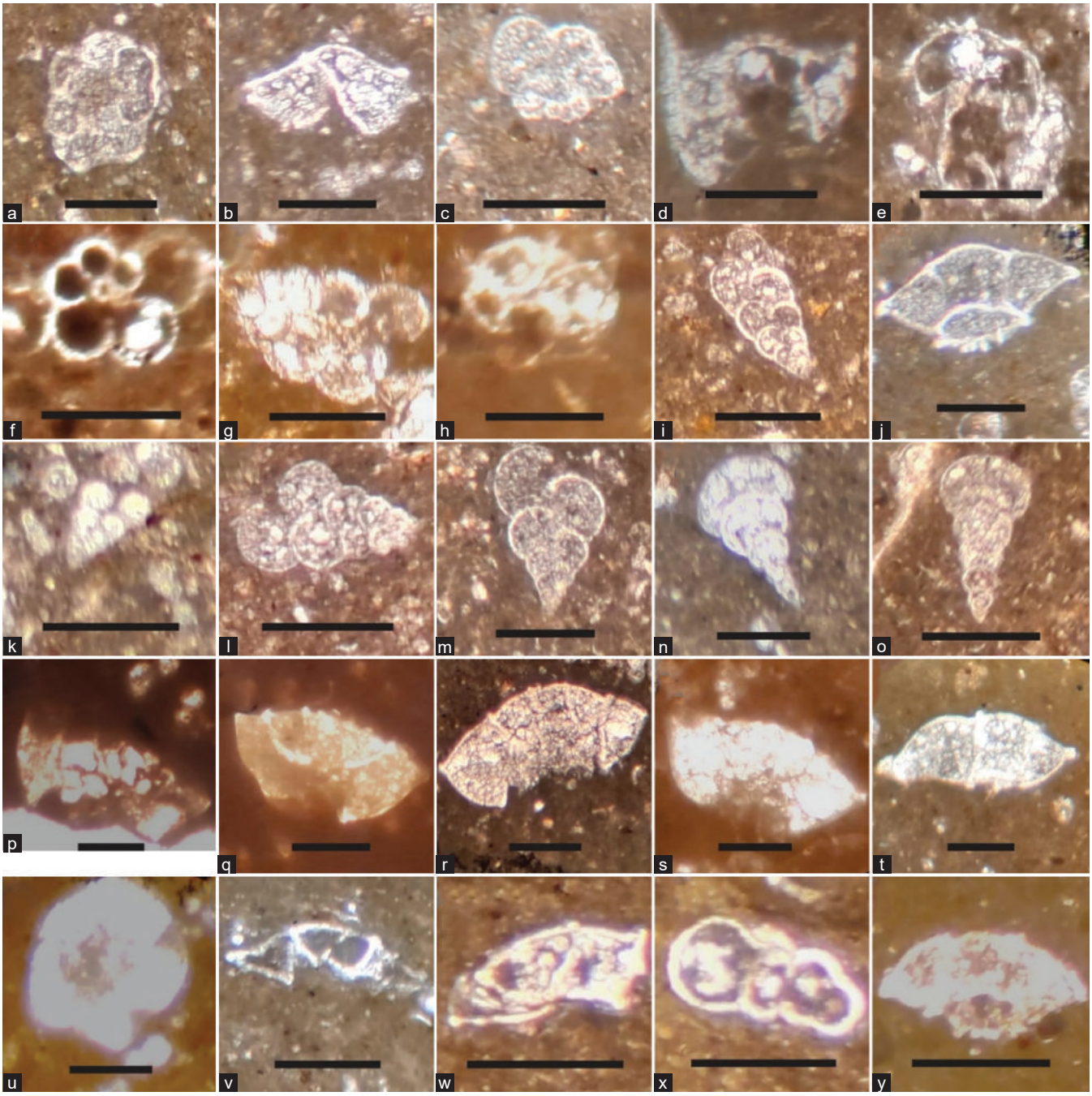

Fig. 5. (a) *Racemiguembelina fructicosa* (Egger, 1900), sample no. DT-10. (b) *Abathomphalus intermedius* (Bolli, 1951), sample no. DT-10. (c) *Abathomphalus mayaroensis* (Bolli, 1951), sample no. DT-10. (d) *Gansserina gansseri* (Bolli, 1951), sample no. DT-9. (e) *Globotruncana arca* (Cushman, 1926), sample no. DT-9. (f) *Hedbergella holmdelensis* (Olsson 1964), sample no. DT-9. (g) *Pseudoguembelina costellifera* (Masters, 1976), sample no. DT-9. (h) *Rugoglobigerina* sp., sample no., sample no. DT-9. (i) *Heterohelix navarroensis* (Loeblich 1951), sample no. DT-10. (j) *Globotruncanita conica* (White, 1928), sample no. DT-10. (k) *Planoheterohelix moremani* (Cushman, 1938), sample no. DT-10. (l) *Planoheterohelix planata* (Cushman, 1938), sample no. DT-10. (m) *Planoheterohelix globulosa* (Ehrenberg, 1840), sample no. DT-10. (n) *Pseudotextularia elegans* (Rzehak, 1891), sample no. DT-10. (*o*) *Pseudotextularia nuttalli* (Voorwijk, 1937), sample no. DT-10. (p) *A. mayaroensis* (Bolli, 1951), sample no. DT-15. (*q*) *Gansserina wiedenmayeri* (Gandolfi, 1955), sample no. DT-15. (r) *Globotruncana orientalis* (El Naggar 1966), sample no. DT-15. (s) *Globotruncana rosetta* (Carsey, 1926), sample no. DT-15. (t) *Pseudoguembelina hariaensis* (Nederbragt, 1991), sample no. DT-15. (u) *Rugoglobigerina hexacamerata* (Brönnimann, 1952), sample no. DT-15. (v) *Contusotruncana*, sample no. DT-19. (w) *Globotruncana dupeublei* (Caron, Gonzalez, Robazynski & Wonders in Robaszynski, et al., 1984) Sample No. DT- 19. (x) *Rugoglobigerina hexacamerata* (Brönnimann, 1952) SampleNo. DT-19. (y) *Globotruncana orientalis* (El Naggar 1966) Sample No. DT-19. The Bar scale = 0.5 mm.

marker with a thickness of 3.6 m, and they determined its age as middle late Maastrichtian. The abundant occurrence of these planktic foraminifera has been recognized by Hammoudi (2011), *Globotrunana aegyptiaca*, *Globotrunana*

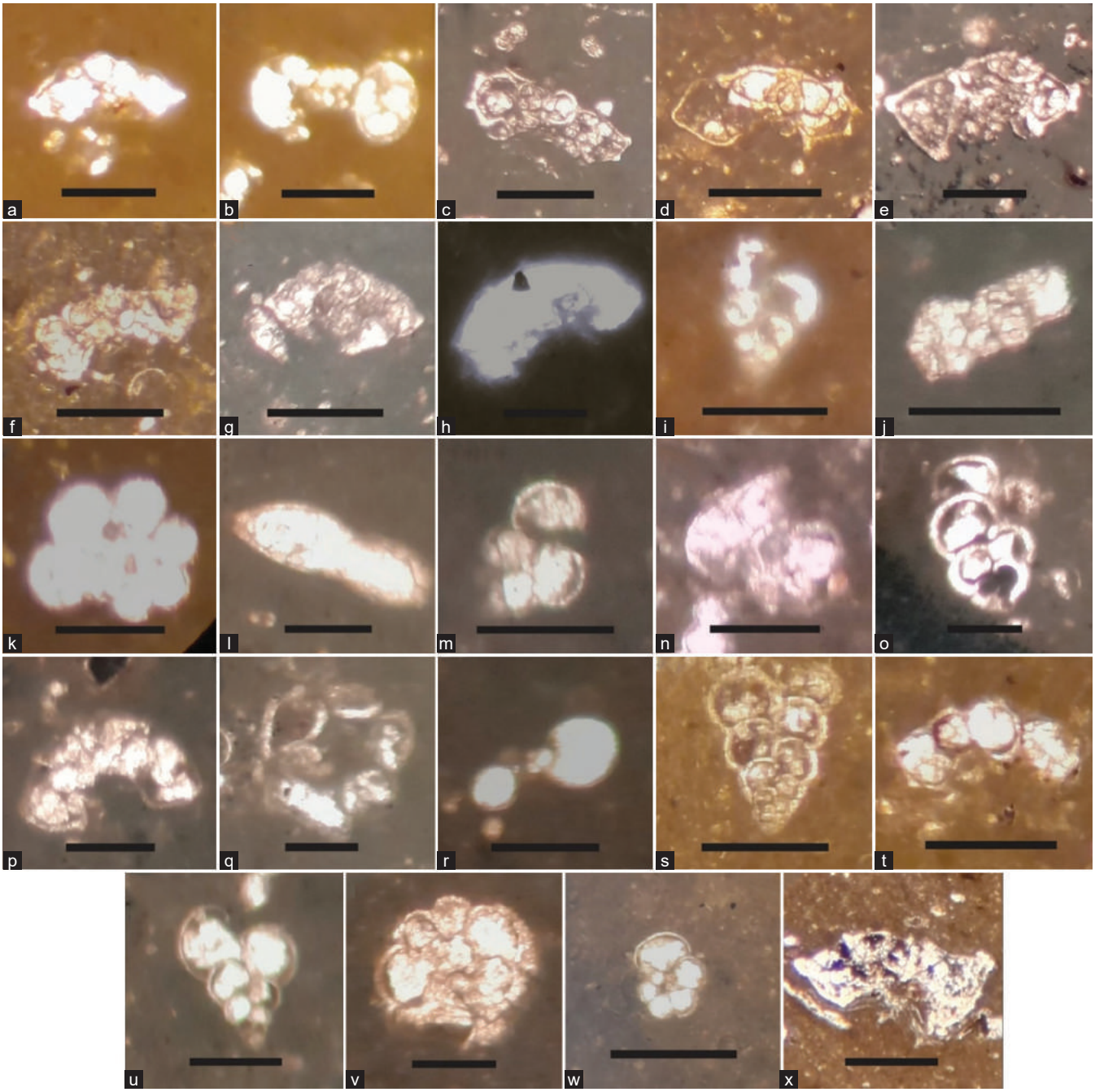

Fig. 6. (a) *Globotruncana orientalis* (El Naggar 1966), sample no. DT-22. (b) *Rugoglobigerina pennyi* (Bronnimann, 1952), sample no. DT-22. (c) *Abathomphalus mayaroensis* (Bolli, 1951), sample no. DT-27. (d) *Globotruncana falsostuarti* (Sigal, 1952), sample no. DT-27. (e) *Globotruncana dupeublei* (Caron, Gonzalez, Robazynski & Wonders in Robaszynski, et al., 1984), sample no. DT- 27- (f) *Globotruncanita angulata* (Tilev, 1951), sample no. DT-27. (g) *Globotruncana stephensoni* (Pessagno 1967), sample no. DT-27. (h) *Globotruncanita conica* (White, 1928), sample no. DT-29. (i) *Pseudotextularia intermedia* (De Klasz, 1953), sample no. DT-29. (j) *Abathomphalus mayaroensis* (Bolli, 1951), sample no. DT-55. (k) *Rugoglobigerina rotundata* (Bronnimann, 1952), sample no. DT-55. (l) *Globotruncanella petaloidea* (Gandolfi, 1955), sample no. DT-57. (m) *Guembelitria cretacea* (Cushman, 1933), sample no. DT-57. (n) *Plummerita hantkeninoides* (Bronnimann, 1952), sample no. DT-57. (o) *Archaeoglobigerina blowi* (Pessagno 1967), sample no. DT-57. (p) *Contusotruncana contusa* (Cushman, 1926), sample no. DT-57. (q) *Contusotruncana*, sample no. DT-57. (r) *Globigerinelloides subcarinatus* (Bronnimann, 1952), sample no. DT-57. (s) *Planoheterohelix globulosa* (Ehrenberg, 1840). (t) *Globotruncanella petaloidea* (Gandolfi, 1955), sample no. DT-57. (u) *Heterohelix globulosa* (Ehrenberg, 1840). (v) *Rugoglobigerina hexacamerata* (Brönnimann, 1952), sample no. DT-57. (w) *Rugoglobigerina rugosa* (Plummer, 1927), sample no. DT-53 (x) *Globotruncanita stuartiformis* (Dalbiez, 1955), sample no. DT-19. The Bar scale = 0.5 mm.

arca, *Globotrunana esnehensis*, *Contusutruncana contusa*, *R. rugosa*, *R. macrocephala*, *R. scotti*, *Rugoglobogerina hexacamerata*, *H. holmdelensis*, *H. monmouthensis*, *Hetrohelix planata*, *Hetrohelix glabrans*, *Hetrohelix globulosa*, *Hetrohelix navaroensis*, and she considered the CF3 Zone as a subzone within the *A. mayaroensis* Zone also

http://dx.doi.org/10.14500/aro.11587

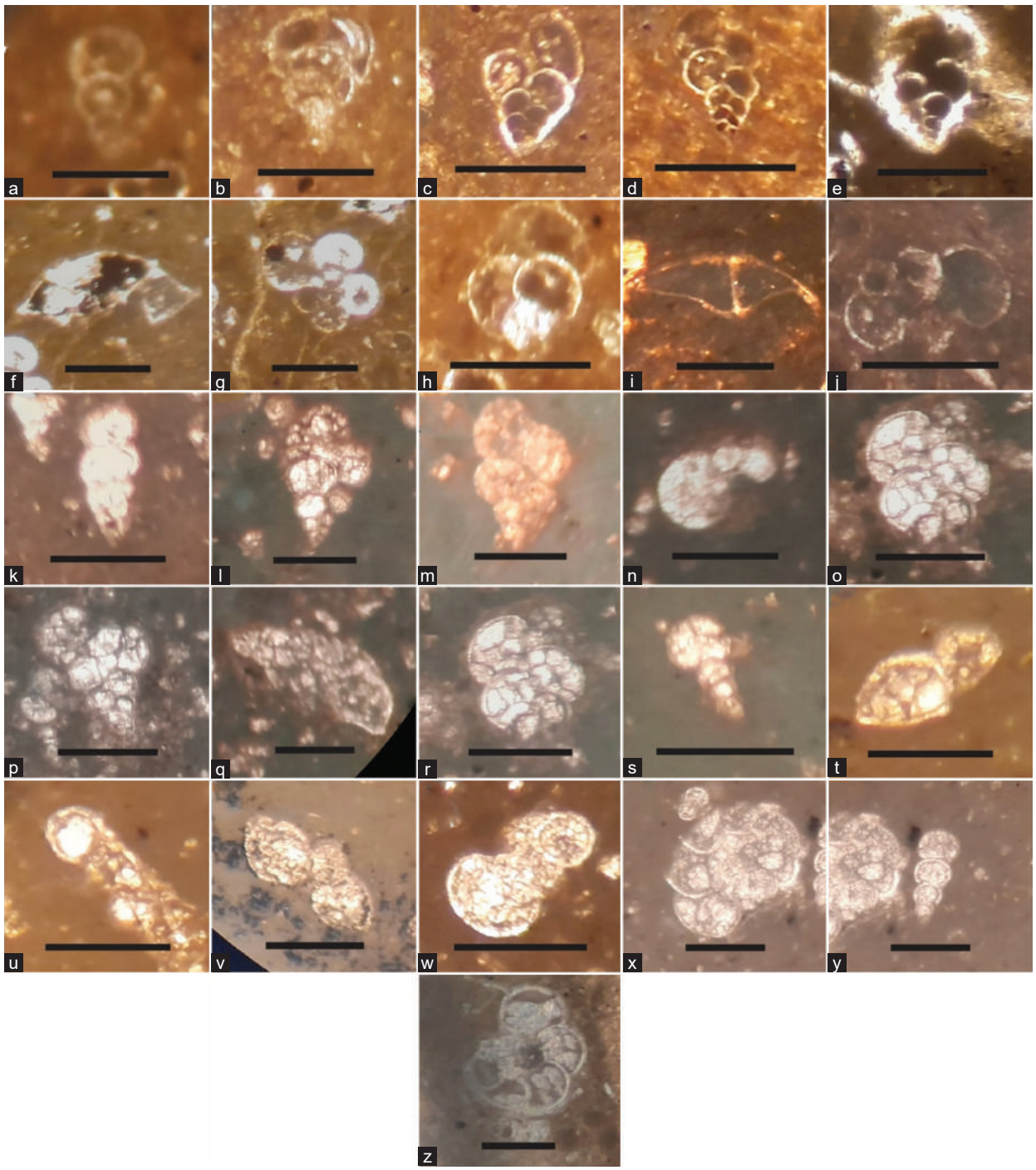

Fig. 7. (a) *Woodringina claytonensis* (Loeblich and Tappan, 1957), sample no. DT-61. (b) *Spiroplectammina dentata* (Alth, 1850) sample no, DT-61, (c) *Chiloguembelina morsei* (Kline 1943), sample no. DT-61, (d) *Guembelitria* cretacea (Cushman, 1933), sample no. DT-61, (e) *G. cretacea* (Cushman, 1933), sample no. DT-61, (f) *Hedbergella monmouthensis* (Olsson, 1960), sample no. DT-61, (g) *H. monmouthensis* (Olsson, 1960), sample no. DT-61, (h) *Parasubbotina pseudobulloides* (Plummer, 1927), sample no. DT-61, (i) *Parvularugoglobigerina extensa* (Blow, 1979), sample no. DT-61, (j) *Subbotina triangularis* (White, 1928), (k) *Woodringina claytonensis* (Loeblich and Tappan, 1957), sample no. DT-61, (l) *Chiloguembelina* sp., sample no. DT-63, (m) *Chiloguembelina morsei* (Kline, 1943), sample no. DT-63, (n) *Eoglobigerina eobulloides* (Morozova, 1959), sample no. DT-63, (o) *Eoglobigerina eobulloides simplicissima* (Blow, 1979), sample no. DT-63, (p) *G. cretacea* (Cushman, 1933), sample no. DT-63, (q) *Parvularugoglobigerina eugubina* (Luterbacher and Premoli Silva, 1964), sample no. DT-63, (r) *P. pseudobulloides* (Plummer, 1927), sample no. DT-63, (s) *Pseudonodosaria appressa* (Loeblich and Tappan, 1955), sample no. DT-63, (t) *Globanomalina compressa* (Plummer, 1927), sample no. DT-65, (u) *Hedbergella holmdelensis* (Olsson, 1964), sample no. DT-65, (v) *Globanomalina compressa* (Plummer, 1927), sample no. DT-65, (w) *Globanomalina archeocompressa* (Blow, 1979), sample no. DT-65, (x) *P. eugubina* (Luterbacher and Premoli Silva, 1964), sample no. DT-65, (y) *Woodringina claytonensis* (Loeblich and Tappan, 1957), sample no. DT-65, (z) *Globanomalina archeocompressa* (Blow, 1979), sample no. DT-70. Bar scale = 0.5 mm.

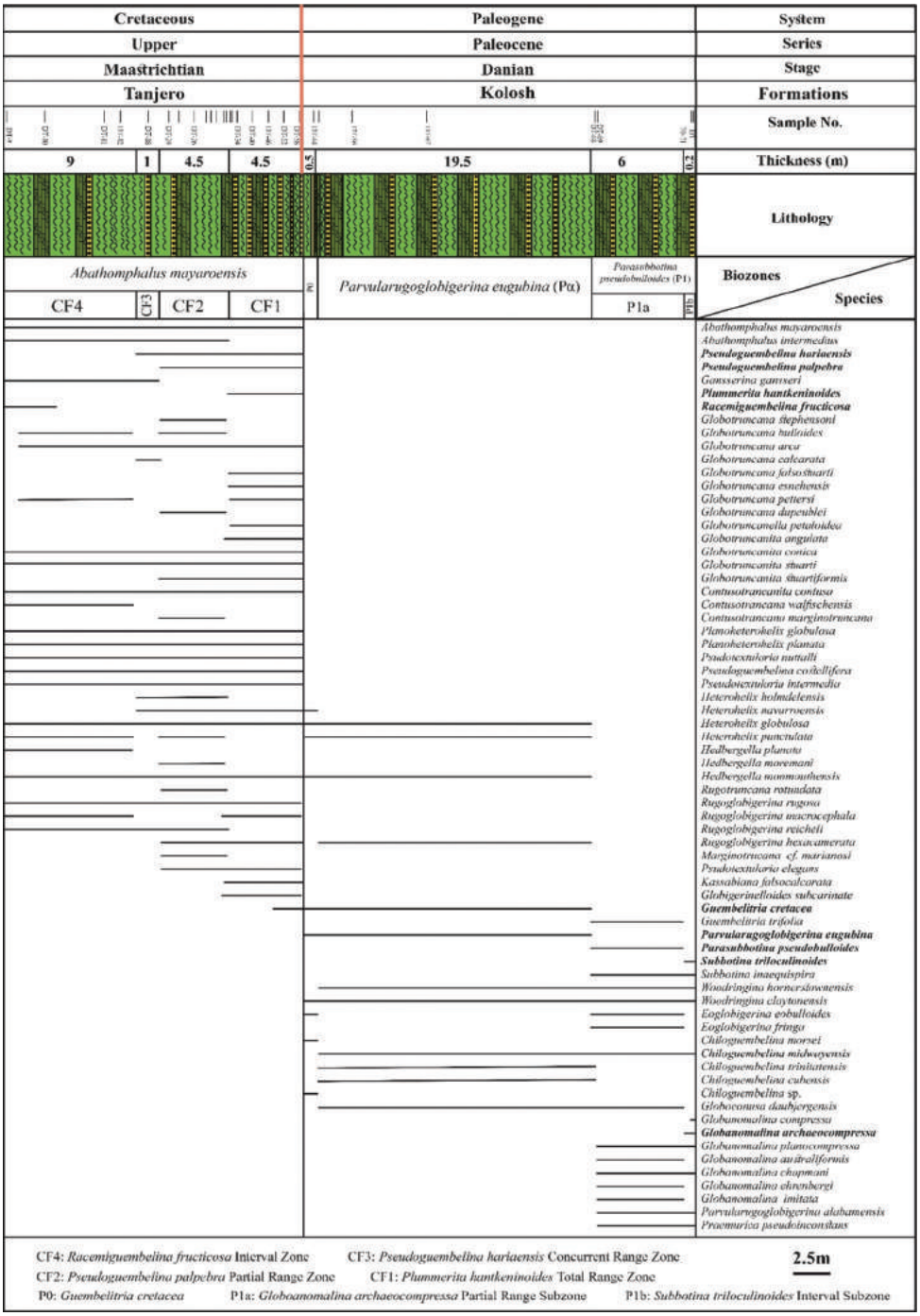

Fig. 8. Biostratigraphic range chart of identified planktic foraminifera across K/Pg boundary in the Dartw section. Biozones are based on Li and Keller (1998a; 1998b).

determined the age of this subzone as late Maastrichtian. Sharbazheri, Ghafor and Muhammed (2011) recorded this zone from the Smaquli area with 35-m thickness. They documented an increase in the abundance of planktic foraminifera within this zone, documenting the species *P. hariaensis*, *H. navaroensis*, *H. globulosa*, *Hetrohelix striata*, *Hetrohelix punctulata*, *Hetrohelix nuttalli*, *Hetrohelix reussi*, *P. carseyae, P. brazoensis*, *P. acervulinoides*, *R. rugosa*, *R. scotti*, *R. hexacamerata*, *R. macrocephala*, *Rugoglobigerina pennyi, Rugoglobigerina Reicheli*, *Rugoglobigerina rotundata*, *G. gansserina*, *Globtruncanita stuartiformis*, *G. conica, Globotruncanita pettersi*, *Globotruncanita angulata*, *Ganserina. aegyptiaca*, *Ganserina falsostuarti*, *Ganserina dupeublei*, *Ganserina lapparenti*, *Contustruncana contusa*, *Contusutruncana plicata*, *Contusutruncana patelliformis*, *P. elegans*, *P. deformis*, *Racemegumbelina fructicosa*, *P. costulata*, *P. palpebra*, *P. excolata*, *Hedbegella monmouthensis*, *H. holmdelensis*, *A. mayaroensis*, *Guembulina cuvillieri*, and *Guembelitria cretacea*.

The study of Salih, Al-Mutwali and Aldabbagh, 2015 in Northern Iraq documented a 6 m section of this zone with well-preserved, abundant planktonic foraminifera species

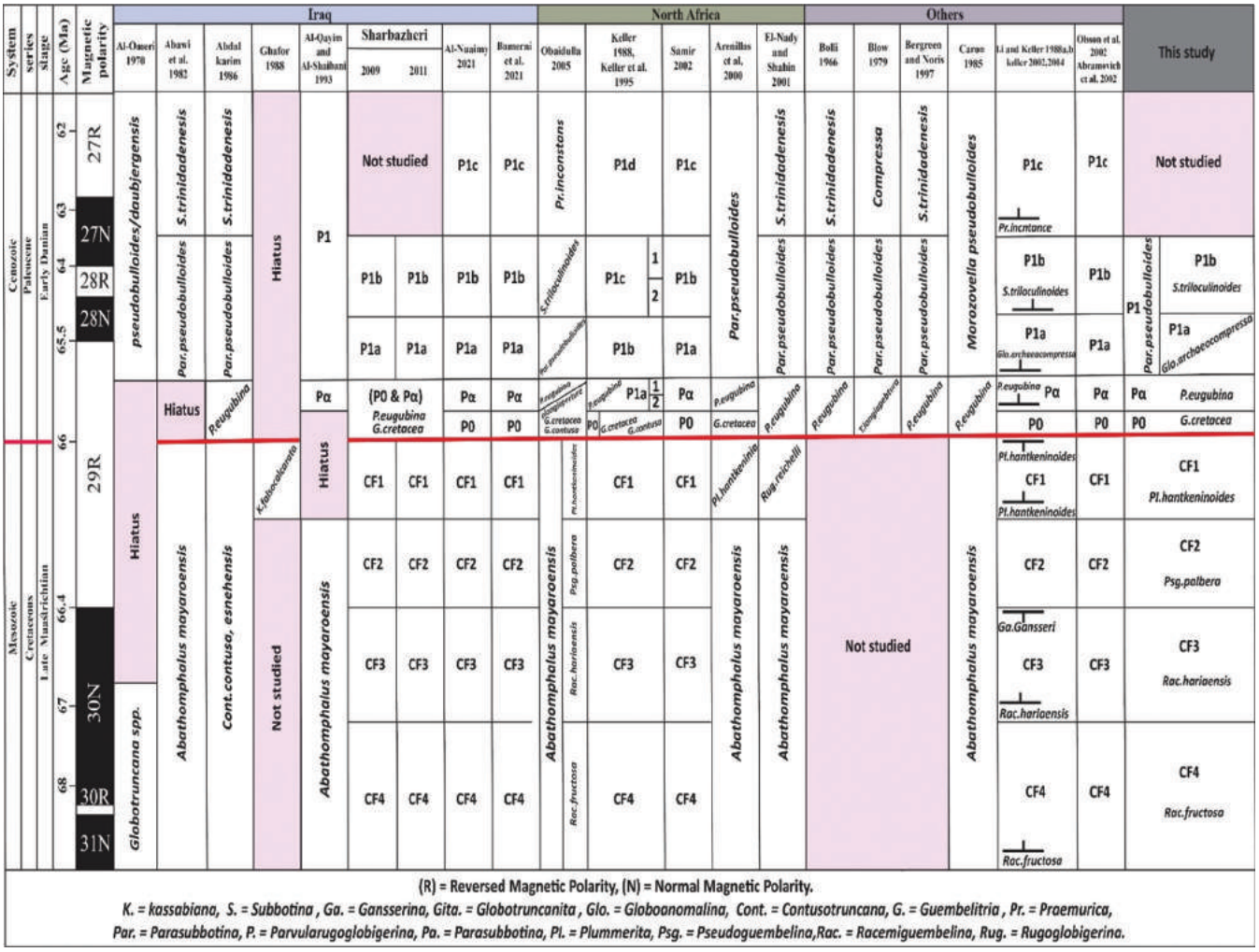

(R) = Reversed Magnetic Polarity, (N) = Normal Magnetic Polarity.

K. = kassabiana, S. = Subbotina , Ga. = Gansserina, Gita. = Globotruncanita , Glo. = Globoanomalina, Cont. = Contusotruncana, G. = Guembelitria , Pr. = Praemurica, Par. = Parasubbotina, P. = Parvularugoglobigerina, Pa. = Parasubbotina, Pl. = Plummerita, Psg. = Pseudoguembelina,Rac. = Racemiguembelina, Rug. = Rugoglobigerina.

Fig. 9. Biostratigraphic correlation of the planktic foraminiferal biozones of this study with other studies.

including *P. hariaensis*, *Ganserina gansseri*, *H. globulo*sa, *Heterohelix labellosa*, *Heterohelix navaroensis*, *H. striata*, *P. acervulinoides*, *P. brazoensis*, *P. carseyae*, *Pseudogumbelina elegans*, *Pseudogumbelina nuttalli*, *Racemegumbelina fructicosa*, *Racemegumbelina powelli*, *Pseudogumebelina. costulata*, *Pseudogumebelin excolata*, *Pseudogumbelina kempensis*, *Pseudogumebelina palpebra*, *H. holmdelensis*, *H. monmouthensis*, *C. contusa*, *Cont*usotruncana *patelliformis*, *Ganaserina aegyptiaca*, *G. arca*, *Globotruncana dupeublei*, *Globotruncana esnehensis*, *G. falsostuarti*, *Globotruncana mariei*, *Globotruncana rosetta*, *Globotruncana ventricosa*, *Globotrucanita stuarti*, *G. stuartiformis*, *Globotrucanita subspinosa*, *G. havanensis*, *G. petaloidea*, *Rugglobigerina hexacamerata*, *R. macrocephala*, *R. rugosa*, *Rugoglobigerina Scotti*. They reported the age of this zone to be middle–late Maastrichtian. Bamerni, et al. (2021) recorded this zone in the Duhok area, which spans an interval of 9 m in the Per Fat section and 6 m in the Xezava section and they documented these planktic foraminifera, *A. mayaroensis*, *Ab. intermedius*, *R. macrocephala*, *Racemegumbelina fructicosa*, *P. acervulinoides*, *Contusutruncana. contusa*, *H. monmouthensis*, *Ganserina gansseri*, *Psudigumbelina. palpebra*, *Psudigumbelina costulata*, *P. elegans*, *Globotrunana arca*, *Globotrunana aegyptiaca*, *G. esnehensis*, *G. stuarti*, *Globotrucanita conica*, *G. stuartiformis*, *Archaeoglobigerina cretacea*, *Trintella scotti*, *H. striata*, *H. globulo*sa, *H. punctulata*, and *R. rugosa*. The current biozone (CF3), as mentioned above, can be connected to the DSDP site 525A region zone reported by Li and Keller (1988a) and Abramovich and Keller (2002) in Madagascar. Premoli Silva and Sliter, (1995) from Tunisia. Keller and Pardo (2004) in Eastern Tethys. Samir (2002) and Obaidalla (2005) in Egypt. Sharbazheri (2007; 2010) in NE Iraq, and it is correlated according to Abawi, Kireem and Yousef (1982) and Abdel-Kireem (1986a) with the middle part of *A. mayaroensis* Zone recorded in the Northeast of Iraq, Premoli Silva and Sliter (1999) in Italy, Premoli Silva and Sliter (1999) in Egypt.

The age calculation of this biozone by Li and Keller (1998a), recorded the time span between 66.83 Ma to 65.45 Ma. In the studied section, estimating absolute ages based on magnetochron age between a time span between 66.80 Ma and 66.44 Ma, and moderate rate of sedimentation. Its age is middle late maastrichtian with 1 m thick.

P. palpebra partial range subzone (CF2)

This zone spans the interval from the LAD of *G. gansseri* to the FAD *P. hantkeninoides* (Li and Keller, 1998a; 1998b). In the Dartw section, this zone spans 4.5 m of grey shale (Fig. 8). It is recognized at the Tanjero Formation and is represented in the Dartw section by an interval extending from the samples DT-22, and DT-32. The assemblage includes this planktic foraminifera: *A. intermedius*, *A. mayaroensis, C. contusa, Globotruncana conica, Globotruncana dupeublei, Contusotrancana marginotruncana, hexacamerata Globotrucanita arca, G. stuarti, G. stuartiformis, Globotruncana dupluberti, G. bulloides, Globotruncana stephensoni, H. holmdelensis, H. monmouthensis, H. globulos*a*, Heterohelix moremani, Heterohelix punctulate; H. navarroensis, P. hariaensis, Rugotruncana rotundata, P. hantkeninoides, R. hexacamerata, R. reicheli, R. rugosa, psudotextularia elegans. Marginotrucana cf. marianosi.*

The age estimation of this biozone by Li and Keller (1998a) records the upper late Maastrichtian, with a time span of 65.45 Ma to 65.30 Ma. In the studied section, estimating absolute ages based on magnetochron age between a time span between 65.4 Ma and 65.30 Ma, providing a high rate of sedimentation, its age is upper late Maastrichtian with 4.5 m thick.

P. hantkeninoides total range subzone (CF1)

The biozone CF1 is defined by the total range of *P. hantkeninoides*, which marks the last 300 ky of the Maastrichtian (Li and Keller, 1998a; 1998b and Olsson, et al., 1999). In the Dartw section, zone CF1 spans the uppermost 4.5 m of dark green calcareous shale. It is recognized at the Tanjero Formation and is represented in the Dartw section by an interval extending from the samples DT-32 and DT-58. Species identified in this interval include: *A. mayaroensis, G. aegyptiaca, P. hantkeninoides*, *Globotruncanita arca, Globotruncanita esnehensis, Globotruncanita. falsostuarti, Globotruncanita. petaloidea, Globotruncanita angulata, G. conica, Globotruncanita contusa, Globotruncanita pettersi, G. stuarti, G.stuartiformis, H. globulos*a*, H. navarroensis, H. monmouthensis, Kassabiana falsocalcarata, P. hantkeninoides, P. hariaensis, P. palpebra, P. elegans, R. macrocephala, Rugoglobigerina riecheli*, *R. rugosa, G. cretacea. R. hexacamerata, G. subcarinate* (Fig. 3). The CF1 subzone was introduced by Masters (1984), at the K-Pg boundary in Tunisia and Egypt. Coccioni and Premoli Silva (2015) stated that the zonal marker is very rare and sporadic in the classic Tethyan Gubbio section (Italy). Sharbazheri, Ghafor and Muhammed (2009; 2011) and Al-Nuaimy, et al. (2020) recorded the CF1 Zone in their study from the upper part of the Maastrichtian deposits in Kurdistan region/Iraq. They also stated that the characteristic planktic foraminiferal assemblage of this zone gradually decreased in both species richness and individual numbers from the *P. palpebra* Zone to the *P. hantkeninoides* Zone. Mousa, Al-Dulaimi, and Mohammed (2020) recorded the C1 zone in the Western Desert of Iraq and they documented common occurrences of *A. intermedius*, *A. mayaroensis*, *Glla. pschadae*, *H. monmouthensis*, *P. palpebra*, *R. hexacamerata*, the age of this zone estimated by the latest Maastrichtian. Recently *P. hantkeninoides* Zone was recorded by Bamerni et al. (2020) in the Dohuk area, North-east Iraq, with high-resolution biostratigraphic analysis of the K-Pg boundary and shows a great diversity of the planktic foraminiferal assemblages compared to the CF2 and CF3 biozones. They recorded planktic foraminifera; the most abundant taxa are *P. hantkeninoides*, *Plummerita reicheli*, *Plummerita* cf. *hantkeninoides*, *P. elegans*, *Pseudotextularia nuttalli*, *P. intermedia*, *G. stuarti*, *Globotruncanita. conica*, *Globotruncanita. stuartiformis*, *Racemegumbelina powelli*, *Plummerita carseyae*, *Plummerita brazoensis*, *Plummerita acervulinoides*, *H. striata*, *H. globulos*a, *Heterohelix labelosa*, *Heterohelix. reussi*, *Heterohelix. navaroensis*, *Heterohelix carinata*, *R. rugosa*, *R. macrocephala*, *Racemegumbelina fructicosa*, *Pseudigumbelina costulata*, *P. hariaensis*, *P. palpebra*, *Pseudoguembelina kempensis*, *Gansserina arca*, *Ganserina rosetta*, *C. contusa*, *Contusutruncana fornicata*, *C. patelliformis*, *H. monmouthensis*, *Rugglobigerina hexacamerata*, *Archaeoglobigerina blowi*, and *Gublerina cuvillieri.*

CF1 biozone in the study section had an assemblage of planktonic foraminifera, which is comparable to the zone reported by Nederbragt, (1991) in Tunisia; Keller and Pardo (2004) in Eastern Tethys Israel; Samir (2002) and Obaidalla (2005) in Egypt; Li and Keller (1988a) from South Atlantic DSDP Site 525A; Abramovich and Keller (2002) in Madagascar; Abramovich and Keller (2002) in DSDP Site 525A, and Stinnesbeck, et al. (2002) from USA.

The present zone of *P. hantkeninoides* is equal to *A. mayaroensis* in their upper majority from all parts of the world (Canudo, Keller and Molina, 1991); Chacon and Martin-Chivelet, (2005) in Spain; Premoli Silva and Sliter (1999) from Italy; Abramovich, et al. (2005) in the eastern Mediterranean; Govindan, Ravindran and Rangaraju (1996) from India; Maestas, et al. (2003) in USA, California; Martínez (1989) and Molina, et al. (2005) from south USA, and corresponding to *Plummerita richly* Zone of Elnady and Shahin (2001) from Egypt.

The estimation of this zone age indicates the uppermost late Maastrichtian (Li and Keller, 1998a), with a complete estimate of absolute ages based on magnetochron ages 65.30 Ma to 65.00 Ma. In the studied section, estimating absolute ages based on magnetochron age between a time span between 65.35 Ma and 65.10 Ma, high rate of sedimentation, its age is latest Maastrichtian with 4.5 m thick.

C. Biostratigraphy of Kolosh Formation-Early Danian

Twenty-five species from ten genera of planktic foraminifera have been identified in the Kolosh Formation (Fig. 7). Based on the stratigraphic ranges of the recognized species, three biozones have been recognized and were arranged from older to younger (Fig. 8), the recognized biozones in this study were correlated with different locations (Fig. 9).

The Early Danian Zones in the studied section started from the *G. cretacea* zone (P0) to the *Parasubbotina*

pseudobulloides zone (P1), representing the presence of the Danian succession in the studied section, these zones are:

G. cretacea (P0) interval zone

The base of the zone (P0) coincides with the base of dark fine-grain sandstone with plant debris, content, and the extinction of all tropical and subtropical species and within a few centimeters of the first appearance of Danian species including *G. cretacea***,** and *Parvularugoglobigerina eugubina.* The *G. cretacea* (P0) biozone is defined by the Interval range Zone of *G. cretacea* and occurs between the Hos of the Cretaceous planktic foraminiferal genera (e.g., *Plummerita*, *Abathomphalus*, *Globotruncana*, *Globotruncanita*). The *G. cretacea* interval zone is recognized at the base of the Danian Kolosh Formation and is represented in the Dartw section by an interval extending from the samples DT-61 to DT-64 with a thickness of 0.5 m of dark green calcareous shale. This zone includes minute-sized (dwarf forms) biserial and simple planktic foraminiferal taxa of the late Cretaceous such as *H. globulosa*, *H. navarroensis, Hx*eterohelix *punctulata*, *Hedbergella. monmouthensis*. The zone includes these planktic foraminifera *Woodringina claytonensis, P. pseudobulloides, Eoglobigerina eobulloides, Chiloguembelina morsei, Chiloguembelina* sp., *Parvularugoglobigirina eugubina.* The Kolosh Formation is subdivided into three main zones and two subzones that are early Paleocene (Danian) in age (Fig. 8). The similarities of these biozones are shown clearly in the earliest Danian, where the simple forms and dwarf are associated with some Cretaceous biserial foraminifera, in addition to the opportunistic occurrence of *G. cretacea*. In the field, the base of the P0 Zone is mostly identifiable by the color change of the dark fine-grain sandstone with plant debris content of the Upper Cretaceous Tanjero Formation to the alternation of calcareous shale with argillaceous limestone of the Danian Kolosh Formation.

This zone was introduced as an indication for sediments of lowermost Dania and the index is marked as early Danian by many authors (Smit and Ten Kate, 1982; Keller, 1988; Arenillas, et al., 2000; Sharbazheri, Ghafor and Muhammed, 2009; 2011), this zone is a thin interval between last appearance of *P. hantkeninoides* and *P. eugubina*. P0 is characterized by the bloom of the disaster opportunists *Guembelitria* species. *Guembelitria* is considered the only survivor that can be used as an environmental proxy for severe biotic stress conditions (Keller and Padro, 2004). *G. cretacea* as the index for P0 was first used by Smit and Ten Kate (1982), later Keller (1988) subdivided it into P0a (*G. cretacea*) and P0b (*Globoconusa conusa*) but then P0 was reviewed as the top of mass extinction and LO of *P.eugubina* (Keller, et al., 1995). P0 in Iraq was not well defined until 21st century, most probably due to the consequence of distant sample interval in the work (Kassab, 1972; Abawi, Kireem and Yousef, 1982; Ghafor, 1988; Al-Qayim and Al-Shaibani, 1989). The *G. cretacea* Zone in this study was correlated with Sharbazheri, Ghafor and Muhammed (2009; 2011), Al-Nuaimy, et al. (2020), and Bamerni et al. (2021) inside Iraq and other records of the P0 zone globally (Fig. 9). The age estimation of this biozone by Olsson, et al. (2000) and Keller and Pardo (2004), Keller (2002) they record the earliest Paleocene (Danian), with the period of 65.00 Ma to 64.97 Ma estimating absolute ages based on magnetochron ages. In the current study, estimating absolute ages based on magnetochron age between a time span from 65.05 Ma to 64.09 Ma. Its age is the Earliest Paleocene (Danian) with 0.5 m thick.

P. eugubina (Pα) total range zone

The Pα is a biozone defined by the total range of the nominal taxon *P. eugubina*. The *P. eugubina* Total Range Zone is identified in the studied section from the sample DT-65 to DT-68, with a thickness of 19.5 m of alternation of dark grey calcareous shale, alternation of calcareous shale with argillaceous limestone and sandstone. This zone has an increase in the diversity and abundance of the Danian cosmopolitan planktic foraminifera including: *Parvularugoglobigirina eugubina, G. cretacea - P. pseudobulloides, Globoconusa. daubjergensis*, *Woodringina hornerstownensis*, *Woodringina claytonensis*, *Chiloguembelina midwayensis*, *Chiloguembelina. trinitatensis*, *Chiloguembelina. cubensis*, besides the abundant and continuous extension of *G. cretacea*, this zone also has minute-sized, simple late Cretaceous taxa such as *Heterhelix globulosa*, *H. punctulata*, and *H. monmouthensis*. The P*α* in the section correlated to Bamerni, et al. (2021) in northern Iraq, Sharbazheri, Ghafor and Muhammed (2009; 2011), and Al Nuaimy, et al. (2020) in Northeastern Iraq. Bamerni, et al. (2021) recorded 52 and 27cm thickness for two sections in Duhok and documented the occurrence of *Globoconusa daubjergensis, Woodringina hornerstownensis, Woodringina claytonensis Eoglobigerina bulloides*, *Eoglobigerina fringa*, *Eoglobigerina edita*, *Chiloguembelina midwayensis, Chiloguembelina trinitatensis, Chiloguembelina cubensis*, *Globanomalina archaeocompressa*, *Globanomalina australiformis*, *Globanomalina chapmani*, *Globanomalina planocompressa*, *Guembelitria trifolia, Parasubbotina* aff. *pseudobulloides* Besides the abundant and continuous extension of *G. cretacea*, this zone also has minute-sized, simple late Cretaceous taxa such as *H. globulo*sa, *H. striata*, *H. punctulata*, *Heterohelix labelosa*, *Heterohelix navaroensis*, *H. monmouthensis*, *Pseudigumbelina. costulata*, *Archaoglobigerina blowi* and *R. hexacamerata*. The age estimation of this biozone by Olsson, et al. (2000); Li and Keller (1998a); Keller and Pardo (2004), Keller (2002), records the earliest Paleocene (Danian), with the period of 64.97 Ma to 64.90 Ma estimating absolute ages based on magnetochron ages. In the current study, estimating absolute ages based on magnetochron age between a time- span between 64.96 Ma and 64.90 Ma. Its age is the Earliest Paleocene (Danian)with 19.5-m thick.

P. pseudobulloides (P1) total range zone

P. pseudobulloides zone is defined by the total Range zone of *Parasubbotina pesudobulloides,* this zone is subdivided into two subzones (P1a, and P1b), 6.2 m thick from the sample numbers DT-68 to DT0-71. Leonov and Alimarina (1961) introduced *Globorotalia* (*Turborotalia*)

pseudobulloides-Globorotalia daubjergens, later Bolli (1966) renamed as *Globigerina pseudobulloides* PRZ. Berggren and Miller (1988) and Berggren, et al. (1995) defined this zone by LOD of *P.eugubina* and LOD of *Praemurica uncinate.*

Globoanomalina archaeocompressa (P1a) partial range subzone

This Subzone is defined as a partial range of the nominal taxon, between the FAD of *G. archaeocompressa* and FAD of *Subbotina triloculinoides, G. archaeocompressa* Subzone (P1a) is represented in the studied section in the sample DT-69 and DT-70 with a thickness of 6 m. Many Danian planktonic foraminiferal species are identified throughout this subzone: - *P. pseudobulloides, Guembelitria trifolia*, *Subbotina inaequispira*, *Woodringina hornerstownensis*, *Woodringina claytonensis*, *Globaanomalina archaeocompressa*, *Globaanomalina planocompressa*, *Globaanomalina australiformis*, *Globaanomalina chapmani*, *Globaanomalina ehrenbergi*, *Globaanomalina imitate*, *Globoconusa daubjergensis*, *Chilogumbelina midwayensis*, *Eoglobigerina eobulloides*, *Eoglobigerina fringa*, *Chiloguembelina midwayensis, Pararugoglbigerina alabamensis*, and *Praemurica pseudoinconstans*. The *G. archaeocompressa* (P1a) subzone spans an interval of 6 m in the studied section. this zone is comparable with the P1a subzone of Sharbazheri, Ghafor and Muhammed (2009; 2011) and Al-Nuaimy, et al. (2020). It is also comparable with the global record of this zone (Fig. Correlation). Bamerni, et al. (2021) recorded 2 and 2.5 m thickness of this zone in Duhok with occurrence if identified population as *Gumbelirita cretacea*, *Gumbelirita trifolia*, *Wodringina hornerstownensis*, *Wodringina claytonensis*, *Globanomalina archaeocompressa*, *Gloanomalina planocompressa*, *Globanomalina australiformis*, *Globanomalina chapmani*, *Gloanomalina. ehrenbergi*, *Gloanomalina Imitate*, *Globocnusa daubjergensis*, *Chiloguembelina. midwayensis*, *Eoglobigerina eobulloides, Eoglobigerina fringe, Praemurica alabamensis*, *Praemurica pseudoinconstans*, and *Praemurica inaequispira*. The age estimation of this interval depends on Magnetic polarity and recorded datum events by Olsson, et al. (2000) and Keller and Pardo (2004), Keller (2002) with the period of 64.90 Ma from the end of *P. eugubina* to 64.50 Ma first occurrence of *S. triloculinoides*, estimating absolute ages based on magneto chron ages 400 Ky with 10 Ky/m. In the current study, estimating absolute ages based on magnetochron age between a time span between 64.90 Ma and 64.50 Ma. Its age is the earliest Paleocene (Danian) with 6 m thick.

S. triloculinoides (P1b) interval subzone

This subzone represents the biostratigraphic interval between the LO of *S. triloculinoides* and the LO of *Globanomalina planocompressa*. In the studied section, it extends from the samples DT-70 and DT-71, with a thickness of 0.2 m of alternation of dark grey calcareous shale (marl) with argillaceous limestone, 3 m sandstone beds of 6 cm thick at the top. Argillaceous limestone beds are 40 cm thick between very thick beds of calcareous shale. sandstones are medium-grained and mostly friable. In addition to the abundance of the marker species of this subzone *S. triloculinoides*, it also shows the continuation of the previous P1a subzone taxa such as *Woodringina hornerstownensis*, *Woodringina claytonensism S. triloculinoidesm, Globaanomalina planocompressa*, *Globaanomalina chapmani*, *Chilogumbelina midwayensis*, *Pararugoglbigerina alabamensis*, and *Praemurica pseudoinconstans*. The P1b zone was introduced by Berggren and Miller (1988), and the zone was revised by Berggren and Miller (1988). The zone correlated to P1b of Sharbazheri, Ghafor and Muhammed (2009; 2011) and Al-Nuaimy, et al. (2020). Its intervals span 2 and 4 m in the Duhok area, Northeastern Iraq, by Bamarnii, et al. (2021). They also recorded these species assemblage in Duhok as *Woodringina hornerstownensis*, *Woodringina claytonensis*, *Globaanomalina. archaeocompressa*, *Globaanomalina planocompressa*, *Globaanomalina chapmani*, *Praemurica pseudoinconstans*, *Pararugoglbigerina alabamensis, Subbotina inaequispira*, and *Chiloguembelina midwayensis.*

The age estimation of this interval depends on Magnetic polarity and recorded datum events by (Olsson, et al. (2000) and Keller and Pardo (2004), Keller (2002) with the time span of 64.5 Ma from the first occurrence of, *S. triloculinoides*, to FAD of *Globanomalina compressa* and/or *Praemurica inconstans* at the top of 63 Ma. In the current study, estimating absolute ages based on magnetochron age between a time-span between 64.50 Ma and 63.01 Ma, Its age is the Earliest Paleocene (Danian), with 0.2 m thick.

V. Conclusion

The Cretaceous/Plaeogene boundary in the Dartw section, south-west of Sulaymaniyah, reveals an expanded late Maastrichtian to Early Danian, and the boundary transition covers the uppermost part of the Tanjero Formation (late Maastrichtian) and the entire Kolosh Formation (Danian). Planktic foraminifera were very abundant and diversified during the late Cretaceous and early Danian in the studied section. The biozonation of the K-Pg boundary in the Dartw section shows continuous sedimentation based on the recognized planktic foraminifera, which subdivided into four zones of the Upper Cretaceous Tanjero Formation:

(i). *R. fructicosa* Interval Zone (CF4).
(ii). *P. hariaensis* Concurrent Range Zone (CF3)
(iii). *P. palpebra* Partial Range Zone (CF2),
(iv). *P. hantkeninoides* Total Range Zone (CF1),

While three Danian planktic foraminiferal biozones and two subzones have been recorded from the Kolosh Formation:

(i). *G. cretacea* (P0) Interval Zone,
(ii). *P. eugubina* (Pα) Total Range Zone, and
(iii). *P. pseudobulloides* (P1) Partial-Range Zone
  (a) *G. archaeocompressa* (P1a) Partial Range Subzone, and
  (b) *S. triloculinoides* (P1b) Interval Subzone.

Late Maastrichtian planktic foraminifera were much diversified and some species reached a very large size. The present biostratigraphic study provides compelling evidence for a complete K/Pg transition at the studied locality in the Dartw section.

A. Declaration

The authors declare that they have no conflicts of interest.

References

Abawi, T.S., Kireem, M.R.A., and Yousef, J.M., 1982. Planktonic foraminiferal stratigraphy of Shiranish formation, Sulaimaniah-Dokan region, northeastern Iraq. *Revista Espanola de Micropaleontologia*, 14(1), pp.153-164.

Abdel-Kireem, M.R., 1986. Contribution to the stratigraphy of the upper Cretaceous and the lower tertiary of the Sulaimaniah-Dokan region, northeastern Iraq. *Neues Jahrbuch für Geologie und Paläontologie-Abhandlungen*, 172, pp.121-139.

Abramovich, S., and Keller, G., 2002. High stress late Maastrichtian paleoenvironment: Inference from planktonic foraminifera in Tunisia. *Palaeogeography, Palaeoclimatology, Palaeoecology*, 178(3-4), pp.145-164.

Ahmed, S.H., Qadir, B.O., and Müller, C., 2015. Age determinations of cretaceous sequences based on calcareous nannofossils in Zagros Thrust and Folded Zone in Kurdistan Region-Iraq. *Journal of Zankoy Sulaimani-Part A* (*JZS-A*), 17(3), pp.185-196.

Al-Barzinjy, S.T.M., 2005. *Stratigraphy and Basin Analysis of Red Bed Series from Northeastern Iraq, Kurdistan Region, Unpublished Ph.D. Thesis*. University of Sulaimani University, Iraq, p.159.

Al-Khalaif, S., and Al-Mutwali, M., 2020. Biostratigraphy and sequence stratigraphy and depositional environment of Kolosh formation in Dohuk Area, Northern Iraq. *Iraqi National Journal of Earth Science*, 20(2), pp.18-42.

Al-Mashaikie Sa'ad, Z., and Mohammed, I.J., 2018. New discovery of olivine/pyroxene-rich sandstones in the Kolosh formation, Dyana Area, NE Iraq: An approach to provenance and tectonics of the sedimentary basin. *Iraqi Bulletin of Geology and Mining*, 14(2), pp.81-96.

Al-Mutwali, M.M., and AL-Doori, M.A., 2012. Planktonic foraminiferal biostratigraphy of Shiranish formation in Dohuk area/northern Iraq. *Iraqi National Journal of Earth Science*, 12(3), pp.17-40.

Al-Nuaimy, Q.A.M., Sharbazheri, K.M.I., Karim, K.H., and Ghafor, I.M., 2020. Cretaceous/paleogene boundary analysis by planktic foraminiferal biozonation in the Western Zagros fold-thrust belt (Smaquli valley), Sulaimani Governorate, NE-Iraq. *Kirkuk University Journal, Scientific Studies*, 15(3), pp.45-81.

Al-Qayim, B., and Al-Shaibani, S., 1989. Stratigraphic analysis of Cretaceous-Tertiary contact, Northwest Iraq. *Journal of Geological Society*, 22(1), pp.41-52.

Al-Qayim, B., Omer, A., and Koyi, H., 2012. Tectonostratigraphic overview of the Zagros suture zone, Kurdistan region, Northeast Iraq. *GeoArabia*, 17(4), pp.109-156.

Al-Qayim, B.A., Kharajiany, S.O.A., and Wise, S.W. Jr., 2020. Biostratigraphic analysis of the K/Pg boundary using calcareous nannofossil from Sulaimani area, Kurdistan Region, Iraq. *Kuwait Journal of Science*, 47(4), pp.92-105.

Al-Shaibani, S.K., Al-Hashimi, H.A., and Ghafor, I.M., 1993. Biostratigraphy of the cretaceous-tertiary boundary in well Tel-Hajer No-1, Sinjar Area, Northwest Iraq. *Iraqi Geological Journal*, 26(2), pp.77-97.

Alth, A., 1850. Geognostisch-palaeontologische Beschreibung der nächsten Umgebung von Lemberg. *Haidinger's Naturwissenschftliche Abhandlungen*, 3(2), pp.171-284.

Alvarez, L.W., Alvarez, W., Asaro, F., and Michel, H.V., 1980. Extraterrestrial cause for the Cretaceous-tertiary extinction. *Science*, 208(4448), pp.1095-1108.

Alvarez, W., Claeys, P., and Kieffer, S.W., 1995. Emplacement of Cretaceous-tertiary boundary shocked quartz from Chicxulub crater. *Science*, 269(5226), pp.930-935.

Arenillas, I., Alegret, L., Arz, J.A., Liesa, C., Meléndez, A., Molina, E., Soria, A.R., Cedillo-Pardo, E., Grajales-Nishimura, J.M., and Rosales-Domínguez, C., 2002. *Cretaceous-tertiary boundary planktic foraminiferal mass extinction and biochronology at La Ceiba and Bochil, Mexico, and El Kef, Tunisia. Special Papers*. Geological Society of America, United States, pp.253-264.

Arenillas, I., Arz, J.A., Molina, E., and Dupuis, C., 2000. The Cretaceous/paleogene (K/P) boundary at Aïn Settara, Tunisia: Sudden catastrophic mass extinction in planktic foraminifera. *The Journal of Foraminiferal Research*, 30(3), pp.202-218.

Arenillas, I., Belhai, D., Arz, J.A., Metsana-Oussaid, F., and Gilabert, V., 2022. Hypothesis testing on the planktic foraminiferal survival model after the KPB mass extinction: Evidence from Tunisia and Algeria. *Fossil Record*, 25, pp.43-63.

Bakkal, K.K., Ghafor, I.M., and Kassab, I.I.M., 1993. Biostratigraphy of shiranish formation in Hijran area northeastern Iraq. *Journal of Science and Nature*, 2(2), pp.34-39.

Bamerni, A., Al-Qayim, B., Hammoudi, R.A., and Frontalini, F., 2021. High-resolution biostratigraphic analysis of the cretaceous-paleogene boundary in the Kurdistan region (NW Iraq). S*tratigraphy*, 18(4), pp.251-268.

Bamerni, A., Al-Qayim, B.A., and Hammoudi, R.A., 2020. High resolution biostratigraphic analysis of the Danian stage, per fat section, Duhok Area, Kurdistan Region, North of Iraq. *The Iraqi Geological Journa*l, 53, pp.113-126.

Bellen, R.C., Dunnington, H.V., Wetzel, R., and Morton, D.M., 1959. Lexique stratigraphic international Asia, Iraq, Congress Geol. *International Commission de Stratigraphique*, 3, p.333.

Belza, J., Goderis, S., Montanari, A., Vanhaecke, F., and Claeys, P., 2017. Petrography and geochemistry of distal spherules from the K-Pg boundary in the Umbria-Marche region (Italy) and their origin as fractional condensates and melts in the Chicxulub impact plume. *Geochimica et Cosmochimica Acta*, 202, pp.231-263.

Berggren, W.A., and Miller, K.G., 1988. Paleogene tropical planktonic foraminiferal biostratigraphy and magnetobiochronology. *Micropaleontology*, 34, pp.362-380.

Berggren, W.A., Kent, D.V, Swisher, C.C., and Aubry, M.P., 1995. A revised Cenozoic geochronology and chronostratigraphy. In: Berggren, W.A., Kent, D.V., Aubry, M.A., and Hardenbol, J., eds. *Geochronology, Time Scales and Global Stratigraphic Correlation.* Society for Sedimentary Geology, Lynn Riggs Blvd.

Blow, W.H., 1979. *The Cenozoic Globigerinidae*, Vol. 1-3, Brill Publishers, Leiden, Netherlands, p1413, p264.

Bolli, H., 1951. The genus *Globotruncana* in Trinidad, BWI: Notes on occurrence, nomenclature and relationships between species. *Journal of Paleontology*, 25, pp.187-199.

Bolli, H.M., 1966. *Zonation of Cretaceous to Pliocene Marine Sediments Based on Planktonic Foraminifera.* Geologisches Institut der Eidg, Technischen Hochschule und der Universität, Berlin.

Bonté, P., Delacotte, O., Renard, M., Laj, C., Boclet, D., Jehanno, C., and Rocchia, R., 1984. An iridium rich layer at the Cretaceous/Tertiary boundary in the Bidart section (Southern France). *Geophysical Research Letters*, 11(5), pp.473-476.

Brönnimann, P.T., 1952. Globigerinidae from the upper cretaceous (Cenomanian-Maestrichtian) of Trinidad, B.W.I. *Bulletin of American Paleontology,* 34, pp.5-71.

Canudo, J.I., Keller, G., and Molina, E., 1991. Cretaceous/Tertiary boundary extinction pattern and faunal turnover at Agost and Caravaca, SE Spain. *Marine Micropaleontology*, 17(3-4), pp.319-341.

Caron, M., 1985. Cretaceous planktic foraminifera. In: Bolli, H.M., Saunders, J.B., and Perch Nielsen, K., eds. *Plankton Stratigraphy*. Cambridge University Press, Cambridge, pp.17-86.

Carsey, D.O., 1926. *Foraminifera of the Cretaceous of Central Texas*. Bulletin No 2612. University of Texas, Austin, pp.1-56.

Chacon, B., and Martín-Chivelet, J., 2005. Major palaeoenvironmental changes

in the Campanian to Palaeocene sequence of Caravaca (Subbetic zone, Spain). *Journal of Iberian Geology*, 31(2), pp.299-310

Coccioni, R., and Premoli Silva, I., 2015. Revised upper Albian-Maastrichtian planktonic foraminiferal biostratigraphy and magneto-stratigraphy of the classical Tethyan Gubbio section (Italy). *Newsletters on Stratigraphy*, 48(1), pp.47-90.

Courtillot, V., Besse, J., Vandamme, D., Montigny, R., Jaeger, J.J., and Cappetta, H., 1986. Deccan flood basalts at the Cretaceous/Tertiary boundary? *Earth and Planetary Science Letters*, 80(3-4), pp.361-374.

Cushman, J.A., 1926. Some foraminifera from the Mendez Shale of Eastern Mexico. Contributions from the *Cushman Laboratory for Foraminiferal Research*, 2(1), pp.16-26.

Cushman, J.A., 1933. Some new foraminiferal genera. Contributions from the Cushman Laboratory for Foraminiferal Research, 9(2), pp.32-38.

Cushman, J.A., 1938. Cretaceous species of *Guembelina* and related genera. *Contributions from the Cushman Laboratory for Foraminiferal Research*, 14(1), pp.2-28.

Dalbiez, F., 1955. The Genus *Globotruncana* in Tunisia. *Micropaleontology*, 1(2), p.161.

De Klasz, I., 1953. Einige neue oder wenig bekannte Foraminiferen aus der helvetischen Oberkreide der bayerischen Alpen, südlich Traunstein (Oberbayern). *Geologica Bavarica*, 17, pp.223-244.

Egger, J.G., 1899. *Foraminiferen und Ostrakoden Aus den Kreidemergeln der Oberbayerischen Alpen*. Vol. 21. Germany: Verlag der K. Akademie.

Ehrenberg, C.G., 1840. *Uber die Bildung der Kreidefelsen und des Kreidemergels Durch Unsichtbare Organismen*. Physikalische Abhandlungen der Koniglichen Akademie der Wissenschaften zu Berlin, pp.59-147.

El Naggar, Z.R., 1966. *Stratigraphy and Planktonic Foraminifera in the Upper Cretaceous-Lower Tertiary Succession in the Esna-Idfu Region*. Bulletin No 2. British Museum of Natural History, Nile Valley, Egypt, UAR, p.291.

Elnady, H., and Shahin, A., 2001. Planktonic foraminiferal biostratigraphiy and paleobathymetry of the late cretaceous-early tertiary succession at northeast Sinai, Egypt. *Egypt Journal Paleontology*, 1, pp.193-227.

Font, E., Adatte, T., Sial, A.N., De Lacerda, L.D., Keller, G., and Punekar, J., 2016. Mercury anomaly, Deccan volcanism, and the end-Cretaceous mass extinction. *Geology*, 44(2), pp.171-174.

Gandolfi, R., 1955. The genus Globotruncana in Northeastern Colombia. Bulletins of American Paleontology, 36, pp.7-118.

Ghafor, I.M., 1988. *Planktonic Foraminifera and Biostratigraphy of the Aaliji Formation and the Nature of its Contact with the Shiranish Formation in Well Tel-Hajar No. 1. Sinjar Area, Northwestern Iraq*. *Unpublished. Thesis*. Department of Geology, Salahaddin University, Iraq.

Ghafor, I.M., 2000. Spores and pollen of upper cretaceous lower tertiary in Higran area, Kurdistan, Iraq. *Zanco Journal of Pure and Applied Science*, 12(2), 47-62.

Govindan, A., Ravindran, C.N., and Rangaraju, M.K., 1996. Cretaceous stratigraphy and planktonic foraminiferal zonation of the Cauvery basin, South India. *Memoirs of the Geological Society of India*, 37, pp.155-188.

Hammoudi, R., 2011. High resolution biostratigrahpy of the K/T boundary in the Higran Section, Shaqlawa Area, Northern Iraq. *Iraqi National Journal of Earth Science*, 11(1), pp.23-48.

Hildebrand, A.R., Boynton, W.V., and Zoller, W.H., 1984. Rhenium enriched Kilauea volcano aerosols: Evidence for a volcanogenic component in the K/T boundary clay layer. *Bulletin of the American Astronomical Society*, 16, p.679.

Hildebrand, A.R., Penfield, G.T., Kring, D.A., Pilkington, M., Camargo Z, A., Jacobsen, S.B., and Boynton, W.V., 1991. Chicxulub crater: A possible Cretaceous/Tertiary boundary impact crater on the Yucatan Peninsula, Mexico. *Geology*, 19(9), pp.867-871.

Ismael, K.M., Khanaqa, P.A., and Karim, K.H., 2011. Biostratigraphy of Bluish Marl Succession (Maastrichtian) in Sulaimanyia, Area, Kurdistan Region NE-Iraq. *Iraqi National Journal of Earth Science*, 11(2), pp.81-99.

Jassim, S.Z., and Goff, J.C., 2006. *Geology of Iraq*. Dolin, Sro, Distributed by Geological Society of London, Brno.

Jaza, I.M., 1992. *Sedimentary Facies Analysis of the Tanjero Formation in Sulaimaniya District, NE-Iraq. Unpublished. M.Sc. Thesis*. Salahaddin University, Erbil, p.121.

Karim, K.H., 2004. *Basin analysis of Tanjero Formation in Sulaimaniya area, NE-Iraq, Unpublished. PhD. Thesis*. Sulaimani University, Erbil, p135.

Karim, K.H., and Hamza, B.J., 2023. Relation between Walash and Kolosh Formations and geology of their equivalent metamorphosed greywackes and arenites in Sulaimaniyah Governorate, Kurdistan Region, Northeast Iraq. *Tikrit Journal of Pure Science*, 28(6), pp.122-145.

Kassab, I.I.M., 1972. *Micropaleontology of the Upper Cretaceous to Lower Tertiary of Northern Iraq. Unpublished Ph. D. Thesis, University of London*, p.310.

Keller, G., 1988. Extinction, survivorship and evolution of planktic foraminifera across the Cretaceous/Tertiary boundary at El Kef, Tunisia. *Marine Micropaleontology*, 13(3), pp.239-263.

Keller, G., 2003. Guembelitria-dominated late Maastrichtian planktic foraminiferal assemblages mimic early Danian in central Egypt. *Marine Micropaleontology,* 47(1-2), pp.71-99.

Keller, G., 2014. Deccan volcanism, the Chicxulub impact, and the end-Cretaceous mass extinction: Coincidence? Cause and effect. In: *Geological Society of America Special Papers*. Vol. 505, pp.57-89.

Keller, G., and Pardo, A., 2004. Disaster opportunists Guembelitrinidae: Index for environmental catastrophes. *Marine Micropaleontology*, 53(1-2), pp.83-116.

Keller, G., Li, L., and MacLeod, N., 1996. The cretaceous/tertiary boundary stratotype section at El Kef, Tunisia: How catastrophic was the mass extinction? *Palaeogeography, Palaeoclimatology, Palaeoecology*, 119(3-4), pp.221-254.

Keller, G., Mateo, P., Monkenbusch, J., Thibault, N., Punekar, J., Spangenberg, J.E., Abramovich, S., Ashckenazi-Polivoda, S., Schoene, B., and Eddy, M.P., 2020. Mercury linked to Deccan Traps volcanism, climate change and the end-Cretaceous mass extinction. *Global and Planetary Change,* 194, p.103312.

Kharajiany, S.O.A., Al-Qayim, B.A., and Wise, S.W. Jr., 2019. Calcareous nannofossil stratigraphy of the Upper Cretaceous-lower Paleocene sequence from the Chinarok section, Sulaimaniah area, Kurdistan region, NE Iraq. *Iraqi Bulletin of Geology and Mining*, 15(1), pp.1-14.

Kharajiany, S.O.A., Wise, S.W., and Al-Qayim, B.A., 2020. The Danian sediments and the K/Pg boundary determination using calcareous nannofossil from Sulaimani area, Kurdistan Region/Iraq. *Carbonates and Evaporites*, 35(3), pp.1-14.

Kline, V.H., 1943. Clay County fossils, Midway *Foraminifera and Ostracoda*. *Mississippi State Geological Survey, University of Mississippi Bulletin*, 53, pp.1-98.

Koeberl, C., 1989. Iridium enrichment in volcanic dust from blue ice fields, Antarctica, and possible relevance to the K/T boundary event. *Earth and Planetary Science Letters*, 92(3-4), pp.317-322.

Lawa, F.A., and Qadir, H.A., 2023. New biostratigraphic ideas about the cretaceous/paleogene boundary from selected sections in Kurdistan-Mesopotamian foreland basin, Northern Iraq. *Iraqi National Journal of Earth Science*, 23(2), pp.124-156.

Leonov, G.P., and Alimarina, V.P., 1961. *Stratigraphy and Foraminifera of Cretaceous-Paleogene "Transition" Beds of the Central Part of the North Caucasus*. Moscow University Geology Faculty, Moscow, pp.29-60.

Li, L., and Keller, G., 1998a. Diversification and extinction in Campanian-Maastrichtian planktic foraminifera of Northwestern Tunisia. *Eclogae Geologicae Helvetiae*, 91(1), 75-102.

Li, L., and Keller, G., 1998b. Maastrichtian climate, productivity and faunal turnovers in planktic foraminifera in South Atlantic DSDP sites 525A and 21. *Marine Micropaleontology*, 33(1-2), pp.55-86.

Loeblich Jr. A.R., 1951. Coiling in the *Heterohelicidae*. *Contributions from the Cushman Foundation for Foraminiferal Research*, 2(3), pp.106-110.

Loeblich, A.R., and Tappan, H., 1955. *Revision of some glanduline Nodosauridae (Foraminifera). Smithsonian Miscellaneous Collections*, 126(3), pp.1-18.

Loeblich, A.R., and Tappan, H., 1957. Planktonic Foraminifera of Paleocene and early Eocene Age from the Gulf and Atlantic coastal plains. In: Loeblich, A.R. Jr., Tappan, H., Beckmann, J.P., Bolli, H.M., Montanaro Gallitelli, E., and Troelsen, J.C. (eds) *Studies in Foraminifera. U.S. National Museum Bulletin No* 215, pp.173-198.

Luterbacher, H., and Premoli-Silva, I., 1964. Biostratigrafia del limite Cretaceo-Terziario nell'Appennino Centrale. *Rivista Italiana di Paleontologia*, 70, pp.67-128.

Madhavaraju, J., and Lee, Y.I., 2010. Influence of deccan volcanism in the sedimentary rocks of late Maastrichtian-Danian age of cauvery basin Southeastern India: constraints from geochemistry. *Current Science*, 98, pp.528-537.

Maestas, Y., MacLeod, K.G., Douglas, R., Self-Trail, J., and Ward, P.D., 2003. Late cretaceous foraminifera, paleoenvironments, and paleoceanography of the Rosario Formation, San Antonio del Mar, Baja California, Mexico. *The Journal of Foraminiferal Research*, 33(3), pp.179-191.

Martínez R.J., 1989. Foraminiferal biostratigraphy and paleoenvironments of the Maastrichtian Colon mudstones of northern South America. *Micropaleontology*, 35, pp.97-113.

Maruoka, T., 2019. *Mass Extinction at the Cretaceous-Paleogene* (*K-Pg*) *Boundary, Astrobiology: From the Origins of Life to the Search for Extraterrestrial Intelligence*. Springer, Germany, pp.303-320.

Masters, B.A., 1984. Comparison of Planktonic Foraminifers at the Cretaceous-Tertiary Boundary from the El Haria Shale (Tunisia) and the Esna Shale (Egypt). In: *Proceedings of the 7th Exploration Seminar*, pp.310-324.

Mateo, P., Keller, G., Adatte, T., Bitchong, A.M., Spangenberg, J.E., Vennemann, T., and Hollis, C.J., 2020. Deposition and age of Chicxulub impact spherules on Gorgonilla Island, Colombia. *GSA Bulletin*, 132(1-2), pp.215-232.

Molina, E., Alegret, L., Arenillas, I., and Arz, J.A., 2005. The Cretaceous/Paleogene boundary at the Agost section revisited: Paleoenvironmental reconstruction and mass extinction pattern. *Journal of Iberian Geology*, 31(1), pp.135-148.

Morozova, V.G., 1959. Stratigraphy of the Danian-Montian deposits of the Crimea according to the *Foraminifera. Doklady Akademii Nauk*, 124(5), 1113-1115.

Mousa, A.K., Al-Dulaimi, S.I., and Mohammed, I.Q., 2020. Biostratigraphy of the late cretaceous/early Paleocene successions at KH 5\6 and KH 5\8 core interval, Western Desert of Iraq. *The Iraqi Geological Journal*, 53(1), pp.104-125.

Mustafa, A.I., Mansurbeg, H., and Mohialdeen, I.M.J., 2022. Petrography and Clay Mineral Variations Across the Cretaceous/Paleogene (K/Pg) Boundary, Sulaimani, Kurdistan Region, Iraq. *Iraqi Geological Journal*, 55(2), 16-34.

Nederbragt, A.J., 1991. Late Cretaceous biostratigraphy and development of *Heterohelicidae* (planktic foraminifera). *Micropaleontology*, 37, pp.329-372.

Obaidalla, N.A., 2005. Complete Cretaceous/Paleogene (K/P) boundary section at Wadi Nukhul, southwestern Sinai, Egypt: Inference from planktic foraminiferal biostratigraphy. *Revue de Paléobiologie*, 24(1), p.201.

Olsson, R.K., 1960. Foraminifera of latest Cretaceous and earliest Tertiary age in the New Jersey Coastal Plain. *Journal of Paleontology,* 34, pp.1-58.

Olsson, R.K., 1964. Late Cretaceous planktonic foraminifera from New Jersey and Delaware. *Micropaleontology*, 10(2), pp.157-188.

Olsson, R.K., Berggren, W.A., Hemleben, C., and Huber, B.T., 1999. Atlas of Paleocene planktonic foraminifera. *Smithsonian Contributions to Paleobiology*, 85. pp.1-252.

Pessagno, E.A., 1967. Upper Cretaceous planktonic foraminifera from the western Gulf Coastal Plain. *Palaeontographica Americana*, 5, pp.245-445

Plummer, H.J., 1927. *Foraminifera of the Midway Formation in Texas*, Bulletin No, 2644. University of Texas, Austin, pp.1-206.

Renne, P.R., Deino, A.L., Hilgen, F.J., Kuiper, K.F., Mark, D.F., Mitchell, W.S., Morgan, L.E., Mundil, R., and Smit, J., 2013. Time scales of critical events around the cretaceous-paleogene boundary. *Science*, 339(6120), pp.684-687.

Robaszynski, F., Caron, M., Gonzales Donoso, J.M., Wonders, A.A.H., and The European Working Group on Planktonic *Foraminifera*., 1984. Atlas of late cretaceous globotruncanids. *Revue de Micropaléontologie*, 26(3-4), pp.145-305.

Robaszynski, F., Caron, M., Gonzalez, D. J. M. and Wonders, A. A.H., 1984. Atlas of Late Cretaceous Globotruncanids Revue de Microp., Vol. 26, No. 3 - 4, pp. 145- 305.

Rzehak, A., 1891. Die Foraminiferenfauna der alttertiären Ablagerungen von Bruderndorf in Niederösterreich, mit Berücksichtigung des angeblichen Kreidevorkommens von Leitzersdorf. *Annalen des Naturhistorischen Museums in Wien*, 6(Häft 1), pp.1-12.

Sahib, G.M., and Al-Dulaimi, S.I.M., 2022. Biostratigraphy of the late cretaceous-early paleocene succession in selected wells, Jambur Oil field, Kirkuk, Northern Iraq. *The Iraqi Geological Journal*, 55, pp.223-240.

Salih, M.S., Al-Mutwali, M.M., and Aldabbagh, S.M., 2015. Geochemical study of the Cretaceous-Tertiary boundary succession exposed at Duhok Dam area (eastern Tethys): Northern Iraq. *Arabian Journal of Geosciences*, 8(1), pp.589-603.

Samir, A.M., 2002. Biostratigraphy and paleoenvironmental changes in the upper Cretaceous-Early Paleogene deposits of Gabal Samara section, Southwestern Sinai. Egypt. *Egypt Journal of Paleontology*, 2, pp.1-40.

Sarigül, V., Hakyemez, A., Tüysüz, O., Can Genç, Ş., Yilmaz, İ.Ö., and Özcan, E., 2017. Maastrichtian-Thanetian planktonic foraminiferal biostratigraphy and remarks on the K-Pg boundary in the southern Kocaeli Peninsula (NW Turkey). *Turkish Journal of Earth Sciences*, 26(1), pp.1-29.

Schulte, P., Alegret, L., Arenillas, I., Arz, J.A., Barton, P.J., Bown, P.R., Bralower, T.J., Christeson, G.L., Claeys, P., Cockell, C.S.,… & Willumsen, P.S., 2010. The Chicxulub asteroid impact and mass extinction at the Cretaceous-Paleogene boundary. *Science,* 327(5970), pp.1214-1218.

Scotese, C.R., 2011. Paleogeographic and Paleoclimatic Atlas. In: *AAPG Search and Discovery Article, 30192*. *AAPG 2011Annual Convention and Exposition.*

Sharbazheri, K., Ghafor, I., and Muhammed, Q., 2009. Biostratigraphy of the cretaceous/tertiary boundary in the Sirwan Valley (Sulaimani Region, Kurdistan, NE Iraq). *Geologica Carpathica*, 60(5), p.381-396.

Sharbazheri, K.M., Ghafor, I.M., and Muhammed, Q.A., 2011. Biostratigraphy of the Cretaceous/Paleogene boundary in Dokan area, Sulaimaniyah, Kurdistan Region, NE Iraq. *Iraqi Bulletin of Geology and Mining*, 7(3), pp.1-24.

Sigal, J., 1952. *Apercu Stratigraphique sur la Micropaleontologie du Cretace. XIXème Congrès Géologique International, Alger. Monographies Regionales*. Vol. 1. pp.3-43.

Silva, I.P., and Sliter, W.V., 1999. Cretaceous paleoceanography: evidence from planktonic foraminiferal evolution. In: *Evolution of the Cretaceous Ocean-Climate System*. Vol. 332. Geological Society of America, United States, p.301.

Sissakian, V.K., and Al-Jiburi, B.S.M., 2014. Stratigraphy of the high folded zone. *Iraqi Bulletin of Geology and Mining*, 6, pp.73-161.

Smit, J., and Hertogen, J., 1980. An extraterrestrial event at the Cretaceous-Tertiary boundary. *Nature*, 285, pp.198-200.

Smit, J., and Ten Kate, W., 1982. Trace-element patterns at the Cretaceous-Tertiary boundary-consequences of a large impact. *Cretaceous Research*, 3(3), pp.307-332.

Stinnesbeck, W., Keller, G., Schulte, P., Stüben, D., Berner, Z., Kramar, U., and Lopez-Oliva, J.G., 2002. The Cretaceous-Tertiary (K/T) boundary transition at Coxquihui, state of Veracruz, Mexico: Evidence for an early Danian impact event? *Journal of South American Earth Sciences,* 15(5), pp.497-509.

Tilev, N., 1951. *Etude des Rosalines maestrichtiennes (genre Globotruncana) du Sud-Est de la Turquie (Sondage de Ramandağ)*. Maden Tetkik ve Arama Enstitüsü Yayınlarından - Publications de l'Institut d'Etudes et de Recherches Minières de Turquie Séreis No B 16, pp.1-101.

Toumarkine, M., and Luterbacher, H., 1985. Paleocene and eocene planktic foraminifera. In: Bolli, H.M., Saunders, J.B., and Perch-Nielsen, K., eds. *Plankton Stratigraphy*. Cambridge University Press, Cambridge, pp.87-154.

Voorwijk, G.H., 1937. Foraminifera from the upper cretaceous of Habana, Cuba. *Koninklijke Nederlandse Akademie van Wetenschappen*, 40(2), pp.190-198.

Wade, B.S., Pearson, P.N., Berggren, W.A., and Pälike, H., 2011. Review and revision of Cenozoic tropical planktonic foraminiferal biostratigraphy and calibration to the geomagnetic polarity and astronomical time scale. *Earth-Science Reviews*, 104(1-3), pp.111-142.

White, M.P., 1928. Some index *Foraminifera* of the Tampico embayment of Mexico, part I and part II. *Journal of Paleontology*, 2, pp.177-215.

General Information

ARO's Mission: ARO seeks to publish those papers that are most influential in their fields or across fields and that will significantly advance scientific understanding. Selected papers should present novel and broadly important data, syntheses, or concepts. They should merit the recognition by the scientific community and general public provided by publication in ARO, beyond that provided by specialty journals.

We welcome submissions from all fields of natural science and technology, and from any source. We are committed to the prompt evaluation and publication of submitted papers. ARO is published biannually; selected papers are published online ahead of print.

Submission

Manuscripts should be submitted by the correspondent authors of the manuscript via the on-line submission page. Regardless of the source of the word-processing tool, only electronic Word (.doc, .docx, .rtf) files can be submitted on-line. There is no page limit. Only online submissions are accepted to facilitate rapid publication and minimize administrative costs. Submissions by any other one but the authors will not be accepted. The submitting author takes responsibility for the paper during submission and peer review. If for some technical reason submission through the email is not possible, the author can contact aro.journal@koyauniversity.org for support. Before submitting, please check ARO's guide to authors thoroughly to avoid any delay in the review and publication process.

Authors are explicitly responsible for the language of their texts. Paper should be submitted in a well written in understandable English. Authors should not expect the editor or editorial board to rewrite their paper. Prior to submission, authors should have their paper proofread by a possible academic native speaker of English.

- Submit the Article with contact Information
- File name should be your article title
- Don't submit your article in multiple journals, we are taking only minimum time for the review process. please don't waste our time
- Once the paper is accepted, it can't be withdrawn
- Please follow publication ethics and regulation
- Avoid plagiarism and copied material
- Strictly Follow ARO's template

Terms of Submission

Papers must be submitted on the understanding that they have not been published elsewhere and are not currently under consideration by another journal or any other publisher. ARO accepts original articles with novel impacts only. Post conference papers are not accepted "as is", however, regular papers on the same topic but with a different title can be submitted. The new paper should contain significant improvements in terms of extended content, analysis, comparisons with popular methods, results, figures, comments, etc. Please do not forget that the publication of the same or similar material in ARO constitutes the grounds for filing an (auto) plagiarism case.

The submitting author is responsible for ensuring that the article’s publication has been approved by all the other co-authors. It is also the authors’ responsibility to ensure that the articles emanating from a particular institution are submitted with the approval of the necessary institution. Only an acknowledgement from the editorial office officially establishes the date of receipt. Further correspondence and proofs will be sent to the author(s) before publication unless otherwise indicated. It is a condition of submission of a paper that the authors permit editing of the paper for readability. All enquiries concerning the publication of accepted papers should be addressed to aro.journal@koyauniversity.org.

Peer Review

All manuscripts are subject to peer review and are expected to meet standards of academic excellence. Submissions will be considered by an editor and "if not rejected right away" by peer-reviewers, whose identities will remain anonymous to the authors.

Guide to Author

We welcome submissions from all fields of science and from any source. We are committed to the prompt evaluation and publication of submitted papers. Selected papers are published online ahead of print. Authors are encouraged to read the instructions below before submitting their manuscripts. This section is arranged into an overview of the of the speedy guidelines below and is more detailed in the bottom section of this page.

Manuscript Preparation

Submitting your manuscript will be in two stages namely before final acceptance and after.

Stage One:

For the initial submission, the manuscript should be prepared electronically in Microsoft Word (.doc, .docx, .rtf) and PDF formats. Submit it through the online submission system after completing the registration. The Word file should be in a single-column format, double-spaced, with Times New Roman font, and 12-point font size. The authors' names and affiliations should be removed from the manuscript for the double-blind review process. Referencing and citation should follow the Harvard/ARO system. You can download the stage-one manuscript template by clicking here.

Stage Two:

Once the manuscript is accepted, the production team of ARO Journal will prepare the camera-ready paper.

Units of Measurement

Units of measurement should be presented simply and concisely using System International (SI) units.

Title and Authorship Information

The following information should be included;

- Paper title.
- Full author names.
- Affiliation.
- Email addresses.

Abstract

The manuscript should contain an abstract. The abstract should be self-contained and citation-free and should not exceed 250 words.

Introduction

This section should be succinct, with no subheadings.

Materials and Methods

This part should contain sufficient detail so that all procedures can be repeated. It can be divided into subsections if several methods are described.

Results and Discussion

This section may each be divided by subheadings or may be combined.

Conclusions

This should clearly explain the main conclusions of the work highlighting its importance and relevance.

Acknowledgements

All acknowledgements (if any) should be included at the very end of the paper before the references and may include supporting grants, presentations, and so forth.

References

References must be included in the manuscript and authors are responsible for the accuracy of references. Manuscripts without them will be returned. ARO is following Harvard System of Referencing. (Learn how to import and use Harvard Styling in your Microsoft Office by following this link:
http://bibword.codeplex.com/releases/view/15852)

Preparation of Figures

Upon submission of an article, authors are supposed to include all figures and tables in the PDF file of the manuscript. Figures and tables should be embedded in the manuscript. Figures should be supplied in either vector art formats (Illustrator, EPS, WMF, FreeHand, CorelDraw, PowerPoint, Excel, etc.) or bitmap formats (Photoshop, TIFF, GIF, JPEG, etc.). Bitmap images should be of 300 dpi resolution at least unless the resolution is intentionally set to a lower level for scientific reasons. If a bitmap image has labels, the image and labels should be embedded in separate layers.

Preparation of Tables

Tables should be cited consecutively in the text. Every table must have a descriptive title and if numerical measurements are given, the units should be included in the column heading. Vertical rules should not be used.

ARO Reviewer/Associate Editor Application Form

ARO is a scientific journal of Koya University (p-ISSN: 2410-9355, e-ISSN: 2307-549X) which aims to offer a novel contribution to the study of Science. The purpose of ARO is twofold: first, it will aim to become an ongoing forum for debate and discussion across the sciences and Engineering. We hope to advance our problem solving capacity and deepen our knowledge regarding a comprehensive range of collective actions. Second, ARO accepts the challenges brought about by multidisciplinary scientific areas and aspires to expand the community of academics who are able to learn from and help to produce advances in a variety of different disciplines.

The Journal is seeking reviewers who can provide constructive analysis of papers thus enhancing the overall reputation of the Journal. If any expert is interested in participating in the review process, we highly encourage you to sign up as a reviewer for our Journal and help us improve our presence in the domain of your expertise. Appropriate selection of reviewers who have expertise and interest in the domain relevant to each manuscript are essential elements that ensure a timely, productive peer review process. We require proficiency in English.

How to apply

To apply for becoming a reviewer of ARO, please submit the application form by following the link:
https://aro.koyauniversity.org/user/register

To apply for becoming a member of the Editorial Board of ARO, please submit the application form by completing the application form.

Both Associate Editor and Reviewers should specify their areas of research and expertise. Applicants must have a doctorate (or an equivalent degree), and if Master degree they need to have significant publishing experience. Please note that;

- You will need to write your full official name.
- Please provide an email which reflects your official name, such as nameOne.NameTwo@... , or your institute's official email.
- All data need to be written in English.

Note: For more information, kindly visit the following websites:

1. aro.koyauniversity.org.
2. http://libweb.anglia.ac.uk/referencing/harvard.htm.
3. http://bibword.codeplex.com/releases/view/15852.

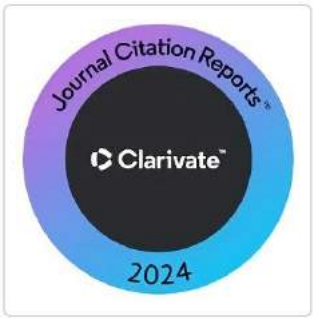
Journal Citation Reports
Clarivate
2024


PRESERVED IN
CLOCKSS


PRESERVED IN
LOCKSS


PKP
PUBLIC
KNOWLEDGE
PROJECT


DOAJ
SEAL


INDEXED IN
DOAJ


Journal
TOCs
The latest Journals Tables of Contents


ingenta


Dimensions


ZEITSCHRIFTEN
DATENBANK


SHERPA
RoMEO


scinapse


Scilit


ScienceGate


ROAD
DIRECTORY
OF OPEN ACCESS
SCHOLARLY
RESOURCES


ResearchGATE
scientific network


OAJSE


Microsoft
Academic


OCLC
WorldCat


Google
Scholar


Crossref


BASE


publons


ACADEMIA

KOYA UNIVERSITY

Koya University is a young University established in 2003 and it is located in the city of Koya (Koysinjaq), short distance to the East of regional capital city of Erbil (Arbil, Hewlêr) in Kurdistan Region of Iraq. It is on the foothills of beautiful High Mountain. Its campus has been carefully laid out to embrace the beautiful mountainous nature. The Koya University has a Faculty system which enhances the interactions between similar academic fields. Today, Koya University has four Faculties: Engineering, Science and Health, Humanities and Social Sciences and Education in addition to the School of Medicine, which all consist of twenty-five scientific departments in different fields, such as Petroleum Engineering, Geotechnical Engineering, Software Engineering, Physics, Chemistry, Clinical Psychology, Social Science, Medical Microbiology and Sport Education.

ARO-The Scientific Journal of Koya University is a biannual journal of original scientific research, global news, and commentary in the areas of Science and Technology. ARO is a Peer-reviewed Open Access journal with CC BY-NC-SA 4.0 license. It provides immediate, worldwide and barrier-free access to the full text of research articles without requiring a subscription to the journal, and has no article processing charge (APC). ARO Journal seeks to publish those papers that are most influential in their fields or across fields and that will significantly advance scientific understanding. ARO Journal is a member of ROAD and Cross-ref agencies and has got ESCI, DOAJ seal, SHERPA/RoMEO deposit policy, and

ARO

The Scientific Journal of Koya University

Koya University (KOU)
University Park
Danielle Mitterrand Boulevard
Koya KOY45, Kurdistan Region - Iraq

DOI: 10.14500/2307-549X p-ISSN: 2410-9355 e-ISSN: 2307-549X